

**SYNTHESIS AND CHARACTERIZATION OF  
CALCIUM PHOSPHATE CEMENT BASED  
MACROPOROUS SCAFFOLDS**

**A Thesis Submitted to  
the Graduate School of Engineering and Sciences of  
İzmir Institute of Technology  
in Partial Fulfillment of the Requirements for the Degree of  
DOCTOR OF PHILOSOPHY  
in Chemical Engineering**

**by  
Erdem ŞAHİN**

**July 2012**

**İZMİR**

## **ACKNOWLEDGEMENTS**

I express my deepest gratitude to my family for giving me all I needed to complete this work; to my fiancée for helping ease the burdens of life; to my advisor for supporting and directing my work: and to the almighty for answering my calls on faith, will and patience.

# ABSTRACT

## SYNTHESIS AND CHARACTERIZATION OF CALCIUM PHOSPHATE CEMENT BASED MACROPOROUS SCAFFOLDS

The goal of this thesis is to synthesize unique, clinically relevant macroporous calcium phosphate cement blocks to be utilized both in vivo and in vitro tissue engineering applications. Calcium phosphate cements which essentially consist of hydroxyapatite or brushite are constantly improved to overcome their inherent shortcomings such as low strength, low functional porosity, and low resorption. Recent literature on the topic points to monetite forming cements as an alternative phase. A novel method to utilize monetite that is finer and stronger with respect to brushite in load bearing scaffold applications is introduced in the results section of this thesis as a contribution to ever growing literature on this scope. In the preliminary study on the conversion extent of apatite forming cement, ionic strength of the setting liquid was determined as the prime effective factor on monetite conversion extent. Subsequently brushite forming  $\beta$ -tricalcium phosphate – monocalcium phosphate monohydrate cement system was modified by NaCl and citric acid so that brushite formation was selectively inhibited. Singular and synergistic monetite promoting effects of NaCl and citric acid were determined by monitoring the kinetics of cement setting in excess setting liquid. Spectrometric studies revealed the difference in brushite and monetite crystal surface site density which enabled selective inhibition of brushite and promotion of monetite by the synergistic effect of NaCl and citric acid. Proposed phase control mechanism enables tailoring the composition of biphasic cements comprising of a predetermined monetite content and brushite or hydroxyapatite.

In the final stage of the thesis, size distributed NaCl particles were introduced into the cement paste containing optimum amount of citric acid to enable complete monetite formation. Resultant macroporous monetite blocks were characterized in terms of microporosity, macroporosity, density, morphology, strength, phase composition, and surface area. Interconnectivity of the cement was optimized based on the correlation of porogen size distribution and morphological data.

## ÖZET

### GÖZENEKLİ KALSİYUM FOSFAT ÇİMENTOSU BAZLI DOKU İSKELELERİNİN SENTEZİ VE KARAKTERİZASYONU

Bu çalışmada klinik uygunluğu olan, özgün, kalsiyum fosfat çimentosu bazlı gözenekli doku iskeleleri sentezi amaçlanmıştır. Kalsiyum fosfat çimentosunun yüksek yüzey alanı, yüksek biyoaktivitesi ve yüksek biyobozunurluğu dolayısıyla özellikle kemik dokusu iskeleleri için bu malzeme sınıfı üzerinde yoğunlaşmıştır. Doku iskelelerinin en önemli özelliklerinden olan gözeneklilik ve mukavemet kalsiyum fosfat çimentolarının zayıf özellikleridir. Yüksek biyobozunurluğa sahip bruşit fazını oluşturan kalsiyum fosfat çimentosu formülasyonunun iyonik modifikasyonla üstün mukavemete sahip alternatif bir faz olan monetit oluşturması sağlanmıştır. Sitrik asit ve sodyum klorürün bruşit çimentosu reaksiyon kinetiği üzerindeki tekil ve sinerjistik etkileri araştırılmış ve azami monetit verimi sağlayan optimum konsantrasyonları belirlenmiştir. Aynı zamanda sertleşme geciktirici ve gözenek yapıcı olarak da etkinliği olan sitrik asit ve sodyum klorürün sertleşme sıvısına eklentisi ile monetit fazınca zengin, gözenekli bloklar elde edilmiştir. Blokların iç yapı, gözenek ve mekanik karakterizasyonları doku iskelesi uygulamalarına uygunluklarını göstermiştir. Çalışmanın son kısmında gözenek yapıcı ve çimento parçacıklarından oluşan katı faza 5-200 mikrometre arasında boyut dağılımı uygulanarak çimento matrisinin paketlenmesi ve yoğunluğu artırılmış ve yararsız mikrogözenek azaltılarak blokların doku iskelesi etkinlikleri artırılmıştır. Deneysel tasarım ve istatistiksel analiz yöntemleri ile geniş bir aralıktaki olası tüm boyut dağılımları incelenmiş ve 100 mikrometre boyutundaki parçacıkların ağırlıkta olduğu dengeli bir boyut dağılımının en yüksek gözenek bağlantısına yol açtığı bulunmuştur. Kimyasal ve fiziksel modifikasyonlar sonucu sentezlenen monetit bazlı makrogözenekli doku iskelelerinin klinik uygulamalar için yeterli olduğu düşünülmektedir.

# TABLE OF CONTENTS

LIST OF FIGURES .....	ixx
LIST OF TABLES .....	xviii
CHAPTER 1. INTRODUCTION .....	1
CHAPTER 2. THE BONE.....	5
CHAPTER 3. THE BONE REGENERATIVE SCAFFOLD.....	11
CHAPTER 4. CALCIUM PHOSPHATE CEMENTS .....	19
4.1. Component Phases of Calcium Phosphate Cements.....	31
4.2. Types of Calcium Phosphate Cements and Their Properties.....	46
4.2.1 Apatite Cements .....	46
4.2.2. Brushite Cements.....	51
4.3. Thermodynamics of Calcium Phosphate Cement Setting Reaction .....	53
4.4. Kinetics of Calcium Phosphate Cement Setting Reaction .....	65
4.4.1. Effect of Ionic Modifiers on the Kinetics of Calcium Phosphate Cement Setting .....	74
4.4.2. Methods of Analysis of the Kinetics of Calcium Phosphate Cement Setting .....	82
CHAPTER 5. MATERIALS AND METHODS .....	86
5.1. Investigation of the Effect of Several Factors on the Extent of Calcium Phosphate Cement Setting.....	86

5.2. Ionic Modification of the $\beta$ -TCP-MCPM Cement System by NaCl and Citric Acid Addition.....	89
5.3. Modification of the Morphology of Macroporous Cement Blocks by A Variable Porogen Size Distribution Approach .....	91
5.4. Quantitative Phase Analysis by X-Ray Diffraction .....	95
5.4.1. The External Standard Method.....	97
5.5. Porosity Determination by Archimedes' Water Intrusion Method.....	101
5.6. Morphological Analysis of Macroporous Blocks .....	102
5.7. Rheological Analysis of Porogen Suspensions and Determination of Maximum Packing Density .....	106

## CHAPTER 6. CHEMICAL MODIFICATION OF CALCIUM PHOSPHATE

CEMENT MICROSTRUCTURE.....	108
6.1. Analysis of the TTCP-MCPM cement setting mechanism.....	108
6.1.1. Effect of Ionic Strength .....	114
6.1.2. Effect of Temperature.....	115
6.1.3. Effect of pH .....	116
6.1.4. Effect of Setting Liquid Saturation.....	117
6.1.5. Effect of Precursor Size.....	118
6.2. Investigation of the Effect of Ionic Modifiers on the Setting Kinetics of the $\beta$ -TCP – MCPM cement system.....	120
6.2.1. The Singular Effects of NaCl and Citric Acid Modifiers on Brushite Cement Setting Kinetics .....	125
6.2.1.1. Analysis of the Free Drift Runs .....	126
6.2.1.2. Analysis of the pH-stat Runs .....	134
6.2.2. Synergistic Effect of NaCl and Citric Acid on Brushite Cement Setting Kinetics.....	146
6.2.3. Controlling the Phase Composition of the $\beta$ -TCP-MCPM Cement System via Synergistic Effect of NaCl on Citric Acid .....	160

CHAPTER 7. PHYSICAL MODIFICATION OF CALCIUM PHOSPHATE CEMENT BLOCKS BY A VARIABLE POROGEN SIZE DISTRIBUTION APPROACH .....	173
7.1. Rheological Determination of Maximum Packing Density for a Set of Size Distributed NaCl Particles .....	174
7.2. Microstructural Characterization of Macroporous Cement Blocks ....	187
7.3. Mechanical Characterization of Macroporous Cement Blocks .....	208
7.4. Morphological Analysis of the Scaffold Microstructure .....	219
7.5. General Evaluation of the Morphological Analysis Results.....	246
 CHAPTER 8. CONCLUSIONS .....	 251
 REFERENCES .....	 254
 APPENDIX A. DETAILED MORPHOLOGICAL ANALYSES OF THE SAMPLES.....	 268

## LIST OF FIGURES

<u>Figure</u>	<u>Page</u>
Figure 1.1. Distribution of type of materials studied in the studies submitted to the World Biomaterials Congress. ....	2
Figure 1.2. Distribution of type of ceramics studied in World Biomaterials Congress.....	3
Figure 2.1. Cross section of a human femur. ....	6
Figure 3.1. Backscattered electron image of a secondary osteon in rat femur clearly showing the relatively hypermineralized cement line forming the interface between the new bone (top) and the old bone (bottom).....	13
Figure 3.2. Macroporous scaffolds prepared by (a) NaCl/PVA fiber leaching (b) solid free form fabrication, (c) polymer reverse replica techniques. ....	17
Figure 4.1. Calorimetric curve showing the heat evolution rate as a function of time. ....	23
Figure 4.2. SEM pictures of cement at various periods of reaction: (a) after 15 min; (b) after 1 hr; (c) after 64 hrs; (d) after 360 hrs. ....	24
Figure 4.3. Correlation between the conversion of cement reaction and compressive strength.....	26
Figure 4.4. Decrease in solubility of calcium phosphates with increasing Ca/P ratio. ....	32
Figure 4.5. Morphology of MCPM crystals. ....	34
Figure 4.6. Representation of the crystal structure of brushite viewed along the a axis with the b axis horizontal and the c axis vertical.....	35
Figure 4.7. Morphology of DCPD with OCP crystals grown on its face. ....	36
Figure 4.8. Representation of the crystal structure of monetite viewed along the a axis with the b axis horizontal and the c axis vertical.....	38
Figure 4.9. Morphology of DCP. ....	39
Figure 4.10. Morphology of $\beta$ -TCP. ....	39
Figure 4.11. Morphology of $\alpha$ -TCP. ....	40
Figure 4.12. Morphology of TTCP.....	41



Figure 4.13. Morphology of OCP crystals.....	43
Figure 4.14. Morphology of HA crystals.....	45
Figure 4.15. Comparison of cement and natural bone mechanical properties to bone mechanical properties. ....	53
Figure 4.16. Solubility isotherms of different calcium phosphates in equilibrium with their solutions for the ternary system $\text{Ca}(\text{OH})_2$ - $\text{H}_3\text{PO}_4$ - $\text{H}_2\text{O}$ at 37 °C in a representation of $\log [\text{Ca}]$ versus pH.....	58
Figure 4.17. Relative positions of the isotherms for acidic and basic cement precursors as they approach the equilibrium condition at singular point in hypothetical $\text{A}(\text{OH})_n$ - $\text{H}_n\text{B}$ - $\text{H}_2\text{O}$ system.....	59
Figure 4.18. Supersaturations of brushite cement end products brushite and monetite predicted by the Pitzer ion interaction model. ....	65
Figure 4.19. Illustration of growth at a crystal surface by attachment of molecules to step edges on either islands or dislocation spirals.....	67
Figure 4.20. Rate determining growth mechanisms as a function of supersaturation.....	70
Figure 4.21. Generally applicable prediction of growth rates as a function of supersaturation and solubility. ....	71
Figure 4.22. Kossel model for the sites of impurity adsorption: a) kink sites, b) step sites, c) face sites.....	75
Figure 4.23. Variation in brushite growth with citrate concentration.....	76
Figure 4.24. Heat flow of the exothermic setting reaction of brushite cement versus time for fixed P/L 2.0 g/mL and three different citric acid retardant concentrations.....	79
Figure 4.25. Solubility of KCl in the KCl-NaCl-Water ternary system. ....	82
Figure 4.26. Typical relaxation curves for precipitation of(a) a pure phase, (b) two phases forming successively, and (c) two phases forming simultaneously over a certain period. ....	84
Figure 5.1. Optical microscope images of cement precursor (A) $\beta$ -TCP, (B) MCPM, NaCl less than (C) 38 $\mu\text{m}$ , (D) 75 $\mu\text{m}$ , (E)150 $\mu\text{m}$ , and (F) 212 $\mu\text{m}$ . The scale is 1 mm, smallest ticks corresponding to 10 $\mu\text{m}$ . ....	94
Figure 5.2. The balance setup for measuring the buoyant force and specific density. ....	102
Figure 5.3. Image processing sequence for sample 32. ....	105

Figure 5.4. Morphological parameters measured in the image analysis.....	105
Figure 6.1. Correlation of compressive strength with HA formation ratio.....	113
Figure 6.2. Correlation of compressive strength with setting time.....	114
Figure 6.3. Effect of ionic strength variation on analysis responses. ....	115
Figure 6.4. Effect of temperature variation on analysis responses. ....	116
Figure 6.5. Effect of pH variation on analysis responses. ....	117
Figure 6.6. Effect of phosphate saturation variation on analysis responses. ....	118
Figure 6.7. Effect of precursor size variation on analysis responses.....	118
Figure 6.8. Schematic representation of the calcium and phosphate concentrations during brushite cement setting.....	122
Figure 6.9. Variation in the pH of the setting solution for $\beta$ -TCP – MCPM cement with brushite seeds. ....	126
Figure 6.10. Variation of pH in free drift runs with increasing NaCl concentration.....	127
Figure 6.11. Phase composition of samples from free drift in liquid containing various NaCl concentrations. ....	128
Figure 6.12. Variations in pH of the setting liquid observed in free drift. ....	129
Figure 6.13. Phase composition of the precipitate set in liquids containing various citric acid concentrations.....	130
Figure 6.14. Free calcium concentrations of calcium phosphates in citrate solutions as determined by ICP-AES.....	131
Figure 6.15. Citrate concentration in the supernatant of various aqueous calcium phosphate solutions as determined by UV spectroscopy. ....	133
Figure 6.16. Net citrate adsorption as a function of initial citric acid concentration.....	134
Figure 6.17. Cumulative base uptake of $\beta$ -TCP – MCPM cement with brushite seeds.....	135
Figure 6.18. Cumulative base uptake curves for cement setting with various NaCl concentrations.....	136
Figure 6.19. Variation in time of maximum growth rate with NaCl concentration.....	137
Figure 6.20. Variation of growth rates with increasing NaCl concentration.....	138
Figure 6.21. Phase composition of calcium phosphate cement set in the presence of varying NaCl concentration.....	138

Figure 6.22. Initial base uptake in NaCl containing solutions during the pH-stat runs.....	139
Figure 6.23. Plot of $-\log(\alpha^{-n} d\alpha/dt)$ versus $-\log(1 - \alpha)$ for brushite seeded $\beta$ -TCP – MCPM cement in pure water at pH 4.2. ....	140
Figure 6.24. Crystal morphology of samples set in 1-6 M NaCl aqueous solution (A-F).....	143
Figure 6.25. Cumulative base uptake curves for cement setting with various citric acid concentrations. ....	144
Figure 6.26. Phase composition of calcium phosphate cement set in the presence of varying citric acid concentration. ....	145
Figure 6.27. Double sigmoidal curves obtained from pH-stat analysis of sample set in 0.1 M citric acid and 6 M NaCl solution. ....	147
Figure 6.28. Total base uptake of samples set in 0.1 M citric acid solution.....	148
Figure 6.29. pH variation of samples set in 0.1 M citric acid solution.....	149
Figure 6.30. Total base uptake of samples set in 0.19 M citric acid solution.....	150
Figure 6.31. pH variation of samples set in 0.19 M citric acid solution.....	150
Figure 6.32. Total base uptake of samples set in 0.28 M citric acid solution.....	152
Figure 6.33. pH variation of samples set in 0.28 M citric acid solution.....	152
Figure 6.34. Total base uptake of samples set in 0.35 M citric acid solution.....	153
Figure 6.35. pH variation of samples set in 0.35 M citric acid solution.....	153
Figure 6.36. Shift in the time of maximum monetite growth rate curves as functions of citric acid (left) and NaCl (right) concentrations.....	154
Figure 6.37. Variation of $\beta$ -TCP (A), brushite (B), monetite (C) content and brushite/monetite ratio (D) with citric acid and NaCl concentrations. ....	157
Figure 6.38. XRD patterns for samples prepared with various NaCl concentrations. ....	161
Figure 6.39. Variation of $\beta$ -TCP residue amount by monetite formation.....	162
Figure 6.40. The relation between porosity and monetite formation.....	163
Figure 6.41. Variation of brushite to monetite transformation with increasing NaCl concentration. ....	165
Figure 6.42. Variation in compressive strengths of samples prepared using various NaCl concentrations. ....	166

Figure 6.43. Variation of normalized compressive strength with monetite amount.....	167
Figure 6.44. (a-g) SEM images of samples prepared with NaCl concentration varying from 0 to 6 M respectively. (h) Morphology of monetite and brushite crystals from sample prepared with 6 M NaCl. ....	169
Figure 7.1. Flow behavior of (a) NaCl suspensions and (b) PEG200. ....	176
Figure 7.2. Graphical determination of maximum packing density for sample 16.....	177
Figure 7.3. Graphical representation of the experiment results.....	178
Figure 7.4. Variation in maximum packing densities.....	178
Figure 7.5. Design cube for 3 size distributions used in combination.....	182
Figure 7.6. Variation of maximum packing density in the binary system.....	183
Figure 7.7. Synergistic effect of -53, -38, -212 size groups on the packing density.....	183
Figure 7.8. Synergistic effect of -75, -38, -212 size groups on the packing density.....	184
Figure 7.9. Adverse effect of combination of -53 and -75 size groups on packing density. ....	184
Figure 7.10. Ternary diagram for variation of packing density in the -38, -75, -212 size group system.....	186
Figure 7.11. Change in the sample volumes due to size distribution of the solid phases.....	190
Figure 7.12. Change in packing density as a result of size distribution of the solid phases.....	190
Figure 7.13. Net improvement in sample packing due to size distribution of solid phases.....	191
Figure 7.14. Change in porosity of the samples as a result of size distribution of solid phases.....	192
Figure 7.15. Change in microporosity of the samples due to the size distribution of solid phases.....	193
Figure 7.16. Linear relationship between packing density and microporosity of samples containing about 85% monetite.....	193
Figure 7.17. Linear proportionality between monetite content and microporosity of samples with 0.68 packing density.....	194

Figure 7.18. Strong correlation between packing improvement and reduction in microporosity. ....	194
Figure 7.19. Change in macroporosity of the samples as a result of size distribution of solid phases. ....	195
Figure 7.20. Correlation between packing improvement by size distribution and reduction in total porosity. ....	196
Figure 7.21. Correlation between packing density and macro-microporosity.....	197
Figure 7.22. Variation of Porosity as a function of packing density. ....	197
Figure 7.23. Correlation of micro, macro and total pore volumes with improvement in packing by size distribution.....	198
Figure 7.24. Change in open and closed porosities due to size distribution of the solid phases. ....	200
Figure 7.25. Correlation between packing improvement by size distribution and sample density.....	201
Figure 7.26. Correlation between theoretical density and measured density of the samples.....	202
Figure 7.27. Change in the phase composition of the samples as a result of size distribution of solid phases. ....	203
Figure 7.28. Correlation between monetite formation and brushite content of the samples.....	204
Figure 7.29. Correlation between monetite formation and $\beta$ -TCP content of the samples.....	206
Figure 7.30. Correlation between brushite formation and $\beta$ -TCP content of the samples.....	206
Figure 7.31. Phase compositions of dry and wet samples from sample set 3.....	208
Figure 7.32. Representative stress-strain diagram for all samples. ....	209
Figure 7.33. Correlation between porosity and elastic modulus of the samples. ....	210
Figure 7.34. Correlation between density and elastic modulus of the samples.....	210
Figure 7.35. Correlation between porosity and yield strength of the samples.....	212
Figure 7.36. Correlation between density and yield strength of the samples. ....	212
Figure 7.37. Correlation between porosity and ultimate compressive strength of the samples.....	213
Figure 7.38. Correlation between density and ultimate compressive strength of the samples.....	213

Figure 7.39. Correlation between porosity and elastic modulus of samples containing about 85% monetite. ....	214
Figure 7.40. Correlation between porosity and yield strength of samples containing about 85% monetite. ....	214
Figure 7.41. Correlation between porosity and ultimate compressive strength of samples containing about 85% monetite.....	215
Figure 7.42. Correlation between monetite content and yield strength of samples having 67% porosity. ....	216
Figure 7.45. Mean pore diameter distribution for all samples.....	221
Figure 7.46. Histogram of sample mean pore diameter.....	222
Figure 7.47. Mean area distribution of all samples.....	223
Figure 7.48. Histogram of sample mean area. ....	223
Figure 7.49. Total area distribution of all samples. ....	225
Figure 7.50. Histogram of sample total area.....	225
Figure 7.51. Mean perimeter distribution for all samples.....	226
Figure 7.52. Histogram of sample mean perimeter. ....	226
Figure 7.53. Total perimeter distribution for all samples. ....	227
Figure 7.54. Histogram of sample total perimeter. ....	227
Figure 7.55. Radius ratio distribution for all samples.....	229
Figure 7.56. Histogram of sample radius ratio. ....	229
Figure 7.57. Coarse (a) and fine (b) dominant particle systems. ....	234
Figure 7.58. Particle interaction models. ....	235
Figure 7.59. Mosaic display of micrographs for sample 16 taken at 100x magnification. ....	238
Figure 7.60. Mosaic display of micrographs for sample 7 taken at 100x magnification. ....	239
Figure 7.61. Monetite crystals of sample 2 in focus.....	240
Figure 7.62. Brushite rich region of sample 2 .....	241
Figure 7.63. Correlation between brushite content and specific surface area of cement samples. ....	242
Figure 7.64. Monetite rich region of sample 1 in focus.....	243
Figure 7.65. Cellular monetite crystals of sample 1 on a pore wall. ....	244
Figure 7.66. Microstructure of sample 37 around macropore walls. ....	245

Figure 7.67. SEM image of the microstructure of sample containing 80% porosity at 100 times magnification.....	248
Figure 7.68. SEM image of the microstructure of sample containing 80% porosity at 250 times magnification.....	249
Figure 7.69. SEM image of the microstructure of sample containing 80% porosity at 500 times magnification.....	249
Figure 7.70. SEM image of the microstructure of sample containing 80% porosity at 2500 times magnification.....	250
Figure 7.71. SEM image of the microstructure of sample containing 80% porosity at 10000 times magnification.....	250

# LIST OF TABLES

<b><u>Table</u></b>	<b><u>Page</u></b>
Table 4.1. Properties of Calcium Phosphate Cement Precursors .....	33
Table 4.2. Several apatite cement formulations with TTCP precursor and their calculated free energy changes .....	49
Table 4.3. Various apatite CPC formulations and their properties .....	50
Table 4.4. Brushite calcium phosphate cement formulations and properties .....	52
Table 4.5. Mechanical properties of apatite and brushite cements .....	53
Table 4.6. Singular points between calcium phosphates in the system Ca(OH) <sub>2</sub> - H <sub>3</sub> PO <sub>4</sub> -H <sub>2</sub> O at 37 °C (Source: Fernandez, Gil et al. 1994) .....	60
Table 4.7. Points of inflection for different growth models and values of m .....	85
Table 5.1. Chemical reagents used in all experiments and their properties .....	88
Table 5.2. Mass ratio for the packing determination experiment variables .....	93
Table 5.3. Mass for 7 blocks produced in the mechanical experiment .....	95
Table 5.4. Diffraction parameters of the phases analyzed quantitatively using the external standard method .....	100
Table 6.1. Ruggedness Test Results .....	111
Table 6.2. Conversion extent of the cement samples .....	113
Table 6.3. Rate constants obtained graphically and numerically for samples with varying NaCl concentration .....	141
Table 6.4. Elemental analysis of samples set in 1-6 M NaCl aqueous solution .....	143
Table 6.5. Phase composition of samples calculated by quantitative XRD analysis .....	156
Table 6.6. Growth rate constants and the probable growth mechanisms for monetite precipitation .....	158
Table 6.7. Results of quantitative XRD, Archimedes porosity, and mechanical analysis for all samples .....	164
Table 6.8. Calculated parameters of trendlines for variation of compressive strength with porosity .....	170
Table 7.1. Data used for extrapolation to maximum packing density .....	177
Table 7.2. Results of the rheometric analysis of maximum packing density .....	180
Table 7.3. Analysis of variance table for maximum packing density .....	181



Table 7.4. Results of the Archimedean analysis for all samples .....	199
Table 7.5. Results of the quantitative phase analysis for all samples.....	205
Table 7.6. Results of mechanical characterization for all samples.....	218
Table 7.7. Unit volume, mass and number equivalent of particle sizes .....	220
Table 7.8. Top 10 samples with the highest total pore area and their size distribution .....	232
Table 7.9. Top 10 samples with the highest total pore perimeter and their size distribution .....	233
Table 7.10. Top 10 samples with the highest effectiveness factor and their size distribution .....	236
Table 7.11. Optimum size distribution deduced from the morphological analysis .....	248

# CHAPTER 1

## INTRODUCTION

Musculoskeletal trauma is one of the major health concerns in the world due to ageing of the population and the ever growing acceptance of active life style. Annually millions of bone and joint operations are conducted throughout the world, of which bone grafting constitutes the majority. A surgical implant such as bone graft has been defined in general, as an object made from non-living material that is introduced into the human body with the intention of staying therein during a certain period of time in order to fulfill a specific function (Williams 1973). From a functional point of view, implants are used for:

- a) Replacing a damaged, diseased or worn part of the anatomy, for example, total joint replacements.
- b) Simulating an absent part of the anatomy, such as breast prostheses.
- c) Assisting in the healing process of a tissue, including the plates for bone fractures, temporary grafts for treating burns and surgical adhesives.
- d) Correcting congenital, traumatic or pathological deformities, as in the example of spinal plates.
- e) Rectifying the operation mode of a certain organ, such as pacemaker.

This general classification is made based on the realization of whether a given implant works properly, by taking into account the characteristics of the implant material and its usage. The properties of a material are basically classified into three: chemical properties, physical properties and mechanical properties. The chemical properties of the material, determined through reactions between material and the surrounding environment in the body, control the ability of the implant to maintain their functionality over the period of use and are perhaps more important in many ways than the other two. Physical and mechanical properties are those that control the functional characteristics of most active implants. For example, the properties of mechanical strength and rigidity makes the stainless steel suitable for the manufacture of osteosynthesis plates, the electrical resistivity of an epoxy resin makes it useful in pacemaker encapsulation, the fatigue life of polypropylene makes this material suitable

in joint replacements and so on. The selection of a material based on properties required by the application and the characteristics of the material determines the functional suitability of the implant.

Of a total of 2500 papers and posters accepted for program of the 7<sup>th</sup> World Biomaterials Congress held in Sydney in 2004, approximately 44% is devoted to the aspect of materials used to make biomaterial implants (Leeuwenburgh et al. 2008). Figure 1.1. shows the type and percentage of the materials allocated to the 44% of work classified by materials. Of note is the high percentage of work, 48%, performed on polymeric materials due to the high versatility of these materials. Ceramics have been studied extensively in bone regeneration applications due to their inertness and stiffness. The number of studies focusing on them is increasing with time as composites are finding new applications as (Leeuwenburgh et al. 2008).

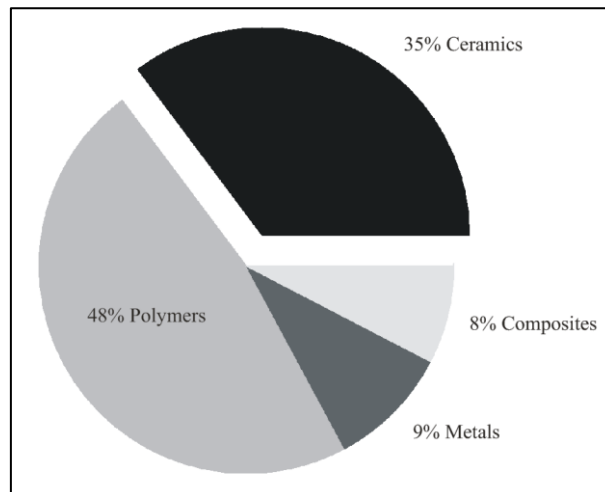


Figure 1.1. Distribution of type of materials studied in the studies submitted to the World Biomaterials Congress.

The types of ceramics are detailed in Figure 1.2. This is the group that is of interest and which is related to the content of this thesis. More specifically, percentage of works devoted to calcium phosphates is of interest, which is 55%, compared to 45% of the combined works devoted to bioglasses (25%) and other bioactive or inert ceramics (20%). About half within this 55% were related to hydroxyapatite synthesis by high temperature sintering techniques while the other half of the studies were investigating the possibility of obtaining calcium phosphates, more or less soluble than hydroxyapatite, by dissolution and precipitation techniques as in cements.

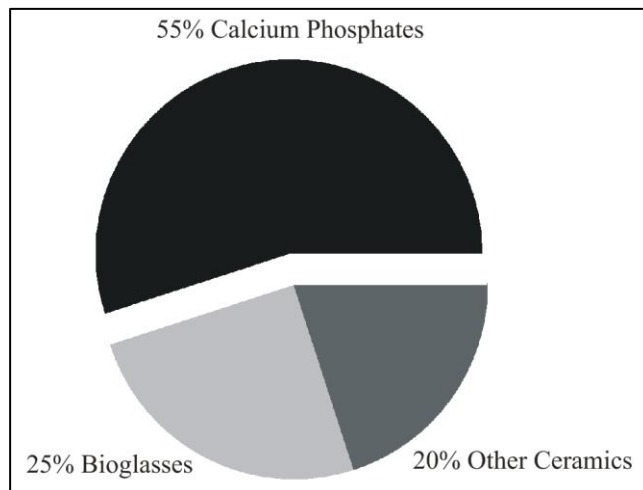


Figure 1.2. Distribution of type of ceramics studied in World Biomaterials Congress.

Bioactivity of calcium phosphates, specifically hydroxyapatite ceramics, aroused enormous interest to these materials in the 70's, in applications related to hard tissues. The Orthopaedics, Plastic Surgery and Dentistry try to solve problems related to bone tissue. Diseases such as osteoarthritis, osteoporosis, osteosarcoma, caries, and large losses of bone caused by traumatic means are associated with problems of substitution, filling, fixation, osseointegration and biocompatibility issues that are difficult to resolve. Calcium phosphate cements were developed as a response to the growing need in clinics for bone tissue engineering scaffolds and bone filler materials to be used in the regeneration of large orthopaedic defects and fixation of orthopaedic implants. Due to excellent regenerative ability of bone, defects can be rectified by supplying the void space with bone grafts or scaffolds. The principle of bone reconstructive surgery is to replace the defective bone with a new functional and viable substitute (Laurencin et al. 1999). Synthetic calcium phosphates were aimed to have all the required properties of allografts and additionally be available “off-the-shelf”. They were designed to achieve a suitable combination of physical properties to match those of the replaced tissue with a minimal toxic response in the host (Hench 1980). The wealth of information present today on physicochemical and biological properties of calcium phosphates enables material and tissue engineers develop efficient strategies addressing the current shortcomings of the bone grafts (de Groot 1984; Wang et al. 2008). Some of these properties are discussed in the forthcoming sections to illustrate some intrinsic biological advantages of calcium phosphates.

Calcium phosphate cements are materials formed by a combination of a solid mixture of calcium phosphates and an aqueous solution. Despite the simplicity of the idea, all the properties of the calcium phosphate cements, such as setting time, compressive strength, porosity, solubility, resorption rate in vivo, and so on are affected by a large number of parameters. For this reason, from the standpoint of the technological development of a particular calcium phosphate cement formulation, application of statistical techniques is important in order to prepare clinically relevant bioactive constructs. Extensive tissue engineering applications of calcium phosphate cements in literature shows that there is still room for improvement in service properties of these materials. Better control of chemical and microstructural characteristics of the cement powders can improve the setting properties, phase structure and contribute to a better ultimate strength. Chemical modification of the setting liquid can result in the formation of alternative setting products with finer microstructures. Introduction of pore forming agents into the cement powder or paste in combination with compaction techniques such as particle size distribution can improve the cellular response to the macroporous cement constructs. The incorporation of biodegradable polymers in the cement formulations can improve the rheological properties and the workability of the cement pastes helping to improve the surgical procedures to become less invasive. By optimizing the osteoconduction and resorption of the calcium phosphate cements, through microstructural modifications and the incorporation of bone growth factors, it is expected that the process of bone healing can be accelerated.

Several of the above mentioned strategies are applied in this work in order to produce clinically relevant calcium phosphate cement based scaffolds. Chemical modification of the brushite forming cement formulation enabled preferred formation of metastable monetite phase and improved the mechanical properties. Pore interconnectivity was enhanced, microporosity was minimized and macroporosity was increased while keeping the strength constant by improved packing as a result of physical modification of the macroporous construct and utilization of particles with size distribution. Chemical, physical and mechanical characterizations of the macroporous calcium phosphate cement based blocks revealed their relevancy for clinical applications.

## CHAPTER 2

### THE BONE

The ideal bone graft material has to have properties similar to bone in order to function adequately as a bone substitute (Hench et al. 2002). Understanding the structure of the bone, the mechanism of bone formation, and the biochemical factors that affect these mechanisms is therefore the prerequisite of bone tissue engineering. Bone mineral was recognized in the 1920s as being an analog of the naturally occurring mineral, hydroxyapatite (Boskey 2005). The unit cell of crystalline hydroxyapatite has the chemical formula  $\text{Ca}_{10}(\text{PO}_4)_6(\text{OH})_2$ ; however, analysis of bone mineral shows a Ca:P molar ratio ranging from 1.3:1 to 1.9:1. This, in part, is due to the contribution of the organic phosphate in the bone matrix to this ratio, but is also related to the nature of the bone mineral itself. It is now recognized that bone mineral is a hydroxyl-deficient, calcium-deficient, carbonated apatite. Deposition of nanosized mineral in bone during development and remodeling is a complex process that involves the cell, the organic extracellular matrix, and physicochemical processes. Bone mineral optimally has a broad range of compositions and sizes, but the mineral crystals are always associated with the collagen matrix. Type I collagen is the principal component of the organic matrix of bone, accounting for approximately 30% of the dry nondemineralized matrix.

Bone can be divided into two basic morphological types, cortical and trabecular, each with its unique morphology, mechanical properties, and function. Cortical or compact bone comprises the outer shell of bones; it is relatively dense and appears solid in histological sections. Trabecular or cancellous bone is a web-like matrix of individual trabecular rod- or plate-like elements connected to one another in three dimensions. It is concentrated at the epiphyses and metaphyses of long bones and is present in all round bones and irregular-shaped bones such as vertebrae. Figure 2.1 shows a human femur where the trabeculae are aligned along the lines of stress. The plates of trabecular bone project from the medial cortex of the femoral neck to support the femoral head and neck; and trabeculae have formed arcs extending from the lateral femoral cortex to the femoral head (Buckwalter 1995). Bone is a metabolically active tissue capable of adapting to local mechanical conditions, a phenomenon described by Wolff's Law.

Although cortical and trabecular bone demonstrate similar mechanical properties, cortical bone is a relatively rigid material with a somewhat steeper stress–strain slope, and which yields over a shorter portion of its curve (Cullinane 2005). The mechanical properties of bone are dependent on the specific constituent materials comprising the bone matrix. For example, compressive stress resistance is predominantly a mineral phase property while tensile load resistance is predominantly a collagen-related property (Burr 2002). Although bone can be broken down to its constituent materials, and its collective material properties reflect those constituent materials, its conglomerate material properties are unique and not simply a sum of its parts.

Trabecular or cancellous bone is an extremely anisotropic material and is less stiff than cortical bone, having a stress–strain slope that is less steep, and that yields over a greater portion of its stress–strain curve. This yielding creep behavior is related to the failure of individual trabecular elements over the loading cycle (Cullinane 2005). Cortical bone also exhibits creep behavior, but to a lesser degree than trabecular bone. Trabecular bone material properties vary widely with the principal orientation of the trabecular elements.

There are 206 pieces of whole-bones in human body. Irrespective of the size and position of the bone, the whole-bone strength is determined by a combination of four physical features (Frost 2001):

- i. Bone’s stiffness, ultimate strength, resilience, true density
- ii. The kinds of bone and their amounts in a cross section
- iii. The size, shape and the distribution of the bony tissue in space
- iv. Fatigue damage or microdamage

Like bone mass, whole-bone strength increases during growth, plateaus in young adults and declines afterwards. Two biological processes manipulate the above listed physical properties of bone, by the action of independently working osteoblasts, osteoclasts, precursor, stem and other cells. Bone modelling is known to increase bone’s strength by moving bone surfaces in tissue space to form the final cross sectional size and shape of bones. Bone remodelling on the other hand, either conserves the amount of bone or deplete it by the successive actions of osteoclasts and osteoblasts in small packets of bone. Bone depletion that accounts for the decline of bone mass up to 40% by ageing is triggered by disuse of a bone region (Brown et al. 2002).

Bone remodelling is a continuous process of bone resorption and formation throughout lifetime (Robling et al. 2006). Positive balance exists approximately during the first 30 years and bone formation rate slows down as one gets older. The main physiological role of bone remodelling is thought to be adaptation of the skeleton to the variety of mechanical loads. Remodelling occurs in microscopic, discrete cavities of old bone in all parts of the skeleton by the action of osteoblasts, osteoclasts and uncharacterized mononuclear cells (Pivonka et al. 2008). The bone remodelling units cover around 100 microns of old bone tissue and the average turnover period is estimated at about 3-4 months. It is thought to be regulated by numerous factors including mechanical, vascular, genetic, nervous, nutritional, hormonal and local growth factors (Pivonka et al. 2008). It is believed that the most common factor is the mechanical impulses that generate electrical signals by piezoelectric bone mineral (Pivonka et al. 2008). The effects of loading on bone remodelling are characterized by a U-shaped curve. Remodelling rate is maximum in the case of overuse or underuse and at the physiological loading range, bone remodelling is minimized. This complex process is described as a cycle of five stages:

a) Passive stage

Approximately 80% of the cancellous bone surface and 95% of the intracortical bone surface is inactive. Bone remodelling units occur along the endosteal surface of bones by local regulatory signals (Parfitt 1984).

b) Activation

There exists a non-mineralized, collagenous membrane on the passive bone surface which is around 1 micron thick (Chow et al. 1992). It separates mineralized bone and bone cells and is needed to be removed for the osteoclast resorption to take place. Following removal of this collagenous membrane, mononuclear cells migrate to the surface of the bone and differentiate to form multinuclear osteoclasts. During these processes, it is believed that the activity of lining cells such as release of collagenase and signalling are involved.

c) Resorption

Newly formed mature osteoclasts degrade organic and mineralized bone matrix through a series of acidic reactions, resulting in the creation of a cavity termed as the



Howship's lacuna (Parfitt 1984). Osteoclasts resorb around two thirds of the final cavity and the last part is decomposed by mononuclear cells. Upon termination of the resorption phase, the cavity reaches a mean depth of about 60-100 microns from the surface. It is thought that bone lining cells are active as well for the termination of the resorption stage. The resorption of bone may be modified by different factors including systemic and local hormones (Pivonka et al. 2008).

d) Reversal

Between the end of resorption and the beginning of formation, bone creation is coupled to previous bone degradation via deposition of a thin and dense mineral cement layer on the bone surface by macrophages(Parfitt 1984). The cement line acts to bind old and new synthesised bone and is crucial for the preparation of the surface for bone formation (Davies et al. 1997).

e) Formation, mineralization and passivation

Differentiated osteoblasts fill the bone remodelling unit by two steps: osteoid synthesis and mineralisation. Due to high density of osteoblasts, rapid deposition of extracellular matrix components such as collagen type I and organisation of the collagen fibers into lamellar structure occurs in the first step up to 2-3 microns/day (Parfitt 1984). The second step begins as the unmineralized matrix reaches a width of 20 microns and continues until the cavity is filled and all the cells remaining on the bone surface is transformed to lining cells. The bone surface returns to its original passive state except that a pristine bone is present underneath (Parfitt 1984).

Mechanical loads deform and strain bones. Strains indirectly but strongly influence the strength and architecture of load bearing bones. Where strains exceed a modeling threshold range, modelling slowly increases bone strength. Those responses make bones strong enough to keep typical peak strains from exceeding the modeling threshold that is lower than the bone's ultimate strength. The result is healthy bones stronger than needed for their peak loads. When strains stay below a lower remodelling threshold range, disuse mode remodelling permanently removes bone, particularly around bone marrow. When strains exceed that threshold, conservation mode remodelling begins to reduce or stop the bone loss (Frost 2001).

In the case of bone healing in fractures, similar biological processes take place in the defective region. A soft tissue termed callus forms in the region with new vessels,

osteoblasts making woven bone and chondroblasts making hyaline cartilage. Callus fills the gaps, surrounds, embeds and welds to the fragments of the fracture or graft without a distinct structure. Once the callus mineralizes, remodelling cells begin to replace it and any graft material with packets of new lamellar bone that can support the largest local compression and tension strains. Guided by those strains, modelling begins to modify the shape and size of the callus to make it stronger. Small strains help to guide the remodelling and modelling processes of bone healing as well. Without any strains, disuse mode remodelling tends to remove the callus and healing retards or fails. It is known that excessive strains also retard bone healing. The permissible strains lie in the range 0.0001-0.002 while bone's fracture strain is known to be around 0.025 (Frost 2001).

In order for a load bearing implant to function properly, it should keep typical peak strains in the supporting bone below its microdamage threshold while keeping them above the remodelling threshold. Microdamage is the overall microscopic fatigue damage that accumulates in the bones to the point of stress fractures. Microdamage threshold is estimated to be around 60 MPa (Frost 2001). In this mild overload range, strains might help modelling to strengthen the supporting bone and prevent its removal by disuse mode remodelling.

## CHAPTER 3

### THE BONE REGENERATIVE SCAFFOLD

The general concept of bone tissue engineering is based on the formation of a construct to encourage the regeneration of the damaged tissue. The tissue engineering construct is composed of the scaffold, viable cells and biologically active agents. The scaffold acts as a temporary three dimensional support for seeding, proliferation and differentiation of cells. Activity of the cells is managed by bioactive molecules incorporated within the scaffold or supplied from the environment. In addition, scaffold supports vascular invasion throughout its lattice, undergoes resorption and replacement by new bone as it is formed. Porosity and interconnectivity are very critical for new bone tissue formation. An elaborate list of properties are expected from the ideal scaffold (Agrawal et al. 2001). The ideal scaffold should:

1. be biocompatible
2. be biodegradable or capable of being remodeled
3. biodegrade in tune with the repair or regeneration process
4. be very porous
5. be highly permeable to allow for proper diffusion
6. have the correct pore size for the candidate cells
7. possess adequate mechanical properties to provide the correct microstress environment for cells
8. provide a surface conducive for cell attachment
9. encourage the formation of extracellular matrix by promoting cellular functions
10. possess the ability to carry biomolecular signals such as growth factors.

Selection or synthesis of the appropriate scaffold materials is governed by the physical, the mass transport, and the biological interaction requirements of each specific

application. These properties or design variables are specified by the intended scaffold application and environment into which the scaffold will be placed.

In order to model an ideal scaffold material, it is imperative to understand the mechanism of bone bonding to the implant surface. This has been a controversial subject in the biomaterials literature as until recently a complete theory based on experimental evidence was not presented. J.E.Davies' study that shed light into this blurry subject involved the analysis of implant surface resorption and cement line which subsequently forms in place of the resorbed material (Davies 2007). First it should be remembered that skeleton system constantly undergoes remodeling throughout life and this results in the exquisite lamellar microarchitecture of both cortical and trabecular mature bone. Like other connective tissues of the body, bone comprises cells embedded in an abundant extracellular matrix. However, unlike most other connective tissues, the extracellular matrix is mineralized to provide unique physiological functions. As the major structural element of the skeleton, bone provides not only locomotor support and protection, but also a dynamic mineral and protein reservoir. The constant remodeling of bone tissue provides a mechanism for scar-free healing and regeneration of damaged bone tissue and also plays, through endocrine control, a vital role in the calcium and phosphate balance of the body fluid.

According to Davies, it is the cement line, secreted during remodelling as a non-collagenous mineralized matrix by differentiating osteoblasts, that interdigitates and interlocks with the demineralized collagenous matrix left by the resorbing osteoclast and thus playing a critical physical role in the establishment of the interface of new bone and old bone. It is only after the formation of the cement line that the differentiated osteoblast assembles collagen fibres extracellularly which become encrusted in the forming cement line and themselves become mineralized to produce the vast majority of the volume of normal bone matrix (Davies 1996). In this manner the cement line becomes a relatively hypermineralized matrix which matures in and around the submicron topography presented by the resorbed bone surface (Davies 1996).

From the early work of Hench (Hench 1980), the mechanism for the bone-bonding phenomenon has been generally accepted to be a chemical interaction that results in collagen, from the bony compartment, being incorporated in the chemically active surface of the implant. Even recently published works on bone remodeling completely discount the histological reality of the cement line and adopt the view that the first formed matrix in bone at remodeling sites is collagen. Davies claims that in the

The material surface must provide a highly topographically complex, and sufficiently stable surface with which the initial cement line matrix can interdigitate, and subsequently interlock as cement line maturation occurs. Also microtopographically complex surfaces promote osteoconduction by both increasing the available surface area for fibrin attachment, providing surface features with which fibrin becomes entangled; and potentiating the activation of platelets, which will produce density gradients of cytokines and growth factors through which leukocytes and osteogenic cells will enter the healing compartment (Davies 2003).

Above mentioned theory by Davies helps one understand how calcium phosphate materials, whether they are employed as lithomorphs or coatings, provide the advantages of accelerating early healing and bone bonding over most other endosseous materials. Calcium phosphates are known to readily adsorb proteins to their surfaces. Potentiating protein adsorption on calcium phosphate surfaces could be expected to increase the binding of fibrinogen that would lead to increased platelet adhesion and possibly, result in increased platelet activation that would accelerate healing. Increasing protein adsorption could also include an increase of or improvement in fibrin binding to the implant surface resulting in an earlier establishment of the three-dimensional matrix through which osteogenic cells have to migrate to reach the implant surface. Thus, calcium phosphate coatings could have a biphasic effect on both platelet activation and fibrin binding (Davies 2003). Furthermore Davies claims that platelet activation on calcium phosphate surfaces is a function of the surface topography of the calcium phosphate, rather than due to the presence of calcium and phosphate ions on the surface of the material. Thus the effect of calcium phosphates on early healing is solely dependent on the inherent physical characteristics of the surface. Contrary to the generally accepted theory of mechanism for the bone-bonding phenomenon being a chemical interaction that results in collagen, from the bony compartment, interdigitating with the chemically active surface of the implant; Davies demonstrates that in cases of de novo bone formation at implant surface, bonding is achieved by micro-mechanical interdigitation of the cement line with the material surface. Therefore surface microtopography of calcium phosphates is critical to not only the osteoconduction, but also whether the elaborated bone matrix will bond to that surface or not (Davies 2003).

The most important requirement for a bone scaffold material aside from surface topography is biocompatibility. Through decades tissue engineers have come up with evolving definitions of biocompatibility but the most complete definition is given

recently by David F. Williams as (Williams 2008): “The ability of a biomaterial to perform its desired function with respect to a medical therapy, without eliciting any undesirable local or systemic effects in the recipient or beneficiary of that therapy, but generating the most appropriate beneficial cellular or tissue response in that specific situation, and optimising the clinically relevant performance of that therapy.”

About 60 wt% of bone is made of carbonate substituted apatite  $\text{Ca}_{10}(\text{PO}_4)_6(\text{OH})_{2-2x}(\text{CO}_3)_x$  therefore it is clear why hydroxyapatite ( $\text{Ca}_{10}(\text{PO}_4)_6(\text{OH})_2$ ) and related calcium phosphates have been intensively investigated as the major component of scaffold materials for bone tissue engineering. Calcium phosphates have excellent biocompatibility due to their close chemical and crystal resemblance to bone mineral. Numerous *in vivo* and *in vitro* assessments have shown that calcium phosphates, whether bulk, coating, powder, porous and crystalline or amorphous, always support the attachment, differentiation, and proliferation of osteoblasts and mesenchymal cells, with hydroxyapatites being the most efficient among them (Rezwan et al. 2006). According to Hench, because hydroxyapatite implants have low reliability under tensile load, such calcium phosphate bioceramics can only be used as powders, or as small, unloaded implants such as in the middle ear, dental implants with reinforcing metal posts, coatings on metallic implants, low-loaded porous implants where bone growth acts as a reinforcing phase, and as the bioactive phase in a composite (Hench 1993).

Formation of tissues with desirable properties relies on scaffold material mechanical properties on both the macroscopic and the microscopic level. Macroscopically, the scaffold must bear loads to provide stability to the tissues as they form while maintaining its original volume. As mentioned above, bone modelling around the implant site necessitates stress signals to be in a medium range in order to increase the bony tissue amount while keeping the bone from disuse remodelling or fracture. For a scaffold to transmit the correct stress range, its stiffness should be similar to that of bone. Cell growth and differentiation and ultimate tissue formation on the microscopic level are dependent on mechanical input to the cells (Drury et al. 2003). As a consequence, the scaffold must be able to both withstand specific loads and transmit them in an appropriate manner to the surrounding cells and tissues.

The desired kinetics for scaffold degradation depends on the tissue engineering application. Degradation is essential in many small and large molecule release applications and in functional tissue regeneration applications. It is important to

understand and control both the mechanism and the rate by which scaffold material is degraded. In the case of load-bearing tissue such as articular cartilage and bone, scaffold matrix must provide sufficient temporary mechanical support to withstand *in vivo* stresses and loading. The biomaterial must be selected and designed with a degradation and resorption rate such that the strength of the scaffold is retained until the tissue engineered transplant is fully remodeled by the host tissue. Bone is able to remodel *in vivo* under physiological loading. Therefore it is a requirement that the degradation and resorption kinetics have to be controlled in such a way that the bioresorbable scaffold retains its physical properties for at least 6 months. Thereafter, it will start losing its mechanical properties and should be metabolized by the body without a foreign body reaction after 12-18 months (Hutmacher et al. 2005).

The success of scaffolds for tissue engineering is also coupled to the appropriate transport of gases, nutrients, proteins, cells, and waste products into, out of, and within the scaffold. Here, the primary mass transport phenomenon of interest, at least initially, is diffusion. The rate and distance a molecule diffuses in a scaffold depend on both the material and molecule characteristics and interactions. Diffusion rates will be affected by the molecular weight and size of the diffusing species compared to the size of the macro and micro pores present in the matrix. Ultimately, diffusion requirements and subsequent material choice depend on the scaffold application. In the case of small and large molecule delivery, limiting free diffusion out of the scaffold may be a priority. In contrast, enhancing the supply of oxygen and nutrients and the removal of waste products is essential to the survival of implanted cells. *In vivo*, most cells exist within 100 microns of a capillary, and diffusion is usually adequate for cell and tissue survival over this distance. However, for larger distances, other means of transport like simultaneous angiogenesis that necessitates interconnected pores in the order of 150 to 500 microns, must be incorporated (Drury et al. 2003). Porous scaffolds with large void volume and large surface area to volume ratio are also needed to maximize space for cell seeding, attachment and growth. Small pores are preferable to attain a large surface area provided that the pore size is greater than the diameter of cells which is typically around 10 microns (Khan 2004). Both the rate and distribution of osteogenesis throughout the implant are affected by the size and number of interconnecting channels, and pore size and porosity may not be the primary determinants for osteoconductivity.

In addition to the design and material selection of the scaffold, success of the tissue engineering construct depends on the viability of the cells and biologically active agents that are either present in vivo or artificially added to the construct. Scaffolds act as a conduit for the delivery of cells, genetic material and growth factors to the site of interest (Kakar 2005). Bone marrow cells and differentiated mesenchymal stem cells have been used in the tissue engineering of bone, and in particular the repair of osseous defects (Connolly 1995). The ability of bone marrow cells to heal bony defects can be potentiated by adding osteoinductive agents such as human bone morphogenetic proteins. Bone morphogenetic proteins, transforming growth factors, fibroblast growth factors are proteins secreted by cells and function as signaling molecules. They comprise a family of molecules that have autocrine, paracrine or endocrine effects on appropriate target cells. In addition to promoting cell differentiation, they have direct effects on cell adhesion, proliferation and migration by modulating the synthesis of proteins, other growth factors and receptors (Kakar 2005). Combination of these biologically active agents with scaffold material ensures an adequate host response upon implantation. Heat treated scaffold materials are unable to host active agents so that loading and release of these agents are restricted to a small class of biomimetic materials of which calcium phosphate cement constitutes the majority. The following section provides an in-depth look into the properties of calcium phosphate cements.



## CHAPTER 4

### CALCIUM PHOSPHATE CEMENTS

In the most general sense of the word, cement is a binder, a substance that sets and hardens independently and can bind other materials together. In every era of human history cementitious materials are made use of in load bearing structures. From Egyptians to Romans every major civilization left their marks on earth via gigantic structures made of stone, sand and cement. In the ancient history gypsum and limestone were burnt to obtain cementitious materials similar to volcanic ashes that were used as mortar in stone structures. The cement that we know of had been developed in the 19th century following William Aspdin's discovery of Portland cement. It is a synthetic mixture of calcium silicates formed in a molten matrix from a suitably proportioned and homogeneously prepared mixture of calcareous components. The material consists of a suitable ratio of  $3\text{CaOSiO}_2$  to  $2\text{CaOSiO}_2$  that when ground to an optimum particle size distribution forms a paste with water which sets and hardens by means of hydration reactions and which, after hardening, retains its strength and stability even under water (Hewlett 2004). Calcium silicates dissolve and precipitate in the presence of small amount of water by virtue of their high solubility. Hydrated silicate crystals precipitate out of the solution by a vigorous exothermic reaction, entangle and bind everything in the structure of the cement. Inherent solubility of many calcium compounds in water has motivated material scientists to discover more cementitious calcium compounds.

Calcium phosphate cements (CPC) were discovered by LeGeros, Brown and Chow in the 1980s as an alternative to bulky bone graft bioceramics to set in situ and fill bone or dental defects. According to Chow, the discovery of the first CPC was in fact a result of decades of basic studies on calcium phosphate solubility behaviors. Based on solubility phase diagrams, calcium phosphate scientists were aware of the fact that both tetracalcium phosphate (TTCP) and dicalcium phosphate anhydrate (DCPA) are much more soluble than hydroxyapatite (HA) under neutral pH conditions. Further, a slurry containing appropriate amounts of these compounds can produce continuous HA precipitation while maintaining the solution composition relatively constant. Studies on the reactions of TTCP and DCPA were conducted with the aim of

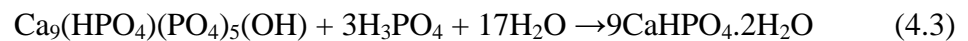
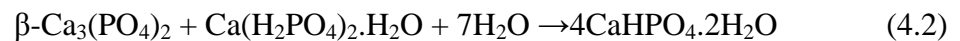
developing slurries for remineralizing carious lesions. It was observed that some of the TTCP + DCPA aqueous pastes became a hardened mass when left in test tubes for a few hours. Thus unaware of the consequences, Chow et al. discovered a new type of self-hardening cements that consisted of only calcium phosphates and formed HA as the product. In subsequent years, results from a series of animal studies revealed that implanted CPC was gradually replaced by new bone without a loss in volume. This CPC composition received approval by the US Food and Drug Administration in 1996, thus becoming the first commercially available CPC for use in humans (Chow 2009). Since then, many compositions have been proposed most of which are given in subsequent chapters of this report.

Despite the large number of formulations, CPC can only have two different setting products: apatite and brushite. Compared to sintered calcium phosphate ceramics, calcium phosphate cements have two major advantages. Firstly, CPCs are nanocrystalline and hence have a very high specific surface area. Values as high as 100 m<sup>2</sup>/g can be reached. By comparison, sintered ceramics have surface areas close to or below 1 m<sup>2</sup>/g. Secondly, CPCs enable the synthesis of granules and blocks of low-temperature calcium phosphates such as dicalcium phosphate dihydrate, octacalcium phosphate, or precipitated apatite (Bohner et al. 2005). CPCs are made of an aqueous solution and of one or several calcium phosphates. Upon mixing, the calcium phosphates dissolve and precipitate into a less soluble calcium phosphate. During the precipitation reaction, the calcium phosphate crystals grow and become entangled, thus providing a mechanical rigidity to the cement. When CPC is mixed with the setting solution, it becomes a slurry that can be shaped to any contour and set to harden under physiological conditions. Under ideal conditions, continuing dissolution of the reactants supplies calcium and phosphate ions to the solution, while HA formation depletes these ions. All studies show that the microstructure of cement evolves during the setting and hardening processes (Fernandez et al. 1998).

Chemical composition of calcium phosphate cements may include all ionic compounds of oligoelements occurring naturally in a human body. The list of possible additives includes the following cations: Na<sup>+</sup>, K<sup>+</sup>, Mg<sup>2+</sup>, Ca<sup>2+</sup>, H<sup>+</sup> and anions: PO<sub>4</sub><sup>3-</sup>, HPO<sub>4</sub><sup>2-</sup>, H<sub>2</sub>PO<sub>4</sub><sup>-</sup>, CO<sub>3</sub><sup>2-</sup>, HCO<sub>3</sub><sup>-</sup>, SO<sub>4</sub><sup>2-</sup>, HSO<sub>4</sub><sup>-</sup>, Cl<sup>-</sup>, F<sup>-</sup>, SiO<sub>4</sub><sup>2-</sup>. Therefore, the preparation of mixed-type cements consisting of calcium orthophosphates and other calcium salts like gypsum, calcium sulfate hemihydrate, calcium pyrophosphate, calcium polyphosphates, calcium carbonate, calcium oxide, calcium hydroxide, calcium

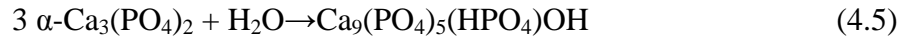
aluminate, calcium silicate, strontium orthophosphate, as well as cements made of ion-substituted calcium orthophosphates such as  $\text{Ca}_2\text{KNa}(\text{PO}_4)_2$ ,  $\text{NaCaPO}_4$ ,  $\text{Na}_3\text{Ca}_6(\text{PO}_4)_5$ , magnesium-substituted calcium deficient hydroxyapatite (CDHA), strontium-substituted CDHA are possible. The aqueous solution facilitating the setting and hardening of the cement might be distilled water, phosphate-buffered saline, an aqueous solution of sodium orthophosphate, orthophosphoric acid, aqueous solution of citric acid, or even revised simulated body fluid (Dorozhkin 2008).

Two types of setting reactions are possible. First, the setting reaction can occur according to an acid-base reaction, i.e. a relatively acidic Calcium phosphate phase reacts with a relatively basic calcium phosphate to produce a relatively neutral calcium phosphate (Bohner 2000). Typical examples are the cement of Brown and Chow, where tetracalcium phosphate (basic) reacts with dicalcium phosphate (neutral) to form PHA (slightly basic), the cement of Lemaitre where  $\beta$ -tricalcium phosphate ( $\beta$ -TCP, slightly basic) reacts with monocalcium phosphate monohydrate (MCPM, acidic) to form dicalcium phosphate dihydrate (DCPD, neutral), and a variation of Lemaitre's formulation where MCPM is substituted by orthophosphoric acid while  $\beta$ -TCP is replaced by calcium deficient hydroxyapatite according to the reactions:



The second type of setting reaction is defined as hydrolysis of a metastable calcium orthophosphate and the initial and final calcium phosphates have the same Ca/P molar ratio. Typical examples are amorphous calcium phosphate (ACP),  $\alpha$ -TCP, and TTCP which form calcium deficient hydroxyapatite upon contact with an aqueous solution:





It should be remembered that these equations are valid for the in vitro conditions only. There are evidences that samples of calcium phosphate cement retrieved 12 hours after hardening in vivo already contained carbonateapatite even though the initial cement mixture did not contain carbonate as one of the solid components. The mass fraction of carbonate in the 12 hour samples was about 1 % (Dorozhkin 2008). The results suggest that under the in vivo conditions, carbonate is readily available and this allows formation of carbonateapatite in favor of carbonate-free calcium deficient hydroxyapatite.

Furthermore calcium phosphate cement precursors are mainly classified into three groups: those containing TTCP,  $\alpha$ -TCP and  $\beta$ -TCP as the main phase. TTCP and  $\alpha$ -TCP are the only calcium phosphates that can individually transform to hydroxyapatite (Monma 2006). Also a self setting cement can be prepared from the thermal decomposition product of hydroxyapatite (Dorozhkin 2008). Surface dissolution of reactant particles at an earlier stage and diffusion through the HA layer at later periods describe the dynamics of cement hardening process (Liu et al. 1997). Dissolution of the initial calcium orthophosphates and mass transport are the primary activities in an aqueous environment, in which the dissolved reactants form a supersaturated microenvironment with regard to the precipitation of the final product. The relative stability and solubility of various calcium orthophosphates is the major driving force for the setting reactions that occur in these cements. Mixing of the calcium phosphate precursors with aqueous setting solution induces various chemical transformations, where crystals of the initial calcium orthophosphates rapidly dissolve and precipitate into crystals of HA or DCPD with possible formation of intermediate precursor phases such as ACP and octacalcium phosphate (OCP) (Dorozhkin 2008).

Thermodynamic analysis of the conventional TTCP containing cement formulation reveals the general setting mechanism for calcium phosphate cements (Liu et al. 2003). Calcium phosphate cement setting reaction is an exothermic reaction consisting of several steps. Monitoring the heat evolution by an isothermal calorimeter shows that these steps are the initiation period (A), induction period (B), acceleration

period (C), deceleration period (D), and termination period (E) as given in Figure 4.1. In the initiation period of 5–10 minutes, water is absorbed and then covers the surface of the grains upon mixing calcium phosphate powder with water. This is a physical exothermic process. In the induction period or latency, the particle dissolution contributes to a rise in concentration of the Ca and P containing species in the solution. With the different dissolution rates of TTCP and DCPA, the pH translates towards the basic region until the solution is supersaturated, and then HA crystallizes from the solution. The acceleration period is a fast reaction controlled region. In the deceleration period, rate of hydration reaction decreases and the reaction order changes from surface reaction controlled to diffusion controlled after the hydrate product grows around the raw material particle surfaces. The hydrate product layer is destroyed by osmotic pressure and crystallization interior stress, and leads to the increase of the reaction rate and another slight exothermic peak (Liu et al. 2003). The total area under the curve gives the total heat evolved during setting reaction. Various factors influence the heat liberation including the presence of crystal seed, reaction temperature, Ca/P ratio, particle size of the raw materials.

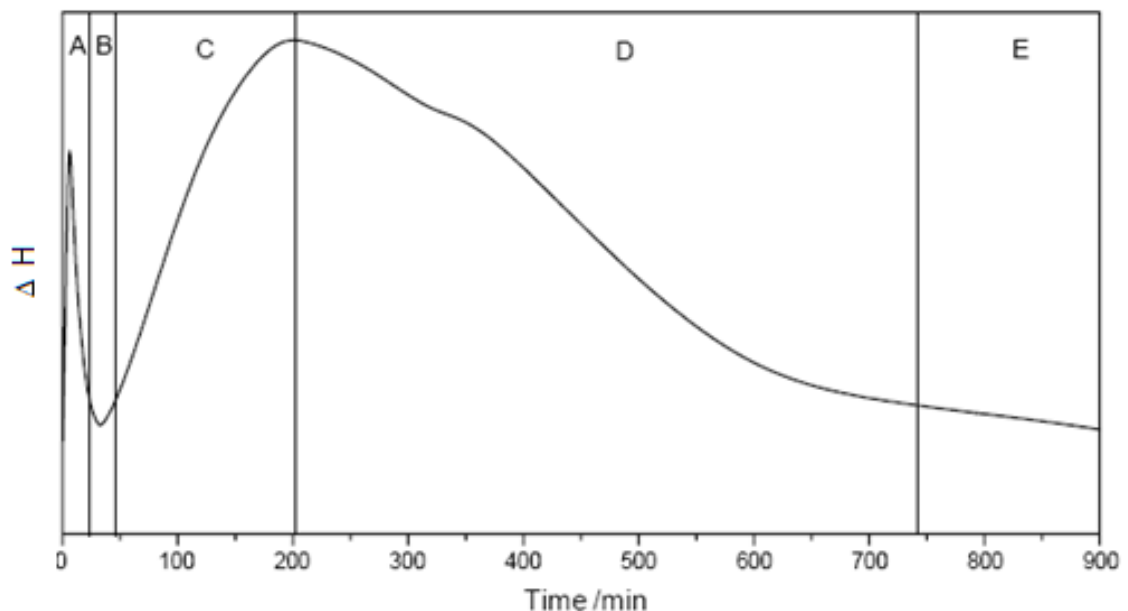


Figure 4.1. Calorimetric curve showing the heat evolution rate as a function of time. (Source: Liu et al. 2003).

After conversion, materials occupied originally by reactant particles are wrinkled and consist of small acicular crystals. Different morphologies of crystals are formed in different ways: the needlelike crystal intergrains are formed by dissolution control at the earlier stage; the wrinkled crystals are formed by diffusion control at the later stage. The dissolution process is controlled by the specific surface area of DCPA which greatly affects the hardening process (Liu et al. 1997).

Hydration of the conventional formulation is controlled by the dissolution of reactant particles in the first 4-h period, and since the rate of dissolution is proportional to the surface area of the particles which is basically constant in CPC specimens in the earlier stage, the precipitation rate of HA is linear with time. HA forms among the reactant particles which enhances the binding of solids, or around the particles which reduces the distance of grains (Liu et al. 1997). All of these lead to a rise in compressive strength. Setting of calcium orthophosphate cements occurs in general within the initial 6 hours, yielding an 80% conversion to the final product. The volume of cements stays almost constant during setting (Dorozhkin 2008). Therefore, increases in the compressive strengths are linear both with time and the extent of conversion. However, when a shell of HA is formed around the reactants, the rate of HA formation is controlled by the transport of water and ions through such a shell and decrease with an increase of the thickness of the HA shell. The hydration of the residual DCPA engulfed by the shell of HA leads to an internal force which is harmful to the compressive strength since the densities of DCPA and HA are different. Thus, the compressive strengths decrease with the process of hydration at the later stage (Liu et al. 1997).

Both the extent of conversion and the compressive strength of the cement initially increase drastically with time, subsequently reaching a saturation level. This decrease of the reaction rate as a function of time is correlated with the surrounding of the  $\alpha$ -TCP particles by layers of CDHA. The compressive strength is highly correlated with extent of conversion of the hydrolysis reaction as seen in Figure 4.3. This correlation is deduced from the analysis of the XRD peak intensities of the reactants and products by Fernandez et al. (Fernandez et al. 1996).

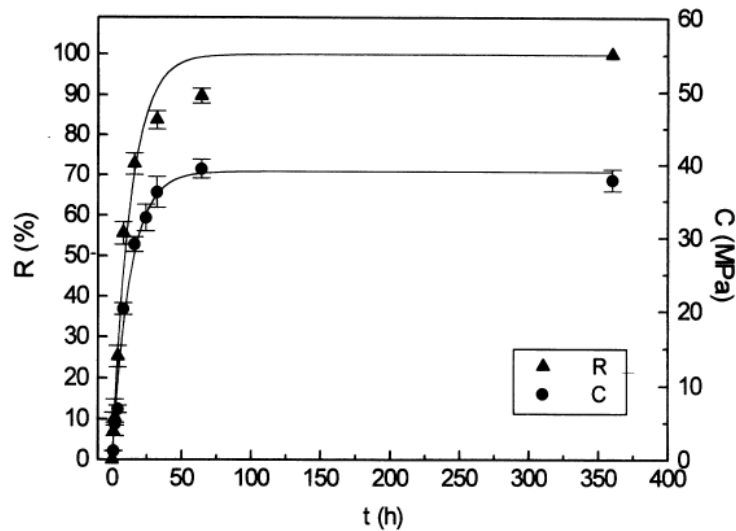


Figure 4.3. Correlation between the conversion of cement reaction and compressive strength. (Source: Fernandez et al. 1996)

CPC setting time corresponds typically to a precursor conversion close to 5–20% whereas maximum mechanical properties have been reported to be reached after 90% reacted fraction (Bohner 2008). There are currently two standardized methods to study the setting and hardening processes of cements, namely: Gillmore needles method (ASTM C266–89) and Vicat needle method (ASTM C191–92). The idea of both methods is to examine visually the surface of cement samples to decide whether the cement has already set, i.e., if no mark can be seen on the surface after indentation. Gillmore needles have been used with success to measure the initial and final setting times of calcium orthophosphate cements. A light and thick needle is used to measure the initial setting time I, while a heavy and thin needle is used for the final setting time F. The clinical meaning is that the cement paste should be implanted before time I and that the wound can be closed after time F. A cement should not be deformed between times I and F because in that stage of the setting process any deformation could induce cracks (Dorozhkin 2008).

The manipulation of the setting times of CPCs is significant as they should meet the requirements of surgical procedures. The initial setting time should be adjusted so as to allow sufficient time gap for shaping and filling. After the filling, it is not advisable to disturb the set cement until its hardening because any mechanical strain during this period will produce cracks and adversely affect the strength. Therefore it requires the shortest possible final setting time so that the wound closure is not delayed. An initial

setting time of about 8 minutes and a final setting time of < 15 minutes are recommended for orthopedic applications. The initial setting time denotes the end of workability of the putty after wetting, and the final setting time indicates the hardening of the set mass (Komath et al. 2000). Both the initial and final setting times decrease markedly with increasing powder/liquid (P/L) ratio.

The powder/liquid ratio is one of the most significant parameters that have a direct effect on porosity and hence mechanical properties of the calcium phosphate cements. The cement paste should neither be too dry nor too fluid for ease of moldability and cohesion during injection. Low powder/liquid ratio is beneficial for homogeneous reaction and moldability and high powder/liquid ratio leads to low porosity after setting is complete. The effect of liquid ratio on mechanical properties was clearly demonstrated in the study by Xu et al. on incorporation of dissolved chitosan lactate in the liquid as plasticizer (Xu et al. 2002). There is a linear decrease of strength and elastic modulus with decreasing powder/liquid ratio due to higher pore fraction. However injectability is improved with decreasing P/L. Variations in injectability by P/L ratio appear to be valid to certain extent only. For example, injectability was found to be unaffected by P/L ratio within the range of 3.85–4.50 g/ml, but drops by nearly 100% between P/L ratio of 4.50 and 5.00 g/ml (Dorozhkin 2008). Hofmann's calorimetric analysis of brushite cement with different concentrations of citric acid retarder and varying P/L ratio demonstrated the decrease in the setting time with higher P/L ratio but also revealed that the height of the exothermic peak corresponding to the maximum heat flow decreased as well.

CPCs can reach mechanical properties comparable to those of sintered calcium phosphate blocks with the same porosity after setting. Some studies have reported clear correlations between the mechanical properties, the conversion extent of the reactants, and the crystalline microstructure and a clear effect of the ageing temperature on the crystalline microstructure (Fernandez et al. 1998)., The set products of all calcium orthophosphate cements are brittle as is common for all ceramics, have both a low impact resistance and a low tensile strength within 1–10 MPa, whereas the compressive strength varies within 10–100 MPa. The latter value exceeds the maximum compressive strength of human trabecular bone. The compressive strength of these cements twelve weeks after implantation was found to be still significantly higher (60–70 MPa) than that of normal bone. The chemical composition of the cement, the particle size and the relative proportion of the reactants in the mixture, the powder and/or liquid additives



acting as accelerators or retarders, the liquid-to-powder ratio and the ageing conditions affect the compressive strength (Fernandez et al. 1998). Comparative mechanical properties of brushite and apatite cements will be given in the subsequent section.

One of the main reasons for the weakness of these materials is their high level of porosity, which makes it easier for micro and macro cracks to run through the mass. The pores are less than 10  $\mu\text{m}$  in diameter, and after the cement is set, about 43% of the volume is occupied by the pore phase. Porosity may be controlled to a certain extent by adjusting particle size and powder/liquid ratio. The negative effects of these two parameters on porosity of cements were reported by Almirall et al. (Almirall et al. 2004). In the case of macropore introduction to the cement matrix by the incorporation of porogens, the microporosity was influenced by the amount of macropore forming agents as follows:

$$\% \text{ MicP} = (100 - \text{MacP}) \times \text{mean I-MicP} \quad (4.7)$$

where MicP is the microporosity, MacP is the macroporosity and mean I-MicP is the average inherent microporosity fraction of the porogen free cement. The overall microporosity of the entire sample is lower because the sample contained less CPC per unit volume due to more macroporosity. As a result, with increase of macroporosity, the microporosity of the cement decreases. Although this is beneficial for the resorbability of the cement, mechanical properties of macroporous cement are greatly reduced compared to macropore free cements (Takagi et al. 2001). In general strength,  $\sigma$  of ceramics vary as an exponential function of porosity, P as given below and so does the strength of CPCs: (Rice 1998)

$$\sigma = \sigma_0 \exp(-KP) \quad (4.8)$$

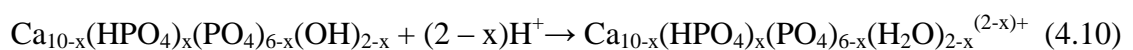
$\sigma_0$  is the strength of the material with zero porosity and K is a constant. Also this equation is modified by Le Huec to take pore size into account (Le Huec et al. 1995):

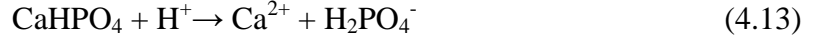
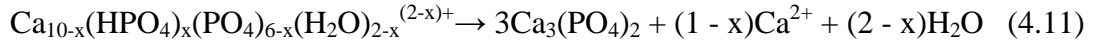
$$\sigma = (E_0 R / (\pi c))^{0.5} \exp(-KP) \quad (4.9)$$

where  $E_0$  is the modulus of zero porosity,  $R$  is fracture surface energy and  $c$  is the average pore size. This equation shows that strength increases at a given porosity as the pore size is decreased and takes into account the fact that when porosity changes, pore size may also change. A point is reached where the macropore size equals the dimension of the inherent micropores with decreasing cement porosity, hence the critical flaw size is reached. Porosity alone controls the strength at this level and below according to the former equation and a marked decrease in the slope of the  $\ln$  strength vs porosity graph is observed at low porosity (Barralet et al. 2002).

Calcium phosphate cements are able to provide short-term biologically desirable properties and then be replaced by new bone. The overall dissolution behavior of calcium phosphate cement is a combination of a solution-mediated process and a cell-mediated process. The resorption properties of bioceramics are generally believed to relate to the solubility of their constitutive phases. The implanted calcium orthophosphates might be resorbed by two possible mechanisms, namely: an active resorption, mediated by the cellular activity of macrophages, osteoclasts, and other types of living cells and a passive resorption due to either chemical dissolution or chemical hydrolysis (brushite cements only) in the body fluids (Dorozhkin 2008). An important in vivo characteristic of HA-forming CPC is that it does not dissolve spontaneously in a normal physiological fluid environment, yet is resorbable under cell-mediated acidic conditions. Although DCPD is soluble in normal physiological fluids, studies have shown that resorption of DCPD-forming CPC was also essentially cell mediated (Chow 2009).

The kinetics of passive resorption depends on porosity of the samples, ionic substitutions, Ca/P ratio, crystallinity and pH of the cement–tissue interface. The active resorption is due to cellular activity; however, it is also related to the passive one. Solution pH near macrophages and osteoclasts can drop to 5 by the excretion of lactic acid, whereas near osteoblasts solution pH can become as high as 8.5 by the excretion of ammonia (Dorozhkin 2008). Dissolution chemistry of CDHA and therefore, of the hardened apatite cements in acidic media might be described as a sequence of four successive chemical equations:





The pore dimensions in hardened cements are too small to allow fast bone ingrowth. Besides, unless special efforts have been performed, the pores are not interconnected. Due to these reasons, osteoclastic cells are able to degrade the hardened cements after injection layer-by-layer only, starting at the bone–cement interface throughout its inner part. This is the main drawback of the classical cement formulations when compared to calcium orthophosphate ceramic scaffolds with an open porosity (Dorozhkin 2008). Bone substitution depends on porosity, bulk site, crystallinity, chemical composition, particle size, powder/liquid ratio of the cement and anatomic site. Also the growth rate of a newly forming bone depends on age, sex, and general metabolic health of the recipient. It may take 3 to 36 months for the cement to be completely resorbed and replaced by bone considering these factors (Ambard et al. 2006). A linear degradation rate of 0.25 mm/week has been reported in literature (Dorozhkin 2008).

Resorption of calcium phosphate cements is not desired at the onset of hardening *in vivo* due to washout of loose calcium phosphate particles by the surrounding body fluid before maintaining mechanical rigidity. The implant should be placed into the wound site between the initial and final setting times therefore washout constitutes a problem for the cement formulations with long setting time. Besides improving setting times, it is possible to have stable cement prior to implantation that sets in contact with body fluids. These are called premixed cements and are essentially pastes formed by calcium phosphate particles mixed with a nonaqueous but water miscible liquid like glycerol. Also several studies show that incorporation of a gelling agent such as hydroxypropyl methylcellulose, carboxymethyl cellulose, alginate, chitosan, into CPC provides good washout resistance (Takagi et al. 2003). However, generally premixed CPC have lower mechanical properties probably related to the volume initially taken up by the non-aqueous liquid (Chow 2009).

Injectability of CPC is of crucial importance for surgical procedures utilizing minimally invasive procedures such as in vertebroplasty and kyphoplasty or for delivery

of the cement into a very narrow space as in root canal obturation. CPC injectibility depends on many factors and may be quite poor in certain cases which results in liquid–solid phase separation called filter-pressing. Bohner’s study shows that the injectibility of CPC’s is generally improved by a decrease of P/L, the use of round particles, the addition of citrate ions, and the addition of viscous polymer solutions (Bohner et al. 2005). In addition to a large number of parameters relating to CPC composition, the injectibility of a setting cement depends strongly on the post-mixing time interval relative to the cement setting time. In this regard, premixed CPCs that are described earlier and do not harden until being placed into the defect would be of advantage in that the injectibility would remain essentially constant with time (Chow 2009).

It is generally accepted that calcium phosphate materials, including CPCs, are osteoconductive but not osteoinductive. CPC materials can be a suitable substrate for various osteoinductive factors currently under development because its pH can be controlled quite precisely, and it can be made macroporous which is essential for efficient delivery systems. Incorporation of osteoinductive factors like bone morphogenetic protein, transforming growth factor, platelet-derived growth factor, and basic fibroblast growth factor should be one of the most effective ways to improve the efficacy of CPC materials for repairing defects with insufficient available bone surfaces (Chow 2009).

#### **4.1. Component Phases of Calcium Phosphate Cements**

Solids occurring in the system  $\text{Ca}(\text{OH})_2\text{-H}_3\text{PO}_4\text{-H}_2\text{O}$  can all be precipitated at appropriate pH and temperature in aqueous calcium phosphate solutions. However few are stable in physiologically relevant conditions. DCPD (dicalcium phosphate dihydrate), OCP (octacalcium phosphate), CDHA (calcium deficient hydroxyapatite) and PHA (precipitated apatite) are those calcium phosphates obtained as the product of calcium phosphate cement setting reactions. Other metastable and thermally synthesized calcium phosphates are utilized in CPC as reactants due to their solubility in water. In general the solubility and acidity of calcium phosphates increase with decreasing Ca/P ratio as seen in Figure 4.4. Calcium orthophosphates are obtained by neutralizing phosphoric acid which has four protonated forms (Leon 2009). Oligo-elements like Na, K, Mg, Zn, carbonate and chloride are also suitable as reactants for the synthesis of

calcium phosphates. Properties of calcium phosphates present in CPC along with some other common precursors are listed in Table 4.1.

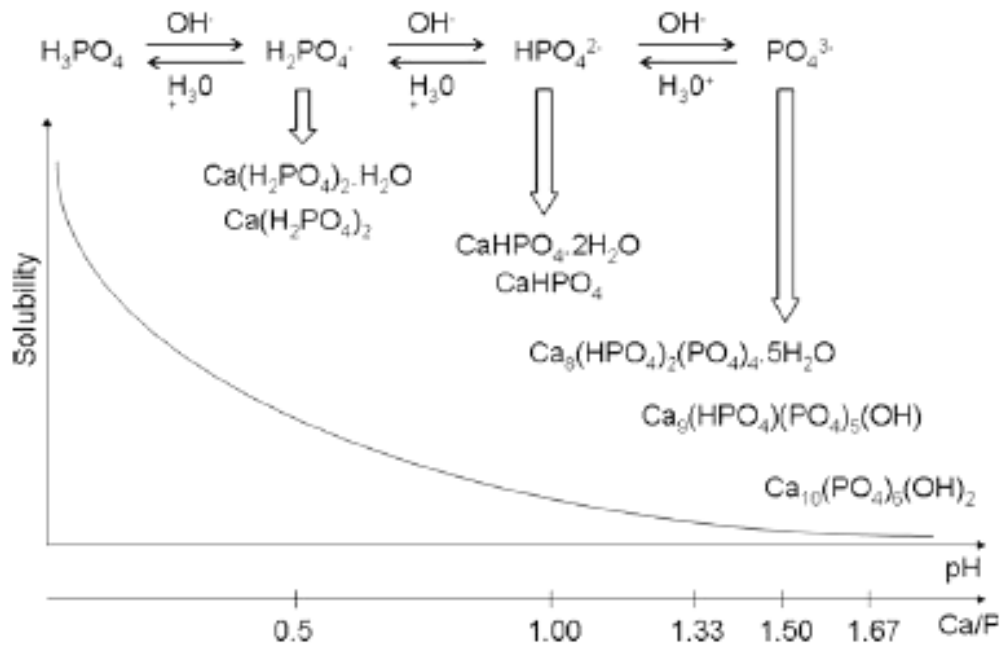


Figure 4.4. Decrease in solubility of calcium phosphates with increasing Ca/P ratio. (Source: Leon, 2009)

Most calcium phosphates used in cements are calcium orthophosphates with the exception of calcium pyrophosphate ( $\text{Ca}_2\text{P}_2\text{O}_7$ ), i.e. they contain the orthophosphate group  $\text{PO}_4^{3-}$ . Most calcium orthophosphates are sparingly soluble in water, but all dissolve in acids. The most important property of calcium phosphates is probably their solubility in water because the in vivo behavior of calcium phosphates can be predicted to a large extent by their solubility. The in vivo degradation rate of calcium phosphates at pH 7.0 is in the following order:



Even though all parameters except the composition are kept constant, this order is not always observed experimentally: the surface of a highly-soluble calcium phosphate is reactive and may become covered with a poorly soluble calcium phosphate, hence reducing its degradation rate (Bohner 2000).

Table 4.1. Properties of Calcium Phosphate Cement Precursors

Phases	Chemical Formula	Ca/P Ratio	Molecular Weight (g)	Density (g/cc)	Solubility at 25°C $-\log(K_{sp})$	pH stability range in aq.	Mineral
Tetracalcium phosphate	$\text{Ca}_4\text{P}_2\text{O}_9$	2.00	366	3.05	38-44	Cannot be precipitated	Hilgenstockite
Hydroxyapatite	$\text{Ca}_{10}(\text{PO}_4)_6(\text{OH})_2$	1.67	1004	3.16	116.80	9.5-12	Hydroxyapatite
Calcium deficient hydroxyapatite	$\text{Ca}_{10-x}(\text{HPO}_4)_x(\text{PO}_4)_{6-x}(\text{OH})_{2-x}$ $0 < x < 1$	<1.67	966-1004		85.10	6.5-9.5	--
$\beta$ -Tricalcium phosphate	$\text{Ca}_3(\text{PO}_4)_2$	1.50	310	3.07	28.90	Cannot be precipitated	--
$\alpha$ -Tricalcium phosphate	$\text{Ca}_3(\text{PO}_4)_2$	1.50	310	2.86	25.50	Cannot be precipitated	--
Amorphous calcium phosphate	$\text{Ca}_3(\text{PO}_4)_2 \cdot n\text{H}_2\text{O}$ $n=3-4.5$	1.50	364-391		25.70	Metastable (6.0-12)	--
Whitlockite	$\text{Ca}_{10}(\text{HPO}_4)(\text{PO}_4)_6$	1.43	1071	3.13	81.70	Metastable	Whitlockite
Octocalcium phosphate	$\text{Ca}_8(\text{HPO}_4)_2(\text{PO}_4)_4 \cdot 5\text{H}_2\text{O}$	1.33	982		96.6	Metastable (6.0-7.0)	--
Dicalcium phosphate dihydrate	$\text{CaHPO}_4 \cdot 2\text{H}_2\text{O}$	1.00	172	2.34	6.59	2.0-6.5	Brushite
Dicalcium phosphate anhydrate	$\text{CaHPO}_4$	1.00	136	2.93	6.90	2.0-6.0	Monetite
Calcium Pyrophosphate	$\text{Ca}_2\text{P}_2\text{O}_7$	1.00	254	3.09	--	Cannot be precipitated	--
Monocalcium phosphate monohydrate	$\text{Ca}(\text{H}_2\text{PO}_4)_2 \cdot \text{H}_2\text{O}$	0.50	252	2.22	Highly soluble	Metastable (0.1-2.0)	--
Calcium Oxide	$\text{CaO}$	--	56	3.35	Reactive	--	Lime
Calcium Hydroxide	$\text{Ca}(\text{OH})_2$	--	74	2.24	5.10	--	Portlandite
Calcium Carbonate	$\text{CaCO}_3$	--	100	2.71	8.32	--	Calcite

***Monocalcium phosphate monohydrate*** (MCPM;  $\text{Ca}(\text{H}_2\text{PO}_4)_2 \cdot \text{H}_2\text{O}$ ) is the most acidic and the most soluble CaP at almost all pH values. It precipitates from highly acidic solutions. MCPM crystallizes into a triclinic structure with two formula units per cell. The crystal morphology of MCPM resembles thin plates as seen in Figure 4.5. The anhydrous form of monocalcium phosphate precipitates at temperatures above 100 °C and under acidic conditions. MCPM is not biocompatible due to its acidity and solubility, and thus cannot be used alone as a bone substitute. However, it can be used in combination with basic calcium phosphate compounds (Bohner 2000). One such formulation involves MCPM and CaO to form DCPD by the following reaction:

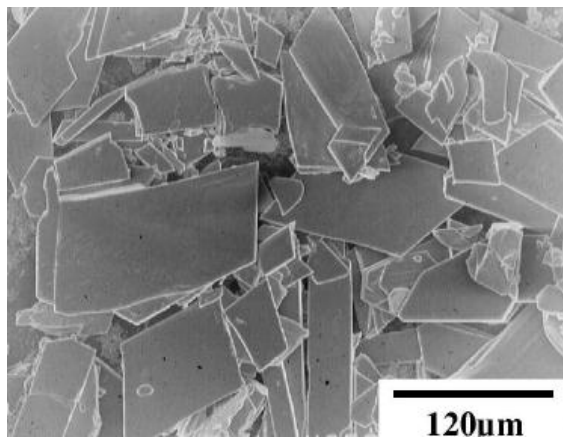
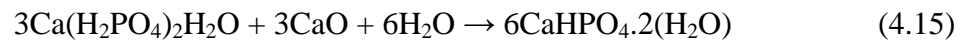


Figure 4.5. Morphology of MCPM crystals.  
(Source: Bohner, 2000)

***Dicalcium phosphate dihydrate*** (DCPD;  $\text{CaHPO}_4 \cdot 2\text{H}_2\text{O}$ ) also known as brushite, is biocompatible, biodegradable and osteoconductive. It has monoclinic crystal structure with the lattice parameters  $a) 5.812$   $b) 15.180$   $c) 6.239 \text{ \AA}$ ,  $\beta) 116.42^\circ$ . DCPD has been detected in fracture callus, bone and kidney stones. It is considered as an intermediate in both bone mineralization and enamel dissolution. It has a Mohr hardness of 2.5 (Kodaka et al. 1999). DCPD is metastable and can be converted into DCP (pH < 6), OCP (pH = 6-7) or PHA (pH > 7). It transforms into dicalcium phosphate anhydrous at temperatures above 80 °C. In vivo DCPD is converted into PHA or biodegraded and replaced by bone (Bohner 2000). Dicalcium phosphate dihydrate crystals consist of

synthesized in aqueous solutions at room temperature by using soluble calcium ( $\text{Ca}(\text{NO}_3)_2 \cdot 4\text{H}_2\text{O}$ ,  $\text{CaCl}_2 \cdot 2\text{H}_2\text{O}$ , or  $\text{Ca}(\text{CH}_3\text{COO})_2 \cdot \text{H}_2\text{O}$ ) and phosphate ( $\text{NH}_4\text{H}_2\text{PO}_4$ ,  $(\text{NH}_4)_2\text{HPO}_4$ ,  $\text{Na}_2\text{HPO}_4$ ,  $\text{NaH}_2\text{PO}_4$ ,  $\text{KH}_2\text{PO}_4$ , or  $\text{K}_2\text{HPO}_4$ ) salts on adjusting the Ca/P molar ratio to 1 (Tas et al. 2004). Pure DCPD powders can also be synthesized, for instance, by reacting a suspension of  $\text{Ca}(\text{OH})_2$  with stoichiometric amounts of  $\text{H}_3\text{PO}_4$ , as long as the solution pH is kept in the acidic range.

Both DCPD and DCPA phases are successfully used as starting materials in the preparation of the powder components of self-hardening apatite cements. DCPD is also the final precipitation product of cements developed by Mirtchi et al. that set under acidic conditions (Mirtchi et al. 1989). Such formulations have superior in vivo resorbability, as opposed to conventional apatitic cements. The scientific basis behind this fact can be clearly explained by the dissolution data published by Tang et al. (Tang et al. 2003). It is seen that DCPD has a dissolution rate of  $4.26 \times 10^{-4}$  mole/ $\text{m}^2 \cdot \text{min}$  at a pH value of 5.5, and this rate is about 3.4 times greater than that of  $\text{Ca}_3(\text{PO}_4)_2$  ( $1.26 \times 10^{-4}$ ). The dissolution rate for carbonated apatite was also reported by the same researchers to be as  $1.42 \times 10^{-6}$  which is significantly lower.

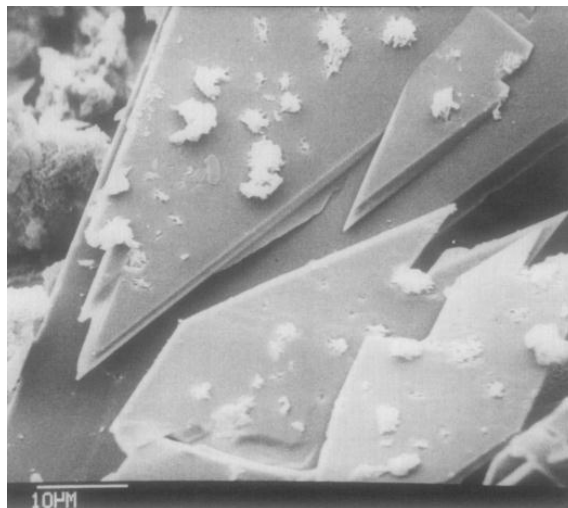


Figure 4.7. Morphology of DCPD with OCP crystals grown on its face.  
(Source: Tas, Bhaduri et al. 2004)

**Dicalcium phosphate** (DCP;  $\text{CaHPO}_4$ ) powder has been tested in vivo and has proven to be biocompatible and biodegradable. It has triclinic crystal structure with the



following lattice parameters:  $a$ ) 6.91,  $b$ ) 6.627,  $c$ ) 6.998Å,  $\alpha$ ) 96.34°,  $\beta$ )103.82°,  $\gamma$ ) 88.33°. It has a Mohr hardness of 3.5 (Kodaka et al. 1999). Monetite molecular structure consists of CaHPO<sub>4</sub> chains bonded together by Ca-O bonds and three types of hydrogen bonds. Two distinct sets of pairs of PO<sub>4</sub> units are found in each primitive cell shown schematically in Figure 4.8 (Xu et al. 1999). Removal of both water molecules from brushite causes the formation of a more compact structure, in which the acidic proton of the HPO<sub>4</sub><sup>2-</sup> groups is structurally disordered. DCP has been reported to be present in fracture callus and possibly in bone. Brushite is converted to monetite near 80 °C and monetite to calcium pyrophosphate above 430 °C upon heating. (Rabatin 1960; Tas et al. 2004; Gbureck et al. 2005). Heat treatment in the presence of water vapour was found to increase the rate of transformation of brushite to monetite (Ball et al. 1973; Lausier et al. 1977; Sivakumar et al. 1998). Temperatures as low as 40 °C were reported for monetite formation in the presence of water vapour (Mirtchi et al. 1989). Crystallization of monetite is also favored to crystallization of brushite in more acidic solutions (Bohner et al. 1997; Bohner et al. 2000). Even though monetite is the most stable calcium phosphate at low pH, it results normally from the recrystallization of brushite, which precipitates faster than monetite. The conversion is faster in water and at higher temperature and acidity (Bohner 2000). Monetite is slightly more stable ( $K_{sp} = 1.83 * 10^{-7} \text{ mol}^2/\text{l}^2$ ) than brushite ( $K_{sp} = 2.59 * 10^{-7} \text{ mol}^2/\text{l}^2$ ) in the pH range between 2 and 7. The rate of crystal growth of brushite however is several orders of magnitude higher than that of monetite causing the cement mixtures set to form mainly brushite in the presence of an aqueous phase. The formation of the thermodynamically stable reaction product is thus kinetically inhibited.

Although brushite and monetite form readily from a calcium phosphate solution, they are thermodynamically metastable with respect to HA and serve as precursor phases. The order of the precipitation from a supersaturated solution is governed not only by the thermodynamic solubility product but also by kinetic factors. Thus, the solid-phase first precipitated undergoes changes in solution toward phases of higher stability. The sequence of calcium phosphate precipitation in general, has been observed by the relative solubility of the different solid phases at constant pH and temperature. Van Kemenade and de Bruyn showed that the Ostwald rule of stages was obeyed, regardless of solution conditions under which the relaxation experiments were made (Van Kemenade M. J. J. M. 1987). Homogenous formation of HA at low supersaturation was never observed but was always preceded by the growth of

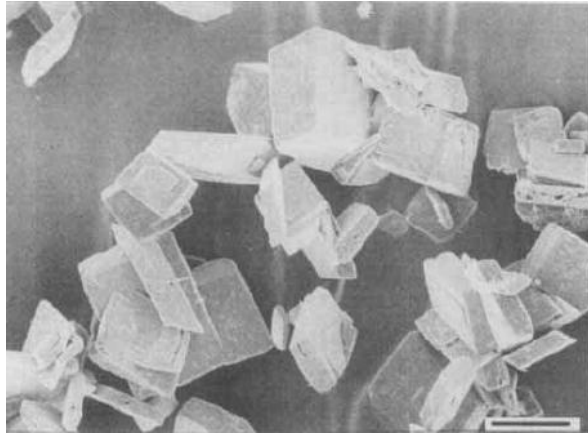


Figure 4.9. Morphology of DCP. Bar=10 microns.  
(Source: Desai, Bhaduri et al. 2007)

***β-Tricalcium phosphate*** ( $\beta$ -TCP;  $\beta$ -Ca<sub>3</sub>(PO<sub>4</sub>)<sub>2</sub>) has rhombohedral crystal structure with the following lattice parameters  $a=b$ ) 10.4183,  $c$ ) 37.3464 Å,  $\gamma$ ) 120°. It can be obtained only by a thermal treatment above at least 650°C. The crystal morphology of  $\beta$ -TCP is shown in Figure 4.10.  $\beta$ -TCP is degradable and it occurs by osteoclastic activity.  $\beta$ -TCP is the main component of brushite CPC (Bohner 2000). The formulation of brushite cement invented by Mirtchi et al. is as follows:

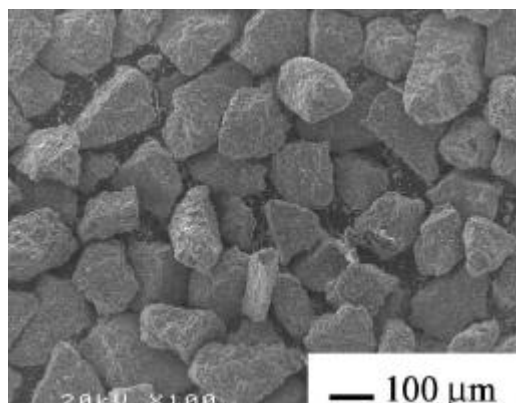
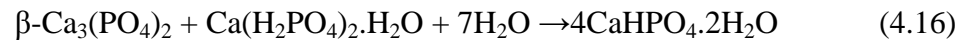


Figure 4.10. Morphology of  $\beta$ -TCP.  
(Source: Bohner, 2000)

***α-Tricalcium phosphate*** ( $\alpha$ -TCP;  $\alpha$ -Ca<sub>3</sub>(PO<sub>4</sub>)<sub>2</sub>) has exactly the same chemical composition as  $\beta$ -TCP with a different crystallographic structure. It has monoclinic structure with the following lattice parameters: *a*) 12.887, *b*) 27.280, *c*) 15.219Å,  $\beta$ ) 126.20°. This difference makes  $\alpha$ -TCP much more soluble than  $\beta$ -TCP.  $\alpha$ -TCP is normally obtained by heating  $\beta$ -TCP above 1125°C, and quenching it to prevent the reverse transformation.  $\alpha$ -TCP is readily transformed into PHA with a Ca:P molar ratio of 1.50 in an aqueous solution which is used to make apatite CPC.  $\alpha$ -TCP has become the major precursor component of most apatite CPC.  $\alpha$ -TCP is biocompatible and more biodegradable than  $\beta$ -TCP (Bohner 2000). Crystal morphology of  $\alpha$ -TCP is shown in Figure 4.11. Reactions of  $\alpha$ -TCP with water are as follows:

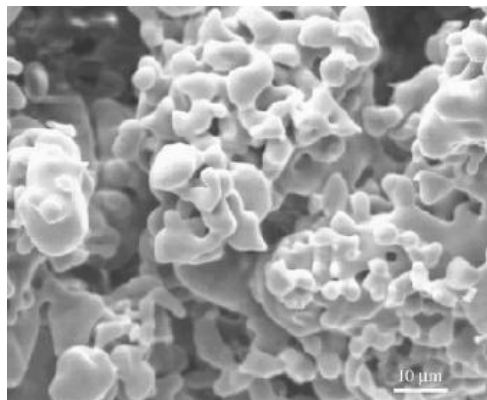
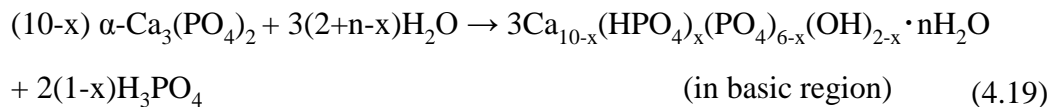
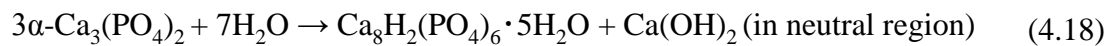
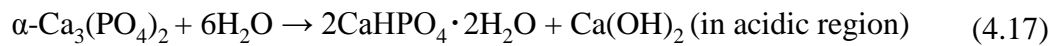
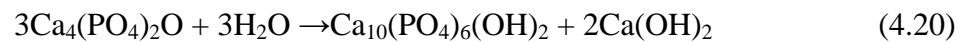


Figure 4.11. Morphology of  $\alpha$ -TCP.  
(Source: Bohner, 2000)

***Tetracalcium phosphate*** (TTCP; Ca<sub>4</sub>(PO<sub>4</sub>)<sub>2</sub>O) is only obtained by a solid-state reaction at high temperatures around 1400 °C, usually between equimolar quantities of DCP and CaCO<sub>3</sub>. The crystal morphology of TTCP is shown in Figure 4.12. TTCP is

the most soluble calcium phosphate below a pH of 5. It is also the most basic calcium phosphate. TTCP is biocompatible and despite its high solubility poorly biodegradable (Bohner 2000). TTCP hydrolyzes to hydroxyapatite in 80 hours at 80 °C but it remains unreacted in water at room temperature for 4 weeks. The low reactivity has been attributed to the formation of a thin, insoluble HA layer around the TTCP particles, inhibiting further hydrolysis (Gbureck et al. 2004). The hydrolysis reactions producing hydroxyapatite and calcium deficient hydroxyapatite are as follows:



$\text{Ca}(\text{OH})_2$  released from TTCP renders biomaterials antimicrobial due to high pH and is utilized in dentistry.

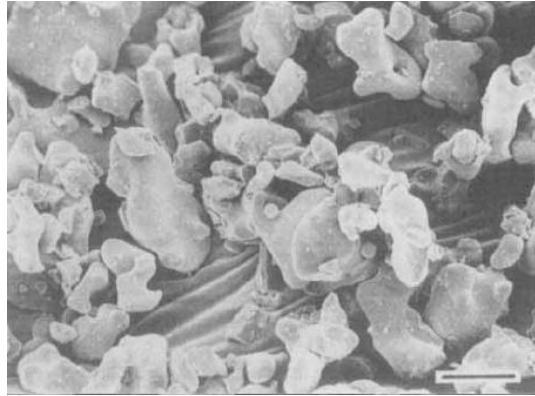
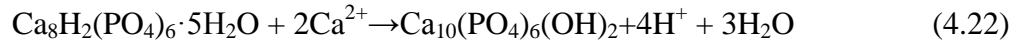


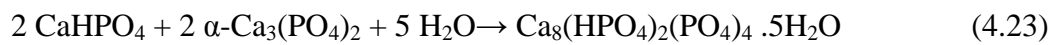
Figure 4.12. Morphology of TTCP. Bar=10 microns.  
(Source: Gbureck, 2004)

**Octacalciumphosphate** (OCP;  $\text{Ca}_8\text{H}_2(\text{PO}_4)_6 \cdot 5\text{H}_2\text{O}$ ) is a precursor in the formation of apatitic calcium phosphates in teeth, bones and other biominerals. It has triclinic crystal structure with the following lattice parameters: *a*) 19.692, *b*) 9.523, *c*) 6.835Å,  $\alpha$ ) 90.15°,  $\beta$ ) 92.54°,  $\gamma$ ) 108.65°. It has needlelike crystal structure as shown in Figure 4.13. OCP is also biocompatible, biodegradable and osteoconductive. Obtaining OCP with a cementitious reaction is difficult because it crystallizes very slowly. OCP is

also metastable and often occurs as a transient intermediate in the precipitation of the thermodynamically more stable PHA (Bohner 2000). The hydrolysis of the OCP to apatitic phases may occur either by the dissolution of OCP, followed by the precipitation of HA, or by a direct solid-state transformation:



One of the cementitious reactions that form OCP is as follows:



However hydrolysis of  $\alpha$ -TCP is feasible in most cases:



OCP has similar crystal structure to HA and they grow epitaxially on each other. OCP has a layered structure involving apatitic and hydrated layers. The apatitic layers have calcium and phosphate ions distributed in a manner similar to that of HA, while the hydrated layer contains lattice water and less densely packed calcium and phosphate ions. It has been found that the hydrated layer of the OCP unit cell forms an interphase between HA and the surrounding solution. If this occurs, the epitaxial intergrowth of OCP and HA is favored. Either the transformation of OCP or simultaneous growth of both phases yields an eventual apatitic phase having calcium ion deficiencies. The transformation is never complete, leaving unhydrolyzed regions of OCP associated with the precipitated apatite. OCP hydrolysis reaction has been found to be accelerated by  $\text{CO}_3^{2-}$ ,  $\text{HPO}_4^{2-}$ , and  $\text{Ca}^{2+}$  ions (Johnsson et al. 1992).

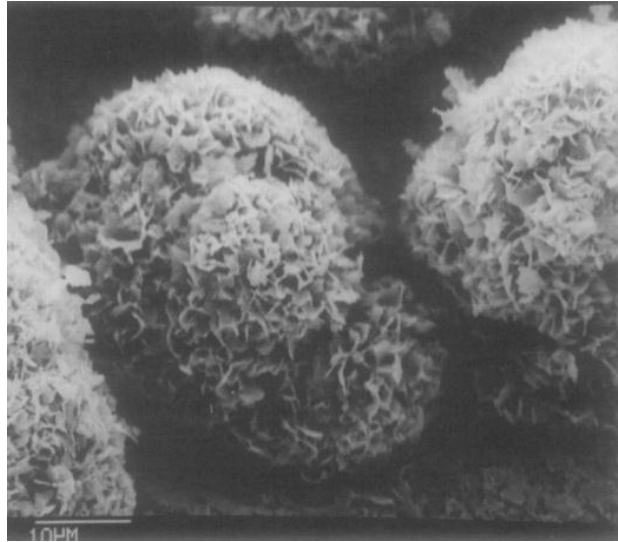


Figure 4.13. Morphology of OCP crystals.  
(Source: Johnsson and Nancollas, 2002)

**Precipitated hydroxyapatite** (PHA;  $\text{Ca}_{10-x}(\text{HPO}_4)_x(\text{PO}_4)_{6-x}(\text{OH})_{2-x}$ ) chemistry is very complex, because precipitated hydroxyapatite can have a Ca:P molar ratio from 1.50 to 1.67. PHA with a Ca:P molar ratio of 1.50 is often called calcium-deficient hydroxyapatite (CDHA) or tricalcium phosphate (TCP). The latter name has led to confusion with  $\beta$ -TCP, which has almost the same chemical composition, but a different crystalline structure. Crystals of PHA may have either monoclinic or hexagonal unit cells. In the more stable monoclinic form with the following lattice parameters:  $a$ ) 9.84214,  $b=2a$ ,  $c$ ) 6.8814Å,  $\gamma$ )  $120^\circ$ , rows of phosphate ions are located along the  $a$  axis, with calcium and hydroxide ions localized between the phosphate groups. Calcium ions are placed in two triangles surrounding two hydroxide ions and in larger hexagons surrounding these calcium positions. The hydroxide ions are situated either above or below the calcium ion planes. The rows of hydroxide ions are directed, alternately, upward or downward. The hexagonal form of PHA with the following lattice parameters:  $a=b$ ) 9.4302,  $c$ ) 6.8911Å,  $\gamma$ )  $120^\circ$ , generally found in biological apatites, has a structure similar to the monoclinic form, but with columns of calcium and hydroxide groups located in parallel channels. Ion substitution can readily occur in these channels, and this may account for the high degree of substitution found in natural apatites. In hexagonal PHA, the hydroxide ions are more disordered within each row, when compared with the monoclinic form, pointing either upward or downward in the structure. This induces strains that are compensated for by substitution or ion vacancy;

hexagonal PHA is therefore seldom a stoichiometric phase (Wang et al. 2008). PHA is obtained by precipitation in an aqueous solution above a pH of 7. Crystals are normally poorly crystalline and of submicron dimensions. PHA has a very large specific surface area, typically 25-100 m<sup>2</sup>/g. It is thus very similar to the apatite present in bone. The main difference is the absence of impurities in the structure, mainly carbonate and magnesium ions (Bohner 2000).

The solubility of PHA increases with a decrease of the Ca:P molar ratio, crystallinity, and of the crystal size. The solubility of TCP (PHA with a Ca:P molar ratio of 1.50) is estimated to be close to that of  $\beta$ -TCP. PHA decomposes upon heating into  $\beta$ -TCP (Ca:P = 1.50), into a mixture of  $\beta$ -TCP and HA ( $1.67 > \text{Ca:P} > 1.50$ ), or into pure HA (Ca:P = 1.67). The decomposition temperature lies above 700 °C. Apart from brushite CPC, all commercial CPC have PHA or a carbonated PHA as the main end-product of the setting reaction. The main difference between the cements after the setting reaction lies in the Ca:P molar ratio, in the cement porosity and the crystallinity of the PHA (Bohner 2000).

At low supersaturations and ambient pH, PHA initially grows as needle-like crystals in the direction of the c-axis whose lengths increase with the extent of reaction. The needlelike crystal structure is shown in Figure 4.14. The nucleation at low supersaturations is called primary nucleation while at high supersaturations, PHA precipitates as a result of both primary, heterogeneous and secondary nucleation at a faster rate. Secondary nucleation is the polynuclear formation of dendritic-like overgrowths on crystal faces normal to the c-axis, which eventually break off into separate entities (Ishikawa et al. 1994). The precipitation of PHA is always found to be preceded by one or more precursors in a sequence that is in agreement with the Ostwald rule of stages. Homogeneous formation of PHA at medium to high concentrations is almost never observed. Accordingly at pH greater than 6.8 and calcium and phosphate concentrations each higher than 0.01 M, heterogeneous formation of ACP is followed by subsequent nucleation of OCP or DCPD which serve as a template for PHA formation (Song Y. 2002). HA is the most stable phase for a large pH interval as seen in Fig 4.16. At pH 6.7 the isotherms for OCP and DCPD intersect. DCPD has the higher solubility above this value and is therefore less stable than OCP. As Ostwald rule of stages predicts that the phase which is thermodynamically least stable forms first, HA precipitation is preceded by first DCPD, then OCP formation above pH 6.7. (Van Kemenade M. J. J. M. 1987).

A high degree of substitution is observed in apatites due to the diffusion of ions in or out of OH<sup>-</sup> channels within the structure, facilitating the exchange of OH<sup>-</sup> ions for water or for other ions. These channels at the crystal surfaces form parallel grooves containing adsorbed water, phosphate, OH<sup>-</sup>, and foreign ions. Ion vacancies in Ca<sup>2+</sup> or OH<sup>-</sup> positions compensate for excess or depleted charges due to substitution. Typical ion substitutions in biological apatites are F<sup>-</sup> for Cl<sup>-</sup> or OH<sup>-</sup>, carbonate for phosphate or OH<sup>-</sup>, and Sr<sup>2+</sup>, Mg<sup>2+</sup>, or Na<sup>+</sup> for Ca<sup>2+</sup> (Wang et al. 2008).

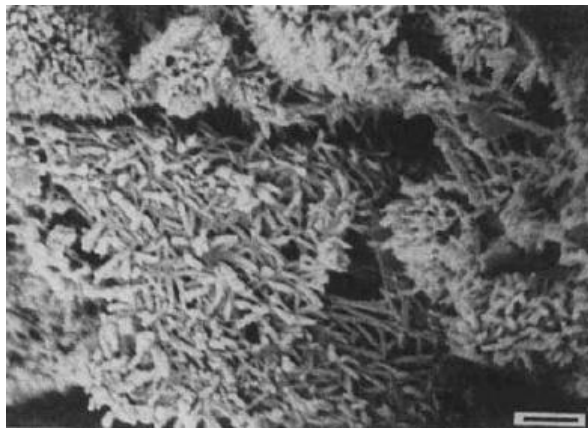


Figure 4.14. Morphology of HA crystals. Bar = 1 micron.  
(Source: Ishikawa and Eanes, 1994)

**Amorphous Calcium Phosphate** (ACP,  $\text{Ca}_3(\text{PO}_4)_2 \cdot n\text{H}_2\text{O}$ ) is basically a tricalcium phosphate with little long range order. It is generally agreed that, both in vitro and in vivo, calcium phosphate precipitation reactions at sufficiently high supersaturation and neutral to basic conditions result in the initial formation of an amorphous calcium phosphate with a molar calcium/phosphate ratio of 1.18 to 2.5. The chemical composition of ACP is strongly dependent on the solution pH. ACP phases with Ca/P ratios in the range of 1.18:1 precipitates at pH 6.6, 1.53:1 at pH 11.7 and even as high as 2.5:1 at higher pH. ACP consists of roughly spherical  $\text{Ca}_9(\text{PO}_4)_6$  clusters close-packed to form larger spherical particles with water in the interstices. These amorphous clusters serve as seeds during PHA crystallization via a stepwise assembly process and were presumed to pack randomly with respect to each other, forming large 300-800 Å spheres (Wang et al. 2008). ACP is a highly unstable phase and hydrolyzes almost instantaneously to more stable phases. Conversion to more stable calcium



phosphate phases takes place by an autocatalytic solution-mediated crystallization process. In the alkaline condition with pH 10, formation of poorly crystalline PHA proceeds without change in the local calcium environment, but with the development of longer range order. An internal rearrangement process is responsible for the ACP-PHA transformation rather than a dissolution-precipitation process. In more acidic solutions, a precipitate of DCPD is formed. In the presence of other ions or under in vivo conditions, ACP may persist for appreciable periods due to kinetic stabilization (Johnsson et al. 1992). The lifetime of the metastable amorphous precursor in aqueous solution was reported to be a function of the presence of additive molecules and ions, pH, ionic strength, and temperature. The induction periods for the formation of ACP and the lifetime of this phase are also increased at lower supersaturations (Wang et al. 2008).

## **4.2. Types of Calcium Phosphate Cements and Their Properties**

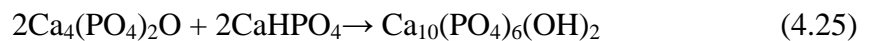
Calcium phosphate cements are generally classified into apatite and brushite cements, and their properties are summarized in the following sections.

### **4.2.1 Apatite Cements**

All existing formulations of calcium orthophosphate cements are divided into two major groups, apatite and brushite cements. The final product of the cement is of paramount importance because it determines the solubility and therefore in vivo bioresorbability. Since the chemical composition of mammalian bone is similar to ion substituted calcium deficient hydroxyapatite, apatite cements have been more extensively investigated. All apatite CPC formulations have precipitated hydroxyapatite (PHA) as the end-product of the reaction, and have a long intrinsic setting time. To remedy this shortcoming, the amount of mixing liquid should be reduced to a minimum (Komath et al. 2000). Therefore, all apatite CPC are viscous, easily moldable, but tend to be difficult to inject. Fine reagents should be used to reduce the intrinsically long setting duration, in particular DCP particles that are limiting factor in the reaction. Another approach is to replace DCP with a markedly more soluble and hence reactive calcium phosphate, such as MCP or MCPM, provided that this reaction does not lead to

the formation of an intermediate product such as DCP or DCPD. However, the dissolution rate of MCPM is so fast that acidic pH values are obtained in the mixing liquid leading to the precipitation of DCPD. Besides controlling the dissolution rate of the reagents, it is important to control the time until hardening occurs. This can be best achieved by using apatite powders as nucleating agent or a mixing liquid with a Ca/P molar ratio of 1.5 that is close to the saturation limit for CDHA precipitation. A setting time in the range of 10-15 minutes can normally be obtained with these additives. For example the long setting periods (> 60 min) normally observed in TTCP + DCPD cements are reduced to acceptable levels by adding accelerators like disodium hydrogen phosphate ( $\text{Na}_2\text{HPO}_4$ ). The slow precipitation is due to the rate limiting nature of dissolution of the reactants which prevents the supersaturation of  $\text{PO}_4^{3-}$  ions. The function of the accelerator is to impart  $\text{PO}_4^{3-}$  ions to the medium to create sufficient supersaturation (Komath et al. 2000). However the use of a phosphate solution appears inadequate because the presence of phosphate ions in the mixing liquid reduces the dissolution rate of reagents and was seen to prolong the overall reaction time (Bohner 2007).

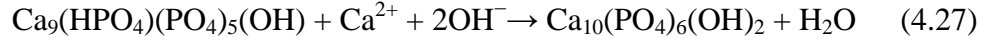
The conventional CPC formulation has been investigated by Ishikawa et al. in detail using various molar ratios, particle sizes, P/L ratios and the results agree that the reaction proceeds by complete dissolution of DCPA and partial dissolution of TTCP particles. Precipitated HA either in stoichiometric or calcium deficient forms nucleates and grows on TTCP particles, thereby reducing their dissolution rate. The reaction sequence however is dependent on the molar ratio of the reactants (Ishikawa et al. 1999). It is reported that different reactions take place at different molar concentrations and HA might exhibit various Ca/P ratios, depending on the TTCP/DCPA ratio in the mixture. For CPC (1:1) the ideal cement setting reaction forms stoichiometric HA:



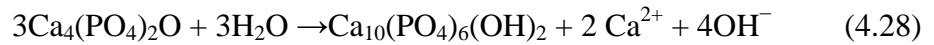
However presence of large amount of residual TTCP in the cement after 24 hours means that the cement setting did not follow the above equation and instead formed a nonstoichiometric calcium deficient HA as follows:



Calcium deficient HA transforms to the thermodynamically more stable stoichiometric HA with time if calcium ions are present in the aqueous solution:



Increasing consumption of TTCP at later stages of the reaction corresponds to hydrolysis of TTCP to stoichiometric or calcium deficient HA:



Since the instantaneous Ca/P consumption of the systems show that stoichiometric ratio of 1.67 is rarely consumed, the setting reaction does not follow the ideal reaction path. Thus at any time in the studied molar ratio range, two main reactions occur either separately or simultaneously. One is the formation of calcium deficient HA from TTCP and DCPA. The other is maturation of calcium deficient HA by transformation to stoichiometric HA using the  $\text{Ca}^{2+}$  formed by the hydrolysis of TTCP to stoichiometric HA or calcium deficient HA.

Studies investigating this cement system indicate that the dissolution of DCPA is the control step in the hydration of CPC. Solubility of DCPA under neutral conditions is far lower than that under basic conditions. Although increasing the specific surface area of DCPA can improve the dissolution rate of DCPA, this measure only slightly increases the degree of supersaturation and the hydration rate. However, increasing the surface area of TTCP causes its dissolution rate to rise, which leads to an increase in pH, and results in a sharp rise in the solubility of DCPA and the supersaturation of HA in the solution. Therefore, the hydration rate rises dramatically, which explains why increasing the SSA of TTCP has a much greater effect on the hydration rate than increasing the SSA of DCPA (Liu et al. 2003).

From a theoretical standpoint, any calcium phosphate that is more acidic than HA can react directly with TTCP to form PHA or CDHA according to the reactions tabulated in Table 4.2.

Table 4.2. Several apatite cement formulations with TTCP precursor and their calculated free energy changes

Apatite Cement Formulations	Free Energy Change $\Delta G$ , kJ
$7 \text{Ca}_4(\text{PO}_4)_2\text{O} + 2 \text{Ca}(\text{H}_2\text{PO}_4)_2 \cdot \text{H}_2\text{O} \rightarrow 6 \text{Ca}_5(\text{PO}_4)_3\text{OH} + 3 \text{H}_2\text{O}$	-2590.6
$2 \text{Ca}_4(\text{PO}_4)_2\text{O} + \text{Ca}(\text{H}_2\text{PO}_4)_2 \cdot \text{H}_2\text{O} \rightarrow \text{Ca}_9(\text{HPO}_4)(\text{PO}_4)_5\text{OH} + 2 \text{H}_2\text{O}$	-759.3
$\text{Ca}_4(\text{PO}_4)_2\text{O} + \text{CaHPO}_4 \cdot 2\text{H}_2\text{O} \rightarrow \text{Ca}_5(\text{PO}_4)_3\text{OH} + 2 \text{H}_2\text{O}$	-357.7
$3 \text{Ca}_4(\text{PO}_4)_2\text{O} + 6 \text{CaHPO}_4 \cdot 2\text{H}_2\text{O} \rightarrow 2 \text{Ca}_9(\text{HPO}_4)(\text{PO}_4)_5\text{OH} + 13 \text{H}_2\text{O}$	-1074.4
$\text{Ca}_4(\text{PO}_4)_2\text{O} + \text{CaHPO}_4 \rightarrow \text{Ca}_5(\text{PO}_4)_3\text{OH}$	-357.7
$3 \text{Ca}_4(\text{PO}_4)_2\text{O} + 6 \text{CaHPO}_4 \rightarrow 2 \text{Ca}_9(\text{HPO}_4)(\text{PO}_4)_5\text{OH} + \text{H}_2\text{O}$	-1074.4
$3 \text{Ca}_4(\text{PO}_4)_2\text{O} + \text{Ca}_8\text{H}_2(\text{PO}_4)_6 \cdot 5\text{H}_2\text{O} \rightarrow 4 \text{Ca}_5(\text{PO}_4)_3\text{OH} + 4 \text{H}_2\text{O}$	-1093.4
$3 \text{Ca}_4(\text{PO}_4)_2\text{O} + 3 \text{Ca}_8\text{H}_2(\text{PO}_4)_6 \cdot 5\text{H}_2\text{O} \rightarrow 4 \text{Ca}_9(\text{HPO}_4)(\text{PO}_4)_5\text{OH} + 14 \text{H}_2\text{O}$	-2590.6
$\text{Ca}_4(\text{PO}_4)_2\text{O} + 2 \text{Ca}_3(\text{PO}_4)_2 + \text{H}_2\text{O} \rightarrow 2\text{Ca}_5(\text{PO}_4)_3\text{OH}$	-356.6

Combinations of TTCP + OCP,  $\alpha$ -TCP + TTCP and  $\beta$ -TCP + TTCP have singular points very close to the solubility isotherm of PHA. Therefore, they have a very low degree of supersaturation and the setting reactions are so slow that these systems are not suitable for cement setting. Only pairs formed by mixing TTCP + MCPM, TTCP + DCPD and TTCP + DCP offer appropriate combinations from the viewpoint of the hardened cement properties. The TTCP + MCPM combination does not usually produce one-step reactions. Formation of DCPD is favored as an intermediate of the reaction kinetics during the setting process (Fernandez 1996). Yet the final product of the reaction remains HA or CDHA due to the stoichiometry of the system. The TTCP + DCPD and TTCP + DCP combinations have been the most studied. These combinations allow the preparation of cements which harden in a suitable time at body or room temperature within a neutral pH range. The most important results obtained from the research on this system indicate that besides the thermodynamic factors, kinetic factors that control the dissolution of both phases are significant, especially in a system where time is limited. The kinetic and thermodynamic factors in control of this system can be extrapolated to other calcium phosphate systems.

Until the mechanisms that control the kinetic processes of setting and hardening of each system is known, the thermodynamic conclusions that are drawn from analysis of the solubility diagrams and relative stability of the various phosphates should be taken as only first approximation, but never as a true explanation of what actually is

happening. Table 4.3 lists various formulations of apatite calcium phosphate cements obtained from literature and their properties.

Table 4.3. Various apatite CPC formulations and their properties.

Components	Precipitate	P/L	Setting Time (minutes)	Porosity (%)	Strength (MPa)	Ref.
<b>TTCP DCPD</b>	HA TTCP trace	2	> 10	52	10-12	(Komath et al. 2000)
<b><math>\alpha</math>-TCP</b>	HA	--	30	55	18	(Monma 2006)
<b><math>\alpha</math>-TCP DCPD</b>	OCP	--	10	48	19	(Monma 2006)
<b>DCPD CaCO<sub>3</sub></b>	HA	--	60	64	3	(Monma 2006)
<b><math>\alpha</math>-TCP TTCP DCP, HA</b>	HA	--	10	--	90	(Monma 2006)
<b><math>\alpha</math>-TCP CaCO<sub>3</sub> MCPM</b>	HA	--	9	--	38	(Monma 2006)
<b><math>\alpha</math>-TCP TTCP MCP</b>	HA	--	18	--	10	(Monma 2006)
<b><math>\alpha</math>-TCP TTCP DCPA CaCO<sub>3</sub>, HA</b>	HA	--	7	--	87	(Monma 2006)
<b>TTCP DCPA</b>	HA	--	20	--	50	(Monma 2006)
<b>ACP DCPD</b>	HA	--	20	--	5	(Monma 2006)
<b><math>\alpha</math>-TCP HA</b>	HA	3	28	--	52	(Khairoun et al. 1997)
<b><math>\alpha</math>-TCP CaCO<sub>3</sub>, HA</b>	HA	3.3	13	--	45	(Khairoun et al. 1997)
<b>MCP Ca(OH)<sub>2</sub> HA</b>	HA	2.5	5	45	17	(Yang et al. 2002)
<b><math>\alpha</math>-TCP DCPA <math>\beta</math>-TCP, HA</b>	CDHA	3.3	8	--	40	(Fernandez et al. 1996)
<b>MCPM CPP</b>	Ca <sub>5</sub> K <sub>4-x</sub> Na <sub>x</sub> (HPO <sub>4</sub> ) <sub>4</sub> (PO <sub>4</sub> ) <sub>2</sub> (H <sub>2</sub> O)	2	10	--	8	(Driessens et al. 2002)
<b>MCPM CPSM</b>	Ca <sub>5</sub> K <sub>4-x</sub> Na <sub>x</sub> (HPO <sub>4</sub> ) <sub>4</sub> (PO <sub>4</sub> ) <sub>2</sub> (H <sub>2</sub> O)	2	20	--	12	(Driessens et al. 2002)
<b>MCPM CaO</b>	HA	2	10	--	20	(Boudeville et al. 1999)

## 4.2.2. Brushite Cements

Mirtchi and Lemaitre introduced this type of cements in 1987. Brushite calcium phosphate bone cements have the advantage of being resorbable in comparison to apatite cements but suffer in application from their fast, water-consuming setting reaction and their low mechanical strength. DCPD is the product of the setting reaction of so-called brushite cements. All brushite CPCs are obtained by an acid-base reaction. The paste of brushite CPC is acidic during setting because brushite can only precipitate at a pH value lower than 6. The pH of the cement paste slowly changes towards the equilibrium pH after setting. If the cement paste contains an excess of basic phase, the equilibrium pH is given by the intersection of the solubility isotherm of the basic phase with that of DCPD (Bohner 2000). For example, the equilibrium pH of  $\beta$ -TCP + MCPM, HA + MCPM, and TTCP + MCPM are 5.9, 4.2 and 7.6, respectively. Several formulations have been already proposed up to now including  $\beta$ -TCP + MCPM,  $\beta$ -TCP +  $H_3PO_4$ , and TTCP + MCPM + CaO (Dorozhkin 2008). The setting time of brushite CPC depends very much on the solubility of the basic phase: the higher the solubility of the basic phase, the faster the setting time. Therefore, the setting time of a CPC made of MCPM and a basic calcium phosphate is in the following order: HA >  $\beta$ -TCP >  $\alpha$ -TCP. Brushite CPC can be initially very liquid in contrast to apatite CPC and still set within a short period of time. However despite initial high reactivity, the hardening reaction of brushite cements typically lasts one day until completion (Bohner 2000). This is likely to be due to the fact that at the end of the setting reaction, the pH of the paste increases which decreases the solubility of the reagents. Two strategies can be proposed to control the start of the setting reaction: (i) using inhibitors of crystal nucleation and growth which leads to an early end to the setting reaction, or (ii) using less soluble reagents (Bohner 2007).

Unlike apatite cements, which consume relatively small amounts (1 mole per 3 moles of powder reactant in  $\beta$ -TCP systems) or no water (TTCP/DCPA systems) during setting, the brushite cement system consumes a lot of water during setting reaction (up to 6 moles per 1 mole of powder reactant), theoretically allowing for the formation of cements with low or almost zero porosities (Hofmann et al. 2009). The disadvantage of brushite forming systems is their high rate of crystal growth leading to very short setting

times and their high dissolution rate leading to low mechanical strength. Table 4.4 lists some of the brushite cement formulations found in the literature and their properties.

Table 4.4. Brushite calcium phosphate cement formulations and properties

Components	Precipitate	P/L	Setting Time (minutes)	Porosity (%)	Strength (MPa)	Ref.
$\beta$ -TCP MCPM	Brushite	4	4.5 $\pm$ 0.5	11	51.6 $\pm$ 7	(Hofmann et al. 2009)
$\beta$ -TCP $H_3PO_4$	Brushite	1.5	5		9 $\pm$ 2	(Gorst et al. 2006)
$\beta$ -TCP MCPM	Brushite	3.3	6.5 $\pm$ 1	32	12.5 $\pm$ 2.5	(Barralet et al. 2004)
$\beta$ -TCP $H_3PO_4$	Brushite	1.75	3	43	1	(Grover et al. 2003)
TTCP MCPM CaO	Brushite	--	12	--	5	(Constantz et al. 1998)
$\beta$ -TCP $H_4P_2O_7$	Brushite	2.25	10	20	25	(Grover et al. 2006)
HA $H_3PO_4$	Brushite	1.5	3	47	8	(Lilley et al. 2005)
Mg-HA $H_3PO_4$	Mg-Brushite	1.5	4	66	3	(Lilley et al. 2005)

The mechanical properties of calcium phosphate cements depend on two conditions: a) the precipitate should grow in the form of clusters of crystals which have a high degree of rigidity, b) the morphology of the crystals should enable entanglement of the clusters. In Driessen's study of 450 different CPC formulations, about 40% set in a time shorter than 60 minutes. However only part of these formulations led to cement bodies having a considerable strength. It was found that both compressive and diametral tensile strength were maximum for stoichiometric compositions with respect to the reaction products (Driessens et al. 1994).

Extensive research on mechanical properties of calcium phosphate cements have been done and results show that apatite cements are more suitable for structural applications while brushite cements are useful as void filler. This is clearly demonstrated by Charriere et al. through the comparison of the mechanical properties of the two cement types. The apatite cement was composed of dicalcium phosphate and calcium carbonate while brushite cement was made of  $\beta$ -tricalcium phosphate and monocalcium phosphate monohydrate. Compression, tensile and shear strengths and moduli of the set cements were measured and compared to those of trabecular and cortical bones. Table 4.5 gives the ultimate values and Figure 4.15 gives the graphical comparison of these properties. Although apatite cement properties exceed those of

trabecular bone, it should be remembered that cements contain about 40% microporosity while that required for a scaffold for trabecular bone substitution is around 70%. With the introduction of controlled macroporosity, the mechanical properties of apatite cement would match those of trabecular bone (Charriere et al. 2001).

Table 4.5. Mechanical properties of apatite and brushite cements  
(Source: Charriere and Terrazzoni 2001)

	Tension		Compression		Poisson's ratio (dimensionless)	Shear	
	Modulus (GPa)	Strength (MPa)	Modulus (GPa)	Strength (MPa)		Modulus (GPa)	Strength (MPa)
Brushite	$6.6 \pm 0.4$	$1.3 \pm 0.3$	$7.9 \pm 0.3$	$10.7 \pm 2.0$	$0.16 \pm 0.03$	$2.7 \pm 0.4$	$2.9 \pm 0.4$
Hydroxyapatite	$12.3 \pm 0.8$	$3.5 \pm 0.9$	$13.5 \pm 0.8$	$75.0 \pm 4.2$	$0.14 \pm 0.02$	$4.8 \pm 0.3$	$9.8 \pm 2.6$

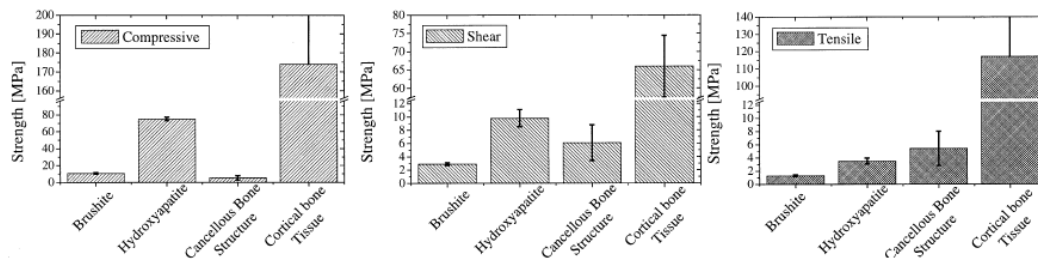


Figure 4.15. Comparison of cement and natural bone mechanical properties to bone mechanical properties. (Source: Charriere, Terrazzoni et al. 2001)

### 4.3. Thermodynamics of Calcium Phosphate Cement Setting Reaction

In the fundamental CPC formulation of  $\text{CaO}$  and  $\text{H}_3\text{PO}_4$ , when powders of calcium oxides are stirred in an acid-phosphate solution, they dissolve slowly and release calcium cations in the solution. These cations react with the phosphate anions within the solvent and form a precipitate of salt molecules. These molecules form an ordered structure and grow into crystals under the proper conditions. This ordered crystalline solid of the reaction products is the CPC. Thus, CPC formation is a result of the following three steps:

- I. The acid phosphates dissolve in water, release phosphate anions, and form an acid-phosphate solution of low pH.



- II. The calcium oxides dissolve gradually in the low pH solution and release  $\text{Ca}^{2+}$  cations.
- III. The phosphate anions react with the newly released cations and form a coordinated network and consolidate into a CPC.

The proper conditions to form a CPC are governed by the rate of reactions that control each of these three steps. Since acid phosphates selected for use in the CPC process are soluble, their dissolution rate is comparatively high and, hence, uncontrollable. The phosphate reaction between dissolved cations and anions described in step III is also inherently fast and, again, cannot be controlled. Thus, the only reaction that can be controlled is the dissolution of calcium oxides given in step II. On the other hand a calcium oxide that dissolves fast will also react too fast and produce only a precipitate but not a well-coordinated network of cement. If the dissolution rate is too low, calcium oxide powder will remain mostly unreacted in the solution as powder. The product resulting from the slow reaction forms a thin coating on the surface of individual particles of calcium oxides in such cases. This coating acts like a shield and inhibits further dissolution of the powder hindering the formation of cement. For this reason, it is crucial that appropriate calcium oxides, based on their moderate solubility, are selected to synthesize CPCs (Wagh 2004).

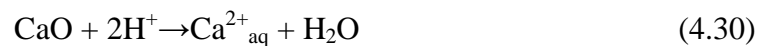
The dissolution of acid phosphates, or that of calcium oxides, is an endothermic or heat absorbing reaction. As a result, there is some cooling effect on the slurry due to the first two steps given above. However, the acid–base reaction described in step III is inherently exothermic, so it generates heat during the reaction. The amount of net heat generated and the rate at which it is produced are also important factors in forming the CPCs. The heating due to the acid–base reaction more than compensates for the initial cooling resulting from the dissolution steps, and the net effect of all three steps is to heat the slurry.

Once calcium ions are dissociated and screened in an acid solution that is rich with phosphate anions, the kinetics of transformation to a CPC is very similar to that of the conventional sol–gel process of fabricating ceramics with the major difference here being that the acid–base reaction used in forming CPCs carries the mixture all the way to the formation of ceramics, while in the sol–gel process the gels are ultimately sintered to form superior ceramics (Wagh 2004). Three main steps describe the kinetics of the CPC formation:

1. *Aquosol formation by dissociation:* When calcium oxides are stirred into an acid solution, they dissolve slowly, and release cations and oxygen-containing anions. The calcium cations react with water molecules and form positively charged “aquosols” by hydrolysis.
2. *Acid–base reaction and the formation of gel by condensation:* The sols subsequently react with the aqueous phosphate anions to form the hydrophosphate salts, while the hydroxonium and oxygen react to form water. As calcium oxide powder is stirred in water, more aquosols are formed in the solution and they start connecting to each other. This leads to the formation of a gel of loosely connected salt molecules.
3. *Saturation and crystallization of the gel into a ceramic:* As the reaction proceeds, this process introduces more and more reaction products into the gel, and it thickens. At this point, it becomes difficult to mix the slurry. The gel now crystallizes around the unreacted core of each grain of calcium oxide into a well-connected crystal lattice that grows into monolithic cement.

The dissolution is the controlling step in the formation of the CPC. It determines which oxides will form a ceramic and which will not, while the hydration step determines the pH range in which the cement will be formed. Formation of a well crystallized cement or a poorly crystallized precipitate will depend on how slowly or rapidly the dissolution of the oxides occurs in the acid solution (Wagh 2004).

When the alkaline oxide CaO is stirred in phosphoric acid, the pH of the solution rises slowly due to the neutralization of this acid. The acid dissolves sufficiently even at the initial low pH, and  $\text{H}_3\text{O}^+$  and  $\text{H}_2\text{PO}_4^-$  anions are readily available to react with the ions produced by the dissolution of calcium oxides. Subsequently, consolidation of the precipitate in the neutral solution leads to the formation of calcium phosphates. CaO dissolves according to the following equation:



The dissolution constant  $K$  for this reaction is defined as:

$$K = \frac{[\text{Ca}^{2+}(\text{aq})][\text{H}_2\text{O}]}{[\text{H}^+]^2[\text{CaO}]} \quad (4.31)$$

where brackets indicate molar concentration of individual species. This quantity determines whether calcium oxide satisfies the condition of slow dissolution and will form calcium phosphate in a given pH range. Taking the logarithm of the dissolution constant gives:

$$\log K = \log \left[ \frac{[\text{Ca}^{2+}(\text{aq})]}{[\text{CaO}]} \right] + \left[ \log \frac{[\text{H}_2\text{O}]}{[\text{H}^+]^2} \right] \quad (4.32)$$

$$\log \frac{[\text{H}_2\text{O}]^{1/2}}{[\text{H}^+]} = \text{pH} \quad (4.33)$$

The negative logarithm of the dissolution product  $\text{pK}_{\text{sp}}$  is called the solubility product constant for 1 mole of calcium oxide:

$$\text{pK}_{\text{sp}} = -\log K = -2 \text{pH} - \log[\text{Ca}^{2+}] \quad (4.34)$$

It indicates the extent of dissolution of a particular chemical species in a given solution (Wagh 2004). Brown and Chow has shown that the thermodynamic solubility product depends on the purity of the compound, which in turn, depends on the method of preparation. Deviations from constant solubility can also be caused by a solid surface with high free energy and high solubility formed during thermal preparation. A constant solubility is obtained after this surface layer is removed by repeated washing. Free ions like fluoride, carbonate and magnesium influence the structure of the calcium phosphates and therefore have specific effects on their solubilities. Fluoride and citrate decrease and carbonate and magnesium increase the solubility of hydroxyapatite (Amjad 1998).

A ternary system with two phases, a solution and a solid salt, in equilibrium at a known temperature and pressure, has one degree of freedom according to Gibbs' phase rule. The geometric figure defined is a line called the solubility isotherm when it is represented in a phase diagram. The solubility isotherm fixes compositions of all saturated solutions in relation to that salt. The solubility isotherm of a calcium phosphate can be calculated taking into account the solubility product constant, dissociation constants of phosphoric acid  $\text{H}_3\text{PO}_4$  and calcium hydroxide  $\text{Ca}(\text{OH})_2$ , stability constants of the different formed complexes and an appropriate model to

calculate the activity coefficients of the different chemical species involved (Fernandez et al. 1999). Solubility constants of the main calcium phosphates at 25 °C are given in Table 4.1 in the order of decreasing Ca/P. Increasing the calcium to phosphorus ratio Ca/P is associated with an increase in the basicity of these salts.

Relative stability of different calcium phosphate salts for different pH values can be obtained from Figure 4.16 showing the solubility diagrams for the ternary system  $\text{Ca}(\text{OH})_2\text{-H}_3\text{PO}_4\text{-H}_2\text{O}$  at 37 °C. The solubility isotherms of different calcium phosphate salts in equilibrium with their saturated solution are shown, in a representation of the logarithm of calcium concentration of the saturated solution versus pH. A common characteristic of the isotherms in Figure 4.16 is that they have a negative slope in the neutral and acid regions ( $\text{pH} < 7$ ) of the solubility diagrams. This means that these compounds became more soluble as the pH decreases. The extent of the slope gives an idea of the solubility increase of the salt as the pH decreases. In that sense, the isotherm slope is taken as a measure of the salt basicity because the solubility of a basic salt will be greater than the one of an acid salt for an equal decrease in pH. According to this criterion, DCPD and DCP are acid salts in comparison to OCP,  $\alpha$ -TCP,  $\beta$ -TCP, HA and TTCP since they have lower negative slopes (Fernandez et al. 1999). The isotherms show that the amount dissolved at equilibrium depends on the thermodynamic solubility product of the compound and the pH of the solution. The pH dependency is due to the fact that orthophosphoric acid is both a weak acid and a polybasic acid; the concentrations of  $\text{HPO}_4^-$ ,  $\text{H}_2\text{PO}_4^{2-}$  and  $\text{PO}_4^{3-}$  change dramatically with the pH of the solution (Amjad 1998).

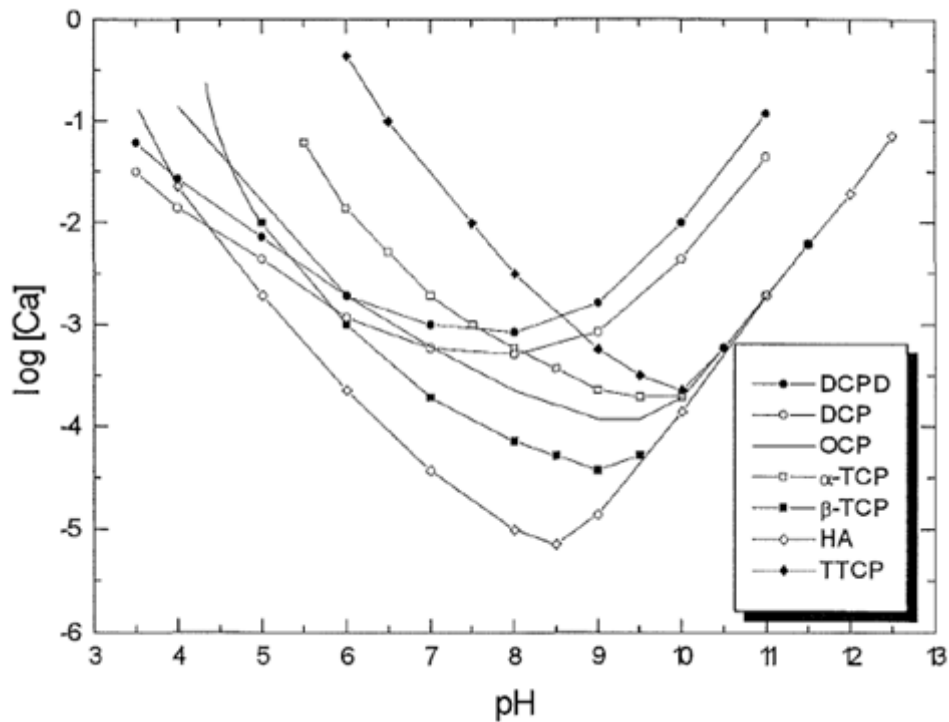


Figure 4.16. Solubility isotherms of different calcium phosphates in equilibrium with their solutions for the ternary system  $\text{Ca}(\text{OH})_2\text{-H}_3\text{PO}_4\text{-H}_2\text{O}$  at 37 °C in a representation of  $\log [\text{Ca}]$  versus pH. (Source: Chow, 1991)

According to the solubility diagram shown in Figure 4.16 it can be observed that, at 37 °C, HA is the least soluble salt down to a pH of 4.2; for pH values lower than this, DCP is the least soluble salt. Also, it can be observed that for pH values lower than 8.5 the most soluble salt is TTCP; for pH values higher than 8.5, the most soluble salt is DCPD. MCPM which is not shown in the graph is also highly soluble regardless of pH around  $\log[\text{Ca}] = -1$ . TTCP and DCPA were used as the starting materials in the first HA-forming CPC because these are the most soluble salts and thus would provide the greatest driving force for the HA-forming reaction. Since all non-HA calcium phosphate compounds are more soluble than HA at a pH above 4.4, these compounds can also be used as starting materials for HA-forming cements. In these cases, a smaller driving force for the HA-forming reaction is in effect, and use of a setting accelerator, most commonly a sodium phosphate solution, is required to produce rapid cement hardening (Chow 2009). Although several non-HA calcium phosphate phases, such as OCP and whitlockite, are more soluble than HA under neutral pH conditions, they can be the major phase in the cement products. This is because these phases precipitate more

rapidly than HA under certain solution conditions. Because DCPD and DCPA are the least soluble calcium phosphates under acidic pH, they are the products formed in acidic CPC formulations. All other calcium phosphate phases being more soluble under these pH conditions, can be used as the starting materials for the DCPD or DCPA-forming cements (Chow 2009).

Singular points for binary calcium phosphate mixtures are given in Table 4.6 (Fernandez et al. 1999). They predict the thermodynamic behavior of several compounds in a solution. For example, if two compounds are in excess in a more acid solution than the singular point, the more basic compound will dissolve and the more acid will precipitate as in point  $P_1$  of Figure 4.17 since, at that pH, the solution is supersaturated in relation to the more acid compound. This dissolution-precipitation process continues until pH and composition reach the singular point, where both compounds will be in equilibrium with the solution and neither will precipitate. The conclusion would be similar if the initial mixture composition is located in a more basic solution than the singular point. In that case, the more acid compound will dissolve and the more basic will precipitate as in point  $P_2$  of Figure 4.17 since, at that pH, the solution is supersaturated in relation to the most basic compound. Finally, the singular point pH will be reached as has been explained above. The singular points for  $\text{Ca}(\text{OH})_2\text{-H}_3\text{PO}_4\text{-H}_2\text{O}$  system can be used to predict the extent of reaction for the particular calcium phosphate precursors in consideration.

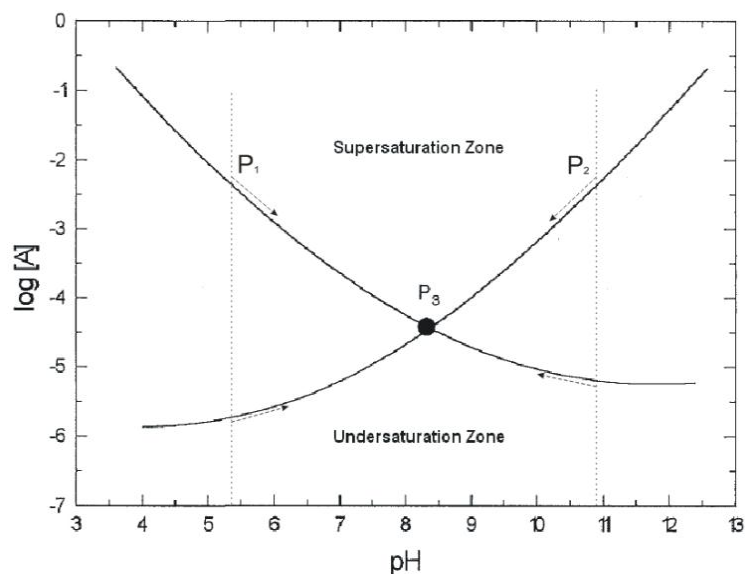


Figure 4.17. Relative positions of the isotherms for acidic and basic cement precursors as they approach the equilibrium condition at singular point in hypothetical  $\text{A}(\text{OH})_n\text{-H}_n\text{B-H}_2\text{O}$  system.

Table 4.6. Singular points between calcium phosphates in the system  $\text{Ca}(\text{OH})_2\text{-H}_3\text{PO}_4\text{-H}_2\text{O}$  at 37 °C (Source: Fernandez, Gil et al. 1994)

Pairs	Chemistry description	pH ( $p = 1.013 \times 10^{-25}$ Pa)	pH ( $p = 1.66$ MPa)
TTCP-MCPM	$\text{Ca}_4(\text{PO}_4)_2\text{O-Ca}(\text{H}_2\text{PO}_4)_2\cdot\text{H}_2\text{O}$	6.5	5.3
TTCP-DCPD	$\text{Ca}_4(\text{PO}_4)_2\text{O-CaHPO}_4\cdot 2\text{H}_2\text{O}$	8.5	6.5
TTCP-DCP	$\text{Ca}_4(\text{PO}_4)_2\text{O-CaHPO}_4$	8.8	6.8
TTCP- $\alpha$ -TCP	$\text{Ca}_4(\text{PO}_4)_2\text{O-}\alpha\text{-Ca}_3(\text{PO}_4)_2$	9.5	N/A
TTCP-OCP	$\text{Ca}_4(\text{PO}_4)_2\text{O-Ca}_8(\text{HPO}_4)_2(\text{PO}_4)_4\cdot 5\text{H}_2\text{O}$	10.0	N/A
TTCP- $\beta$ -TCP	$\text{Ca}_4(\text{PO}_4)_2\text{O-}\beta\text{-Ca}_3(\text{PO}_4)_2$	11.3	N/A
$\alpha$ -TCP-MCPM	$\alpha\text{-Ca}_3(\text{PO}_4)_2\text{-Ca}(\text{H}_2\text{PO}_4)_2\cdot\text{H}_2\text{O}$	5.5	5.5
$\alpha$ -TCP-DCPD	$\alpha\text{-Ca}_3(\text{PO}_4)_2\text{-CaHPO}_4\cdot 2\text{H}_2\text{O}$	7.8	N/A
$\alpha$ -TCP-DCP	$\alpha\text{-Ca}_3(\text{PO}_4)_2\text{-CaHPO}_4$	8.2	N/A
$\beta$ -TCP-MCPM	$\beta\text{-Ca}_3(\text{PO}_4)_2\text{-Ca}(\text{H}_2\text{PO}_4)_2\cdot\text{H}_2\text{O}$	4.4	4.4
$\beta$ -TCP-DCPD	$\beta\text{-Ca}_3(\text{PO}_4)_2\text{-CaHPO}_4\cdot 2\text{H}_2\text{O}$	5.4	5.7
$\beta$ -TCP-DCP	$\beta\text{-Ca}_3(\text{PO}_4)_2\text{-CaHPO}_4$	6.0	6.0
OCP- $\beta$ -TCP	$\text{Ca}_8(\text{HPO}_4)_2(\text{PO}_4)_4\cdot 5\text{H}_2\text{O-}\beta\text{-Ca}_3(\text{PO}_4)_2$	4.7	4.7
OCP-DCPD	$\text{Ca}_8(\text{HPO}_4)_2(\text{PO}_4)_4\cdot 5\text{H}_2\text{O-CaHPO}_4\cdot 2\text{H}_2\text{O}$	6.2	6.2
OCP-DCP	$\text{Ca}_8(\text{HPO}_4)_2(\text{PO}_4)_4\cdot \text{OH-CaHPO}_4$	6.9	N/A
HA-MCPM	$\text{Ca}_{10}(\text{PO}_4)_6(\text{OH})_2\text{-Ca}(\text{H}_2\text{PO}_4)_2\cdot\text{H}_2\text{O}$	3.5	3.3
HA-DCPD	$\text{Ca}_{10}(\text{PO}_4)_6(\text{OH})_2\text{-CaHPO}_4\cdot 2\text{H}_2\text{O}$	3.8	3.1
HA-DCP	$\text{Ca}_{10}(\text{PO}_4)_6(\text{OH})_2\text{-CaHPO}_4$	4.3	4.3
MCPM-DCP	$\text{Ca}(\text{H}_2\text{PO}_4)_2\cdot\text{H}_2\text{O-CaHPO}_4$	2.7	2.7
MCPM-DCPD	$\text{Ca}(\text{H}_2\text{PO}_4)_2\cdot\text{H}_2\text{O-CaHPO}_4\cdot 2\text{H}_2\text{O}$	3.2	3.5

Different kinds of calcium phosphate phases may precipitate from saturated solutions under proper physical and chemical environment. The supersaturation of a system with respect to a given calcium phosphate indicates the thermodynamic driving force of the precipitation reaction. The calculated values for supersaturation help to understand and interpret the precipitation of calcium phosphates. It is defined as the ratio of concentration of a solute in the solution to its solubility.

The driving force of crystallization is the difference between the chemical potentials of the solute in the liquid and the solid phases. These two chemical potentials are equal at equilibrium conditions. The chemical potential of the solute in the crystals may then be expressed as the potential in the solution at equilibrium. The general expression of the chemical potential in a solution is

$$\mu = \mu_0 + RT \ln a \quad (4.35)$$

where  $\mu_0$  is the standard chemical potential of the crystallizing product,  $R$  the gas constant,  $T$  the absolute temperature and  $a$  is its activity in the solution. The theoretical value of the supersaturation then is

$$\mu - \mu^* = RT \ln \left( \frac{a}{a^*} \right) \quad (4.36)$$

where  $\mu^*$  and  $a^*$  are the chemical potential and the activity of the solute in the solution at equilibrium, respectively. In the case of an ionic reaction between ions  $A^{y+}$  and  $B^{x-}$  the chemical potential to be used can be expressed as

$$\mu = x(\mu_{A0} + RT \ln(a_A)) + y(\mu_{B0} + RT \ln(a_B)) \quad (4.37)$$

Thus the driving force of the crystallization is

$$\Delta\mu = x(\mu_A - \mu_A^*) + y(\mu_B - \mu_B^*) = RT \ln \left( \frac{a_A^x a_B^y}{a_A^{*x} a_B^{*y}} \right) \quad (4.38)$$

or

$$\Delta G = -\frac{R}{v} \ln \frac{IP}{K_S^0} = -\frac{RT}{v} \ln S \quad (4.39)$$

where  $IP$  is the ionic product of the precipitating phase,  $K$  is the thermodynamic solubility product,  $v$  is the number of ions in a unit formula of the precipitating calcium phosphate phase,  $R$  the gas constant,  $T$  the absolute temperature and  $S$  the supersaturation ratio.  $\Delta\mu$  is the difference of chemical potential for one molecule  $A_xB_y$ , and the supersaturation is defined as:

$$S = \left( \frac{a_A^x a_B^y}{a_A^{*x} a_B^{*y}} \right) = \left( \frac{a_A^x a_B^y}{K} \right) \quad (4.40)$$

where the numerator of the last term is the ionic activity product of a compound in solution and  $K$  is the solubility product. The ionic activity product is the product of the concentration and the activity coefficient of the complex. There are many equations available for calculation of activity coefficients of ionic species in solution. Debye-Huckel law is only suitable for dilute electrolyte solutions where the main deviation from ideality is assumed to be due to long-range coulomb interactions between ions and is generally accurate for solutions with an ionic strength  $<0.01$  M (Sheikholeslami et al. 2003):

$$-\log a_A = C_y^2 [I^{1/2}] \quad (4.41)$$



where I is the ionic strength and the coefficient  $C_y$  is a constant for a fixed temperature:

$$C_y = 0.3770 + 4.684 \times 10^{-4} (T - 273.15) + 3.74 \times 10^{-6} (T - 273.15)^2 \quad (4.42)$$

Expansion of the Debye-Huckel law by Davies resulted in successful prediction of ionic activity coefficient and is applicable to solutions with an ionic strength  $< 0.15$  M:

$$-\log a_A = C_y^2 \left[ I^{1/2} / (1 + I^{1/2}) - 0.3I \right] \quad (4.43)$$

The total ionic strength of the solution is given as:

$$I = \frac{1}{2} \sum_i c_i z_i^2 \quad (4.44)$$

in which  $c_i$  is the molar concentration of each ion unit (Lu et al. 2005).

For complex systems like electrolyte solutions, the ion specific interaction equation developed by Pitzer is an expansion of Debye-Huckle and is valid up to 6 M (Sheikholeslami et al. 2003). The activity coefficient given by Pitzer takes into account the ion interaction due to electrostatic forces, long and short-range interactions between ions in solution (Pitzer 1973):

$$\begin{aligned} \ln \gamma_X = (|z_+|)^2 \left\{ -A\Phi \left[ \frac{\sqrt{I_x}}{1 + 1.2\sqrt{I_x}} + \frac{2}{1.2} \ln(1 + 1.2\sqrt{I_x}) \right] + \sum_c \sum_a m_c m_a \beta_{ca}'' + \sum_c \sum_{c''} m_c m_{c''} \Phi_{cc''}'' \right. \\ \left. + \sum_a \sum_{a''} m_a m_{a''} \Phi_{aa''}'' \right\} + \sum_a m_a \left\{ 2\beta_{Xa} + \frac{1}{2} \left( \sum_c m_c |z_c| + \sum_a m_a |z_a| \right) \ell_{Xa} \right\} \\ + \sum_c m_c \left( 2\Phi_{Xc} + \sum_a m_a \Psi_{Xca} \right) + \sum_a \sum_{a''} m_a m_{a''} + |z_+| \sum_c \sum_a m_c m_a \ell_{ca} \end{aligned} \quad (4.45)$$

where subscripts X, c, and c'' represent cationic species and Y, a, and a'' represent anionic species; X and Y are cation and anion of interest with charge  $z_+$  and  $z_-$ ;  $v_+$  and  $v_-$  are number of cation and anion moles dissociated in one mole of salt, respectively. The summation index, c or a, denotes the sum over all cations or anions in the system while the double summation index, c and c'' or a and a'', denotes the sum over all

distinguishable pairs of dissimilar cations or anions;  $m$  is the molality of the species;  $I$  is the ionic strength of the solution,  $A$  is the temperature dependent constant and ion interaction parameters for 1-1 (NaCl), 1-2 (Na<sub>2</sub>SO<sub>4</sub>), 2-1 (CaCl<sub>2</sub>) are given as follows:

$$A_{\phi} = 0.3770 + 4.684 \times 10^{-4} (T - 273.15) + 3.74 \times 10^{-6} (T - 273.15)^2 \quad (4.46)$$

$$\beta_{ij} = \beta_{ij}^{(0)} + \beta_{ij}^{(1)} \left\{ \frac{2}{(2\sqrt{I_S})^2} [1 - (1 + 2\sqrt{I_S}) \exp(-2\sqrt{I_S})] \right\} \quad (4.47)$$

$$\beta_{ij}^* = \frac{\beta_{ij}^{(1)}}{I_S} \left\{ \frac{-2}{(2\sqrt{I_S})^2} \left[ 1 - \left( 1 + 2\sqrt{I_S} + \frac{(2\sqrt{I_S})^2}{2} \right) \exp(-2\sqrt{I_S}) \right] \right\} \quad (4.48)$$

The Pitzer ion interaction approach is based on sets of theoretically and empirically derived equations that account for the interactions between the particular ions present in a solution and for indirect forces arising from the ion-solvent interaction. It takes into consideration various combinations of ion-ionic interactions in a solution: cation-anion; cation-cation and anion-anion; cation-cation-anion and anion-anion-cation; cation-neutral molecule and anion-neutral molecule interaction. A valuable simplification Pitzer introduced is the assumption that the semi-empirical ion interaction parameters for simple solutions are identical with those in multiple electrolyte solutions (Krumgalz 2001). The parameters  $\beta_{c,a}$ ,  $\beta_{c,a}^v$ , etc. determined from single electrolyte solutions and from mixed solutions with either a common cation or anion. These constants are given by Pitzer and other researchers (Pitzer et al. 1973; Pitzer et al. 1974).

Pitzer model has been adopted in literature concerning various application areas from geochemistry to wastewater treatment due to its advantages that include avoiding some of the restrictions or assumptions such as the intrinsic limitation to low or moderate concentrations or the extrapolation of solution properties beyond the solubility limit of electrolytes in pure water (Krumgalz 2001). Solubility and precipitation of different salts, are known to be determined by the ionic composition of the solution. The theoretical prediction of thermodynamic properties of multiple electrolyte solutions is the ultimate point one can reach in order to be able to control the phases present in a complex medium. The solubilities of solutes in complex systems can be calculated

provided that equilibrium constants are known and activity coefficients can be theoretically calculated. The equations developed by Pitzer have been quite successful in predicting the thermodynamic properties of mixed electrolyte solutions over a wide range of solution concentrations, and were found to be especially effective for the prediction of thermodynamic properties of ionic activity coefficients and osmotic coefficients, apparent molal heat capacities and apparent molal volumes.

Bromley also has independently developed a system of representation and estimation for activity coefficients of strong electrolytes (Bromley 1973). The model is described as a simplification of the Pitzer system. The third virial coefficient is omitted, and the second virial coefficient is modified into a form, still dependent on ionic strength, but with a single parameter  $B$  which is in effect a relationship between  $\beta_1$  and  $\beta_0$ . It is shown that the  $B$  values can be approximated from two parameters for each ion  $B_m$  and  $\delta_m$  or  $B_X$  and  $\delta_X$  by the following equation.

$$B = B_m + B_X + \delta_m \delta_X \quad (4.49)$$

The system investigated in this study consists of the calcium phosphate precursors,  $\beta$ -TCP, MCPM, ionic modifiers citric acid, NaCl and calcium phosphate products brushite and monetite. In this complex system calcium and phosphate concentrations are always expected to be more than the equilibrium saturation concentrations for end products brushite and monetite for the entire range of ionic strength studied. The factors that may act to cease the supersaturation are any physical or chemical modifications on precursor surface that hinder its dissolution completely. Citric acid is known to chelate calcium ions and bind to  $\beta$ -TCP surfaces (van der Houwen et al. 2003) and premature cement precipitation on  $\beta$ -TCP grains are known to form a surface barrier against their dissolution (Wang et al. 2008). Whether ionic strength of the solution is able to cease or lower the supersaturation is predictable using Pitzer or Bromley approach. Ion activity coefficients calculated using Pitzer approach in addition to the instantaneous or estimated calcium, phosphate concentration and the solubility constants for brushite and monetite together enable calculation of supersaturation with respect to these phases as a function of ionic strength. Application of the Pitzer model to this system necessitates available data on ion interaction parameters for  $\text{Ca}^{2+}$ ,  $\text{HPO}_4^{2-}$ ,  $\text{Na}^+$ ,  $\text{Cl}^-$ , and  $\text{C}_6\text{H}_5\text{O}_7^{3-}$  ions. These constants were

obtained from research papers of Pitzer and Bromley (Bromley 1973; Pitzer et al. 1973). Variation of brushite and monetite supersaturation with respect to ionic strength that is calculated by the author is graphically represented in Figure 4.18. Accordingly, both supersaturations of brushite and monetite and the difference between their supersaturations decrease exponentially with the increasing ionic strength of the solution.

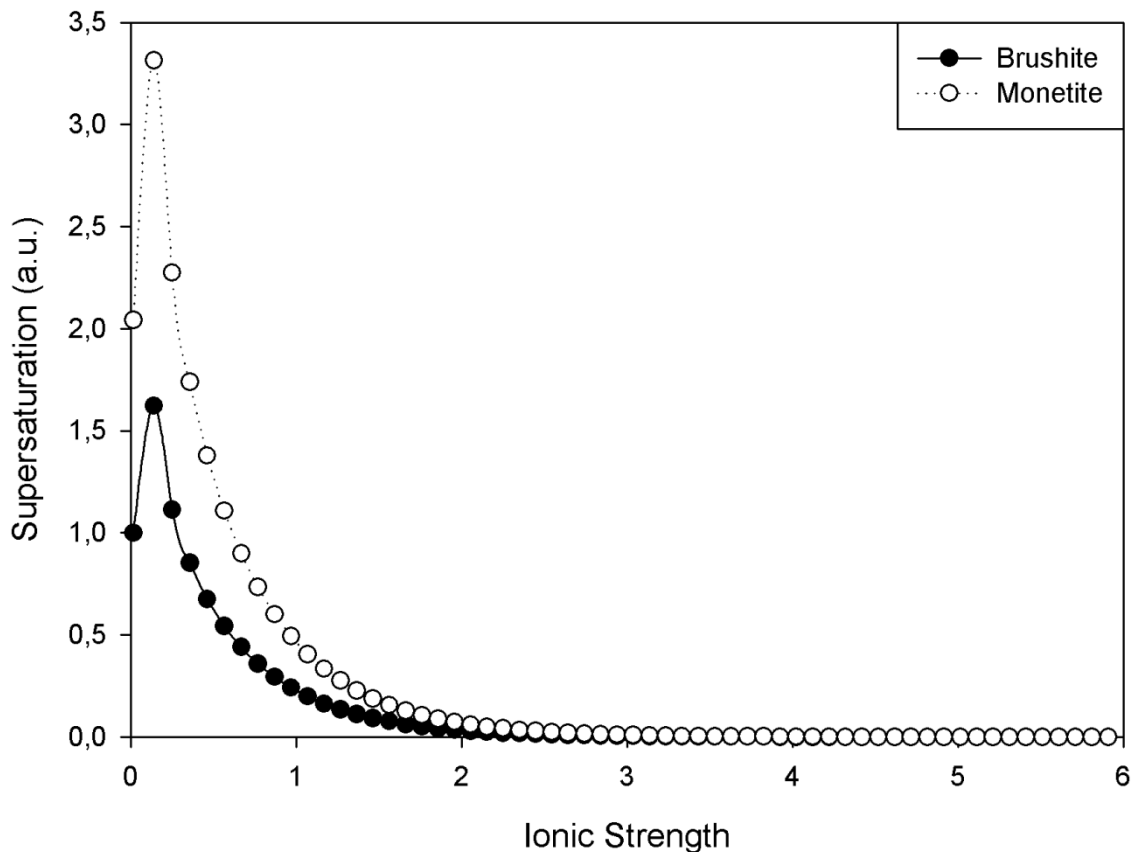


Figure 4.18. Supersaturations of brushite cement end products brushite and monetite predicted by the Pitzer ion interaction model.

#### 4.4. Kinetics of Calcium Phosphate Cement Setting Reaction

Although the likelihood of precipitation of a particular calcium phosphate phase is ultimately determined by the thermodynamic driving force of formation, kinetic factors may be considerably more important in controlling the nature of the solids formed. Ostwald's Rule of Stages postulated in 1897 states that the crystal phase that nucleates in a supersaturated solution is not the phase that is thermodynamically stable at that temperature and pressure but rather another metastable phase that is closest in free energy to the parent phase. There are also examples of phase transformations where

a metastable phase exists but does not form due to immediate transformation into another phase. It is possible to observe the metastable intermediate by slowing down the kinetics of the reaction.

Calcium phosphate cements must react slowly in order to provide sufficient time to the surgeon for implantation, and fast enough to prevent delaying the operation. Also its setting time and the extent of reaction should be balanced to impart strength to the final product. It is therefore essential to perfectly understand and control the kinetics of CPC setting reactions. The setting reaction of CPCs consists of three stages:

- I. Dissolution of reactants to saturate the mixing liquid in calcium and phosphate ions
- II. Nucleation of crystals
- III. Growth of crystals

It is demonstrated in many CPC experiments that nucleation occurs during the mixing stage. This is explained as flash-like formation of very small critical nuclei at very high local supersaturation. HA growth was always preceded by formation and growth of precursors like ACP, OCP, DCPD, and DCP. The precursor phase influences the kinetics of the precipitation of subsequent phases by serving as template material for heterogeneous nucleation of these phases and their further growth. On the other hand, the solution composition and therefore the supersaturation with respect to other solid phases is also modified by the precipitation of a precursor phase (Van Kemenade M. J. J. M. 1987). The metastable precursors serve as template for heterogeneous nucleation of these phases, their further growth and subsequent transformation to HA.

Crystal growth takes place by the deposition and incorporation of dissolved solute molecules onto steps on the crystal surfaces, causing them to advance quickly along the surface, perpendicular to the step. The growth of crystals by facets usually occurs in the classic spiral pattern given in Figure 4.19 whereby one or more screw dislocations on the crystal surface provide a continuing source of steps. The important parameters controlling the growth rate are the energy required to create a step at the crystal surface and the free-energy barrier for an adsorbed solute molecule to be incorporated into the crystal. In this process, the incorporation of these growth units into kinks is rate-determining at relatively low supersaturation. Kink sites are the most reactive portions of step edges. At higher supersaturations, a "birth and spread" growth model predicts two-dimensional nucleation on existing crystal surfaces.

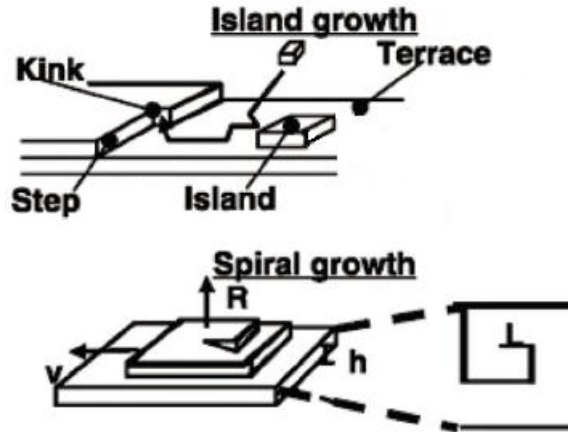


Figure 4.19. Illustration of growth at a crystal surface by attachment of molecules to step edges on either islands or dislocation spirals. (Source: Wang, Nancollas et al. 2008)

There are three alternative growth models applicable to calcium phosphate cements:

- A. Diffusion controlled continuous growth – Applicable to early stage cement setting where nucleation sites are away from the dissolving particles.
- B. Mononuclear growth – Surface nucleation controlled growth of metastable phases.
- C. Polynuclear growth – Applicable to heterogeneous growth of highly supersaturated stable phases.

Among many theories describing crystal dissolution and crystallization, not one model completely covers all the stages of these processes. The most basic diffusion theory claims that both dissolution and crystallization processes are purely diffusion controlled and the rate of dissolution at a given temperature and under equal concentrations equals the rate of crystallization. Surface energy theory states that the crystal faces with minimum energy grow first and disappear. Layer theory assumes that flat crystal surfaces are in fact made up of moving layers of monatomic height and contain numerous kinks that enable growth units to be incorporated during growth. This is a highly ideal model that leaves dislocations and imperfections out of consideration. It is now realized that screw dislocations acting as a source of infinite kinks promote rapid growth. Burton-Cabrera-Frank theory was developed to account for the growth rate in terms of spiral geometry and supersaturation of the solution. Mononuclear growth proceeds with a layer mechanism where the formation of a surface nucleus is

assumed to be the rate-limiting step in the addition of a new layer to the growing crystal. Polynuclear model states that growth develops from surface nucleation that occur on faces, corners and edges of the crystal and further nuclei develop on the monolayer nuclei as they spread across the crystal face. Although most of these theories generally consider crystal growth as a simple two-stage process consisting of bulk diffusion and surface integration, a more complex process in the following order may be taking place (Mullin 2001):

1. Bulk diffusion of hydrated ions through the diffusion boundary layer
2. Bulk diffusion of hydrated ions through the adsorption layer
3. Surface diffusion of hydrated or dehydrated ions
4. Partial or total dehydration of ions
5. Integration of the ions into the lattice
6. Counter diffusion of released water through the adsorption layer
7. Counter diffusion of water through the boundary layer

Crystal growth mechanisms covered by various models may occur simultaneously and have a combined effect on the crystal growth rate. Nielsen states that when two mechanisms act in parallel, the individual rates are additive and the one that gives the faster rate is rate-determining. When two mechanisms act consecutively, they share the driving force and the slower one is rate determining (Nielsen 1984).

It must be emphasized that it is difficult to divide systems into those that are limited by diffusion and those that are limited by integration with respect to crystal growth (Mersmann 2001). First, the growth limitation depends on supersaturation. Furthermore, small crystals under 100 microns often grow under integration limitation, whereas the growth of large crystals of the same system can be described by the assumption of a purely diffusive resistance and an indefinitely fast integration reaction. It can be assumed that large crystals exhibit sufficient dislocations and, therefore, sufficient integration sites so that growth will not be limited by the integration reaction.

The influence of solution supersaturation on crystal growth rate is explained in the context of several models as such: Although the screw dislocation mechanism causes a certain roughening of the crystal surface, the density of energetically favorable surface sites is small and the increase in the growth rate with increasing supersaturation is moderate. There is a possible change in growth mechanisms with increasing supersaturation and surface nucleation becomes a source of much higher densities of

kink sites. It is considered that adsorbed growth units collide with each other and form clusters and, finally nuclei. For a two-dimensional cluster to be stable, sufficient growth units must join together to form a nucleus of critical size on the crystal surface. Once this has been achieved, other growth units can join onto the corners of the nucleus so that crystal growth takes place over the entire surface area. Growth depends on the ratio of the spreading rate to the time required for another nucleus to be formed on the smooth surface. Thus all growth models have varying degree of dependency on supersaturation. The general relation of supersaturation to growth rate applicable to three models follows (Mersmann 2001):

$$v = A\sigma^p \exp\left(-\frac{B}{\sigma}\right) \quad (4.50)$$

where  $v$  is the growth rate,  $\sigma$  is the supersaturation,  $A$ ,  $p$ , and  $B$  are constants. For the mononuclear model, the spreading rate of the layer is very rapid compared to the surface nucleation rate and  $p= 0.5$ . The other extreme configuration is the polynuclear mechanism, where the spreading rate of the layer is slow compared to new nuclei formed; in this case,  $p= -1.5$ . There exists an intermediate model, birth and spread model, which considers nuclei born on incomplete layers and growing at a constant step advancement independently from each other. This model relates crystal growth to supersaturation with a constant  $p=5/6$ . Polynuclear or activated growth mechanism exhibits a very strong dependency of growth on supersaturation, because with increasing supersaturation, the time elapsing between two nucleation events decreases rapidly. For a distinct range of small supersaturation, almost no growth occurs, and when supersaturation rises above a critical value, the growth rate increases rapidly to the domain of limiting bulk diffusion.

In principle, the growth rate follows the scheme presented in Figure 4.20. Viewed on a molecular scale, crystal growth preferably takes place at energetically favorable surface sites. Only the imperfections present at the crystal surface, such as screw dislocations, act as possible sources for integration sites for very low supersaturations. With increasing supersaturation, the formation of surface nuclei from adsorbed growth units becomes more probable and new sources for integration sites are possibly created by a birth and spread mechanism (B+S). Generally, the surface nucleation mechanisms exhibit a very strong dependency of the growth rate on



supersaturation. The spreading of the nuclei loses ground compared to new nuclei by further increasing the supersaturation, continuously roughening the surface by polynuclear mechanism (PN), and thus forming numerous energetically favorable integration sites. The course of the growth rate with supersaturation continues to be controlled solely by bulk diffusion with a rough surface providing enough favorable sites for approaching growth units.

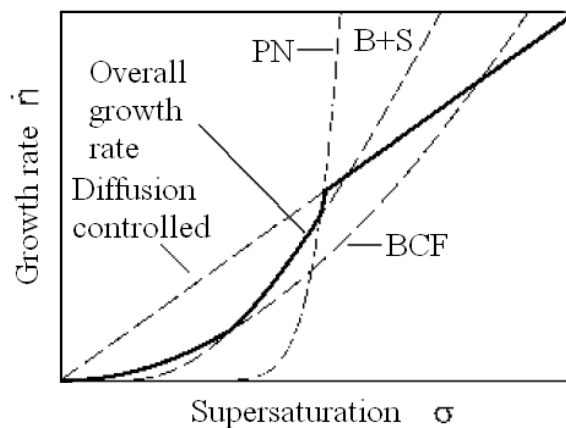


Figure 4.20. Rate determining growth mechanisms as a function of supersaturation. (Source: Mersmann, 2001)

In general, it is difficult to predict the controlling step for crystal growth. The growth rate for the integration stage increases approximately with (solubility)<sup>4/3</sup> for a given supersaturation (Mersmann 2001). The supersaturation  $S$  must be much higher for sparingly soluble substances in order to obtain a fast growth rate of  $10^{-9} < G < 10^{-7}$  m/s. When new crystals are formed by primary nucleation at low levels of supersaturation  $S < 10$ , the nuclei are smooth and appreciable growth is gained only by the polynuclear growth mechanism with the characteristic strong increase in the growth rate with supersaturation. In contrast, nuclei produced in the range  $20 < S < 100$  exhibit molecular rough surfaces and their growth can be described by combination of diffusion and integration controlled growth. Based on experimental and theoretical data, Mersmann reaches the following conclusions on the dependence of growth mechanisms on supersaturation and solubility that can be deduced from Figure 4.21 where  $\Delta C$  is the concentration gradient,  $C^*$  is the equilibrium concentration and  $C_c$  is the molar density:

brushite cement solution at relatively low ionic strengths is around 0.1. According to the figure, corresponding growth rate for brushite cement in pure water is in the range  $10^{-5}$ - $10^{-8}$  m/s which is considered a fast reaction by Mersmann.

van Kemenade developed a set of equations simplified by certain restrictions for the diffusion controlled, mononuclear and polynuclear growth mechanisms based on Nielsen's fundamental work on crystallization kinetics theory, (Van Kemenade M. J. J. M. 1987). These restrictions are that the precipitate particles are monodisperse, isotropic, and the concentration does not change by more than ten during the experiment. Accordingly the following derivations were done for each mechanism.

Growth can be described by following the advancement of the reaction as a function of time. If the concentration of monomers in solution is  $c(0)$  at  $t = 0$  and  $c(t)$  at time  $t$ , then the extent of reaction  $\alpha$  can be defined as

$$\alpha(t) = \frac{c(0)-c(t)}{c(0)-c(\infty)} \quad (4.51)$$

where  $c(\infty)$  is the saturation concentration. The relation between particle size ( $r$ ) and the extent of the reaction ( $\alpha$ ) can be written as

$$r(t) = r(\infty)[\alpha(t)]^{1/3} \quad (4.52)$$

where  $r(\infty)$  is the particle size at the end of the reaction. A relation between  $\alpha$  and  $t$  can be derived for the different growth models.

#### **Diffusion controlled growth:**

Nielsen's relation for linear growth rate ( $\dot{r}$ ) is expressed as

$$\dot{r} = \frac{v \cdot D}{r} (c(t) - c(\infty)) \quad (4.53)$$

with  $v$  the molecular volume and  $D$  the diffusion coefficient. Combining equations 4.51-4.53 yields

$$\dot{\alpha} = K_D \alpha^{1/3} (1 - \alpha) \quad (4.54)$$

where

$$K_D = \frac{3v.D}{r(\infty)^2} (c(0) - c(\infty)) \quad (4.55)$$

### Mononuclear growth:

Nielsen's expression for size-dependent rate of growth is,

$$\dot{r} = \beta \cdot r^2 \cdot d \cdot J_{2D} \quad (4.56)$$

where  $r^2$  represents the surface area of one layer with thickness  $d$ ,  $J_{2D}$  is the flux of surface nuclei, and  $\beta$  is a shape factor. Nielsen approximates the flux expression as

$$J_{2D}(t) = kc(t)^m \quad (4.57)$$

with a constant value of exponent  $m$ , which is justified if the concentration  $c(t)$  does not change more than one decade during the experiment. For a degree of reaction defined by

$$c(t) = c(0) \cdot (1 - \alpha(t)) \quad (4.58)$$

Derivation yields

$$\dot{\alpha} = K_m \cdot \alpha^{4/3} (1 - \alpha)^m \quad (4.59)$$

where

$$K_m = 3k\beta d \cdot r(\infty) \cdot c(0)^m \quad (4.60)$$

### Polynuclear growth:

Nielsen's relation for growth by polynuclear layers is expressed as

$$\dot{r} = 0.6(J_{2D})^{1/3} \cdot w^{2/3} \cdot d \quad (4.61)$$

where  $w$  is the spreading velocity across the surface which is limited by surface diffusion as

$$w = d^2 D (c(t) - c(\infty)) \quad (4.62)$$

Derivation yields

$$\dot{\alpha} = K_p \pi \alpha^{2/3} (1 - \alpha)^p \quad (4.63)$$

where  $p = (m+2)/3$  and

$$K_p = 1.8 r(\infty)^{-1} (k d^7 D^2 c(0)^{m+2})^{1/3} \quad (4.64)$$

Hence, for both diffusion controlled and integration controlled growth models the growth rate can be described by a general growth equation of the form:

$$\dot{\alpha} = K \alpha^n (1 - \alpha)^m \quad (4.65)$$

where the term  $\alpha^n$  represents the dependence of growth rate on the surface area or size of the monodisperse particles and the term  $(1 - \alpha)^m$  represents the dependence on the decreasing supersaturation during the precipitation.

#### **4.4.1. Effect of Ionic Modifiers on the Kinetics of Calcium Phosphate Cement Setting**

Any substance other than the material being crystallized is considered an impurity. It may be an unintentionally added species or an electrolyte in the solvent. Impurities may suppress growth entirely, enhance it or exert a highly selective effect, acting only on certain crystallographic faces. The mechanism of actions are various. Impurities can change the properties of the solution, equilibrium saturation concentration and hence the supersaturation. They can alter the characteristics of the

adsorption layer at the crystal-solution interface, influencing the integration of growth units. If there is a lattice similarity, they can be incorporated into the crystal. They can adsorb selectively on to different crystal faces at kinks, steps and faces and retard their growth rates as schematically represented in Figure 4.22 (Mullin 2001). Mullin states that if kink site adsorption is possible, very low impurity levels in the solution is enough for growth retardation. More and more impurity would be needed if the preferred adsorption mode is step site and face site adsorption respectively.

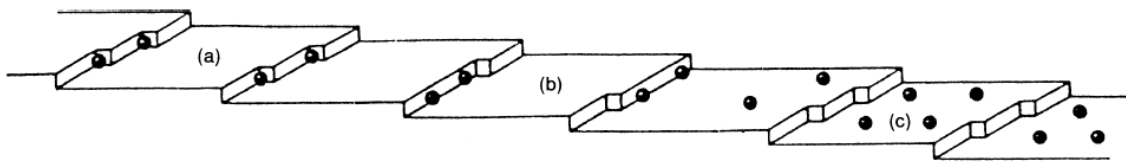


Figure 4.22. Kossel model for the sites of impurity adsorption: a) kink sites, b) step sites, c) face sites. (Source: Mullin, 2001)

Four mechanisms of microscopic crystallization dynamics influenced by impurities have been proposed: (1) step pinning, (2) incorporation, (3) kink blocking, and (4) step edge adsorption. Each of these major mechanisms for growth inhibition exhibits a characteristic dependence of step speed on supersaturation and impurity concentration. The influences of impurities on crystal growth are attributed to their adsorption at kinks, edges, and terraces of a growing surface according to a classical theory of growth inhibition, thus reducing the growth rate by hindering the movement of growth steps. Citrate is found to decrease the step density in brushite (Wang et al. 2008).  $Mg^{2+}$  and  $Zn^{2+}$  ions, amino acids, proteins and carbonate ions have been reported to inhibit hydroxyapatite growth and also prolong the setting reaction of CPCs (Bohner 2007).

A classical model of growth inhibition known as the Cabrera-Vermilyea (C-V) model attributes the influences of impurities on crystal growth to their adsorption at kinks, edges, and terraces of a growing surface, thus reducing the growth rate by hindering the movement of growth steps (Wang et al. 2008). Impurities adsorbed at step edges or on the terraces ahead of migrating steps create a field of “impurity stoppers” that act to block the motion of elementary steps, thereby decreasing their velocity. When the average spacing between impurity molecules is less than a critical distance,

the steps are unable to advance. As a consequence, the C-V model predicts the presence of a “dead zone” region of positive supersaturation where no growth occurs. As the supersaturation is increased further and the critical diameter becomes smaller, the steps begin to squeeze through the “fence” of impurities and the step speed rises rapidly, eventually reaching that of the pure system. Nancollas et al. demonstrated the inhibitory effect of citrate on brushite surfaces as seen in Figure 4.23 (Tang et al. 2005). Citrate is also found to decrease the step density in brushite (Wang et al. 2008).  $Mg^{2+}$  and  $Zn^{2+}$  ions, amino acids, proteins and carbonate ions have been reported to inhibit hydroxyapatite growth and also prolong the setting reaction of CPCs (Bohner 2007).

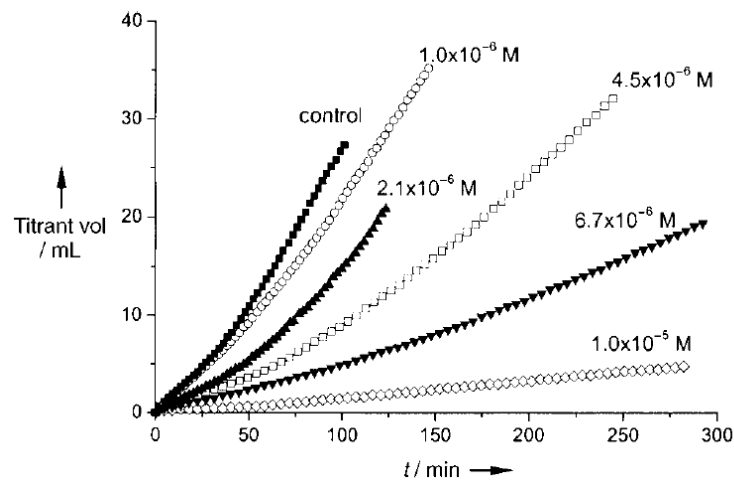


Figure 4.23. Variation in brushite growth with citrate concentration. (Source: Tang and Darragh 2005)

Carbonate ions have the most significant effect on CPC microstructure such that incorporation of carbonate in the apatite cement causes a decrease in precipitated crystallite size. The size and shape of the crystallites change from long needles to smaller rods to tiny spheroids (Takagi et al. 2001). Carbonate ions inhibit HA growth due to adsorption at surface sites and also the less favorable coordination in phosphate or hydroxide sites in the lattice (Johnsson et al. 1992). It has been reported that carbonate substitutes mainly for phosphate. Charge balance may be achieved by a cation incorporation, and the substitution of carbonate usually results in poorly crystalline structures. In cases where carbonate occupies the phosphate sites, the smaller size induces strain in the lattice, leading to a unit cell contraction (Wang et al. 2008). It is reported that the supersaturation required for precipitation of slightly carbonated apatite

was higher than that of apatite in simulated body fluid (Lu et al. 2005). Carbonate ions disturb the crystallization of the growing apatite crystallites to such an extent that, depending upon the amount of carbonate added, the material may give an amorphous X-ray diffraction pattern. A submicron structure of interconnected microcrystals are responsible for the improved final mechanical properties of the cement formulation with addition of calcium carbonate. Moreover, carbonate ions cause the bonding in the apatite to become weaker and more isotropic, which results in the small spheroidal crystals and in faster dissolution rates (Fernandez et al. 1998).

The crystallization of calcium phosphates must also take into account the probable positive influence of biomacromolecules in the solution phase. A common feature of proteins that control mineralization is the presence of segments in a relatively rigid conformation having high affinities for apatite surfaces. Even though a protein may have charged groups in favorable positions, the possibility of nucleation initiation decreases if they do not bind sufficient calcium ions. Mineralization takes place under high supersaturation by the adsorption of spontaneously precipitated crystallites onto a layer of immobilized proteins if the HA binding groups are in favorable positions. Highly oriented layers of crystals, such as those in bone and enamel, are formed by adsorption of crystal faces on to proteins at the sites of mineralization. These crystals continue an oriented overgrowth directed by their adsorption to the proteins (Nancollas et al. 1994). Anionic proteins are more effective on HA crystallization. Examples are type I collagen, osteocalcin, statherin, acidic amino acids aspartic and glutamic acid (Koutsopoulos et al. 2000; Wang et al. 2008).

Electrolytes that modify the surface charge of precipitated calcium phosphates also significantly affect the growth mechanism through electrostatic hinderance. The effect of polyelectrolytes on the formation and properties of ACP and on the nucleation and growth morphology of the crystalline phase is explained as a dual role in inducing and/or inhibiting crystal nucleation in the ACP-apatite transformation system by Nancollas et al (Wang et al. 2008). Accordingly, the polyelectrolyte molecules adsorb reversibly on the surfaces of ACP particles in a random conformation at low concentrations. A large number of small, highly charged particles are created as a consequence, which concentrate oppositely charged  $\text{Ca}^{2+}$  or  $\text{HPO}_4^{2-}$  ions and thus provide effective sites for secondary nucleation. The flexible polyelectrolyte chains spread out into a flat position at high concentrations, at the surface of ACP particles.

This type of adsorption process is considered irreversible and inhibits the transport of ions to the template surface, thus inhibiting secondary nucleation.

Two basic explanations in general are brought for the combined influence of impurity concentration and supersaturation on crystal growth:

- i) Growth is only suppressed in the low range of supersaturation while at higher supersaturation the impurity effect disappears completely
- ii) Growth rate suppression occurs throughout a very wide range of supersaturation

Generally it is observed that impurity adsorption rate decreases as the supersaturation is increased (Mullin 2001).

Analogously to crystal growth, dissolution is accompanied by the movements of dissolution steps on the crystal surface. Impurity molecules can adsorb on some active sites on these steps, blocking their movement (Hurle 1993). This reduction in the step velocity,  $v$ , or the kinetic effect of impurity adsorption, leads to a decrease in the crystal dissolution rate. Alternatively, adsorption of additive at step edges may result in a reduction of edge free energy,  $\gamma$ , an important thermodynamic parameter in crystal dissolution models, and an increase in the crystal dissolution rate.

Dissolution depends on at least two interrelated factors: one is the nucleation rate  $R$  (creation of pits) and the other the rate of step movement,  $v$ . Additives present in solution, especially organic molecules, that may complex with free impurities will reduce their competition with surface dissolution units, resulting in an increase in the concentration of the latter. The additive molecules may interact with the surface layers, resulting in a decrease in the barrier for the formation of dissolution steps. Since  $R$  is very sensitive to changes in the barrier, this can result in a considerable increase in dissolution rate. On the other hand, the velocity,  $v$ , is not influenced by the barrier, but may be reduced markedly due to kinetic effects, interpreted in terms of the adsorption of inhibitor molecules on crystal surfaces. The dissolution rate of  $\beta$ -TCP is mainly controlled by the direct formation of dissolution steps, suggesting that for citric acid, the former effect, or the promotion of nucleation, dominates. HA dissolution is mainly controlled by reactions at kinks and dissolution steps. Thus, the retardant effect on  $v$  dominates in the presence of citric acid and HA dissolution is inhibited. However, the dissolution mechanism of DCPD at such high undersaturations is complex and controlled mainly by volume diffusion.



In common with the behavior of many other weak acid additives, citric acid (CA) probably influences dissolution through adsorption at active sites on the crystal surfaces and binding to calcium ions (Tang et al. 2005). The electrostatic effects are important since CA is an organic triacid becoming more negatively charged with increasing pH. The species  $C_6H_7O^-$  (20%) and  $C_6H_6O^{2-}$  (75%) dominate at pH 5.5, while at pH 6.2, most CA molecules exist in the forms  $C_6H_6O^{2-}$  (55%) and  $C_6H_5O^{3-}$  (45%). CA has more functional anionic groups for metal ion binding at higher pH, and therefore has a greater influence on dissolution. The decrease in heat evolution with increasing citric acid concentration clearly demonstrates that fact in Figure 4.24 from Hofmann's calorimetric analysis of brushite cement setting reaction, (Hofmann et al. 2006).

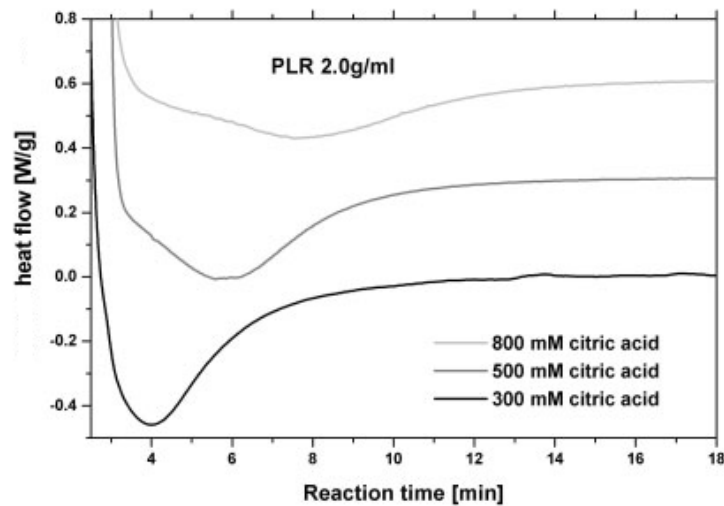


Figure 4.24. Heat flow of the exothermic setting reaction of brushite cement versus time for fixed P/L 2.0 g/mL and three different citric acid retardant concentrations. (Source: Hofmann and Nazhat 2006)

Besides acting as an inhibitor impurity, citrate also is an effective electrolyte that modifies the surface charge of calcium phosphate crystals. Barralet et al. have shown that citrate ions can reduce viscosity of apatite cements by increasing the surface charge of the reactants (Barralet et al. 2005). This had three important consequences; high powder/liquid ratio resulting in workable mixes producing stronger cements, compacted mixes to produce very low porosity, high strength materials, and injectable cement mixes.

Constant composition kinetic studies of the mineralization of DCPD and OCP show that these phases are less influenced by inhibitor molecules than is HA (Nancollas et al. 1994). The influence of fluoride ion is especially interesting in view of its positive effect on HA crystal growth. The hydroxyapatite surface has a remarkable affinity for fluoride. Fluoride is readily incorporated from solution into the HA surface, but although the formation of a fluoroapatite film prevents the onset of apatite dissolution, the fluoride ion does not penetrate into the bulk material but remains at the surface. It is relatively easy to replace surface hydroxyl groups by fluoride ions, but the fluoride is not expected to penetrate deeply into the apatite material itself. Possible modes of incorporation of fluoride include ion exchange, adsorption, and crystal growth of calcium fluoride, fluoroapatite ( $\text{Ca}_5\text{F}(\text{PO}_4)_3$ ), or fluorohydroxyapatite solid solutions ( $\text{Ca}_5\text{F}_x(\text{OH})_{1-x}(\text{PO}_4)_3$ ) (Wang et al. 2008).

Moreover, HA dissolution is inhibited by the presence of compounds such as bisphosphonates, polyphosphates or pyrophosphoric acid (Bohner 2007). Bisphosphonates which are metabolically stable analogs of pyrophosphate, bind strongly to hydroxyapatite crystals and suppress osteoclast-mediated bone resorption and crystal growth. The oxygen atom that binds the two phosphate groups of pyrophosphate (P–O–P) is substituted by a carbon atom (P–C–P) in bisphosphonates (Panzavolta et al. 2009). The utility of two potent aminobisphosphonates, Alendronate and Pamidronate in TTCP-DCPA cements is investigated in the study by Panzavolta et al. It is seen that initial and final setting times increase on increasing the content of bisphosphonate. The increase is greater for the final setting time, and it is more evident for Alendronate than for Pamidronate, in agreement with the greater affinity of Alendronate for calcium ions (Panzavolta et al. 2009).

Magnesium ions, polyphosphates, and citrate in apatite CPCs strongly inhibit nucleation (Bohner 2007). Whereas polyelectrolytes and certain proteins like amelogenin and phosphovitin are known to promote HA nucleation. Most notable is the effect of citrate on nucleation rate which also influences the calcium ion saturation, mechanical strength and setting liquid amount. It is revealed in a recent study that the presence of citrate influences the precipitate both in terms of size and perfection of the crystal lattice. Citrate addition increased the supersaturation required for HA nucleation due to adsorption of citrate onto the newly formed calcium phosphate nuclei (van der Houwen et al. 2003). The carboxyl groups are situated in the  $\text{OH}^-$  or  $\text{PO}_4^{3-}$  sites of the HA increasing the imperfections of the formed apatitic lattice and making possible for

high amounts of impurities to be included in the structure. The formation of HA was not totally inhibited by citrate however the cell parameters of the precipitate are modified. Crystal size range of HA decreases from 50-100 nm with deionized water to 5-50 nm with citrate solution.

Several studies were performed to investigate calcium phosphate nucleation inhibition by polyphosphates as calcium phosphates are the main precursors in urine responsible for formation of kidney stones as effective and common heterogeneous nuclei for calcium oxalate crystallization. The work by Grases quantitatively determines the inhibition potential of major polyphosphates present in the body (Grases et al. 2000). The author suggests that phytate, a substance present in normal urine, exerts a potent action as crystallization inhibitor of calcium salts. Accordingly, the effectiveness in preventing brushite crystallization decreases in the sequence:

*phytate > polyphosphate > EDTPO > etidronate > pyrophosphate > triphosphate > medronate* (4.66)

A vital salivary protein in the development of enamel, amelogenin was found to kinetically promote HA nucleation, producing elongated rod-like HA crystals at a concentration as little as 5.0 µg/mL (Wang et al. 2008). Similarly, phosvitin, a representative phosphoprotein was found to promote heterogeneous HA nucleation while inhibiting ACP to HA transformation (Onuma 2005). Immobilized phosvitin acts as the favored nucleation site for HA; therefore, the heterogeneous nucleation and growth of HA on phosvitin-adsorbed ACP was promoted.

Besides impurities, the solvent itself plays an important role in crystal growth. Parameters such as the type of liquid and its structure and the degree of dissociation can affect the growth rate. It is necessary to take into account not only the microstructure of the crystal surface but also any kind of adsorbed species. In particular, the solvent affects crystallization kinetics significantly in the case of electrolyte solutions. As the water molecule itself dissociates into H<sup>+</sup> and OH<sup>-</sup>, usually at least a five-component system is in contact with the ionic crystal surface. The dissociated ions are hydrated to specific hydration numbers with a specific hydration enthalpy depending on the valency and the reciprocal ionic radius (Mersmann 2001). As this hydrate layer has to be removed during the growth process to a certain degree, any change in the structure of the solvated

ions affects growth kinetics too. Metal ions tend to form different complex species, depending on the pH, which contain hydroxide or hydronium ions, respectively, thus changing the charge of the complex and affecting the hydration enthalpy. On the other hand, the crystal surface itself has a hydrate layer, which changes with pH and results in a surface charge on the crystal (Mersmann 2001). There is a great deal of experimental evidence for the importance of solution conditions such as pH and ionic strength in the literature, which points to a distinct dependence of growth rates on these parameters. Experimental results in Figure 4.25 obtained for the ternary system KCl–NaCl–H<sub>2</sub>O by König et al reveal that the solubility of the aqueous KCl or NaCl solution is reduced in the presence of a third component (König 1987).

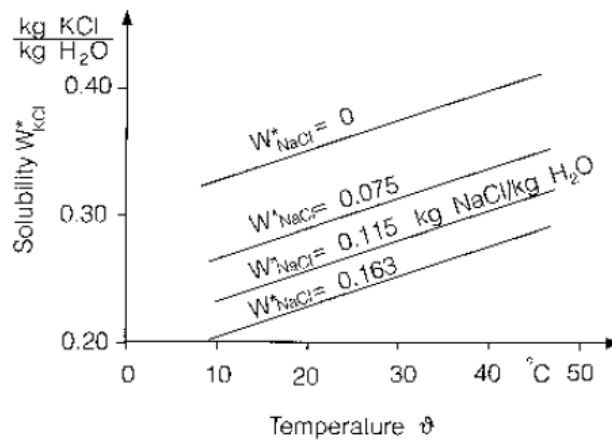


Figure 4.25. Solubility of KCl in the KCl–NaCl–Water ternary system. (Source: König, 1987)

#### 4.4.2. Methods of Analysis of the Kinetics of Calcium Phosphate Cement Setting

Introduction of seeded growth techniques enabled the kinetic study of crystallization of calcium phosphates. Methods such as free drift, pH-stat and constant composition have been developed in order to model calcium phosphate cement precipitation. Following the addition of test surfaces of known surface area to metastable supersaturated solutions, the free drift method involves the monitoring of the decrease in pH and changes in calcium and phosphate concentrations. The degree of supersaturation varies considerably during the reaction since the solubility of calcium

phosphate phases is strongly dependent on pH. Although changes in pH are avoided by use of a glass electrode and potentiostat to control base addition in the pH-stat method,, the concentrations of crystal lattice ions again decreased during the reaction, resulting in the possible formation of multiple phases (Nancollas et al. 1994). This problem is avoided in the constant-composition method, in which the concentrations of lattice ions are maintained at the initial values by titration with solutions containing calcium, phosphate, and hydroxide ions from coupled burets. The volume of titrant,  $V$ , added as a function of time is recorded. Adjustment of titrant solution stoichiometry to match the precipitated phases enables the activities of all ionic species to be maintained constant during extended periods of time. A particular advantage of this method is that it facilitates the study of rates of mineralization at fixed points on the solubility isotherms with the formation of sufficient solid phases for reliable characterization, even at very low supersaturations. Also a relatively large extent of crystallization can be achieved even at very low supersaturation enabling the characterization of new precipitates. Another advantage is the ability to monitor the times for crystal phases to nucleate and grow on foreign surfaces. The induction time, taken as the time needed to reach steady-state nucleation and growth at the solid surfaces, is measured as the time from the addition of seeding surfaces to the intersection of a tangent ( $dV/dt$ ) with the time axis (Nancollas et al. 2000).

A highly reproducible parameter in precipitation kinetics for the constant composition method, known as relaxation time, is indicative of the initiation of the growth stage in supersaturated calcium solutions. It is defined as the time when the precipitation rate is at maximum. As a result of an increasing surface area and a decreasing supersaturation during the relaxation, a sigmoidal shape of the precipitation extent curve is expected with only one inflection point. At this point, where the growth rate reaches its maximum value, the relaxation time  $t_R$  is obtained (Van Kemenade M. J. J. M. 1987). For a complex-precipitating system where the precipitation involves growth of more than one phase, the relaxation curve is more complicated in form and its analysis is not straight forward. In Figure 4.26, a typical example of a relaxation curve for a single growing phase is shown. In Figure 4.26b, a two-stage precipitation is shown, where the formation of phase I is followed by the subsequent formation of phase II. This results in two sigmoidal curves where which give a relaxation time for each precipitating phase. As the formation of the two phases will not be independent, a simple analysis of the second relaxation time is difficult. Figure 4.26c represents a

precipitation curve where over a certain period both phases I and II are precipitating simultaneously. This results in inflection points in the overall growth curve which cannot be interpreted as relaxation times for growth of the phases.

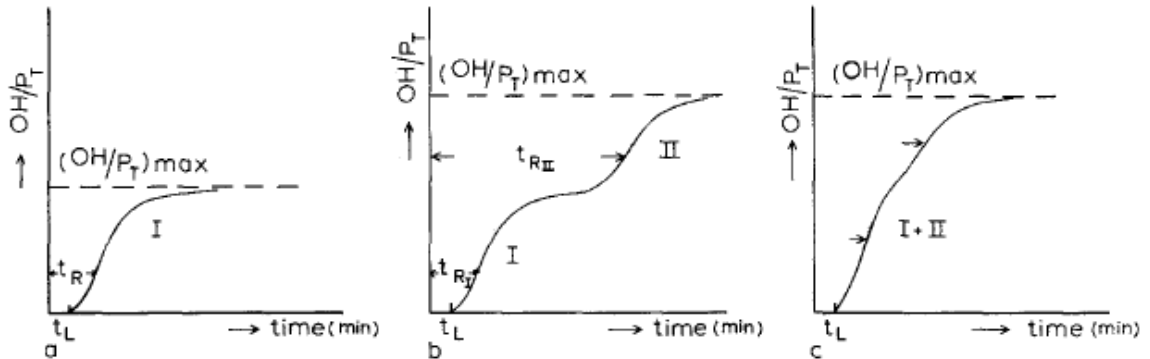


Figure 4.26. Typical relaxation curves for precipitation of (a) a pure phase, (b) two phases forming successively, and (c) two phases forming simultaneously over a certain period. (Source: van Kemenade, 1987)

In these curves the precipitation extent is represented by the base uptake of the precipitating solution at constant pH condition due to decrease of pH with precipitation. The period before the first base uptake is defined as the lag time. Nucleation consumes only small amounts of the precipitating species that cannot be detected by measuring change in pH. The measured uptake of base during the constant pH relaxation is thus almost entirely the result of growth processes. The value of  $\alpha$  at the inflection point can be obtained by applying the condition  $da/dt = 0$  and is seen to have the following dependence on the growth rate exponents  $n$  and  $m$ :

$$\alpha(t_R) = \frac{n}{n+m} \quad (4.66)$$

It is seen in Table 4.7 that  $\alpha(t_R)$  has a single characteristic value for a diffusion-controlled growth mechanism but, as expected, will have different values depending on the magnitude of  $m$  for the other growth mechanisms. In order to identify the growth mechanism responsible for the observed relaxation behavior it is necessary to fit the relaxation curves to straight lines. This may be done by plotting  $-\log(\alpha^{-n} da/dt)$  versus  $-\log(1 - \alpha)$  for  $n = 1/3, 2/3$  and  $4/3$  and assuming  $m$  to be constant. The latter assumption

is justified in the case of the layer growth mechanisms if the concentration of the precipitating species does not change by more than ten in the relaxation experiment.

Table 4.7. Points of inflection for different growth models and values of m

<b>Growth model</b>	<b>n</b>	<b>m</b>	<b><math>\alpha</math></b>
Diffusion controlled	1/3	1	0.25
Polynuclear	2/3	1	0.40
		2	0.25
		3	0.18
		4	0.14
		5	0.12
Mononuclear	4/3	1	0.57
		2	0.40
		3	0.31
		4	0.25
		5	0.21

## CHAPTER 5

### MATERIALS AND METHODS

The ultimate goal of this thesis is to synthesize a unique clinically relevant macroporous calcium phosphate cement construct. This aim could only be achieved if the steps of the study were precisely planned and supportive to the subsequent steps in a long project run. Three study periods that each provided insight and understanding to the subsequent one were determined as follows:

1. Focusing on a particular calcium phosphate cement system in order to understand the factors governing setting kinetics, and deduction of generally applicable strategies to improve setting.
2. Optimizing a calcium phosphate cement system with the information gathered from the first step and to obtain a robust, dense cement with high conversion extent.
3. Processing the calcium phosphate cement developed at the previous step by macropore induction methods, particularly salt leaching method, in order to produce a strong yet porous and biodegradable cement.

#### **5.1. Investigation of the Effect of Several Factors on the Extent of Calcium Phosphate Cement Setting**

The first study was conducted on the Tetracalcium phosphate- Monocalcium phosphate monohydrate cement system. This is the thermodynamically most feasible system in which both precursors are expected to dissolve completely and convert to more stable brushite, monetite or hydroxyapatite phases. The occurrence and the rate of transformation of the cement end products hydroxyapatite, brushite and monetite was controlled by various kinetic parameters including Ca/P ratio, pH, temperature, ionic strength, liquid saturation, seed size, and precursor particle size. The precursors used in the experiment were commercial ceramic powders except TTCP, which was synthesised in laboratory according to the method proposed by Sargin et al (Sargin et al. 1997). Accordingly,  $\text{CaCO}_3$  and  $\text{CaHPO}_4$  were mixed in a stoichiometric ratio and were heated at  $1400\text{ }^\circ\text{C}$  for 5 hours. The batch was quenched from this temperature to prevent TTCP



decomposition. Table 5.1 gives the properties of the precursors employed during the experiments.

The size of the ceramic powders were determined by sedigraph and zetasizer analysis. The default particle sizes were taken as the high level and the low level was set as half the original size. The size reduction was achieved by the use of a planetary ball mill with agat container and balls rotating at 300 rpm. The required duration of milling was determined by trials done with the precursors at various time periods. The zetasizer data suggest that 4 hours of wet milling is enough to reduce the particle size to half. The liquid medium used for wet milling was ethanol for water soluble calcium phosphates or deionized water for hydroxyapatite. Ionic strength was varied by using 0.1 M NaCl solution. Initial pH was set at 7.5 or 5.5, equal distances from the singular point at 6.5 of TTCP-MCPM system, using 0.1 M NaOH and 0.1 M H<sub>3</sub>PO<sub>4</sub>. The saturation of the setting liquid was set using 0.1 M and 0.01 M NaH<sub>2</sub>PO<sub>4</sub> aqueous solution. The increase in ionic strength by NaH<sub>2</sub>PO<sub>4</sub> was compensated by reducing the original strength to add up to the original values. Oven was used to heat the precursors to 50 °C and to store the samples after setting. Room temperature was the low level for temperature variable and may have been subject to a few degrees of change due to the seasonal changes during the experiment. Ca/P ratio of the precursors were adjusted by using two different weight ratio of TTCP and MCPM. Setting liquid contained deionized water, HA seed, NaCl solution and NaH<sub>2</sub>PO<sub>4</sub> solution. The powder/liquid ratio was set as 2.5 g/ml due to strong dependency of mechanical properties to the pore content and hence the amount of the liquid.

The mixing of the cement powder with setting liquid was done in test tubes using a vortex shaker. Setting liquid was added to the cement powder and the mixture was shaken for 1 minute to ensure homogeneous mixing. The wet mixture resembling a paste was then packed into teflon moulds containing cylindrical holes 10 mm in diameter and 20 mm in height according to the ASTM C 773 standard for compressive testing of ceramics. The moulds were filled and the cement was compacted by a syringe piston using moderate force. The cement paste amount was enough to produce 7 samples with the same dimensions. Each of these samples were frozen in liquid nitrogen at the intervals of 15, 30, 60 minutes, and 2, 4, 24 hours. The last sample was aged for 10 days and then dried in vacuum furnace.

The main aim of the study was to analyze the phase transformations and quantitatively determine the composition at each measurement interval. To do so,

external standard method was utilized. For its stable structure, small number of peaks and abundance, corundum is the universally accepted external standard material. The external standard method is based on the comparison of the intensity of the major peak of a material in a 1-to-1 weight ratio mixture with corundum to the intensity of the major peak of corundum. Reference intensity ratio, also given in the JCPDS cards of most materials, is used to estimate the concentration of one material in a mixture of phases with known coefficient of mass absorption.

The ultimate compressive strength of the cement blocks was determined as the other response for experiment using a uniaxial mechanical testing machine. Cylinders 20 mm in height and 10 mm in diameter with flat base and top were placed between uniaxial pressing bars and the machine compressed the samples at a rate of 1 mm/min. Stress-strain diagrams were obtained with clear indication of modulus and compressive strength for each sample. As mentioned above, slight differences in powder/liquid ratio resulted in a wide range of strength values, making comparison of sample groups inaccurate. Instead mechanical test results were used to correlate to the phase conversion ratio at various intervals.

Table 5.1. Chemical reagents used in all experiments and their properties

Precursor	Formula	Supplier	Purity	Mean Particle Size( $\mu\text{m}$ )	$d_{50}(\mu\text{m})$
TTCP	$\text{Ca}_4\text{P}_2\text{O}_9$	As Synthesized	--	20.0	20.0
HA	$\text{Ca}_{10}(\text{PO}_4)_6(\text{OH})_2$	Sigma-Aldrich	>96%	6.0	3.0
$\beta$ -TCP	$\text{Ca}_3(\text{PO}_4)_2$	Fluka/Sigma	>96%	6.9/5.0	5.0/3.5
DCP	$\text{CaHPO}_4$	Sigma	>99%	20.1	24.0
MCPM	$\text{Ca}(\text{H}_2\text{PO}_4)_2 \cdot \text{H}_2\text{O}$	Sigma-Aldrich	>96%	33.4	30.0
DCPD	$\text{CaHPO}_4 \cdot 2\text{H}_2\text{O}$	Aldrich	>99%	35.0	33.0
Ca Carbonate	$\text{CaCO}_3$	Sigma	>99%	--	--
Citric Acid	$\text{C}_6\text{H}_8\text{O}_7$	Merck	>99%	--	--
NaCl	NaCl	Merck	>99%	<500	<500
Na Phosphate	$\text{NaH}_2\text{PO}_4$	Sigma-Aldrich	>98%	--	--
Phosphoric Acid	$\text{H}_3\text{PO}_4$	Merck	>99%	--	--
Na Hydroxyide	NaOH	Merck	>99%	--	--
HCl	HCl	Merck	>99%	--	--
Polyethylene glycol	$\text{C}_{2n}\text{H}_{4n+2}\text{O}_{n+1}$	Merck	>99%	--	--

## 5.2. Ionic Modification of the $\beta$ -TCP-MCPM Cement System by NaCl and Citric Acid Addition

The second study focused on the effect of ionic modifiers on brushite cement setting kinetics as ionic strength was found as the prominent factor contributing to the setting extent and strength of the cement studied in the first study. Setting kinetics of the  $\beta$ -TCP – MCPM cement system in the presence of NaCl and citric acid was analyzed using potentiometric titrator to measure base uptake as the extent of growth at a fixed pH value of 4.2. This value is chosen for its proximity to 4.3 which is the singular point between monetite and hydroxyapatite to prevent any hydroxyapatite formation. The observable effects of ionic modifiers NaCl and citric acid on the kinetics of the cement setting reaction were isolated by keeping other kinetic factors constant. Introduction of seeds reduced the supersaturation build-up so that precipitates formed close to equilibrium conditions. Eliminating variations in temperature and pH also made it possible to investigate the effects of ionic modifiers on the relaxation period at various concentrations.

Effect of ionic strength and impurities on the setting reaction of stoichiometric cement formulation was investigated by adding NaCl and citric acid to the setting liquid of the powder mixture prepared by combining 1.55 gr  $\beta$ -TCP, 1.26 gr MCPM and 0.1 gr brushite seed. NaCl and citric acid concentration in 100 ml of deionized water were varied in the ranges of 0-6 M and 0-0.5 M respectively. 0.1 M NaOH was used as titration base. Variation of base uptake and the pH were recorded as a function of time for the observable period of 9999 seconds. Precipitation products were centrifuged, frozen and freeze-dried in order to investigate the phase structure by XRD, SEM and EDX analysis. The amount of citric acid initially added as planned in the range 0.1 M to 0.5 M in the pH-stat runs was diluted by the high volume of concentrated NaOH added to balance the pH drop caused by citric acid. As calcium phosphate cement powders were mixed after the removal of extra solution, the kinetics of the reactions were not affected by this dilution. Free drift runs in addition were conducted under the same conditions in order to observe the variation in pH as an indication of CPC growth.

Spectrometric analyses of citrate adsorption on the components of the cement system  $\beta$ -TCP, brushite and monetite phases were done by using ICP-AES and UV spectrophotometry by mixing the components with citric acid for 24 hours in order to determine the free calcium and citrate concentrations in the supernatant solution.

Calcium concentrations of the three phases mixed with varying citric acid solution between 0 and 0.5 M were determined by using Varian ICP atomic emission spectrometer. Nitric acid 5% (Merck, 65% purity) was added to each sample prior to analysis to minimize chemical associations and related problems. Citrate concentrations in the supernatant solutions were determined by measurement of absorption at 214nm ultraviolet light in Shimadzu-UV 2450 spectrophotometer. Supernatant solutions were diluted to 1/100 by adding ultrapure water in order to obtain absorbances within the range 0 to 1. Specific surface area or the Blaine value of the three calcium phosphate powders  $\beta$ -TCP, brushite and monetite were measured by a ToniPERM cement air permeability tester according to the ASTM C 204 standard.

In addition to the analysis of brushite cement setting in pH-stat and free drift conditions, mechanical and microstructural characterization of cement blocks prepared by addition of both citric acid and NaCl was done in order to investigate the synergistic effect of ionic modifiers on cement block properties. Three replicate sets of cement blocks were prepared to demonstrate the control of cement phase structure with ionic strength of the setting liquid by adding 0.3 M citric acid and NaCl varying between 0M and 6 M concentration to deionized water. The pH of the setting liquid was adjusted to 4.2, the singular point between monetite and hydroxyapatite by NaOH and citric acid additions. The powder/liquid ratio was set as 2.5. A total of 5 samples were produced for each set in PTFE molds with dimensions of 20 mm height and 10 mm diameter. Set samples were aged in humidifying oven at 30 °C and 85% relative humidity for 72 hours. Samples were subjected to porosity evaluation by Archimedes method subsequent to leaching in deionized water for 72 hours. Wet samples were dried in vacuum oven at 30 °C for 120 hours prior to mechanical testing. Compressive strength of dry samples was determined with an Instron uniaxial testing machine and the fractured cements were subjected to phase analysis by XRD. Phase composition of the samples was needed to calculate the theoretical density required in porosity calculations. The fracture surfaces of the samples were examined and morphology of the microstructure was evaluated using SEM.

XRD analysis was conducted by using Philips X'Pert Pro powder diffractometer with Cu K $\alpha$  radiation at a generator voltage of 45 kV, and a tube current of 40 mA. All XRD patterns were obtained at a scan range of 5-60°, scan step size of 0.05 and 5 seconds per step. External standard method was employed for the semiquantitative XRD analysis. Besides the expected  $\beta$ -TCP, brushite and monetite phases, additional

phases were observed including NaCl, sodium citrate dihydrate and sodium calcium phosphate. Monocalcium phosphate monohydrate was not observed in any of the samples due to its high solubility. A significant amount of NaCl and sodium citrate dihydrate was formed during the centrifugal separation of the precipitates from the setting liquid. Their quantities were calculated with their corresponding RIR values and subtracted from the total concentration. The remaining weight percent values were totalled up to 100%.

### **5.3. Modification of the Morphology of Macroporous Cement Blocks by A Variable Porogen Size Distribution Approach**

In the third and final study, optimization of the 3 dimensional pore architecture was intended by introduction of size distributed NaCl porogens to the optimized monetite rich cement matrix. Two successive experiments were conducted for the minimization of microporosity and optimization of macroporosity by adjusting the size distributions of solid particles of the cement block. First, theoretical maximum packing density for combinations of NaCl size distributions were determined via rheological analysis of set of samples carefully selected to represent all possible combinations by an experimental design model. Maximum packing density values for different NaCl size distribution obtained from the initial experiment were used to adjust the NaCl porogen volume for cement block samples with constant cement volume and sample volume. Packing densities of the samples were correlated with porosity, density, and strength of cement blocks.

The solid particles consist of cement precursors  $\beta$ -tricalcium, monocalcium phosphate monohydrate, monetite seed and sodium chloride grouped into 6 particle size distributions below 38, 53, 75, 106, 150 and 212 micrometers. Commercial NaCl particles as large as 500 micrometers were ground using planetary ball mill, mortar and pestle and then sieved through openings at the respective sizes. Optical microscope images of some of the solid particles used in the experiments are given in Figure 5.1.

Maximum packing densities of different combinations of NaCl size distributions were determined by analysis of their rheological properties using a rotational rheometer. Thirty eight combinations determined through an experimental design study were dispersed in Polyethylene Glycol 200, a slightly viscous and shear thickening non-Newtonian liquid polymer at solid loadings of 10%, 20%, 30%, 40% and 50% by

volume. Viscosity versus shear rate curves for a shear rate range of 0-500 were obtained for each sample. Viscosity values at rates sufficiently high to obey the model assumptions and sufficiently low to prevent phase separation at high rates were needed to insert into the model equation developed by Liu in order to determine the maximum packing density as a function of solid loading (Liu 2000).

Significant size distributions were aimed to be determined by variation of the amount of several or all of the NaCl size groups according to the experimental design order given in Table 5.2. Each size group was added to the samples in amounts ranging from 0 to 1 grams. Each sample was mixed with PEG 200 at 10% to 50% solid loading. A well-mixed suspension was analyzed in rheometer in terms of shear stress and viscosity as a function of shear rate. This design permits the analysis of singular and combined effects of each NaCl size group on the viscosity and maximum packing density of the samples.

Cement precursor volume was kept constant in the preparation of macroporous cement blocks, and maximum packing density data from the rheology study was used to adjust the porogen volume in order to obtain a constant sample unit volume for all runs. Constant cement precursor and water volume are mixed with the appropriate porogen volume in plastic syringes with a diameter of 12.5 mm. The sample unit volume is adjusted to  $2.7 \text{ cm}^3$  for the 25 mm required according to the compressive strength sample standard of 2:1 height to diameter ratio for ceramics. Mixing of the solid particles with setting liquid was done on a vortex shaker oscillating at a frequency of 40 Hertz in order to improve packing. Mixed samples were compressed at the same time via syringe piston under moderate pressure by hand. Seven replicates of each sample set given in Table 5.3 were produced for several destructive characterization methods. Samples were left to set in closed syringe molds upon mixing for 7 days at room temperature. Exactly one week later samples were removed gently from the molds and immersed into pure water for 24 hours in order to leach out the NaCl completely. Wet leached samples were instantly analyzed for density and porosity in Archimedes' apparatus and then left in vacuum oven to dry at room temperature and 1 millibar pressure for 7 days. Completely dried samples were weighed again for density and porosity calculations. Subsequently, rigid dry samples were subjected to compressive strength test in uniaxial mechanical testing machine. Fractured block particles were ground in mortar and then analyzed quantitatively in XRD. For each set one unleached sample was sectioned with precision cutter and the cross section was analyzed for pore

morphology under optical microscope. The reason for not leaching is that samples are relatively stronger in the presence of NaCl and cutting produces a smoother rigid surface.

Table 5.2. Mass ratio for the packing determination experiment variables

<b>Std</b>	<b>Run</b>	<b>Factor 1 A:-38 <math>\mu\text{m}</math></b>	<b>Factor 2 B:-53 <math>\mu\text{m}</math></b>	<b>Factor 3 C:-75 <math>\mu\text{m}</math></b>	<b>Factor 4 D:-106 <math>\mu\text{m}</math></b>	<b>Factor 5 E:-150 <math>\mu\text{m}</math></b>	<b>Factor 6 F:-250 <math>\mu\text{m}</math></b>
1	1	1.000	0.740	0.000	0.000	0.000	0.000
38	2	1.000	0.950	0.000	1.000	1.000	1.000
22	3	0.035	0.000	0.135	0.644	0.090	0.536
32	4	1.000	0.000	1.000	1.000	0.000	1.000
6	5	1.000	0.445	1.000	0.310	0.620	0.000
21	6	0.160	0.350	0.000	0.510	1.000	0.535
10	7	0.000	0.405	0.315	0.200	0.345	0.011
20	8	0.160	0.350	0.000	0.510	1.000	0.535
37	9	0.000	1.000	1.000	0.560	1.000	1.000
4	10	0.700	0.095	0.000	1.000	0.070	0.000
13	11	1.000	1.000	0.620	0.130	0.270	0.350
31	12	0.500	0.665	0.450	0.580	0.000	1.000
9	13	0.000	0.795	0.530	1.000	1.000	0.000
19	14	0.000	1.000	0.525	0.528	0.515	0.533
5	15	0.550	1.000	0.000	0.510	0.595	0.000
29	16	0.000	0.000	0.000	0.000	0.000	1.000
3	17	0.000	0.000	1.000	0.775	0.000	0.000
17	18	0.870	0.000	0.735	0.830	1.000	0.415
36	19	0.700	0.140	0.725	0.000	1.000	1.000
18	20	0.000	1.000	0.000	1.000	0.000	0.530
28	21	1.000	0.209	0.005	0.455	0.390	0.780
35	22	0.100	1.000	0.065	0.000	0.625	1.000
2	23	0.275	1.000	1.000	0.000	0.000	0.000
12	24	1.000	1.000	0.575	0.894	0.120	0.275
23	25	0.475	0.650	1.000	1.000	0.535	0.610
7	26	1.000	0.000	0.000	0.000	1.000	0.000
30	27	0.500	0.665	0.450	0.580	0.000	1.000
33	28	1.000	1.000	1.000	0.000	0.220	1.000
26	29	0.000	0.445	0.955	0.005	0.165	0.760
11	30	0.005	0.000	0.640	1.000	0.575	0.260
8	31	0.000	0.000	1.000	0.000	1.000	0.000
25	32	0.000	0.075	0.350	0.000	0.624	0.708
16	33	0.750	0.960	0.570	0.000	1.000	0.410
14	34	0.640	0.000	0.595	0.085	0.180	0.350
34	35	0.045	0.000	0.430	1.000	0.565	1.000
24	36	0.475	0.650	1.000	1.000	0.535	0.610
27	37	1.000	0.209	0.005	0.455	0.390	0.780
15	38	0.640	0.000	0.595	0.085	0.180	0.350

Table 5.3. Mass for 7 blocks produced in the mechanical experiment

Run	NaCl Size Groups						$\beta$ -TCP	MCPM	Total
	-38 $\mu\text{m}$	-53 $\mu\text{m}$	-75 $\mu\text{m}$	-106 $\mu\text{m}$	-150 $\mu\text{m}$	-212 $\mu\text{m}$			
1	9.156	6.775	0.000	0.000	0.000	0.000	8.176	6.172	30.279
2	3.267	3.104	0.000	3.267	3.267	3.267	8.176	6.172	30.522
3	0.325	0.000	1.255	5.985	0.836	4.981	8.176	6.172	27.730
4	3.756	0.000	3.756	3.756	0.000	3.756	8.176	6.172	29.370
5	4.144	1.844	4.144	1.285	2.569	0.000	8.176	6.172	28.334
6	0.834	1.825	0.000	2.660	5.215	2.790	8.176	6.172	27.672
7	0.000	3.679	2.861	1.817	3.134	0.100	8.176	6.172	25.937
8	0.872	1.908	0.000	2.780	5.450	2.916	8.176	6.172	28.273
9	0.000	2.974	2.974	1.666	2.974	2.974	8.176	6.172	27.911
10	5.305	0.720	0.000	7.579	0.531	0.000	8.176	6.172	28.482
11	4.213	4.213	2.612	0.548	1.137	1.474	8.176	6.172	28.544
12	2.175	2.893	1.958	2.523	0.000	4.351	8.176	6.172	28.248
13	0.000	3.062	2.041	3.852	3.852	0.000	8.176	6.172	27.154
14	0.000	4.203	2.206	2.219	2.164	2.240	8.176	6.172	27.380
15	2.851	5.184	0.000	2.644	3.085	0.000	8.176	6.172	28.112
16	0.000	0.000	0.000	0.000	0.000	11.828	8.176	6.172	26.176
17	0.000	0.000	7.085	5.491	0.000	0.000	8.176	6.172	26.924
18	3.289	0.000	2.779	3.138	3.780	1.569	8.176	6.172	28.902
19	2.921	0.584	3.025	0.000	4.172	4.172	8.176	6.172	29.222
20	0.000	5.179	0.000	5.179	0.000	2.745	8.176	6.172	27.450
21	5.332	1.114	0.027	2.426	2.080	4.159	8.176	6.172	29.486
22	0.542	5.418	0.352	0.000	3.387	5.418	8.176	6.172	29.465
23	1.391	5.056	5.056	0.000	0.000	0.000	8.176	6.172	25.851
24	3.656	3.656	2.102	3.268	0.439	1.005	8.176	6.172	28.474
25	1.565	2.142	3.296	3.296	1.763	2.010	8.176	6.172	28.421
26	7.347	0.000	0.000	0.000	7.347	0.000	8.176	6.172	29.041
27	2.410	3.205	2.169	2.795	0.000	4.819	8.176	6.172	29.745
28	3.350	3.350	3.350	0.000	0.737	3.350	8.176	6.172	28.486
29	0.000	2.696	5.787	0.030	1.000	4.605	8.176	6.172	28.466
30	0.029	0.000	3.661	5.721	3.290	1.487	8.176	6.172	28.536
31	0.000	0.000	6.301	0.000	6.301	0.000	8.176	6.172	26.949
32	0.000	0.630	2.939	0.000	5.239	5.944	8.176	6.172	29.099
33	2.819	3.608	2.142	0.000	3.758	1.541	8.176	6.172	28.215
34	5.109	0.000	4.750	0.679	1.437	2.794	8.176	6.172	29.116
35	0.188	0.000	1.800	4.187	2.366	4.187	8.176	6.172	27.076
36	1.575	2.155	3.316	3.316	1.774	2.023	8.176	6.172	28.507
37	5.830	1.219	0.029	2.653	2.274	4.548	8.176	6.172	30.900
38	5.284	0.000	4.912	0.702	1.486	2.890	8.176	6.172	29.621

## 5.4. Quantitative Phase Analysis by X-Ray Diffraction

All cement types contain multiple phases and in some part of the production process are required to be checked for the amounts and proportions of the constituents. For this reason quantitative X-ray diffraction analysis is an integral part of cement characterization. A given substance always produces a characteristic diffraction pattern, whether that substance is present in the pure state or as one constituent of a mixture of substances. Qualitative analysis for a particular substance is accomplished by identification of the pattern of the substance. Quantitative analysis is also possible,



because the intensities of the diffraction lines due to one constituent of a mixture depend on the proportion of that constituent in the specimen (Cullity 1956).

The basis of quantitative phase analysis by powder diffraction is to attempt to equate the concentration of a given phase or phases with the intensity of a single peak, a number of peaks, or even all of the peaks in a pattern. The shape of the peaks is decisive in choosing the intensity measurement method. When the diffraction peak is sharp and non-overlapped, peak height is taken as the representative value as it is considered proportional to the peak area. Background corrected integrated intensities are measured by subtracting the background intensity from the peak height. Background intensity measurement must be made at the start and end points of the peak in the case of broadened peaks. The intensity of a diffraction peak  $hkl$  of phase  $\alpha$  in a multiphase mixture is fully described by the following equation:

$$I_{(hkl)\alpha} = \left[ \frac{I_0 \lambda^3}{64\pi r} \left( \frac{e^2}{m_e c^2} \right)^2 \right] \left[ \frac{M_{hkl}}{V_\alpha^2} [F_{(hkl)\alpha}]^2 \left( \frac{1 + \cos 2\theta^2 \cos 2\theta_m^2}{\sin \theta^2 \cos \theta} \right) \right] \left[ \frac{X_\alpha}{\rho_\alpha (\mu/\rho)_S} \right] \quad (5.1)$$

where the first set of square brackets represent the terms that are constant for a particular experimental setup and the second set of square brackets represent the terms that are constant for each  $(hkl)$  diffraction peak of phase  $\alpha$ . Thus the equation is reduced to a simpler form:

$$I_{(hkl)\alpha} = \frac{K_e K_{(hkl)\alpha} X_\alpha}{\rho_\alpha (\mu/\rho)_S} \quad (5.2)$$

where  $X$  is the weight fraction,  $\rho$  is the density and  $(\mu/\rho)$  is the mass absorption coefficient of phase  $\alpha$ . The fundamental problem in the quantitative analysis of a homogeneous, randomly oriented powder lies in determination of the mass absorption coefficient of the mixture. To solve the weight fraction of phase  $\alpha$ , it is necessary to compute  $(\mu/\rho)$  via

$$\left( \frac{\mu}{\rho} \right)_S = \sum_j \left( \frac{\mu}{\rho} \right)_j X_j \quad (5.3)$$

The total absorption of a multiphase specimen is simply the sum of the products of individual mass absorption coefficients and weight fractions. Solution of this equation requires the weight fraction of each phase. Thus the single intensity equation contains two unknowns and so the problem of quantitative phase analysis is undetermined. Various methods have been developed that supply some required extra information to this equation. These methods include standard additions method, absorption-diffraction method, and Rietveld total pattern method. Among these the external standard method is applicable to the quantitative analysis of calcium phosphate cements due to the complex nature of the powder.

#### 5.4.1. The External Standard Method

If the diffracted intensity from a pure sample of a phase  $\alpha$ , is  $I_\alpha$ , and the intensity is measured under identical experimental conditions from a mixture containing an unknown weight fraction  $W_\alpha$  of phase  $\alpha$  then the weight fraction in the unknown mixture can be calculated from the ratio of the integrated intensities as:

$$W_\alpha = \frac{I_\alpha}{I_\alpha^P} \cdot \frac{(\mu/\rho)_m}{(\mu/\rho)_\alpha} \quad (5.4)$$

where  $(\mu/\rho)_\alpha$  and  $(\mu/\rho)_m$  are the mass absorption coefficients for the pure phase and the mixture, respectively. The mass absorption coefficient of the mixture must be known independently. In the special case of application to calcium phosphate cements, because the elemental composition of the set cement and the starting powder remain the same, regardless of any phase transformations, the mass absorption coefficient of the cement will be equal to that of the starting powder. In external standard method, the complexity of the analysis of multiple phases in a mixture is greatly reduced by referencing all of the pure phase peak intensities to a single standard. The reference intensity ratio for phase  $\alpha$  is defined as:

$$RIR_\alpha = \frac{I_\alpha}{I_S} \quad (5.5)$$

where  $I_a$  is the intensity of the 100% peak of phase  $\alpha$ , and  $I_s$  is the intensity of the 100% peak of a reference phase  $s$ , taken by convention to be  $\alpha$ -Al<sub>2</sub>O<sub>3</sub>, corundum, in a 50:50 mixture by weight. For an external standard, the RIR values must be expressed in terms of the pure intensities, rather than the intensities in a mixture. In a 50:50 mixture by weight,  $W_a = W_s$ , and the ratio of intensities is, by definition, the RIR value. Therefore the weight fraction of phase  $\alpha$  can be expressed in terms of the ratio of the strongest peaks of  $\alpha$  and the reference phase as:

$$W_\alpha = \frac{I_\alpha}{I_\alpha^p} \cdot \frac{(\mu/\rho)_m}{(\mu/\rho)_s} \cdot \frac{1}{RIR_\alpha} \quad (5.6)$$

The integrated intensity of any diffraction peak from a phase with arbitrary Miller indices (hkl) can be expressed as a fraction of the intensity of the strongest diffraction peak of that phase by the relative intensity. So the above equation can be generalized as

$$W_\alpha = \left[ \frac{I_\alpha^{hkl}}{I_\alpha^{REL}} \right] \cdot \left[ \frac{(\mu/\rho)_m}{(\mu/\rho)_s} \right] \cdot \left[ \frac{1}{I_s^p \cdot RIR_\alpha} \right] \quad (5.7)$$

If the RIR values for all components in a mixture are known relative to the reference phase,  $s$ , a single determination of  $I_s^p$  in conjunction with the measurement of  $I_a^{hkl}$  under identical experimental conditions allows solution of the entire system of weight fractions. The use of RIR values is much faster and less prone to error than the determination of all of the weight fractions from the starting equation which would require reference to the integrated intensities of the 100% peak of each phase in its pure form (Prevey 2000).

The mass absorption coefficients of calcium phosphates used in this study and the cement powder are calculated from Elements of X-Ray Diffraction of Cullity (Cullity 1956). The ratio of the intensities of each precursor except MCPM was obtained experimentally by preparing a 1-to-1 weight ratio mixture with AKP50 alumina powder. The values given in Table 5.4 suggest that the X-Ray diffractometer in the CMR is out of sync with the devices used to produce literature values. The intensity of pure corundum was calculated from diffractograms obtained by triple analysis of pure AKP50 powder. Due to differences in the operation variables of the diffractometer, three parallel patterns were obtained with each major peak at slightly different intensity.

Average of the three values was taken as 7600 counts to be used in the above equation. All XRD analysis were done in maximum resolution at a scan range of 5-60°, scan step size of 0.05 and 5 seconds per step using a cassette to ensure high intensity count for the peaks.

The XRD patterns of the samples contain a high number of peaks that mostly overlap each other. At any time the cement powder may contain 6 phases: TTCP, HA, DCPD, DCP,  $\alpha$ -TCP,  $\beta$ -TCP. Each of these phases were identified in the XRD patterns produced and mass balance was made from the results of the quantitative analysis to add the total amount to 100. The characteristic peaks of these phases that do not overlap were carefully determined from the 10 highest peaks of each phase. The intensity of the characteristic peaks given in Table 5.4 were read for each XRD pattern and subtracted from the background intensity to obtain the net intensity. The net intensity is inserted in equation with the relative intensity of the peak, intensity ratio to corundum, corundum maximum intensity, and mass absorption coefficients for the cement and corundum. The result of the equation gives the mass percent of the phase, the peak of which is analyzed. However when the mass balance is done for the phases present, the total adds up to value less than 100. As all the peaks are clearly identified and there are no other minor phases, the values for each phase can safely be expanded to 100% normal value.

Table 5.4. Diffraction parameters of the phases analyzed quantitatively using the external standard method

	JCPDS #	Measured RIR	Literature RIR	Characteristic Peak 2 $\theta$ /Ratio	hkl	Mass Absorption Coefficient
HA	74-0566	0.805	1.06	31.77/0.999	(211)	87.31
				32.89/0.612	(300)	
				25.94/0.466	(002)	
DCPD	72-0713	1.464	1.42	11.65/0.999	(020)	52.52
				20.95/0.794	(12-1)	
				29.30/0.536	(14-1)	
DCP	77-0128	1.27	0.7	26.60/0.999	(200)	50.41
				32.82/0.541	(-202)	
				28.51/0.264	(-1-12)	
TTCP	70-1379	0.77	0.75	29.79/0.999	(040)	92.55
				32.35/0.449	(-212)	
				25.35/0.406	(200)	
$\alpha$ -TCP	09-0348	0.827	--	30.75/0.999	(170)	86.42
				34.18/0.500	(043)	
				24.09/0.400	(132)	
$\beta$ -TCP	09-0169	1.926	1.35	31.03/0.999	(2010)	86.42
				34.37/0.650	(220)	
				27.77/0.550	(214)	
MCPM	70-0090	--	1.14	7.53/0.999	(010)	52.52
				22.87/0.656	(120)	
				24.09/0.631	(-120)	
Corundum	75-1864	--	1	43.36/0.999	(210)	69.49
				35.18/0.900	(104)	
				57.52/0.800	(110)	
NaCl	05-0628	3.71	4.40	31.70/0.999	(200)	74.65
				45.40/0.550	(220)	
				58.58/0.151	(222)	
Sodium Citrate Dihydrate	16-1170	--	0.40	11.25/0.999	(-111)	23.09
				24.03/0.350	(131)	
				17.55/0.300	(-202)	
Sodium Calcium Phosphate	29-1193	--	1.10	32.59/0.999	(211)	67.51
				33.67/0.800	(031)	
				23.16/0.450	(111)	
Cement with Ca/P= 1.00	--	--	--	--	--	70.52
Cement with Ca/P= 1.50	--	--	--	--	--	82.45
Cement with Ca/P= 1.67	--	--	--	--	--	86.01

## 5.5. Porosity Determination by Archimedes' Water Intrusion Method

Archimedes's method is based on the direct proportionality between the density of an object immersed in water and the buoyant force acting on it. When an object is placed in a container of water, the level of the water rises. The level raises the same height as if the volume of water was increased by the submerged volume of the object, or the volume of water the object displaces.

$$V_{submerged} = V_{displaced} \quad (5.8)$$

Archimedes' principle is stated as "A body wholly or partially immersed in a fluid will be buoyed up by a force equal to the weight of the fluid that it displaces" (Resnick 1988). Accordingly, the buoyant force in a fluid with a density  $\rho_F$  is:

$$B = \rho_F V_{displaced} g \quad (5.9)$$

Water is chosen as the test fluid because it is very readily available and is frequently used in the measurement of density. One defines for a material with a density,  $\rho_m$ , a specific density,  $S_m$  as:

$$S_m = \frac{\rho_m}{\rho_w} \quad (5.10)$$

The buoyant force for a wholly immersed object is:

$$B = W_A - W_B \quad (5.11)$$

where  $W_A$  is the weight measured using the balance with the beaker of water before the object is immersed and  $W_B$  is the balance reading for the beaker of water with the object immersed as seen in Figure 5.2. Combining equations 5.9-5.11 gives the specific gravity of the object in terms of three measured weights:

$$S_{object} = \frac{\rho_{object}}{\rho_{water}} = \frac{m_{object}/V_{object}}{B/V_{displaced}g} = \frac{mg}{B} \quad (5.12)$$

$$S_{object} = \frac{W_{object}}{W_A - W_B} \quad (5.13)$$

Obtained density of object is compared to the theoretical density of the object with no porosity in order to estimate the total porosity. The volume of intruded water is calculated as the open pore volume:

$$V_{Pore} = \frac{m_{object}}{\rho_{object}} - \frac{m_{object}}{\rho_{theoretical}} \quad (5.14)$$

$$V_{OpenPore} = \frac{m_{object} - W_B}{\rho_{water}} \quad (5.15)$$

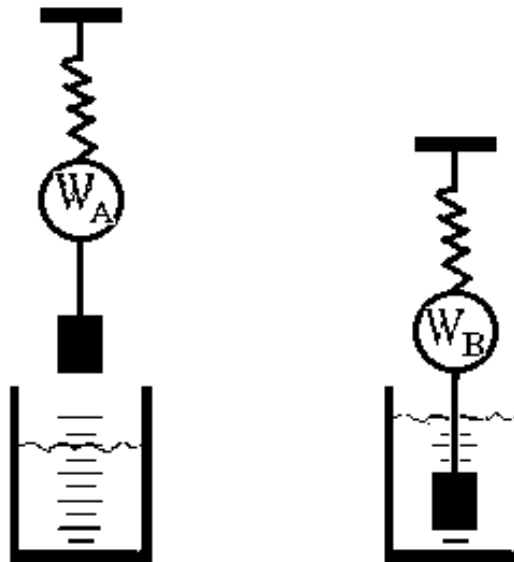


Figure 5.2. The balance setup for measuring the buoyant force and specific density.

## 5.6. Morphological Analysis of Macroporous Blocks

The ideal way to observe the microstructure would be microcomputer tomography analysis which generates a three dimensional image of the whole construct from serial cross sectional analysis (Mather et al. 2008). Scanning electron or optical microscopy are also considered as viable alternatives in cross sectional analysis of macroporous constructs provided that the light intensity and image resolution are sufficiently high to yield high contrast between the pores and matrix phase. Measuring the porosity of materials by digital image analysis of micrographs is a convenient

method for the testing of metallic samples (von Bradke et al. 2005). However applying this method to ceramics produces two sources of error that make the method less reliable and less reproducible: The high optical opacity of the material leads to poor contrast existing at pore edges. This property makes all light microscope methods inferior to electron microscopy for quantitative determination of pore dimensions. The second factor is the influence of the sample preparation technique itself through alteration of the pore shape near the cross-section face. In brittle ceramic materials, edges of the pores tend to break off during grinding and polishing, leading to creation of more conically shaped pores close to the polished surface. This factor again leads to poor edge contrast and to the observed dependence of pore dimensions on the imaging parameters selected.

Optical microscopy was utilized in this morphological analysis of sample microstructure mainly due to the sheer abundance of samples and the large size of the microstructural features analyzed. Above mentioned shortcomings were minimized by two strategies. Instead of cutting through the cross section of the leached porous samples, unleached samples were cut using precision cutter so that both calcium phosphate matrix and NaCl particles were bisected without inducing a major change on the edges of the pores. Sliced samples were then leached in deionized water to expose the contrasting pores and to eliminate the polishing effect of the cutter blade by some surface dissolution of the calcium phosphate matrix, thereby lowering its opacity. Still, some extra reflection from matrix phase occurred due to its opacity but the noise produced was eliminated by image enhancement techniques supported by the image analysis software.

One slice of a sample from each sample set was examined under 50x and 100x magnification. The span of the focused area for 50x magnification was found upon spatial calibration as approximately 620 squaremicrons. The resolution of the micrographs captured by camera was 1024\*768 pixels and 1 pixel corresponded roughly to 0.9 micrometers. Twelve frames of adjacent images were obtained from an examination area of about 6000 squaremicrons from each sliced sample. Reproducibility of the analysis method was improved by examination of a large area on the same slice rather than small areas on various slices. Twelve micrographs with 50x magnification were analyzed using image analysis software in order to measure the porosity and morphology of the pores quantitatively.



The sequence of image analysis subsequent to image acquisition by the camera is shown in Figure 5.3. Well illuminated sample surface is focused and a micrograph with high contrast and high resolution seen in Figure 5.4a is captured by the camera. The raw image file is enhanced using the image analysis software to improve its brightness and contrast so that a binary image consisting of light pores and dark matrix is obtained as seen in Figure 5.3b. Most images contained some noise due to the opacity of the matrix phase that appeared as light regions similar to pores. Noise signals were removed from the micrograph by applying various filters to the enhanced image as seen in Figure 5.3c. Four morphological filters, open-close-dilate-erode were useful to reduce the noise. Briefly open function was used to smooth object contours, separate narrowly connected objects, and remove small dark holes. Close function is used to fill gaps and enlarge protrusions to connect objects that are close together. Dilate function enlarges the edges of bright objects and erodes dark ones. Conversely, erode function is used to erode the edges of bright objects and enlarge dark ones. Finally a binary image exhibiting high fidelity to the source micrograph is obtained. Image analysis software distinguishes the light pores from the dark background and draws an outline while counting them as seen in Figure 5.3d. If for some reason, for example poor contrast, the outline drawn does not have the pore morphology observed in the source micrograph, outline is corrected manually by hand drawing over the inaccurate pore outline. Similarly noises not completely eliminated by the filters are removed manually at the last stage of image analysis.

Once the pores are outlined and counted, image analysis software measures several geometric parameters based on the shape and size of the pore outlines. These are maximum diameter, minimum diameter, mean diameter, radius ratio, aspect ratio, caliper length, caliper width, roundness, perimeter and area. The definitions of each parameter are shown schematically in Figure 5.4. Arithmetic average of the mentioned parameters for all pores are obtained for each image of the sample. Only weighted average of radius ratio was calculated by multiplying with area of each pore. A final average value was deduced for each parameter from 10 images for each sample by discarding the images with the highest and lowest values. That average value represents the sample set and the size distribution used in the fabrication of the sample set.

Selected samples were analyzed for microstructure determination using SEM. Their fracture surfaces were coated with gold prior to examination in secondary electron mode.

## 5.7. Rheological Analysis of Porogen Suspensions and Determination of Maximum Packing Density

The relation between the solid loading and viscosity of suspensions has been the focus of the rheological analysis for many particle systems. Generally, increase in solid loading increases the suspension viscosity. Several models were developed to accurately predict the viscosity of suspensions that are applicable for a range of concentrations. The predictive capacity of the early models taking into account only dilute suspensions are much less accurate for suspensions with highly-concentrated solid fraction. The applicability of the models has much improved for concentrated suspensions by taking the particle size distribution and more importantly, the maximum packing density into account as in the study by Chong et al (Chong et al. 1971):

$$\eta_r = \left[ 1 + \frac{0.75(\phi/\phi_m)}{1-(\phi/\phi_m)} \right]^2 \quad (5.15)$$

In this model  $\eta_r$  is the relative viscosity,  $\phi$  is the packing density, and  $\phi_m$  is the maximum packing density of a given powder. As evident from the equation, suspension viscosity tends to be infinite when the solid concentration in the suspension is close to  $\phi_m$ . The maximum packing density is known to be a function of particle size distribution (Mangels et al. 1983), particle shape and size (Lam 1998). Liu et al. have shown that interparticle repulsive and attractive forces also affect the maximum packing density considerably (Tseng et al. 1999). The large number of parameters affecting maximum packing density makes it hard to theoretically predict the packing behavior of a real suspension. The most frequently used method in determining maximum packing density had been by means of a best-fit procedure to the rheological data for a given suspension until Liu et al. developed an empirical equation primarily for the determination of maximum packing density and verified it by comparing the calculated values with the reported ones available in the literature for a number of suspensions (Liu 2000):

$$\eta_r = [a(\phi_m - \phi)]^{-2} \quad (5.16)$$

where  $\eta_r$  is the relative viscosity calculated by the ratio of the obtained sample viscosity to liquid viscosity,  $\phi_m$  is the maximum packing density,  $\phi$  is the solid loading and  $a$  is a constant obtained by graphically plotting the following relation:

$$1 - \eta_r^{-1/2} = a\phi + b \quad (5.17)$$

where  $a$  is the slope and  $b$  is the intercept of the curve. At the boundary condition of  $\phi = \phi_m$ , the left hand side of the equation equals 1 and one can determine the maximum density as:

$$\phi_m = \frac{1-b}{a} \quad (5.18)$$

The coefficient of -2 at the first equation is valid for high shear rates and must be determined separately at low shear rates. The term  $(\phi_m - \phi)$  is clearly defined as the effective space available for the particles to move in the matrix media. When  $\phi \geq \phi_m$ , the effective space will reduce and the viscosity of suspensions becomes thicker and finally turns to be infinite at the point of  $\phi_m$ . The equation is a two-parameter equation and the parameters  $a$  and  $\phi_m$  can be determined easily via a single  $1 - \eta_r^{-1/2}$  versus  $\phi$  plot through the use of a few viscosity-concentration data.

Aside from determination of the maximum packing density via an extrapolation of the equations, Liu's model makes it possible to predict the viscosity of suspensions. Since the parameters  $a$  and  $\phi_m$  are determined experimentally for a given suspension, the equations form a suspension-specific model which allows the viscosity of a given suspension to be predicted precisely once the parameters are accurately determined. A change in the viscosity of the suspensions was seen for both increased solid loading, particle size and shear rate.

## CHAPTER 6

# CHEMICAL MODIFICATION OF CALCIUM PHOSPHATE CEMENT MICROSTRUCTURE

### 6.1. Analysis of the TTCP-MCPM cement setting mechanism

Tetracalcium phosphate- Monocalcium phosphate monohydrate cement system was studied in order to understand the setting reaction and the governing factors. This is the thermodynamically most feasible system in which both precursors are expected to dissolve completely and convert to more stable brushite, monetite or hydroxyapatite phases. Through an elaborate experimental research period, adequate data were produced to understand the setting kinetics of the system and the effect of statistically important variables on the conversion rate.

As mentioned before, calcium phosphate cement hardening by intergrowth of needlelike hydroxyapatite crystals is facilitated by sequential precipitation, dissolution, reprecipitation and transformation of metastable octacalcium phosphate, brushite and monetite phases. The occurrence and the rate of transformation of these phases are controlled by various kinetic parameters including Ca/P ratio, pH, temperature, ionic strength, liquid saturation, seed presence, particle size, inhibitors and promoters. These variables have direct and synergistic effects on either of the three stages of calcium phosphate cement setting:

- I. Dissolution of reactants to saturate the mixing liquid in calcium and phosphate ions
- II. Nucleation of crystals
- III. Growth of crystals

Setting starts as soon as the setting liquid is supersaturated with respect to a calcium phosphate phase. As seen in Figure 4.16, hydroxyapatite is almost always supersaturated in a calcium phosphate system. However supersaturation is the thermodynamic driving force for precipitation but kinetics determine the rate of the setting reaction. Ostwald's Rule of Stages states that the crystal phase that nucleates in a supersaturated solution is not the phase that is thermodynamically stable at that

temperature and pressure but rather another metastable phase that is closest in free energy to the parent phase (ten Wolde et al. 1999). DCPD and OCP are the metastable phases that mostly occur first in a calcium phosphate cement system. Precipitation of HA is always found to be preceded by one or more phases although HA is the most stable phase for a wide range of pH values. Homogeneous formation of HA at low concentrations is almost never observed due to the activation energy barrier for nucleation that should be overcome with high supersaturation. Particle size, pH and temperature are the important factors that have direct effect on solubility of the precursors and hence the supersaturation of the liquid

It is demonstrated in many CPC experiments that nucleation occurs during the mixing stage. This is explained as rapid formation of very small critical nuclei at very high local supersaturation. These nuclei are never of the most stable phase HA, rather of more soluble calcium phosphate phases OCP and DCPD. They serve as template for heterogeneous nucleation of these phases, their further growth and subsequent transformation to HA. Precipitation consists of nucleation and growth stages and kinetics of the system determines which stage is dominant at the extent of precipitation. The form of the precipitation may vary widely depending upon factors such as the degree of coherency between the precipitates and matrix, the degree of supersaturation, and the availability of heterogeneous nucleation sites. Ionic strength directly affects ionic product and hence supersaturation of a phase. Since the desired precipitate phase in a calcium phosphate cement is hydroxyapatite, the presence of large amount of hydroxyapatite seeds in the setting liquid is expected to improve the nucleation rate.

Growth in CPC takes place by the deposition and incorporation of dissolved calcium and phosphate molecules onto steps on the seed surfaces, causing them to advance quickly along the surface, perpendicular to the step. Growth is driven by supersaturation and individual nuclei could have their growth limited by the decreasing supersaturation in the untransformed volume. When nucleation and growth occur simultaneously as in the case of calcium phosphate cements, the overall transformation rate and microstructural characteristics such as particle or grain size depend on the interplay of nucleation and growth processes (Balluffi 2005). Seed size and surface area have direct influence on the growth of precipitates. Also change in the Ca/P ratio during precipitation is of great importance in the calcium phosphate system where the different crystalline modifications all have different calcium and phosphate contents. By varying the Ca/P ratio, the supersaturations of the different phases can be decreased or

increased. Another factor influencing the growth rate of hydroxyapatite is temperature. It has been shown that while hydroxyapatite exhibiting an acicular, needlelike habit forms at all temperatures, the aspect ratio of the needles increases with increasing temperature (Brown et al. 1991).

Thermodynamic analysis of another TTCP containing cement formulation suggests that setting is an exothermic reaction consisting of several steps (Liu et al. 2003). In the initiating period of 5–10 minutes, water is absorbed and then imbibed the surface of the grains upon mixing calcium phosphate powder with water. This is a physical exothermic process. In the inducing period or latency, the particle dissolution contributes to a rise in concentration of the  $\text{Ca}^{2+}$  and  $\text{PO}_4^{3-}$  ion in the solution. With the different dissolution rates of precursors, the pH translates towards the basicity region until the solution is supersaturated, and then HA crystallizes from the solution. The accelerating period is a fast reaction controlled region. In the decelerating period, hydration reaction decreases and the reaction process converts from surface reaction controlled to diffusion controlled after the hydrate product grows around the particle surface of the raw materials. The hydrate product layer is destroyed by osmotic pressure and crystallization interior stress, and leads to the increase of the reaction rate and another slight exothermic peak (Liu et al. 2003).

Conversion of starting calcium phosphate cement powder to hydroxyapatite is the governing factor for the strength of the cement and high values should be achieved for maximum strength. For the calcium phosphate system covered in this work, different products of HA, DCPD, DCP, OCP are present in the microstructure. Their conversion rates are important individually to understand the setting kinetics. Ultimately forming HA conversion is the one that has to be maximized to achieve strong structure rapidly. Quantitative X-ray diffraction is the most convenient method to analyze the extent of setting reaction for a cement system. In the literature there are numerous studies utilizing internal standard, external standard and direct comparison methods as a means to quantify the composition of multiphase ceramics. Internal standard and direct comparison methods are best applicable to simple systems with small number of phases. For a complex system such as the one studied in this work, containing 6 phases at any time during setting, the more precise external standard method is suitable.

Using quantitative XRD analysis based on external standard method and taking corundum as the external standard, integrated net intensities of each characteristic peak of constituent phases were measured and converted to weight percent concentration for

every sample of all 32 experimental runs. A ruggedness test was applied to sample number to check the effectiveness of the methods and the repeatability of the experiment. This experiment was repeated three times at the same conditions and the quantitative analysis was applied to each sample. As seen in Table 6.1, the calculated concentrations are close especially for the impurity phases  $\alpha$ -TCP and  $\beta$ -TCP. This suggests that the quantitative analysis method is accurate. Small variations in the major phases should mainly be a result of uncontrolled experimental variations including the powder/liquid ratio, room temperature or mixing rate.

Table 6.1. Ruggedness Test Results

HA content	Analysis Period						
	15 min	30 min	60 min	2 hr	4 hr	24 hr	240 hr
2A	24.92	24.94	26.88	32.24	--	--	32.32
2B	18.16	19.77	20.03	--	22.94	28.01	28.78
2C	16.61	17.70	19.93	22.38	26.31	--	33.72
mean	19.90	20.80	22.28	27.31	24.63	28.01	31.61
std. dev.	4.42	3.73	3.98	6.97	2.38	--	2.55
<b>TTCP content</b>							
2A	33.23	34.88	31.35	30.35	--	--	30.44
2B	34.13	32.76	33.11	--	32.56	30.21	29.77
2C	33.44	33.79	34.14	33.42	29.51	--	25.69
mean	33.60	33.81	32.86	31.89	31.03	30.21	28.63
std. dev.	0.47	1.06	1.41	2.17	2.16	--	2.57
<b>DCPD content</b>							
2A	12.87	11.62	11.10	8.12	--	--	8.75
2B	19.95	20.53	19.29	--	18.46	14.21	12.46
2C	23.23	22.39	18.64	15.58	14.71	--	10.41
mean	18.68	18.18	16.34	11.85	16.59	14.21	10.54
std. dev.	5.29	5.76	4.55	5.28	2.65	--	1.86
<b>DCP content</b>							
2A	4.22	4.74	6.26	6.00	--	--	3.64
2B	4.38	4.43	3.69	--	4.15	3.99	3.48
2C	2.74	2.73	3.18	3.71	3.86	--	4.48
mean	3.78	3.97	4.37	4.86	4.01	3.99	3.86
std. dev.	0.90	1.08	1.65	1.62	0.20	--	0.54
<b><math>\alpha</math>-TCP content</b>							
2A	16.41	15.14	16.09	16.36	--	--	17.88
2B	15.18	13.50	15.91	--	13.07	16.76	16.39
2C	15.76	15.68	14.61	15.92	19.69	--	18.52
mean	15.78	14.77	15.54	16.14	16.38	16.76	17.60
std. dev.	0.61	1.13	0.81	0.31	4.68	--	1.09
<b><math>\beta</math>-TCP content</b>							
2A	7.86	8.17	7.74	7.01	--	--	7.22
2B	8.98	9.30	8.25	--	9.16	7.41	8.26
2C	7.70	8.61	8.47	8.36	7.41	--	7.69
mean	8.18	8.69	8.15	7.68	8.28	7.41	7.72
std. dev.	0.43	0.63	0.52	0.65	0.78	--	0.53

The phases of major interest are hydroxyapatite and tetracalcium phosphate. HA is the major end product that imparts strength to the cement and TTCP is the major precursor whose conversion increases the strength. Two high temperature calcium

phosphates  $\alpha$ -TCP and  $\beta$ -TCP formed in large quantities during synthesis of TTCP due to imperfect cooling of the batch. Their total amount approaches TTCP amount and they also act as cement precursors due to their high solubility. The other precursor monocalciumphosphate monohydrate is extremely soluble in water and almost instantly dissolved when mixed with the setting liquid. For this reason it is never observed in the XRD patterns. Brushite and monetite are the intermediate phases that have high solubilities and low supersaturations compared to hydroxyapatite. According to Ostwald's rule of stages their formation is more probable than HA formation but eventually they convert to HA. Their presence in this experiment indicates combination of variables creating kinetic conditions favorable for an alternate route than predicted by thermodynamics. The main responses of the experimental design are TTCP consumption percentage and maximum HA content. The significant variables contributing to both of these responses are expected to increase strength and can be used in the optimization of cement properties. The conversion extent for major phases is given in Table 6.2.

The strength of the cement blocks were seen to be highly correlated with the HA formation ratio as seen in Figure 6.1. The strength evolution graph of the strongest sample 31 shown in Figure 6.2 reveals that significant strength increase occurred at late stages of the setting process. The early high strength of this sample is a result of instant monetite formation from MCPM upon mixing with setting liquid. Since formation of monetite is kinetically favored at the early stages, formation of this relatively stronger phase in contrast to brushite leads to compact cement crystals that can further intergrow with subsequent formation of HA at the later stages. In fact, the strongest cement samples regardless of the porosity variation are the ones going through this two stage multiphase formation mechanism.



Table 6.2. Conversion extent of the cement samples

Run	TTCP conversion %	Max HA content	Max DCPD content	Max DCP content
1	54.14	50.89	2.79	1.18
2	20.71	28.01	20.53	20.53
3	51.96	34.31	3.72	11.99
4	9.31	27.16	1.72	5.36
5	44.05	37.66	0.91	14.81
6	45.20	26.81	22.18	23.71
7	32.11	24.12	24.86	2.05
8	39.65	27.18	23.88	2.09
9	7.21	23.71	7.02	5.68
10	42.92	35.33	20.11	10.31
11	37.58	33.15	2.98	13.83
12	39.95	25.65	23.54	1.98
13	45.78	32.30	16.46	12.20
14	10.46	27.07	4.68	2.39
15	24.95	31.99	2.39	3.96
16	18.96	21.89	2.87	15.30
17	42.88	35.04	11.25	12.02
18	22.15	27.52	8.88	4.03
19	44.04	44.23	5.21	1.50
20	8.66	23.45	24.61	18.44
21	47.28	30.97	24.61	6.51
22	27.98	25.30	28.69	3.18
23	19.91	27.89	2.29	4.86
24	25.97	26.95	1.23	14.18
25	30.63	30.19	1.25	19.77
26	48.19	44.14	10.13	3.19
27	45.34	40.92	1.49	6.09
28	16.46	24.28	1.63	12.64
29	46.96	36.03	5.39	12.65
30	22.10	33.02	7.63	13.90
31	31.50	33.89	1.70	14.58
32	25.93	37.01	6.42	2.31

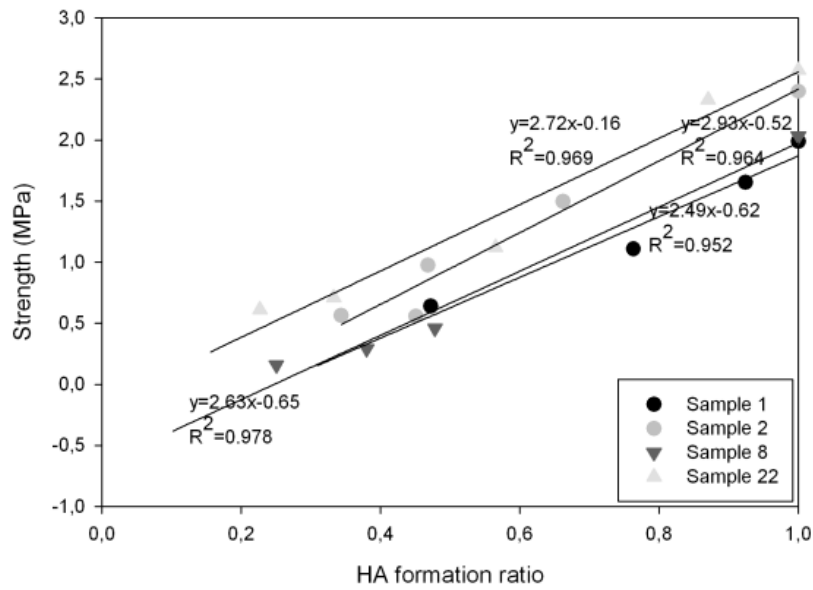


Figure 6.1. Correlation of compressive strength with HA formation ratio.

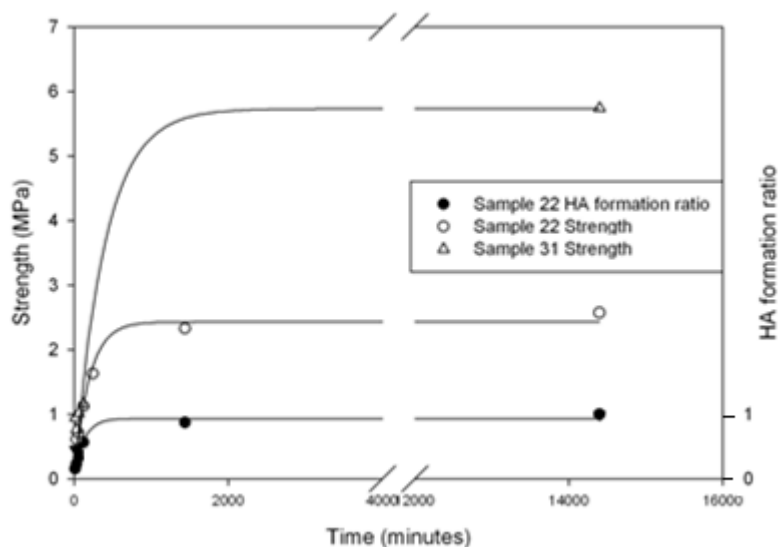


Figure 6.2. Correlation of compressive strength with setting time.

The effect of the experimental parameters Ca/P ratio, pH, temperature, ionic strength, liquid saturation, seed presence, and precursor particle size on the responses TTCP conversion %, and HA formation extent are statistically analyzed by analysis of variance on the data gathered from 32 samples. The most significant factors were determined as the ionic strength, temperature, pH, setting liquid saturation and precursor particle size. Individual effects of these parameters on various responses are presented in detail in the following sections.

### 6.1.1. Effect of Ionic Strength

Ionic strength of the setting liquid was modified by addition of 1 M and 0.1 M NaCl which is the main leachable porogen used for macropore induction. From that point of view, this study provides significant information on the adverse effects that NaCl addition may cause to the developing cement structure. Ionic strength was found to affect the conversion and formation of all phases significantly according to the statistical analysis. It is interesting that only brushite formation was adversely affected by increasing ionic strength. This is explained by brushite being the least supersaturated phase among all stable calcium phosphate phases. Yet, brushite is the first precipitating calcium phosphate phase in pure water setting of conventional brushite cements as

revealed by Ostwald rule of stages. Brushite is expected to lose both supersaturation and kinetic conditions favoring its formation as ionic strength starts to increase. Monetite is slightly more supersaturated than brushite so its formation is also expected to be adversely affected by increase in ionic strength. However monetite formation is positively affected by ionic strength increase as seen in Figure 6.3, though not as much as hydroxyapatite. The results of this study suggest that the small difference in the supersaturation between brushite and monetite provides a barrier that may inhibit brushite and enhance monetite formation. This observation will be further investigated in the subsequent sections.

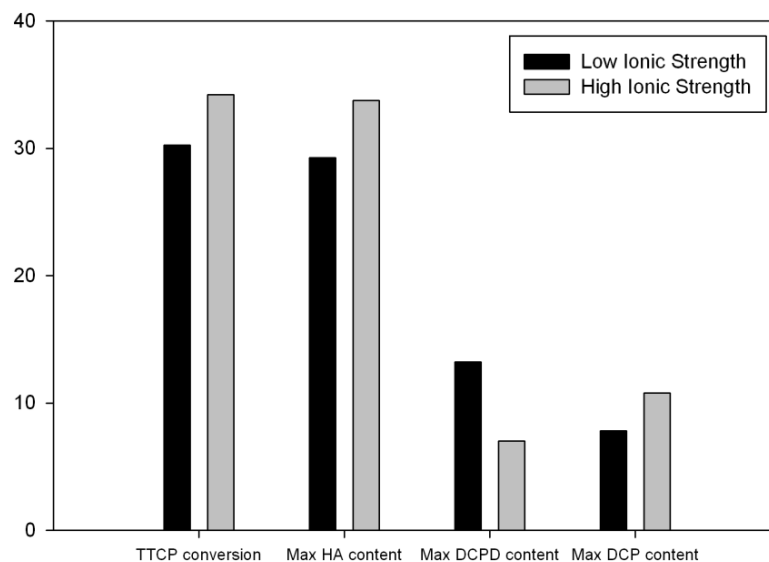


Figure 6.3. Effect of ionic strength variation on analysis responses.

### 6.1.2. Effect of Temperature

Temperature was found to be a significant variable for conversion and formation of brushite and monetite as seen in Figure 6.4. Temperature change between 25 and 50 °C was only insignificant for HA formation. This may result from the balance of the positive effect of temperature on crystal growth and the strong negative influence on dissolution of TTCP due to the exothermic nature of dissolution (Bohner et al. 2008). High correlation of temperature with brushite and monetite formation ratio support that these two intermediate phases are generally formed at the beginning of the setting reaction where dissolution of the precursors is the highest. Positive influence of high

temperature on monetite formation is in agreement with literature as brushite is known to convert to monetite at temperatures in excess of 40 °C (Bohner 2000).

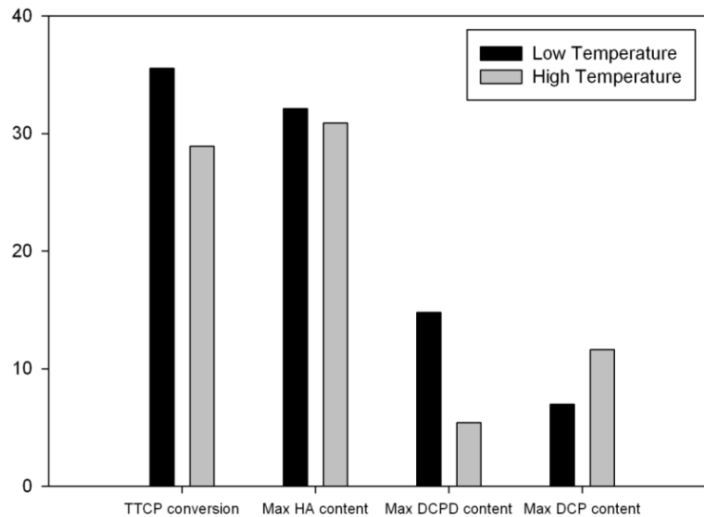


Figure 6.4. Effect of temperature variation on analysis responses.

### 6.1.3. Effect of pH

Initial pH of the setting liquid was found to be significant for only TTCP conversion and HA formation. As seen in Figure 6.5 pH lower than 6.5 favored both processes. TTCP dissolution is favored by acidic conditions and the resultant increase in HA yield is expected. Brushite and monetite formation that compete against HA formation is similarly favored at pH greater than 6.5. The reason may be thermodynamic as the increase in precursor solubility may enhance the formation of the already highly supersaturated hydroxyapatite in place of the metastable brushite and monetite at low pH.

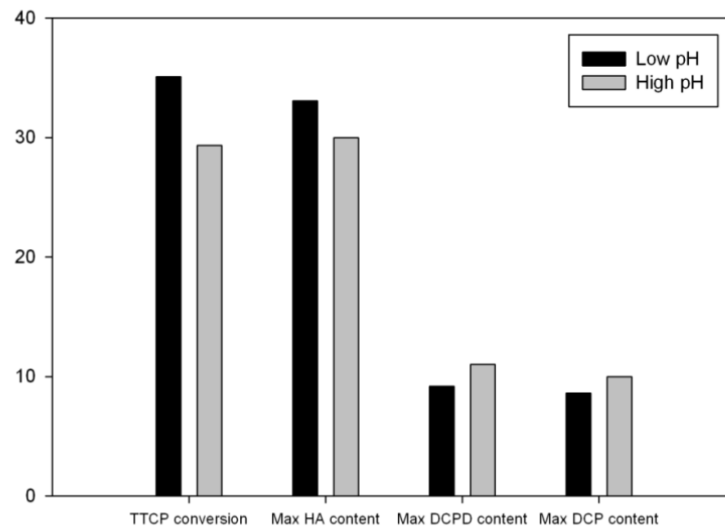


Figure 6.5. Effect of pH variation on analysis responses.

#### 6.1.4. Effect of Setting Liquid Saturation

The saturation level of setting liquid was maintained by addition of 0.1 and 0.01 M  $\text{NaH}_2\text{PO}_4$ .  $\text{HPO}_4^{2-}$  and  $\text{PO}_4^{3-}$  ions supplied by the  $\text{H}_2\text{PO}_4^-$  group are effective in increasing the supersaturation of precipitating calcium phosphate phases. This is reflected on the increase in hydroxyapatite and monetite content of the cement blocks seen in Figure 6.6. Rapidly depleting calcium ion concentration in the solution is balanced by the increased dissolution of TTCP at high initial saturation of the setting liquid.

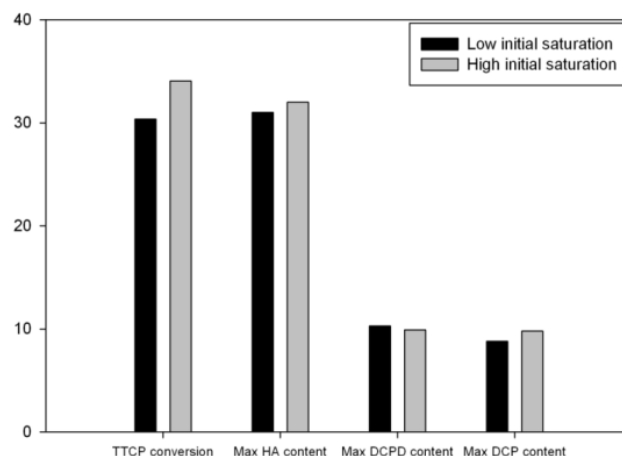


Figure 6.6. Effect of phosphate saturation variation on analysis responses.

### 6.1.5. Effect of Precursor Size

MCPM particle size has a strong negative influence on TTCP conversion and HA formation due to dependence of these processes on high solubility of TTCP facilitated by the low pH provided by rapid dissolution of acidic MCPM phase. In contrast this variable has strong positive influence on brushite formation and small positive influence on monetite formation as a result of the competition between formation of these phases and formation of HA. The effects are seen in Figure 6.7.

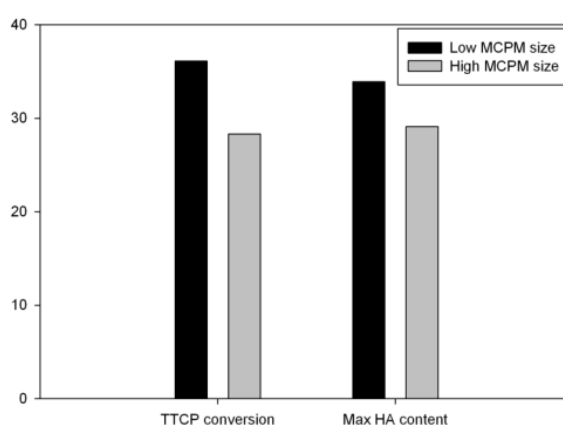


Figure 6.7. Effect of precursor size variation on analysis responses.

The aim of the present study was to understand the setting kinetics of the TTCP-MCPM system, determine the significant variables that have an effect on the kinetics,

and develop strategies to optimize strength of cements applicable to all cement systems. Mechanical tests provided information on the correlation of conversion with strength but they were not used for comparative purposes due to the inaccuracy of strength values. Nevertheless, some strong samples stood out and had a common property. These samples contained significant amounts of both monetite and hydroxyapatite, suggesting a biphasic approach to optimize the strength of calcium phosphate cements. Due to the competition between formation processes of hydroxyapatite and monetite, the variables leading to such a structure were quite different from those resulting in high HA content.

Ionic strength and temperature are the two key variables promoting monetite formation in place of hydroxyapatite. The results on ionic strength are especially important due to its common use as macropore inducing porogen in cements. High initial saturation and low Ca/P ratio increase the thermodynamic driving force of initial monetite formation while reducing that of hydroxyapatite. Interestingly, low pH values were found to promote high HA content and high pH to promote high monetite content probably due to the narrow range of tested pH values in the vicinity of singular point for the TTCP-MCPM system. Low MCPM precursor size favored both formation routes, suggesting that precursor particle size has a strong effect on the kinetics of setting reaction. TTCP and HA seed size were relatively insignificant factors.

The next step in the thesis work is the investigation of ionic modification of the conventional brushite cement system based on the information gathered from this study. Ionic strength will be utilized as a control parameter on the monetite content and impurity effect of citric acid is expected to enable selective inhibition of brushite formation. A robust, strong cement microstructure is aimed as a result. The subsequent final step will involve macropore induction to the obtained strong cement.

## 6.2. Investigation of the Effect of Ionic Modifiers on the Setting Kinetics of the $\beta$ -TCP – MCPM cement system

Understanding the mechanism of setting, thermodynamic and kinetic considerations were completed by literature review and experimental data at the beginning of the thesis. According to the preliminary study it was concluded that calcium phosphate cement setting reaction is essentially an acid-base reaction that consists of dissolution, nucleation and growth steps that are kinetically affected by parameters including precursor size, seed presence, pH, temperature, Ca/P ratio, ionic strength, and liquid saturation. Control of these parameters enables tailor-made cement blocks with desired phase structure, strength, and setting time.

Special emphasis is given to NaCl in this study not only because it is one of the most commonly utilized porogens in scaffold design but also it is a strong electrolyte in aqueous solutions that determines the ionic strength and hence the setting kinetics of the calcium phosphate cements. For hydroxyapatite forming cement systems, the end product is always hydroxyapatite, the most supersaturated phase above pH 4.2. For these cement systems, the effect of ionic strength on suppression of supersaturation does not significantly affect the phase composition of the set cement. However brushite forming cement systems are highly susceptible to fluctuations in ionic strength since brushite is not the most supersaturated phase below pH 4.2. Its dehydrated and stronger form monetite is the most stable phase with the highest supersaturation in brushite forming cement systems. It is clear according to Ostwald rule of stages that precipitation product in a system is not the thermodynamically most stable phase but the phase with free energy closest to the parent phases. This principle also applies to hydroxyapatite forming cements but due to the high supersaturation difference between intermediate phases and hydroxyapatite, the latter eventually forms. In the case of brushite forming acidic cement systems, the supersaturation difference between brushite and monetite is not high. Therefore small variations in the supersaturation due to change in ionic strength may cause significant alterations in the phase structure.

In fact that is what was observed and reported in the previous study. Among the parameters affecting the kinetics of the cement setting reaction, ionic strength was statistically found to be the most significant parameter in terms of the responses including TTCP consumption, brushite formation, monetite formation, and HA formation. Brushite formation was adversely affected by increased ionic strength due to



the above mentioned phenomenon while monetite and hydroxyapatite formation were enhanced at different pH values. The most noteworthy conclusion of the previous study was that a monetite-hydroxyapatite biphasic calcium phosphate cement obtained due to high ionic strength was the strongest of the 32 samples. This was enabled in the pH region higher than 4.2 by elimination of brushite formation as an intermediate phase. Instead monetite was formed and due to its stability, competed with hydroxyapatite for the final phase. However in order to reach a solid conclusion on the phase changing effect, further investigation of cement setting kinetics under high ionic strength was needed.

Scope of the current report is almost entirely restricted to the in depth analysis and application of ionic modification to the calcium phosphate cement setting liquid using NaCl and citric acid. Various thermodynamical and kinetic models were utilized to predict and understand the variation in driving force for the cement setting reaction. Citric acid is chosen due to its multifunctionality also as a setting retardant that enhanced workability of the cement paste. The observed and reported data in the subsequent sections are sound confirmation of the synergistic effect of citric acid and NaCl as ionic modifiers on the brushite to monetite transformation. Relation of the two ionic modifiers with the setting cement enable controlled transformation of brushite cement to monetite cement. This relation has not been covered in calcium phosphate cement literature.

Kinetics for dissolution and growth of the  $\beta$ -TCP – MCPM cement system was observed by conducting controlled growth experiments in both pH free drift and pH-stat condition. Observed pH fluctuations and base uptake point to the dissolution and growth of the proton consuming calcium phosphate phases during conversion of cement precursors in all samples. Setting reaction in a  $\beta$ -tricalcium phosphate – monocalcium phosphate monohydrate cement system is expected to undergo distinct stages shown schematically in Figure 6.8. The setting reaction includes (A) instant dissolution, (B) supersaturation build-up, (C) relaxation periods through which kinetically most favorable phase precipitates. MCPM completely dissolves in the first period due to its high solubility, while  $\beta$ -tricalcium phosphate dissolution continues indefinitely (Bohner et al. 2008). MCPM dissolution supplies  $\text{H}_2\text{PO}_4^-$  ions and  $\beta$ -TCP dissolution supplies  $\text{PO}_4^{3-}$  ions to the solution as well as  $\text{Ca}^{2+}$ . The solution is initially rich in calcium while  $\text{HPO}_4^{2-}$  concentration depends on the equilibrium between phosphoric acid species  $\text{H}_3\text{PO}_4$ ,  $\text{H}_2\text{PO}_4^-$ ,  $\text{HPO}_4^{2-}$ , and  $\text{PO}_4^{3-}$ . Instant MCPM dissolution creates a reservoir of the

thermodynamically stable  $\text{H}_2\text{PO}_4^-$  which dissociates into  $\text{HPO}_4^{2-}$  and  $\text{H}^+$  at a rate determined by the pH and ionic strength of the solution. On the other hand,  $\text{PO}_4^{3-}$  ions released from the relatively slow dissolving  $\beta$ -TCP crystals consume the protons in the solution during conversion to  $\text{HPO}_4^{2-}$  ions, increasing the pH of the solution. Supersaturation is built up until the relaxation period upon which either one of the stable acidic phases, brushite or monetite starts to form, depleting total calcium and phosphate ions. If the kinetics of the system have been modified, for example by a temperature rise, monetite is favored relative to brushite and the precipitation order may change to such an extent that pure monetite formation or simultaneous formation of both phases may be observed (Rabatin 1960).

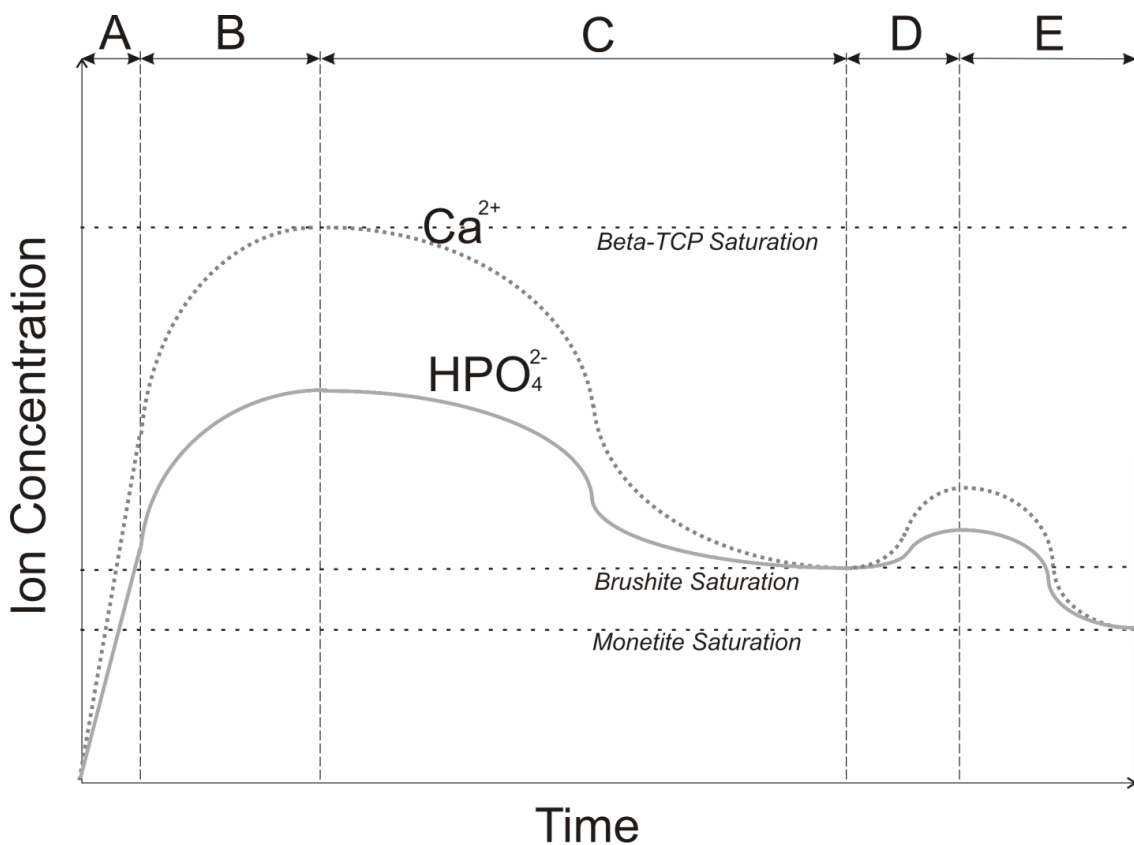


Figure 6.8. Schematic representation of the calcium and phosphate concentrations during brushite cement setting.

Solubility isotherms for the  $\text{CaOH-H}_2\text{O-H}_3\text{PO}_4$  system dictate that in the acidic pH range, the solubility of the phases present in the system under study follows the order of (Fernandez et al. 1999):

The beginning of the relaxation period is only a matter of supersaturation, the thermodynamic driving force of crystallization, once the stoichiometric Ca/P ratio of 1 for the two stable phases brushite and monetite is maintained. The relaxation period continues until the precipitating phase is saturated in the ideal case of ordered kinetics based on Ostwald rule of stages. The supersaturation build-up period consists entirely of  $\beta$ -tricalcium phosphate dissolution since MCPM is expected to completely dissolve at the instant of mixing with excess water. Variations in pH, temperature, ionic strength, impurity concentrations directly alter  $\beta$ -tricalcium phosphate dissolution rate as a result of which, the relaxation period extends or shortens. Kinetically, not thermodynamically most favorable phase precipitates to a large extent at the end of the relaxation period in accord with the Ostwald rule of stages. Secondary supersaturation build-up (D), and secondary relaxation (E) periods are possible within observed experiment time as a result of presence of multiple stable phases due to the difference between solubilities of brushite and monetite.

Among the factors directly affecting the supersaturation of the stable calcium phosphate phases, the most prominent effect is caused by the ionic strength of the cement setting liquid as demonstrated in Figure 4.18 by the highly precise Pitzer model of ionic activity in electrolyte solutions. Accordingly, both supersaturations of brushite and monetite and the difference between their supersaturations exponentially decrease with the increasing ionic strength of the solution.

The ion specific interaction equation developed by Pitzer for complex electrolyte solutions is an expansion of Debye-Huckel equation and is valid up to 6 M (Sheikholeslami et al. 2003). The Pitzer ion interaction approach is based on sets of theoretically and empirically derived equations that account for the interactions between the particular ions present in a solution and for indirect forces arising from the ion-solvent interaction (Pitzer 1973). It takes into consideration various combinations of ionic interactions in a solution. A valuable simplification Pitzer introduced is the assumption that the semi-empirical ion interaction parameters for simple solutions are identical with those in multiple electrolyte solutions (Krumgalz 2001). Ion interaction parameters are determined from single electrolyte solutions and from mixed solutions with either a common cation or anion. The constants used in the calculation of the

supersaturation for calcium phosphates are given by Pitzer (Pitzer et al. 1973; Pitzer et al. 1974).

Another kinetic effect that is directly related to ionic strength is the impurity effect. Impurities may be present in the solvent in trace amounts or intentionally added to alter crystal dissolution and growth. Impurities may substitute for similar ions in the crystal, bind to the surface ions with affinity, hindering step motion, or chelate free ions with affinity in the solution (Orme et al. 2007). Impurities thereby inhibit both dissolution and growth of the crystals. Nancollas et al. demonstrated the general inhibitory effect of citrate on brushite growth as a function of the citric acid concentration (Tang et al. 2005). It is known that at high supersaturations impurities are ineffective as the surface integration rate is too high (Mersmann 2001). In order to enhance impurity effectiveness, supersaturation of the solution should be reduced, for instance by increasing the ionic strength with a simple electrolyte such as NaCl.

NaCl is soluble in water at 25 °C up to 6.143 M. Pitzer's equation predicts the supersaturation of calcium phosphates accurately in a wide range of NaCl concentrations from 0 to about 5 M since the ionic strength of a saturated aqueous calcium phosphate solution is around 0.8. Supersaturations of both brushite and monetite are suppressed to extremely low values around an ionic strength of 2 as seen in Figure 4.18. Theoretically, addition of about 1 M NaCl is sufficient to reduce the supersaturation of calcium phosphates to such low levels that surface integration of ions is expected to become the rate determining step of crystallization. According to Mersmann, crystal growth is controlled by diffusion at high supersaturations and low solubility (Mersmann 2001). Surface integration rate is expected to be surpassed by the increasing diffusion rate as the solubilities of the stable phases increase. If the supersaturation is increased again as in a cement supersaturation build-up period, surface integration becomes increasingly faster to a limit where it exceeds the rate of diffusion.

Role of NaCl and citric acid as ionic modifiers to balance the supersaturation and to control the solubility in brushite cement were investigated in this study as possible control parameters for monetite formation. High supersaturations encountered at low ionic modifier concentrations are expected to result in high crystal growth rates. Dissolution of cement precursors on the other hand are expected to be hindered at high ionic strength and impurity concentrations, further lowering the driving force for crystallization. Growth curves of the conventional brushite cement system set in excess

aqueous solution containing NaCl and citric acid were analyzed in order to determine their effect on monetite phase formation despite the unfavorable kinetic conditions for crystal growth. The results of the study will provide cues for controlling monetite content in acidic cement setting applications under sufficiently high growth rates.

### **6.2.1. The Singular Effects of NaCl and Citric Acid Modifiers on Brushite Cement Setting Kinetics**

MCPM instantly dissolves and supplies  $\text{H}_2\text{PO}_4^-$  and  $\text{Ca}^{2+}$  ions to the solution upon mixing the cement precursors with excess setting liquid. A small fraction of  $\text{H}_2\text{PO}_4^-$  is expected to dissociate to  $\text{H}^+$  and  $\text{HPO}_4^{2-}$  ions due to its relative stability among phosphoric acid species in water at room temperature (Wang et al. 2008).  $\beta$ -TCP dissolves simultaneously to release  $3\text{Ca}^{2+}$  and  $2\text{PO}_4^{3-}$  that can form brushite  $\text{CaHPO}_4 \cdot 2\text{H}_2\text{O}$  provided that the same amount of  $\text{H}^+$  ions are removed from the solution to first form  $\text{HPO}_4^{2-}$  groups, resulting in an overall increase in solution pH as seen in Figure 6.9. The  $\text{H}^+$  ions supplied by  $\text{H}_2\text{PO}_4^-$  ions are expected to increase over time as more  $\text{H}^+$  ions are consumed by dissolving  $\beta$ -TCP species and a net decrease in pH is expected as growth progresses shortly after mixing the reactant with water. Built-up supersaturation is quickly relaxed in the system under study due to the presence of brushite seeds as brushite is known to be preferred to monetite at pH 4.2 and room temperature (Gbureck et al. 2005). The broad peak observed in Figure 6.9 around 100 seconds is an indication of the supersaturation build-up due to fast  $\beta$ -TCP dissolution at lower pH and the subsequent gradual pH fall indicates that brushite growth has speeded up relative to  $\beta$ -TCP dissolution. Precipitation and  $\beta$ -TCP dissolution act to balance the supersaturation and pH until one weakens relative to the other. This interplay between dissolution and precipitation continues indefinitely until the consumption of precursors.

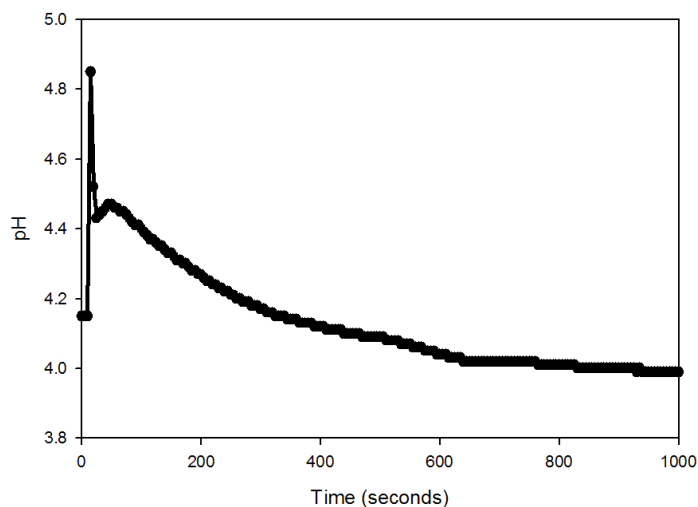


Figure 6.9. Variation in the pH of the setting solution for  $\beta$ -TCP – MCPM cement with brushite seeds.

#### 6.2.1.1. Analysis of the Free Drift Runs

Sodium chloride was introduced into 100 ml of setting liquid up to 6 M concentration. Free drift and monitoring of  $\beta$ -TCP – MCPM cement in the presence of 3% seed were conducted at ambient temperature. The initial sharp peak corresponding to simultaneous dissolution of MCPM and  $\beta$ -TCP diminished gradually with increasing NaCl concentration. Increasing the NaCl concentration shifted the instantaneous pH of the setting liquid to a lower value, by about  $\Delta\text{pH}=0.2$  with each 1 M increase as seen in Figure 6.10. This is attributed to the decrease in solubility of calcium source  $\beta$ -TCP as sodium, a monovalent cation, is expected to decrease the equilibrium concentration of cations with similar electron affinity (König 1987). The pH drop observed with increasing NaCl concentration was a result of dissociation of  $\text{H}_2\text{PO}_4^-$  into  $\text{HPO}_4^{2-}$  and  $\text{H}^+$  with the absence of the  $\text{H}^+$  consuming  $\text{PO}_4^{3-}$  ions. The supersaturation build-up represented by the broad peak also occurred later compared to pure water and a higher peak was observed for lower NaCl concentrations. The height and slope of the broad peak decreased with increasing NaCl concentration up to 6 M where supersaturation build-up was finally not detected due to effective suppression of  $\beta$ -TCP dissolution at the highest ionic strength attained.

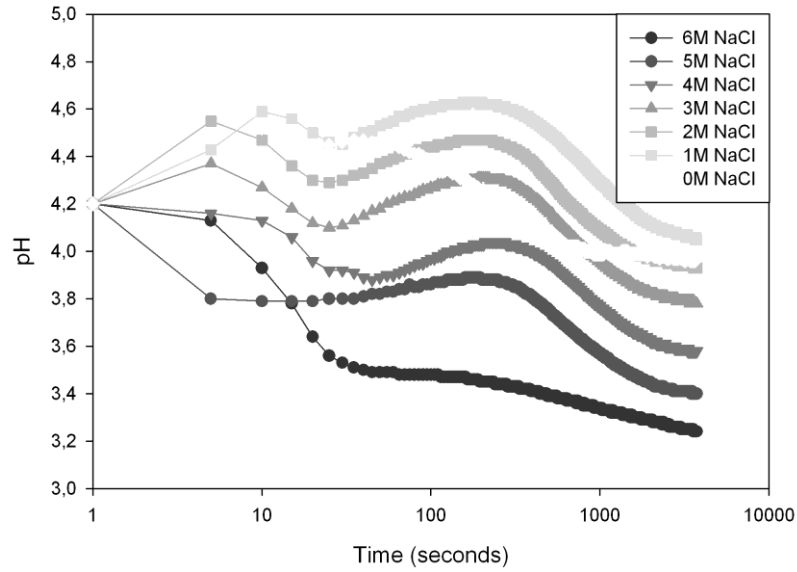


Figure 6.10. Variation of pH in free drift runs with increasing NaCl concentration.

Phase composition of free drift samples given in Figure 6.11 reveals that NaCl addition inhibited  $\beta$ -TCP dissolution remarkably despite the observed pH drop. Brushite amount decreased and monetite amount increased especially at low and high NaCl concentrations. A slight increase in brushite amount was detected above 2 M NaCl where the growth kinetics are thought to be controlled by diffusion as surface integration of the  $\text{Ca}^{2+}$  and  $\text{HPO}_4^{2-}$  species are expected to become slower due to the suppression of activity coefficients at increasingly higher ionic strengths. Another change in growth kinetics may be responsible for the inhibition of brushite growth encountered above 4 M NaCl as diffusion is also slowed down by suppressed solubility of  $\beta$ -TCP at high ionic strengths. Monetite formation was positively affected by the changes in growth kinetics due to its thermodynamic stability at low pH attained by increasing NaCl concentration.

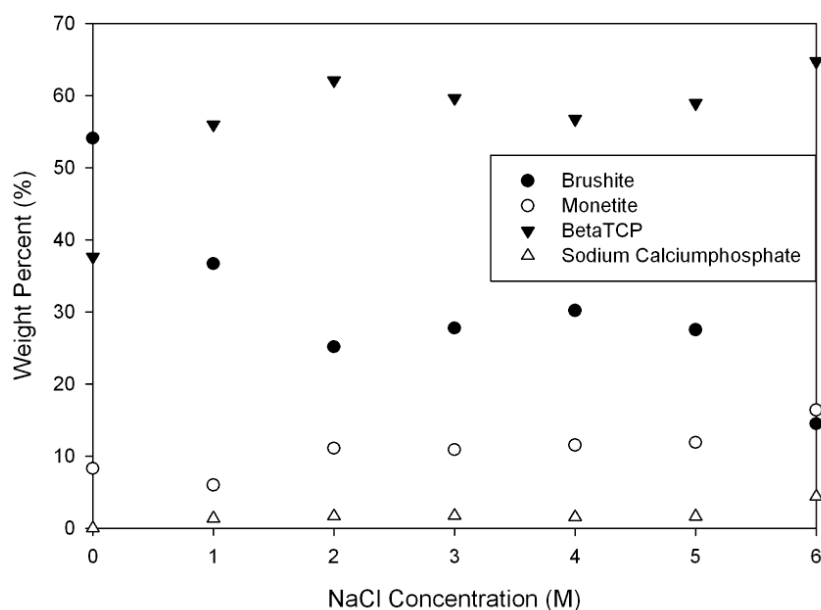


Figure 6.11. Phase composition of samples from free drift in liquid containing various NaCl concentrations.

Free drift analysis of cement setting in water containing 0 to 0.5 M citric acid showed significant differences in the pH of the liquid with varying citric acid concentration. Final pH of the cement liquid gradually increased from 3.86 to 4.04 by increasing citric acid concentration from 0.1 M to 0.5 M as seen in Figure 6.12. The observed effect was not caused by the acidity of citric acid since all cement samples were mixed into aqueous solution at pH 4.2. The adsorption of the citrate groups on the dissolving and precipitating crystals is more likely the source of the variation in pH. The initial rise of pH due to the release of  $H^+$  consuming  $PO_4^{3-}$  ions does not occur in citrate solutions. A late fall in the pH corresponding to the dissociation of  $H_2PO_4^-$  groups to  $HPO_4^{2-}$  and  $H^+$  followed by gradual increase in pH indicative of supersaturation build-up before relaxation is observed for all citric acid concentrations. Phase compositions given in Figure 6.13 reveal that  $\beta$ -TCP dissolution is inhibited with the smallest addition of citrate into the liquid and the extent of precipitation is lowered with less  $\beta$ -TCP dissolution.



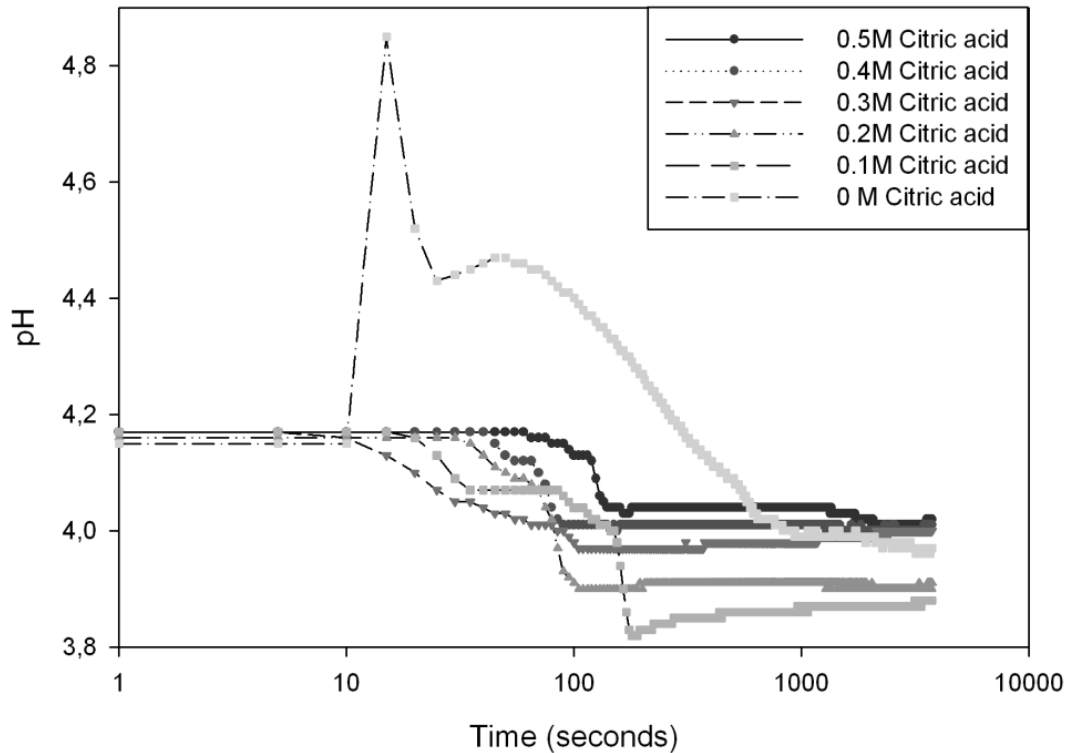


Figure 6.12. Variations in pH of the setting liquid observed in free drift.

Phase composition of the precipitates in Figure 6.13 obtained from free drift runs shows a more intense effect of introducing citric acid to the system as the  $\beta$ -TCP residue more than doubles with 0.1 M citric acid addition. Further increasing the citric acid concentration does not affect the  $\beta$ -TCP dissolution significantly. Also the brushite/monetite ratio is found to significantly decrease with initial citric acid addition in both free drift and pH-stat runs. The change in solubility and the resultant narrowing of the supersaturation gap between brushite and monetite is thought to cause this variation so that brushite becomes more stable but kinetically less favored.

Different conclusions are given in literature on the effect of citric acid on brushite/monetite phase equilibria. In a similar study investigating the shelf life of the  $\beta$ -TCP-MCPM cement system, Gbureck et al. has shown that 0.1 M citric acid effectively inhibits the formation of monetite phase that would otherwise be formed from the cement precursors at ambient laboratory conditions without any additives (Gbureck et al. 2005). Monetite formation was attributed in that study to the lack of stoichiometric water required for cement precursors to completely transform to brushite despite the crystal growth rate of brushite being several orders of magnitude higher than that of monetite. On the other hand, Hofmann's study on the effect of additives at much higher

concentrations revealed that monetite content in the  $\beta$ -TCP-MCPM cement system was increased from 7% to 33% in expense of brushite, upon setting in aqueous solution containing 0.5 M to 1.5 M citric acid (Hofmann et al. 2006). However, increase in monetite content was not attributed to insufficient water as much lower powder/liquid ratio were used than the stoichiometric ratio of 4.5. Previous research supports the possibility of monetite formation in brushite cements at citric acid concentrations exceeding a certain limit where its adsorption on calcium phosphate surfaces becomes effective probably due to the enhanced ionic strength.

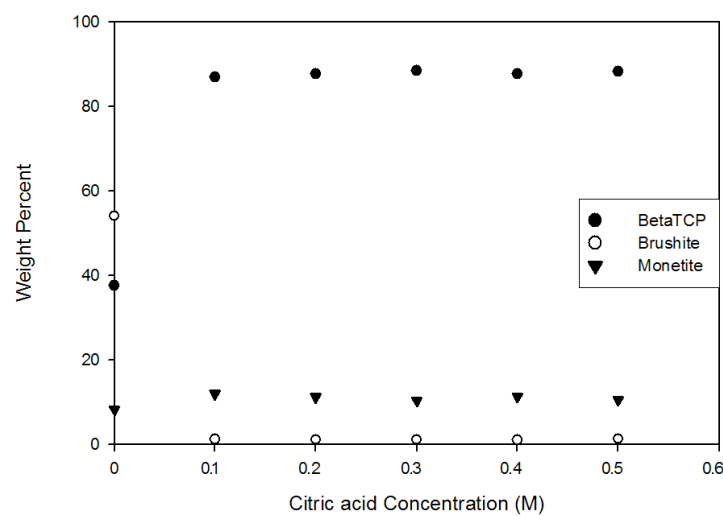


Figure 6.13. Phase composition of the precipitate set in liquids containing various citric acid concentrations.

Citrate groups were explained to adsorb to the calcium phosphate surfaces through interaction with the calcium ions (Hofmann et al. 2006) and the positively charged hydrated surfaces (Giocondi et al. 2010). Impurity adsorption is known to be effective at only low supersaturations. The ionic strength at increasing citrate concentrations decreases the calcium phosphate supersaturation so that the impurity effect becomes effective on the cement phase structure even at 0.1 M citric acid concentration as seen in Figure 6.13. The decrease in brushite/monetite ratio observed in Figure 6.13 with increasing citrate concentration can be explained by the relative stabilization of brushite as the gap between solubilities and thus supersaturations of brushite and monetite becomes narrower at higher impurity concentration and ionic strength. This hypothesis was tested using ICP atomic emission spectroscopy on the

supernatant solutions of pure  $\beta$ -TCP, brushite and monetite in the presence of citrate groups. The pH of the citrate solutions was adjusted to 4.2 and equal amounts of calcium phosphates were mixed in the solutions containing various citric acid concentrations for 24 hours. The equilibrium pH of the calcium phosphate solutions in pure water reached the highest value for  $\beta$ -TCP as this phase had the highest solubility at any pH value.  $\beta$ -TCP was also the phase with solubility most susceptible to pH variation. Initial low calcium concentration in all solutions was due to a difference in equilibrium pH of about  $\Delta\text{pH}=2.0$  between pure water (pH $\sim$ 7) and citric acid solution (pH $\sim$ 5). Calcium concentrations shown in Figure 6.14 demonstrate the linear relationship between brushite solubility and citric acid concentration above 0.1 M citric acid. The decreasing trend in calcium concentration was not observed for monetite as its calcium concentration remained in the same range with small fluctuations. Brushite had the lowest solubility at the highest citric acid concentration contrary to the solubility isotherms observed in pure water.

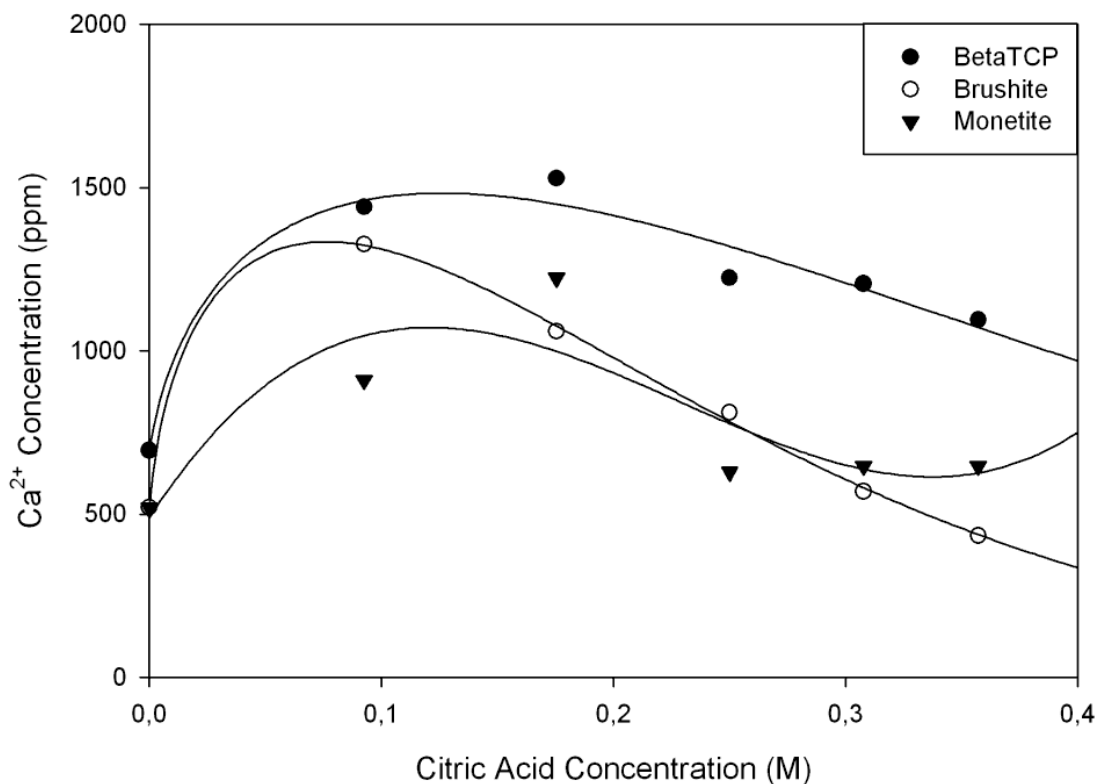


Figure 6.14. Free calcium concentrations of calcium phosphates in citrate solutions as determined by ICP-AES.

Adsorption of citrate groups on calcium phosphates is proportional to the calcium/phosphate ratio at the surface of the calcium phosphate crystals, density of surface calcium ions, and the magnitude of surface positive charge.  $\beta$ -TCP which has a Ca/P of 1.5 is known to host more citrate groups than brushite and monetite (Alkhraisat et al. 2008). Giocondi et al. revealed in their latest study that citrate molecules adsorb on brushite crystals rather as a surfactant than binding onto the dominant (010) surface sites due to the presence of a hydrate layer (Giocondi et al. 2010). The proposed mechanism of the inhibition of brushite growth in that study was adsorption on the hydrated surface and increase in the surface free energy which in turn resulted in a decrease in step density at low citrate concentrations. On the other hand at high citrate concentrations, citrate molecules bound onto the polar [101] calcium terminated steps with no decrease in step density on the (010) plane. The SFM analysis of adsorption of osteocalcin, another macromolecule with calcium affinity, on brushite surface by Flade et al. revealed that the calcium phosphate ions in the (010) plane are not able to interact with macromolecules (Flade et al. 2001).

Insensitivity of monetite solubility to citrate concentration as opposed to the linear dependency of brushite solubility to citrate concentration is attributed to the higher density of surface calcium ions on monetite crystals compared to the dominantly hydrated surface of brushite and the lower surface area of monetite powder. Specific surface areas of the powders determined by the Blaine method were  $0.582 \text{ m}^2/\text{g}$  for  $\beta$ -TCP,  $0.462 \text{ m}^2/\text{g}$  for brushite and  $0.301 \text{ m}^2/\text{g}$  for monetite. The highest solubility observed in the ICP analysis for  $\beta$ -TCP is most likely due to the highest surface area of this powder. It is known that changes occur at the surface of monetite when in contact with water at  $37 \text{ }^\circ\text{C}$ , such that dissolution is hindered by slow topotactic growth of a nanometer thin calcium deficient apatite formation on the surface (Lebugle et al. 1999). Lebugle et al. revealed by XPS analysis that the release of calcium and phosphate ions decrease with time and the Ca/P ratio of the solution decreases simultaneously as the crystallization of apatitic calcium phosphate on monetite surface consumes calcium ions. This incongruity in monetite dissolution is a function of time and temperature and is not expected to reduce the calcium concentration of samples prepared for ICP analysis due to the short period of analysis time. Overall, monetite surface may be able to accommodate more citrate ions and still release calcium ions but brushite dissolution is confined to the step edges on the dominant (010) faces where calcium and phosphate ions are exposed to the solution. Surface exposed calcium ratio of brushite is expected

to decrease linearly with increasing citrate concentrations, according to the trend given in Figure 6.14 while that of monetite should stay relatively constant despite the slow formation of surface apatitic layer.

The mechanism of citrate adsorption on brushite and monetite was further investigated by measuring the concentration of citrate in the supernatants of aqueous calcium phosphate solutions via UV spectrophotometry. Similar adsorption capacities of equal masses of brushite and monetite phases subjected to UV analysis seen in Figure 6.15 do not reflect the higher surface calcium density of monetite because of the lower surface area of monetite powder used in the analysis. The lower citrate concentration in  $\beta$ -TCP solution supernatant was mainly due to the higher Ca/P ratio of that phase. While small fluctuations in the net adsorption exists as seen in Figure 6.16, brushite and monetite generally adsorb similar amounts of citrate despite the higher surface area of brushite used in the study. The surface attachment of citrate on the charged hydrated brushite surface layer proposed by Giocondi et al. is also thought to be an effective adsorption mechanism due to the low surface calcium density.

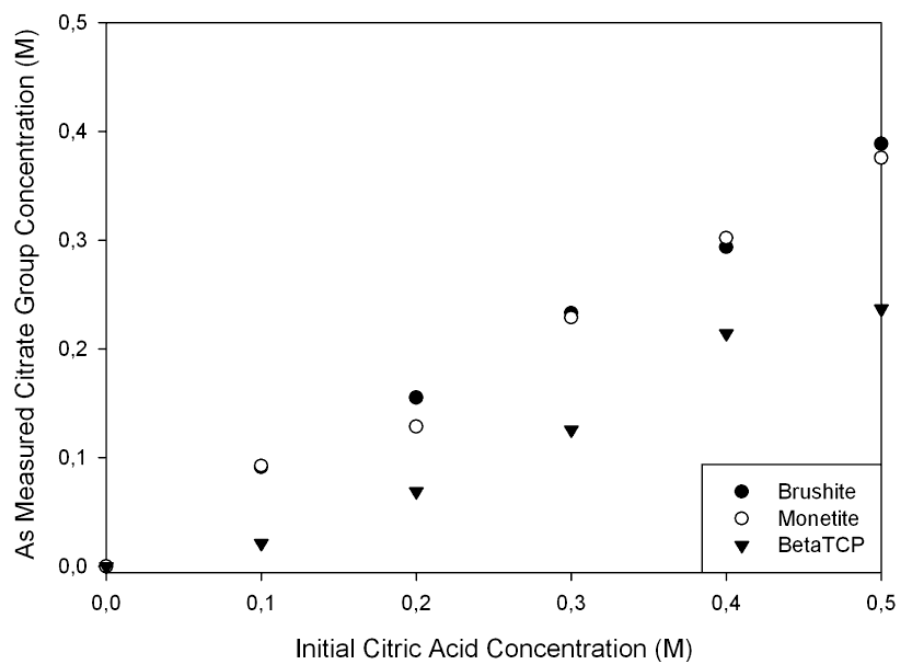


Figure 6.15. Citrate concentration in the supernatant of various aqueous calcium phosphate solutions as determined by UV spectroscopy.

The decrease in brushite solubility relative to monetite may be due to the higher density of surface calcium ions on monetite crystals. Increasing ionic strength of the citrate solution is expected to enhance surface integration of citrate groups. Thus the supersaturation gap between brushite and monetite is expected to be narrower by effective citrate adsorption on both surfaces, decreasing the available surface growth sites on brushite much more effectively. Citrate adsorption at the scarcely available brushite surface calcium ions is expected to be much more effective at high ionic strengths induced by a neutral electrolyte like NaCl, thereby constituting a synergistic effect.

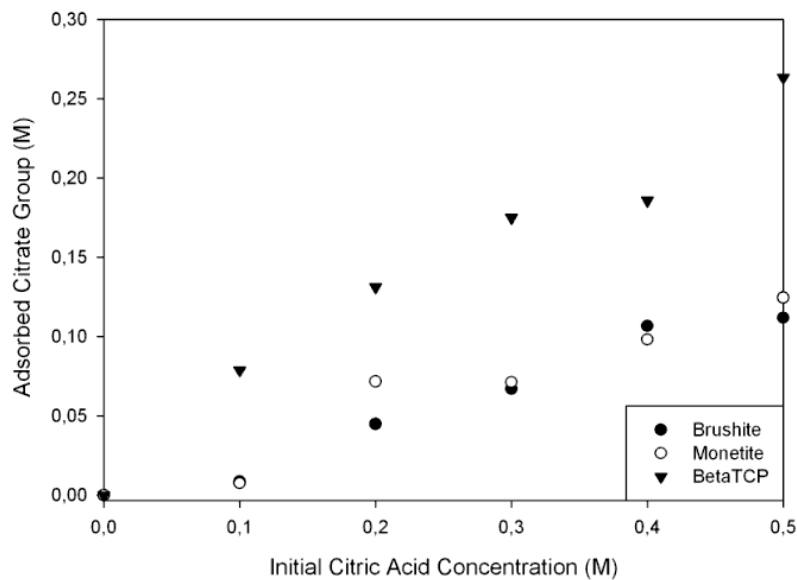


Figure 6.16. Net citrate adsorption as a function of initial citric acid concentration.

### 6.2.1.2. Analysis of the pH-stat Runs

The pH-stat instrument used in this work is responsive when the pH drops below 4.2 and did not detect and respond to the pH fluctuations in the initial dissolution lagtime period. The recorded data contain kinetic information about growth on the existing brushite seeds after the initial mixing and dissolution period. The growth curve given in Figure 6.17 for CPC set in pure water is a well defined sigmoidal curve that represents the relaxation period in reverse. The inflection point of the sigmoidal curve represents the point of maximum growth rate and the end plateau indicates the kinetic balance between  $\beta$ -TCP dissolution and brushite growth which occurs when concentration of the forming phase is close to saturation.

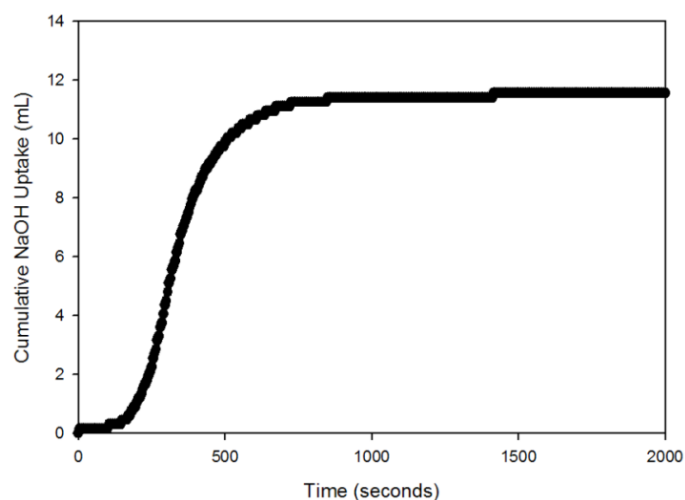


Figure 6.17. Cumulative base uptake of  $\beta$ -TCP – MCPM cement with brushite seeds.

Figure 6.18 gives the cumulative base uptake of cement setting in water containing 0 to 6 M NaCl. Pure setting liquid produces a well-defined sigmoidal curve representative of a relaxation period that starts and ends relatively faster than NaCl containing setting liquid up to 3 M concentration. The addition of small amounts of NaCl extends the relaxation period significantly. Double sigmoidal curves observed in our current research on the synergistic effect of NaCl and citric acid was observed where the second curve may be attributed to monetite formation. Cement setting in the presence of NaCl is retarded by NaCl additions up to 3 M and confined to earlier times upon increasing the NaCl concentration as seen in Figure 6.19. Observed variation is parallel to the variation in calcium phosphate supersaturation as predicted by Pitzer ion interaction model given in Figure 4.18 since crystal growth rate is proportional to supersaturation. Sodium chloride may promote monetite precipitation with inhibition of mainly brushite growth, at concentrations higher than 3 M in the presence of citric acid.

Sigmoidal curves observed in Figure 6.18 were curve fitted to perfect sigmoids and their derivatives were taken in order to obtain the variation of growth rate as a function of time. As seen in the growth rate curves given in Figure 6.20, the peak rates corresponding to the inflection points of the sigmoidal curves shift to lower times with increasing NaCl concentration. The area under the rate curves give the total base uptake at infinite time. Equal values of total base uptake for all concentrations of NaCl confirm that the main effect of NaCl is shifting the maximum growth rates to early times within

the observed experiment period. Compresses of the growth period of cement end products with increasing NaCl concentration is attributed to the increasingly rapid consumption of  $\text{HPO}_4^{2-}$  ions supplied by stable  $\text{H}_2\text{PO}_4^-$  groups at the solution pH as a result of the exponential decrease in their supersaturation as predicted in Figure 4.18. Constituent ions of brushite and monetite are expected to be integrated rapidly to crystal surfaces without a need for supersaturation build up at high ionic strengths attained.

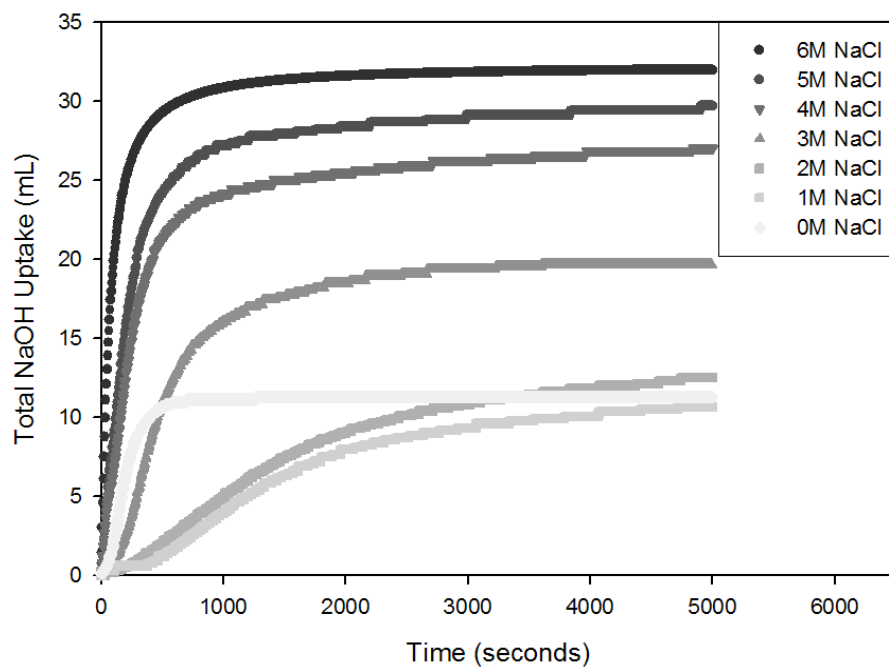


Figure 6.18. Cumulative base uptake curves for cement setting with various NaCl concentrations.

Calcium and phosphate ions are depleted quickly at high NaCl concentrations due to their depressed activity and sudden formation of the growing phases as evident from the sharper sigmoidal curves. The supersaturation build-up and relaxation periods are compressed with increasing NaCl concentrations and a change in growth model is thought to occur from diffusion controlled to surface integration controlled around 3 M NaCl. It is seen in Figure 6.21 that brushite and monetite are present in all NaCl concentrations and their mass percentages remain relatively constant until an intermediate NaCl concentration. Brushite/monetite ratio starts to decrease consistently with increasing NaCl concentration above 3 M NaCl. This may be attributed to the drop of pH observed in the free drift runs as a result of  $\text{H}_2\text{PO}_4^-$  dissociation to  $\text{HPO}_4^{2-}$  and  $\text{H}^+$ .



The equilibrium pH of the NaCl containing setting liquids drops below 4.2 at 3 M NaCl as seen in Figure 6.10. Consequently, an extra initial base uptake is observed in pH-stat runs exceeding 3 M NaCl as seen in Figure 6.22, adding to the slope and extent of the total base uptake curves. Calculated net base uptakes that are due solely to the growth of the brushite and monetite phases give comparable reaction extents for all NaCl concentrations which accounts for the similar total mass content around 50-60% deduced from phase compositions given in Figure 6.21. Whether observed change in brushite/monetite ratio is due to ionic strength or initial drop in pH can be resolved by comparing the phase composition of the pH-stat runs and free drift runs where pH was allowed to decrease throughout setting. While lower pH values in free drift runs favored monetite rather than brushite, similar increase in monetite content relative to brushite in constant pH runs reveals that high ionic strength is effective in the suppression of brushite supersaturation. Overall higher brushite content observed in pH-stat runs compared to the free drift runs with lower pH shows that brushite is favored relative to monetite at higher pH as reported in literature (Aberg et al. 2010).

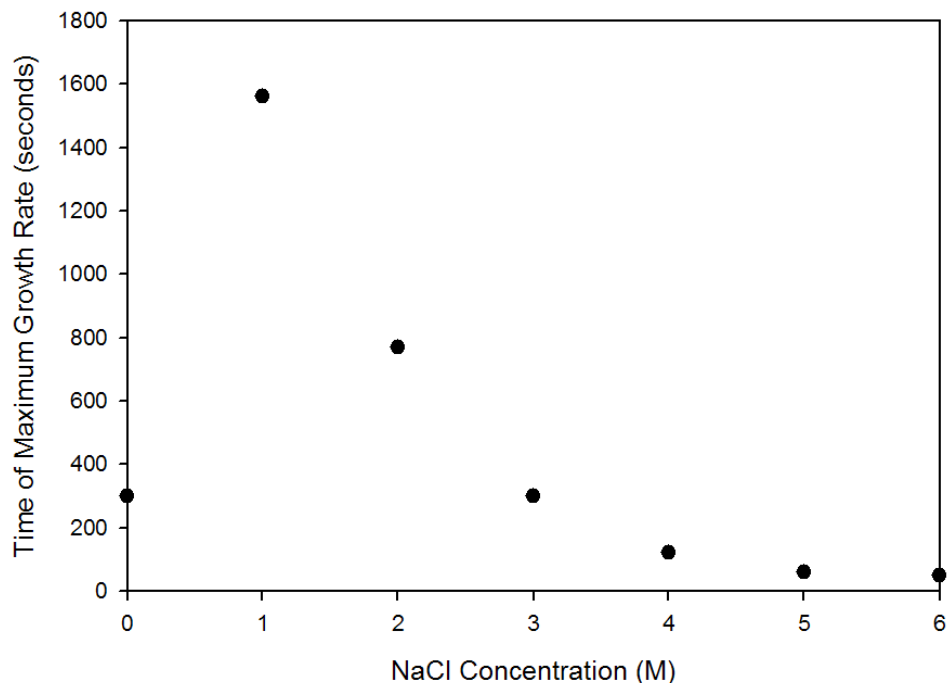


Figure 6.19. Variation in time of maximum growth rate with NaCl concentration.

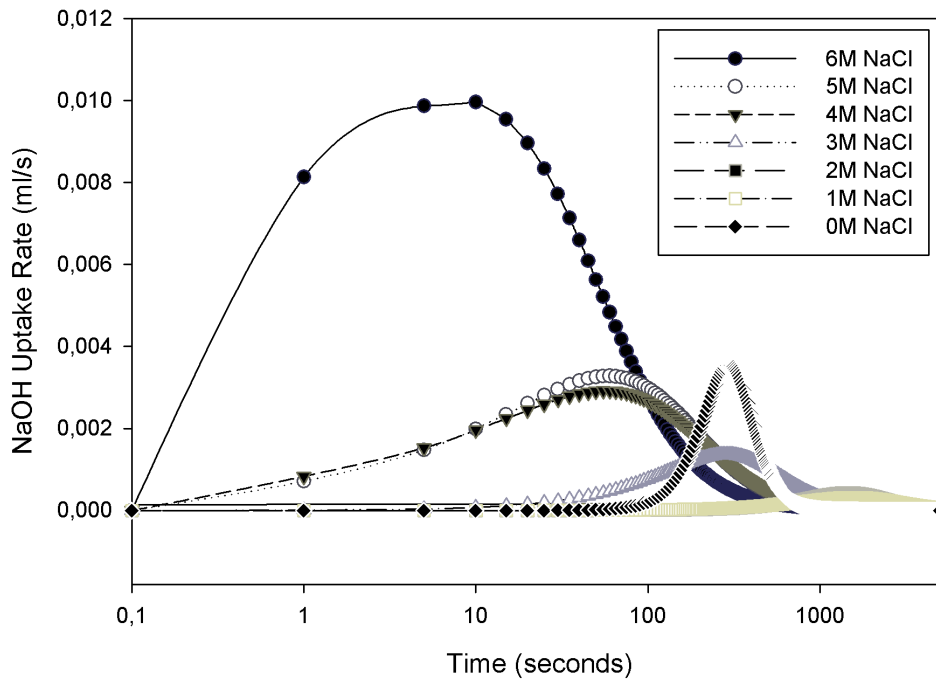


Figure 6.20. Variation of growth rates with increasing NaCl concentration.

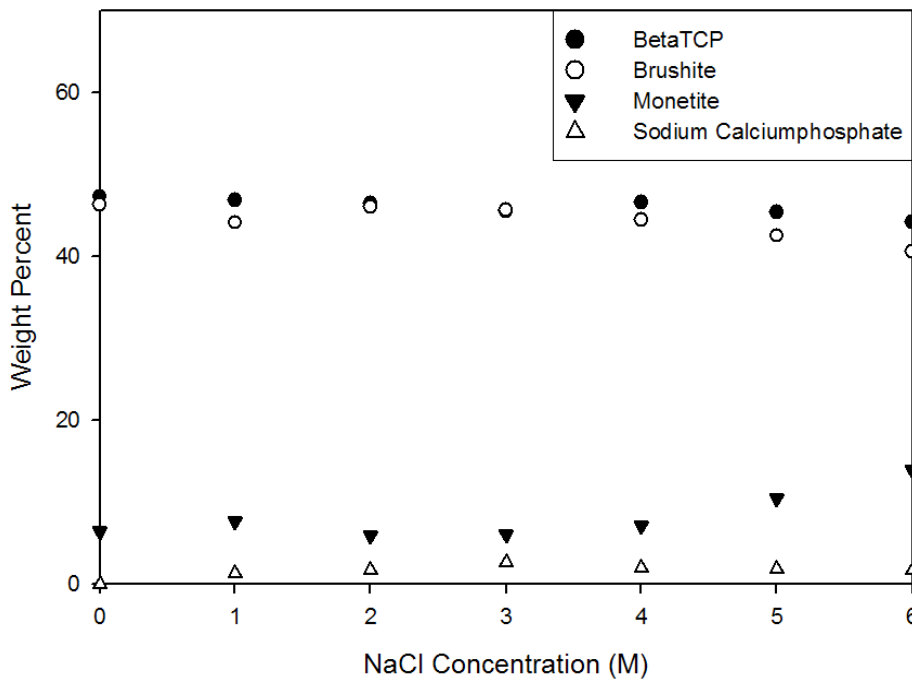


Figure 6.21. Phase composition of calcium phosphate cement set in the presence of varying NaCl concentration.

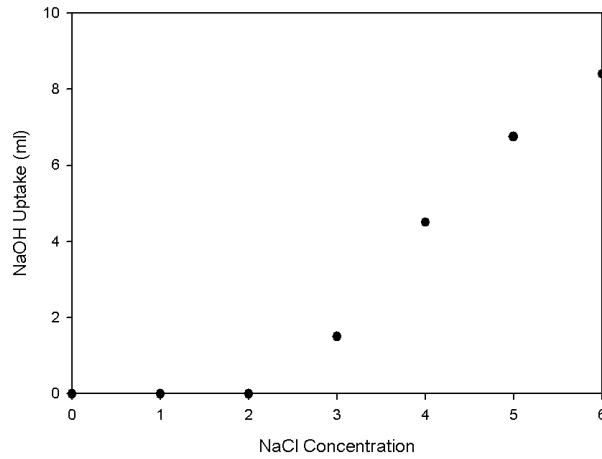


Figure 6.22. Initial base uptake in NaCl containing solutions during the pH-stat runs.

Growth kinetics of the brushite cement in NaCl containing water was analyzed via the method of Van Kemenade. According to the general formula based on Nielsen's fundamental studies on crystal growth mechanisms, it is possible to distinguish the rate determining growth mechanism among diffusion controlled, mononuclear, and polynuclear layer growth mechanism. The following equation is applicable for the three mechanisms:

$$\dot{\alpha} = K\alpha^n(1 - \alpha)^m \quad (6.2)$$

A plot of  $-\log(\alpha^{-n} d\alpha/dt)$  versus  $-\log(1 - \alpha)$  for  $n = 1/3, 2/3$  and  $4/3$  should yield a straight curve with slope  $m$ . The extent  $\alpha$  is calculated from the sigmoidal base uptake graphs by fitting a curve that gives the maximum base uptake at infinite time and taking the ratio of the total base uptake to that value. The rate  $d\alpha/dt$  is obtained by taking the derivative of the fit curve as is done in the growth rate graphs. Furthermore Van Kemenade relates the relaxation extent to the constants  $n$  and  $m$  accordingly:

$$\alpha(t_R) = \frac{n}{n+m} \quad (6.3)$$

Values of  $m$  obtained via both methods were compared for consistency and the  $n$  value giving the least variation is accepted for the rate determining growth mechanism for each sample. A representative plot of  $-\log(\alpha^{-n} d\alpha/dt)$  versus  $-\log(1-\alpha)$  for brushite seeded cement in pure water is given in Figure 6.23. Curve for polynuclear layer growth mechanism gives a constant slope for nearly all values so the growth rate determining stage in brushite cement in pure water is polynuclear layer growth. The same conclusion is reached from the graph of monetite seeded cement in pure water.

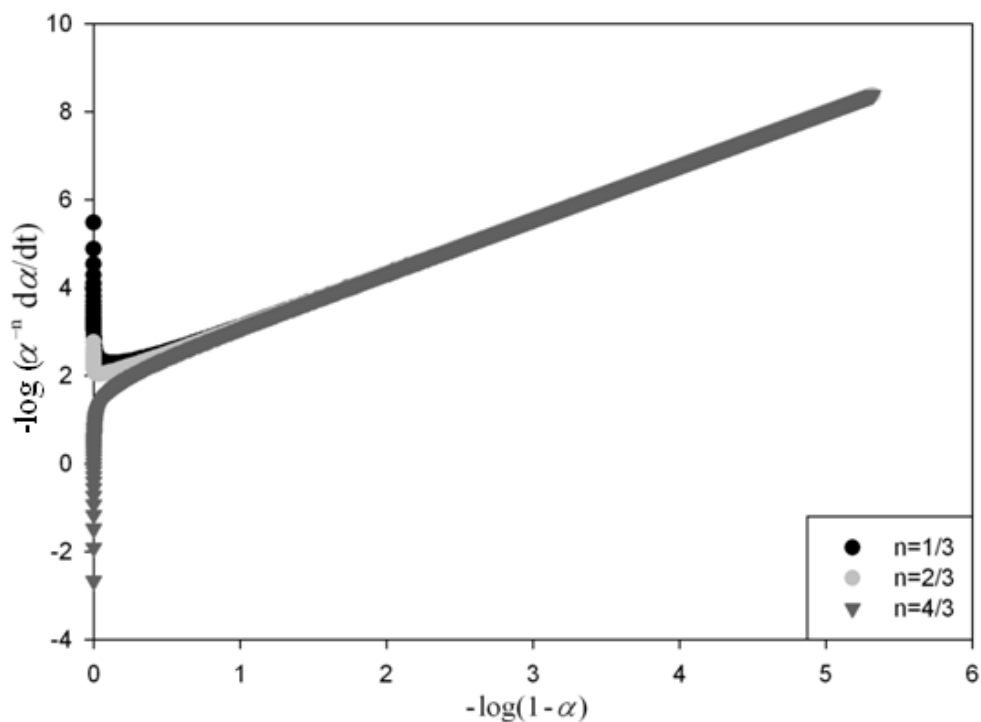


Figure 6.23. Plot of  $-\log(\alpha^{-n} d\alpha/dt)$  versus  $-\log(1 - \alpha)$  for brushite seeded  $\beta$ -TCP – MCPM cement in pure water at pH 4.2.

The shaded cells in Table 6.3 highlight the proposed rate determining growth mechanism for each sample precipitated in water with varying NaCl concentration. Although  $m$  values obtained both from slope of the curves and from relaxation extents are not integers as found in literature, the consistency of their values is indicative of the rate determining growth mechanism at the considered NaCl concentration. Deviation in values from integers may be the result of precipitating particles not to be strictly monodisperse. Van Kemenade states that diffusional growth acts to narrow, and mononuclear growth acts to broaden the polydispersity while polynuclear growth has no effect on particle size distribution. Proposed mechanisms are only diffusion controlled

and polynuclear growth controlled models, suggesting that particle size distribution does not further increase during precipitation. Besides all plots give a constant slope similar to that of Figure 6.23, indicating that restriction of no concentration change during experiment applies to this system.

Table 6.3. Rate constants obtained graphically and numerically for samples with varying NaCl concentration

NaCl M	Graphically Obtained m			Calculated m			Absolute Difference in m		
	n=1/3	n=2/3	n=4/3	n=1/3	n=2/3	n=4/3	n=1/3	n=2/3	n=4/3
<b>0</b>	1.371	1.372	1.375	0.708	1.417	2.833	0.663	0.044	1.458
<b>0.5</b>	1.679	1.764	1.936	1.718	3.436	6.871	0.039	1.671	4.935
<b>1</b>	1.685	1.752	1.884	1.763	3.526	7.052	0.078	1.775	5.168
<b>1.5</b>	1.537	1.603	1.736	1.182	2.364	4.727	0.355	0.760	2.991
<b>2</b>	1.519	1.578	1.680	1.074	2.148	4.295	0.445	0.569	2.615
<b>2.5</b>	1.489	1.462	1.448	0.877	1.754	3.508	0.612	0.292	2.060
<b>3</b>	1.482	1.496	1.523	0.970	1.940	3.879	0.512	0.444	2.356
<b>3.5</b>	1.542	1.556	1.583	1.163	2.325	4.650	0.379	0.770	3.067
<b>4</b>	1.725	1.739	1.769	2.164	4.327	8.654	0.439	2.588	6.886
<b>4.5</b>	1.646	1.659	1.687	1.561	3.121	6.242	0.085	1.462	4.555
<b>5</b>	1.686	1.700	1.728	1.743	3.486	6.971	0.056	1.785	5.243
<b>5.5</b>	1.667	1.681	1.708	1.735	3.470	6.939	0.068	1.789	5.231
<b>6</b>	1.864	1.878	1.905	1.817	3.634	7.269	0.047	1.757	5.363

For most of the samples the rate determining growth mechanism is found as diffusion. That means among diffusion and surface integration controlled growth, diffusion is slower in these samples. This is confirmed by Figure 4.21 where low solubility accounts for diffusion controlled growth for a large range of supersaturations. Also Mersmann developed a set of criteria based on both theoretical and experimental data. Accordingly, for systems containing sparingly soluble phases with low solubility and high levels of supersaturation, the growth is diffusion controlled. All NaCl concentrations resulting in diffusion controlled growth are known to reduce  $\beta$ -TCP dissolution and supersaturation of brushite. However due to presence of seeds with some degree of surface roughness, integration step may have become faster compared to diffusion of scarcely available bulk calcium phosphate ions. According to Mersmann, crystals formed at low levels of supersaturation  $S < 10$ , have smooth surfaces and appreciable growth is gained only by the polynuclear growth mechanism with the characteristic strong increase in the growth rate with supersaturation. In contrast, nuclei produced in the range  $20 < S < 100$  exhibit molecular rough surfaces and their growth can be described by combination of diffusion and integration controlled growth. In the

case of heterogeneous nucleation on already present micron sized seeds, surface integration may not be the rate determining step. Brushite seeded cement systems in pure water are controlled by polynuclear layer growth according to Table 6.3. This may be attributed to significantly higher solubility of  $\beta$ -TCP in pure water and the resultant high diffusion rates. A change in growth mechanism is observed between NaCl concentrations of 2 M and 3.5 M. This anomaly is probably related to the occurrence of maximum relaxation extent and start of pH drop around those concentrations. From kinetic considerations, the solubility should have increased and supersaturation should have decreased around this concentration region. Solubility increase is consistent with observed pH drop and the resultant increase in  $\beta$ -TCP dissolution. Strong increase in  $\beta$ -TCP dissolution coupled with exponential decrease in supersaturation above that concentration region may have produced the peak relaxation extent.

Phase evolution of the cement samples with increasing NaCl concentration is exhibited in the SEM images given in Figure 6.24. Majority of the observed crystals are identified as smooth brushite plates elongated in the planar direction. Crystal sizes remain in a few micrometers range throughout all solution concentrations.  $\beta$ -TCP crystals are mostly hidden in the background and only the precipitated crystals reside in the surface of the samples. Smooth, rigid brushite plates are seen to evolve into the stacked sheet structure at high ionic strengths that is characteristic of monetite crystals as evident in Figures 6.24D-F. Atomic percentages of the constituent elements Ca, P and O were determined via energy dispersive X-ray analysis and were compared to the elemental ratio deduced from the X-ray diffraction quantitative phase analysis. The results shown in Table 6.4 are in close agreement except the small deviation in especially P content. The reason for that mismatch is due to experimental restrictions as some  $\beta$ -TCP was removed from the EDX analyzed sample in the leaching water used in order to remove NaCl. Whereas XRD analysis was done in the presence of excess NaCl and its quantity was subtracted from the total phase percentage to obtain the calcium phosphate phase composition. Ca/P ratio around 1.23 for the XRD analyzed samples indicate a higher  $\beta$ -TCP content while the increase in brushite and monetite content at maximum NaCl concentration is reflected by the decline in Ca/P ratio.

The relaxation curves of all samples set in citric acid solution reach stability within the first few minutes of mixing in the solution similar to the free drift observations. Figure 6.25 shows that even 0.1 M citric acid addition effectively inhibits any extended dissolution of  $\beta$ -TCP and the relaxation period is extremely compressed. Almost all precipitation and setting is seen to occur in the first few minutes and abruptly cease as the forming phase is saturated. Only sample set in 0.5 M citric acid solution exhibited a portion of the secondary relaxation curve around 4000 seconds, possibly due to high ionic strength inducing a suppression of the supersaturation of the kinetically favored brushite phase. Such a change in the kinetics of cement setting is expected to narrow the gap between supersaturations of the two thermodynamically stable phases and change the order of precipitation. The constant decrease in brushite content seen in Figure 6.26 confirms the inhibitory effect of citrate adsorption on brushite growth. The shift in the relaxation curves to shorter periods is analogous to the shift observed in NaCl addition which further demonstrates the suppression effect due to high ionic strength with increasing citric acid concentration.

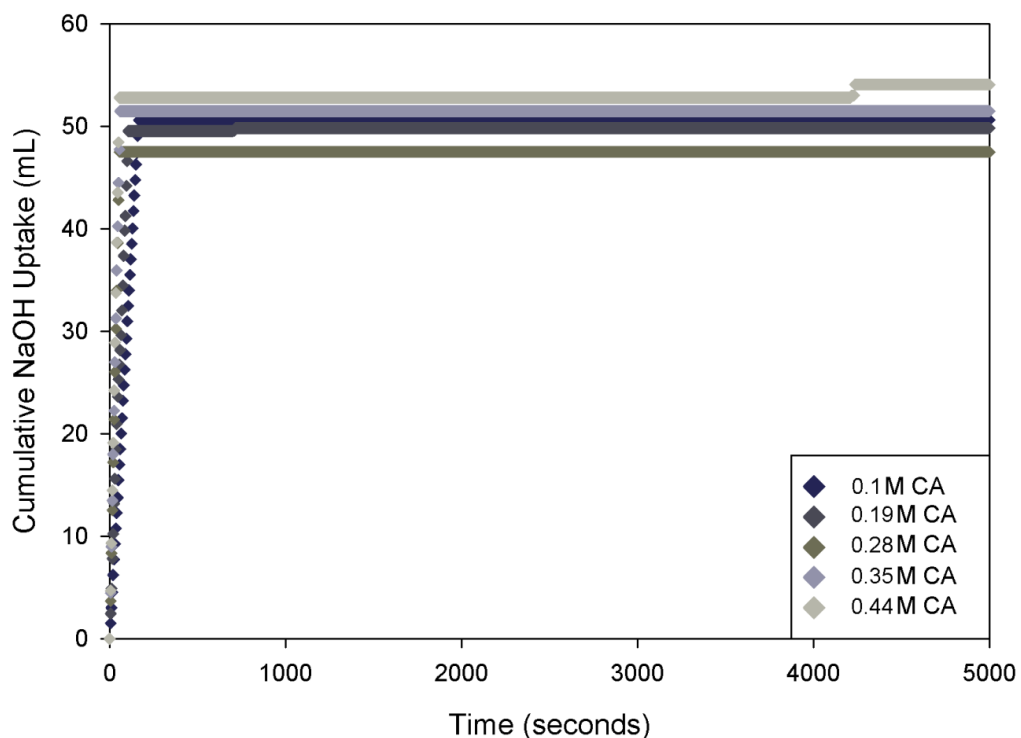


Figure 6.25. Cumulative base uptake curves for cement setting with various citric acid concentrations.

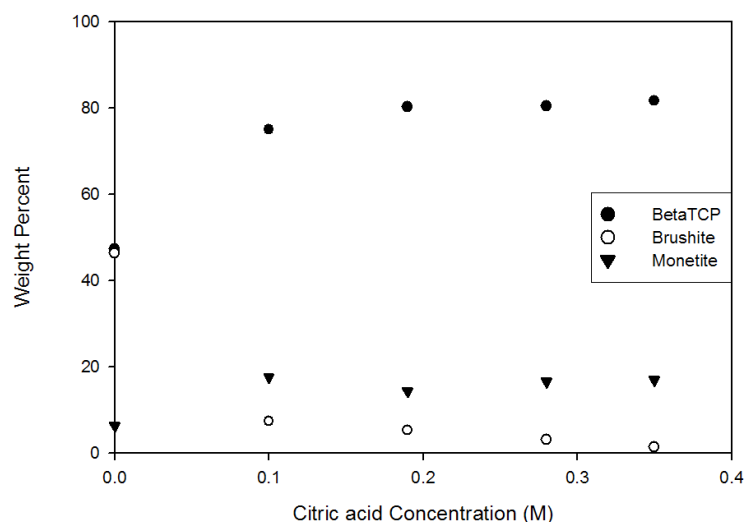


Figure 6.26. Phase composition of calcium phosphate cement set in the presence of varying citric acid concentration.

Overall, citric acid, or more specifically citrate was found to singularly alter the setting kinetics of the  $\beta$ -TCP – MCPM cement system to such an extent that the solubility of  $\beta$ -TCP was reduced remarkably and the kinetically favorable phase was changed from brushite to monetite with small amounts of additions up to 0.4 M. The weight percentages in Figure 6.26 calculated by quantitative XRD do not show high conversion extent as the  $\beta$ -TCP residue amounts to 80%. This is due to the overall suppression of  $\beta$ -TCP and brushite dissolution and growth. However it should be considered that the volume of water used in pH-stat and free drift runs was about 100 times larger than used in cement setting applications. Excessive dilution of the cement setting liquid lowered the acidity and supersaturations considerably with respect to the cement setting liquid added in clinical applications to a powder/liquid ratio around 3. In the latter case, MCPM is also supersaturated and constantly acts to lower the pH by dissolution. The monetite conversion extent observed in these cement setting experiments is seen to magnify since  $\beta$ -TCP solubility is exponentially proportional to acidity and monetite is known to be kinetically favored to brushite at such acidic conditions (Hofmann et al. 2006). Also impurity effectiveness of citrate molecules is much lower for cement setting with low liquid volume at high calcium phosphate supersaturations. Therefore, another ionic species is needed to lower the calcium phosphate supersaturation by decreasing the activity coefficient of calcium and phosphates as predicted by the Pitzer equation. Sodium chloride is the best candidate to be used as the electrolyte for modification of the ionic strength of the cement system



considering its singular monetite promoting effect. The investigation of the synergistic effects of both citrate groups and NaCl on  $\beta$ -TCP – MCPM cement system presented in the following section reveals that NaCl can effectively balance the supersaturation to activate citrate groups in order to modify the phase composition of brushite cements in favor of monetite.

### **6.2.2. Synergistic Effect of NaCl and Citric Acid on Brushite Cement Setting Kinetics**

The same conditions of the previous pH-stat experiment setup was replicated for the investigation of the synergistic effect of NaCl and citric acid with the addition of 0.1-0.5 M citric acid as an active impurity in the aqueous solution. Numerous studies point to the  $\text{Ca}^{2+}$  chelating ability, dissolution inhibitor and resultant cement setting retarding properties of citric acid. Due to its strong potential to singly alter setting kinetics of brushite cements, no studies investigating its effect in relation with another electrolyte like NaCl are present in the literature. However literature on effect of citric acid on brushite to monetite transformation as an ionic modifier exists as mentioned in the previous section. Results obtained from pH-stat setting of  $\beta$ -TCP – MCPM cement system reveal that due to synergistic effect of citric acid and NaCl, brushite to monetite transformation is possible even at 0.1 M citric acid concentration.

In all citric acid added experiment runs, NaOH uptake as a function of time gives a double sigmoidal curve for the NaCl concentration range 2 M to 6 M. A representative curve for 0.1 M citric acid and 6 M NaCl containing sample is shown in Figure 6.27. Figure 6.27a is the combined overall curve obtained from the pH-stat titrator and the Figure 6.27b is the overlay of the curves for brushite and monetite precipitation respectively. A sharp base uptake at the onset of mixing was recorded for all samples, corresponding to instant dissolution and growth of the kinetically favorable phase brushite. The second sigmoidal curve that represents monetite precipitation follows its own path and is a separate precipitation reaction with its own driving force that starts and completes after brushite precipitation. If the start of monetite precipitation coincided with brushite growth so that simultaneous growth of both phases takes place, the sigmoidal curves would merge into a single curve. In other words the monetite growth curve would be hidden as in the case of high NaCl concentration

curves given in Figures 6.29 and 6.30. Monetite growth was observed in 3 hours for NaCl concentrations exceeding 2 M concentration.

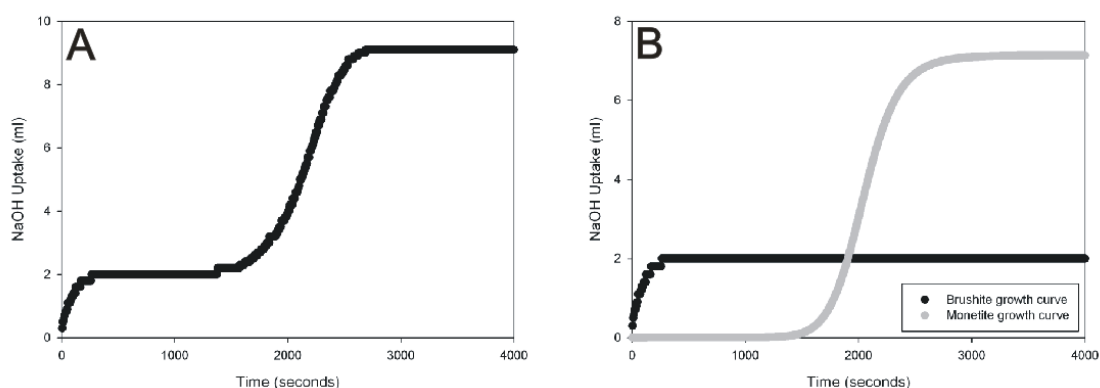


Figure 6.27. Double sigmoidal curves obtained from pH-stat analysis of sample set in 0.1 M citric acid and 6 M NaCl solution.

Only single sigmoidal curves were observed at low concentrations of NaCl for all citric acid concentrations; whereas at concentrations exceeding 2 M NaCl, a second sigmoidal curve was observed corresponding to the second relaxation period as seen for four citric acid concentrations in Figures 6.28-6.34. The occurrence of a distinct second sigmoidal curve is thought to be the result of suppression of the supersaturations of both brushite and monetite due to high ionic strength, and the selective inhibition of brushite growth by adsorbing citrate ions. The shortening of the extent of the first sigmoidal curve is an indication of the inhibition of brushite growth. The second sigmoidal curves are seen to occur at earlier times at increasing NaCl concentrations. That observation may be the result of either a change in pH, temperature or ionic modification on growth kinetics. Since titration was done at constant pH and temperature, it is certain that ionic modification of the solution lowered the brushite saturation limit close to that of monetite at increasing NaCl concentration so that both the initial brushite precipitation and the later monetite precipitation occurred increasingly rapidly. The result is that monetite was kinetically favored at high NaCl concentration in the presence of citric acid. Supersaturation gap between brushite and monetite, calculated via Pitzer's ion interaction model is thought to be narrowed with the adsorption of citrate molecules on scarcely available calcium ions on the hydrated brushite surfaces at low supersaturations induced by NaCl. The density of surface calcium ions on brushite surface is much lower (Giocondi et al. 2010), so that citrate adsorption alters the solubility and growth of brushite more compared to monetite.

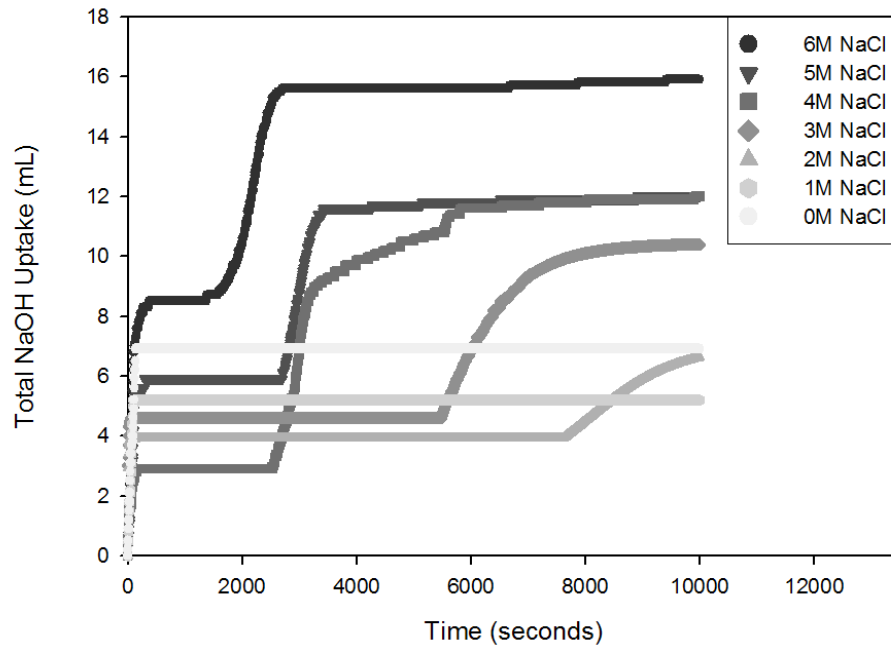


Figure 6.28. Total base uptake of samples set in 0.1 M citric acid solution.

The shift in the detection of second sigmoidal curves with increasing NaCl concentration that is observed in Figure 6.28 is correlated with the earlier occurring supersaturation build-up and relaxation periods indicated in the pH fluctuation curves given in Figure 6.29. The pH's of the solutions elevate prior to the onset of monetite formation as a result of the supersaturation build-up maintained by  $\beta$ -TCP dissolution. The supersaturation build-up and second relaxation periods are observed for all NaCl concentrations above 2 M but only 5 M and 6 M NaCl solution periods are visible in Figure 6.29 due to limited data. Sample set in 5 M NaCl solution reached the highest supersaturation build-up around 2500 seconds while 6 M sample exhibited a small peak around 1000 seconds. The height of the supersaturation peaks in Figure 6.29 and thus the  $\beta$ -TCP solubility decreases with increasing ionic strength as expected. Notice the late supersaturation build-up for 6 M sample subsequent to monetite formation. That is due to increasingly faster  $\beta$ -TCP dissolution compared to monetite growth which ceases with time. Further supersaturation build-up may result in growth of hydroxyapatite if pH, temperature, and Ca/P of the solution create favorable kinetic conditions. Similarly supersaturation build-up retardation is seen in Figure 6.31 for samples set in 0.19 M citric acid solution.

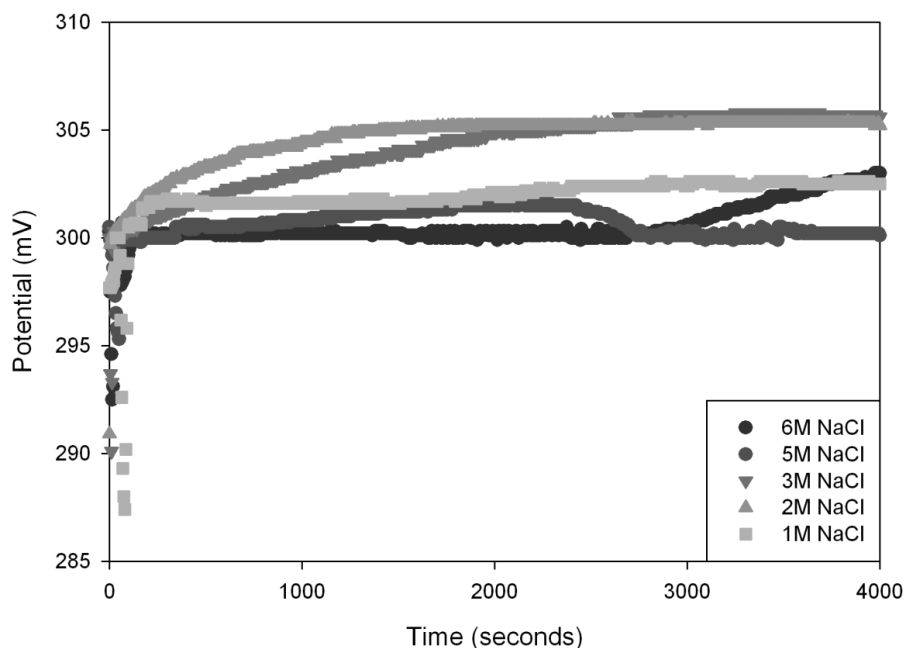


Figure 6.29. pH variation of samples set in 0.1 M citric acid solution.

Increasing citric acid concentration is seen to slightly affect the total base uptake of the samples as seen in Figures 6.30, 6.32, 6.34. The heights of the second sigmoidal curves are also shortened with increasing citric acid concentration which is an indication of suppression of monetite supersaturation as well as brushite. Monetite growth curves are seen to merge with the brushite growth curves with increasing citric acid concentration. The inflection points of the curves are barely seen for 3 M and 4 M samples in Figure 6.30. This is an indication of the narrowing of the supersaturation gap between brushite and monetite with increasing citric acid adsorption on both surfaces and the resultant reduction in their dissolution and growth. The shift in the monetite growth period to earlier times is observed in both total base uptake and pH-drift graphs. The monetite curves of high NaCl samples are on the verge of merging with the initial brushite curve indicating the suppression effect of high ionic strength as predicted by the Pitzer's model. With further increase in citric acid which inhibits the growth of both phases, although more of brushite, the supersaturation gap between the two phases is expected to close.

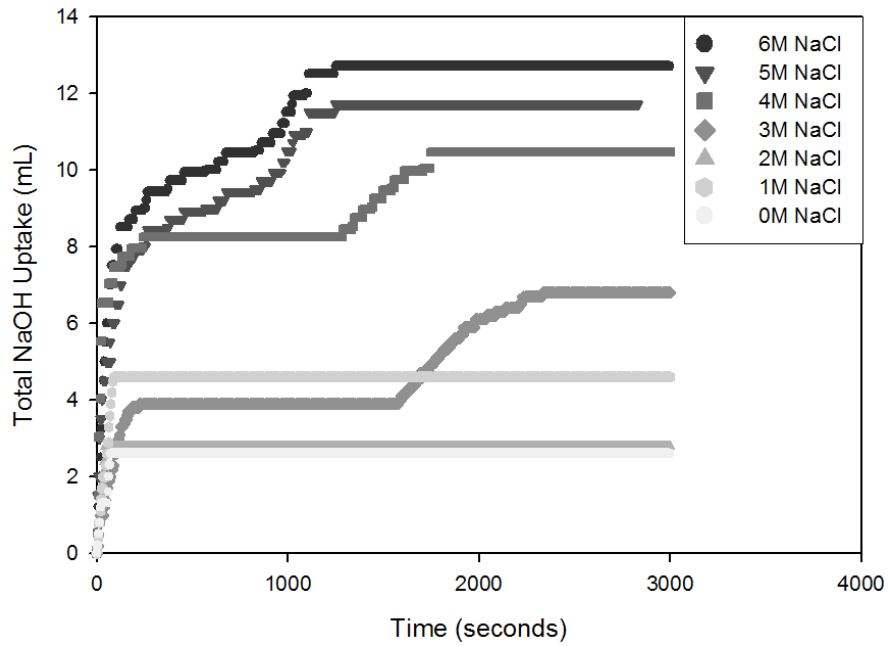


Figure 6.30. Total base uptake of samples set in 0.19 M citric acid solution.

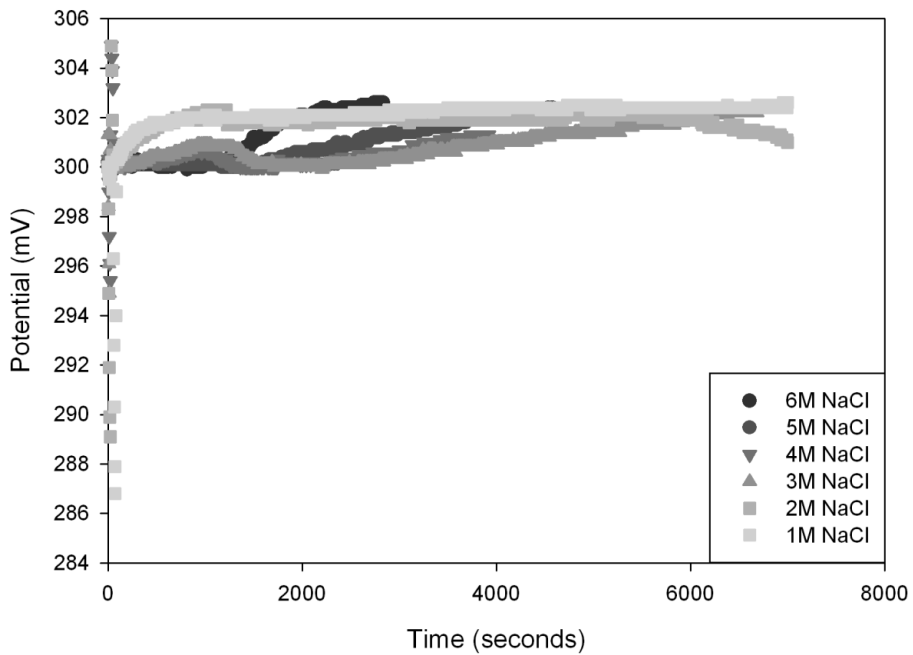


Figure 6.31. pH variation of samples set in 0.19 M citric acid solution.

Higher citric acid concentrations are seen to decrease the extent of cement growth in Figures 6.32 and 6.34 as indicated by the shortening of both single and double curves. Increase in citric acid concentration enables lower NaCl concentration samples

to display second sigmoidal curves, although significantly shorter in height than the lower citric acid containing samples. It is thought that only a portion of the second sigmoidal curves be detected due to the time monetite growth takes to deplete the OH<sup>-</sup> ions supplied by the long supersaturation build-up prior to relaxation as seen for the 2 M sample in Figure 6.33. The start of the relaxation period that could not be detected by the pH-stat titrator is around 2500 seconds as indicated by the top of the broad supersaturation build-up peak. Therefore the increased ionic activity of the citrate groups brings the kinetics of the cement growth close to simultaneous growth of brushite and monetite with even 2 M NaCl addition. The impurity effect of citric acid is considered more effective on the narrowing of the supersaturation gap than the ionic strength effect of NaCl based on these results.

The occurrence of the supersaturation build-up peak and the second relaxation period at earlier times as seen in Figure 6.33 reveals that the supersaturation gap between brushite and monetite is extremely narrowed at the extreme ionic strengths attained at high citric acid and NaCl concentrations. Citric acid adsorption produces an even stronger effect of growth inhibition by both decreasing the solubility of  $\beta$ -TCP and inhibiting the growth of both brushite and monetite. The selective inhibition of brushite relative to monetite is thought to be possible at some intermediate citric acid concentration as monetite growth is also inhibited significantly at high citric acid concentrations. This is indicated by low monetite content given in the Table 6.5. Notice the constant increase in pH of all samples set in 0.4 M citric acid in Figure 6.35. The supersaturations are so suppressed that monetite growth rate cannot approach the dissolution rate of  $\beta$ -TCP which is hindered by citrate adsorption.

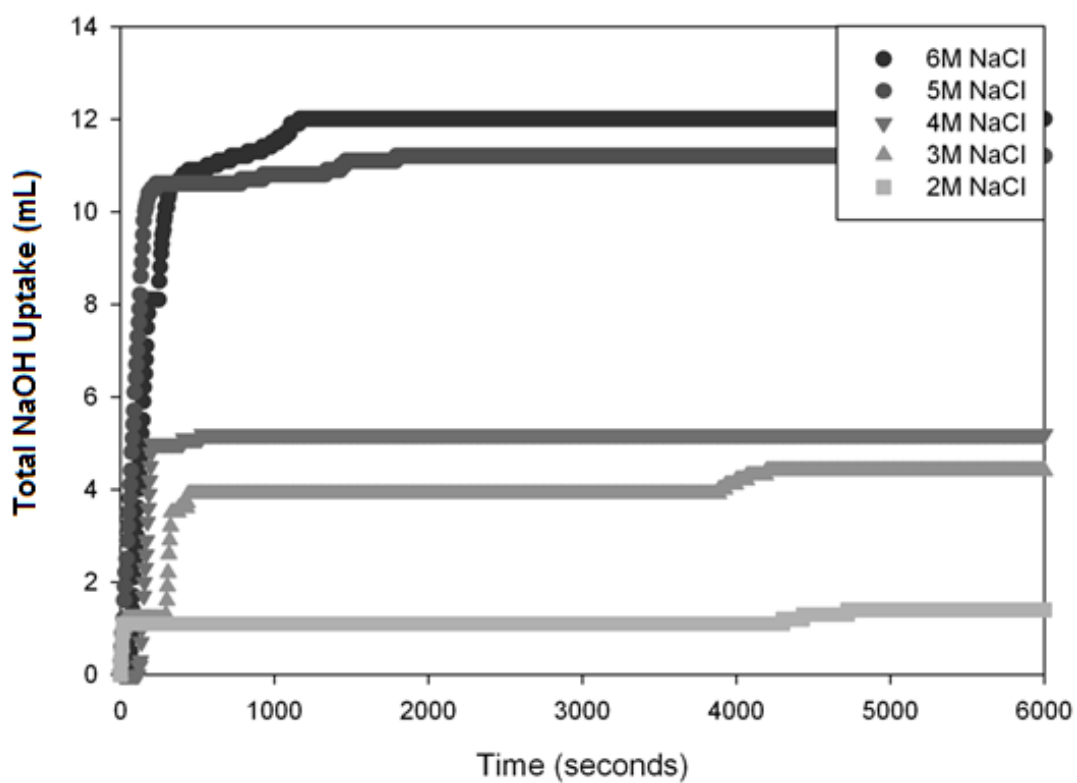


Figure 6.32. Total base uptake of samples set in 0.28 M citric acid solution.

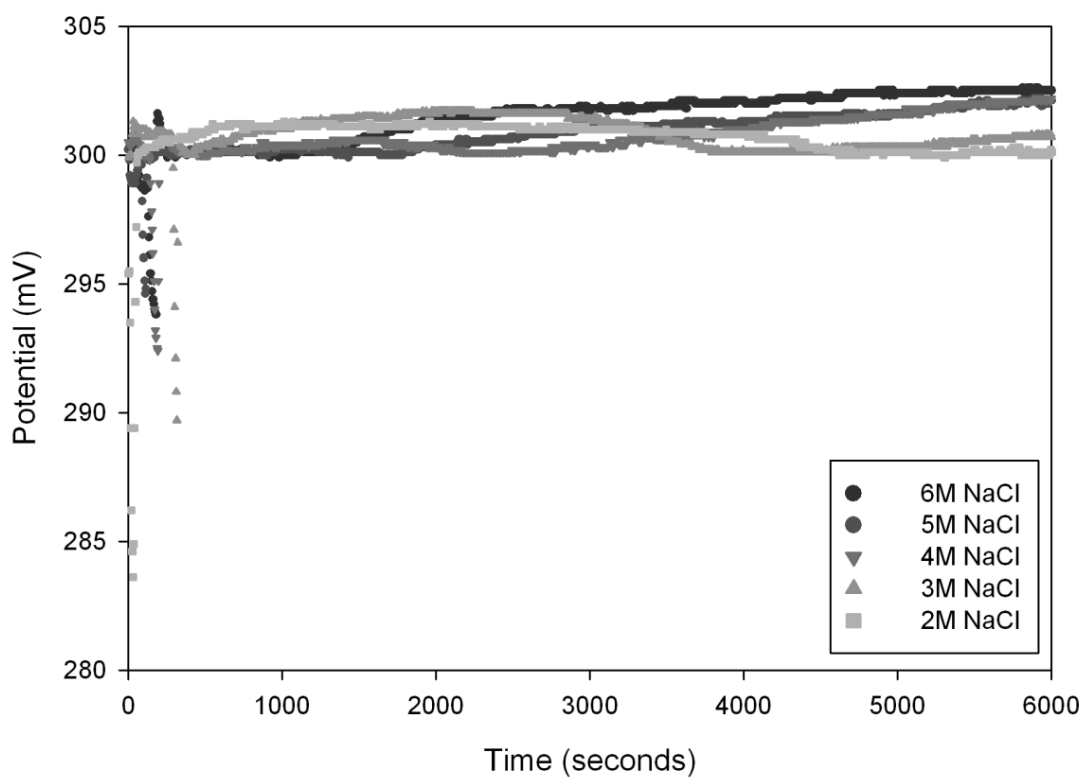


Figure 6.33. pH variation of samples set in 0.28 M citric acid solution.

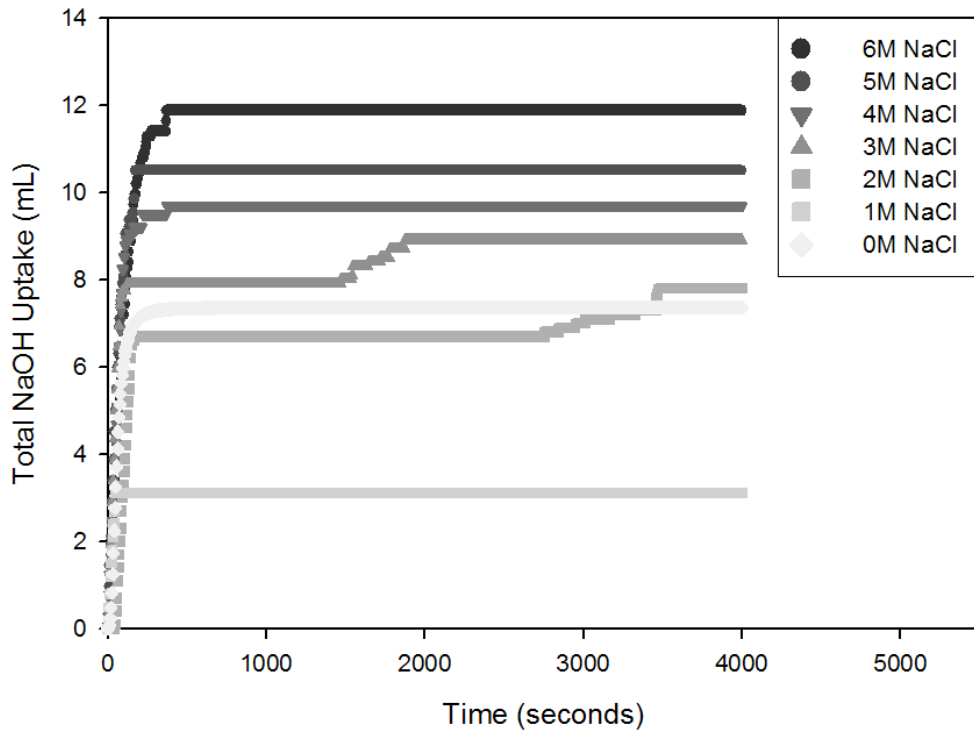


Figure 6.34. Total base uptake of samples set in 0.35 M citric acid solution.

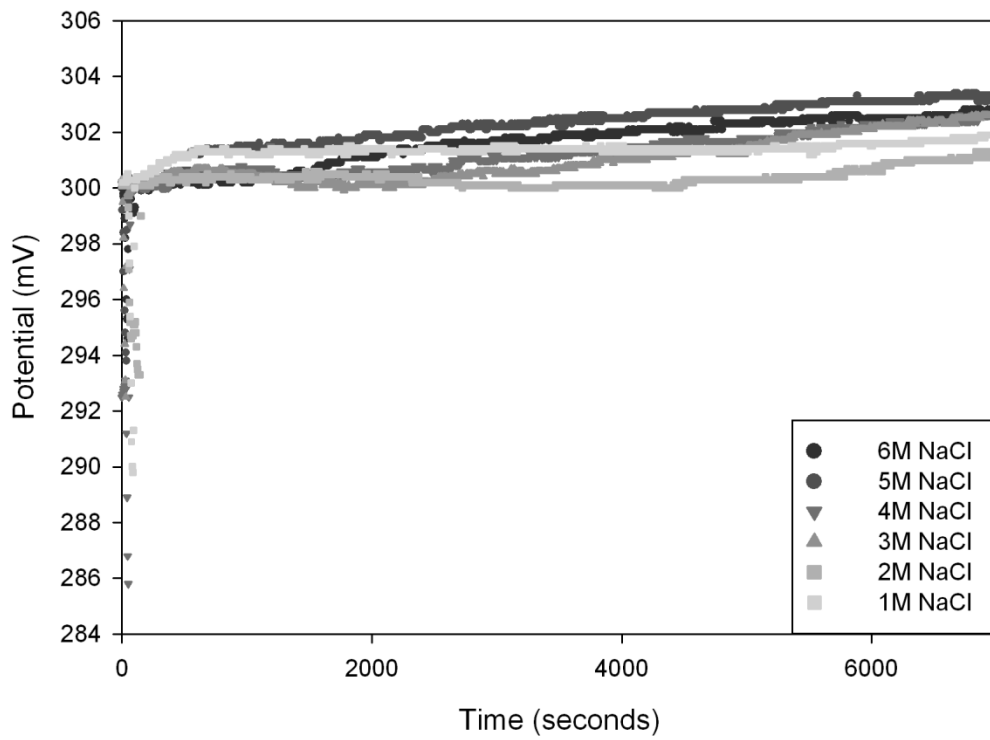


Figure 6.35. pH variation of samples set in 0.35 M citric acid solution.



The second sigmoidal curves for all samples were isolated by curve fitting and their derivatives were calculated as a representation of the monetite growth rate. The pH-drift data were used as a guide to determine the start and end of the second relaxation period. The maxima in the derivative curves corresponding to the inflection point of the sigmoidal curves represent the maximum monetite growth rates. Calculated maximum growth rates were displaced to earlier times as seen in Figure 6.36 by increasing NaCl and citric acid concentration. Only the second sigmoidal curves for samples set in 0.35 M citric acid at 4,5, and 6 M NaCl could not be distinguished from the initial sigmoidal curve which is an indication of simultaneous precipitation of the two phases according to van Kemenade (Van Kemenade M. J. J. M. 1987).

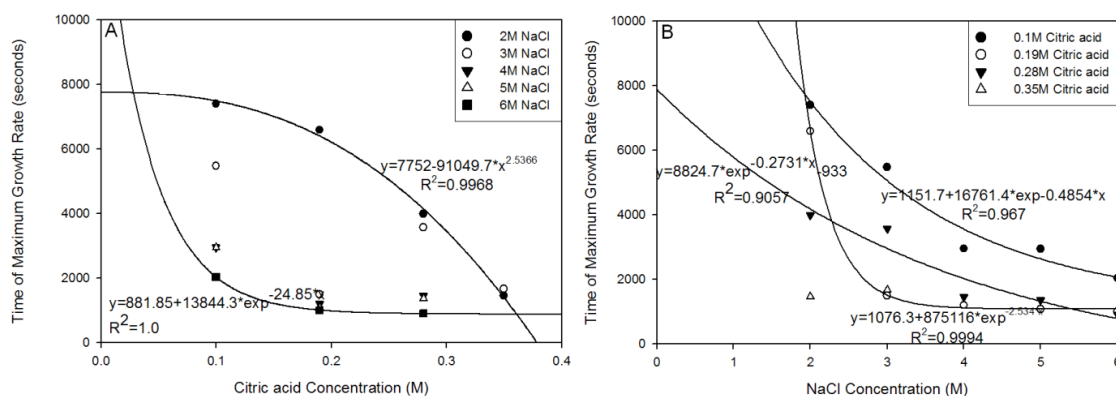


Figure 6.36. Shift in the time of maximum monetite growth rate curves as functions of citric acid (left) and NaCl (right) concentrations.

In contrast to the synergistic effect of citric acid and NaCl on the monetite growth rate, the singular effect of citric acid is known to prolong the growth rate of brushite cement (Bohner et al. 1999). The promoting effect of NaCl on monetite precipitation above 3 M concentration was demonstrated in the previous section. The variation in maximum monetite growth rate as a function of NaCl concentration are exponential as given in Figure 6.36b, similar to the Pitzer relation of supersaturation as a function of ionic strength. Maximum growth rate occurs fastest at 0.19 M citric acid concentration and maximum NaCl. As seen in Figure 6.36a, the maximum monetite growth occurs at an extended time for 0.19 M citric acid and 2 M NaCl compared to higher citric acid concentrations as expected. Monetite precipitation is promoted to times even earlier than those in solutions containing higher citric acid upon increasing the NaCl concentration above 3 M. The synergistic effect of NaCl and citric acid on

monetite transformation of brushite cement is most effective at 0.19 M citric acid and high NaCl concentrations. In other words, the supersaturation gap between brushite and monetite is thought to be minimized around that concentration so that monetite becomes the kinetically favorable phase. This is confirmed by the enhanced ratio of monetite to brushite obtained from quantitative XRD analysis given in Table 6.5.

Comparable monetite content present in all samples with and without a second sigmoidal curve indicates that the monetite growth curves are either merged or too far separated with the single brushite growth curve observed. Those samples exhibiting double sigmoidal curves such as the ones set in 0.19 M citric acid, 4-6 M NaCl solutions are kinetically favored to have more monetite. Samples set in high citric acid and high NaCl solutions exhibit a merged curve due to the narrowing of the supersaturation gap at extreme ionic activity of the modifiers and their growth extents are low as indicated by their high total  $\beta$ -TCP residue seen in Table 6.5. Brushite content significantly increases upon reaching 3 M NaCl where an uncontrolled pH drop occurs in the solution due to increased NaCl concentration, resulting in an increase in  $\beta$ -TCP solubility and brushite precipitation as explained in the previous section.  $\beta$ -TCP solubility returns to the initial levels with increasing NaCl concentration that enables enhanced citrate adsorption at calcium ions on the surface of calcium phosphates with lower supersaturation. This observed trend is only absent in 0.19 M citric acid such that the solubility of  $\beta$ -TCP continues to increase with NaCl concentration as well as the growth rate of monetite. Brushite/monetite ratio also starts to increase at higher citric acid concentrations meaning that the synergistic effect is getting weaker above 0.19 M citric acid regardless of NaCl concentration. Higher citrate concentrations more effectively inhibit  $\beta$ -TCP dissolution and brushite-monetite growth as indicated by the increase in  $\beta$ -TCP content in Table 6.5.

Table 6.5. Phase composition of samples calculated by quantitative XRD analysis

0.1 M Citric acid					0.19 M Citric acid			
NaCl	$\beta$ -TCP	Brushite	Monetite	SCP	$\beta$ -TCP	Brushite	Monetite	SCP
0 M	75.05±2.24	7.41±0.94	17.56±1.68	0	80.33±4.19	5.31±0.29	14.38±2.14	0
1 M	74.19±1.61	8.14±0.16	15.22±0.87	2.45±0.11	79.07±0.98	0.80±0.04	15.61±2.33	4.53±0.08
2 M	73.42±0.88	6.67±0.09	17.34±0.92	2.56±0.07	77.62±0.14	1.83±0.11	16.12±0.89	4.43±0.06
3 M	69.89±0.50	11.25±0.17	16.55±1.52	2.31±0.08	75.65±1.14	3.49±0.14	16.57±3.50	4.29±0.13
4 M	73.72±0.49	10.01±0.12	13.82±0.35	2.44±0.05	75.58±0.50	2.88±0.10	18.33±0.05	3.21±0.08
5 M	74.71±1.35	7.59±0.10	15.09±0.05	2.60±0.14	70.19±0.31	3.25±0.07	22.66±0.11	3.90±0.05
6 M	74.13±0.50	8.66±0.21	14.76±0.63	2.45±0.10	72.12±0.21	4.25±0.24	20.20±0.14	3.46±0.10

0.28 M Citric acid					0.35 M Citric acid			
NaCl	$\beta$ -TCP	Brushite	Monetite	SCP	$\beta$ -TCP	Brushite	Monetite	SCP
0 M	80.41±3.39	3.07±0.03	16.52±1.55	0	81.66±1.32	2.88±0.05	15.45±1.13	0
1 M	77.75±3.94	4.39±0.15	13.90±0.74	3.96±0.09	81.69±1.69	2.89±0.02	11.23±0.93	4.19±0.14
2 M	76.92±1.28	4.31±0.78	14.84±1.09	3.92±0.14	75.37±0.82	10.47±0.26	10.30±0.45	3.86±0.09
3 M	77.90±0.47	8.59±0.92	9.54±0.53	3.97±0.08	72.42±0.17	9.11±0.12	14.60±0.37	3.87±0.05
4 M	77.93±0.33	7.11±0.22	10.99±1.55	3.97±0.23	78.41±1.27	7.73±0.15	9.84±0.51	4.02±0.19
5 M	78.04±0.22	7.08±0.31	10.91±0.68	3.98±0.17	83.15±0.53	2.52±0.03	10.06±0.67	4.26±0.10
6 M	82.36±0.60	3.52±0.11	9.92±0.35	4.20±0.15	81.32±0.67	2.34±0.05	12.17±0.98	4.17±0.22

Variations of phase compositions with citric acid and NaCl concentration are given in Figures 6.37a-c for  $\beta$ -TCP, brushite and monetite respectively. Increase in citric acid concentration alone caused a rise in reactant  $\beta$ -TCP residue amount and fall in brushite up to 0.19 M citric acid. Introduction of NaCl did not change that order but enhanced the increase and decrease in the phases towards highest NaCl concentration. Initially without NaCl, cement setting in the presence of citric acid is thought to be limited by diffusion as surface integration is expected to be quite fast at high supersaturations. Addition of NaCl gradually slows the surface integration rate of calcium and phosphate ions as well as diffusion rate indefinitely to the point where surface integration is suppressed compared to diffusion and supersaturation gap between brushite and monetite narrows. Once surface integration rate diminishes, hydrated brushite crystals with adsorbed citrate groups are more rarely grown and brushite/monetite ratio changes further in favor of monetite as the NaCl concentration reaches 6 M. Monetite growth rate exceeds that of selectively inhibited brushite due to higher surface area of fine monetite crystals and absence of a hydrated layer on the surface calcium ions. This mechanism is most clearly observed in Figure 6.37d for samples set with 0.19 M citric acid.

Monetite amount nearly doubled in expense of brushite despite much lower solubility of  $\beta$ -TCP in the presence of 0.19 M citric acid compared to no ionic modifier. NaCl concentration above the critical value of 3 M provided effective activation of citrate adsorption, particularly on brushite surface calcium sites as previously hypothesized. The variation of brushite/monetite ratio as a function of citric acid and

NaCl shown in Figure 6.37d clearly supports the hypothesis as the lowest brushite/monetite ratio is observed around 0.19 M citric acid concentration and 6 M NaCl.

Kinetic analysis method of Van Kemenade was applied to the growth curves for varying NaCl concentrations in order to estimate the growth rate and rate determining growth mechanisms for monetite precipitation. Table 3.6 gives the rate constants obtained from both slope of  $-\log(\alpha^{-n} d\alpha/dt)$  versus  $-\log(1 - \alpha)$  curves and the relation with relaxation time.

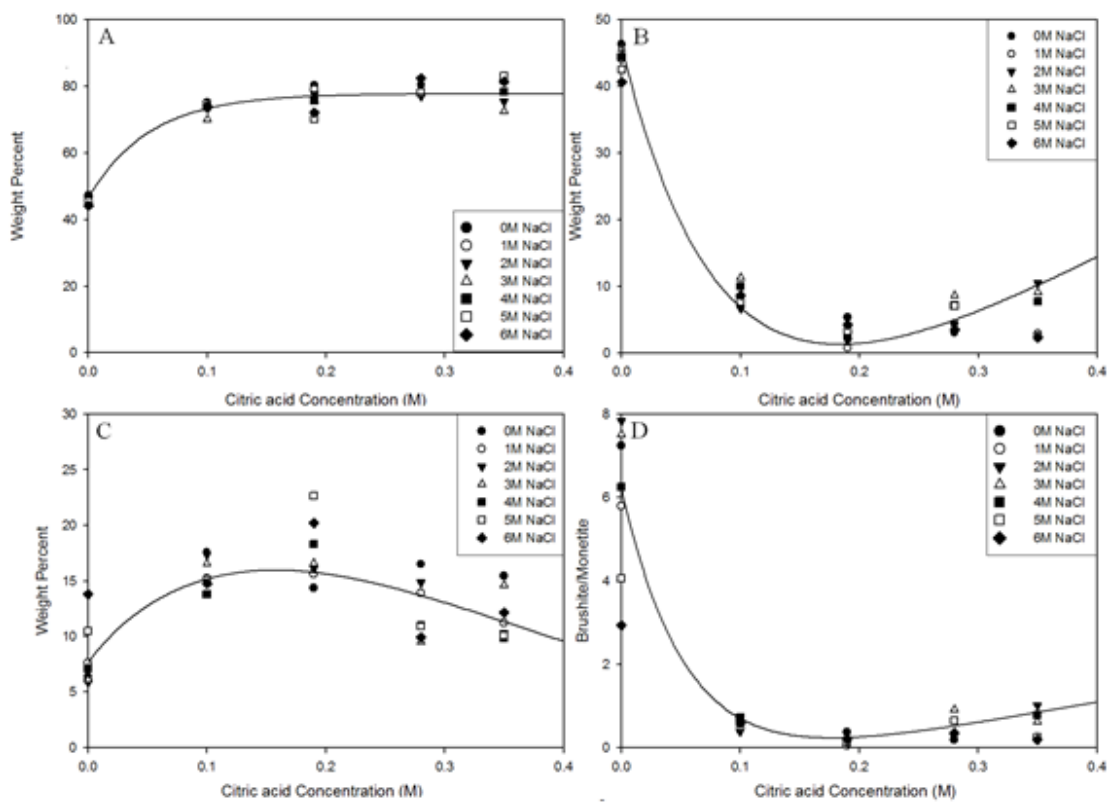


Figure 6.37. Variation of  $\beta$ -TCP (A), brushite (B), monetite (C) content and brushite/monetite ratio (D) with citric acid and NaCl concentrations.

Table 6.6. Growth rate constants and the probable growth mechanisms for monetite precipitation

NaCl M	Graphically Obtained m			Calculated m			Absolute Difference in m		
	n=1/3	n=2/3	n=4/3	n=1/3	n=2/3	n=4/3	n=1/3	n=2/3	n=4/3
<b>0.1 M Citric acid</b>									
0	N/A	N/A	N/A	N/A	N/A	N/A	N/A	N/A	N/A
1	N/A	N/A	N/A	N/A	N/A	N/A	N/A	N/A	N/A
2	1.091	1.112	1.154	0.428	0.857	1.713	0.663	0.255	0.559
3	1.093	1.101	1.116	0.411	0.822	1.644	0.682	0.279	0.528
4	1.056	1.069	1.097	0.396	0.793	1.585	0.659	0.276	0.489
5	1.048	1.048	1.050	0.363	0.727	1.453	0.684	0.322	0.403
6	1.075	1.075	1.075	0.384	0.767	1.534	0.691	0.308	0.459
<b>0.19 M Citric acid</b>									
0	N/A	N/A	N/A	N/A	N/A	N/A	N/A	N/A	N/A
1	N/A	N/A	N/A	N/A	N/A	N/A	N/A	N/A	N/A
2	1.034	1.035	1.037	0.360	0.720	1.440	0.674	0.315	0.403
3	1.106	1.107	1.108	0.420	0.839	1.678	0.686	0.268	0.570
4	1.097	1.097	1.097	0.412	0.824	1.648	0.685	0.273	0.551
5	1.054	1.054	1.054	0.381	0.761	1.523	0.673	0.292	0.469
6	1.062	1.062	1.062	0.363	0.727	1.453	0.699	0.336	0.391

The n value giving the least variation in m values was n=2/3 corresponding to polynuclear surface growth. With increasing NaCl concentration the variation in m values decreases for n=4/3 corresponding to mononuclear surface growth. Mononuclear growth is less dependent on supersaturation as the spreading rate of the precipitating layer is very rapid compared to the surface nucleation rate. So mononuclear growth is commonly the rate determining mechanism for low supersaturations as in the case with monetite precipitation. Inhibition of  $\beta$ -TCP dissolution by adsorbing citrate groups is expected to slow the diffusion rate and make the overall growth rate diffusion controlled. However even lower surface integration rates in the case of suppressed supersaturation may have resulted in the observed growth scheme. Effect of increasing ionic strength to suppress  $\beta$ -TCP solubility is expected to change the rate determining growth mechanism from polynuclear to mononuclear according to Figure 4.21.

The discussion as to why the optimum monetite yield occurs at 0.19 M citric acid concentration may be addressed to the fact that high citric acid concentration effectively inhibits both brushite and monetite precipitation as revealed by Bohner et al (Bohner et al. 1999). Citrate groups stabilize the reactants by inhibiting their dissolution and hence supersaturation build-up. At sufficiently high citrate concentration,  $\beta$ -TCP dissolution is inhibited regardless of the pH of the setting liquid. As previously shown

in the analysis of singular effect of citric acid on brushite cement setting, citric acid enables selective inhibition of brushite precipitation especially at high ionic strengths. Brushite supersaturation increases to match that of monetite with the relative decrease in solubility so that it is only thermodynamically favored. Monetite solubility is less affected by citrate adsorption due to higher density of surface dissolution sites. Suppression effect of NaCl on the other hand is effective on supersaturations of all ionic species in solution. Supersaturation suppression and growth rate inhibition of all species is expected above a certain citric acid concentration. Therefore it is reasonable to encounter an optimum citric acid concentration at which level brushite growth is effectively inhibited while monetite growth is not inhibited. In fact at 0.19 M citric acid monetite precipitation is enhanced as the competition of supersaturated solution calcium and phosphate ions to grow on a crystal surface ceases as citrate groups block brushite active surface sites.

Increasing NaCl concentration facilitated effective citrate adsorption as hypothesized, particularly at scarcely available active growth sites on hydrated brushite surfaces. Moderate increase in monetite content was observed in excess cement setting liquid at constant pH of 4.2. Full conversion of the  $\beta$ -TCP – MCPM cement to monetite is possible by utilization of the synergistic effect of NaCl and citric acid at even low powder/liquid ratio and low setting pH encountered in laboratory practice.

The significance of the synergistic effect of NaCl and citric acid on brushite cement setting kinetics is that NaCl concentration is used as a control parameter on the phase composition and porosity of brushite cements. Previously, monetite transformation was considered as an undesired degradation due to lack of control in transformation processes that mostly utilized elevated temperatures. However monetite hardness is known to be higher than brushite and its theoretical strength was found much higher than brushite. Another significance of this novel method is the ability to obtain phase pure monetite cement in the presence of excess NaCl. As a porogen NaCl is an integral part of many scaffold design templates. It is now certain that by the synergistic effect of citric acid and NaCl, brushite forming cement systems will react to form monetite blocks in the presence of excess NaCl particles.

### **6.2.3. Controlling the Phase Composition of the $\beta$ -TCP-MCPM Cement System via Synergistic Effect of NaCl on Citric Acid**

Cement blocks consisting of  $\beta$ -TCP-MCPM precursors, monetite seeds, 0.3 M citric acid containing setting liquid with varying NaCl concentration in the range 0-6 M was produced with the expectation of controlling the monetite content with NaCl concentration. Variation in XRD results given in Figure 6.38 confirmed that as expected a phase pure brushite cement was not the resultant product for varying NaCl concentrations. Phase transformation of brushite to monetite was observed for the samples set with liquid containing 0.3 M citric acid and NaCl at a critical concentration of 2 M as recorded quantitatively in Table 6.7. Monetite transformation started at NaCl concentration of 2 M and seemed complete at a NaCl concentration of 5 M. The simultaneous presence of brushite at the highest NaCl concentration may be attributed to fluctuations in saturation due to dilution of the setting liquid with water excluded from MCPM and monetite during dissolution and crystallization. The lower ionic strength of the diluted liquid in the vicinity of monetite crystals is expected to increase supersaturation of brushite and facilitate its nucleation. Hence an intimate mixture of both phases in the structure is expected.

The increase in ionic strength of the setting liquid containing 0.3 M citric acid by successive NaCl addition to the limit of saturation was the factor enabling phase transformation to monetite. Furthermore, a residual  $\beta$ -TCP phase was found to gradually increase with ionic strength. The underlying mechanism for the varying amount of phases is the variation in relative dissolution rates of the precursors in accord with fluctuations in solution pH and supersaturation. Thermodynamic considerations dictate that the driving force for both dissolution and precipitation of calcium phosphates, supersaturation, is suppressed to extremely low values in the presence of high concentrations of electrolytes as predicted by the Pitzer's ion interaction model.

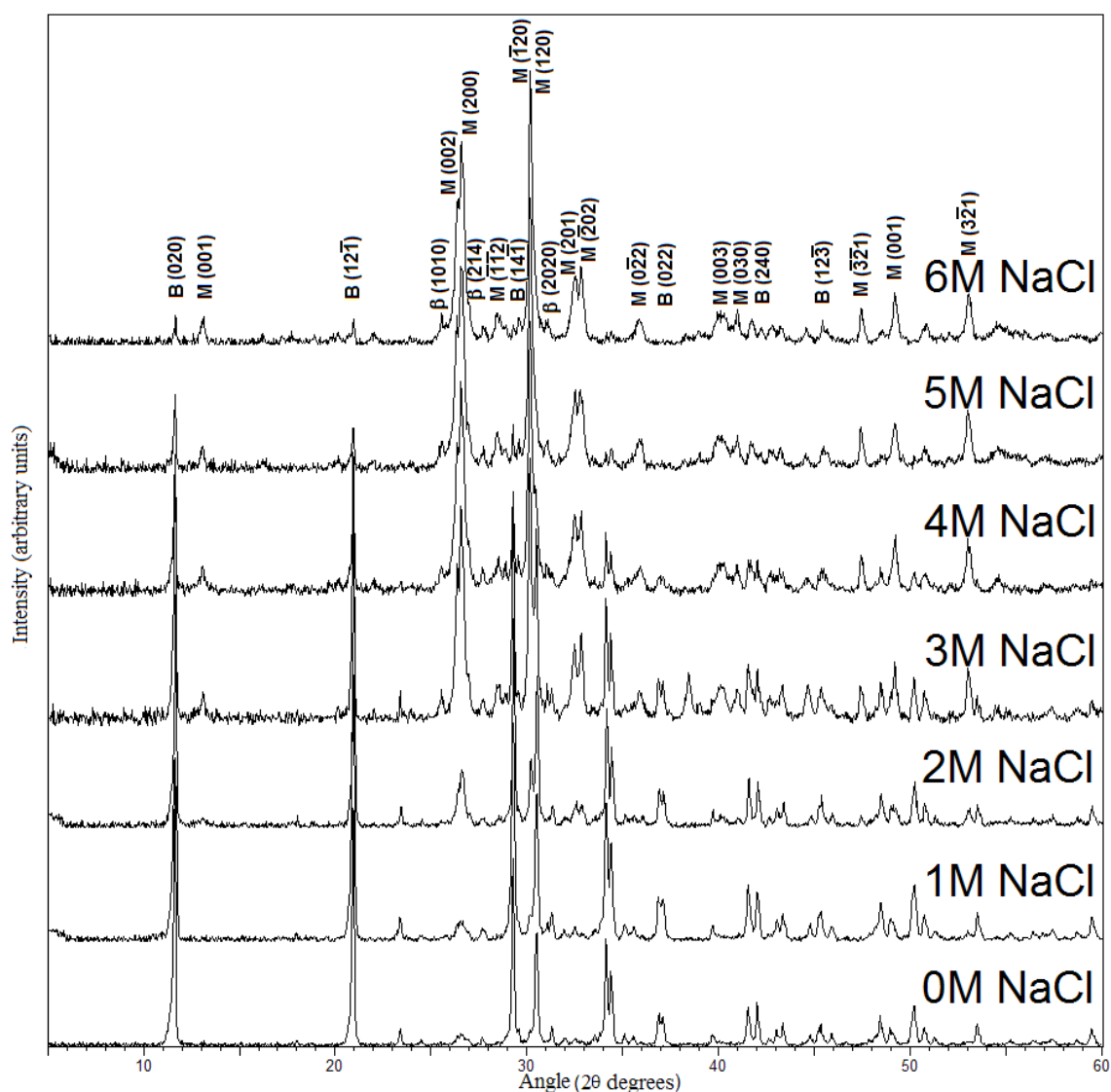


Figure 6.38. XRD patterns for samples prepared with various NaCl concentrations.

The variation of undissolved  $\beta$ -TCP with monetite amount is demonstrated in Figure 6.39. The ability of citrate ions to interact with  $\beta$ -TCP surface and inhibit its dissolution was tested by ICP analysis in the previous section. In addition, water excluded from monetite has a dilution effect on the pH of the setting liquid, further increasing the pH and lowering  $\beta$ -TCP dissolution. Higher residual  $\beta$ -TCP amount is thus attributed to its lower solubility at high ionic strength.



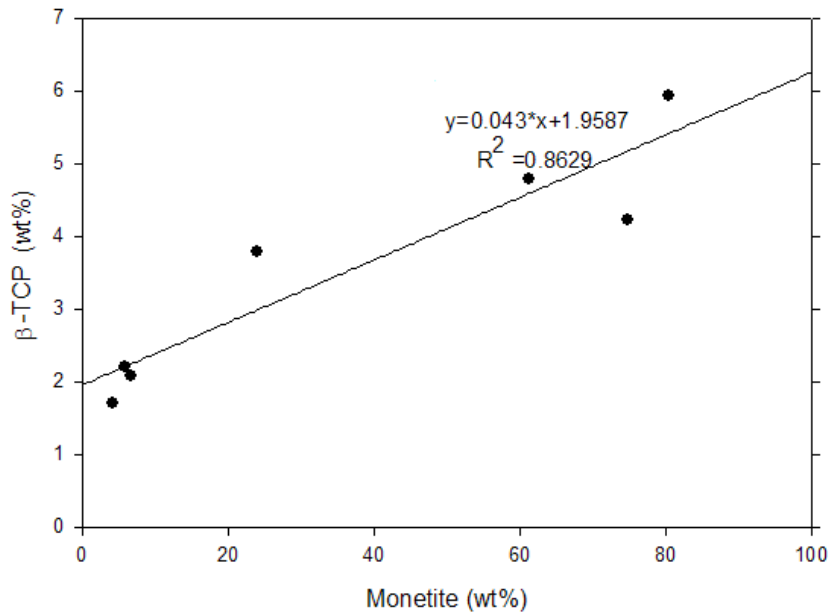


Figure 6.39. Variation of  $\beta$ -TCP residue amount by monetite formation.

In brushite crystal structure, lattice water molecules are interlayered between the calcium phosphate chains. Monetite crystal structure is denser than brushite due to the exclusion of water molecules (Wang et al. 2008). It is also less soluble due to absence of water. This contraction results in isolated reservoirs of water that form pores upon drying. Formation of monetite is accompanied by a gradual increase in porosity as seen in Figure 6.40. In theory, porosity is linearly dependent on monetite amount. For the P/L ratio of 2.5 used in this study and 5% residual  $\beta$ -TCP, the theoretical dependence of porosity is expressed as:

$$P\% = 0.215[\text{DCPA}\%] + 40.91 \quad (6.4)$$

Here the initial 40.91% porosity is the sum of the initial 9.5% shrinkage and the voids occupied by water exceeding the stoichiometric amount. As monetite is preferentially crystallized, excluded water sums up to a maximum porosity of 62.4%. The highest porosity obtained in this study was 52.45% for the samples containing an average of 5.2% undissolved  $\beta$ -TCP and 14.5% brushite. The evolution of porosity with monetite formation shown in Figure 6.40 gives a similar relationship to the theoretical relation of Equation 6.4:

$$P\% = 0.194[\text{DCPA}\%] + 36.50 \quad (6.5)$$

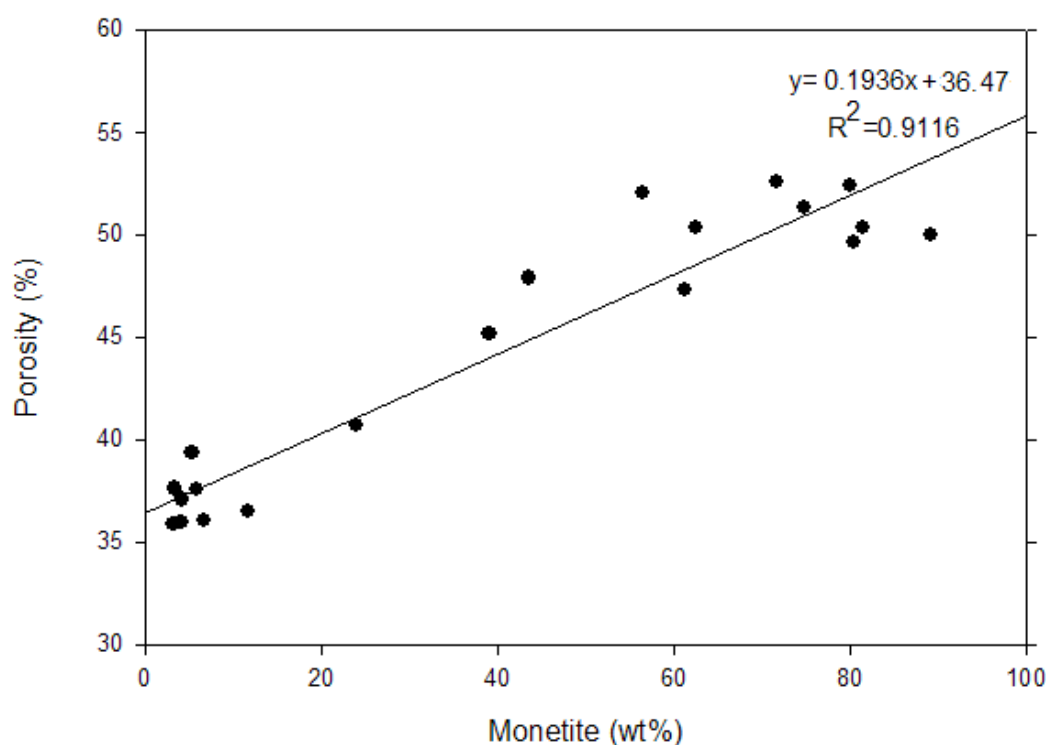


Figure 6.40. The relation between porosity and monetite formation.

Multiple mechanisms were suggested at the maximum citric acid concentration for increased monetite formation. These are chelation of calcium ions and interaction with  $\beta$ -TCP surface by citric acid to reduce the supersaturation of both brushite and monetite. In addition, Bohner et al conclude in their study on citric acid addition to brushite cements that low concentrations up to 0.3 M citric acid provide effective inhibition of monetite transformation due to small decrease in supersaturation (Bohner et al. 1999). Barrere et al studied calcium phosphate precipitation in enhanced simulated body fluid containing up to 0.7 M NaCl and concluded that high ionic strength reduced ionic diffusion and nucleation sites, lowering the supersaturation and favoring heterogeneous nucleation (Barrere et al. 2002). A similar mechanism is thought to take place for brushite cement set in highly saline conditions, with the combined effects of ionic modifiers citric acid and NaCl. Decrease in supersaturation of both brushite and monetite to the level of undersaturation for brushite, decreased solubility of  $\beta$ -TCP at low pH combined with enhanced heterogeneous nucleation of monetite on brushite

crystals is the proposed mechanism of increased monetite formation with higher NaCl concentration at a fixed citric acid concentration of 0.3 M.

Table 6.7. Results of quantitative XRD, Archimedes porosity, and mechanical analysis for all samples

Sample	Phase Composition				Porosity %	Compressive Strength MPa	Normalised Strength MPa
	$\beta$ -TCP wt%	MCPM wt%	DCPD wt%	DCPA wt%			
0A	1.43±0.09	0	95.28±0.7	3.29±0.62	37.63±4.01	10.88±0.33	8.21
0B	1.38±0.05	0	93.36±1.41	5.28±1.37	39.38±3.87	12.44±2.57	10.32
0C	2.33±0.47	0	93.45±1.37	4.21±1.1	37.37±3.61	11.88±2.56	8.24
1A	1.56±0.37	0	94.3±1.18	4.15±0.8	37.06±2.86	11.76±4.22	8.60
1B	1.37±0.33	0	95.42±0.63	3.21±0.3	36.52±1.49	10.96±1.96	7.52
1C	3.72±0.45	0	90.39±1.42	5.87±0.91	37.60±1.18	11.39±3.99	8.58
2A	1.89±0.65	0	94.06±0.86	4.05±0.23	35.94±1.04	11.05±0.58	7.61
2B	2.41±0.02	0	86.02±4.05	11.59±4.06	36.52±1.89	12.31±1.80	8.74
2C	1.96±1.05	0	91.45±4.28	6.59±3.23	36.06±1.34	11.86±0.09	8.21
3A	4.41±0.71	0	56.56±1.02	39.04±1.7	45.20±0.27	7.72±1.87	9.84
3B	3.93±0.44	0	52.48±0.15	43.6±0.31	47.90±1.87	9.17±0.72	12.09
3C	3.03±0.28	0	73.03±1.66	23.95±1.4	40.67±3.22	10.22±2.47	9.10
4A	5.3±0.58	0	38.31±4.54	56.38±3.97	52.02±1.00	9.07±1.22	14.97
4B	6.16±1.06	0	31.37±8.53	62.46±7.49	50.36±0.68	8.21±2.00	12.37
4C	2.93±0.57	0	35.88±12.4	61.21±12.9	47.36±2.11	9.48±1.06	12.14
5A	3.63±0.44	0	24.8±1.6	71.59±1.15	52.60±0.38	8.68±0.65	14.78
5B	3.27±1.24	0	7.58±1.18	89.15±1.39	50.02±0.48	10.35±0.86	15.32
5C	5.77±3.67	0	19.45±6.35	74.8±10.04	51.34±1.74	9.08±1.58	14.44
6A	5.21±1.11	0	14.53±1.37	80.01±2.12	52.45±2.03	6.41±1.47	10.83
6B	5.95±0.62	0	12.6±1.44	81.43±2.07	50.40±3.19	10.95±1.59	16.54
6C	6.67±1.49	0	12.85±5.01	80.49±4.69	49.62±1.46	10.45±2.31	15.13

The finding of critical NaCl concentration of 2 M introduces a significant control parameter in brushite cements containing NaCl porogen for the purpose of inducing macroporosity. Sodium chloride has a solubility in water at room temperature of 6.143 M. Figure 6.41 reveals that a portion of the macroporous brushite cement will transform to monetite upon using NaCl porogen and the accompanying water filled pore formation will increase the porosity significantly. Stability of brushite at the initial concentrations and stability of monetite at final concentrations give the curve a sigmoidal character with a sudden variation at the intermediate NaCl concentrations.

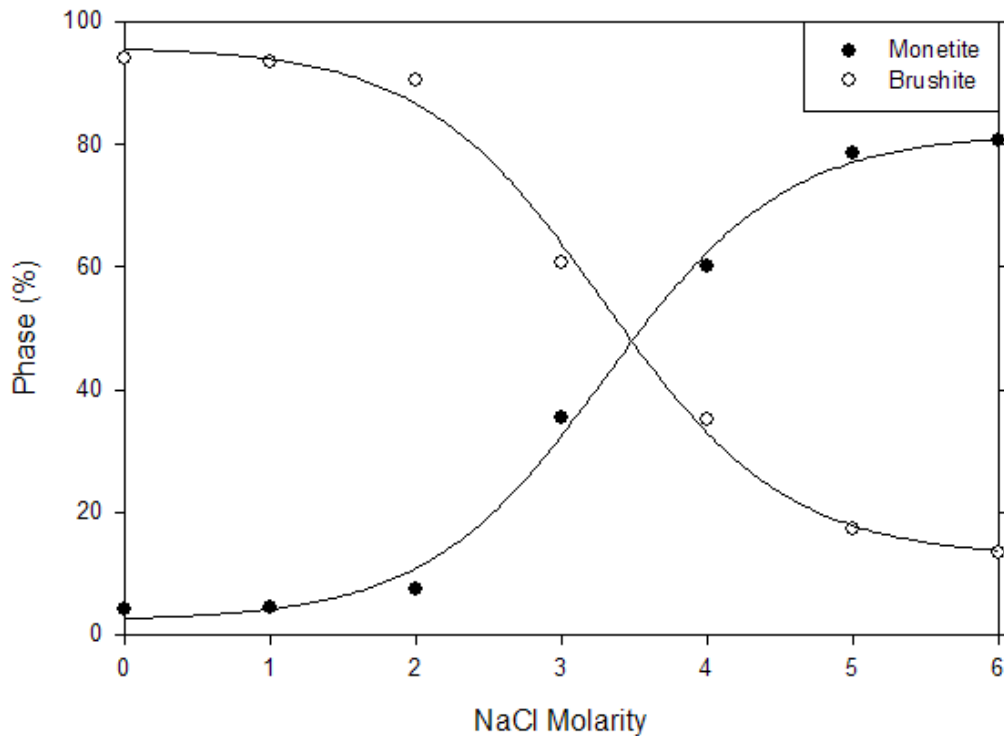


Figure 6.41. Variation of brushite to monetite transformation with increasing NaCl concentration.

Up until now, transformation of brushite to monetite was considered detrimental to the mechanical properties of cement blocks (Bohner et al. 1997; Bohner et al. 1999; Hofmann et al. 2006). In order to rightfully assess the material specific properties of monetite and consider utilization of rarely used monetite and its high temperature decomposition product calcium pyrophosphate in scaffolds, there is need to make a distinction between the inferiority of highly porous monetite crystal structure to porous brushite crystal structure and the mechanical differences between dense monetite and brushite structures. Previous studies make no such distinction and consider monetite inferior to brushite in terms of mechanical properties overall. However it is clear from the findings of this study that strength reduction through brushite to monetite transformation is due solely to extra pore formation. Equally of importance is the fact that the expected strength decrease is compensated by the relatively higher strength of monetite so the resultant relation of strength to porosity is weaker than expected. Figure

6.42 shows the variation of strength for sample sets prepared using varying NaCl concentrations with corresponding porosities.

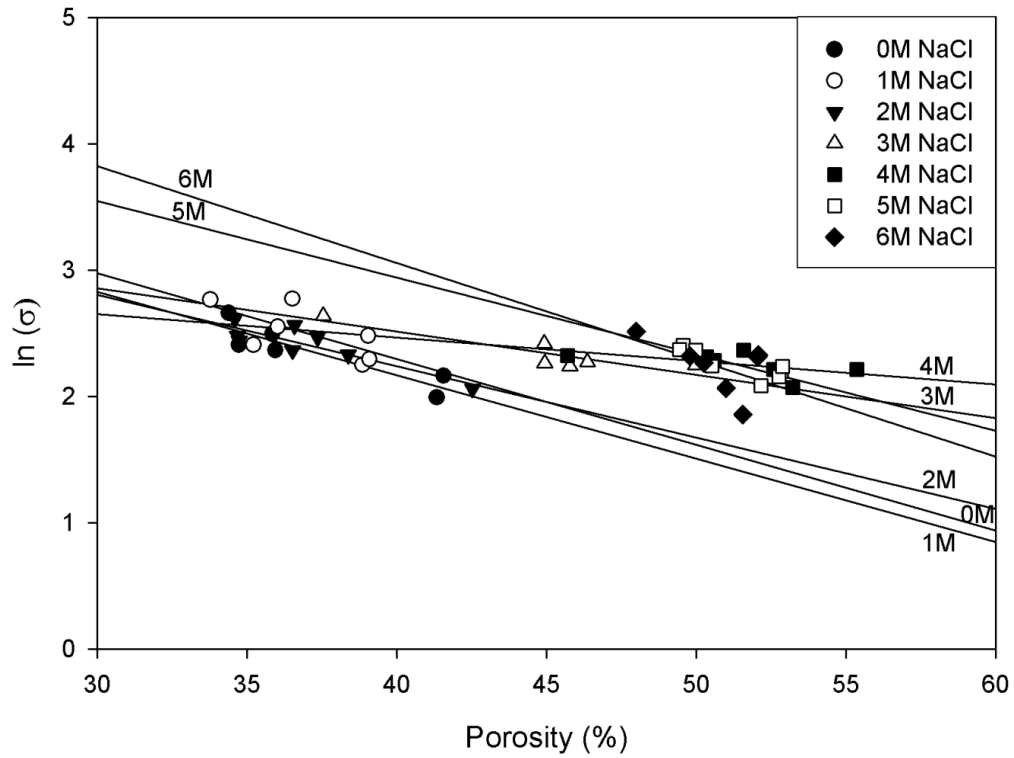


Figure 6.42. Variation in compressive strengths of samples prepared using various NaCl concentrations.

The relation between compressive strength of brittle ceramics and porosity was approximated by Rice et al. in the form of an exponential function as:

$$\sigma = \sigma_0 e^{(-bP)} \quad (6.6)$$

where  $\sigma$  is the strength at porosity  $P$ ,  $\sigma_0$  is zero-porosity strength, and the constant  $b$  is the stress concentration factor that is mainly dependent on pore morphology (Rice 1998). The constant  $b$  is obtained from the slope of the curve representing variation of strength with porosity. Fracture mechanics of ceramics predicts that  $b$  is between 0.04 and 0.07 for most ceramics with regular pore morphology (de Groot 1984). Most ceramics contain pores that are ellipsoidal in shape corresponding to stress

concentration factors in the range 0.04-0.07 (Rossi 1968; Rice 1998). Larger macropores are known to intensify the stress more than smaller macropores (Liu 1997). Studies on mechanical properties of calcium phosphates reported a range of values between 0.035 and 0.108 depending on the pore size and shape (de Groot 1984; Liu 1997; Liu 1998). The average value of 0.054 obtained from experimental data reveals that the stress concentration factor is within the range expected from calcium phosphates.

The resulting variation of normalized compressive strength with increasing monetite amount is given in Figure 6.43. Enhancement in strength during brushite to monetite transformation is evident from the slope of the trendline. The higher strength of monetite rich structure than brushite rich structure despite presence of residual  $\beta$ -TCP may be attributed to stronger fine monetite crystals, and formation of nanoscale colloidal pores during monetite formation instead of disc-like macropores efficient in stress intensifying.

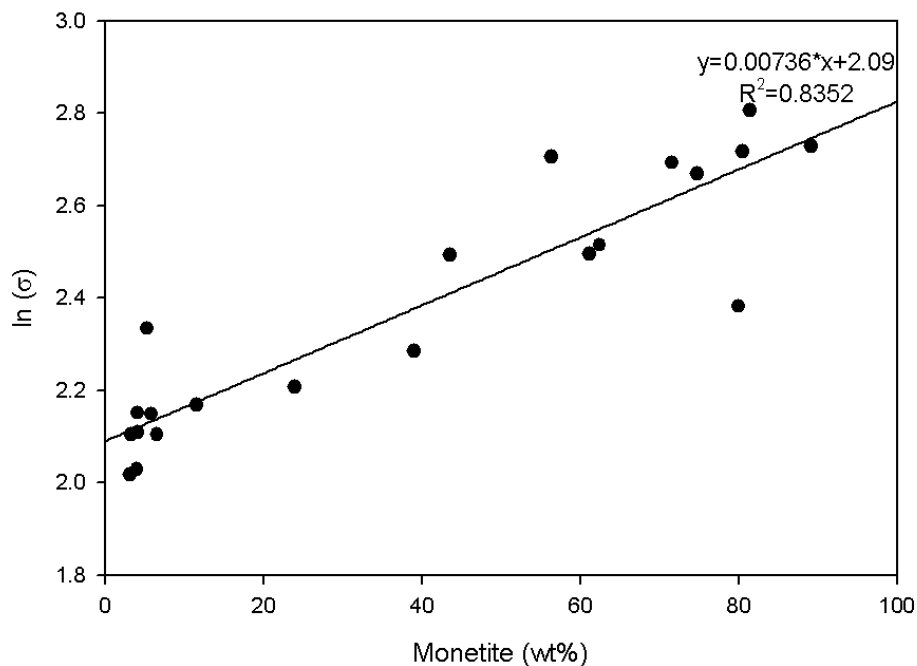


Figure 6.43. Variation of normalized compressive strength with monetite amount.

Pore morphology of the evolving microstructure of the calcium phosphate cement blocks shown in Figure 6.44 reveals that increasing monetite formation and porosity has no effect on macropore shape and size. Disc-like pores of a few hundred

microns in diameter and 10-20 microns in thickness aligned at random directions are present in all samples. These pores are the result of packing defects and air gaps occurred during the mixing process. Excess water both from the starting precursors and from the exclusion by monetite crystals fill the gaps and lead to macropores upon drying. Large spherical or ellipsoidal pores are seldom present but interparticle porosity in the nanoscale is present as seen in Figure 6.44h. These so called colloidal pores have been found to account for about 90% of total porosity volume in hydraulic cements (Kendall et al. 1983). Mechanical properties of hydraulic cements are dependent on the length of the crack-like macropores and the volume fraction of the colloidal pores (Kendall et al. 1983). As seen in Figure 6.44, relative size of crack-like pores stays the same regardless of the ionic strength of the solution. Therefore observed strength reduction with monetite formation is mainly due to increase in nanoscale interparticle porosity volume as a result of monetite formation.

Disc-like pores in ceramics are more effective in stress intensifying than ellipsoidal or spherical pores (Rossi 1968). Accordingly, slopes of the trendlines in Figure 6.42 are expected to be much steeper. Relatively higher strength of monetite rich structure is evident as the intercept of 5 M and 6 M NaCl containing samples are higher irrespective to the pore morphology. To demonstrate newly forming monetite phase counteract the stress intensifying effect of increasing porosity clearly, a normalization was applied to the compressive strength of samples to cancel out the variation in porosity. Mean compressive strengths of all samples were extrapolated to mean porosity of 43.5% according to the average relation derived from Figure 6.42:

$$\ln(\sigma) = 4.702 - 0.054[P\%] \quad (6.7)$$

Variation of compressive strength for individual sample sets with porosity given in Figure 6.42 reveals varying stress concentration factors due to varying NaCl concentration. The coefficients of trendlines of all sample sets in Figure 6.42 are given in Table 6.8. Accordingly, brushite rich samples had an average theoretical dense strength around 100 MPa which is close to the dense strength value given in literature (Hofmann et al. 2009), while the strength values for monetite rich samples were more than twice that value. Stress concentration factors of both brushite and monetite rich samples are similar while the samples containing comparable amounts of both phases result in lower constants possibly due to a change in pore structure by the voids formed as a result of mismatch in crystal densities of brushite and monetite.

Table 6.8. Calculated parameters of trendlines for variation of compressive strength with porosity

NaCl Molarity	b	$\ln \sigma_0$	$\sigma_0$	R <sup>2</sup>
0	0.0660	4.81	122.54	0.817
1	0.0679	5.01	150.23	0.572
2	0.0566	4.50	90.38	0.767
3	0.0343	3.89	48.74	0.790
4	0.0186	3.21	24.80	0.518
5	0.0607	5.37	214.93	0.690
6	0.0766	6.12	455.37	0.517

The crystal structure of brushite and monetite are quite different as seen closely in Figure 6.44h. Brushite crystals are smooth, rigid, equiaxed blocks that are less than 10 microns in average size while monetite crystals are in the form of stacked sheets of a few microns length and a few nanometers in thickness. The comparatively finer structure of monetite crystals gives a fuzzy look to the microstructure at macroscales. The study by Sheikholeslami on the precipitation of a similar calcium compound, CaSO<sub>4</sub> in moderate ionic strengths up to 1.5 M NaCl reveals that lower supersaturation at high ionic strength is responsible for an induction period during spontaneous nucleation (Sheikholeslami et al. 2003). The longer the observed induction period, higher the growth rate and larger the crystals are. Monetite crystals in this study nucleated on readily available brushite crystals so that their nucleation rate was also expected to be high. Since the principle mechanism of setting and hardening of calcium phosphate cements is the intergrowth of individual crystals, and compressive strength of ceramics is a function of grain size, fine monetite crystals are expected to be more



efficient in load bearing despite the presence of micro voids between crystal sheets. Nevertheless the disc-like morphology of macropores in all samples suggests a high stress concentration factor should be used in modeling the dependence of strength on porosity.

The dependence of stress concentration factor  $b$  to pore shape for ceramics with a Poisson's ratio close to 0.2 is approximated by Rossi et al as:

$$100 * b \cong \left( \frac{5a}{4c} + \frac{3}{4} \right) \quad (6.8)$$

where  $a$  is the axis of diameter and  $c$  is the perpendicular axis to the diameter of the average pore. Thus, a disc-like pore is expected to raise the stress concentration much higher than a spheroid or rod-like pore (Rossi 1968). Poisson's ratio of brushite and monetite is recorded in literature as 0.16 (Charriere et al. 2001). Therefore above relation is also valid for brushite and monetite blocks. The average coefficient derived from Figure 6.42, 0.054, gives an  $a/c$  ratio of 3.72, a representation of slightly disc-like average pore shape. A bimodal pore size distribution consisting of large disc-like pores and nanoscale pores may account for the observed variation in stress concentration factor. Transformation of brushite to monetite is the sole mechanism that the enhancement of the compressive strength of highly porous CPC can be addressed in this study. Monetite blocks can be of valuable use as scaffold material provided that the inherent macroporosity created during mixing process is eliminated.

The attempt to apply the synergistic effect of NaCl and citric acid to design of monetite rich porous scaffolds resulted in enhanced monetite formation, microporosity and strength of the macroporous blocks. In addition to synergistic effect of citric acid and NaCl on controlling the phase composition and porosity of the blocks, citric acid improved workability of cement paste by retardation of brushite formation and NaCl acted to induce macroporosity upon drying. As evidenced in the kinetic studies, a critical NaCl concentration around 3 M was found to rapidly enhance monetite formation. Mechanical testing of the blocks revealed higher strength of monetite in contrast to brushite despite increased microporosity due to monetite formation. Mechanical models enabled determination of theoretical brushite strength around 100 MPa in accord with literature. Theoretical strength of monetite rich samples were than twice that value. SEM analysis of the microstructure revealed that pore morphology was not affected by

phase transformation and the strength reduction was due solely to micropore formation accompanying monetite transformation.

The results of this study strengthen the realization of biphasic monetite – hydroxyapatite cements encountered in the previous study, as an enhanced scaffold material. Being able to control monetite amount in brushite cements make it possible to control hydroxyapatite amount by conversion of the brushite phase in media such as simulated body fluid. Hence a balance in strength and resorbability of scaffold blocks can be reached depending on the extent of transformation. One other aim of this PhD thesis is to obtain the densest possible calcium phosphate cement possible prior to macropore induction. This is achievable by introducing size distribution to the precursor particles and porogens. In order to optimize packing ratio, rheology of cement precursors consisting of various particle size distributions are aimed to be analyzed. The correlation between cement viscosity and packing ratio may enable optimization of cement density based on size distribution of the precursors.

## CHAPTER 7

### **PHYSICAL MODIFICATION OF CALCIUM PHOSPHATE CEMENT BLOCKS BY A VARIABLE POROGEN SIZE DISTRIBUTION APPROACH**

The ultimate goal of the present study is to produce novel bone tissue engineering scaffolds consisting of calcium phosphate cement as the dense matrix and NaCl as the porogen. Previous studies have shown that NaCl concentration in the cement setting liquid can be used as a control parameter in the presence of citric acid, to induce monetite phase precipitation as the final phase for the  $\beta$ -TCP-MCPM brushite forming cement system. Physical and mechanical properties of monetite are superior to brushite such that it has higher surface area and strength. Cement block samples prepared in this study are modified so as to consist majorly of monetite phase.

In the broadest sense scaffold is a 3 dimensional porous construct that has high surface area, high porosity with interconnectivity, and is made of bioactive materials for inducing a cellular response in vivo or in vitro. Scaffolds designed for in vivo applications require a certain strength in order to withstand body forces and maintain rigidity. Strength and porosity are two equally important yet opposing properties for scaffold design. It is an accepted rule that strength of a ceramic decreases roughly by half with every 10% increase in porosity. Building a 3 dimensional construct that is both macroporous and strong necessitates refinement of all the physical properties of the materials constituting the scaffold structure. The aim of this study is to minimize the useless microporosity formed in cement due to packing defects and optimize macroporosity in terms of interconnectivity by adjusting the size distribution of solid particles of the cement block.

Materials utilized in dense matrix formation and macropore formation in this study are calcium phosphate cement and NaCl. The most important physical property of the constituent materials is the particle size. Finer cement precursor particles are known to enhance dissolution and increase the scaffold strength while larger NaCl particles are known to induce porosity that is useful for effective cellular colonization of the scaffold. This mutual beneficial relationship of strength and porosity is worth investigating as there are not many material design parameters other than porogen size distribution that

favor improvements in both strength and porosity. Furthermore, particle size distribution of cement precursor is an energy consuming inefficient process due to the necessity to grind the particles to the submicron size range. Packing of nanosized particles are generally obstructed by the formation of agglomerates as individual particles rarely pack independently. The approach tried in this study is utilization of the fine cement precursors as the lower limit of the range of particle size distribution for the solid phase also including NaCl porogen particles that are distributed near the higher limit of the distribution range. Maximum packing densities of NaCl suspensions were used as a baseline for the engineering of the cement block samples. Cement precursor volume and sample unit volume was kept constant while porogen volume was calculated as a function of maximum packing densities obtained from the rheological analysis of the suspensions. It is hypothesized that addition of fine cement precursor to the size distributed porogen mixture will improve the packing density in the presence of the setting liquid medium.

### **7.1. Rheological Determination of Maximum Packing Density for a Set of Size Distributed NaCl Particles**

Two successive experiments were conducted for minimization of the microporosity and optimization of the macroporosity by adjusting the size distributions of solid particles of the cement block. First, theoretical maximum packing density for combinations of NaCl size distributions were determined via rheological analysis of set of samples carefully selected to represent all possible combinations by an experimental design model. Maximum packing density values for different NaCl size distribution obtained from the first experiment were used to adjust the NaCl porogen volume for cement block samples with constant cement volume and sample volume. Packing densities of the samples were correlated with porosity, density, and strength of cement blocks.

Significant size distributions were aimed to be determined by variation of the amount of several or all of the NaCl size groups. Each size group was added to the samples in amounts ranging from 0 to 1 grams. A well-mixed suspension was analyzed in rheometer in terms of shear stress and viscosity as a function of shear rate. This design permits the analysis of singular and combined effects of each NaCl size group on the viscosity and maximum packing density of the samples. Rheological analysis of

PEG200 filled with NaCl was done at the shear rate range 0 to 500 1/s. Initially 5 solid loadings from 10% to 50% were prepared for the samples. Increasing the solid content had the effect of increasing the shear thinning character of the suspension. For high solid loadings the liquid polymer had the tendency to separate from NaCl at high shear rates greater than 300 1/s. The effect of phase separation on viscosity in the 50% solid loaded suspension is seen clearly in the viscosity – shear rate given in Figure 7.1a. The viscosity curve was seen to reach a plateau region at high shear rates for samples without phase separation. Viscosity values taken at 200 1/s shear rates are close to the constant viscosity value reached at the plateau region, so all viscosity readings were done for all samples at 200 1/s rate for consistency. The viscosity – shear rate graph for PEG200 was obtained first in order to calculate the relative viscosity values. As seen in Figure 7.1b, PEG200 is a slightly shear thickening non-Newtonian fluid with a relatively low viscosity for relevant shear rates considered. It was seen that generally PEG200 filled with NaCl particles exhibited shear thinning non-Newtonian fluid behavior.

Maximum packing densities of different combinations of NaCl size distributions were determined by analysis of their rheological properties using a rotational rheometer. Thirty eight combinations determined through an experimental design study were dispersed in Polyethylene Glycol 200, a slightly viscous, slightly shear thickening non-Newtonian liquid polymer at solid loadings of 10%, 20%, 30%, 40% and 50% by volume. Viscosity versus shear rate curves for a shear rate range of 0-500 1/s were obtained for each sample. Viscosity values at rates sufficiently high to obey the model assumptions and sufficiently low to prevent phase separation at high rates were needed to insert into the model equation developed by Liu et al. in order to determine the maximum packing density as a function of solid loading as seen in Figure 7.2.

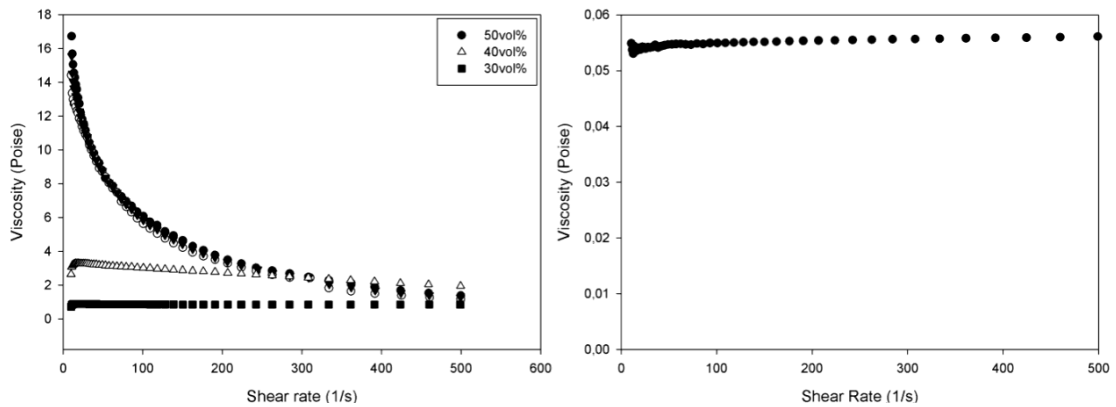


Figure 7.1. Flow behavior of (a) NaCl suspensions and (b) PEG200.

Calculated relative viscosity values and solid loadings were used to plot the model equation developed by Liu et al. (Liu 2000):

$$1 - \eta_r^{-1/2} = a\phi + b \quad (7.1)$$

The slopes and intercepts of the extrapolated trendlines were obtained graphically as seen in Figure 7.2 for sample 16. Theoretically at maximum solid loading or maximum packing density, the relative viscosity of the sample reaches infinity and the left hand side of the equation equals 1. Equating the horizontal axis to 1 by extrapolating the trendline, maximum packing factor is obtained at the intersection point. Liu's model is only applicable to suspensions with high solid loading. It is seen in Figure 7.2 that taking the low solid loadings into account decreases the slope and intercept of the trendline significantly. Subsequent samples were analyzed using three solid loadings and the useless low solid loadings were not taken into account. After analysis of all the samples it was seen that even 30% solid loading was too low to obtain a statistically significant trendline so 30% solid loading data were also discarded. Table 7.1 shows the change in maximum packing factor values with different data points being taken into account.

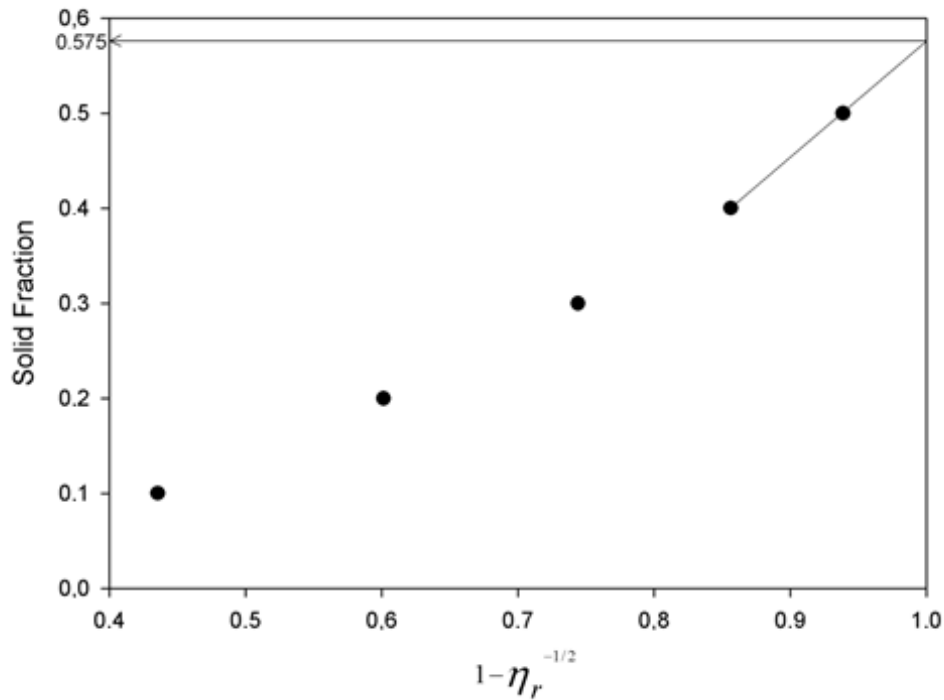


Figure 7.2. Graphical determination of maximum packing density for sample 16.

Table 7.1. Data used for extrapolation to maximum packing density

Data points used	Maximum packing density $\phi_m$	$R^2$
All	0.522	0.982
20%, 30%, 40%, 50% solid loading	0.539	0.985
30%, 40%, 50% solid loading	0.557	0.992
40%, 50% solid loading	0.575	1.000

Maximum packing densities of all 38 samples were calculated accordingly and the results are given in Table 7.2. At the first glance of data, it is evident that increasing the size distribution has a positive effect on the maximum packing density of the samples. The variation of maximum packing density of the samples is shown in Figure 7.3. As seen in Figure 7.4, maximum packing densities for all samples lie within the range between 0.566 and 0.689. A packing density change that large is sufficient to double the strength of a porous ceramic block. The mean packing density for all samples is close to the packing density obtained from random packing of uniform sized spheres, which means that introduction of size distribution cancelled the negative effect of irregular angular particle shape of NaCl particles on packing.

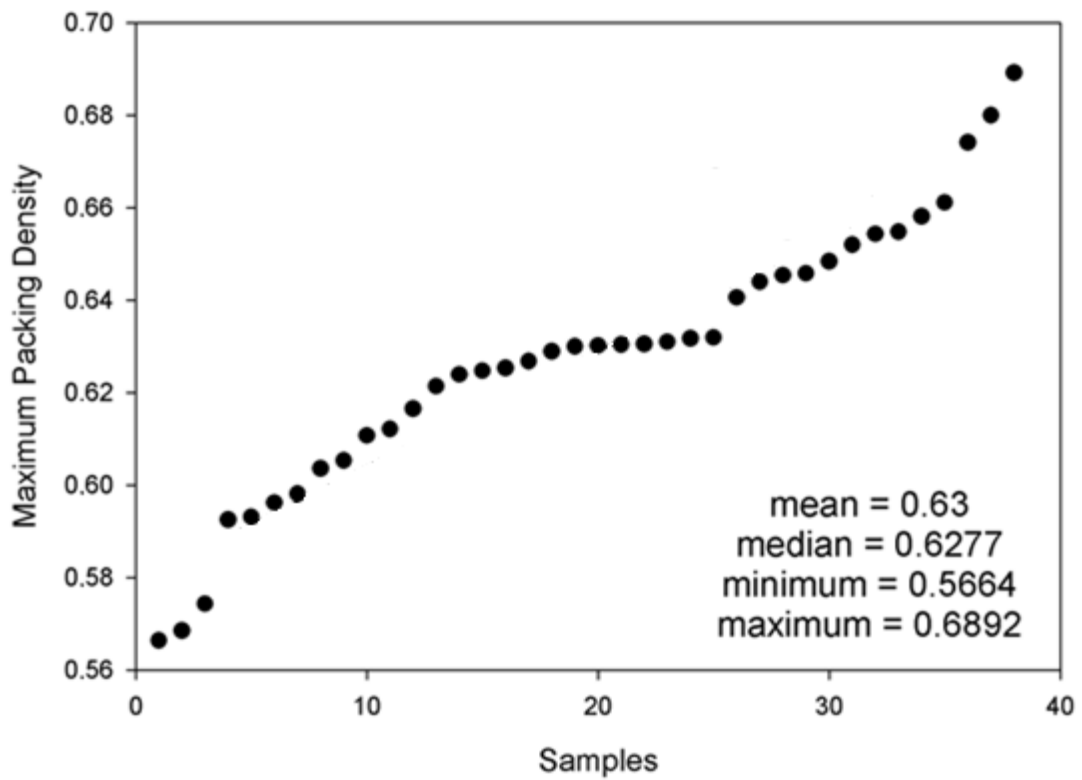


Figure 7.3. Graphical representation of the experiment results.

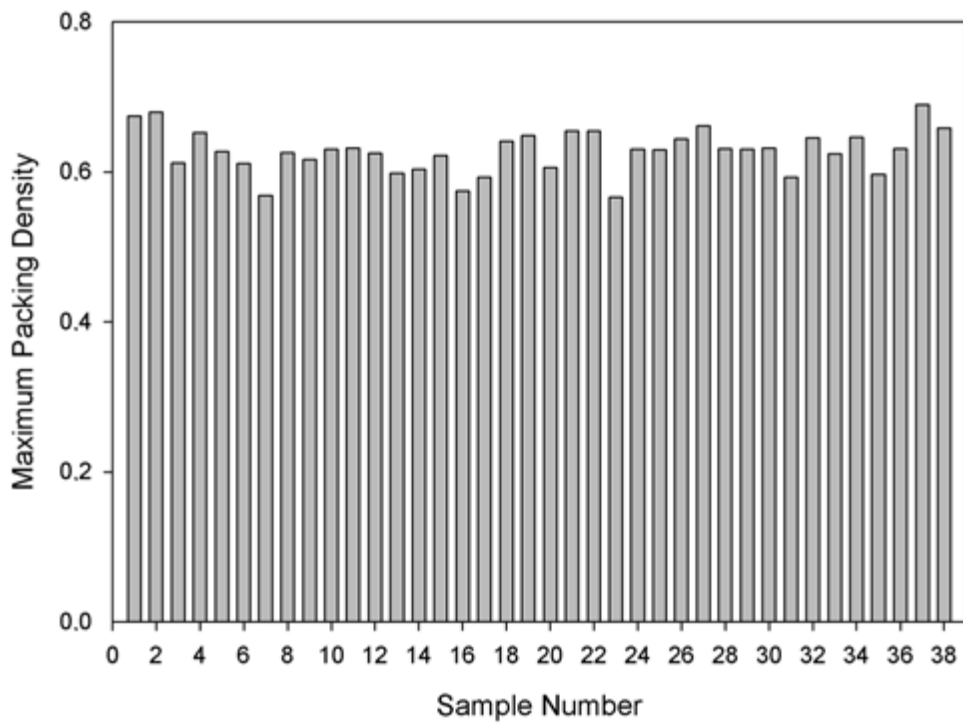


Figure 7.4. Variation in maximum packing densities.



Experimental design software package Design Expert was used to analyze the rheological data. Analysis of variance table was constructed by the software and the results are tabulated in Table 7.3. Values of "Prob > F" less than 0.0500 indicate model terms are significant. In this case A, F, BC are significant model terms. Particle size groups less than 38 and 212 microns are necessary to obtain a well packed structure and particle groups with sizes less than 53 and 75 micrometers are effective in decreasing the maximum packing density significantly when used in combination. Values greater than 0.1000 indicate the model terms are not significant. That means all other particle size groups and the combination of these factors have insignificant effect on the maximum packing density. The overall effect of particle size distribution on maximum packing density is given by the following representative equation:

$$\begin{aligned} \text{maximum packing density} = & 0.63 + 0.022 * A - 0.005964 * B - 0.007033 * C - 0.0008291 * \\ & D - 0.0002856 * E + 0.015 * F - 0.003341 * A * B - 0.009871 * A * C - 0.003166 * A * D - \\ & 0.008934 * A * E - 0.006357 * A * F - 0.016 * B * C + 0.0028 * B * D - 0.0003648 * B * E \\ & + 0.007126 * B * F + 0.001585 * C * D - 0.003726 * C * E + 0.001075 * C * F + 0.003986 * \\ & D * E - 0.006557 * D * F + 0.002881 * E * F \end{aligned} \quad (7.2)$$

Although 38 samples cover most of the experiment design space, still some data points lie outside the model equation given above. This equation is valid in the presence of all 6 size groups and takes into account their singular and synergistic effects. An experimental design consisting of only 3 factors A, B and F on the other hand predicts maximum packing densities beyond the estimation of the model equation. Figure 7.5 shows the design cube for combination of 3 factors, each represented by one axis. The significant effects of particle size groups -38 and -212 are evident from the difference in values at the two sides of the axes. It is interesting to see that particle size group -53 micrometers has a slight positive effect on the maximum packing density in the presence of the other two size groups. In fact at the corner farthest from the origin, the maximum packing density exceeds the maximum value obtained in the experiment. This synergistic effect of three particle size distributions, two small and one large seems to result in the optimum packing density for NaCl particles.

Table 7.2. Results of the rheometric analysis of maximum packing density

Std	Run	Factor 1 A:38 microns	Factor 2 B:53 microns	Factor 3 C:75 microns	Factor 4 D:106 microns	Factor 5 E:150 microns	Factor 6 F:212 microns	$\Phi_m$
1	1	1	0.74	0	0	0	0	0.6741
38	2	1	0.95	0	1	1	1	0.68
22	3	0.035	0	0.135	0.644	0.09	0.536	0.6121
32	4	1	0	1	1	0	1	0.652
6	5	1	0.445	1	0.31	0.62	0	0.6268
21	6	0.16	0.35	0	0.51	1	0.535	0.6107
10	7	0	0.405	0.315	0.2	0.345	0.011	0.5685
20	8	0.16	0.35	0	0.51	1	0.535	0.6253
37	9	0	1	1	0.56	1	1	0.6165
4	10	0.7	0.095	0	1	0.07	0	0.6304
13	11	1	1	0.62	0.13	0.27	0.35	0.6319
31	12	0.5	0.665	0.45	0.58	0	1	0.6247
9	13	0	0.795	0.53	1	1	0	0.5981
19	14	0	1	0.525	0.528	0.515	0.533	0.6036
5	15	0.55	1	0	0.51	0.595	0	0.6214
29	16	0	0	0	0	0	1	0.5743
3	17	0	0	1	0.775	0	0	0.5925
17	18	0.87	0	0.735	0.83	1	0.415	0.6406
36	19	0.7	0.14	0.725	0	1	1	0.6484
18	20	0	1	0	1	0	0.53	0.6053
28	21	1	0.209	0.005	0.455	0.39	0.78	0.6548
35	22	0.1	1	0.065	0	0.625	1	0.6543
2	23	0.275	1	1	0	0	0	0.5664
12	24	1	1	0.575	0.894	0.12	0.275	0.6302
23	25	0.475	0.65	1	1	0.535	0.61	0.6289
7	26	1	0	0	0	1	0	0.644
30	27	0.5	0.665	0.45	0.58	0	1	0.6611
33	28	1	1	1	0	0.22	1	0.6305
26	29	0	0.445	0.955	0.005	0.165	0.76	0.63
11	30	0.005	0	0.64	1	0.575	0.26	0.6317
8	31	0	0	1	0	1	0	0.5931
25	32	0	0.075	0.35	0	0.624	0.708	0.6454
16	33	0.75	0.96	0.57	0	1	0.41	0.6239
14	34	0.64	0	0.595	0.085	0.18	0.35	0.6458
34	35	0.045	0	0.43	1	0.565	1	0.5962
24	36	0.475	0.65	1	1	0.535	0.61	0.631
27	37	1	0.209	0.005	0.455	0.39	0.78	0.6892
15	38	0.64	0	0.595	0.085	0.18	0.35	0.6581

Table 7.3. Analysis of variance table for maximum packing density

Source	Sum of Squares	df	Mean Square	F Value	p-value Prob > F
Model	0.024445806	21	0.001164086	3.053561767	0.0133
A-38	0.01101139	1	0.01101139	28.88442881	- 0.0001
B-53	0.000729724	1	0.000729724	1.914168297	0.1855
C-75	0.001003947	1	0.001003947	2.633494842	0.1242
D-106	1.36E-05	1	1.36E-05	0.035779879	0.8523
E-150	1.54E-06	1	1.54E-06	0.00404449	0.9501
F-212	0.004036288	1	0.004036288	10.58775173	0.005
AB	0.000178016	1	0.000178016	0.466962364	0.5042
AC	0.001121565	1	0.001121565	2.942023684	0.1056
AD	0.000130387	1	0.000130387	0.342024044	0.5668
AE	0.000930683	1	0.000930683	2.441312475	0.1377
AF	0.000394152	1	0.000394152	1.033916837	0.3244
BC	0.002761722	1	0.002761722	7.244387235	0.016
BD	0.000106786	1	0.000106786	0.280115746	0.6039
BE	1.61E-06	1	1.61E-06	0.004219557	0.949
BF	0.00061033	1	0.00061033	1.600982162	0.2239
CD	2.74E-05	1	2.74E-05	0.071776092	0.7922
CE	0.000154492	1	0.000154492	0.40525373	0.5334
CF	1.24E-05	1	1.24E-05	0.032449943	0.8593
DE	0.000180984	1	0.000180984	0.474747141	0.5007
DF	0.000497388	1	0.000497388	1.304718132	0.2702
EF	9.38E-05	1	9.38E-05	0.246026018	0.6266
Residual	0.006099558	16	0.000381222		
<i>Lack of Fit</i>	0.004660968	11	0.000423724	1.472707033	0.3514
<i>Pure Error</i>	0.00143859	5	0.000287718		
Cor Total	0.030545363	37			

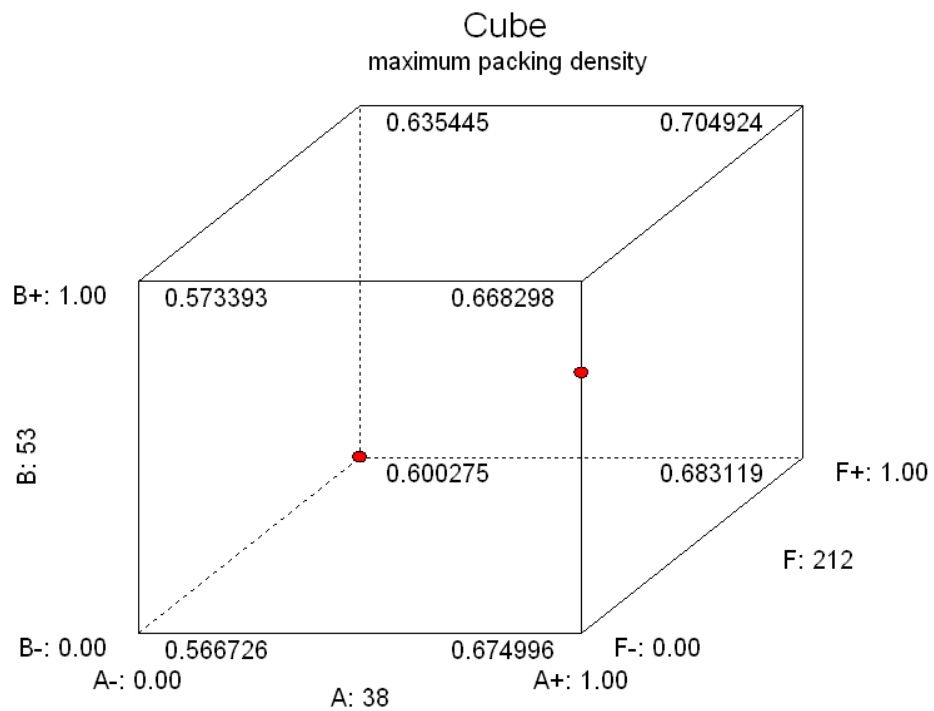


Figure 7.5. Design cube for 3 size distributions used in combination.

Three dimensional response surface graphs obtained from the analysis software are quite useful to understand the synergistic effect of particle size groups -38 and -212 micrometers. As seen on Figure 7.6, simultaneous presence of a significant amount of both size groups improves the maximum packing density considerably. It should be noted that small size group of -38 micrometers is more effective to improve packing than the large particle size group. That may be attributed to the presence of more irregularities on the coarse NaCl crystals than the equiaxed fine crystals that are broken down using intensive force. The mechanism of improvement in the packing density is probably filling of the large gaps formed due to stacking of irregular coarse crystals by the fine equiaxed crystals.

Response surface diagrams used to analyze the multicomponent NaCl mixture give a more clear idea on the contribution of each size group to the packing density than binary and ternary diagrams. For example even though the effect of two dominant particle size groups -38 and -212 could be explained by a binary diagram where the optimum ratio lies somewhere around 0.5, this diagram would neglect the slight improvement in packing density when either -53 or -75 size groups were added. Still ternary diagrams consisting of corners occupied by -38, -212, and either -53 or -75 groups can be constructed from the response surface diagram if only a ternary system would be desired. The data points needed to construct a ternary diagram of packing density for -38, -75, and -212 size groups used in combination are obtained and converted to a ternary diagram. The resultant ternary diagram is shown in Figure 7.10. As seen in the figure, the maximum packing density is shifted to the -38 micrometers size group. The packing density is not as high around other size group corners that means that fine particles have to be dominant in that ternary system for high packing density. Also highest packing density is obtained near the -38 side of the center and there exists a plateau of stable particle packing towards the -212 micrometers size group. The packing density decreases abruptly while moving towards the -75 size group corner, therefore a small amount of -75 micrometers particles are needed at most.

The increase in packing density near the -38 micrometers particle group is an indication of the elimination of coagulations or agglomerations formed by fine NaCl particles during the processing of the suspension. NaCl particles were dispersed in PEG200 without the aid of any dispersant by hand mixing for about 10 minutes in a mortar. The agglomerates were broken down by grinding at the same time with mixing using the pestle. Mixing of the NaCl particles with cement precursors during the preparation of cement blocks is also expected to eliminate the agglomerations of fine particles by the use of vortex shaker and cement liquid medium. The same packing behavior of NaCl particles are expected to occur in cement blocks, possibly with the strengthening effect of even finer cement precursors.

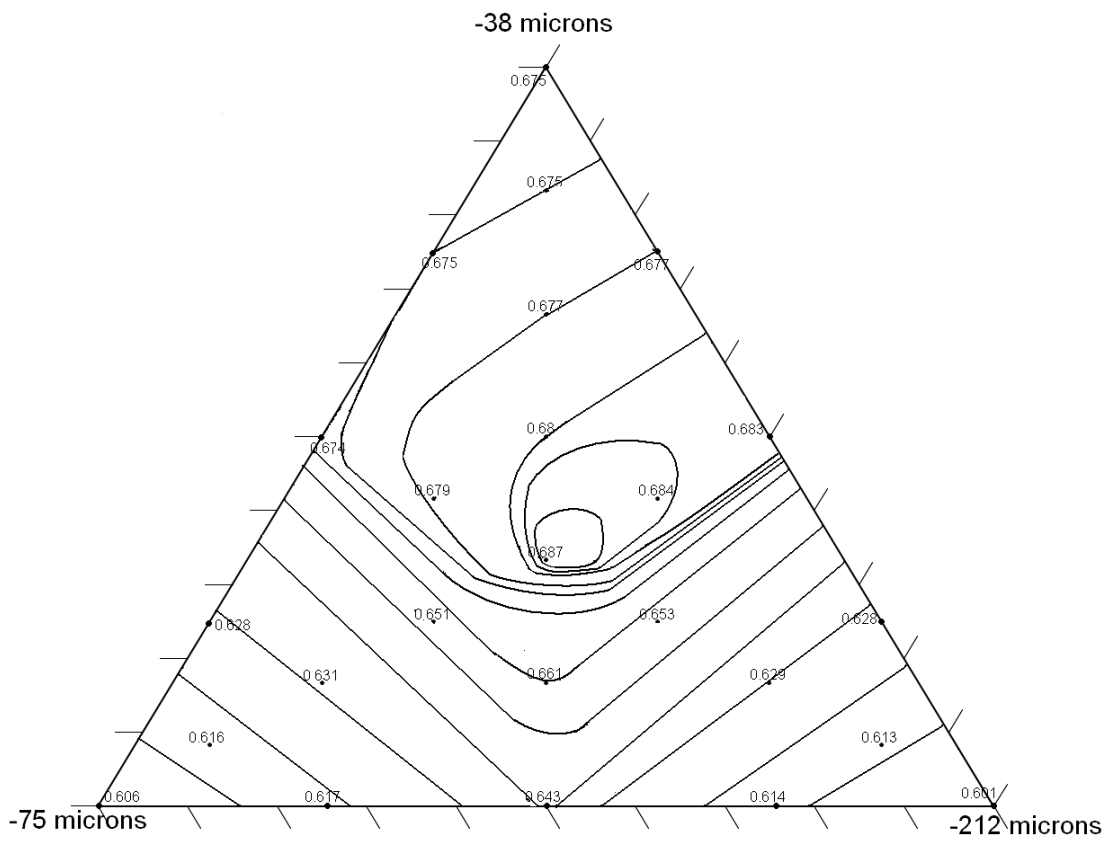


Figure 7.10. Ternary diagram for variation of packing density in the -38, -75, -212 size group system.

## 7.2. Microstructural Characterization of Macroporous Cement Blocks

Size distribution of cement precursors have been shown to effectively improve packing of the cement blocks and reduce microporosity to a quarter of the expected value when unisized precursors are used (Hofmann et al. 2009). A similar approach is taken in this study however by introducing size distribution to the porogen particles in addition to cement precursors. The aim was to closely pack both porogen and precursor particles in order to both eliminate microporosity and improve pore interconnectivity. Microporosity is defined in this context as porosity not larger than a few microns that is produced naturally during the cement setting process as a result of imperfections in packing. Pores that are produced intentionally by the addition of large porogens with sizes ranging to a few hundred micrometers are referred as macropores.

Cement block samples produced in this study are tailored to fit the maximum packing data obtained from the rheological study of the porogen particles. Addition of fine cement precursors to the porogen particles is expected to change the size distribution and an overall improvement in packing is foreseen. In order to observe the effect of the increase in solid particle size distribution, equal amounts of cement precursors are added to each porogen group tested in the rheometry experiment. Unit volumes of the cement blocks have to vary if constant porogen amount is used as the packing densities of each porogen group differ. Alternatively porogen amount may be adjusted according to the maximum packing density data and a constant sample unit volume is expected. Thereby the quantity of microporosity which is a function of packing density as derived by the following equations, is expected to decrease with an equal increase in macroporosity:

$$\phi = \frac{P+C}{V_S} \quad (7.3)$$

$$V_{Por} = MicP + P \quad (7.4)$$

$$Porosity = \frac{V_{Por}}{V_S} \quad (7.5)$$

$$Porosity = \frac{MicP+P}{V_S} \quad (7.6)$$

$$Porosity = \frac{MicP + \phi V_S - C}{V_S} \quad (7.7)$$

$$(Porosity - \phi)V_S = MicP - C \quad (7.8)$$

$$MicP = (Porosity - \phi)V_S + C \quad (7.9)$$

$$\frac{MicP}{V_S} = \frac{(Porosity - \phi)V_S + C}{V_S} \quad (7.10)$$

$$Microporosity = (Porosity - \phi) + \frac{C}{V_S} \quad (7.11)$$

$$Microporosity = Porosity_{Arc} - \left( \frac{Porogen Volume}{Estimated Sample Volume} \right) \quad (7.12)$$

where  $\phi$  is the packing density, P, MicP and C are the volumes of porogens, micropores, and cement precursors respectively. Sample volume, and total pore volume are denoted as  $V_S$ , and  $V_{Por}$ . It is possible to reduce microporosity by improving the packing of the solid phase and also by minimizing the water content of the cement. Water volume introduced to the sample powders at a fixed powder/liquid ratio of 4 is not included in the above equations since the expected volume of micropores are much larger and are able to accommodate all excess water inside. Other fixed parameters in the experiment, sample volume of 2.713 cm<sup>3</sup>, cement precursor volume of 0.777 cm<sup>3</sup>, and total porosity of 71.34% were adjusted to obtain similar porous cement blocks with varying porogen size distributions to effectively monitor the effect of size distribution on microporosity, interconnectivity and mechanical properties. The sensitivity of mechanical properties to the total porosity of cement blocks necessitates small tolerance to variations in sample porosity in order to compare their mechanical properties.

The results of the Archimedean analysis reveal that solid size distribution is effective in improving the packing density of porous cement blocks even further than the maximum packing densities as expected. Increase in packing density with introduction of fine cement precursors was accompanied by reduction in sample volumes, microporosities and total pore volumes. The quantity of improvement however was not uniform for all samples as expected. Packing densities of porous



cement blocks with porogen size distributions yielding lower maximum packing densities were enhanced significantly more compared to samples with porogen size distributions exhibiting already high maximum packing densities in the rheometry experiment. Such porogen size distributions with high maximum packing densities commonly consisted of higher small porogen particles that majorly occupied the space between larger porogen particles. Small improvement in packing densities of porous cement blocks consisting of these porogen size distributions upon addition of the finer cement precursors reveals that fine porogen particles and finer cement precursors function similarly as gap fillers between large porogen particles. So a simple hierarchy of fine and coarse particles exists and the proximity of these two particle size groups to each other is seen to affect the packing density adversely due to the overlap of particle sizes and the consequent interaction between them.

Archimedean measurements gave mean sample volumes much lower than the estimated value of  $2.713 \text{ cm}^3$  for some samples with initially low maximum packing densities as seen in Figure 7.11. The porous cement blocks consisting of size distributed particles with high maximum packing densities were less compacted due to the presence of fine cement precursors. Final packing densities of the porous cement blocks were calculated by taking the obtained sample volumes into account in addition to the cement precursor and porogen volumes for each sample. As shown schematically in Figure 7.12, the volume of the solid phase divided by the total sample volume gave the final packing density which also determines the microporosity. Considerable improvement in packing densities were attained due to introduction of fine cement precursors, particularly for the samples containing not-so-packable porogen size distributions. For example, one of the lowest packable samples, Sample 16, containing only the largest -212 micrometers porogen particles, was compacted down from 57% packing to 70% packing density as seen in Figure 7.13. Only one sample was insensitive to finer cement precursor addition, Sample 37 that majorly consisted of the finest porogen particles of -37 micrometers size. Detailed statistical analysis of the significant size groups affecting the final packing density will be given later in the report.

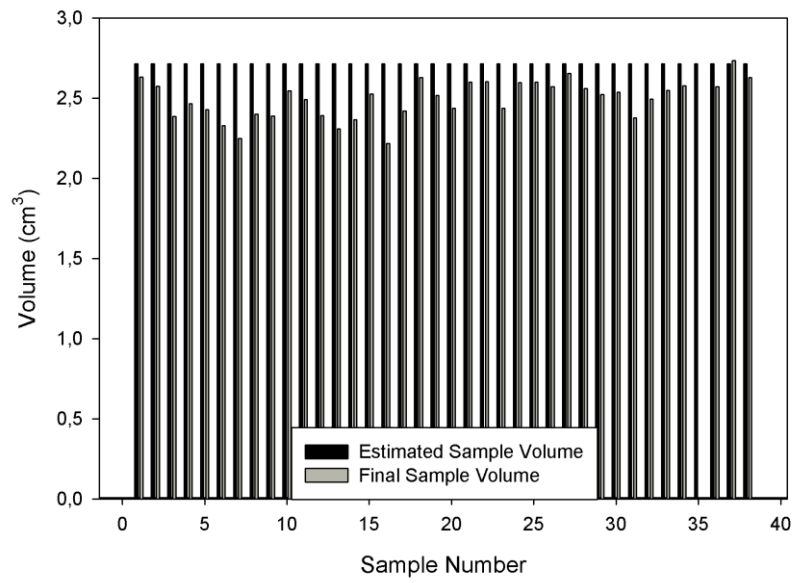


Figure 7.11. Change in the sample volumes due to size distribution of the solid phases.

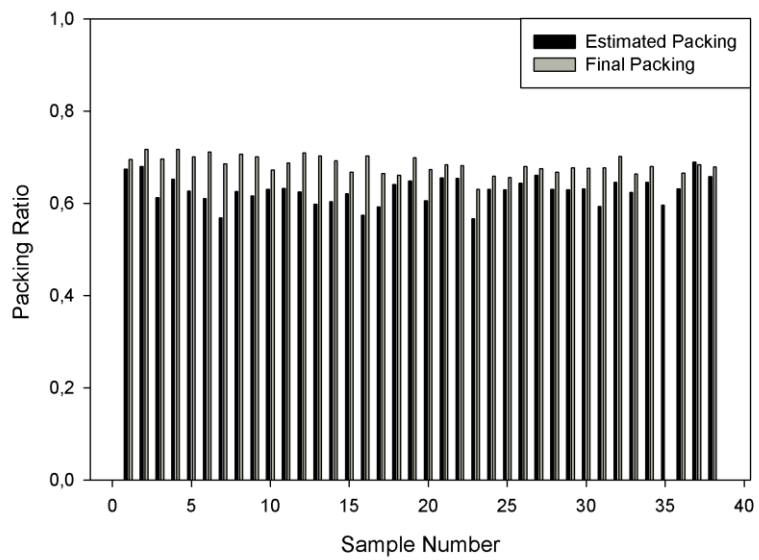


Figure 7.12. Change in packing density as a result of size distribution of the solid phases.

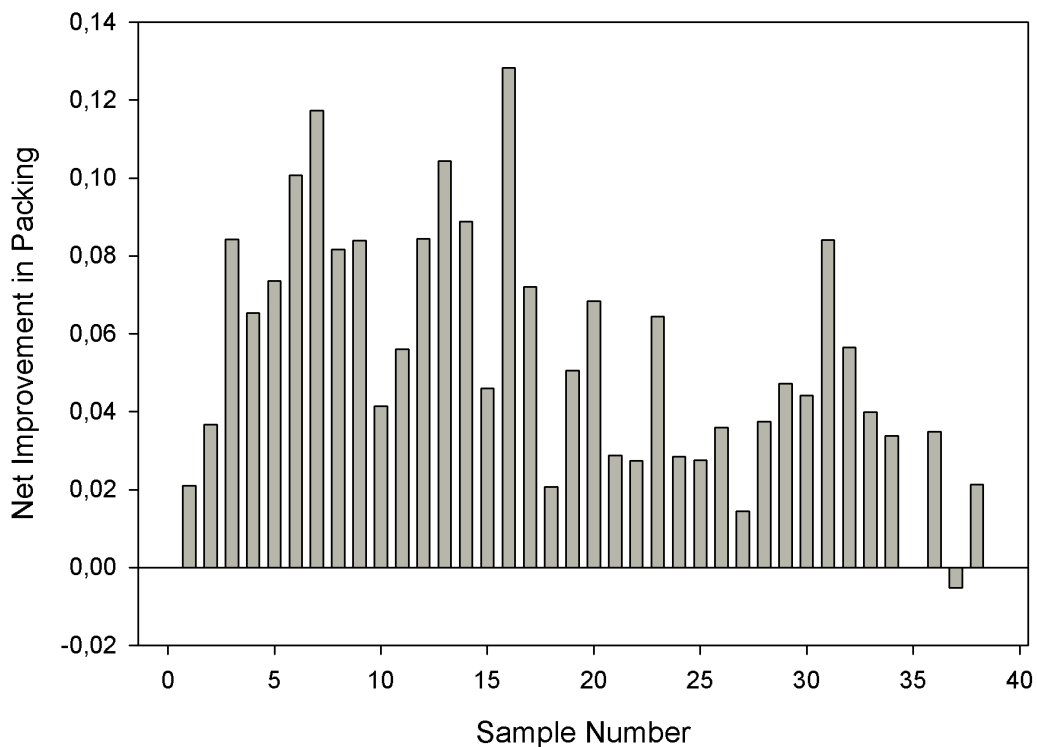


Figure 7.13. Net improvement in sample packing due to size distribution of solid phases.

The observed reduction in volumes of the porous cement blocks was due solely to the reduction in porosity, particularly microporosity as given in Figures 7.14 and 7.15. The infiltration of fine cement precursors to the void spaces between larger porogen particles reduced the packing defects and helped densify the cement matrix by local dissolution of the cement precursors  $\beta$ -TCP, MCPM and precipitation of nano-to-micrometer size monetite crystals in the space filled with cement liquid. The densification effect would be even greater if the end product of the cement reaction was brushite that binds two water molecules into its atomic structure rather than monetite which was aimed to be produced via the synergistic effect of citric acid and NaCl. Monetite formation results in some shrinkage of the cement structure due to its higher density than brushite ( $2.9 > 2.34 \text{g/cm}^3$ ) resulting in micropores around fine monetite crystals. Therefore microporosity is a function of both packing density and monetite content of the porous cement blocks. Although same experimental materials and processes were used for the synthesis of porous cement blocks, not all samples contained a high monetite content. The phase analysis of the cement matrix given in detail later in the report shows that monetite content of the samples ranges between 85

to 55%, so it is not healthy to compare the relation between packing densities and microporosity for all samples. Rather, smaller sample groups with similar monetite content and similar packing densities were analyzed and a direct relation between microporosity, packing density and monetite content was observed as seen in Figure 7.16 and 7.17. The strong relation between packing density and microporosity is seen clearly in Figure 7.18 as the differential microporosity at corresponding net packing for all samples are highly correlated and the variation observed in the figure is mostly due to the variation in monetite content of the samples.

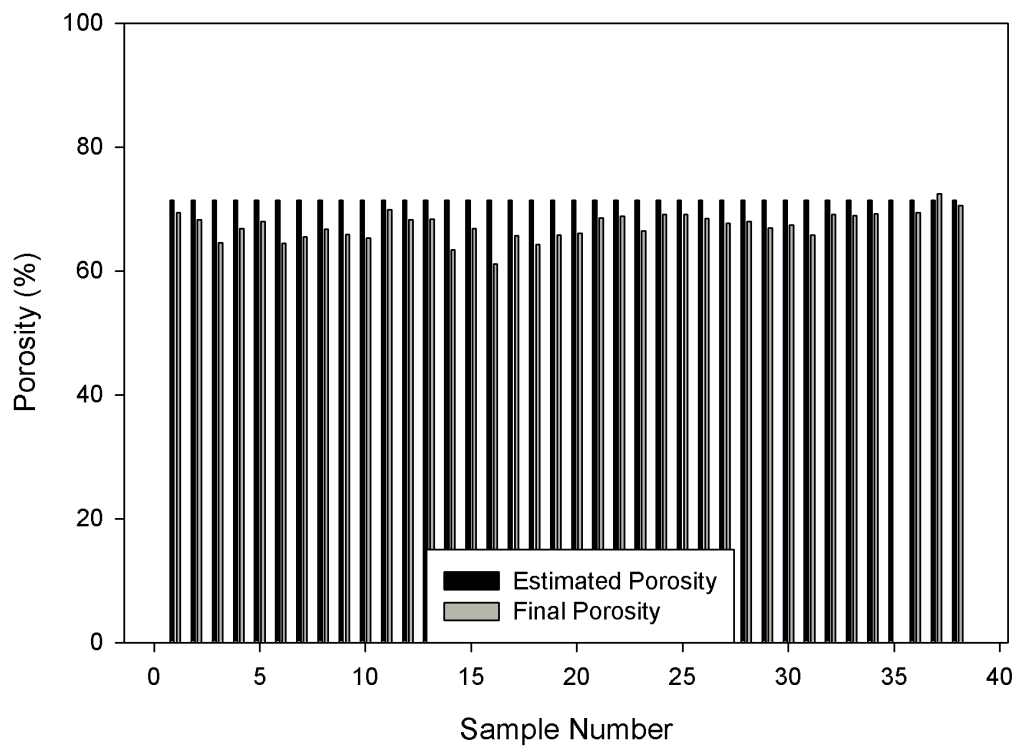


Figure 7.14. Change in porosity of the samples as a result of size distribution of solid phases.

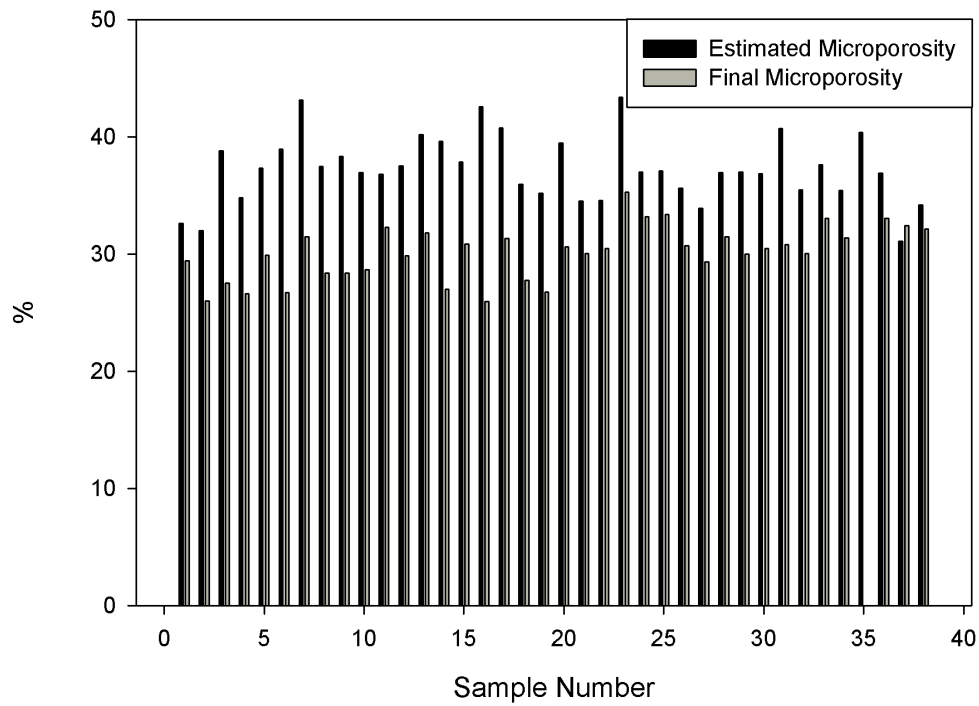


Figure 7.15. Change in microporosity of the samples due to the size distribution of solid phases.

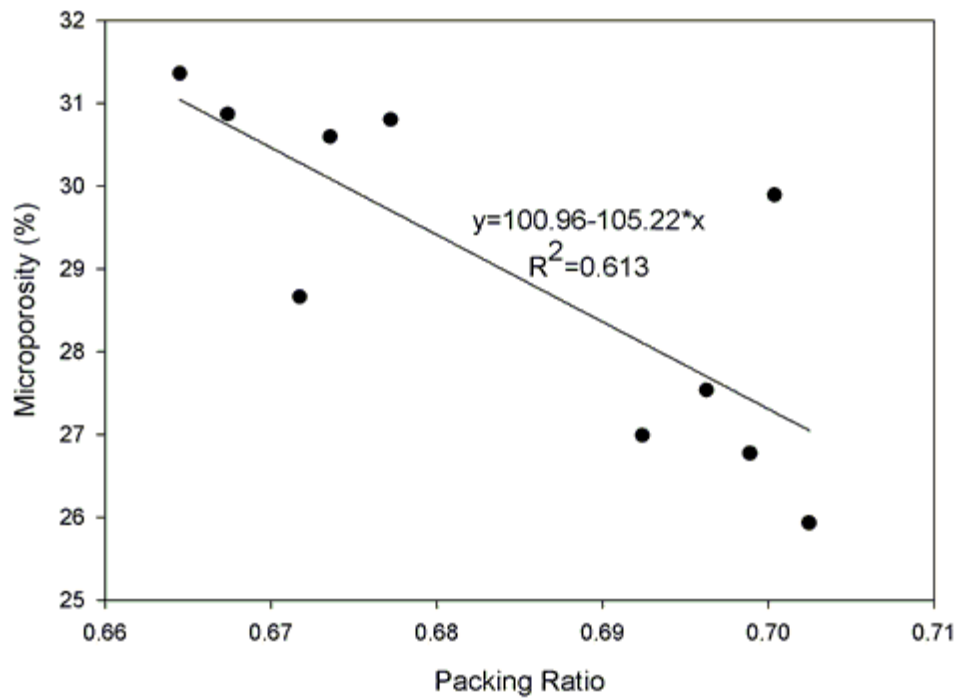


Figure 7.16. Linear relationship between packing density and microporosity of samples containing about 85% monetite.

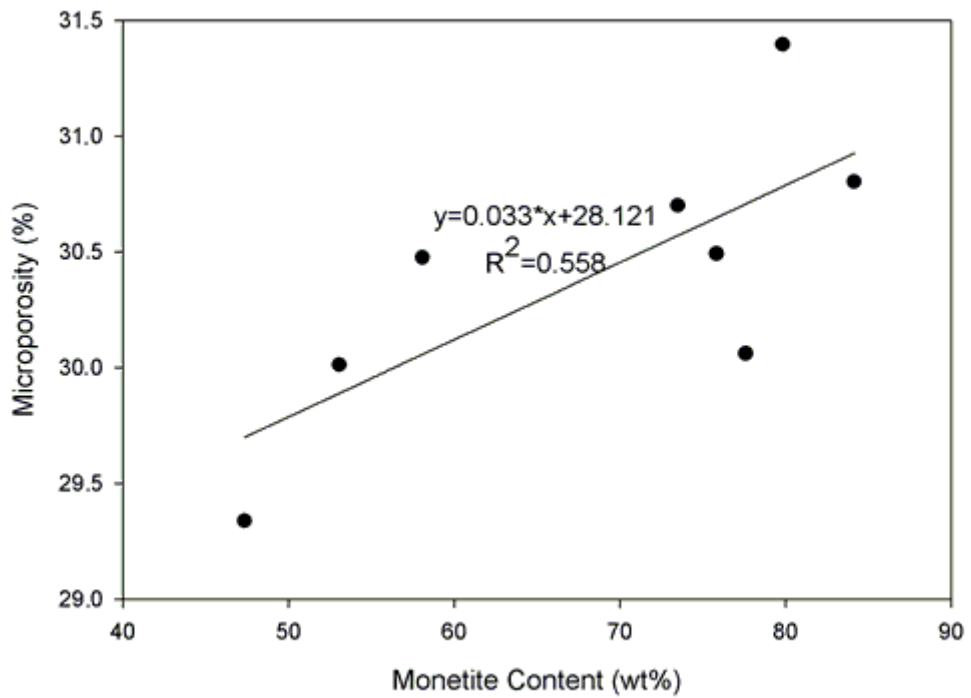


Figure 7.17. Linear proportionality between monetite content and microporosity of samples with 0.68 packing density.

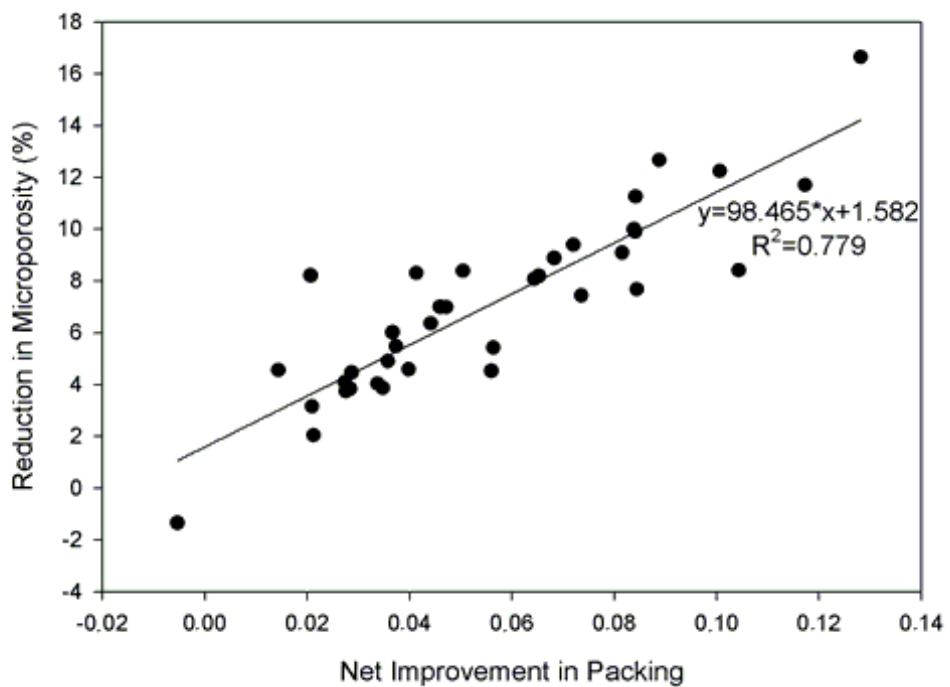


Figure 7.18. Strong correlation between packing improvement and reduction in microporosity.

Macroporosity of porous cement blocks were calculated from the ratio of initial porogen volume to final volume of the porous cement blocks. Macroporosity of the samples increased parallel to microporosity but the magnitude of change was smaller as seen in Figure 7.21. The result is net reduction in total sample porosity. Volume measurements by Archimedean method is prone to errors especially due to mass losses during sample molding, demolding and handling. To minimize the errors, a reproducible sample preparation process by which equal molding periods, forces and care was applied to all 266 samples was used. Six samples for each of 38 sets were leached in deionized water for equal durations prior to Archimedean analysis of sample dimensions and densities. Only Sample 35 was accidentally wasted during leaching as a result of contact with magnetic stirrer. Other measurements for 37 remaining samples were done accurately and the arithmetic mean was taken as the representative value. Small standard deviations given in Table 7.4 confirm the validity of the Archimedean measurements.

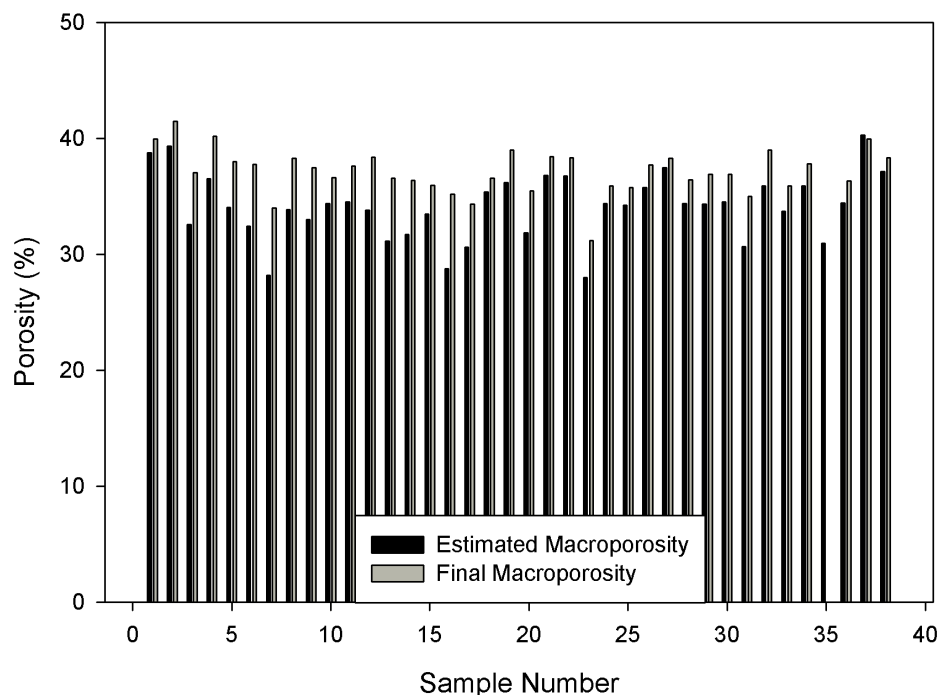


Figure 7.19. Change in macroporosity of the samples as a result of size distribution of solid phases.

The strong correlation between differential packing density and the reduction in microporosity as seen in Figure 7.18 is reflected also in the effect of packing

enhancement on the reduction in total porosity as given in Figure 7.20. Observed correlation is not as strong due to the variable porogen volume designed according to the estimated maximum packing densities to keep the total porosity constant. The increase in macroporosities seen in the previous figure is solely due to the higher porogen amount used in preparation of the samples with higher maximum packing densities. However the net reduction in total porosity with packing improvement is a promising result for the particle size distribution approach, considering the strong dependence of cement mechanical properties on porosity.

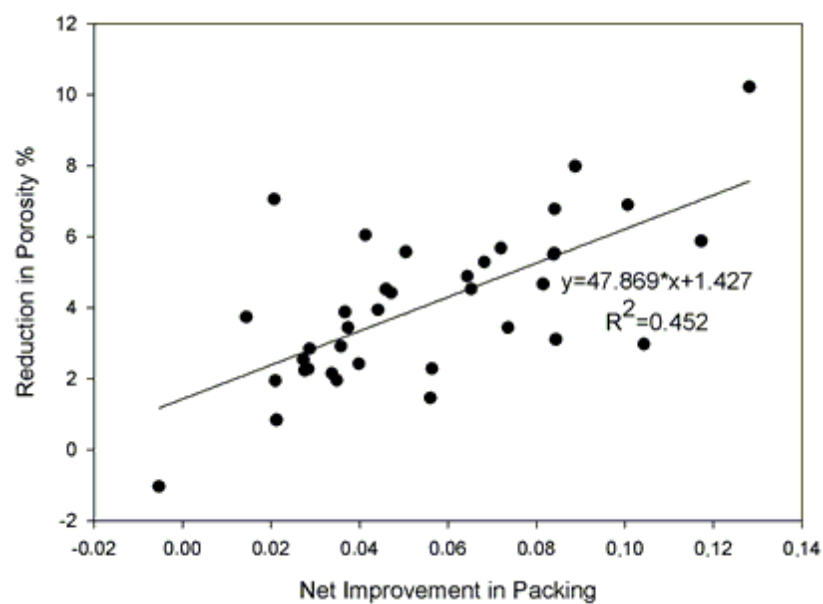


Figure 7.20. Correlation between packing improvement by size distribution and reduction in total porosity.

Correlations between the final packing density and macro-microporosities exist as well as seen in Figure 7.21. Considerable variation is present in macroporosity data especially for samples with low initial maximum packing densities and high final packing densities. Microporosity is more correlated with final packing ratio as significant factor for compaction of the cement blocks. On the contrary, total porosity of all samples are quite variable as a function of the final packing density as seen in Figure 7.22. Comparable increase and decreases in the macro and microporosities respectively cancel out each other, resulting in more or less similar porosity values for all packing densities. Another reason for the variation is the presence of additional phase factors including monetite content and the  $\beta$ -TCP residue amount that hinder the densification and hence the microporosity of the cement microstructure.



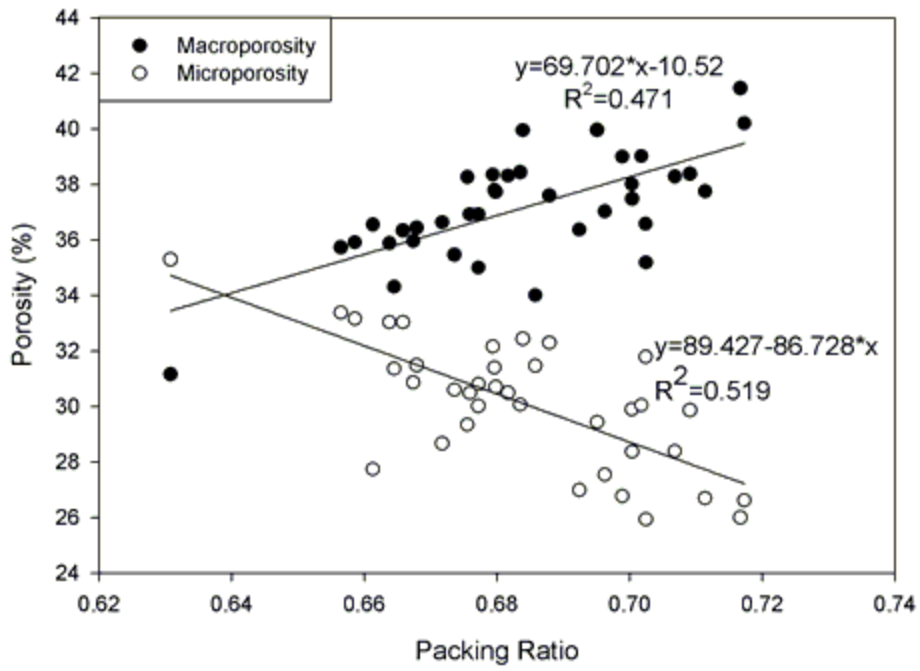


Figure 7.21. Correlation between packing density and macro-microporosity.

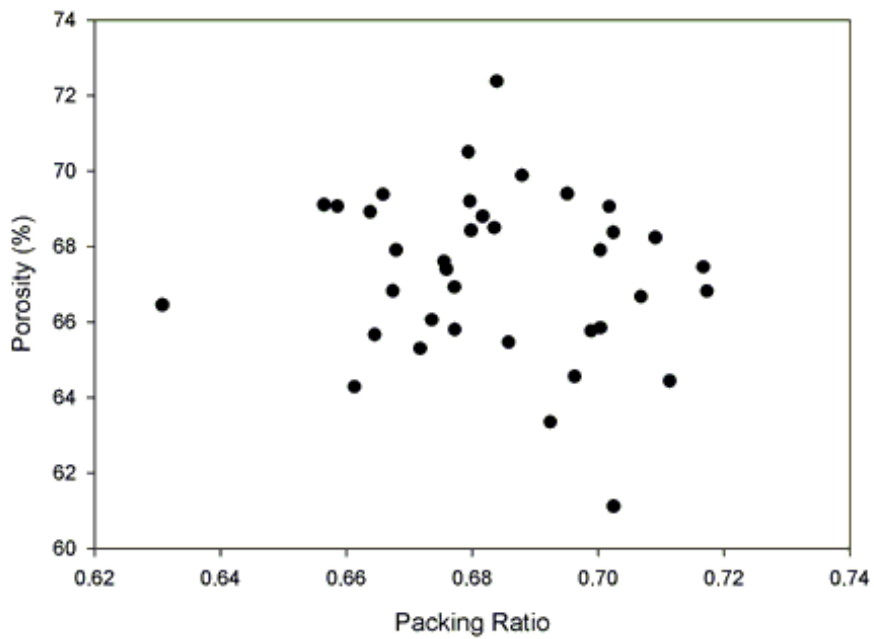


Figure 7.22. Variation of Porosity as a function of packing density.

The overall effect of packing density improvement upon introduction of fine cement precursors on the porosity of cement blocks is most clearly observed by taking the total, macro and micropore volumes into account as a function of the net packing density. Both micropore and macropore volumes are seen in Figure 7.23 to decrease with improvement of the packing density of the solid phase. Previously observed increase in macroporosity is a consequence of the relatively slow reduction of macropore volume in contrast to total pore volume as seen in Figure 7.23. Total pore volume decreases much faster than macropore volume as a function of packing improvement as the sum of macropore and micropore volumes. The decrease in macropore volumes is the result the mismatch between the final packing density and the initial maximum packing density that the porogen amount depends on. The decrease confirms the conclusion that packing improvement takes place in samples with low initial maximum packing densities. Slightly lower correlation between micropore volume and improvement in packing stems from the fact that initially well packed samples with low micropore volume are not improved considerably in packing. Micropore volume is more sensitive to final packing density regardless of the initial maximum packing density.

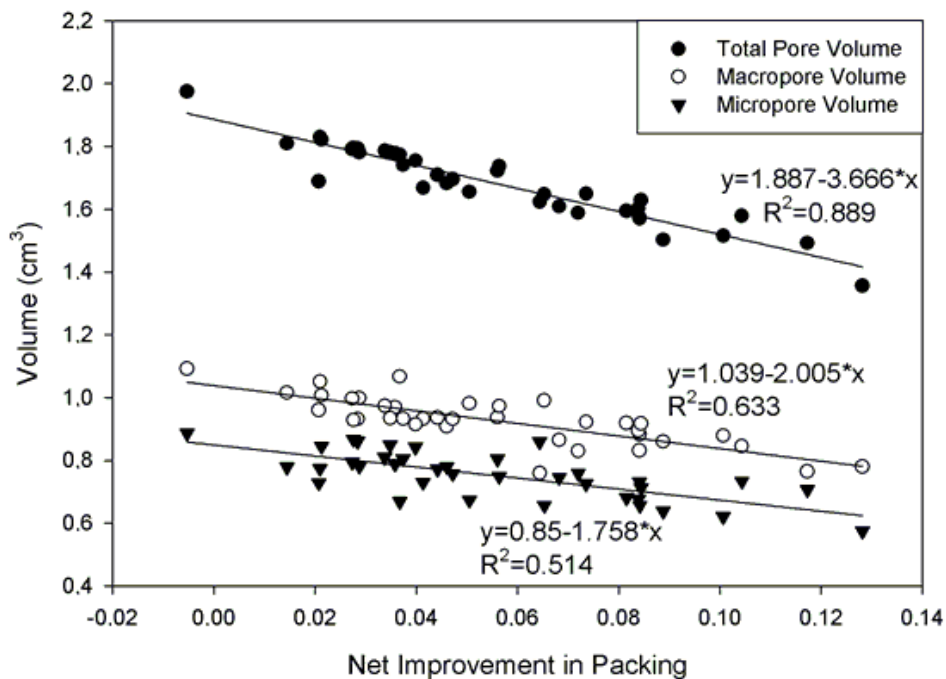


Figure 7.23. Correlation of micro, macro and total pore volumes with improvement in packing by size distribution.

Table 7.4. Results of the Archimedean analysis for all samples

Sample	Theoretical Density (g/cm <sup>3</sup> )	Archimedean Density (g/cm <sup>3</sup> )	+/-	Porosity	+/-	Sample Volume (cm <sup>3</sup> )	+/-	Pore Volume (cm <sup>3</sup> )	+/-	Open Pore %	+/-	Closed Pore %	+/-	Packing
Dense	2.90	1.59	0.01	45.26	0.26	2.40	0.01	1.08	0.02	76.49	1.03	23.51	1.03	0.58
1	2.87	0.88	0.01	69.39	0.36	2.63	0.02	1.83	0.01	87.77	1.61	12.23	1.61	0.70
2	2.80	0.91	0.04	68.20	0.68	2.60	0.02	1.77	0.03	87.99	0.79	12.01	0.79	0.72
3	2.90	1.03	0.02	64.56	0.84	2.38	0.00	1.57	0.03	83.68	3.57	16.32	3.57	0.70
4	2.83	0.94	0.04	66.81	1.29	2.47	0.02	1.65	0.04	84.91	1.46	15.09	1.46	0.72
5	2.90	0.93	0.04	67.90	1.53	2.43	0.05	1.65	0.06	85.45	1.32	14.55	1.32	0.70
6	2.73	0.97	0.01	64.44	0.49	2.33	0.06	1.51	0.03	83.50	2.72	16.50	2.72	0.71
7	2.91	1.00	0.02	65.46	0.60	2.25	0.07	1.49	0.03	80.75	5.34	19.25	5.34	0.69
8	2.85	0.95	0.01	66.67	0.42	2.40	0.03	1.59	0.01	79.80	2.88	20.20	2.88	0.71
9	2.86	0.99	0.05	65.84	1.61	2.39	0.04	1.60	0.05	81.25	1.59	18.75	1.59	0.70
10	2.88	1.01	0.03	65.29	0.90	2.55	0.04	1.67	0.03	72.20	1.08	27.80	1.08	0.67
11	2.92	0.87	0.02	69.89	0.64	2.49	0.06	1.72	0.06	83.71	1.13	16.29	1.13	0.69
12	2.89	0.92	0.02	68.24	0.74	2.39	0.09	1.63	0.07	81.21	1.95	18.79	1.95	0.71
13	2.89	0.90	0.06	68.37	2.23	2.31	0.05	1.58	0.02	83.94	3.57	16.06	3.57	0.70
14	2.90	1.09	0.07	63.35	2.29	2.36	0.08	1.50	0.05	66.30	3.05	33.70	3.05	0.69
15	2.90	0.96	0.02	66.82	0.66	2.53	0.03	1.68	0.02	75.02	1.22	24.98	1.22	0.67
16	2.92	1.14	0.01	61.12	0.47	2.22	0.02	1.36	0.01	75.75	5.30	24.25	5.30	0.70
17	2.90	0.99	0.02	65.66	0.64	2.42	0.03	1.59	0.03	76.13	4.47	23.87	4.47	0.66
18	2.83	1.01	0.03	64.28	0.97	2.63	0.03	1.69	0.04	66.58	1.45	33.42	1.45	0.66
19	2.91	1.01	0.06	65.77	1.97	2.52	0.07	1.66	0.07	72.88	3.74	27.12	3.74	0.70
20	2.87	0.98	0.02	66.06	0.72	2.44	0.03	1.61	0.03	75.06	2.23	24.94	2.23	0.67
21	2.86	0.90	0.03	68.49	1.00	2.60	0.04	1.78	0.05	77.52	1.50	22.48	1.50	0.68
22	2.86	0.89	0.03	68.80	1.02	2.60	0.05	1.79	0.06	79.55	2.00	20.45	2.00	0.68
23	2.84	0.95	0.01	66.45	0.50	2.44	0.04	1.62	0.04	80.53	0.83	19.47	0.83	0.63
24	2.80	0.86	0.01	69.07	0.51	2.60	0.02	1.79	0.03	85.01	0.88	14.99	0.88	0.66
25	2.78	0.87	0.02	69.10	0.68	2.60	0.03	1.80	0.03	84.70	2.71	15.30	2.71	0.66
26	2.80	0.88	0.02	68.43	0.66	2.57	0.06	1.78	0.04	81.60	1.00	18.40	1.00	0.68
27	2.67	0.87	0.02	67.61	0.92	2.65	0.05	1.81	0.05	84.64	1.88	15.36	1.88	0.68
28	2.76	0.89	0.01	67.90	0.39	2.56	0.02	1.74	0.02	86.98	1.21	13.02	1.21	0.67
29	2.69	0.88	0.02	66.92	0.74	2.52	0.01	1.70	0.03	86.78	1.39	13.22	1.39	0.68
30	2.72	0.89	0.02	67.40	0.76	2.54	0.03	1.71	0.04	86.66	2.05	13.34	2.05	0.68
31	2.91	1.00	0.03	65.80	0.93	2.38	0.02	1.57	0.01	80.55	1.52	19.45	1.52	0.68
32	2.87	0.89	0.02	69.06	0.82	2.50	0.04	1.74	0.02	82.74	3.04	17.26	3.04	0.70
33	2.74	0.85	0.01	68.92	0.37	2.55	0.04	1.75	0.04	89.50	0.91	10.50	0.91	0.66
34	2.86	0.88	0.03	69.19	0.92	2.58	0.03	1.79	0.04	84.87	1.83	15.13	1.83	0.68
35	2.77	0.95	0.06	65.74	2.22	1.94	0.09	1.28	0.10	86.02	6.29	13.98	6.29	0.66
36	2.72	0.83	0.01	69.38	0.32	2.57	0.02	1.78	0.02	89.86	1.00	10.14	1.00	0.67
37	2.83	0.79	0.02	72.38	0.81	2.73	0.04	1.97	0.03	90.13	1.73	9.87	1.73	0.68
38	2.87	0.85	0.02	70.50	0.77	2.63	0.07	1.82	0.07	83.66	1.52	16.34	1.52	0.68
Mean	2.84	0.95	0.03	66.66	0.90	2.48	0.04	1.66	0.04	81.58	2.17	18.42	2.17	0.68
Median	2.86	0.92	0.02	67.40	0.76	2.52	0.04	1.68	0.03	83.50	1.61	16.50	1.61	0.68

Archimedean analysis is based on the buoyancy of water that penetrates the pores of a rigid block. The penetration is a factor of sample immersion time, water diffusivity and material structure. Ceramics contain a high amount of cracks and micropores that enable the penetration of water if sufficient time is given. Porous cement blocks were analyzed subsequent to 24 hours of leaching in deionized water for porogen leaching purpose. Upon removal of NaCl porogen, water completely fills all accessible pores and micropores. The dry volume and weight of the sample blocks are known so that the the penetrated water volume is subtracted from the sample volume to obtain the inaccessible closed pores. Closed pore amount calculated does not reflect the microporosity as anticipated in this study. Some large micropores contribute to open porosity and some small micropores are trapped inside the cement matrix so that the total closed pore amount is found lower than the microporosity as given in Figure 7.24. Still open porosity obtained by Archimedean analysis gives an indication of the interconnectivity of the pore structure. Closed porosity is seen to increase for samples with low size distribution and decrease for samples containing at least 5 size distributions. Statistical analysis will be presented later in the report for more detailed analysis of interconnectivity.

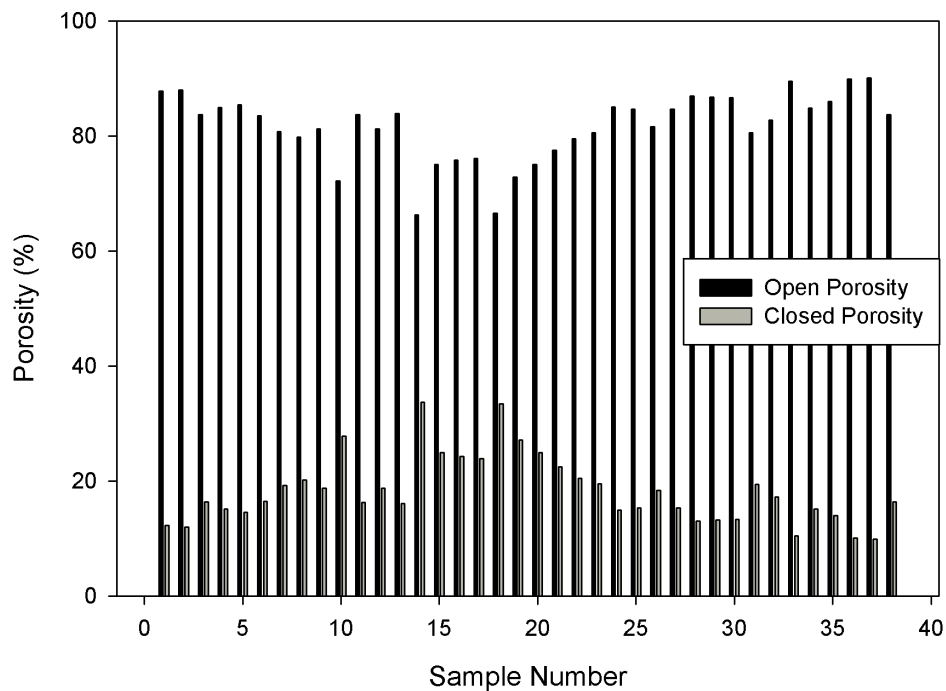


Figure 7.24. Change in open and closed porosities due to size distribution of the solid phases.

Densities of the samples show variation with packing density similar to porosity due to presence of multiple factors affecting it besides packing density like phase structures. These factors are canceled out by taking the net improvement in packing into account. Figure 7.25 shows a direct proportionality between improvement in packing and density of the porous cement blocks as expected from the similar negative relation between porosity and packing improvement. Variations in phase structure of the cement blocks introduce difficulties in controlling the porosity and density of the porous cement blocks as the porosity and density of the final phases are quite different. The major phase monetite has a density of  $2.9 \text{ g/cm}^3$  and is accompanied by micropore formation, while the competing phase brushite has a density of  $2.34 \text{ g/cm}^3$  but has a pore free microstructure. The reactant  $\beta$ -TCP residue amount increases with monetite formation as seen indirectly from Figure 7.26. The reason for the low correlation coefficient is the dependence of dense  $\beta$ -TCP residue to monetite formation .

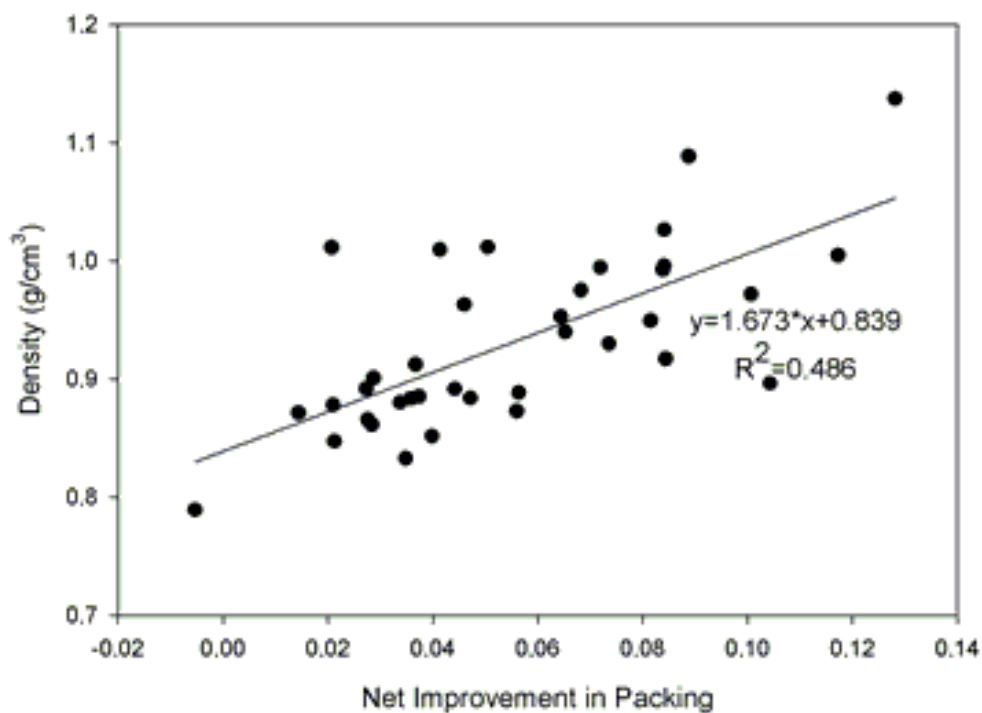


Figure 7.25. Correlation between packing improvement by size distribution and sample density.

The theoretical density of the porous cement blocks is the weighted average of the densities of the constituent phases monetite, brushite and  $\beta$ -TCP. Samples that have high monetite conversion have higher theoretical density than the samples which contain a significant amount of brushite. The Archimedean density calculated by the Archimedean analysis shows that the density of the samples containing higher monetite and  $\beta$ -TCP phases increases exponentially rather than linearly. The reason is that the densest phase  $\beta$ -TCP remains increasingly unreacted in the conditions favoring monetite formation. Monetite is selectively formed by the synergistic effect of ionic modifiers citric acid and NaCl. As mentioned in the previous sections, the ionic modifiers reduce the solubility of  $\beta$ -TCP and brushite while kinetically enabling monetite precipitation in place of brushite. The acidic nature of the cement setting liquid facilitates complete  $\beta$ -TCP dissolution in the absence of any ionic modifier. It is seen in the phase analysis given in Figure 7.27 and Table 7.5 that  $\beta$ -TCP residue as high as 15% exists in monetite rich cement blocks.

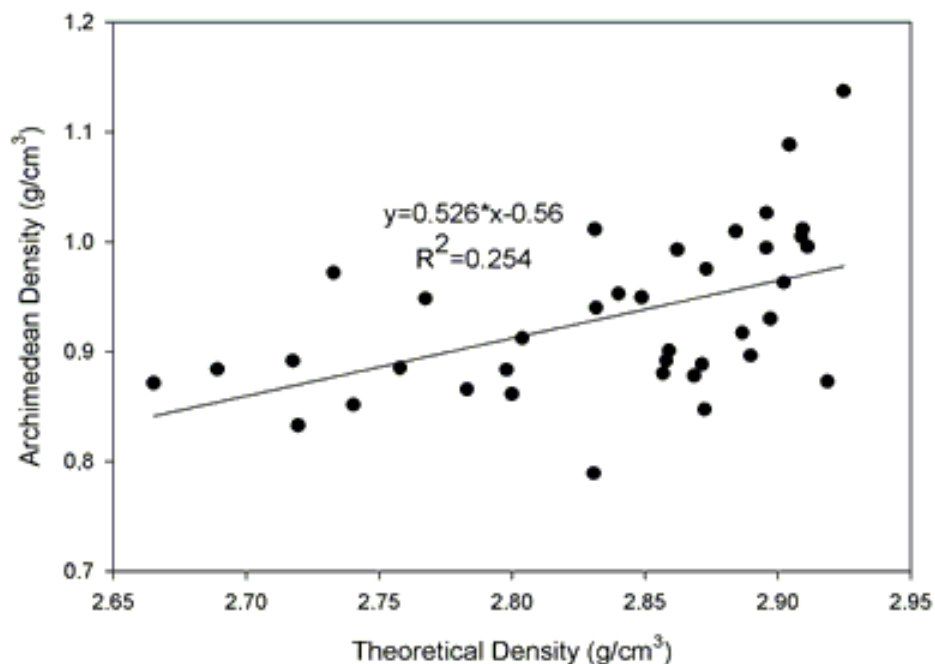


Figure 7.26. Correlation between theoretical density and measured density of the samples.

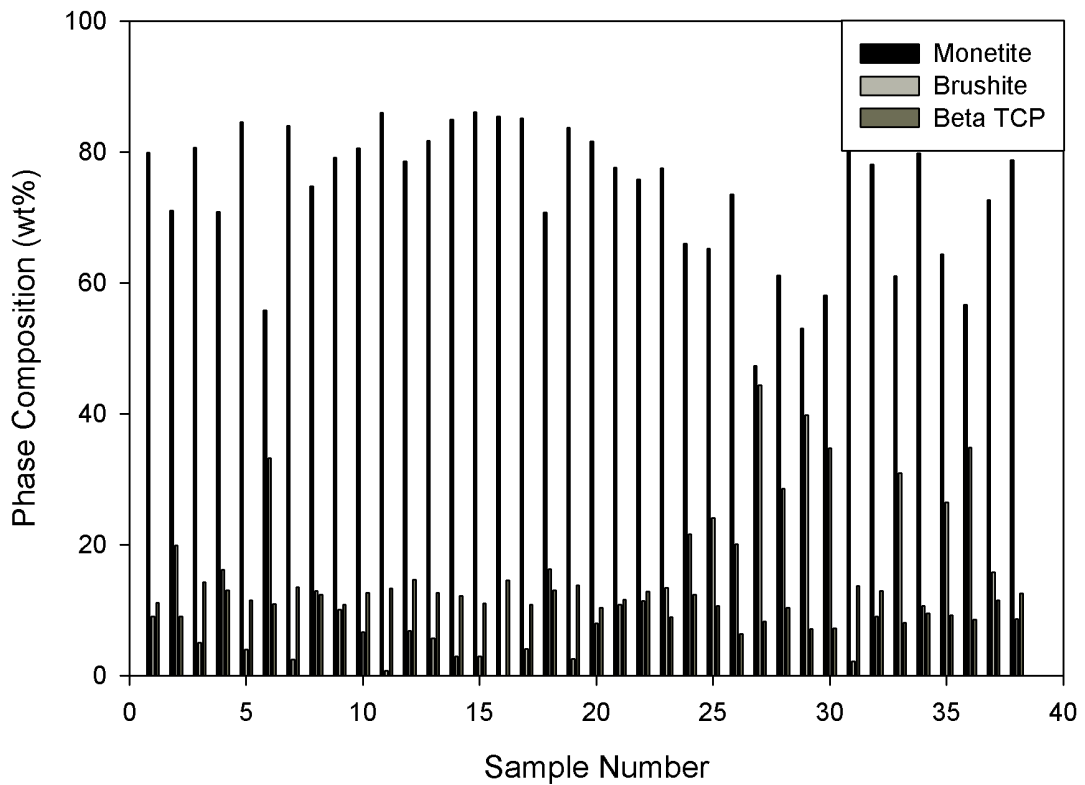


Figure 7.27. Change in the phase composition of the samples as a result of size distribution of solid phases.

Although most porous cement blocks contain high monetite content with an average around 75%, variation in the phase composition exists such that monetite conversion for some samples were as low as 50%. As seen in Figure 7.28, brushite content in these samples increased to about 40% and an average of 11%  $\beta$ -TCP was present. Monetite and brushite are two competing phases for the end product of porous cement blocks as seen clearly from the high correlation between their amounts. Any other by-products stemming from NaCl use such as  $\text{NaH}_2\text{PO}_4$  or sodium calcium phosphate phases were not present in the X-ray diffractograms.

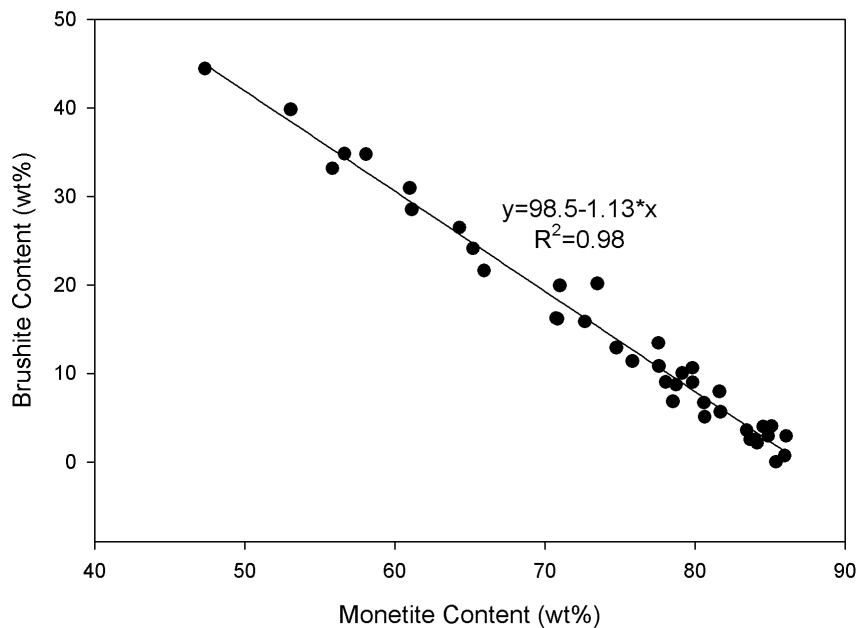


Figure 7.28. Correlation between monetite formation and brushite content of the samples.

Most porous cement blocks contain monetite around 80% and only a handful were seen not to convert to monetite at a great extent. Expected minimum brushite content was achieved for Samples 11 and 16, confirming the validity of the synergistic effect of NaCl and citric acid. In these samples maximum monetite content was around 85% with an increase in  $\beta$ -TCP residue to 15%. Synergistic effect of citric acid and NaCl on the phase evolution of the porous cement blocks is thought to be independent of the size distribution of NaCl particles since the dissolution of NaCl and its molarity in the setting liquid is thought to be constant for all samples regardless of the variations in the particle sizes. Phase purity of the NaCl particles is important in the effectiveness of the synergistic effect as any impurity unintentionally introduced to the cement liquid in addition to citrate groups are expected to change the setting kinetics of monetite by binding on active surface sites. The source of the variation in phase composition especially in the second half of the sets may be introduction of impurities from either grinding, ball milling and sieving or contamination of the phase pure NaCl. Size distribution of NaCl particles was not completely done prior to the experiment as extra NaCl size groups were produced simultaneously throughout porous cement block preparation since the initial stock was depleted around the middle of the experiment process.



Table 7.5. Results of the quantitative phase analysis for all samples

Sample	Monetite		Brushite		B-TCP		Theoretical Density
	Mean	+/-	Mean	+/-	Mean	+/-	
Dense	83.45	2.43	3.59	1.76	12.96	0.67	2.90
1	79.86	3.04	9.00	2.38	11.14	0.66	2.87
2	71.01	5.51	19.92	7.17	9.08	1.65	2.80
3	80.66	0.71	5.08	1.00	14.26	1.71	2.90
4	70.84	4.10	16.15	7.03	13.00	2.93	2.83
5	84.55	1.31	3.99	0.14	11.46	1.45	2.90
6	55.84	2.88	33.18	3.51	10.98	0.63	2.73
7	83.99	5.75	2.51	0.17	13.50	5.92	2.91
8	74.76	6.80	12.89	4.46	12.35	2.34	2.85
9	79.16	0.73	10.03	2.82	10.81	2.09	2.86
10	80.59	1.82	6.69	5.29	12.71	3.47	2.88
11	85.98	3.88	0.71	1.01	13.31	4.89	2.92
12	78.52	1.92	6.83	2.20	14.65	4.12	2.89
13	81.71	10.25	5.66	5.86	12.63	4.39	2.89
14	84.89	1.02	2.92	0.32	12.19	0.70	2.90
15	86.08	1.97	2.92	0.60	11.00	2.57	2.90
16	85.41	2.32	0.00	0.00	14.59	2.32	2.92
17	85.11	0.85	4.06	0.96	10.83	0.11	2.90
18	70.75	6.49	16.24	4.14	13.01	2.35	2.83
19	83.68	0.65	2.52	0.49	13.80	1.14	2.91
20	81.63	0.19	7.96	1.31	10.41	1.49	2.87
21	77.60	6.63	10.82	5.21	11.58	1.42	2.86
22	75.82	1.14	11.38	1.57	12.80	2.71	2.86
23	77.57	5.46	13.44	6.71	9.00	1.24	2.84
24	65.95	4.23	21.63	1.74	12.42	2.49	2.80
25	65.21	3.91	24.12	2.62	10.66	1.29	2.78
26	73.50	3.55	20.14	2.74	6.36	0.81	2.80
27	47.35	7.07	44.42	6.65	8.23	0.41	2.67
28	61.14	1.31	28.52	1.04	10.35	0.27	2.76
29	53.07	1.53	39.81	1.47	7.12	0.06	2.69
30	58.07	12.98	34.75	13.60	7.17	0.62	2.72
31	84.16	0.02	2.15	0.07	13.69	0.09	2.91
32	78.06	4.97	9.02	6.37	12.92	1.39	2.87
33	61.00	11.15	30.95	9.76	8.05	1.39	2.74
34	79.83	2.59	10.61	2.27	9.56	0.32	2.86
35	64.32	2.14	26.46	1.44	9.22	0.70	2.77
36	56.65	2.48	34.80	3.04	8.55	0.56	2.72
37	72.67	0.37	15.85	1.68	11.49	1.31	2.83
38	78.76	1.93	8.71	2.95	12.54	1.02	2.87
Mean	74.34	3.54	14.37	3.17	11.29	1.69	2.84
Median	78.06	2.48	10.61	2.27	11.49	1.39	2.86

Direct relationships between monetite, brushite formation and unreacted  $\beta$ -TCP content are seen clearly in Figures 7.29 and 7.30.

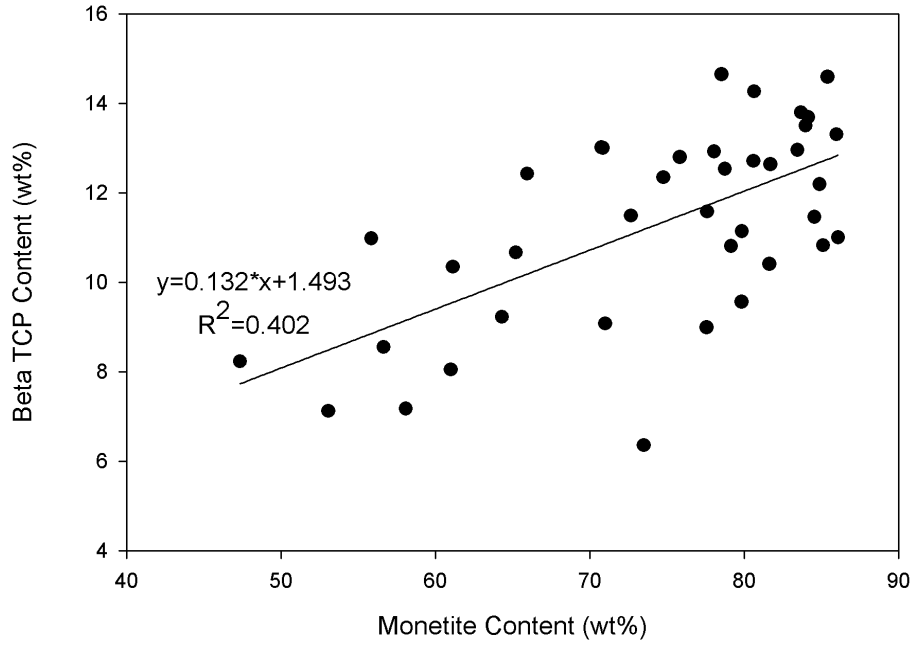


Figure 7.29. Correlation between monetite formation and  $\beta$ -TCP content of the samples.

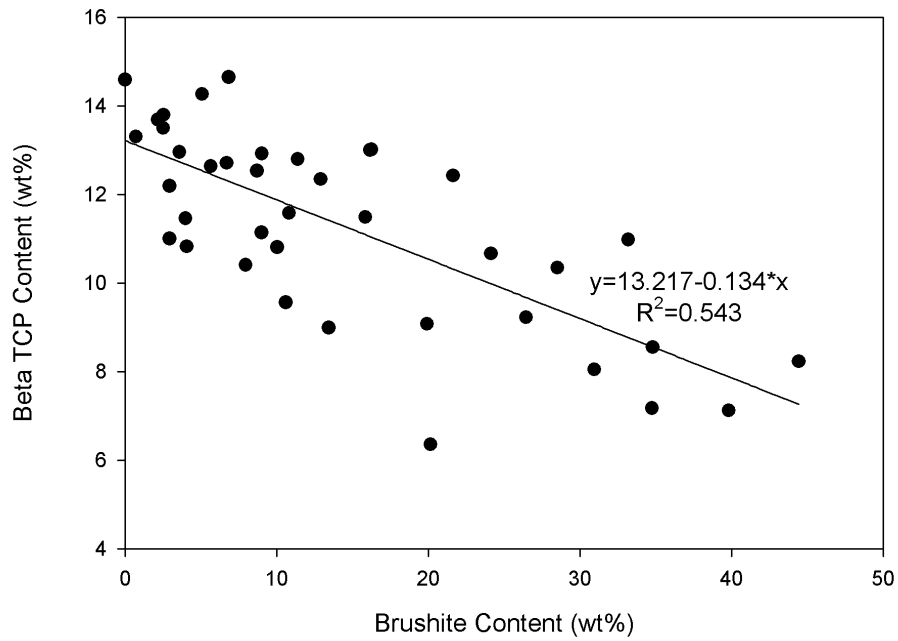


Figure 7.30. Correlation between brushite formation and  $\beta$ -TCP content of the samples.

Common knowledge in the calcium phosphate literature about brushite to monetite transformation is that monetite forms under dry conditions, e.g. upon drying to remove water or in setting with low liquid volume. Mirtchi et al. invented the MCPM- $\beta$ -TCP cement formulation in 1989 and many investigations have been conducted by Bohner and co-workers regarding their phase stability since then (Bohner et al. 1999; Bohner et al. 2000; Gbureck et al. 2005; Bohner 2007; Bohner 2008). When asked about his personal opinion on the synergistic effect of NaCl and citric acid, Bohner suspected that the increased monetite content may originate from drying of the samples instead of the proposed ionic modification method since monetite formation is endothermic while brushite formation is an exothermic reaction (Bohner et al. 2008). Most drying in Bohner's studies were done in ordinary oven by utilization of heat treatment and temperatures as low as 40 °C was reported to effectively facilitate monetite formation. Although the drying of the cement precipitates was done in freeze dryer and cemen blocks in vacuum oven in this study, Bohner's argument is viable since monetite is commonly formed in lack of water. In order to see whether the synergistic effect actually exists or monetite formation is a consequence of drying, vacuum dried and wet samples were compared in terms of phase composition. Wet samples were the as cast samples used for optical microscope analysis. They had been leached in water to remove the porogens and left at room temperature after optical microscope analysis. They were easily crushed and ground in mortar without forming agglomerates due to low water content. The result of the quantitative XRD test confirms that synergistic effect is the sole cause of enhanced monetite formation as the phase compositions before and after vacuum drying were found the same. Fig. 7.31 shows the comparison of dry and wet phase composition of sample 3.

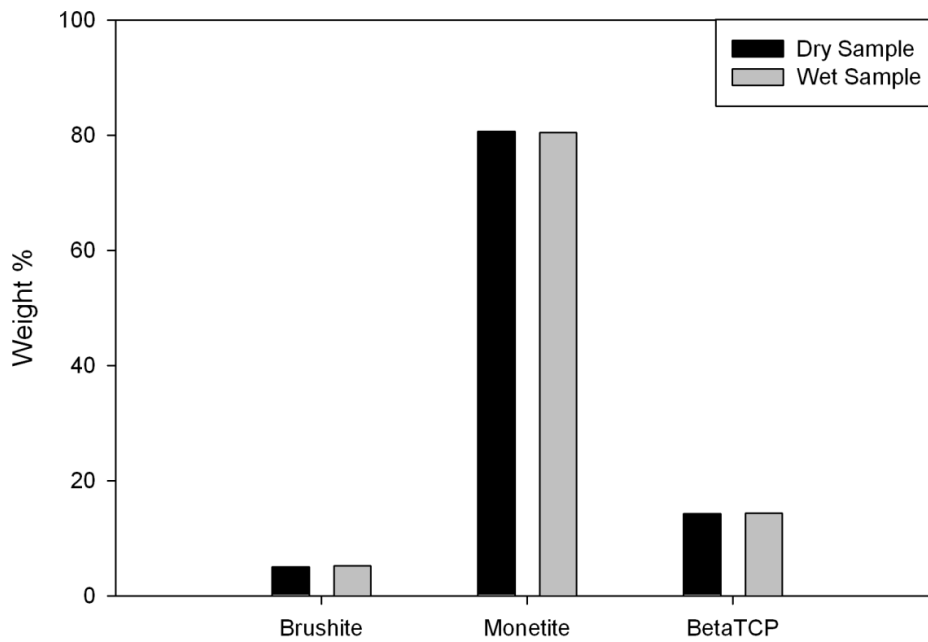


Figure 7.31. Phase compositions of dry and wet samples from sample set 3.

### 7.3. Mechanical Characterization of Macroporous Cement Blocks

Leached and dried porous cement blocks suitable to compressive testing according to the ASTM C 773-88 standard were uniaxially loaded by 5 kN maximum force at a rate of 1 mm/min. A typical stress-strain diagram obtained for a uniform sample is shown in Figure 7.32. The diagram exhibits an initial elastic deformation region, yield point, plastic deformation region, a zig-zag plateau region reflecting the collapse of the pores and filling of the pores by cement particles to reinforce the structure, and finally a peak corresponding to the ultimate compressive strength of the porous cement block. Generally the ultimate compressive strength is reached within a strain quarter of the block height. Some samples were seen to enlarge at the base upon further loading and support unrealistically high loads. Stress-strain graphs for all samples were analyzed up to 0.3 strain to minimize such errors. Three properties were read from the stress-strain diagrams, namely elastic modulus, yield strength, and ultimate compressive strength. Averages of up to 5 samples were taken to concur a representative value for each sample set. The results given in Table 7.6 are quite varied

due to numerous factors affecting the strength of porous cement blocks including porosity, packing density and monetite content.

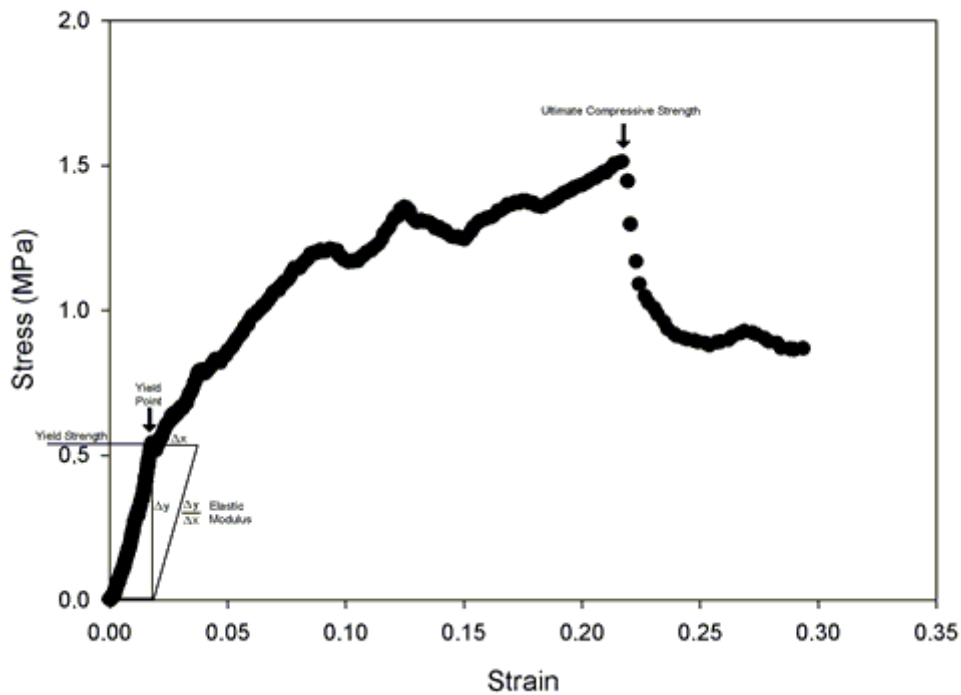


Figure 7.32. Representative stress-strain diagram for all samples.

Although it is hard to correlate the elastic modulus directly to the porosity of porous cement blocks due to other effective factors, a roughly linear relation is obtained considering all samples as seen in Figure 7.33. A similar dependence of elastic modulus on sample density is seen in Figure 7.34. Susceptibility of porous cement blocks to defects during demolding and handling is another factor that results in variation in mechanical properties.

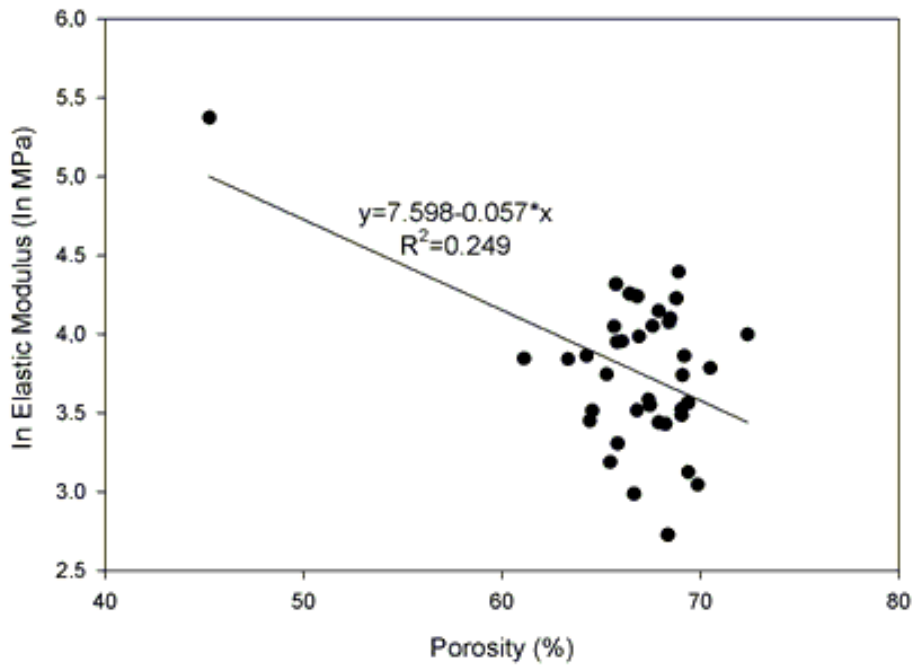


Figure 7.33. Correlation between porosity and elastic modulus of the samples.

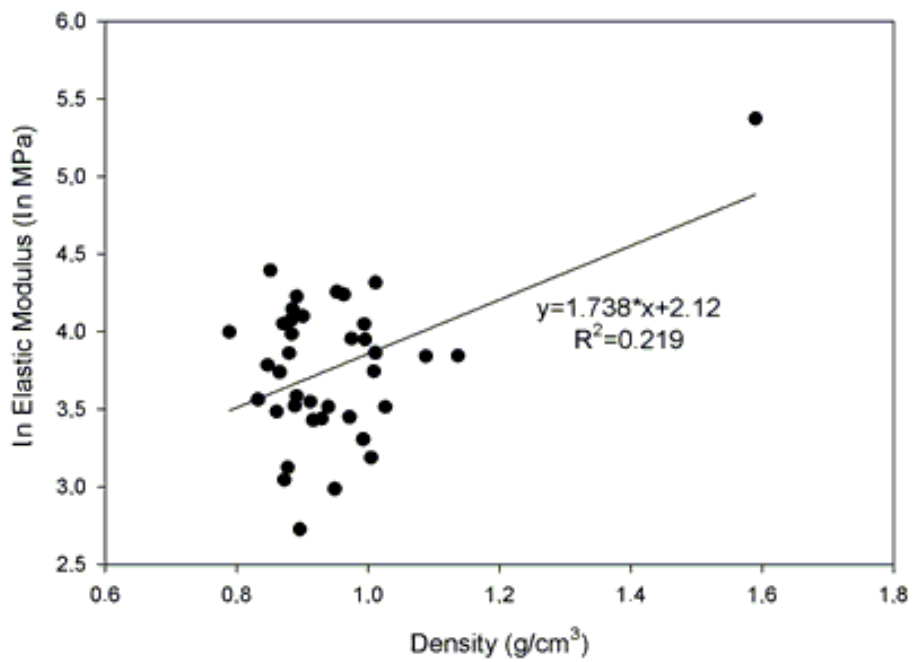


Figure 7.34. Correlation between density and elastic modulus of the samples.

Yield strength and ultimate compressive strength are highly correlated to sample porosity and density as seen in Figures 7.35-7.38. Strength of ceramics in general are exponential functions of porosity and the results show that monetite rich cement is not an exception. Despite the presence of other factors including packing density and variable phase composition, observed high correlation of yield strength and ultimate compressive strength to porosity, reveals that porosity is the governing factor for strength of porous cement blocks. Theoretically it is a widely accepted rule of thumb that strength of ceramics reduces by half with every 10% increase in porosity. The trendlines of strength as a function of porosity conform to this criterion. As an example the dense sample prepared to obtain a baseline for minimum porosity has a strength of 8 MPa at 45% porosity while sample 31 at 65% porosity has a strength of 2 MPa, exactly  $\frac{1}{4}$  of the strength of the dense sample. At the minimum porosity or theoretical dense structure, the average elastic modulus amounts up to 2 GPa, while the theoretical dense yield strength and ultimate compressive strength were obtained by extrapolation around 300 MPa. Theoretical strength value of monetite is higher than that of brushite cements given in literature (Hofmann et al. 2009), which is a confirmation of mechanical superiority of monetite crystal structure than brushite.

Monetite rich cement has a fine crystal structure, higher resorption rate and higher mechanical properties at the same porosity as brushite cement. The only drawback of monetite cement is the extra 19% microporosity formed around monetite crystals as a result of shrinkage during setting reaction. Densification of the microporosity enhances the mechanical properties of monetite rich cement so that its utilization in clinical applications is realized. Densification by size distribution is the approach investigated in this study however other methods such as densification by surface hydroxyapatite deposition in supersaturated calcium phosphate solution also promises success. The effectiveness of size distribution of the solid phase on the minimization of microporosity is most clearly demonstrated above in Figure 7.21 by correlating the microporosities of high monetite containing porous cement blocks to their packing densities. Although its accuracy may be questioned due to the not so high correlation coefficient, the trendline representing the relation between microporosity and packing density reveals that microporosity decreases 1% with every 1% increase in packing density due to size distribution. That means introduction of size distribution to monetite rich cement precursors and porogens effectively eliminates the microporosity introduced to the structure during monetite formation, producing monetite cements with

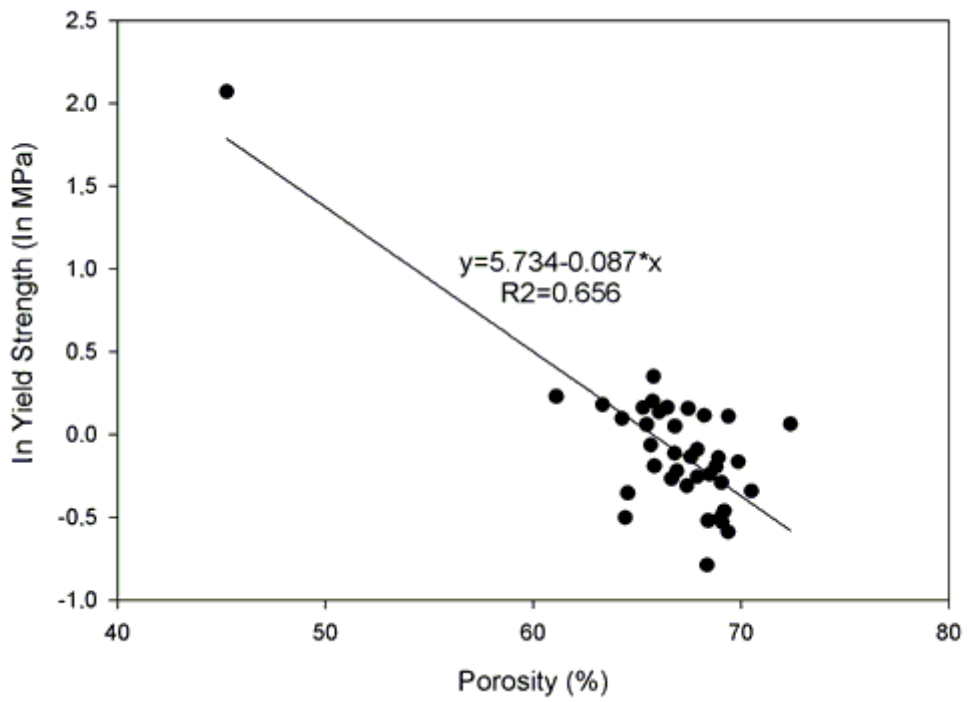


Figure 7.35. Correlation between porosity and yield strength of the samples.

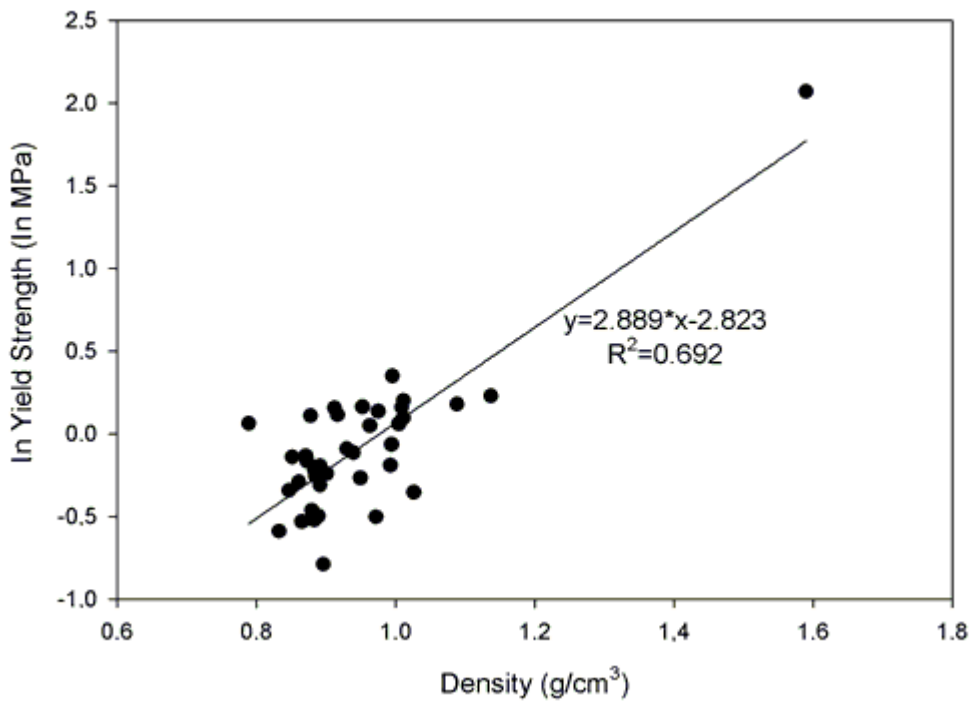


Figure 7.36. Correlation between density and yield strength of the samples.



the same porosity but higher surface area, resorption and mechanical properties than brushite cement. If the  $\beta$ -TCP residue, amounting in average to 11 wt% can be reduced for example by increasing the acidity of the cement liquid, size distribution approach may be considered as a complementary process for the preparation of porous monetite cement blocks.

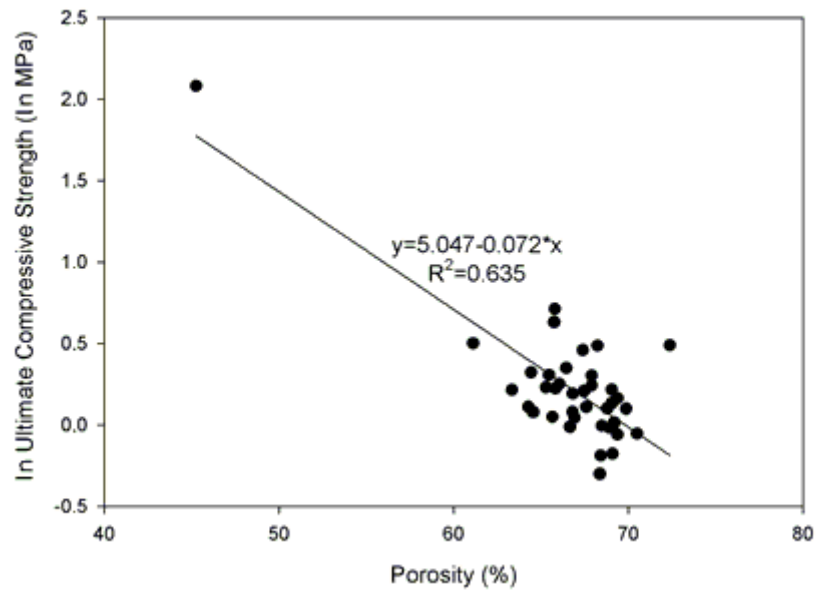


Figure 7.37. Correlation between porosity and ultimate compressive strength of the samples.

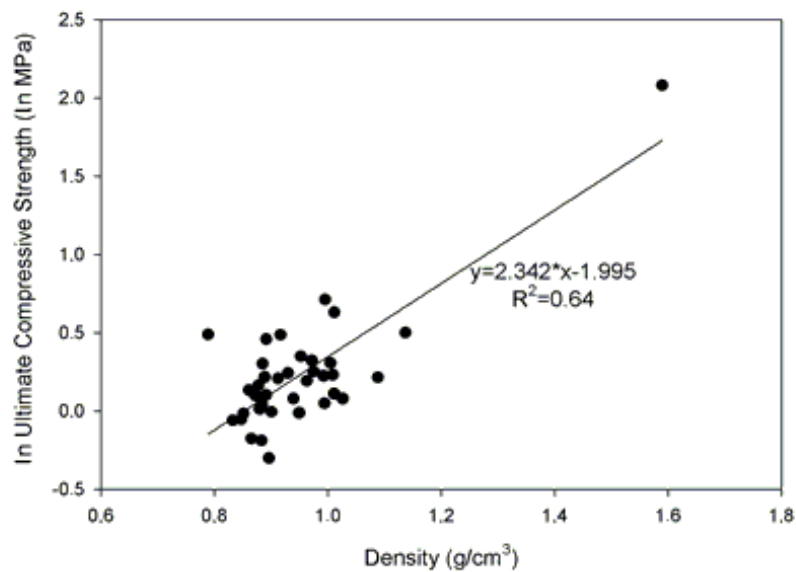


Figure 7.38. Correlation between density and ultimate compressive strength of the samples.

The significance of porosity for mechanical properties of the porous cement blocks are revealed by isolation of the two other factors packing density and monetite content. A smaller sample group with constant monetite content is used to observe the dependence of mechanical properties to porosity, and the resulting graphs give higher correlation coefficients compared to the whole sample group as seen in Figures 7.39-7.41.

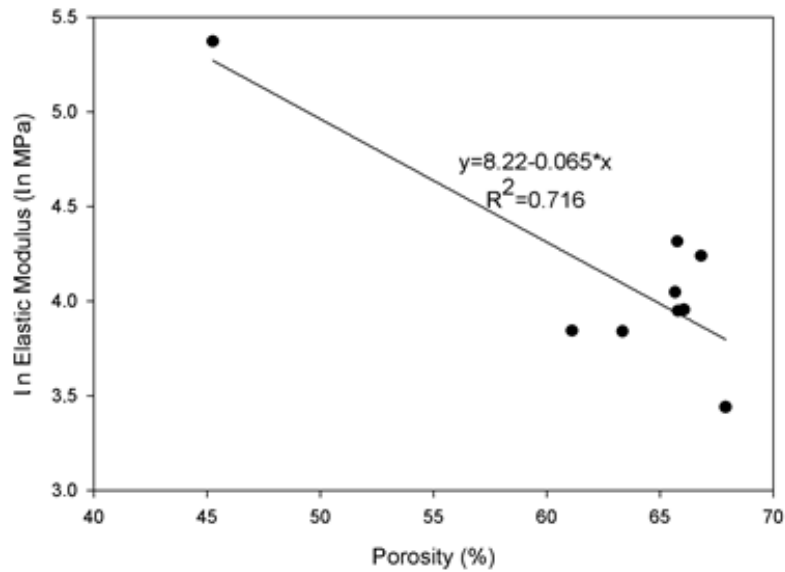


Figure 7.39. Correlation between porosity and elastic modulus of samples containing about 85% monetite.

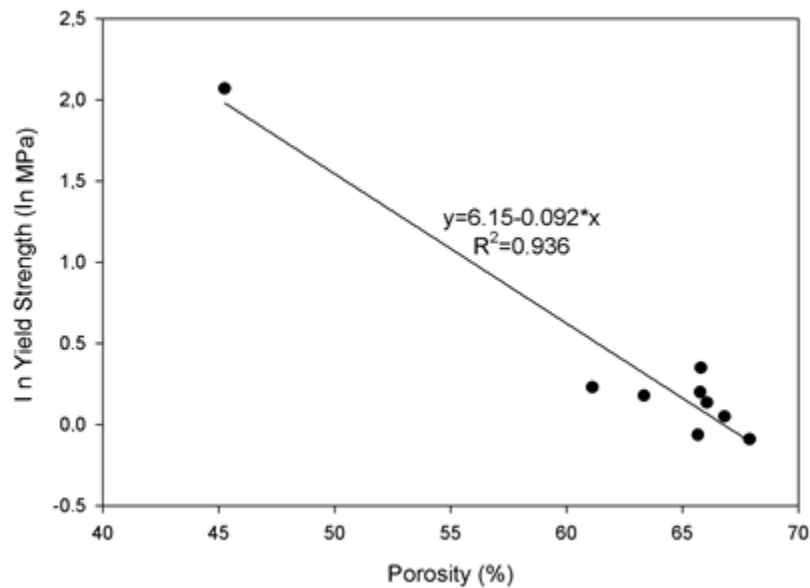


Figure 7.40. Correlation between porosity and yield strength of samples containing about 85% monetite.

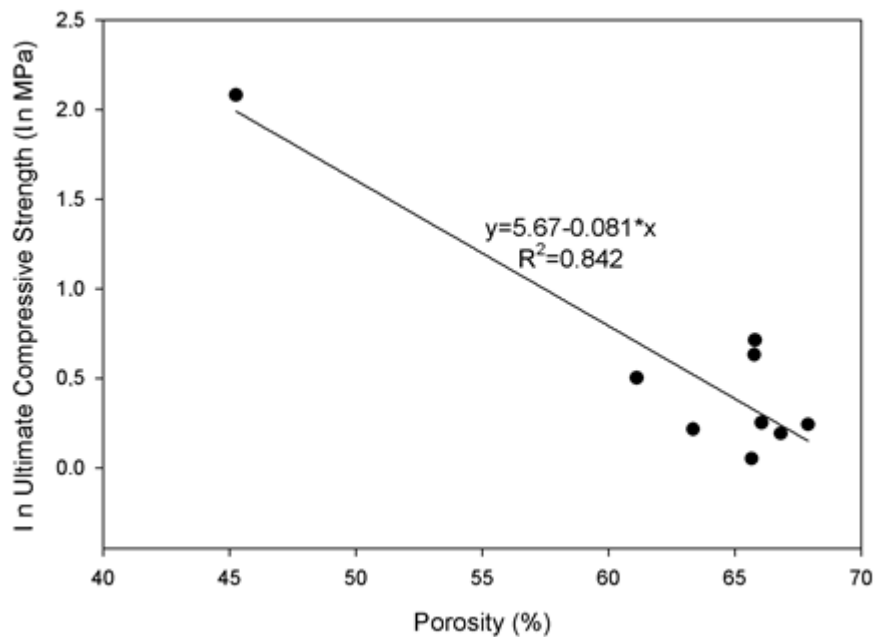


Figure 7.41. Correlation between porosity and ultimate compressive strength of samples containing about 85% monetite.

The theoretical dense yield strengths of the samples were found to be slightly higher than the ultimate compressive strength while the opposite is expected for samples experiencing additional plastic deformation until fracture. The majority of the samples reached ultimate compressive strength shortly after the yield point so that there was not much difference between yield strengths and ultimate compressive strengths on average. Such a load supporting behavior is typical for hard ceramics and it is an indication to the strength of the porous monetite rich cement blocks.

The stress concentration factors obtained from the above figures are similarly around 0.09. That constant obtained from experimental data reveals that the stress concentration factor is within the range expected from calcium phosphates. The stress concentration factor obtained from Figures 7.40-7.41 give an  $a/c$  ratio of 6.6, a representation of slightly disc-like average pore shape. Although irregularity of the porogen shape upon grinding makes it hard to deduce an average pore shape, generally equiaxed nature of the porogens as will be seen later in this report from optical microscope images do not conform to the disc-like shape prediction of Rossi. Undissolved MCPM particles may be the source of the disc-like morphology of the stress intensifying pores.

The dependence of mechanical properties to monetite content can be similarly observed by analyzing a subgroup of samples having the same porosity. Mechanical properties of 5 samples with porosities close to the mean sample porosity of 67% were correlated to the monetite content in Figure 7.42. Depth of the subgroup was low due to high scattering of porosity in the whole sample set. Despite low correlation coefficient, a linear proportionality was obtained for both elastic modulus, yield strength, and ultimate compressive strength with monetite content. The maximum obtainable strength at 67% porosity at full monetite conversion is found as 1.62 MPa while theoretical dense full monetite cement block would have a dense strength of 170 MPa. These values are lower than previously calculated values for samples containing 65% porosity, 85% monetite and zero porosity, 85% monetite. The accuracy of the trendlines for monetite dependence of mechanical properties is low, nevertheless they provide a basic understanding of how strength of porous cement blocks vary with increasing monetite conversion at constant porosity.

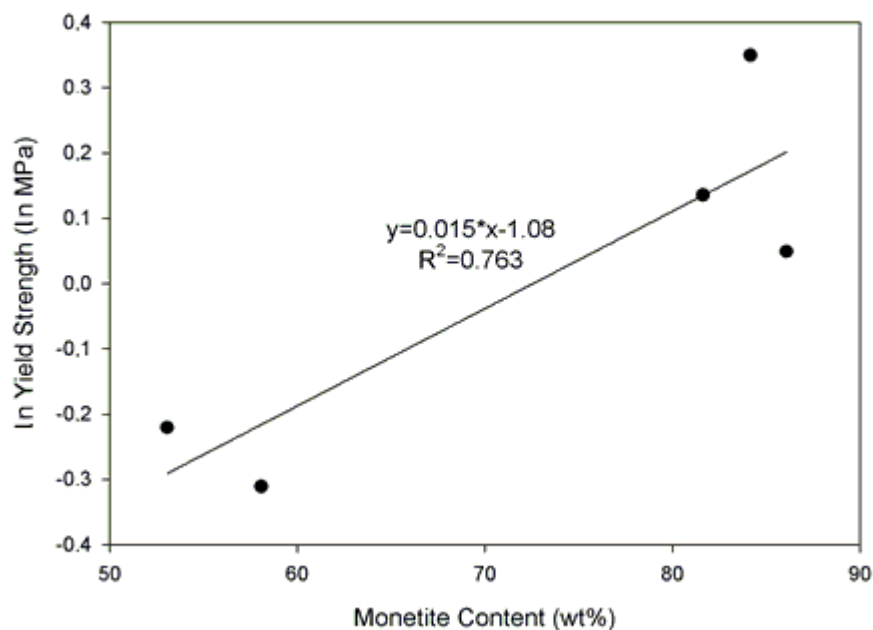


Figure 7.42. Correlation between monetite content and yield strength of samples having 67% porosity.

Of the three significant factors porosity, packing density and monetite content, packing density was seen to have the lowest impact on the mechanical properties. Analysis of subgroups of samples with the same porosity or monetite content did not give any correlation between packing density and mechanical properties. This may be

attributed to the negative proportionality of packing density to micropores which is known to have a lesser role in stress intensification compared to macropores. Packing density is thought to improve strength indirectly by reinforcement of the monetite structure through compaction of the monetite matrix. Correlation between monetite content and mechanical properties are expected to be enhanced by higher packing density. The improvement in mechanical properties with higher monetite conversion would be lower if packing density was lower in average for the porous cement blocks. In fact comparison of the mechanical properties of Samples 12 and 21 given in Table 7.6 confirms this expectation. Both samples contain 68% porosity and around 78% monetite while their packing densities were calculated as 0.71 and 0.68 respectively. Sample 12 with the higher packing density has a yield strength of 1.12 MPa and ultimate compressive strength of 1.63 MPa while the values calculated for Sample 21 are 0.79 MPa and 0.99 MPa respectively. Overall evaluation of the mechanical characterization reveals that porosity is the most significant factor followed by monetite content and packing density. Packing density has an indirect effect on mechanical properties by strengthening of the monetite structure.

Table 7.6. Results of mechanical characterization for all samples

Sample	Mean modulus	+/-	Mean Yield Strength	+/-	Mean Ultimate Strength	+/-	Porosity	Density	Monetite Content	Brushite Content	B-TCP Content	Estimated Packing	Real Packing
	MPa		MPa		MPa		%	g/cm <sup>3</sup>	wt%	wt%	wt%		
Dense	215.30	71.38	7.92	1.37	8.01	1.25	45.26	1.59	83.45	3.59	12.96	Random	0.58
1	22.76	7.31	1.11	0.23	1.18	0.14	69.39	0.88	79.86	9.00	11.14	0.67	0.70
2	34.74	5.95	1.17	0.13	1.23	0.04	67.46	0.91	71.01	19.92	9.08	0.68	0.71
3	37.51	10.15	0.70	0.06	1.18	0.14	64.56	1.03	80.66	5.08	14.26	0.61	0.70
4	33.64	1.11	0.89	0.27	1.08	0.02	66.81	0.94	70.84	16.15	13.00	0.65	0.72
5	31.17	0.98	0.91	0.10	1.27	0.29	67.90	0.93	84.55	3.99	11.46	0.63	0.70
6	31.49	1.51	0.60	0.13	1.38	0.52	64.44	0.97	55.84	33.18	10.98	0.61	0.71
7	24.22	3.15	1.06	0.46	1.36	0.56	65.46	1.00	83.99	2.51	13.50	0.57	0.69
8	19.82	3.16	0.77	0.09	0.99	0.05	66.67	0.95	74.76	12.89	12.35	0.63	0.71
9	27.26	12.47	0.83	0.34	1.25	0.27	65.84	0.99	79.16	10.03	10.81	0.62	0.70
10	42.29	10.53	1.18	0.41	1.26	0.30	65.29	1.01	80.59	6.69	12.71	0.63	0.67
11	20.97	6.15	0.85	0.15	1.10	0.10	69.89	0.87	85.98	0.71	13.31	0.63	0.69
12	30.85	6.90	1.12	0.36	1.63	0.36	68.24	0.92	78.52	6.83	14.65	0.62	0.71
13	15.28	2.23	0.45	0.05	0.74	0.16	68.37	0.90	81.71	5.66	12.63	0.60	0.70
14	46.54	23.44	1.20	0.28	1.24	0.33	63.35	1.09	84.89	2.92	12.19	0.60	0.69
15	69.27	37.52	1.05	0.24	1.21	0.23	66.82	0.96	86.08	2.92	11.00	0.62	0.67
16	46.67	15.08	1.26	0.27	1.65	0.41	61.12	1.14	85.41	0.00	14.59	0.57	0.70
17	57.23	21.51	0.94	0.12	1.05	0.16	65.66	0.99	85.11	4.06	10.83	0.59	0.66
18	47.59	21.43	1.10	0.33	1.12	0.35	64.28	1.01	70.75	16.24	13.01	0.64	0.66
19	74.86	28.29	1.22	0.69	1.88	0.55	65.77	1.01	83.68	2.52	13.80	0.65	0.70
20	52.16	7.00	1.15	0.13	1.29	0.08	66.06	0.98	81.63	7.96	10.41	0.61	0.67
21	60.32	18.04	0.79	0.30	0.99	0.15	68.49	0.90	77.60	10.82	11.58	0.65	0.68
22	68.50	28.76	0.82	0.08	1.11	0.09	68.80	0.89	75.82	11.38	12.80	0.65	0.68
23	70.46	19.61	1.18	0.35	1.42	0.29	66.45	0.95	77.57	13.44	9.00	0.57	0.63
24	32.62	10.80	0.75	0.15	1.14	0.26	69.07	0.86	65.95	21.63	12.42	0.63	0.66
25	42.08	3.19	0.59	0.04	0.84	0.14	69.10	0.87	65.21	24.12	10.66	0.63	0.66
26	58.93	8.82	0.59	0.08	0.83	0.06	68.43	0.88	73.50	20.14	6.36	0.64	0.68
27	57.49	12.38	0.88	0.14	1.11	0.12	67.61	0.87	47.35	44.42	8.23	0.66	0.68
28	63.13	22.96	0.77	0.10	1.35	0.17	67.90	0.89	61.14	28.52	10.35	0.63	0.67
29	53.75	13.00	0.80	0.18	1.04	0.17	66.92	0.88	53.07	39.81	7.12	0.63	0.68
30	35.98	8.79	0.73	0.07	1.58	0.30	67.40	0.89	58.07	34.75	7.17	0.63	0.68
31	51.84	23.95	1.42	0.61	2.04	0.16	65.80	1.00	84.16	2.15	13.69	0.59	0.68
32	33.88	12.89	0.61	0.15	1.24	0.42	69.06	0.89	78.06	9.02	12.92	0.65	0.70
33	80.92	21.49	0.87	0.17	0.98	0.18	68.92	0.85	61.00	30.95	8.05	0.62	0.66
34	47.47	16.83	0.63	0.21	1.01	0.28	69.19	0.88	79.83	10.61	9.56	0.65	0.68
35							65.74	0.95	64.32	26.46	9.22	0.60	
36	35.27	10.72	0.55	0.09	0.94	0.33	69.38	0.83	56.65	34.80	8.55	0.63	0.67
37	54.47	18.73	1.07	0.12	1.63	0.46	72.38	0.79	72.67	15.85	11.49	0.69	0.68
38	43.97	21.97	0.71	0.10	0.95	0.17	70.50	0.85	78.76	8.71	12.54	0.66	0.68
mean	44.79	13.48	0.90	0.21	1.22	0.24	67.22	0.93	74.10	14.65	11.25	0.63	0.68
median	43.97	12.38	0.87	0.15	1.18	0.18	67.43	0.91	77.83	10.71	11.47	0.63	0.68

## 7.4. Morphological Analysis of the Scaffold Microstructure

Cylindrical macroporous constructs made of calcium phosphate cements were subjected to morphological characterization in order to assess their validity as an effective tissue engineering scaffold. Ideal scaffold should possess a total porosity greater than 60%, a large fraction of macropores greater than 50 microns, and as much interconnectivity between the pores as possible for efficient transport of nutrients and cells required for tissue regeneration. Size distribution of NaCl porogen particles is expected to produce various degrees of packing, macroporosity, and interconnectivity based on the distribution of total porogen amount to 6 size groups. Porogen amount for each sample set varied as a function of maximum packing density so that total porosity consisting of macro and microporosity was expected to stay constant at 71.28%. Introduction of finer cement particles deviated the expected packing to higher and total porosity to lower values as explained in the previous section. Most samples were compacted to packing densities even higher than the maximum packing densities calculated for the size distributed porogen. The effect of this packing enhancement on microstructure is expected to be seen as less micropores and higher macroporosity due to compaction of the cylindrical construct.

Measured maximum and minimum diameters given in Table A.1 are close to the caliper length and width values and both can be used to represent the size of the individual pores. However it is the caliper length and width that relate more accurately to the aperture length of the meshed sieves that were used to group the size distributions. Mean diameter of the pores are subject to considerable standard deviation so it is not definitive to represent the sample pore size with one mean pore diameter value. Standard deviations for all parameters given in Table A.1 are high due to the large distribution of pores that are present in great numbers. Coarse pores are present in smaller numbers compared to finer ones as their distribution was based on their masses that is a function of cube of the radius of the NaCl particles. Unit mass of the size groups contains particles increasing in number exponentially with decreasing group size as seen in Table 7.7. A small group of coarse pores, medium group of intermediate pores and large group of fine pores produces considerable deviation in the arithmetic average of the pore sizes and especially pore areas that are proportional to the square of the pore size. Size distribution histograms are more useful in the analysis of pore

morphology of the samples and are given in the following section in the detailed morphological analysis of each samples.

Table 7.7. Unit volume, mass and number equivalent of particle sizes

Particle Size ( $\mu\text{m}$ )	Particle Volume ( $\mu\text{m}^3$ )	Particle Mass ( $\mu\text{g}$ )	Number Equivalent					
			38 $\mu\text{m}$ particle	53 $\mu\text{m}$ particle	75 $\mu\text{m}$ particle	106 $\mu\text{m}$ particle	150 $\mu\text{m}$ particle	212 $\mu\text{m}$ particle
38	54872	0.119	1	0.368573	0.130067	0.046072	0.01625837	0.005758949
53	148877	0.322	2.713169	1	0.352894	0.125	0.044111704	0.015625
75	421875	0.913	7.688347	2.833715	1	0.354214	0.125	0.044276798
106	1191016	2.58	21.70535	8	2.823149	1	0.35289363	0.125
150	3375000	7.31	61.50678	22.66972	8	2.833715	1	0.354214385
212	9528128	20.6	173.6428	64	22.58519	8	2.823149037	1

The most relevant information regarding the macroporosity of the samples is the total area. The sum of all area enclosed inside the pore outlines in two dimensions translates into the volume percentage of macropores in the three dimensional construct. The average pore area of 10 adjacent micrographs from the cross section of all samples gives a well representative macroporosity information. This is confirmed by comparing the macroporosity calculated by the Archimedes' method with the morphologically observed macroporosity. Only 12 of the 38 total porosity values deviate more than 10% from the Archimedean macroporosity. The reason for the majority of these inaccuracies is the presence of large number of fine porogen particles which could not be detected by the image analysis software due to the low contrast of the image. Observed macroporosity for the majority of the samples are comparably close to the Archimedean macroporosity. Ten of these samples exhibited greater macroporosity than expected, majority of which are within the acceptable standard deviation range of 5%. Such samples with high macroporosity are seen to have high interconnectivity due to the proximity of the porogen particles.

For a large sample set of varying pore size distributions, the majority of the samples are seen in Figures 7.45-46 to have a mean pore diameter less than 70  $\mu\text{m}$ . This corresponds to the exact median of the six size distributions grouped at -38, -53, -75, -106, -150, and -212  $\mu\text{m}$ . Samples with more or less balanced size distributions possess a mean pore diameter around 70  $\mu\text{m}$ . Considering the minimum accepted pore size around 50  $\mu\text{m}$  based on clinical research of scaffolds, it can be said that balanced porogen size distributions are required in the preparation of macroporous scaffolds. Abundant fine porogens should be balanced with coarse porogens in order to reach the 70  $\mu\text{m}$  mean diameter limit. Sample 21 that outliers in mean diameter



distribution has such balanced porogen size distribution and is categorized as well interconnected as seen in its detailed morphological analysis given in the appendix. On the other hand, sample 16 another outlier has virtually no interconnectivity due to no size distribution. It contains only -212  $\mu\text{m}$  porogens which rarely connect. Sample 26 which contains one large and one fine porogen size group is seen to have low interconnectivity. Thus, a balanced size distribution of porogens with several size groups is expected to provide efficient scaffold conduit structure.

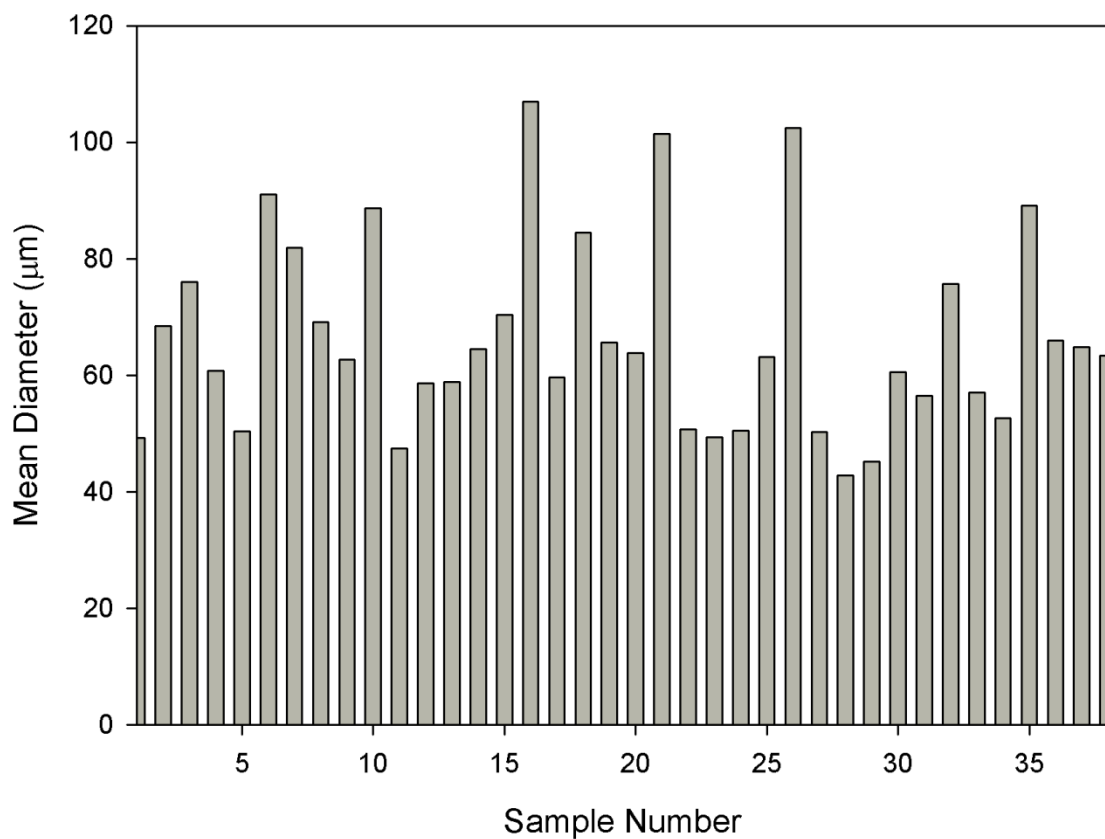


Figure 7.45. Mean pore diameter distribution for all samples.

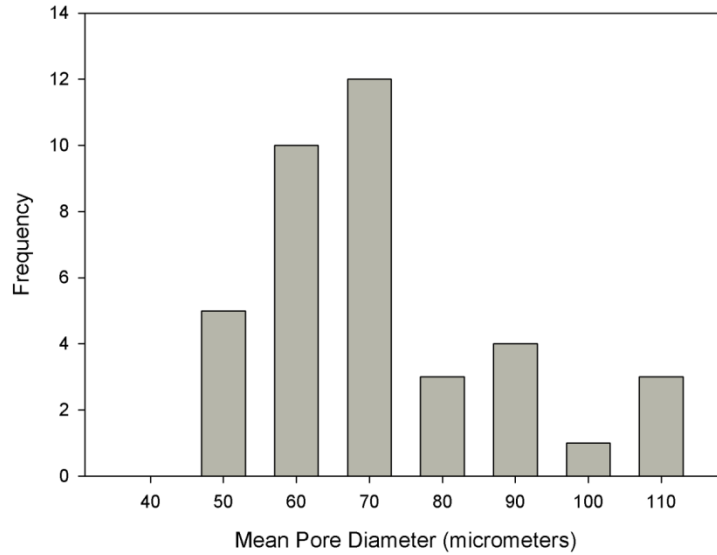


Figure 7.46. Histogram of sample mean pore diameter.

Mean area distribution of the samples is parallel to the mean diameter distribution as seen in Figure 7.47. Mean area corresponding to the mean diameter enables approximation of the geometry of the porogen particles. The median mean area is located at  $5000 \mu\text{m}^2$  as seen in Figure 7.48 and the median mean diameter is located at  $70 \mu\text{m}$ . These values are correlated by the assumption of simple cubic porogen geometry accordingly:

$$D^2 = 4900 \mu\text{m}^2 \approx 5000 \mu\text{m}^2 \quad (7.13)$$

On the other hand spherical assumption is not accurate due to lack of correlation:

$$\pi D^2/4 = 3850 \mu\text{m}^2 \neq 5000 \mu\text{m}^2 \quad (7.14)$$

Prismatic shape of the porogens seen in optical microscope images can thus be approximated as simple cube geometry. Two dimensional area calculated from the sample cross sections is therefore an accurate representation of pore volume in three dimensions. The ratio of the pore volume to sample volume is proportional to the ratio of the pore area to sample area as both are multiplied by the depth of the sample.

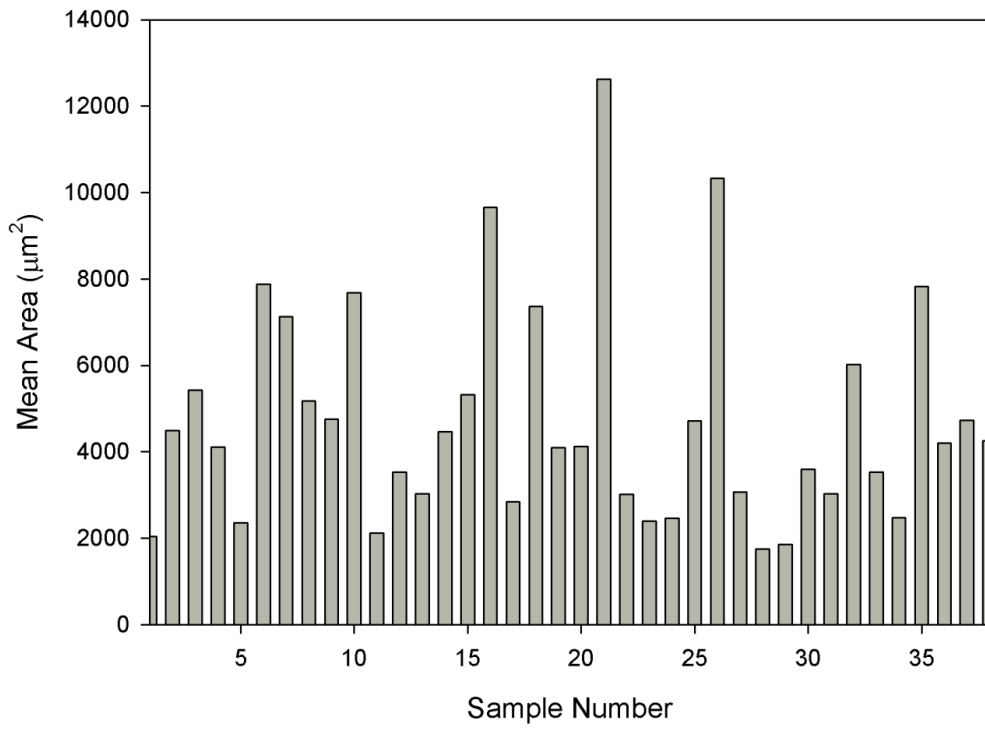


Figure 7.47. Mean area distribution of all samples.

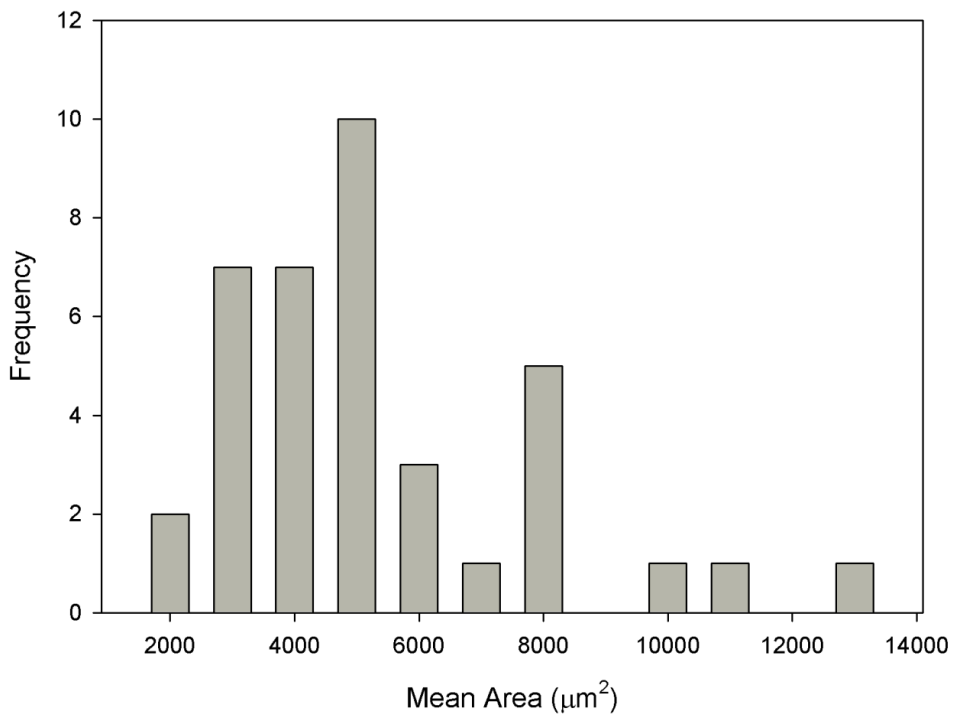


Figure 7.48. Histogram of sample mean area.

Distribution of sample total area is generally parallel to the sample mean diameter and mean area as seen in Figures 7.49-50. Differences exist in the case of unbalanced size distributions such as samples 1 and 16. In the case of balanced size distribution, the total number of pores identified by image analysis software is more or less equal around 40-45. Sample 1 which contains only two fine porogen groups has a mean pore number greater than 100 due to higher number of fine porogens than coarse porogens with the same mass. Similarly, sample 16 which contains only coarse porogens has a mean pore number around 10 due to the small number of large porogens fitting in the observed sample area. Negative exponential dependence of porogen number to porogen size for a fixed amount of porogen makes coarse porogen groups less favorable in the design of scaffolds with optimum mean pore size and interconnectivity. Therefore total pore area is a better indication of the effective scaffold architecture than mean pore area. Effective pore architecture on the other hand necessitates pores to have high surface area in three dimensions or high perimeter in two dimensions.

Mean perimeter distributions of the samples are parallel to the mean diameter distribution as seen in Figure 7.51. The median mean pore perimeter is at 275  $\mu\text{m}$  as seen in Figure 7.52. This value is exactly four times the median mean diameter of 70  $\mu\text{m}$ , which further confirms the simple cubic geometry of the porogens. A similar relationship between mean pore perimeter and total pore perimeter exists as the one between mean pore area and total pore area. Both total area and perimeter reflect the mean values for balanced size distributions while they are opposite the trend in mean values for samples containing either fine or coarse size groups. Samples 1 and 16 which have the least and highest mean diameters are seen to have the highest and the lowest total perimeters in Figure 7.53 due to the inverse relation between porogen number and size. Other outlier samples 27 and 28 which have a balanced porogen size distribution that is slightly moved to the finer side are seen to have the highest total perimeters while having high total areas as well. This makes samples 27 and 28 the best interconnected samples among all the samples. It is interesting that samples 6, 7, and 8 which contain a balanced porogen size distribution that is slightly towards the coarse size have high total perimeters and the highest total area, giving them some of the best interconnected architectures. Similar high interconnectivities observed for samples with balanced porogen size distribution that are slightly deviated from the median points to an

optimum interconnectivity for samples with balanced size distributions centered at the median as in sample 4.

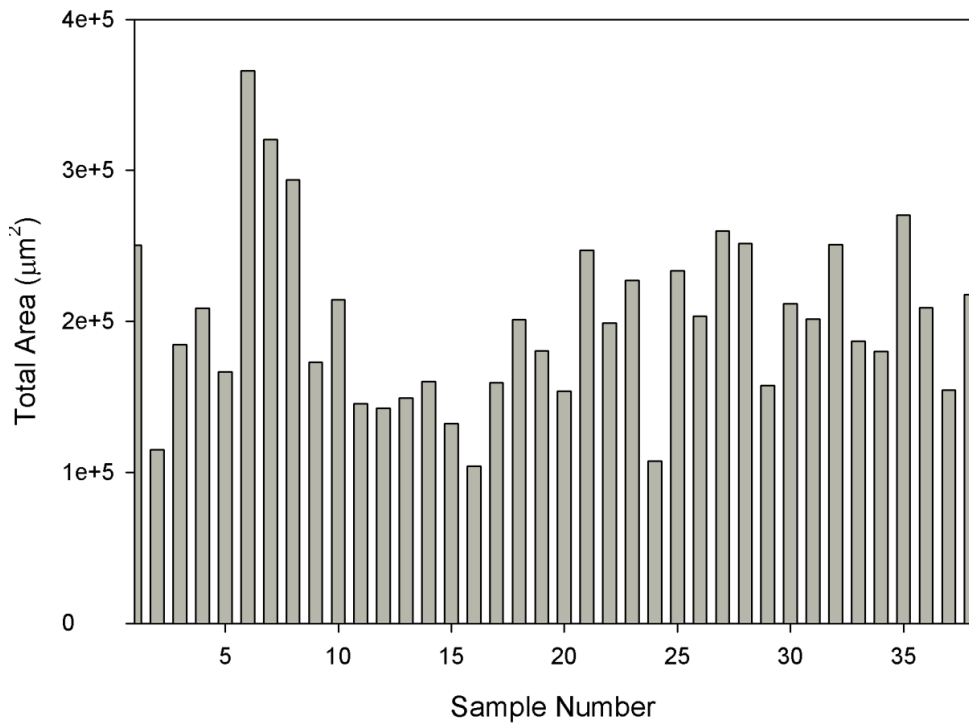


Figure 7.49. Total area distribution of all samples.

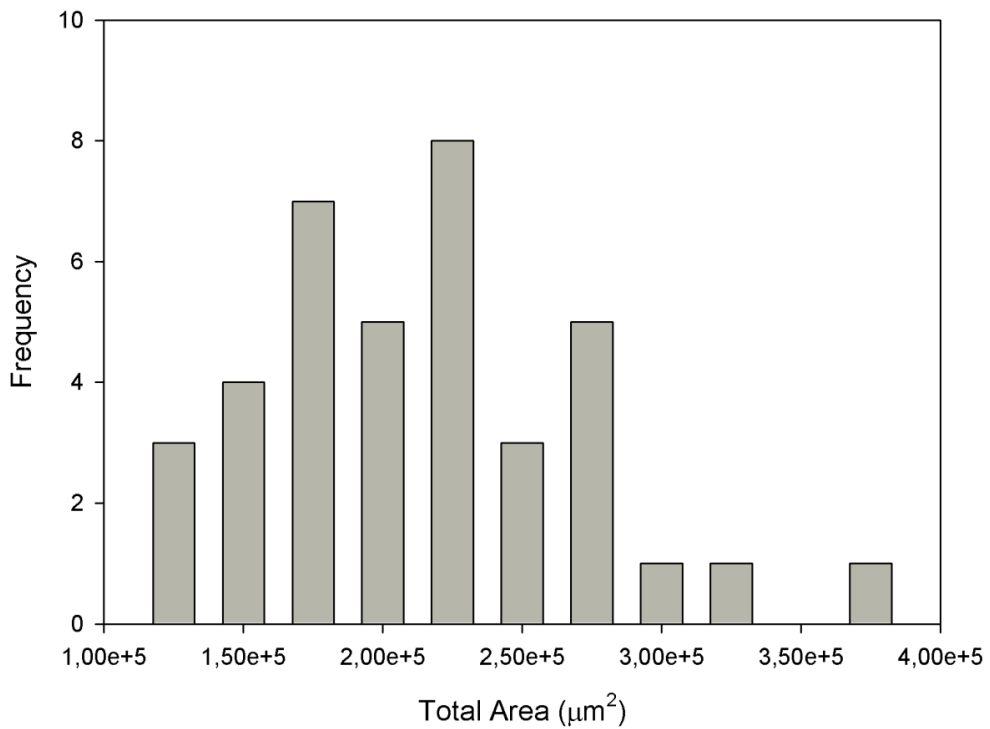


Figure 7.50. Histogram of sample total area.

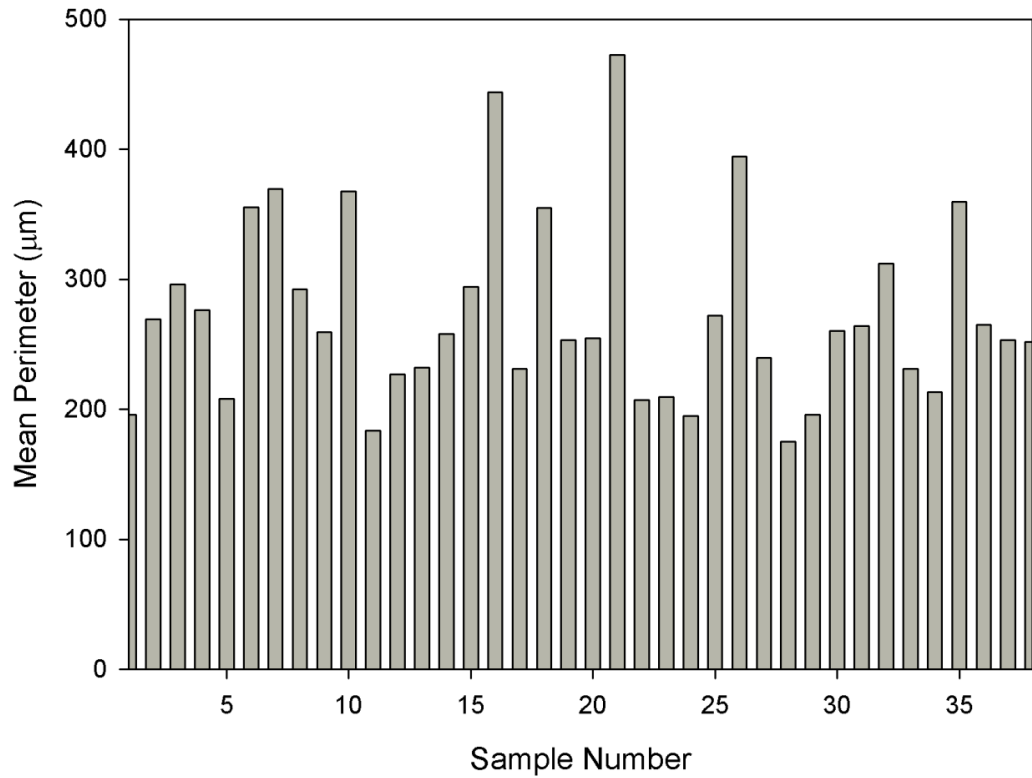


Figure 7.51. Mean perimeter distribution for all samples.

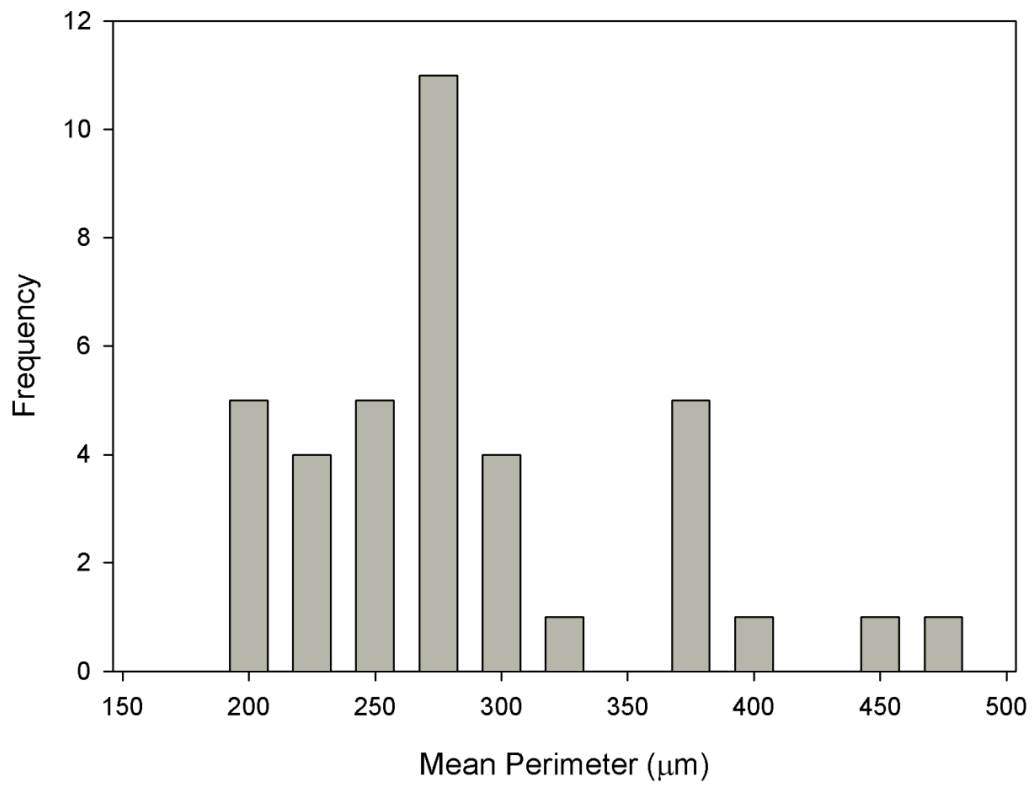


Figure 7.52. Histogram of sample mean perimeter.

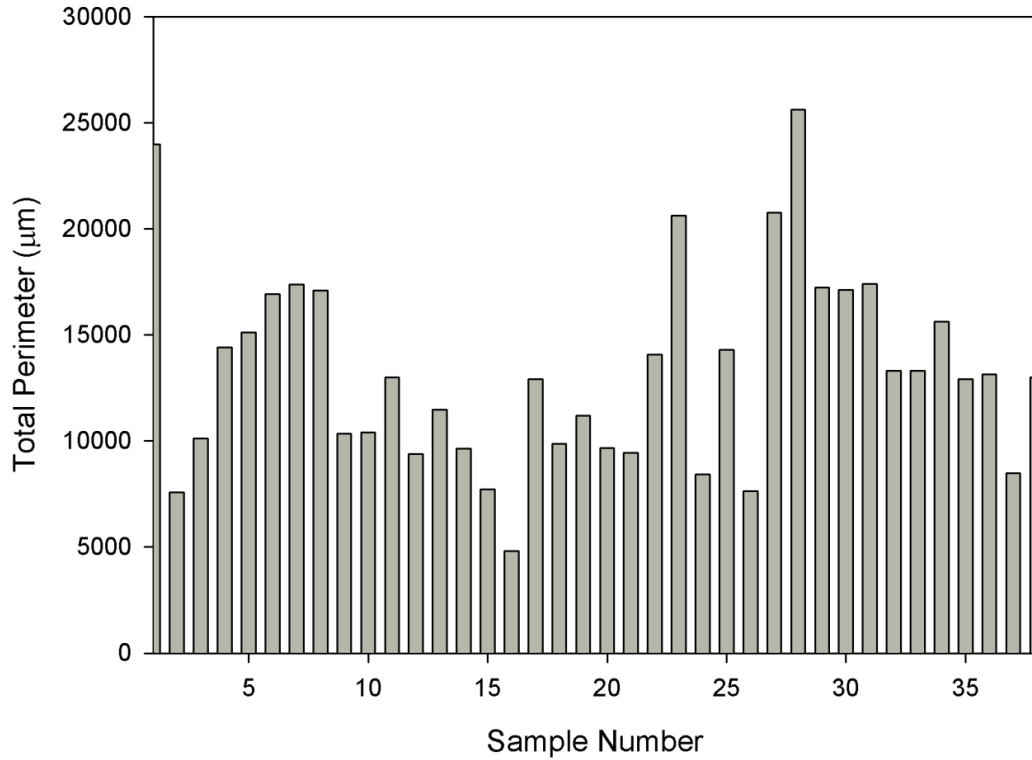


Figure 7.53. Total perimeter distribution for all samples.

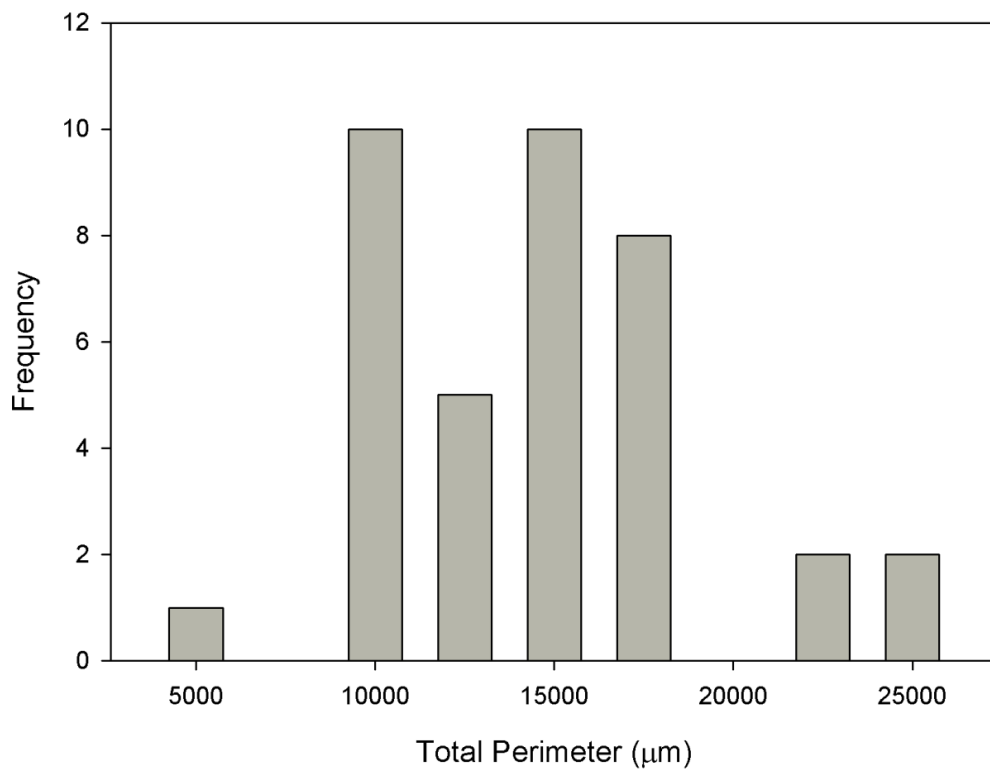


Figure 7.54. Histogram of sample total perimeter.

Image analysis software was able to measure complex features of the sample morphology aside from diameter, area and perimeter. Radius ratio is defined as the ratio of the half width of the largest segment of the pores to the half width of the smallest segment. Equiaxed particles are expected to have radius ratio close to 1 and elongated particles much higher. Connected pores were treated by the image analysis software as one irregular pore that has a high radius ratio. For example 5 equiaxed pores connected side by side give a radius ratio of 5 instead of 1. Thus, radius ratio is a strong indication of the interconnectivity of the samples. Presence of a few interconnected irregular pores that have radius ratio as much as 100 deviates the mean radius ratio significantly. In other words samples with high radius ratio are the ones having some degree of interconnectivity. The majority of the samples seen in the radius ratio distribution given in Figure 7.55 have radius ratio around 2 and are not interconnected. Extent of interconnection for all samples is clearly given by the radius ratio histogram in Figure 7.56 where an exponential decrease in the extent of interconnectivity is deduced. Of all 38 size distribution combinations only less than half result in some degree of interconnectivity. These are the samples with balanced size distributions, the extent being a function of the number of size groups. The only exception to this generalization is sample 1 which has by far the highest number of porogens due to its size distribution being concentrated at the fine side. It has the highest interconnectivity due to the abundance of contact points between individual porogens. However mean diameter of sample 1 is the lowest of all samples meaning that it does not provide an effective conduit structure to be utilized in scaffold design.

Radius ratio and several other parameters such as total area, total perimeter are combined into one parameter that determines the effectiveness of the scaffold architecture. The so called effectiveness factor is therefore the ultimate response obtained from the morphological analysis of the samples in order to determine the optimum size distribution for effective scaffold design.



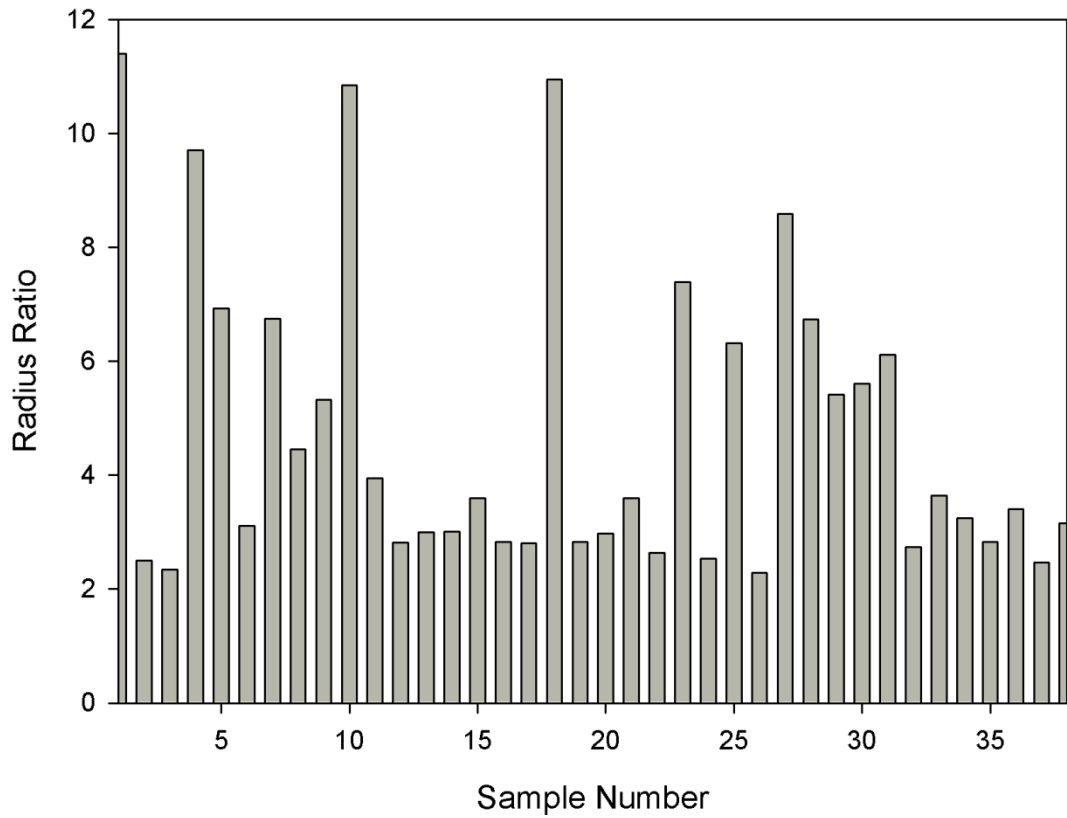


Figure 7.55. Radius ratio distribution for all samples.

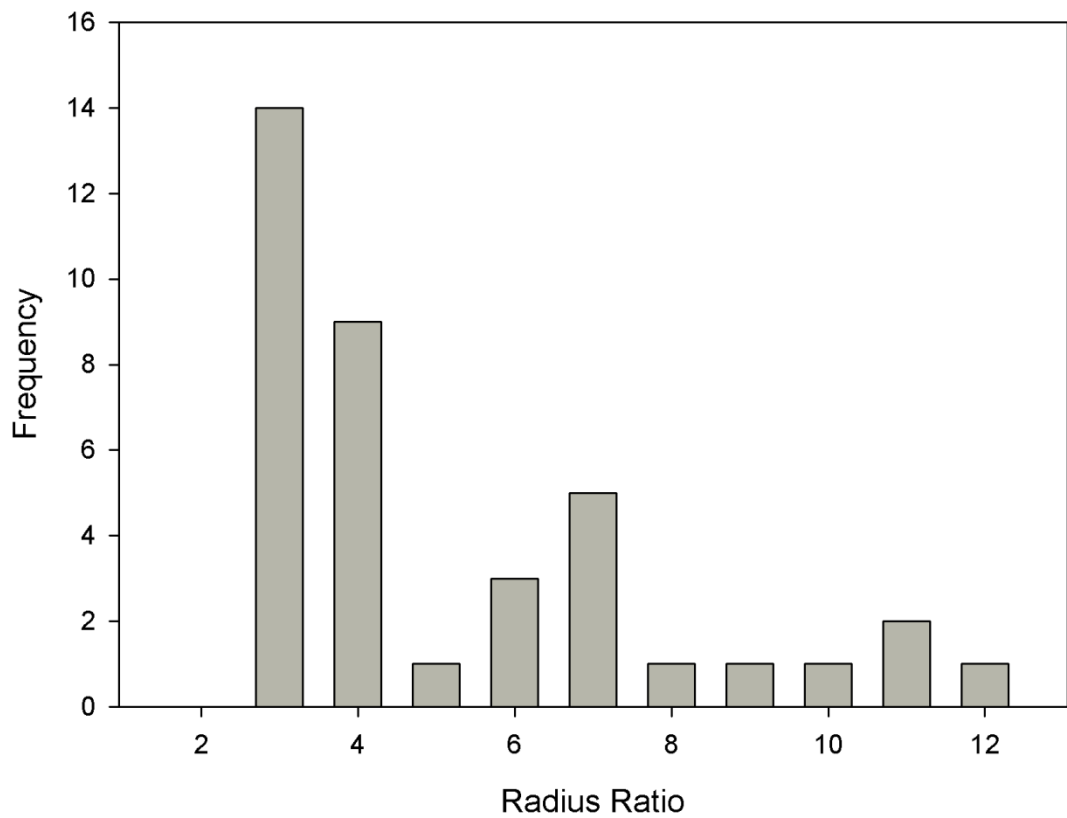


Figure 7.56. Histogram of sample radius ratio.

Direct detection of interconnectivity using image analysis of cross sectional micrographs requires fuzzy image processing tools and tedious work (Bashoor-Zadeh et al. 2010). An indirect model to quantify interconnectivity was developed instead by subjectively correlating various measured parameters with the general interconnectivity of sample sets. It was seen that generally interconnected samples exhibited a few extra-large and elongated pores that appeared at the top of the pore area list of each micrograph. The image analysis software outlined several connected pores as one large pore. For example sample 21 micrograph contained only a few large pores due to the inability of the software to split the interconnected pores to individual pores. Also samples exhibiting high interconnection had both high total area and total perimeter. Another common feature of the interconnected samples was that the large clusters of interconnected pores had a radius ratio much greater than 1, meaning that they are elongated in shape. Combining the commonly correlated parameters for interconnected samples into one parameter, the effectiveness factor was derived by the following equation:

$$\frac{RR \times Area_T \times Per_T \times (Area_3 - 3 Area_M) \times (Per_3 - 3 Per_M)}{10^{16}} \quad (7.15)$$

where RR is the radius ratio,  $Area_T$  is the total area,  $Per_T$  is the total perimeter of the samples,  $Area_3$  is the area of the three largest pores,  $Area_M$  is the mean pore area,  $Per_3$  is the perimeter of the three largest pores, and  $Per_M$  is the mean pore perimeter. The effectiveness factor is dependent on interconnectivity of the pores but does not represent it. It is a measure of the morphological effectiveness of the scaffold rather than a measure of interconnectivity. Correlating the sample interconnectivity quality to the effectiveness factor yields a definitive scale such that samples having effectiveness factor values higher than 50 exhibit some degree of interconnectivity, while those that have values lower than 50 are poorly interconnected. Complete isolation of pores is observed in samples having effectiveness factor around 10. Fourteen such samples exist and the common feature of them is the majority of the porogen size distribution being in the coarser size groups. The ratio of fine NaCl particles to coarser particles is low in these samples, and so is the total particle number. The probability of the proximity of homogeneous distributed porogen particles decreases with decreasing particle number.

Conversely, the samples having a balanced porogen size distribution generally had interconnectivity, accounting to 21 of the 38 samples. Only 3 samples had effectiveness factor lower than 50 without isolated pore structure. They all had a balanced size distribution with the absence of -38 size group. Interconnectivity is expected to be created by void filling of the finer particles between the coarser ones. Finest -38 and -53 size groups are the most important part of the size distribution because of their abundance and void filling capacity. Also their presence as coarser particles among finer cement precursors provides extra size distribution for effective packing.

The highest total pore area of 10 samples listed with their respective size distributions in Table 7.8 show that a high fraction of porogens should consist of coarse porogens to achieve high accessible pore volume. This result is based on the limitations of the optical microscope to capture fine porogens in diameter less than 50  $\mu\text{m}$ . A fraction of fine porogens in about half of the samples was not detected due to the opacity of the sample surface or low surface contrast. The coincidental matching of the size of the omitted pores with the minimum effective pore size for cellular colonization makes the limited morphological data useful as the effective porosity. Detection of isolated fine pores do not improve the assessment of scaffold effectiveness but only add to useless total area in the sample. On the contrary, fine pores that are connected to coarser ones appear as necks or protrusions which add up to the total accessible pore volume analyzed in this study. Another common feature of the samples with highest pore volume is balanced size distribution. Nine of 10 samples were formed from porogens distributed in 5 or more size groups. This is expected as broad size distribution is known to improve packing and more porogens are packed in the observable area of the sample with higher packing. The only exception is sample 1 which consists of two groups of well connected fine pores that were detectable due to high contrast and interconnectivity. Interconnected pores increase the total accessible pore volume by an synergistic effect such that the necks at their connections also add to the total porosity. The highest total area account for 59% macroporosity for sample 6 which means that the microporosity decreased considerably with improved packing from 0.61 to 0.71. The reason for this abrupt increase in macroporosity may be partially heterogeneous porogen distribution in the sample surface examined.

Detection of the second highest total area for sample 7 with the lowest porogen amount is contrary to the expectation of proportionality between pore volume and porogen amount. The fact that sample 7 does not contain -38 size group but other

samples with higher porogen and lower total area do, is an indication of the inaccuracy of the optical microscope image analysis method. A large fraction of the pores that originated from the -38 size group porogens were not accounted for during measurement of the morphological properties. Yet, the measured data is still of value due to the insufficiency of missing fine porosity for effective scaffold permeability.

Table 7.8. Top 10 samples with the highest total pore area and their size distribution

Sample Number		-38 size group	-53 size group	-75 size group	-106 size group	-150 size group	-212 size group	Total NaCl	Total Area ( $\mu\text{m}^2$ )
6	by mass	0.119	0.261	0.000	0.380	0.745	0.399	1.904 gr	366210
	by number	1003413	809005	0	147355	101962	19322	2081057	
7	by mass	0.000	0.526	0.409	0.260	0.448	0.014	1.656 gr	320347
	by number	0	1630386	447497	100641	61264	692	2240481	
8	by mass	0.125	0.273	0.000	0.397	0.779	0.417	1.989 gr	293635
	by number	1048618	845451	0	153993	106555	20193	2174810	
35	by mass	0.027	0.000	0.257	0.598	0.338	0.598	1.818 gr	270572
	by number	226574	0	281601	231970	46251	28996	815392	
27	by mass	0.344	0.458	0.310	0.399	0.000	0.688	2.200 gr	259944
	by number	2897519	1420369	339185	154852	0	33373	4845299	
28	by mass	0.479	0.479	0.479	0.000	0.105	0.479	2.020 gr	251573
	by number	4028961	1484965	524035	0	14411	23203	6075575	
32	by mass	0.000	0.090	0.420	0.000	0.748	0.849	2.107 gr	250649
	by number	0	279087	459611	0	102428	41165	882291	
1	by mass	1.308	0.968	0.000	0.000	0.000	0.000	2.276 gr	250588
	by number	11010287	3002988	0	0	0	0	14013275	
21	by mass	0.762	0.159	0.004	0.347	0.297	0.594	2.163 gr	246998
	by number	6411998	493927	4170	134412	40657	28803	7113967	
25	by mass	0.224	0.306	0.471	0.471	0.252	0.287	2.010 gr	233504
	by number	1882547	949487	515490	182594	34473	13923	3578513	

Samples are listed according to their total perimeter values in a decreasing order in Table 7.9. It is seen that the samples with the highest total perimeter mostly contain finer porogens as expected. The volume/surface area ratio of the equiaxed particles decreases proportionally to the size of the particles. Detection of the second highest total perimeter in sample 1 which contains only fine porogens is parallel to the expectations. Necks and protrusions formed by interconnected pores also contribute to the total surface area of the pores so that the samples with interconnected pore structure have high total perimeter values. Sample 16 is an example to the other extreme case of isolated pore structure. Large isolated pores are the reason for the lowest total perimeter of 4812  $\mu\text{m}$ . Sample 6 which has the highest total area is the lowest among top 10 samples having the highest total perimeter meaning that pore size distributions concentrated at the coarser side may lack the surface features necessary for cellular interaction.

Total perimeter measurements are more affected by the misdetection of -38 size group pores since it is higher for samples having high fraction of fine porogens. The list of samples with lowest total perimeter consists entirely of the ones containing a significant proportion of -38 size group porogens that could not be detected. Samples placed in the second half of Table 7.9 are actually the samples with average total perimeter that exceeded the values of the samples with missing fine porosity.

Table 7.9. Top 10 samples with the highest total pore perimeter and their size distribution

Sample Number		-38 size group	-53 size group	-75 size group	-106 size group	-150 size group	-212 size group	Total NaCl	Total Perimeter ( $\mu\text{m}$ )
28	by mass	0.479	0.479	0.479	0.000	0.105	0.479	2.020 gr	25616
	by number	4028961	1484965	524035	0	14411	23203	6075575	
1	by mass	1.308	0.968	0.000	0.000	0.000	0.000	2.276 gr	23969
	by number	11010287	3002988	0	0	0	0	14013275	
27	by mass	0.344	0.458	0.310	0.399	0.000	0.688	2.200 gr	20752
	by number	2897519	1420369	339185	154852	0	33373	4845299	
23	by mass	0.199	0.722	0.722	0.000	0.000	0.000	1.643 gr	20630
	by number	1672117	2241079	790863	0	0	0	4704059	
31	by mass	0.000	0.000	0.900	0.000	0.900	0.000	1.800 gr	17764
	by number	0	0	985459	0	123182	0	1108641	
7	by mass	0.000	0.526	0.409	0.260	0.448	0.014	1.656 gr	17387
	by number	0	1630386	447497	100641	61264	692	2240481	
29	by mass	0.000	0.385	0.827	0.004	0.143	0.658	2.017 gr	17229
	by number	0	1195091	905084	1678	19547	31891	2153291	
30	by mass	0.004	0.000	0.523	0.817	0.470	0.212	2.027 gr	17128
	by number	34398	0	572683	316957	64315	10301	998654	
8	by mass	0.125	0.273	0.000	0.397	0.779	0.417	1.989 gr	17085
	by number	1048618	845451	0	153993	106555	20193	2174810	
6	by mass	0.119	0.261	0.000	0.380	0.745	0.399	1.904 gr	16919
	by number	1003413	809005	0	147355	101962	19322	2081057	

Both total pore volume and total pore surface area are of significance in the design of an effective scaffold. Of equal importance is the interconnectivity of the pores of the scaffold. Balance is sought between these three properties in this study for optimization of scaffold design. An ideal scaffold would be positioned near the center region towards full interconnectivity of a triaxial diagram consisting of three axes assigned to total pore volume, total pore surface area and interconnectivity. Unfortunately there is no direct method of measuring interconnectivity by image analysis. Open porosity measured by the Archimedes' liquid intrusion method are overestimated values due to the ability of water to penetrate to nanoscale cracks and openings. Only qualitative analysis of the interconnectivity of the macroporous constructs are possible by using the optical micrographs. Common features of the interconnected porous samples such as high area, high perimeter, high radius ratio, high

aspect ratio, low roundness are combined into a single parameter called effectiveness factor in order to optimize the porosity in terms of interconnectivity and establish a correlation between interconnectivity and pore size distribution. Interconnection of pores originating from porogens is a function of the extent of packing of the porogens such that well packed porogens are expected to be more connected. Investigated correlation is expected to be similar to the correlation between the packing density and the size distribution of cement and porogen phases given in the previous chapter. However the proximity of NaCl porogens are not expected to be as high in the abundance of fine cement precursors as in the presence of only size distributed porogens.

Packing theory suggests that the two limiting cases of packing in a simple binary mixture are when there are excess coarse particles, or excess fine particles (de Larrard 1999). In the first case, the coarse particles fill the available space as if no fine particles are present. This case is expected to produce the highest interconnectivity between coarse porogens. In the latter case, the finer particles fully pack in the porosity around coarse particles. These two limiting cases are shown schematically in Figure 7.57. All samples contain about 50 weight % fine cement precursors that result in a fine particle dominant binary mixture in the simplest case. The resultant void filling mechanism is good for packing but not for interconnectivity.

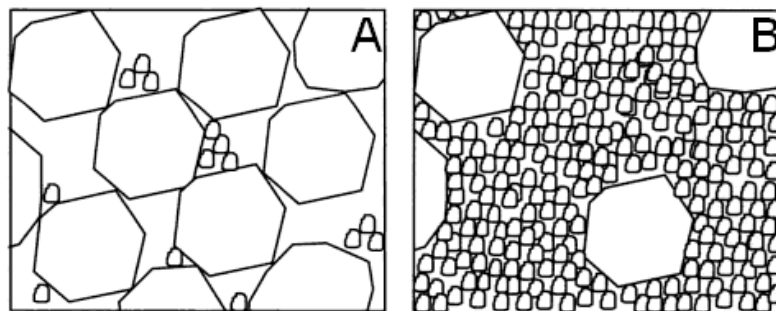


Figure 7.57. Coarse (a) and fine (b) dominant particle systems.

An optimum proportion of coarse to fine particles occurs in binary mixtures without particle interaction. Without interaction means that the local arrangement of an assembly of particles of one size is not disturbed by the vicinity of a particle of the second size. That criterion is generally satisfied when the particle sizes differ greatly. Maximum packing density is obtained around that optimum intermediate proportion.

When the mean sizes of two particle groups in a binary mixture are close to each other, their interactions may lower the packing efficiency considerably. In the case of ternary mixtures, one particle group is usually dominant. For example when the intermediate size particle group is dominant, the other size groups exert forces that limit the packing density of the mixture. The coarse particles exert the so called wall effect on the intermediate particles while the finer particles exert the so called loosening effect as seen in Figure 7.58. These effects are also present in binary mixtures with particle interactions as the particle sizes of the two size groups approach each other.

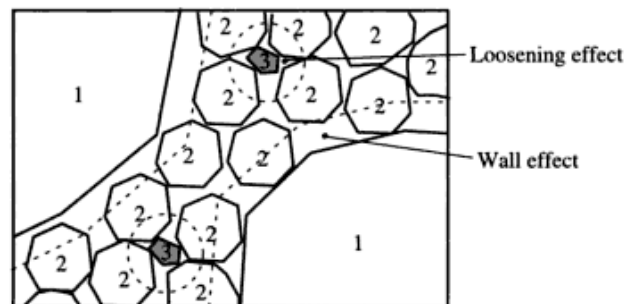


Figure 7.58. Particle interaction models.

The samples with the highest effectiveness factors are listed in decreasing order in Table 7.10. Sample 7 has exceptional interconnection between the pores despite comparatively low porogen amount. Its size distribution is unique in the way that the finest porogens were not included in the mixture and the coarsest size group fraction is negligibly small. Porogen sizes are distributed toward the intermediate size groups. This porogen configuration is thought to result in a poor packing than void filling of the fine porogens due to the size similarity between the porogens and the resultant loosening effect. Interaction of similar size particles is known to reduce packing because of the irregular gaps around the interacting particles (de Larrard 1999). The application of a constant oscillating shear stress during mixing on the other hand induces coagulation of porogens (Kusters et al. 1997). In the initial stage of mixing both NaCl porogens and cement precursors are suspended in the setting liquid and the hydrodynamic shear stress is expected to force them to collide and coagulate. The contact points of the coagulated porogens create the observed interconnections. The separation of interacting similar sized porogens from each other creates a directional coagulation path towards non-interacting coarse porogens. The microstructure observed in sample 7 consists of

intermediate pores coagulated around coarser pores which produced the exceptional interconnectivity.

Table 7.10. Top 10 samples with the highest effectiveness factor and their size distribution

Sample Number		-38 size group	-53 size group	-75 size group	-106 size group	-150 size group	-212 size group	Total NaCl	Effective-ness Factor
27	by mass	0.344	0.458	0.310	0.399	0.000	0.688	2.200 gr	757
	by number	2897519	1420369	339185	154852	0	33373	4845299	
7	by mass	0.000	0.526	0.409	0.260	0.448	0.014	1.656 gr	588
	by number	0	1630386	447497	100641	61264	692	2240481	
4	by mass	0.537	0.000	0.537	0.537	0.000	0.537	2.146 gr	290
	by number	4516306	0	587423	208074	0	26009	5337812	
25	by mass	0.224	0.306	0.471	0.471	0.252	0.287	2.010 gr	289
	by number	1882547	949487	515490	182594	34473	13923	3578513	
8	by mass	0.125	0.273	0.000	0.397	0.779	0.417	1.989 gr	227
	by number	1048618	845451	0	153993	106555	20193	2174810	
1	by mass	1.308	0.968	0.000	0.000	0.000	0.000	2.276 gr	220
	by number	11010287	3002988	0	0	0	0	14013271	
28	by mass	0.479	0.479	0.479	0.000	0.105	0.479	2.020 gr	203
	by number	4028961	1484965	524035	0	14411	23203	6075575	
21	by mass	0.762	0.159	0.004	0.347	0.297	0.594	2.163 gr	188
	by number	6411998	493927	4170	134412	40657	28803	7113967	
6	by mass	0.119	0.261	0.000	0.380	0.745	0.399	1.904 gr	139
	by number	1003413	809005	0	147355	101962	19322	2081057	
10	by mass	0.758	0.103	0.000	1.083	0.076	0.000	2.019 gr	128
	by number	6379673	319115	0	419888	10372	0	7129049	

Maximum packing density obtained for sample 7 porogen configuration was found as one of the lowest, 0.57. Upon mixing with the fine cement precursors however, packing density improved by 12% to 0.69. Hence sample 7 is well packed by the void filling of fine cement precursors around the much coarser size distributed intermediate porogens. Sample 16 which has the same low porogen amount but not distributed in size, was similarly packed by the mechanism of void filling by the fine cement precursors so that its packing density improved significantly from 0.57 to 0.7. Non-interacting single size coarse porogens caused an increase in packing according to the theory. Void filling was partially done by the -38 size group porogens for the other samples with high interconnectivity. Their initial packing density was therefore high and introduction of fine cement precursors resulted in a substantial increase in packing. For example packing density increased from 0.66 to 0.68 for sample 27; 0.65 to 0.72 for sample 4; 0.63 to 0.66 for sample 25; 0.63 to 0.71 for sample 25; and 0.67 to 0.7 for sample 1.



It is seen by comparing samples 7 and 16 that well packing does not necessarily provide well interconnection for a constant porogen amount but it is important for effective utilization of low porogen amount. Much higher interconnectivity would be expected due to the dominant coarse configuration if the coarse porogens in sample 16 were increased in ratio compared to the fine cement precursors. That is seen in the high magnification micrographs of some local high porogen density region of sample 16 given in Figure 7.59. Size distribution of the porogens and the interactions between similar size groups are as important as packing. High interconnectivity of sample 1 suggests that sequential void filling may be a mechanism in well interconnected porous samples. Abundant, finest -38 size group porogens provide effective void filling among the coarser -53 size group in this sample, reaching 0.67 packing density. Packing density is improved to 0.7 upon mixing with fine cement precursors by further filling of the voids, bringing porogens closer to contact. The sequential void filling mechanism may further enhance the packing as size groups are introduced with a balanced porogen size distribution. Fine size groups irrespective of the chemical phases, are found to contribute mainly to the packing of the pores by the binary size approximation while interacting intermediate and coarse porogens are seen to fill the matrix closely due to directional coagulation, resulting in increasing contact points. It is not possible to approximate any sample to the coarse dominant binary distribution case due to addition of about 50% fine cement precursors to the porogens. The size distribution is a balanced binary mixture at best. Local arrangements and interactions of different size groups, for instance loosening and wall effects provide interconnection routes under constant oscillating shear stress. High magnification micrographs of sample 7 given successively in Fig.7.60 provide the necessary clues for the investigated interactions.

0% brushite and the most monetite among all samples with 86%. Consequently the regions captured in the micrographs are expected to be entirely monetite crystals. Figure 7.65 shows the microstructure of sample 11 in detail. Microstructure of the two samples 1 and 11 are almost identical probably due to abundance of monetite in both captured regions.

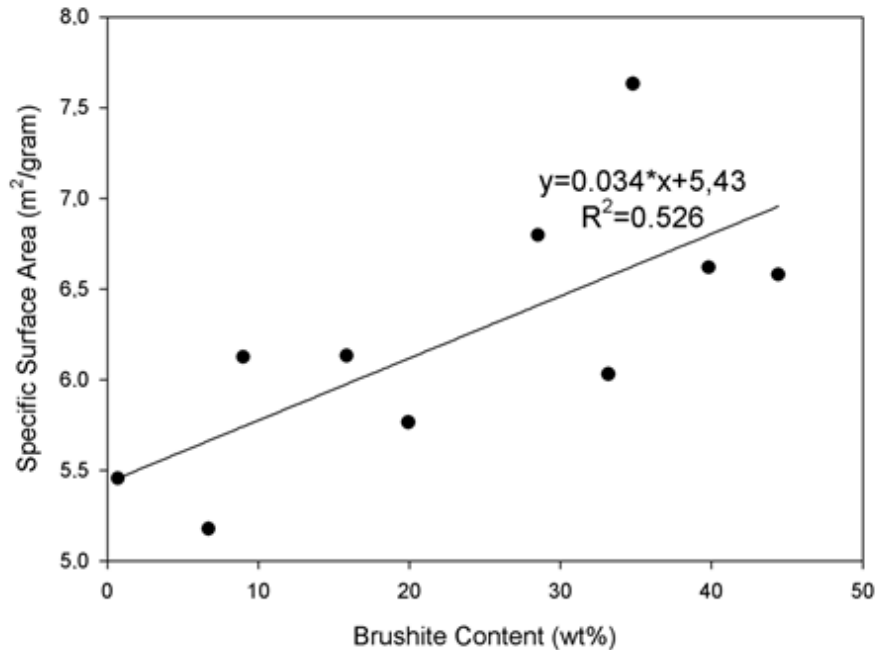


Figure 7.63. Correlation between brushite content and specific surface area of cement samples.

Microstructure of sample 37 seen in Figure 7.66 reveals well connected macropores in Figures 7.66a, b and the monetite crystal morphology in Figures 7.66d-f. Average monetite content of the sample is similar to sample 2 however crystal structure is not as stacked as seen in Figure 7.61. The crystals formed on the pore walls are certainly monetite due to the monetite promoting effect of NaCl but their rosette like structure is different from both samples 1, and 11 which contain almost no brushite in the observed regions and sample 2 which contains a significant amount of brushite.

## 7.5. General Evaluation of the Morphological Analysis Results

In order to produce an effective, fully interconnected large conduit structure, addition of a high number of angular shaped, elongated, coarse, unisized porogens into the cement matrix seem to be the easiest solution since a sufficiently high number of them would produce the fully connected dominant coarse structure seen in Fig. 7.57a. This structure would have the highest pore volume possible, however would lack the essential packing density and the matrix skeleton required for a self supporting scaffold. The delicate balance between porogen ratio and packing ratio is conveniently tuned by the introduction of porogen size distribution. Balanced size distribution of fine-intermediate-coarse porogens is seen to improve packing by sequential void filling mechanism. As porogen size groups differ in size, they behave more like binary mixtures with low interaction among the different size groups. One or more fine porogens that are abundant in number fill the voids around coarser porogens, providing effective packing and enhanced proximity of the porogens. Added fine cement precursor provides a further improvement in packing. The resulting structure consists of close pores not necessarily in contact with each other.

Loosening interactions occur around adjacent size groups, decreasing their packing and separating similar size porogens as fine cement phase fills the defects. On the other hand coarser porogens apply a wall effect to the porogens and cement particles around which is not as effective on packing of the cement phase as the loosening effect due to the size mismatch between them. The separation of fine and intermediate porogens from each other under constant hydrodynamic stress provides the means to group them together around the coarser porogens. Directional coagulation of similar sized fine and intermediate porogens was seen to be the source of interconnection around coarse particles with enhanced contact points. Samples 3, 7, 13, 17, 30, 32, 35 are examples to that mechanism. The sequential void filling mechanism is present in samples consisting of a significant fine porogen amount examples of which are samples 1, 4, 6, 10, 22, 23, 26. Highest interconnectivity is observed in the cases of balanced porogen size distribution in which both mechanisms operate simultaneously. Samples 5, 8, 9, 18, 21, 25, 27, 28, 33 are examples to improved interconnectivity by both active mechanisms.

By examining all the samples it is seen that each mechanism generally produces a limited extent of interconnection. Well packed coarse and fine porogens are rarely connected in sequentially packed samples without the intermediate porogens. Directionally coagulated porous samples by the interaction of similar sized intermediate porogens result in good local interconnection around coarse particles but lack long range continuity due to the lack of high number of fine porogens. Samples containing both fine, intermediate, and coarse porogens are generally more interconnected which is in accord with the theory that size distribution improves packing and interconnection among porogens. Fine tuning of the extent of interconnection can be done by adjusting the proportion of different porogen size groups. It is seen by comparing samples 7 and 13 that higher intermediate porogen amount relative to coarse porogens is essential for effective directional coagulation mechanism. By comparing samples 1 and 23 it is seen that substitution of some of the finest size porogens with an interacting intermediate size group conserved the high interconnectivity while improving the effective pore volume.

Optimization of interconnectivity of the macroporous cement blocks is possible based on these findings. Roughly 2 grams of NaCl porogens are needed for a 70% porous block consisting of 50 weight % cement. This porogen amount may be further increased as all the blocks were seen to be rigid and self supporting in the mechanical characterization at that porosity. First, the total porogen mass known to be safe for a self supporting block is distributed to the adjacent intermediate size groups that are essential for the directional packing mechanism. This porogen configuration produces a not so packed structure without the addition of filler fine cement precursors. Second, an extra amount of both fine and coarse porogens are introduced in order to enhance packing and bring the interconnected pore domains closer. Extra porogen amount is limited by the amount of porosity the cement block requires for self support. The optimum proportion of the size distribution should be around the range given in Table 7.11.

Cement blocks containing NaCl porogen amount and distribution given in Table 7.11 were prepared in order to observe the microstructure and the pore morphology. Archimedeian density of  $0.58 \text{ g/cm}^3$  reveals that the blocks had about 80% porosity. SEM images given in Figures 7.67-7.70 show that pores consist of mostly well defined macropores with a size distribution that is concentrated around 100 micrometers. The macropores look quite packed, indicating the beneficial effect of the balanced size distribution on overall interconnectivity. Crystal morphology of the sample at the pore

## CHAPTER 8

### CONCLUSIONS

The thesis studies consisting of a series of experiments on chemical and physical modification of calcium phosphate cement microstructure done in order to produce a construct possessing the properties of a clinically relevant scaffold were completed successfully and provided valuable information on several aspects of material synthesis and processing. Ionic strength and temperature were seen to have a positive impact on monetite content of apatite forming cement system in accord with the literature given by Bohner and Pitzer. Strong correlation between ionic strength and monetite content provided insight about the modification of setting kinetics and order of precipitation of brushite cements by introduction of NaCl and citric acid as control parameters. Singular effect of NaCl on brushite cement setting kinetics was determined through free drift and pH-stat runs as minimizing the brushite/monetite ratio above 3 M and shortening the period of monetite growth with further increase in concentration. A change in growth model from diffusion controlled to surface integration controlled was seen between 2 M and 3.5 M NaCl as a result of the pH drop observed above 2 M NaCl concentration. Small amounts of citric acid addition to the cement solution around 0.1 M lowered the solubility of  $\beta$ -TCP significantly and the kinetically favorable phase was changed from brushite to monetite due to relative stabilization of brushite at increased concentrations as confirmed by spectrometric studies. The constant decrease in the solubilities of  $\beta$ -TCP and brushite with increasing citric acid concentration determined from the spectrometric analysis was a confirmation of the literature information on the inhibitory effect of citrate groups on the dissolution of  $\beta$ -TCP, brushite and on the growth of brushite crystals. The relative insensitivity of monetite solubility to citric acid on the other hand despite the lower surface area is attributed to the higher density of surface dissolution and growth sites on monetite crystals compared to brushite.

The synergistic effect of NaCl and citric acid is demonstrated by the occurrence of a second relaxation period in the pH-stat analysis of growth which is thought to correspond to monetite growth. Supersaturation gap between brushite and monetite, calculated via Pitzer's ion interaction model is thought to be narrowed with the

adsorption of citrate molecules on scarcely available calcium ions on the hydrated brushite surfaces at low supersaturations induced by NaCl which results in a promotion of monetite content. Citrate groups are expected to inhibit both brushite and monetite growth under low supersaturations above a critical concentration. Brushite/monetite ratio starts to decrease accordingly around the optimum citric acid concentration of 0.19 M. Maximum monetite content and minimum brushite/monetite ratio was obtained at 0.19 M citric acid and 6 M NaCl for all concentrations investigated. Cement blocks prepared from the  $\beta$ -TCP-MCPM system by utilizing the synergistic effect of NaCl and citric acid containing setting liquid yielded high  $\beta$ -TCP conversion and high monetite growth as expected. Cement blocks prepared in the presence of 0.3 M citric acid was seen to have variable brushite and monetite content as function of NaCl concentration. Brushite content decreased from 95% to 12% and monetite content increased from 5% to 80% upon increasing the NaCl concentration from 0 to 6 M. Microstructural analysis of the monetite rich cement blocks revealed that monetite formation was accompanied by formation of micropores around the crystals in the form of thin stacked sheets. Compressive strengths normalized to a single porosity showed positive correlation with increased monetite formation. The application of synergistic effect as a cement phase control mechanism strengthen the realization of biphasic monetite – hydroxyapatite cements encountered in the previous study, as an enhanced scaffold material. Being able to control monetite amount in brushite cements make it possible to control hydroxyapatite amount by conversion of the brushite phase in media such as simulated body fluid. Hence a balance in strength and resorbability of scaffold blocks can be reached depending on the extent of transformation.

The physical properties of the materials constituting the scaffold structure was refined through a series of studies in order to prepare a 3 dimensional construct that is both macroporous and strong. Maximum packing densities of different combinations of NaCl size distributions as determined by their rheological analysis were found to vary in a range between 57% and 69%. Statistical analysis revealed a positive correlation between the amount of -38 and -212 micron sized NaCl particles and maximum packing density. Also -75 micron NaCl size group had a synergistic interaction with -38 size group. The results of the Archimedean analysis reveal that solid size distribution is effective in improving the packing density of porous cement blocks even further than the maximum packing densities. Increase in packing density with introduction of fine cement precursors was accompanied by reduction in sample volumes, microporosities

and total pore volumes. Micropore volume was seen to be directly proportional to monetite content and inversely proportional to packing density. Despite this double dependence of microporosity, it was seen to decrease significantly with packing ratio. Microporosity was found to decrease roughly 1% by every 1% increase in packing density due to size distribution. Mechanical testing revealed the exponential dependence of compressive strength to porosity. Monetite rich cement block with 45% porosity had a compressive strength of 8 MPa while the monetite rich cement block with 65% porosity had a compressive strength of 2 MPa close to the compressive strength of trabecular bone around 2.5 MPa. Hence, it was seen that introduction of size distribution to monetite rich cement precursors and porogens effectively eliminates the microporosity introduced to the structure during monetite formation, producing monetite cements with the same porosity but higher mechanical properties than brushite cement.

Balanced size distribution of fine-intermediate-coarse porogens was seen to improve packing by sequential void filling mechanism. One or more fine porogens that are abundant in number fill the voids around coarser porogens, providing effective packing and enhanced proximity of the porogens. Added fine cement precursor provides a further improvement in packing. The resulting structure consists of close pores not necessarily in contact with each other. On the other hand separation of fine and intermediate porogens from each other under constant hydrodynamic stress provides the means to group them together around the coarser porogens. Directional coagulation of similar sized fine and intermediate porogens were seen to be the source of interconnection around coarse particles with enhanced contact points.

## REFERENCES

- Aberg, J., H. Brisby, H. B. Henriksson, A. Lindahl, P. Thomsen and H. Engqvist (2010). "Premixed Acidic Calcium Phosphate Cement: Characterization of Strength and Microstructure." *Journal of Biomedical Materials Research Part B-Applied Biomaterials* **93B**(2): 436-441.
- Agrawal, C. M. and R. B. Ray (2001). "Biodegradable polymeric scaffolds for musculoskeletal tissue engineering." *J Biomed Mater Res* **55**(2): 141-150.
- Alkhraisat, M. H., F. T. Marino, J. R. Retama, L. B. Jerez and E. Lopez-Cabarcos (2008). "Beta-tricalcium phosphate release from brushite cement surface." *J Biomed Mater Res A* **84**(3): 710-717.
- Almirall, A., G. Larrecq, J. A. Delgado, S. Martinez, J. A. Planell and M. P. Ginebra (2004). "Fabrication of low temperature macroporous hydroxyapatite scaffolds by foaming and hydrolysis of an alpha-TCP paste." *Biomaterials* **25**(17): 3671-3680.
- Ambard, A. J. and L. Mueninghoff (2006). "Calcium phosphate cement: review of mechanical and biological properties." *J Prosthodont* **15**(5): 321-328.
- Amjad, Z. (1998). *Calcium phosphates in biological and industrial systems*, Springer.
- Ball, M. C. and M. J. Casson (1973). "Dehydration of Calcium Hydrogen Phosphate Dihydrate." *Journal of the Chemical Society-Dalton Transactions*(1): 34-37.
- Balluffi, R. W. A., S. M. Carter, W. C. (2005). *Kinetics of Materials*, John Wiley & Sons.
- Barralet, J. E., L. Grover, T. Gaunt, A. J. Wright and I. R. Gibson (2002). "Preparation of macroporous calcium phosphate cement tissue engineering scaffold." *Biomaterials* **23**(15): 3063-3072.
- Barralet, J. E., L. M. Grover and U. Gbureck (2004). "Ionic modification of calcium phosphate cement viscosity. Part II: hypodermic injection and strength improvement of brushite cement." *Biomaterials* **25**(11): 2197-2203.
- Barralet, J. E., M. Tremayne, K. J. Lilley and U. Gbureck (2005). "Modification of calcium phosphate cement with alpha-hydroxy acids and their salts." *Chemistry of Materials* **17**(6): 1313-1319.



- Barrere, F., C. A. van Blitterswijk, K. de Groot and P. Layrolle (2002). "Influence of ionic strength and carbonate on the Ca-P coating formation from SBFx5 solution." *Biomaterials* **23**(9): 1921-1930.
- Bashoor-Zadeh, M., G. Baroud and M. Bohner (2010). "Geometric analysis of porous bone substitutes using micro-computed tomography and fuzzy distance transform." *Acta Biomaterialia* **6**(3): 864-875.
- Bensamoun, S., M.-C. Ho Ba Tho, S. Luu, J.-M. Gherbezza and J.-F. de Belleval (2004). "Spatial distribution of acoustic and elastic properties of human femoral cortical bone." *Journal of Biomechanics* **37**(4): 503-510.
- Bohner, M. (2000). "Calcium orthophosphates in medicine: from ceramics to calcium phosphate cements." *Injury* **31 Suppl 4**: 37-47.
- Bohner, M. (2001). "Calcium phosphate emulsions: possible applications." *Key Eng Mater*: 192-195.
- Bohner, M. (2007). "Reactivity of Calcium Phosphate Cements." *Journal of Materials Chemistry* **17**: 3980–3986.
- Bohner, M. and G. Baroud (2005). "Injectability of calcium phosphate pastes." *Biomaterials* **26**(13): 1553-1563.
- Bohner, M. and U. Gbureck (2008). "Thermal reactions of brushite cements." *J Biomed Mater Res B Appl Biomater* **84**(2): 375-385.
- Bohner, M., U. Gbureck and J. E. Barralet (2005). "Technological issues for the development of more efficient calcium phosphate bone cements: a critical assessment." *Biomaterials* **26**(33): 6423-6429.
- Bohner, M., H. P. Merkle, P. V. Landuyt, G. Trophardy and J. Lemaitre (1999). "Effect of several additives and their admixtures on the physico-chemical properties of a calcium phosphate cement." *Journal of Materials Science-Materials in Medicine* **11**(2): 111-116.
- Bohner, M., H. P. Merkle and J. Lemaitre (2000). "In vitro aging of a calcium phosphate cement." *J Mater Sci Mater Med* **11**(3): 155-162.
- Bohner, M., P. Van Landuyt, H. P. Merkle and J. Lemaitre (1997). "Composition effects on the pH of a hydraulic calcium phosphate cement." *J Mater Sci Mater Med* **8**(11): 675-681.

- Bohner, M. B., T. J. Stark, W. J. (2008). "Controlling the reactivity of calcium phosphate cements." *J. Mater. Chem.*
- Bohner, M. v. L., G. H. Grünenfelder, S. Hirsiger, W. Evison, R. Müller, R. (2005). "Synthesis and characterization of porous b-tricalcium phosphate blocks." *Biomaterials* **26**.
- Boskey, A. L. (2005). *The Organic and Inorganic Matrices. Bone Tissue Engineering*. J. O. Hollinger. New York, CRC Press LLC.
- Boudeville, P., S. Serraj, J. M. Leloup, J. Margerit, B. Pauvert and A. Terol (1999). "Physical properties and self-setting mechanism of calcium phosphate cements from calcium bis-dihydrogenophosphate monohydrate and calcium oxide." *J Mater Sci Mater Med* **10**(2): 99-109.
- Bouler, J. M., M. Trecant, J. Delecrin, J. Royer, N. Passuti and G. Daculsi (1996). "Macroporous biphasic calcium phosphate ceramics: influence of five synthesis parameters on compressive strength." *J Biomed Mater Res* **32**(4): 603-609.
- Bromley, L. A. (1973). "Thermodynamic Properties of Strong Electrolytes in Aqueous-Solutions." *Aiche Journal* **19**(2): 313-320.
- Brown, P. W. and M. Fulmer (1991). "Kinetics of Hydroxyapatite Formation at Low-Temperature." *Journal of the American Ceramic Society* **74**(5): 934-940.
- Brown, S. J., P. Pollintine, D. E. Powell, M. W. Davie and C. A. Sharp (2002). "Regional differences in mechanical and material properties of femoral head cancellous bone in health and osteoarthritis." *Calcif Tissue Int* **71**(3): 227-234.
- Buckwalter, J. A. G., M.J. (1995). "Bone Biology." *The Journal of Bone & Joint Surgery* **77**.
- Burr, D. B. (2002). "Bone material properties and mineral matrix contributions to fracture risk or age in women and men." *J Musculoskelet Neuronal Interact* **2**(3): 201-204.
- Charriere, E., S. Terrazzoni, C. Pittet, P. H. Mordasini, M. Dutoit, J. Lemaitre and P. H. Zysset (2001). "Mechanical characterization of brushite and hydroxyapatite cements." *Biomaterials* **22**(21): 2937-2945.
- Chong, J. S., Christia.Eb and A. D. Baer (1971). "Rheology of Concentrated Suspensions." *Journal of Applied Polymer Science* **15**(8): 2007-&.

- Chow, J. and T. J. Chambers (1992). "An assessment of the prevalence of organic material on bone surfaces." *Calcif Tissue Int* **50**(2): 118-122.
- Chow, L. C. (2009). "Next generation calcium phosphate-based biomaterials." *Dent Mater J* **28**(1): 1-10.
- Connolly, J. F. (1995). "Injectable bone marrow preparations to stimulate osteogenic repair." *Clin Orthop Relat Res*(313): 8-18.
- Constantz, B. R., B. M. Barr, I. C. Ison, M. T. Fulmer, J. Baker, L. McKinney, S. B. Goodman, S. Gunasekaran, D. C. Delaney, J. Ross and R. D. Poser (1998). "Histological, chemical, and crystallographic analysis of four calcium phosphate cements in different rabbit osseous sites." *J Biomed Mater Res* **43**(4): 451-461.
- Cullinane, D. M. S., K.T. (2005). Biomechanics. *Bone Tissue Engineering*. J. O. Hollinger. New York, CRC Press LLC.
- Cullity, B. D. (1956). *Elements of X-Ray Diffraction*, Addison-Wesley.
- Davies, J. E. (1996). "In vitro modeling of the bone/implant interface." *Anat Rec* **245**(2): 426-445.
- Davies, J. E. (2003). "Understanding peri-implant endosseous healing." *J Dent Educ* **67**(8): 932-949.
- Davies, J. E. (2007). "Bone bonding at natural and biomaterial surfaces." *Biomaterials* **28**(34): 5058-5067.
- Davies, J. E. and N. Baldan (1997). "Scanning electron microscopy of the bone-bioactive implant interface." *J Biomed Mater Res* **36**(4): 429-440.
- de Groot, K. (1984). Calcium Phosphate Ceramics: Their Current Status. *Contemporary Biomaterials*. Noyes, William Andrew Publishing.
- de Larrard, F. (1999). *Concrete mixture proportioning: a scientific approach*, Taylor&Francis.
- del Real, R. P., J. G. Wolke, M. Vallet-Regi and J. A. Jansen (2002). "A new method to produce macropores in calcium phosphate cements." *Biomaterials* **23**(17): 3673-3680.

- Descamps, M., T. Duhoo, F. Monchau, J. Lu, P. Hardouin, J. C. Hornez and A. Leriche (2008). "Manufacture of macroporous beta-tricalcium phosphate bioceramics." *Journal of the European Ceramic Society* **28**(1): 149-157.
- Dorozhkin, S. V. (2008). "Calcium orthophosphate cements for biomedical application." *Journal of Materials Science* **43**(9): 3028-3057.
- Driessens, F. C., M. G. Boltong, E. A. de Maeyer, R. Wenz, B. Nies and J. A. Planell (2002). "The Ca/P range of nanoapatitic calcium phosphate cements." *Biomaterials* **23**(19): 4011-4017.
- Driessens, F. C. M., M. G. Boltong, O. Bermudez, J. A. Planell, M. P. Ginebra and E. Fernandez (1994). "Effective Formulations for the Preparation of Calcium-Phosphate Bone Cements." *Journal of Materials Science-Materials in Medicine* **5**(3): 164-170.
- Drury, J. L. and D. J. Mooney (2003). "Hydrogels for tissue engineering: scaffold design variables and applications." *Biomaterials* **24**(24): 4337-4351.
- Fernandez, E. (1996 ). Synthesis & Characterization of Novel Calcium Phosphate Bone Cements in the  $\text{CaHPO}_4 - \alpha\text{-Ca}_3(\text{PO}_4)_2$  System.
- Fernandez, E., F. J. Gil, S. M. Best, M. P. Ginebra, F. C. Driessens and J. A. Planell (1998). "Improvement of the mechanical properties of new calcium phosphate bone cements in the  $\text{CaHPO}_4$ - $\alpha\text{-Ca}_3(\text{PO}_4)_2$  system: compressive strength and microstructural development." *J Biomed Mater Res* **41**(4): 560-567.
- Fernandez, E., F. J. Gil, M. P. Ginebra, F. C. Driessens, J. A. Planell and S. M. Best (1999). "Calcium phosphate bone cements for clinical applications. Part I: solution chemistry." *J Mater Sci Mater Med* **10**(3): 169-176.
- Fernandez, E., M. P. Ginebra, M. G. Boltong, F. C. Driessens, J. Ginebra, E. A. De Maeyer, R. M. Verbeeck and J. A. Planell (1996). "Kinetic study of the setting reaction of a calcium phosphate bone cement." *J Biomed Mater Res* **32**(3): 367-374.
- Flade, K., C. Lau, M. Mertig and W. Pompe (2001). "Osteocalcin-controlled dissolution-precipitation of calcium phosphate under biomimetic conditions." *Chemistry of Materials* **13**(10): 3596-3602.
- Frost, H. M. (2001). "From Wolff's law to the Utah paradigm: Insights about bone physiology and its clinical applications." *Anatomical Record* **262**(4): 398-419.

- Gbureck, U., J. E. Barralet, M. P. Hofmann and R. Thuli (2004). "Nanocrystalline tetracalcium phosphate cement." *J Dent Res* **83**(5): 425-428.
- Gbureck, U., S. Dembski, R. Thull and J. E. Barralet (2005). "Factors influencing calcium phosphate cement shelf-life." *Biomaterials* **26**(17): 3691-3697.
- Gbureck, U., T. Hozel, U. Klammert, K. Wurzler, F. A. Muller and J. E. Barralet (2007). "Resorbable dicalcium phosphate bone substitutes prepared by 3D powder printing." *Adv Funct Mater* **17**(18): 3940-3945.
- Ginebra, M. P., E. Fernandez, E. A. De Maeyer, R. M. Verbeeck, M. G. Boltong, J. Ginebra, F. C. Driessens and J. A. Planell (1997). "Setting reaction and hardening of an apatitic calcium phosphate cement." *J Dent Res* **76**(4): 905-912.
- Giocondi, J. L., B. S. El-Dasher, G. H. Nancollas and C. A. Orme (2010). "Molecular mechanisms of crystallization impacting calcium phosphate cements." *Philos Transact A Math Phys Eng Sci* **368**(1917): 1937-1961.
- Gorst, N. J., Y. Perrie, U. Gbureck, A. L. Hutton, M. P. Hofmann, L. M. Grover and J. E. Barralet (2006). "Effects of fibre reinforcement on the mechanical properties of brushite cement." *Acta Biomater* **2**(1): 95-102.
- Grases, F., M. Ramis and A. Costa-Bauza (2000). "Effects of phytate and pyrophosphate on brushite and hydroxyapatite crystallization. Comparison with the action of other polyphosphates." *Urol Res* **28**(2): 136-140.
- Grover, L. M., U. Gbureck, A. J. Wright, M. Tremayne and J. E. Barralet (2006). "Biologically mediated resorption of brushite cement in vitro." *Biomaterials* **27**(10): 2178-2185.
- Grover, L. M., J. C. Knowles, G. J. Fleming and J. E. Barralet (2003). "In vitro ageing of brushite calcium phosphate cement." *Biomaterials* **24**(23): 4133-4141.
- Hench, L. L. (1980). "Biomaterials." *Science* **208**.
- Hench, L. L. (1993). *An Introduction to Bioceramics*. Singapore, World Scientific Publishing
- Hench, L. L. and J. M. Polak (2002). "Third-generation biomedical materials." *Science* **295**(5557): 1014-1017.

- Hewlett, P. (2004). *Lea's Chemistry of Cement and Concrete*, Elsevier Science & Technology Books.
- Hofmann, M. P., A. R. Mohammed, Y. Perrie, U. Gbureck and J. E. Barralet (2009). "High-strength resorbable brushite bone cement with controlled drug-releasing capabilities." *Acta Biomater* **5**(1): 43-49.
- Hofmann, M. P., S. N. Nazhat, U. Gbureck and J. E. Barralet (2006). "Real-time monitoring of the setting reaction of brushite-forming cement using isothermal differential scanning calorimetry." *Journal of Biomedical Materials Research Part B-Applied Biomaterials* **79B**(2): 360-364.
- Hofmann, M. P., A. M. Young, U. Gbureck, S. N. Nazhat and J. E. Barralet (2006). "FTIR-monitoring of a fast setting brushite bone cement: effect of intermediate phases." *Journal of Materials Chemistry* **16**(31): 3199-3206.
- Hurle, D. T. J. (1993). *Handbook of Crystal Growth*. North-Holland, Amsterdam.
- Hutmacher, D. W. and A. J. Garcia (2005). "Scaffold-based bone engineering by using genetically modified cells." *Gene* **347**(1): 1-10.
- Ishikawa, K., E. D. Eanes and M. S. Tung (1994). "The effect of supersaturation on apatite crystal formation in aqueous solutions at physiologic pH and temperature." *J Dent Res* **73**(8): 1462-1469.
- Ishikawa, K., S. Takagi, L. C. Chow and K. Suzuki (1999). "Reaction of calcium phosphate cements with different amounts of tetracalcium phosphate and dicalcium phosphate anhydrous." *J Biomed Mater Res* **46**(4): 504-510.
- Jalota, S., S. B. Bhaduri and A. C. Tas (2008). "Using a synthetic body-fluid (SBF) solution of 27 mM HCO<sub>3</sub><sup>-</sup> to make bone substitutes more osteointegrative." *Materials Science & Engineering C-Biomimetic and Supramolecular Systems* **28**(1): 129-140.
- Johnsson, M. S. and G. H. Nancollas (1992). "The role of brushite and octacalcium phosphate in apatite formation." *Crit Rev Oral Biol Med* **3**(1-2): 61-82.
- Kakar, S. E., T. A. (2005). *Tissue Engineering of Bone. Bone Tissue Engineering*. J. O. Hollinger. New York, CRC Press LLC.

- Kendall, K., A. J. Howard and J. D. Birchall (1983). "The Relation between Porosity, Microstructure and Strength, and the Approach to Advanced Cement-Based Materials." *Philosophical Transactions of the Royal Society of London Series a-Mathematical Physical and Engineering Sciences* **310**(1511): 139-&.
- Khairoun, I., M. G. Boltong, F. C. M. Driessens and J. A. Planell (1997). "Effect of calcium carbonate on the compliance of an apatitic calcium phosphate bone cement." *Biomaterials* **18**(23): 1535-1539.
- Khan, S. N. L., J.M. (2004). Bone Tissue Engineering: Basic Science and Clinical Concepts. *Orthopaedic Tissue Engineering*. V. M. C. Goldberg, A.I. New York, Marcel Dekker Inc.
- Kodaka, T., M. Kobori, A. Hirayama and M. Abe (1999). "Abrasion of human enamel by brushing with a commercial dentifrice containing hydroxyapatite crystals in vitro." *Journal of Electron Microscopy* **48**(2): 167-172.
- Komath, M., H. K. Varma and R. Sivakumar (2000). "On the development of an apatitic calcium phosphate bone cement." *Bulletin of Materials Science* **23**(2): 135-140.
- Koutsopoulos, S. and E. Dalas (2000). "The effect of acidic amino acids on hydroxyapatite crystallization." *Journal of Crystal Growth* **217**(4): 410-415.
- König, A. E., H.H. Nyvlt, J. (1987). "The influence of sodium chloride on the driving force of the crystallization of potassium chloride from aqueous solution." *Cryst. Res. Technol.* **22**(13).
- Krumgalz, B. S. (2001). "Application of the Pitzer ion interaction model to natural hypersaline brines." *Journal of Molecular Liquids* **91**: 3-19.
- Kumar, M. X., J. Chittur, K. Riley, C. (2000). "Transformation of Modified Brushite to Hydroxyapatite in Aqueous Solution: Effect of Potassium Substitution." *Biomaterials* **20**: 1389-1399.
- Kusters, K. A., J. G. Wijers and D. Thoenes (1997). "Aggregation kinetics of small particles in agitated vessels." *Chemical Engineering Science* **52**(1): 107-121.
- Lam, D. C. C. (1998). "Packing model for bimodal particle packing with aligned fibers." *Journal of Materials Processing Technology* **79**(1-3): 170-176.
- Laurencin, C. T., A. M. Ambrosio, M. D. Borden and J. A. Cooper, Jr. (1999). "Tissue engineering: orthopedic applications." *Annu Rev Biomed Eng* **1**: 19-46.

- Lausier, J. M., C. W. Chiang, H. A. Zompa and C. T. Rhodes (1977). "Aging of Tablets Made with Dibasic Calcium-Phosphate Dihydrate as Matrix." *Journal of Pharmaceutical Sciences* **66**(11): 1636-1637.
- Le Huec, J. C., T. Schaefferbeke, D. Clement, J. Faber and A. Le Rebeller (1995). "Influence of porosity on the mechanical resistance of hydroxyapatite ceramics under compressive stress." *Biomaterials* **16**(2): 113-118.
- Lebugle, A., B. Sallek and A. T. Tai (1999). "Surface modification of monetite in water at 37 degrees C: characterisation by XPS." *Journal of Materials Chemistry* **9**(10): 2511-2515.
- Leeuwenburgh, S. C. G., J. A. Jansen, J. Malda, W. A. Dhert, J. Rouwkema, C. A. van Blitterswijk, C. J. Kirkpatrick and D. F. Williams (2008). "Trends in biomaterials research: An analysis of the scientific programme of the World Biomaterials Congress 2008." *Biomaterials* **29**(21): 3047-3052.
- Leon, B. J., J. A. (2009). *Thin Calcium Phosphate Coatings for Medical Implants*. New York, Springer.
- Lilley, K. J., U. Gbureck, J. C. Knowles, D. F. Farrar and J. E. Barralet (2005). "Cement from magnesium substituted hydroxyapatite." *J Mater Sci Mater Med* **16**(5): 455-460.
- Liu, C., W. Gai, S. Pan and Z. Liu (2003). "The exothermal behavior in the hydration process of calcium phosphate cement." *Biomaterials* **24**(18): 2995-3003.
- Liu, C., H. Shao, F. Chen and H. Zheng (2003). "Effects of the granularity of raw materials on the hydration and hardening process of calcium phosphate cement." *Biomaterials* **24**(23): 4103-4113.
- Liu, C., W. Shen, Y. Gu and L. Hu (1997). "Mechanism of the hardening process for a hydroxyapatite cement." *J Biomed Mater Res* **35**(1): 75-80.
- Liu, D. M. (1997). "Influence of porosity and pore size on the compressive strength of porous hydroxyapatite ceramic." *Ceramics International* **23**(2): 135-139.
- Liu, D. M. (1998). "Preparation and characterisation of porous hydroxyapatite bioceramic via a slip-casting route." *Ceramics International* **24**(6): 441-446.



- Liu, D. M. (2000). "Particle packing and rheological property of highly-concentrated ceramic suspensions:  $\phi(m)$  determination and viscosity prediction." *Journal of Materials Science* **35**(21): 5503-5507.
- Lu, X. and Y. Leng (2005). "Theoretical analysis of calcium phosphate precipitation in simulated body fluid." *Biomaterials* **26**(10): 1097-1108.
- Mangels, J. A. and R. M. Williams (1983). "Injection-Molding Ceramics to High Green Densities." *American Ceramic Society Bulletin* **62**(5): 601-606.
- Mather, M. L., S. P. Morgan, L. J. White, H. Tai, W. Kockenberger, S. M. Howdle, K. M. Shakesheff and J. A. Crowe (2008). "Image-based characterization of foamed polymeric tissue scaffolds." *Biomedical Materials* **3**(1): 015011.
- Mersmann, A. (2001). *Crystallization Technology Handbook*, Marcel-Dekker, Inc.
- Miao, X., Y. Hu, J. Liu and A. P. Wong (2004). "Porous calcium phosphate ceramics prepared by coating polyurethane foams with calcium phosphate cements." *Materials Letters* **58**(3-4): 397-402.
- Mirtchi, A. A., J. Lemaitre and N. Terao (1989). "Calcium phosphate cements: study of the beta-tricalcium phosphate--monocalcium phosphate system." *Biomaterials* **10**(7): 475-480.
- Monma, H. (2006). "Chemical And Biomaterials Aspects Of Calcium Phosphate Cement." *Phosphorous Research Bulletin* **20**: 41-46.
- Mullin, J. W. (2001). *Crystallization*. New Delhi, Butterworth-Heinemann.
- Nancollas, G. H. and M. A. Johnsson (1994). "Calculus formation and inhibition." *Adv Dent Res* **8**(2): 307-311.
- Nancollas, G. H. and W. J. Wu (2000). "Biomineralization mechanisms: a kinetics and interfacial energy approach." *Journal of Crystal Growth* **211**(1-4): 137-142.
- Nielsen, A. E. (1984). "Electrolyte Crystal-Growth Mechanisms." *Journal of Crystal Growth* **67**(2): 289-310.
- Onuma, K. (2005). "Effect of phosvitin on the nucleation and growth of calcium phosphates in physiological solutions." *J Phys Chem B* **109**(16): 8257-8262.

- Orme, C. A. and J. L. Giocondi (2007). Model Systems for Formation and Dissolution of Calcium Phosphate Minerals. *Handbook of Biomineralization: Biomimetic and Bioinspired Chemistry*, Wiley.
- Panzavolta, S., P. Torricelli, B. Bracci, M. Fini and A. Bigi (2009). "Alendronate and Pamidronate calcium phosphate bone cements: setting properties and in vitro response of osteoblast and osteoclast cells." *J Inorg Biochem* **103**(1): 101-106.
- Parfitt, A. M. (1984). "The cellular basis of bone remodeling: the quantum concept reexamined in light of recent advances in the cell biology of bone." *Calcif Tissue Int* **36 Suppl 1**: S37-45.
- Pitzer, K. S. (1973). "Thermodynamics of electrolytes. I. Theoretical Basis and General Equation." *The Journal of Physical Chemistry* **77**(2).
- Pitzer, K. S. and G. Mayorga (1973). "Thermodynamics of Electrolytes .2. Activity and Osmotic Coefficients for Strong Electrolytes with One or Both Ions Univalent." *Journal of Physical Chemistry* **77**(19): 2300-2308.
- Pitzer, K. S. and G. Mayorga (1974). "Thermodynamics of Electrolytes. III. Activity and Osmotic Coefficients for 2-2 Electrolytes." *Journal of Solution Chemistry* **3**(7).
- Pivonka, P., J. Zimak, D. W. Smith, B. S. Gardiner, C. R. Dunstan, N. A. Sims, T. John Martin and G. R. Mundy (2008). "Model structure and control of bone remodeling: A theoretical study." *Bone* **43**(2): 249-263.
- Prevey, P. S. (2000). "X-ray diffraction characterization of crystallinity and phase composition in plasma sprayed hydroxyapatite coatings." *Journal of Thermal Spray Technology* **9**(3): 369-376.
- Qi, X. P., J. D. Ye and Y. J. Wang (2009). "Alginate/poly (lactic-co-glycolic acid)/calcium phosphate cement scaffold with oriented pore structure for bone tissue engineering." *Journal of Biomedical Materials Research Part A* **89A**(4): 980-987.
- Rabatin, J. G. G., R.H. Newkirk, A.E. (1960). "The Mechanism and Kinetics of the Dehydration of Calcium Hydrogen Phosphate Dihydrate." *J. Phys. Chem.* **64**(4): 491-493.
- Rabatin, J. G. G., R.H. Newkirk, A.E. (1960). "The mechanism and kinetics of the dehydration of calcium hydrogen phosphate dihydrate." *J Phys Chem* **64**(4): 491-493.

- Resnick, D. H., R. (1988). *Fundamentals of Physics*, Wiley.
- Rezwan, K., Q. Z. Chen, J. J. Blaker and A. R. Boccaccini (2006). "Biodegradable and bioactive porous polymer/inorganic composite scaffolds for bone tissue engineering." *Biomaterials* **27**(18): 3413-3431.
- Rice, R. W. (1998). *Porosity of ceramics*. New York, M. Dekker.
- Robling, A. G., A. B. Castillo and C. H. Turner (2006). "Biomechanical and molecular regulation of bone remodeling." *Annu Rev Biomed Eng* **8**: 455-498.
- Rossi, R. C. (1968). "Prediction of elastic moduli of composites." *Journal of The American Ceramic Society* **51**(8): 433-439.
- Sargin, Y., M. Kizilyalli, C. Telli and H. Güler (1997). "A new method for the solid-state synthesis of tetracalcium phosphate, a dental cement: X-ray powder diffraction and IR studies." *Journal of the European Ceramic Society* **17**(7): 963-970.
- Schofield, P. F., K. S. Knight, J. A. M. van der Houwen and E. Valsami-Jones (2004). "The role of hydrogen bonding in the thermal expansion and dehydration of brushite, di-calcium phosphate dihydrate." *Physics and Chemistry of Minerals* **31**(9): 606-624.
- Sheikholeslami, R. and H. W. K. Ong (2003). "Kinetics and thermodynamics of calcium carbonate and calcium sulfate at salinities up to 1.5 M." *Desalination* **157**(1-3): 217-234.
- Sivakumar, G. R., E. K. Girija, S. N. Kalkura and C. Subramanian (1998). "Crystallization and characterization of calcium phosphates: Brushite and monetite." *Crystal Research and Technology* **33**(2): 197-205.
- Song Y. , H. H. H., Hoffmann E. (2002). "The Effects of pH and Ca/P Ratio on the Precipitation of Calcium Phosphate " *Chemical water and wastewater treatment VII*.
- Spicer, P. T. and S. E. Pratsinis (1996). "Coagulation and fragmentation: Universal steady-state particle-size distribution." *AIChE Journal* **42**(6): 1612-1620.
- Taboas, J. M., R. D. Maddox, P. H. Krebsbach and S. J. Hollister (2003). "Indirect solid free form fabrication of local and global porous, biomimetic and composite 3D polymer-ceramic scaffolds." *Biomaterials* **24**(1): 181-194.

- Tadic, D. B., F. Schwarz, K. Epple, M. (2004). "A novel method to produce hydroxyapatite objects with interconnecting porosity that avoids sintering." *Biomaterials* **25**: 3335-3340.
- Takagi, S. and L. C. Chow (2001). "Formation of macropores in calcium phosphate cement implants." *J Mater Sci Mater Med* **12**(2): 135-139.
- Takagi, S., L. C. Chow, S. Hirayama and A. Sugawara (2003). "Premixed calcium-phosphate cement pastes." *J Biomed Mater Res B Appl Biomater* **67**(2): 689-696.
- Tang, R. K., M. Darragh, C. A. Orme, X. Y. Guan, J. R. Hoyer and G. H. Nancollas (2005). "Control of biomineralization dynamics by interfacial energies." *Angewandte Chemie-International Edition* **44**(24): 3698-3702.
- Tang, R. K., M. Hass, W. J. Wu, S. Gulde and G. H. Nancollas (2003). "Constant composition dissolution of mixed phases II. Selective dissolution of calcium phosphates." *Journal of Colloid and Interface Science* **260**(2): 379-384.
- Tas, A. C. and S. B. Bhaduri (2004). "Chemical processing of  $\text{CaHPO}_4 \cdot 2\text{H}_2\text{O}$ : Its conversion to hydroxyapatite." *Journal of the American Ceramic Society* **87**(12): 2195-2200.
- ten Wolde, P. R. and D. Frenkel (1999). "Homogeneous nucleation and the Ostwald step rule." *Physical Chemistry Chemical Physics* **1**(9): 2191-2196.
- Tseng, W. J., D. M. Liu and C. K. Hsu (1999). "Influence of stearic acid on suspension structure and green microstructure of injection-molded zirconia ceramics." *Ceramics International* **25**(2): 191-195.
- Turner, C. H., J. Rho, Y. Takano, T. Y. Tsui and G. M. Pharr (1999). "The elastic properties of trabecular and cortical bone tissues are similar: results from two microscopic measurement techniques." *Journal of Biomechanics* **32**(4): 437-441.
- van der Houwen, J. A. M., G. Cressey, B. A. Cressey and E. Valsami-Jones (2003). "The effect of organic ligands on the crystallinity of calcium phosphate." *Journal of Crystal Growth* **249**(3-4): 572-583.
- Van Kemenade M. J. J. M. , D. B. P. L. (1987). "A Kinetic Study of Precipitation from Supersaturated Calcium Phosphate Solutions." *Journal of Colloid and Interface Science* **118**(2).

- von Bradke, M., F. Gitzhofer and R. Henne (2005). "Porosity determination of ceramic materials by digital image analysis--a critical evaluation." *scanning* **27**(3): 132-135.
- Wagh, A. S. (2004). *Chemically Bonded Phosphate Ceramics: Twenty-First Century Materials with Diverse Applications* Elsevier Science
- Wang, L. and G. H. Nancollas (2008). "Calcium orthophosphates: crystallization and dissolution." *Chem Rev* **108**(11): 4628-4669.
- Williams, D. F. (2008). "On the mechanisms of biocompatibility." *Biomaterials* **29**(20): 2941-2953.
- Williams, D. F. R., R. Maisels, D.O. (1973). *Implants in Surgery*. London, W. B. Saunders
- Xu, H. H., J. B. Quinn, S. Takagi and L. C. Chow (2002). "Processing and properties of strong and non-rigid calcium phosphate cement." *J Dent Res* **81**(3): 219-224.
- Xu, J., I. S. Butler and D. F. R. Gilson (1999). "FT-Raman and high-pressure infrared spectroscopic studies of dicalcium phosphate dihydrate (CaHPO<sub>4</sub>·2H<sub>2</sub>O) and anhydrous dicalcium phosphate (CaHPO<sub>4</sub>)." *Spectrochimica Acta Part A: Molecular and Biomolecular Spectroscopy* **55**(14): 2801-2809.
- Yang, Q., T. Troczynski and D. M. Liu (2002). "Influence of apatite seeds on the synthesis of calcium phosphate cement." *Biomaterials* **23**(13): 2751-2760.

# **APPENDIX A**

## **DETAILED MORPHOLOGICAL ANALYSES OF THE SAMPLES**

Table A.1. Morphological measurements done on the microstructure images of the samples

Sample		Mean Diameter		Maximum Diameter		Minimum Diameter		Aspect Ratio		Mean Area		Mean Perimeter		Length	Width	Roundness	Radius Ratio	
		$\mu\text{m}$	+/-	$\mu\text{m}$	+/-	$\mu\text{m}$	+/-		+/-	$\mu\text{m}^2$	+/-	$\mu\text{m}$	+/-	$\mu\text{m}$		+/-		
1	Mean	49.20	17.89	61.63	31.94	37.57	10.29	1.51	0.45	2048.47	1876.33	195.67	117.17	61.88	45.97	1.41	0.59	11.40
	Stdev	3.21		3.42		3.17		0.04		139.47		13.16		3.48	3.28	0.04		8.56
	Median	48.30		60.94		36.46		1.51		2035.49		193.63		60.98	45.16	1.40		9.40
2	Mean	68.45	32.82	87.82	47.50	53.06	24.07	1.63	0.46	4491.57	4449.76	269.37	140.47	88.44	61.49	1.53	0.35	2.50
	Stdev	11.33		14.88		9.28		0.10		1380.47		40.17		15.02	9.83	0.25		0.43
	Median	71.16		89.64		55.90		1.64		4037.18		273.32		90.11	63.22	1.47		2.34
3	Mean	76.00	35.81	97.43	49.91	61.04	28.85	1.59	0.51	5433.27	5266.01	295.91	145.24	94.53	69.89	1.46	0.29	2.34
	Stdev	16.27		20.79		13.15		0.08		1366.55		63.34		20.90	15.88	0.04		0.29
	Median	81.90		103.41		65.36		1.59		5651.46		313.02		102.72	75.10	1.47		2.38
4	Mean	60.71	38.58	81.25	59.84	44.68	26.86	1.67	0.52	4114.20	5553.02	276.19	231.09	81.92	57.12	1.91	0.91	9.71
	Stdev	14.02		18.84		9.94		0.09		1478.32		60.89		18.67	13.98	0.17		12.12
	Median	56.85		75.97		42.09		1.68		3816.96		258.30		76.60	53.20	1.87		5.51
5	Mean	50.43	25.83	66.09	41.51	37.79	18.09	1.71	0.55	2357.86	2878.06	208.28	142.34	66.90	45.96	1.61	0.56	6.92
	Stdev	3.89		5.59		3.63		0.10		280.07		17.21		5.59	3.52	0.06		4.56
	Median	50.33		66.48		37.72		1.70		2436.19		207.42		67.32	45.96	1.61		4.83
6	Mean	91.06	42.69	118.61	59.36	71.55	35.18	1.70	0.62	7878.82	7655.41	355.17	177.69	119.38	82.16	1.55	0.53	3.11
	Stdev	13.43		15.29		11.99		0.13		1791.21		39.18		15.25	12.11	0.24		1.76
	Median	93.67		121.39		74.22		1.67		7999.10		360.60		121.61	85.48	1.45		2.48
7	Mean	81.90	45.01	115.21	73.99	58.62	32.39	1.84	0.61	7125.27	8873.66	369.56	275.41	116.46	76.32	1.94	0.83	6.75
	Stdev	12.40		19.23		9.70		0.09		2054.64		59.65		19.05	11.90	0.25		4.01
	Median	82.69		118.37		59.28		1.82		6923.73		372.69		119.34	79.49	1.88		4.76
8	Mean	69.16	40.84	93.07	63.13	52.19	30.67	1.77	0.64	5179.52	6691.94	292.18	207.48	94.14	63.50	1.78	0.74	4.45
	Stdev	13.69		18.63		11.38		0.08		1676.70		55.76		18.76	12.49	0.20		2.50
	Median	72.36		99.88		53.70		1.79		5952.30		311.54		101.31	69.51	1.80		3.85
9	Mean	62.64	39.04	82.87	61.03	48.11	28.97	1.64	0.56	4751.12	6678.38	259.48	205.95	83.74	57.86	1.58	0.60	5.32
	Stdev	16.44		24.16		12.65		0.16		1498.51		70.79		24.72	14.73	0.13		4.22
	Median	68.08		88.20		54.01		1.61		4739.04		281.22		89.10	64.55	1.53		3.01
10	Mean	88.69	42.28	119.25	67.26	66.80	30.70	1.64	0.52	7681.78	6996.15	367.26	215.41	120.65	82.58	1.57	0.47	10.84
	Stdev	10.93		17.26		7.75		0.09		1492.26		55.50		17.82	11.48	0.12		15.86
	Median	84.37		110.10		66.44		1.64		7288.34		352.35		111.91	78.61	1.53		2.89

Continued on next page

Table A.1. (continued)

Sample		Mean Diameter		Maximum Diameter		Minimum Diameter		Aspect Ratio		Mean Area		Mean Perimeter		Length	Width	Roundness		Radius Ratio
			+/-		+/-		+/-		+/-		+/-		+/-					
11	Mean	47.40	23.76	60.29	35.06	36.14	16.88	1.71	0.58	2124.41	2751.44	183.35	102.28	60.97	41.91	1.49	0.39	3.95
	Stdev	4.22		5.12		4.21		0.05		350.81		15.76		5.23	3.82	0.04		1.76
	Median	46.90		60.58		34.81		1.72		2083.52		183.02		61.22	41.25	1.48		3.21
12	Mean	58.57	33.96	76.80	50.14	44.78	25.58	1.81	0.70	3540.07	5011.11	226.78	139.18	77.34	51.31	1.49	0.34	2.82
	Stdev	5.55		8.70		4.53		0.14		635.26		23.12		8.81	4.62	0.09		0.66
	Median	59.07		76.69		45.80		1.82		3795.17		228.44		77.12	52.84	1.48		2.67
13	Mean	58.85	24.53	76.68	36.37	45.37	19.81	1.74	0.59	3032.76	2619.33	231.82	106.47	77.65	52.77	1.55	0.37	3.00
	Stdev	4.26		5.46		3.90		0.05		385.38		19.65		5.47	4.24	0.06		0.64
	Median	57.88		76.24		43.95		1.73		2856.93		226.30		77.36	51.14	1.56		2.68
14	Mean	64.52	39.68	85.02	56.60	49.49	31.23	1.74	0.60	4463.60	6391.72	257.79	170.78	85.64	58.37	1.57	0.41	3.01
	Stdev	7.01		7.90		7.12		0.08		995.35		25.25		8.21	6.51	0.11		0.80
	Median	64.07		84.83		49.69		1.76		4801.94		259.31		85.63	57.82	1.54		2.91
15	Mean	70.40	40.73	95.19	62.33	53.11	30.97	1.72	0.66	5325.53	5699.23	293.86	200.60	95.65	65.21	1.59	0.54	3.60
	Stdev	14.51		21.56		11.56		0.10		1956.58		73.61		21.61	14.83	0.15		1.26
	Median	64.65		86.04		48.37		1.68		4762.44		259.23		86.69	58.18	1.60		3.32
16	Mean	106.9	31.56	144.01	44.81	81.79	27.74	1.78	0.62	9664.84	0.62	443.87	4915.9	145.07	95.46	1.72	31.1	2.83
	Stdev	11.61		16.64		10.11		0.20		1842.08		48.74		16.57	12.66	0.15		1.48
	Median	106.6		139.73		79.46		1.77		9534.76		425.72		141.06	90.24	1.72		2.34
17	Mean	59.63	19.22	79.00	30.22	45.39	15.48	1.85	0.65	2845.80	1778.45	231.29	81.74	79.98	51.90	1.50	0.32	2.80
	Stdev	4.35		5.76		3.55		0.08		295.48		16.86		5.90	3.18	0.04		0.31
	Median	59.19		77.93		44.93		1.83		2845.43		228.60		79.13	51.34	1.51		2.78
18	Mean	84.49	46.69	117.20	70.86	62.63	36.56	2.00	0.81	7358.15	7201.92	354.54	213.72	118.29	75.35	1.95	0.86	10.95
	Stdev	11.68		13.36		10.52		0.35		1294.59		35.30		13.02	10.50	0.36		15.27
	Median	86.35		118.11		65.13		1.93		7365.78		358.81		119.34	78.05	1.86		3.76
19	Mean	65.67	34.13	86.01	49.06	51.03	26.28	1.74	0.70	4102.07	4493.25	253.27	139.50	86.74	57.71	1.50	0.53	2.83
	Stdev	4.86		6.05		4.24		0.11		416.61		19.64		6.40	4.22	0.11		1.09
	Median	64.75		84.98		50.57		1.74		4041.48		251.92		85.45	57.30	1.48		2.52
20	Mean	63.87	35.67	84.44	54.17	48.97	26.30	1.68	0.52	4120.50	4918.87	254.72	165.61	85.28	58.01	1.49	0.42	2.97
	Stdev	7.67		9.47		6.71		0.06		956.19		31.34		9.27	7.43	0.09		0.53
	Median	64.05		86.98		48.23		1.70		4142.15		260.00		87.27	58.86	1.48		2.94
21	Mean	101.4	65.27	140.99	113.4	74.23	43.90	1.62	0.52	12619.84	17368.9	472.42	444.71	142.91	98.55	1.80	0.86	3.60
	Stdev	14.44		22.25		11.24		0.12		3041.32		74.11		22.20	13.67	0.23		1.13
	Median	99.14		134.61		72.46		1.63		13127.74		479.16		137.29	96.21	1.76		3.82

Continued on next page



Table A.1. (continued)

Sample		Mean Diameter		Maximum Diameter		Minimum Diameter		Aspect Ratio		Mean Area		Mean Perimeter		Length	Width	Roundness		Radius Ratio
			+/-		+/-		+/-		+/-		+/-		+/-				+/-	
22	Mean	50.74	36.25	66.56	51.16	39.18	28.49	1.84	0.77	3019.65	5047.38	207.00	149.58	67.59	45.74	1.91	0.74	2.63
	Stdev	6.13		9.40		4.86		0.17		701.52		26.94		9.59	5.15	0.16		0.24
	Median	51.57		67.29		39.95		1.80		3195.95		208.23		68.23	46.42	1.88		2.53
23	Mean	49.38	23.92	64.81	38.49	37.07	16.97	1.69	0.54	2394.26	2507.81	209.53	128.85	65.30	45.64	1.75	0.64	7.39
	Stdev	4.18		6.67		4.34		0.10		428.24		25.66		6.71	4.29	0.20		8.62
	Median	50.39		65.75		36.07		1.68		2333.93		209.57		66.06	46.79	1.77		4.06
24	Mean	50.47	26.12	64.22	37.88	40.12	20.82	1.66	0.53	2464.63	3072.91	194.61	106.95	64.75	45.46	1.49	0.37	2.54
	Stdev	6.61		9.33		5.73		0.09		599.96		26.66		9.32	5.84	0.12		0.38
	Median	49.92		61.07		40.79		1.65		2911.15		181.81		61.23	44.70	1.50		2.40
25	Mean	63.18	39.33	87.51	63.89	45.60	26.31	1.87	0.70	4712.20	8036.66	272.07	222.88	89.26	58.26	1.73	0.57	6.31
	Stdev	7.85		13.03		5.70		0.12		1965.16		51.79		13.80	9.35	0.15		7.07
	Median	62.99		84.94		43.76		1.87		4523.58		260.76		86.32	57.21	1.67		4.13
26	Mean	102.4	46.47	134.74	65.76	80.99	37.75	1.65	0.48	10334.33	9168.09	394.46	185.98	135.55	91.25	1.46	0.31	2.28
	Stdev	26.45		34.22		22.08		0.11		4202.39		89.36		33.98	22.79	0.15		0.33
	Median	108.6		140.97		86.34		1.67		11382.58		413.63		140.96	96.45	1.43		2.34
27	Mean	50.23	35.26	69.55	59.09	36.38	25.09	1.86	0.66	3067.00	5579.90	239.68	238.36	70.79	47.04	2.30	1.33	8.59
	Stdev	5.04		8.82		3.69		0.07		753.57		48.20		8.76	5.47	0.38		7.62
	Median	49.09		67.40		35.67		1.86		2811.24		228.91		68.70	45.90	2.29		5.63
28	Mean	42.77	22.14	55.68	35.00	31.51	16.20	1.84	0.62	1752.88	2461.34	175.15	108.41	56.56	38.76	1.78	0.75	6.73
	Stdev	3.74		4.39		3.24		0.05		235.92		15.81		4.38	3.66	0.06		3.05
	Median	41.15		54.44		30.03		1.83		1665.99		169.81		55.22	37.12	1.78		5.51
29	Mean	45.19	20.33	59.62	30.25	32.86	16.19	1.89	0.67	1854.49	2187.56	195.66	106.57	60.63	41.24	2.14	1.06	5.41
	Stdev	3.74		4.24		3.54		0.06		281.93		13.89		4.25	3.44	0.19		2.20
	Median	43.53		57.83		31.64		1.88		1793.79		194.74		58.80	40.15	2.13		5.16
30	Mean	60.58	29.66	80.68	43.33	44.95	23.52	1.80	0.60	3594.44	3513.79	260.09	147.78	82.26	56.17	2.12	1.06	5.61
	Stdev	15.62		19.98		13.27		0.10		1480.11		52.57		20.22	14.18	0.42		2.77
	Median	51.24		69.14		36.44		1.81		2703.32		228.77		70.35	47.84	2.10		5.40
31	Mean	56.46	28.21	76.79	42.05	40.81	21.96	1.83	0.59	3027.93	3238.71	263.89	150.98	78.33	53.10	2.53	1.32	6.12
	Stdev	4.67		4.71		4.50		0.11		403.93		23.97		4.84	4.76	0.30		2.66
	Median	54.61		75.91		39.70		1.80		2907.74		253.93		77.12	52.36	2.57		5.42
32	Mean	75.64	44.29	101.76	63.99	57.59	34.86	1.82	0.68	6018.93	7139.31	312.12	196.58	102.73	67.62	1.75	0.60	2.74
	Stdev	8.90		10.89		7.79		0.10		1337.22		28.86		10.64	7.46	0.14		0.60
	Median	78.40		104.73		59.08		1.86		6455.34		320.17		104.97	69.54	1.73		2.50

Continued on next page

Table A.1. (continued)

Sample		Mean Diameter		Maximum Diameter		Minimum Diameter		Aspect Ratio		Mean Area		Mean Perimeter		Length	Width	Roundness		Radius Ratio
			+/-		+/-		+/-		+/-		+/-		+/-					
33	Mean	57.02	32.58	75.66	50.33	43.05	24.17	1.78	0.56	3527.36	5186.39	231.21	151.72	76.57	51.59	1.68	0.53	3.64
	Stdev	12.40		16.57		10.13		0.09		1368.05		47.63		16.40	11.46	0.15		0.91
	Median	62.81		84.33		45.41		1.79		4081.56		257.26		85.33	56.01	1.67		3.57
34	Mean	52.68	23.63	69.33	36.16	39.89	17.68	1.78	0.59	2472.71	2319.03	213.22	104.80	70.09	47.50	1.69	0.46	3.25
	Stdev	5.38		6.35		5.01		0.06		295.41		19.45		6.33	4.78	0.08		0.26
	Median	52.69		70.27		39.00		1.77		2543.90		213.96		70.99	47.20	1.72		3.27
35	Mean	89.08	41.28	122.81	63.14	67.53	31.42	1.83	0.66	7831.73	8593.50	359.42	184.98	124.49	79.59	1.57	0.36	2.83
	Stdev	10.65		18.00		6.94		0.12		3123.66		53.50		19.45	11.23	0.08		0.43
	Median	83.85		114.92		64.34		1.84		6450.38		339.44		116.12	74.36	1.55		2.66
36	Mean	66.00	33.66	88.36	51.14	50.13	25.01	1.79	0.64	4205.24	4732.12	264.99	149.28	89.28	59.02	1.62	0.46	3.40
	Stdev	7.89		10.95		5.77		0.08		891.22		33.88		10.98	7.53	0.04		1.21
	Median	68.24		91.99		51.05		1.83		3998.18		268.70		93.11	58.62	1.61		2.82
37	Mean	64.76	42.26	84.06	60.62	51.02	33.01	1.64	0.49	4728.67	6304.58	253.04	174.32	84.81	58.93	1.51	0.35	2.46
	Stdev	13.40		20.00		10.17		0.12		1561.45		57.48		20.17	12.13	0.10		0.68
	Median	64.46		81.85		48.65		1.64		4578.31		248.14		82.44	59.07	1.52		2.22
38	Mean	63.40	38.87	83.22	56.93	48.72	29.99	1.71	0.56	4253.75	5730.86	252.04	165.77	84.21	57.63	1.55	0.40	3.16
	Stdev	7.26		7.83		7.64		0.14		722.29		22.18		7.76	7.09	0.12		0.98
	Median	61.36		82.32		47.27		1.72		4397.71		249.18		83.20	56.28	1.54		3.00

Table A.2. Morphological properties of all sample sets derived from basic morphological measurements

Sample		Total Area	Total Perimeter	3 Highest Areas	%	3 Highest Perimeters	%	Number of Pores	Macroporosity	Expected Macroporosity	Effectiveness Factor
		$\mu\text{m}^2$	$\mu\text{m}$	$\mu\text{m}^2$		$\mu\text{m}$			%	%	
1	Mean	250588	23969	30135	15.59	1927	10.17	122.6	40.38	39.96	220.13
	Stdev	17163	1692	5510	3.17	346	1.93	8.2	2.77		
	Median	244268	23626	29918	14.93	1871	9.98	125.5	39.36		
2	Mean	114934	7583	39433	41.01	1485	25.72	27.4	18.52	41.05	3.82
	Stdev	23066	1557	13187	11.31	245	6.88	8.3	3.72		
	Median	121235	7220	39087	44.21	1475	27.81	26.0	19.53		
3	Mean	184596	10130	56179	34.34	1745	20.09	37.9	29.74	37.02	14.97
	Stdev	22259	1260	10943	6.05	229	3.28	17.5	3.59		
	Median	192411	10738	60097	32.71	1859	19.80	34.0	31.00		
4	Mean	208716	14410	65064	35.29	2710	21.12	57.3	33.63	40.20	289.83
	Stdev	19618	2349	10956	4.02	962	3.52	20.5	3.16		
	Median	210792	13843	64945	35.63	2312	19.80	55.5	33.96		
5	Mean	166615	15120	37568	27.78	1834	15.67	71.5	26.85	38.01	64.24
	Stdev	21288	1854	8293	6.25	417	4.01	11.3	3.43		
	Median	166652	15104	36806	28.62	1739	16.92	73.5	26.85		
6	Mean	366210	16919	85080	25.68	2237	15.18	48.0	59.01	37.75	138.82
	Stdev	43334	1613	21082	4.72	266	2.60	7.9	6.98		
	Median	360968	16908	76625	26.66	2265	15.53	50.0	58.16		
7	Mean	320347	17387	98460	34.16	3137	20.74	48.7	51.62	34.00	587.71
	Stdev	31391	2579	25988	8.02	714	5.34	13.6	5.06		
	Median	317033	17287	102585	34.84	3027	22.16	47.5	51.08		
8	Mean	293635	17085	78650	30.16	2488	17.06	63.1	47.31	38.28	227.15
	Stdev	58734	3347	29519	8.40	896	5.86	23.7	9.46		
	Median	299769	17734	62221	28.22	2059	15.91	55.5	48.30		
9	Mean	172934	10334	65121	42.92	2235	25.71	40.0	27.86	37.48	70.44
	Stdev	21220	1070	14418	6.43	597	5.72	12.2	3.42		
	Median	162474	10695	64672	46.02	2186	25.33	37.0	26.18		
10	Mean	214205	10401	67253	35.17	2299	25.16	28.7	34.51	36.63	127.84
	Stdev	31128	1597	11445	4.56	446	3.60	6.1	5.02		
	Median	224177	10883	67346	35.91	2369	25.64	31.0	36.12		
11	Mean	145443	12995	35876	32.68	1437	14.67	70.4	23.44	37.59	19.54
	Stdev	12977	1372	10310	8.40	139	2.74	11.5	2.09		
	Median	145013	12689	33274	30.30	1420	15.10	71.5	23.37		

Continued on next page

Table A.2. (continued)

Sample		Total Area	Total Perimeter	3 Highest Areas	%	3 Highest Perimeters	%	Number of Pores	Macroporosity	Expected Macroporosity	Effectiveness Factor
12	Mean	142355	9389	53764	45.68	1792	23.61	42.1	22.94	38.38	18.10
	Stdev	12458	1302	9833	6.74	431	5.38	10.3	2.01		
	Median	137723	9480	52646	46.84	1723	23.48	40.0	22.19		
13	Mean	149435	11488	29683	24.30	1127	12.06	50.1	24.08	36.58	4.57
	Stdev	10638	1026	6717	5.29	315	4.06	6.9	1.71		
	Median	149213	11629	30447	22.94	1092	12.02	51.5	24.04		
14	Mean	159992	9644	62778	46.31	1908	25.12	37.5	25.78	36.36	26.06
	Stdev	23801	1896	19772	15.61	180	8.82	8.8	3.84		
	Median	148553	10458	68246	42.72	1888	21.48	38.5	23.94		
15	Mean	132361	7727	49525	43.59	1836	29.37	27.9	21.33	35.96	11.79
	Stdev	31144	1642	15841	11.44	558	11.15	9.4	5.02		
	Median	135652	7831	45916	45.77	1687	23.72	29.0	21.86		
16	Mean	103961	4814	42934	45.81	1596	36.56	11.1	16.75	35.19	0.52
	Stdev	8561	575	3613	5.12	173	5.33	2.02	1.38		
	Median	102255	4753	42730	45.55	1571	35.47	11.5	16.48		
17	Mean	159361	12924	20359	15.65	1054	9.89	56.5	25.68	34.31	2.46
	Stdev	15064	1305	3249	2.20	65	1.07	7.4	2.43		
	Median	154888	12849	21313	15.80	1053	9.81	54.5	24.96		
18	Mean	201058	9871	67998	37.37	2106	23.93	28.38	32.40	36.54	104.04
	Stdev	31558	2089	16648	3.80	579	2.67	7.60	5.08		
	Median	190829	9431	69505	38.84	1971	24.44	29.00	30.75		
19	Mean	180407	11199	47818	30.94	1585	16.99	44.5	29.07	39.00	16.78
	Stdev	15381	1221	9437	5.93	214	2.81	6.3	2.48		
	Median	177737	11231	46970	29.03	1518	16.16	44.0	28.64		
20	Mean	153904	9654	36130	26.44	1370	17.36	39.2	24.80	35.46	6.35
	Stdev	17631	1020	25431	18.28	695	9.79	8.5	2.84		
	Median	154687	9988	42280	32.72	1461	18.72	36.0	24.92		
21	Mean	247025	9452	133839	59.00	3792	43.54	20.4	39.80	38.43	187.91
	Stdev	39875	1318	43633	10.56	1225	9.51	4.2	6.42		
	Median	242736	9497	129115	62.07	3214	45.34	21.0	39.11		
22	Mean	198985	14077	63258	38.93	2346	20.74	67.7	32.06	38.31	68.78
	Stdev	38025	1770	15598	6.32	1445	10.43	10.8	6.13		
	Median	206713	13851	59033	38.34	1936	18.32	73.0	33.31		
23	Mean	227354	20630	34933	20.23	1708	10.65	95.3	36.63	31.16	103.85
	Stdev	39020	2955	14382	6.01	568	3.02	10.9	6.29		
	Median	227080	20634	31314	19.89	1551	11.75	95.0	36.59		

Continued on next page

Table A.2. (continued)

Sample		Total Area	Total Perimeter	3 Highest Areas	%	3 Highest Perimeters	%	Number of Pores	Macroporosity	Expected Macroporosity	Effectiveness Factor
24	Mean	107541	8427	25682	31.10	1115	17.24	45.3	17.33	35.91	2.23
	Stdev	24240	1476	14926	16.59	326	6.78	11.6	3.91		
	Median	105230	7874	21045	32.33	1135	17.27	47.0	16.96		
25	Mean	233504	14290	88179	43.30	2669	22.77	54.0	37.62	35.73	288.76
	Stdev	41508	2132	46188	15.14	1016	10.81	11.8	6.69		
	Median	225355	14525	78329	40.49	2258	19.27	54.0	36.31		
26	Mean	203373	7633	79934	42.53	2070	27.88	24.5	32.77	37.73	15.14
	Stdev	42331	1664	25805	6.66	292	5.76	15.5	6.82		
	Median	208042	7551	83865	41.49	2187	26.75	20.5	33.52		
27	Mean	259944	20752	79734	37.26	3036	17.98	90.3	41.88	38.27	757.13
	Stdev	18798	2467	19301	8.33	1176	8.01	22.1	3.03		
	Median	259248	19706	79297	36.79	2535	15.36	91.0	41.77		
28	Mean	251573	25616	43472	24.61	1748	9.11	145.8	40.54	36.43	202.71
	Stdev	23316	2824	10452	5.26	173	1.77	18.8	3.76		
	Median	243467	25022	40541	23.72	1731	8.80	148.0	39.23		
29	Mean	157403	17229	29601	26.47	1401	10.95	87.2	25.36	36.91	28.73
	Stdev	21379	2802	11275	9.67	240	3.62	18.1	3.44		
	Median	153843	18244	25274	22.97	1403	11.57	93.5	24.79		
30	Mean	211884	17128	41756	23.56	1790	13.19	70.8	34.14	36.92	63.68
	Stdev	28433	3994	10509	6.15	535	4.20	28.2	4.58		
	Median	197342	18526	41589	24.61	1572	11.89	73.0	31.80		
31	Mean	201618	17406	40151	24.49	1736	11.72	68.0	32.49	34.99	64.26
	Stdev	14112	2083	4897	3.82	169	2.11	11.1	2.27		
	Median	200828	18444	39663	24.13	1781	11.54	68.0	32.36		
32	Mean	250649	13297	74973	33.75	2199	19.21	43.6	40.39	39.01	65.63
	Stdev	24718	1461	19948	7.56	380	4.26	9.2	3.98		
	Median	246665	13565	74376	35.65	2180	19.35	41.0	39.74		
33	Mean	186959	13314	58341	36.77	1881	17.61	62.0	30.12	35.88	51.41
	Stdev	34121	1676	23724	9.86	435	5.41	22.7	5.50		
	Median	188379	12924	57686	35.07	1815	15.83	55.5	30.35		
34	Mean	180253	15635	29062	20.92	1269	10.20	73.0	29.04	37.80	12.49
	Stdev	24969	1800	3469	4.77	57	1.37	6.8	4.02		
	Median	166611	14815	29056	21.17	1257	10.38	73.5	26.85		
35	Mean	270572	12918	72464	28.41	2173	19.52	36.8	43.60	N/A	53.07
	Stdev	52837	1542	63639	16.60	667	6.70	7.7	8.51		
	Median	252786	12141	58128	25.56	1917	18.12	36.0	40.73		

Continued on next page

Table A.2. (continued)

<b>Sample</b>		<b>Total Area</b>	<b>Total Perimeter</b>	<b>3 Highest Areas</b>	<b>%</b>	<b>3 Highest Perimeters</b>	<b>%</b>	<b>Number of Pores</b>	<b>Macroporosity</b>	<b>Expected Macroporosity</b>	<b>Effectiveness Factor</b>
36	Mean	209265	13138	53308	29.52	1848	16.25	51.4	33.72	36.34	40.05
	Stdev	29662	1334	13712	5.53	414	2.53	10.3	4.78		
	Median	199223	13499	45957	29.58	1720	16.26	52.0	32.10		
37	Mean	154628	8472	59469	44.06	1796	25.51	36.2	24.92	39.95	15.13
	Stdev	19416	994	13173	8.25	322	6.10	11.1	3.13		
	Median	158601	8265	59969	46.53	1732	26.58	37.0	25.56		
38	Mean	217629	13013	66541	36.26	1993	18.57	51.4	35.07	38.35	59.47
	Stdev	35881	1544	11677	6.31	185	2.60	5.8	5.78		
	Median	227121	13685	68888	37.28	1990	18.38	51.0	36.60		

## A.1. Morphological Analysis of Sample Set 1

Unique porogen size distribution of sample 1 that is concentrated at the finer side results in a double sequential void filling mechanism as indicated by the high effectiveness factor in Table A.4. Shear abundance of porogens given in Table A.3 formed interconnected pores as seen in Fig.A.1(c-f).

Table A.3. Size distributions of NaCl porogens added into the sample

	-38 $\mu\text{m}$ size group	-53 $\mu\text{m}$ size group	-75 $\mu\text{m}$ size group	-106 $\mu\text{m}$ size group	-150 $\mu\text{m}$ size group	-212 $\mu\text{m}$ size group	Total
By mass (gr)	1.308	0.968	0	0	0	0	2.276
By number	11010287	3002988	0	0	0	0	14013275

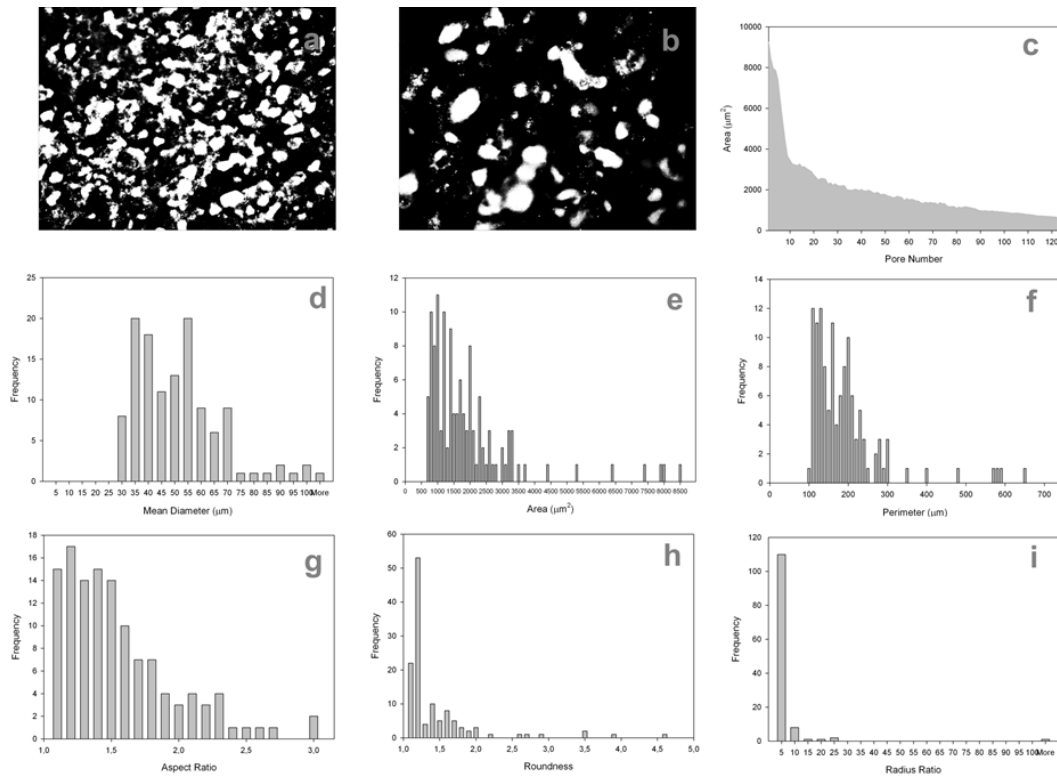


Figure A.1. Representative micrograph taken at 50x magnification (a), random micrograph taken at 100x magnification showing the interaction of pores in detail (b), area distribution (c), size distribution (d), area histogram (e), perimeter distribution (f), aspect ratio distribution (g), roundness distribution (h), radius ratio distribution (i) of pores of the representative sample.

Table A.4. Overall morphological properties of the sample

Total Area ( $\mu\text{m}^2$ )	Total Perimeter ( $\mu\text{m}$ )	3 Highest Areas ( $\mu\text{m}^2$ )	3 Highest Perimeters (%)	3 Highest Perimeters ( $\mu\text{m}$ )	Pore Count	Macro-porosity (%)	Expected Macroporosity (%)	Effectiveness Factor	
250588	23969	30135	16	1927	10	123	40.38	39.96	220.13

## A.2. Morphological Analysis of Sample Set 2

Balanced size distribution seen in Table A.5 with the exception of -75  $\mu\text{m}$  size group is expected to result in some degree of interconnectivity. The low effectiveness factor seen in Table A.6 is due to experimental limitations as low contrast image disabled the detection of fine pores as seen in Fig.A.2(d)

Table A.5 Size distributions of NaCl porogens added into the sample

	-38 $\mu\text{m}$ size group	-53 $\mu\text{m}$ size group	-75 $\mu\text{m}$ size group	-106 $\mu\text{m}$ size group	-150 $\mu\text{m}$ size group	-212 $\mu\text{m}$ size group	Total
By mass (gr)	0.467	0.443	0.000	0.467	0.467	0.467	2.311
By number	3929214	1375791	0	181025	63883	22628	5572541

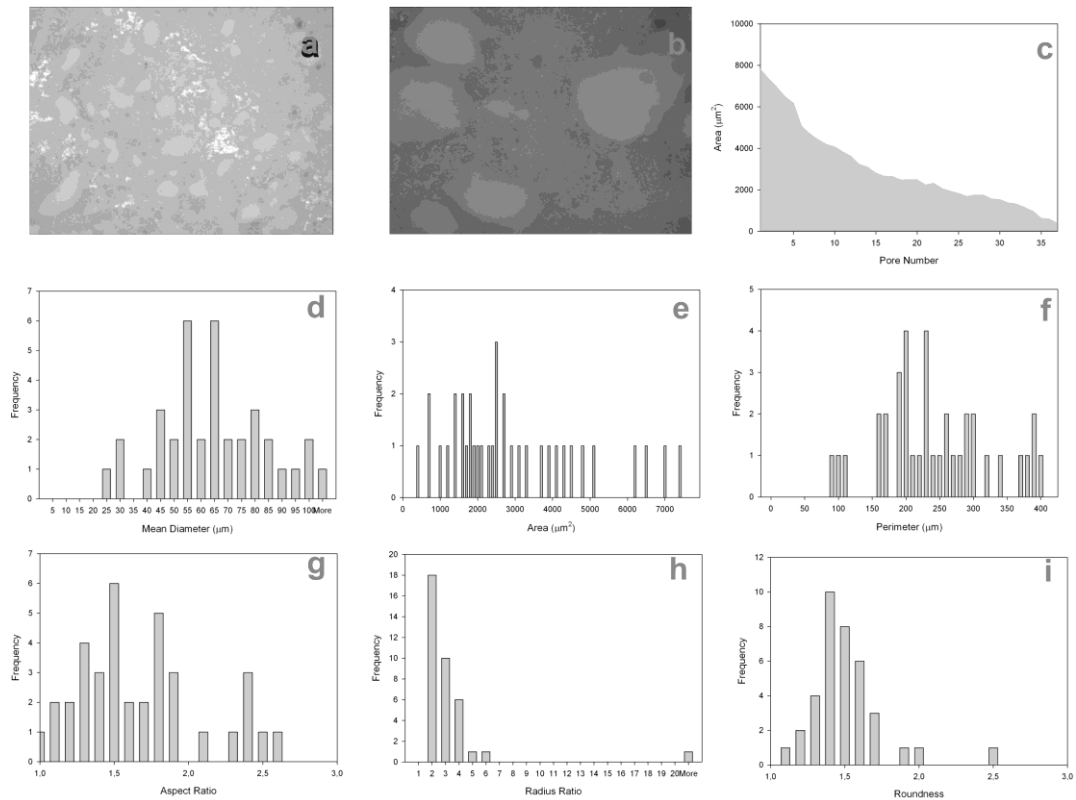


Figure A.2. Representative micrograph taken at 50x magnification (a), random micrograph taken at 100x magnification showing the interaction of pores in detail (b), area distribution (c), size distribution (d), area histogram (e), perimeter distribution (f), aspect ratio distribution (g), roundness distribution (h), radius ratio distribution (i) of pores of the representative sample.

Table A.6. Overall morphological properties of the sample

Total Area ( $\mu\text{m}^2$ )	Total Perimeter ( $\mu\text{m}$ )	3 Highest Areas ( $\mu\text{m}^2$ )	3 Highest Perimeters ( $\mu\text{m}$ )	Pore Count	Macro- porosity %	Expected Macroporosity %	Effectiveness Factor
114934	7583	39433	1485	27	18.52	41.05	3.82



### A.3. Morphological Analysis of Sample Set 3

Absence of fine porogens produced the low number of pores seen in Table A.7 that resulted in close pores without a significant void filling mechanism as seen in Fig.A.3(a-b). Directional coagulation around coarse porogens are rather seen due to the interaction between close size groups. High aspect ratio seen in Fig.A.3(g-i) are due to angular coarse porogen morphology.

Table A.7. Size distributions of NaCl porogens added into the sample

	-38 $\mu\text{m}$ size group	-53 $\mu\text{m}$ size group	-75 $\mu\text{m}$ size group	-106 $\mu\text{m}$ size group	-150 $\mu\text{m}$ size group	-212 $\mu\text{m}$ size group	Total
By mass (gr)	0.046	0.000	0.179	0.855	0.119	0.712	1.912
By number	391137	0	196228	331574	16352	34496	969787

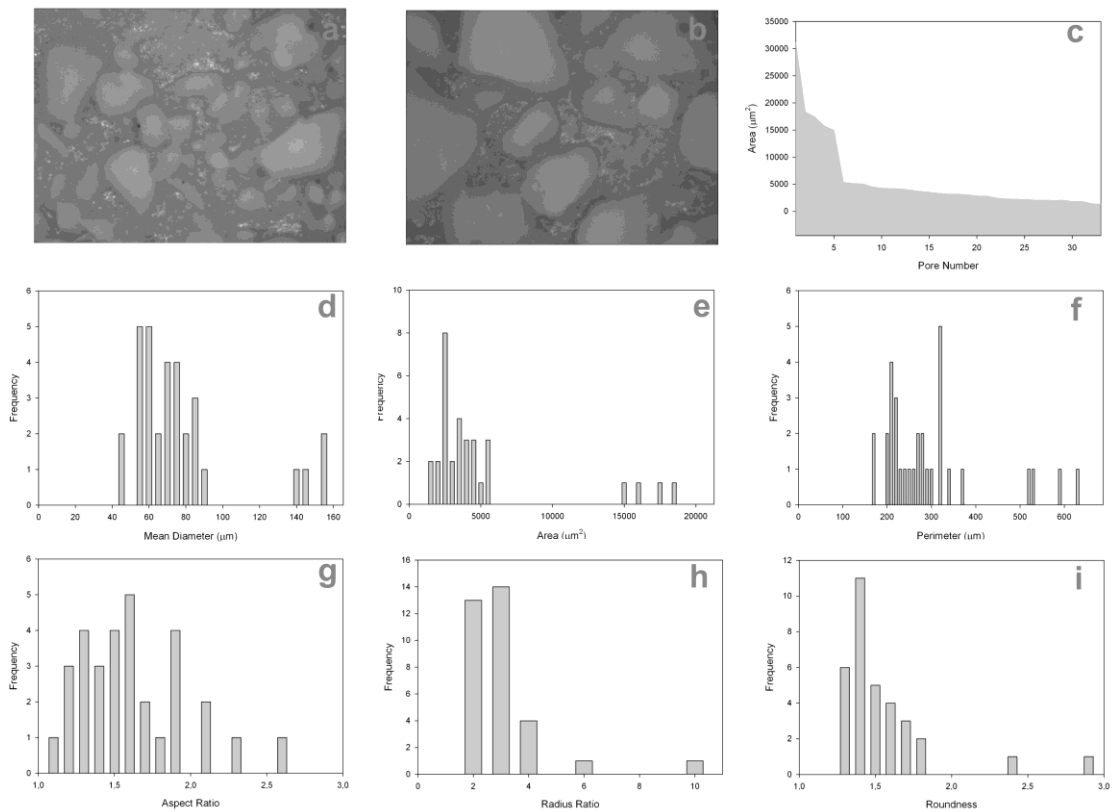


Figure A.3. Representative micrograph taken at 50x magnification (a), random micrograph taken at 100x magnification showing the interaction of pores in detail (b), area distribution (c), size distribution (d), area histogram (e), perimeter distribution (f), aspect ratio distribution (g), roundness distribution (h), radius ratio distribution (i) of pores of the representative sample.

Table A.8. Overall morphological properties of the sample

Total Area ( $\mu\text{m}^2$ )	Total Perimeter ( $\mu\text{m}$ )	3 Highest Areas ( $\mu\text{m}^2$ )	3 Highest Perimeters (%)	Pore Count	Macro-porosity (%)	Expected Macroporosity (%)	Effectiveness Factor		
184596	10130	56179	34	1745	20	38	29.74	37.02	14.97

## A.4. Morphological Analysis of Sample Set 4

The sequenced presence of fine, intermediate and coarse porogens seen in Table A.9 resulted in an interconnected pore morphology seen in Fig.A.4(a) that is indicated by the high effectiveness factor given in Table A.10. Low roundness, high aspect and radius ratio seen in Fig.A.4(g-i) confirm it.

Table A.9. Size distributions of NaCl porogens added into the sample

	-38 $\mu\text{m}$ size group	-53 $\mu\text{m}$ size group	-75 $\mu\text{m}$ size group	-106 $\mu\text{m}$ size group	-150 $\mu\text{m}$ size group	-212 $\mu\text{m}$ size group	Total
By mass (gr)	0.537	0.000	0.537	0.537	0.000	0.537	2.146
By number	4516306	0	587423	208074	0	26009	5337812

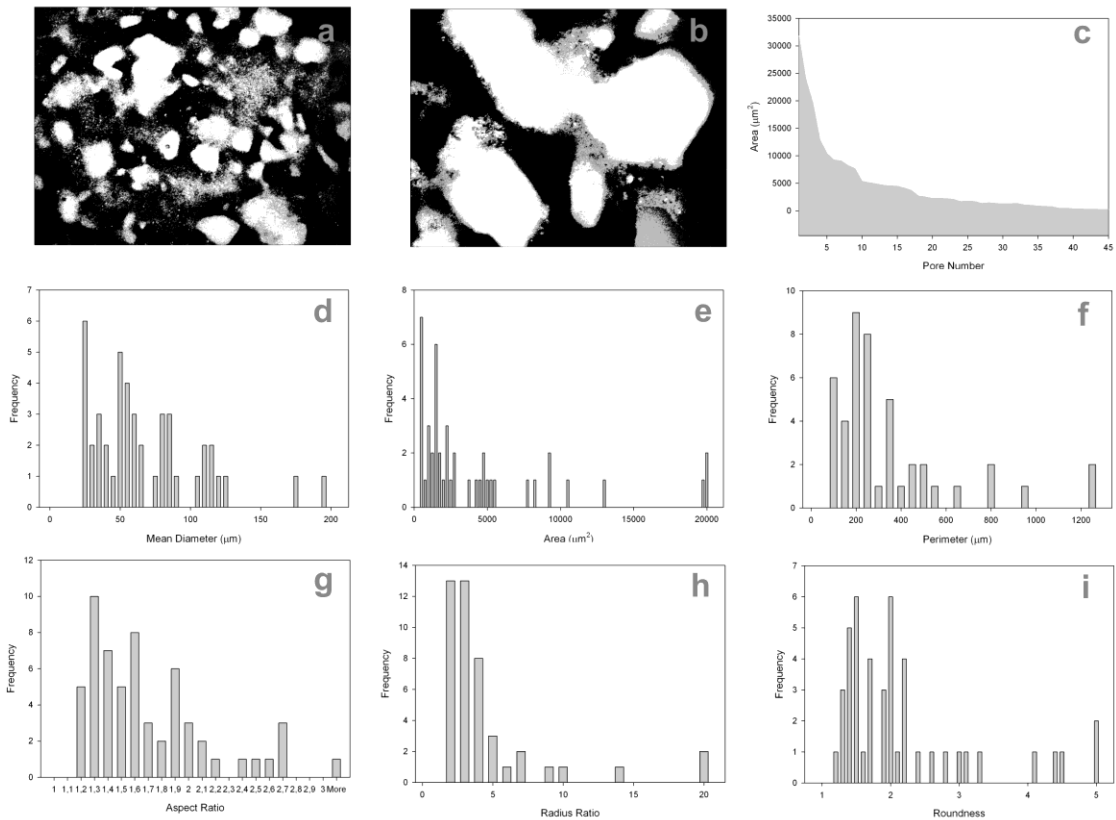


Figure A.4. Representative micrograph taken at 50x magnification (a), random micrograph taken at 100x magnification showing the interaction of pores in detail (b), area distribution (c), size distribution (d), area histogram (e), perimeter distribution (f), aspect ratio distribution (g), radius ratio distribution (h), roundness distribution (i) of pores of the representative sample.

Table A.10. Overall morphological properties of the sample

Total Area ( $\mu\text{m}^2$ )	Total Perimeter ( $\mu\text{m}$ )	3 Highest Areas ( $\mu\text{m}^2$ )	3 Highest Perimeters ( $\mu\text{m}$ )	Pore Count	Macro-porosity %	Expected Macroporosity %	Effectiveness Factor
208716	14410	65064	2710	57	33.63	40.20	289.83

## A.5. Morphological Analysis of Sample Set 5

Balanced porogen distribution without the -212  $\mu\text{m}$  size group given in Table A.11 resulted in some degree of interconnectivity indicated by the medium effectiveness factor given in Table A.12. Macroporosity was not close to the expected value due to partial detection of the abundant finest pores as seen in Fig.A.5(a).

Table A.11. Size distributions of NaCl porogens added into the sample

	-38 $\mu\text{m}$ size group	-53 $\mu\text{m}$ size group	-75 $\mu\text{m}$ size group	-106 $\mu\text{m}$ size group	-150 $\mu\text{m}$ size group	-212 $\mu\text{m}$ size group	Total
By mass (gr)	0.592	0.263	0.592	0.184	0.367	0.000	1.998
By number	4983490	817366	648188	71175	50235	0	6570455

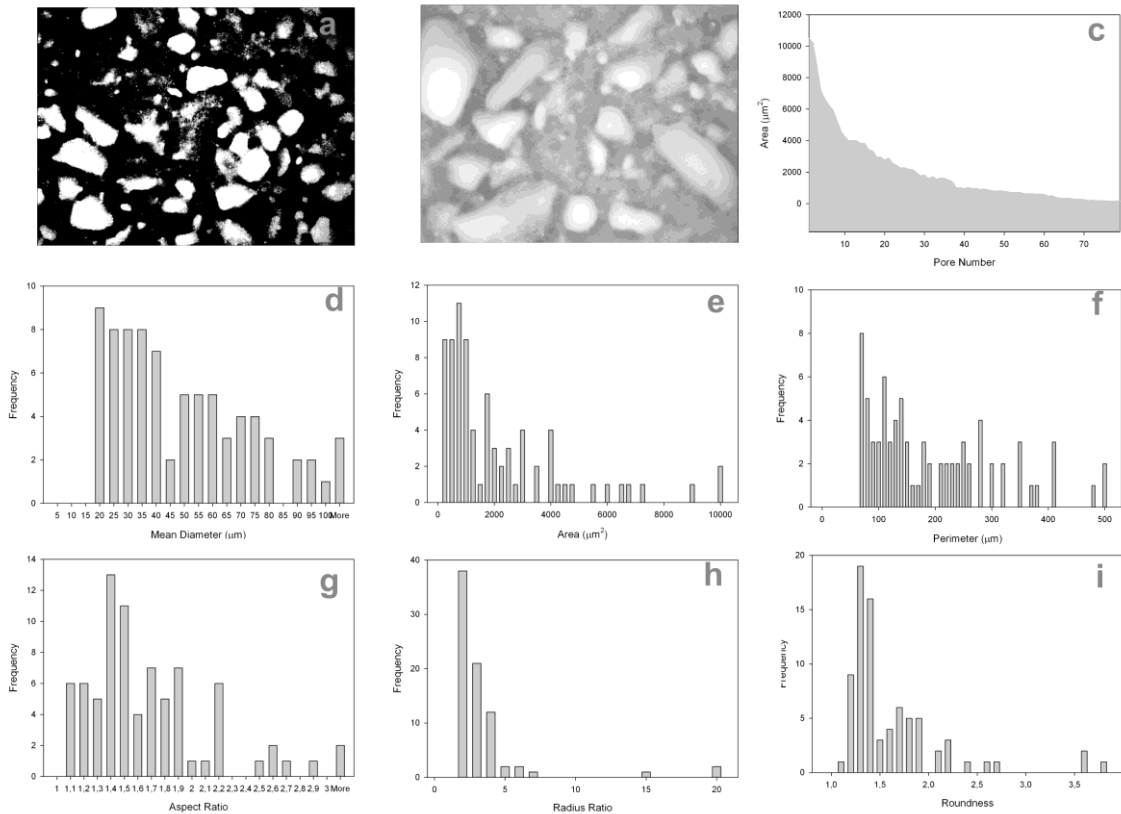


Figure A.5. Representative micrograph taken at 50x magnification (a), random micrograph taken at 100x magnification showing the interaction of pores in detail (b), area distribution (c), size distribution (d), area distribution (e), perimeter distribution (f), aspect ratio distribution (g), radius ratio distribution (h), roundness distribution (i) of pores of the representative sample.

Table A.12. Overall morphological properties of the sample

Total Area ( $\mu\text{m}^2$ )	Total Perimeter ( $\mu\text{m}$ )	3 Highest Areas ( $\mu\text{m}^2$ )	3 Highest Perimeters ( $\mu\text{m}$ )	Macro-porosity %	Expected Macroporosity %	Effectiveness Factor
166615	15120	37568	1834	26.85	38.01	64.24

## A.6. Morphological Analysis of Sample Set 6

Comparable numbers of fine porogens in the balanced size distribution seen in Table A.13 resulted in an effective void filling mechanism responsible for well packed pore structure seen in Fig.A.6(a,b). The large increase in macroporosity given in Table A.14 may be partly due to the heterogeneous distribution of well packed pore regions around the sample surface.

Table A.13. Size distributions of NaCl porogens added into the sample

	-38 $\mu\text{m}$ size group	-53 $\mu\text{m}$ size group	-75 $\mu\text{m}$ size group	-106 $\mu\text{m}$ size group	-150 $\mu\text{m}$ size group	-212 $\mu\text{m}$ size group	Total
By mass (gr)	0.119	0.261	0.000	0.380	0.745	0.399	1.904
By number	1003413	809005	0	147355	101962	19322	2081057

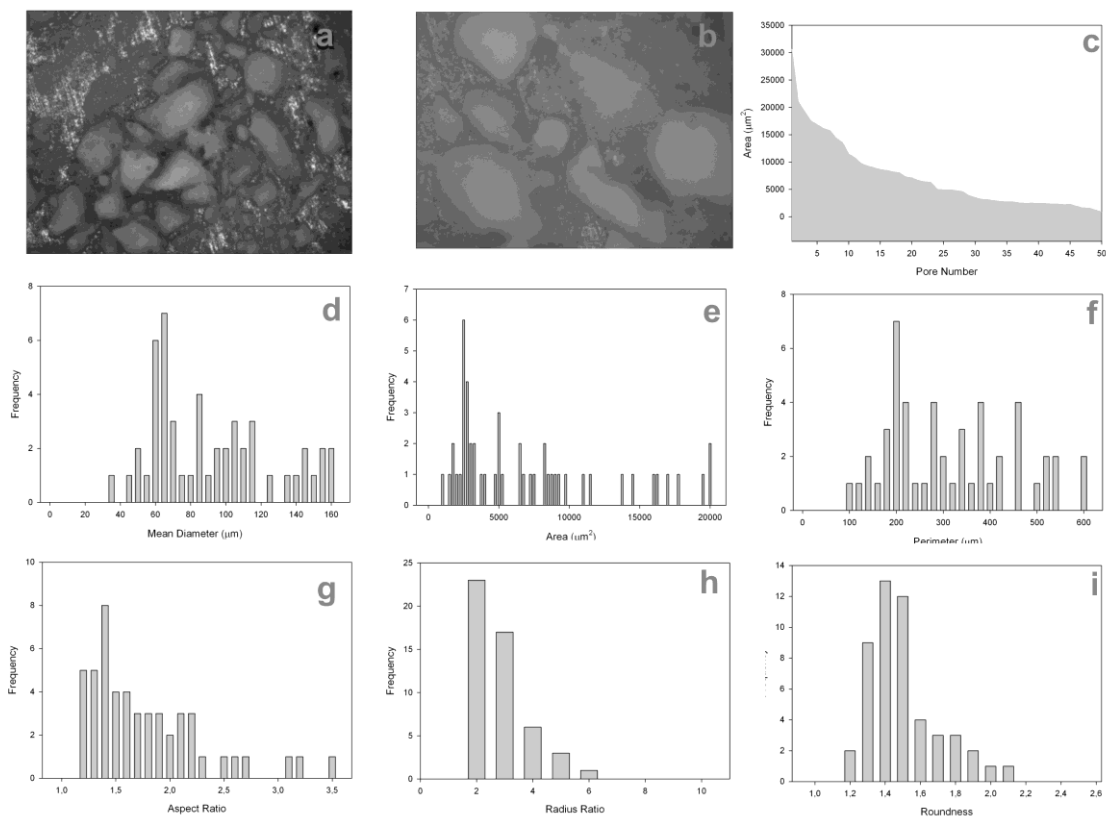


Figure A.6. Representative micrograph taken at 50x magnification (a), random micrograph taken at 100x magnification showing the interaction of pores in detail (b), area distribution (c), size distribution (d), area histogram (e), perimeter distribution (f), aspect ratio distribution (g), roundness distribution (h), radius ratio distribution (i) of pores of the representative sample.

Table A.14. Overall morphological properties of the sample

Total Area ( $\mu\text{m}^2$ )	Total Perimeter ( $\mu\text{m}$ )	3 Highest Areas ( $\mu\text{m}^2$ )	3 Highest Perimeters ( $\mu\text{m}$ )	Pore Count	Macro-porosity %	Expected Macroporosity %	Effectiveness Factor
366210	16919	85080	2237	48	59.01	37.75	138.82

## A.7. Morphological Analysis of Sample Set 7

Unique porogen size distribution of sample 7 with the exclusion of the finest and coarsest size groups as seen in Table A.15 produced the well connected pore structure seen in Fig.A.7(a,b) by the interaction of abundant intermediate porogen particles. This interaction which directs the porogens to group around coarse ones result in an alternative packing mechanism compared to void filling.

Table A.15. Size distributions of NaCl porogens added into the sample

	-38 $\mu\text{m}$ size group	-53 $\mu\text{m}$ size group	-75 $\mu\text{m}$ size group	-106 $\mu\text{m}$ size group	-150 $\mu\text{m}$ size group	-212 $\mu\text{m}$ size group	Total
By mass (gr)	0	0.526	0.409	0.260	0.448	0.014	1.656
By number	0	1630386	447497	100641	61264	692	2240481

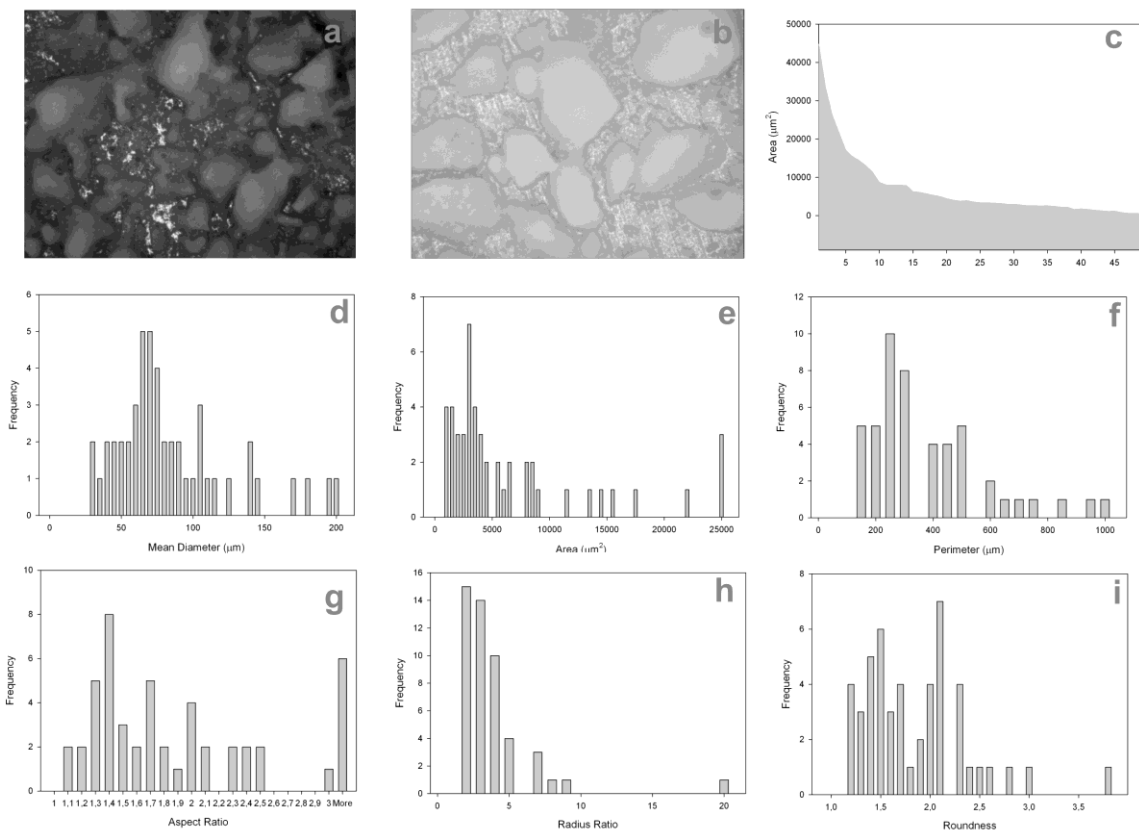


Figure A.7. Representative micrograph taken at 50x magnification (a), random micrograph taken at 100x magnification showing the interaction of pores in detail (b), area distribution (c), size distribution (d), area histogram (e), perimeter distribution (f), aspect ratio distribution (g), roundness distribution (h), radius ratio distribution (i) of pores of the representative sample.

Table A.16. Overall morphological properties of the sample

Total Area ( $\mu\text{m}^2$ )	Total Perimeter ( $\mu\text{m}$ )	3 Highest Areas ( $\mu\text{m}^2$ )	3 Highest Perimeters ( $\mu\text{m}$ )	Pore Count	Macro- porosity %	Expected Macroporosity %	Effectiveness Factor
320347	17387	98460	3137	49	51.62	34.00	587.71

## A.8. Morphological Analysis of Sample Set 8

A similar porogen distribution with sample 6 with a slight increase in the finest and coarsest size groups as seen in Table A.17 resulted in an improved effectiveness factor given in Table A.18. An improved void filling mechanism of finer porogens seen in Fig.A.8(b) is seen to result in well interconnection. Presence of elongated porogens as seen in Fig.A.8(g-i) is another contributing factor.

Table A.17. Size distributions of NaCl porogens added into the sample

	-38 $\mu\text{m}$ size group	-53 $\mu\text{m}$ size group	-75 $\mu\text{m}$ size group	-106 $\mu\text{m}$ size group	-150 $\mu\text{m}$ size group	-212 $\mu\text{m}$ size group	Total
By mass (gr)	0.125	0.273	0.000	0.397	0.779	0.417	1.989
By number	1048618	845451	0	153993	106555	20193	2174810

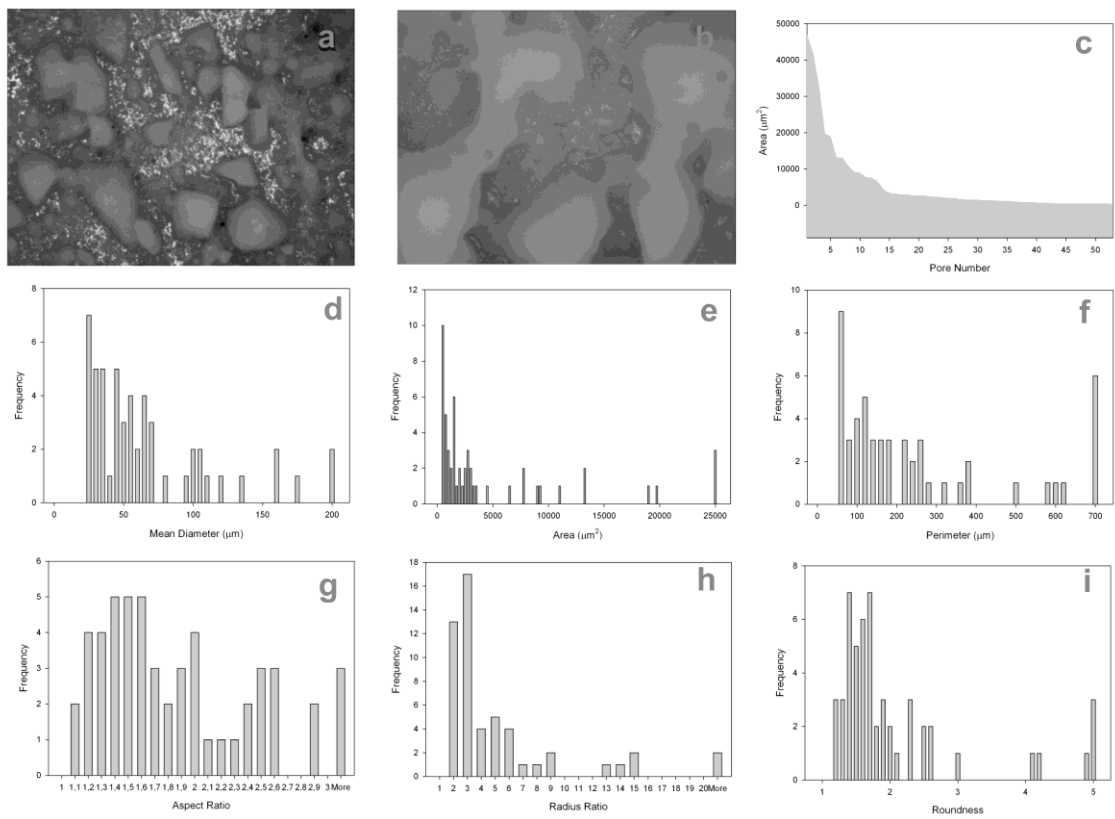


Figure A.8. Representative micrograph taken at 50x magnification (a), random micrograph taken at 100x magnification showing the interaction of pores in detail (b), area distribution (c), size distribution (d), area histogram (e), perimeter distribution (f), aspect ratio distribution (g), roundness distribution (h), radius ratio distribution (i) of pores of the representative sample.

Table A.18. Overall morphological properties of the sample

Total Area ( $\mu\text{m}^2$ )	Total Perimeter ( $\mu\text{m}$ )	Highest Areas ( $\mu\text{m}^2$ )	3 Highest Areas (%)	3 Highest Perimeters ( $\mu\text{m}$ )	3 Highest Perimeters (%)	Pore Count	Macro-porosity (%)	Expected Macroporosity (%)	Effectiveness Factor
293635	17085	78650	30	2488	17	63	47.31	38.28	227.15

## A.9. Morphological Analysis of Sample Set 9

A similar porogen size distribution with sample 7 but a decrease in the fine and increase in the coarsest size group as seen in Table A.19 resulted in a decrease in effectiveness factor. It is also partly due to poor detection of  $-53\mu\text{m}$  pores. Void filling of finer porogens contributes to the interconnection as well as directional coagulation by intermediate interaction as seen in Fig.A.9(b).

Table A.19. Size distributions of NaCl porogens added into the sample

	-38 $\mu\text{m}$ size group	-53 $\mu\text{m}$ size group	-75 $\mu\text{m}$ size group	-106 $\mu\text{m}$ size group	-150 $\mu\text{m}$ size group	-212 $\mu\text{m}$ size group	Total
By mass (gr)	0.000	0.425	0.425	0.238	0.425	0.425	1.938
By number	0	1318296	465219	92281	58152	20598	1954546

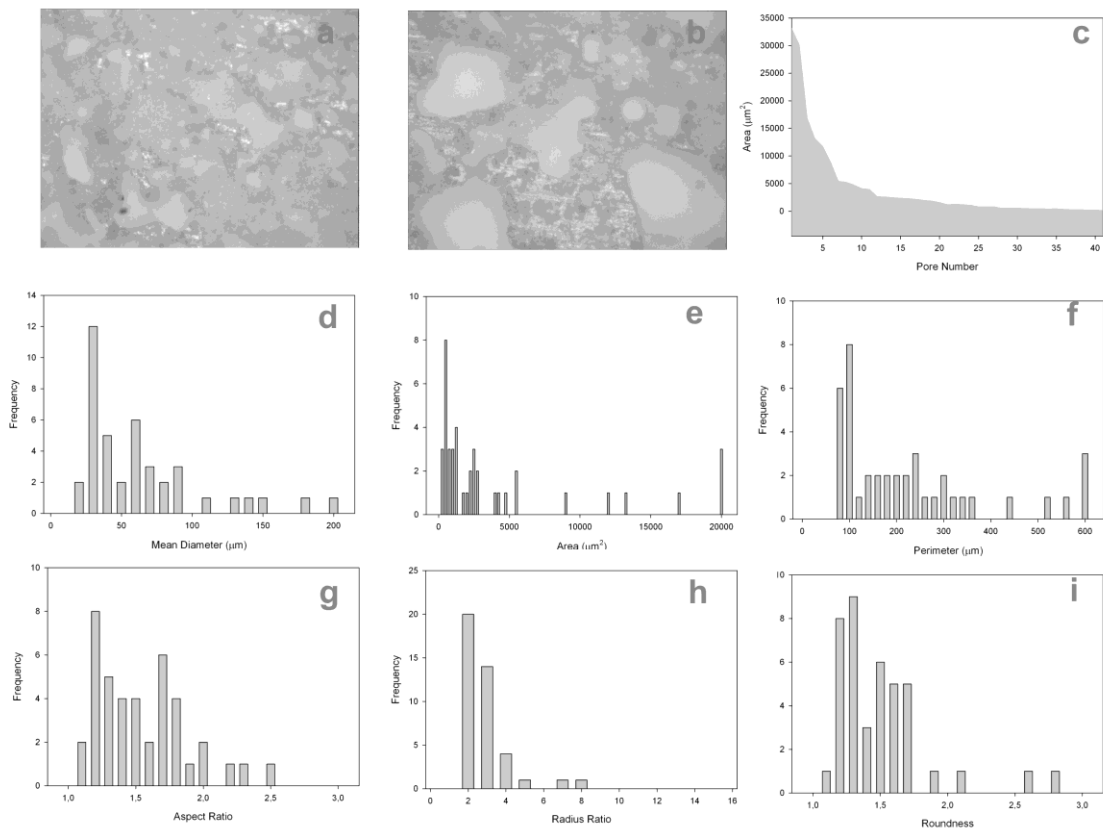


Figure A.9. Representative micrograph taken at 50x magnification (a), random micrograph taken at 100x magnification showing the interaction of pores in detail (b), area distribution (c), size distribution (d), area histogram (e), perimeter distribution (f), aspect ratio distribution (g), roundness distribution (h), radius ratio distribution (i) of pores of the representative sample.

Table A.20. Overall morphological properties of the sample

Total Area ( $\mu\text{m}^2$ )	Total Perimeter ( $\mu\text{m}$ )	3 Highest Areas ( $\mu\text{m}^2$ )	3 Highest Perimeters ( $\mu\text{m}$ )	3 Highest Pore Count	Macro- porosity %	Expected Macroporosity %	Effectiveness Factor
172934	10334	65121	43	2235	26	40	70.44

## A.10. Morphological Analysis of Sample Set 10

Absence of coarse porogen group seen in Table A.21 did not hinder the void filling mechanism of finer porogens among coarse group as indicated by fine necks seen in Fig.A.10(a,b). High total area, perimeter and effectiveness parameter were obtained in Table A.22 due to the relatively high mass and number of porogens. Comparing the aspect ratio and roundness values to samples 7 and 8, it is seen that the elongated particles occur only in coarse size groups.

Table A.21. Size distributions of NaCl porogens added into the sample

	-38 $\mu\text{m}$ size group	-53 $\mu\text{m}$ size group	-75 $\mu\text{m}$ size group	-106 $\mu\text{m}$ size group	-150 $\mu\text{m}$ size group	-212 $\mu\text{m}$ size group	Total
By mass (gr)	0.758	0.103	0.000	1.083	0.076	0.000	2.019
By number	6379673	319115	0	419888	10372	0	7129049

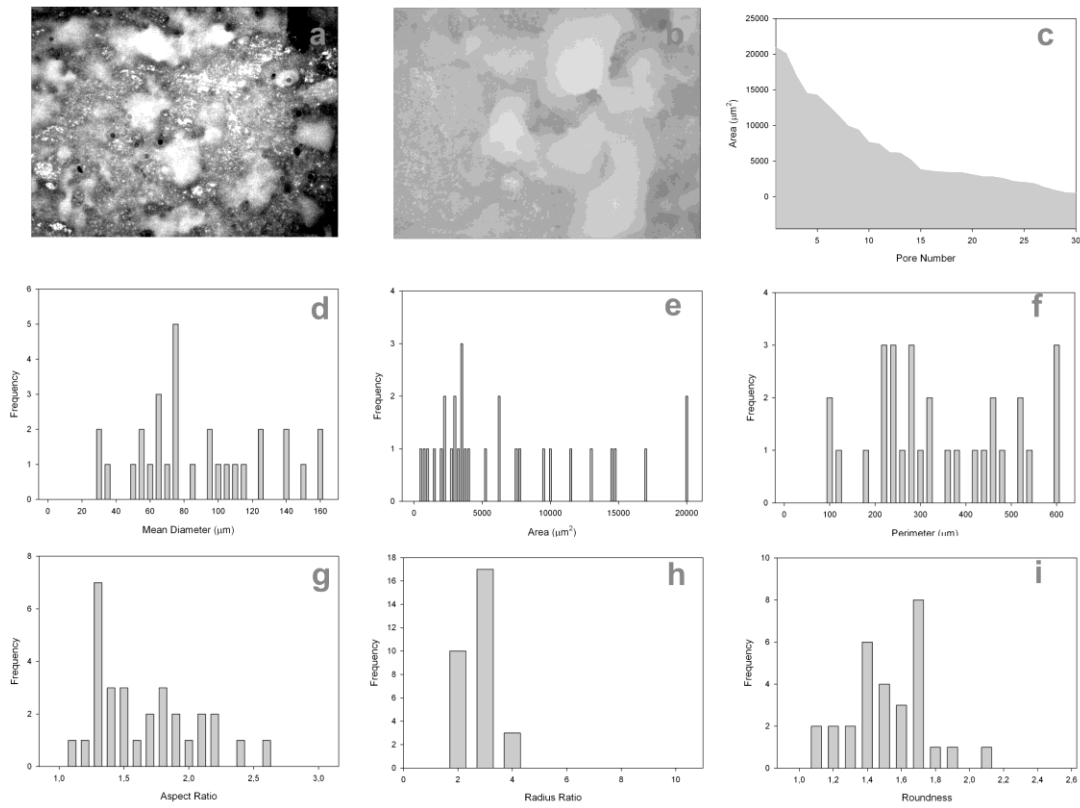


Figure A.10. Representative micrograph taken at 50x magnification (a), random micrograph taken at 100x magnification showing the interaction of pores in detail (b), area distribution (c), size distribution (d), area histogram (e), perimeter distribution (f), aspect ratio distribution (g), roundness distribution (h), radius ratio distribution (i) of pores of the representative sample.

Table A.22. Overall morphological properties of the sample

Total Area ( $\mu\text{m}^2$ )	Total Perimeter ( $\mu\text{m}$ )	3 Highest Areas ( $\mu\text{m}^2$ )	%	3 Highest Perimeters ( $\mu\text{m}$ )	%	Pore Count	Macro-porosity %	Expected Macroporosity %	Effectiveness Factor
214205	10401	67253	35	2299	25	29	34.51	36.63	127.84



## A.11. Morphological Analysis of Sample Set 11

Sample 11 is similar to sample 1 in the abundance of fine porogen particles but total number is reduced by the presence of coarse size groups, resulting in a reduced total perimeter. Fig.A.11(c) shows that almost no joint pores are present and Fig.A.11(a,b) show fine pores are isolated. Low macroporosity seen in Table A.24 is due to poor detection of -38  $\mu\text{m}$  size group as their amount in Fig.A.11(d) is not proportional to their number.

Table A.23. Size distributions of NaCl porogens added into the sample

	-38 $\mu\text{m}$ size group	-53 $\mu\text{m}$ size group	-75 $\mu\text{m}$ size group	-106 $\mu\text{m}$ size group	-150 $\mu\text{m}$ size group	-212 $\mu\text{m}$ size group	Total
By mass (gr)	0.602	0.602	0.373	0.078	0.162	0.211	2.028
By number	5065708	1867082	408507	30340	22237	10211	7404084

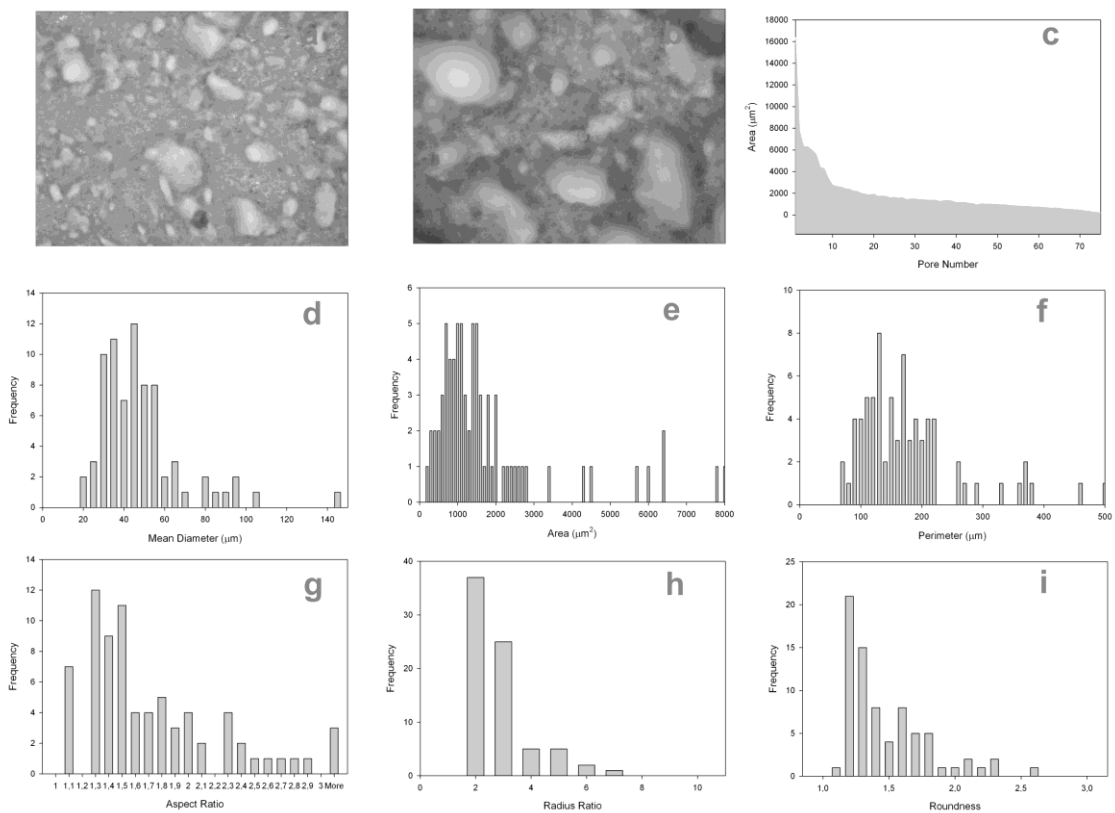


Figure A.11. Representative micrograph taken at 50x magnification (a), random micrograph taken at 100x magnification showing the interaction of pores in detail (b), area distribution (c), size distribution (d), area histogram (e), perimeter distribution (f), aspect ratio distribution (g), roundness distribution (h), radius ratio distribution (i) of pores of the representative sample.

Table A.24. Overall morphological properties of the sample

Total Area ( $\mu\text{m}^2$ )	Total Perimeter ( $\mu\text{m}$ )	3 Highest Areas ( $\mu\text{m}^2$ )	3 Highest Perimeters ( $\mu\text{m}$ )	Pore Count	Macro-porosity %	Expected Macroporosity %	Effectiveness Factor
145443	12995	35876	1437	70	23.44	37.59	19.54

## A.12. Morphological Analysis of Sample Set 12

A large proportion of the total porogen added was fine as seen in Table A.25, however small number of them were detected as seen in Fig.A.12(d). Low total area, parameter, macroporosity seen in Table A.26 is a consequence of this misdetection. Intermediate and coarse pores seen in Fig.A.12(a) seem isolated with a small fraction of fine pores distributed among them.

Table A.25. Size distributions of NaCl porogens added into the sample

	-38 $\mu\text{m}$ size group	-53 $\mu\text{m}$ size group	-75 $\mu\text{m}$ size group	-106 $\mu\text{m}$ size group	-150 $\mu\text{m}$ size group	-212 $\mu\text{m}$ size group	Total
By mass (gr)	0.311	0.413	0.280	0.360	0.000	0.622	1.986
By number	2615876	1282307	306216	139801	0	30129	4374329

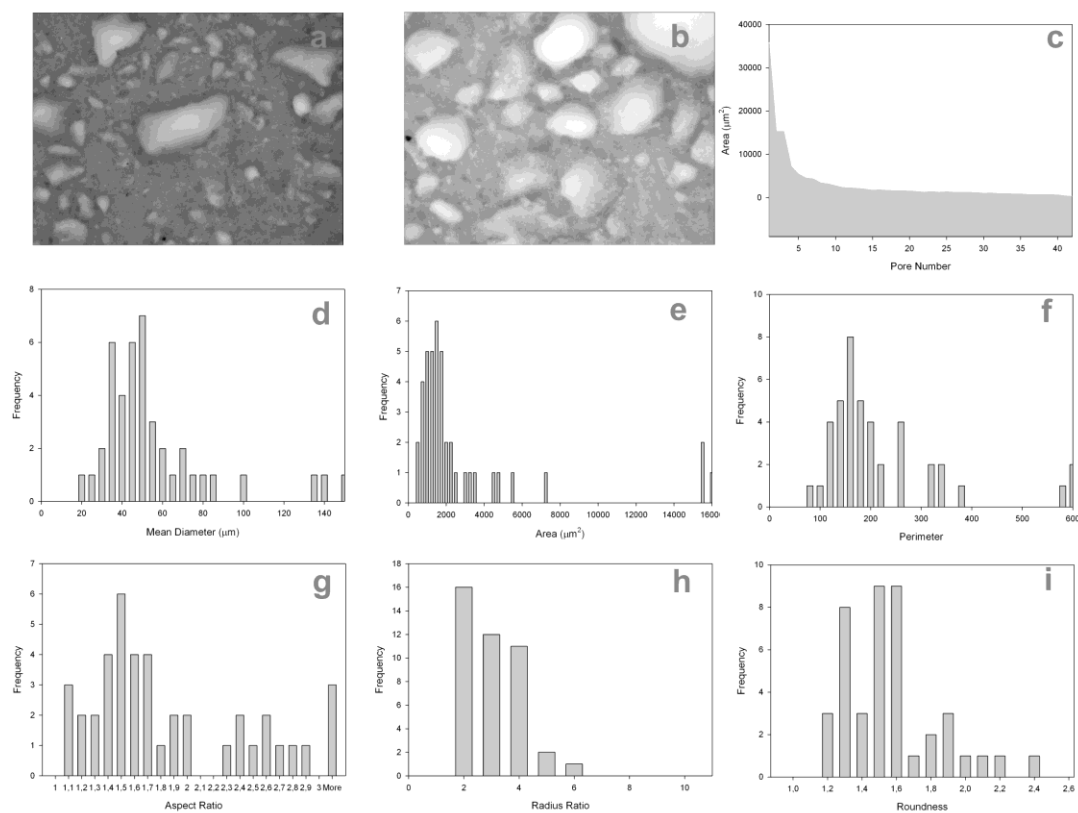


Figure A.12. Representative micrograph taken at 50x magnification (a), random micrograph taken at 100x magnification showing the interaction of pores in detail (b), area distribution (c), size distribution (d), area histogram (e), perimeter distribution (f), aspect ratio distribution (g), roundness distribution (h), radius ratio distribution (i) of pores of the representative sample.

Table A.26. Overall morphological properties of the sample

Total Area ( $\mu\text{m}^2$ )	Total Perimeter ( $\mu\text{m}$ )	3 Highest Areas ( $\mu\text{m}^2$ )	3 Highest Perimeters ( $\mu\text{m}$ )	Pore Count	Macro-porosity %	Expected Macroporosity %	Effectiveness Factor
142355	9389	53764	1792	42	22.94	38.38	18.10

### A.13. Morphological Analysis of Sample Set 13

Sample 13 contains small number of porogens mostly belonging to the coarse-intermediate size groups as seen in Table A.27. Similar size distribution but quite different interconnectivity with sample 7 is due to the decrease in -53 and -75 $\mu\text{m}$  size group porogens. Decrease in total number of intermediates resulted in lower interactions that grouped porogens around coarse ones. It is understood that the quantity of lower size group porogens is important.

Table A.27. Size distributions of NaCl porogens added into the sample

	-38 $\mu\text{m}$ size group	-53 $\mu\text{m}$ size group	-75 $\mu\text{m}$ size group	-106 $\mu\text{m}$ size group	-150 $\mu\text{m}$ size group	-212 $\mu\text{m}$ size group	Total
By mass (gr)	0.000	0.437	0.292	0.550	0.550	0.000	1.830
By number	0	1357149	319287	213388	75303	0	1965127

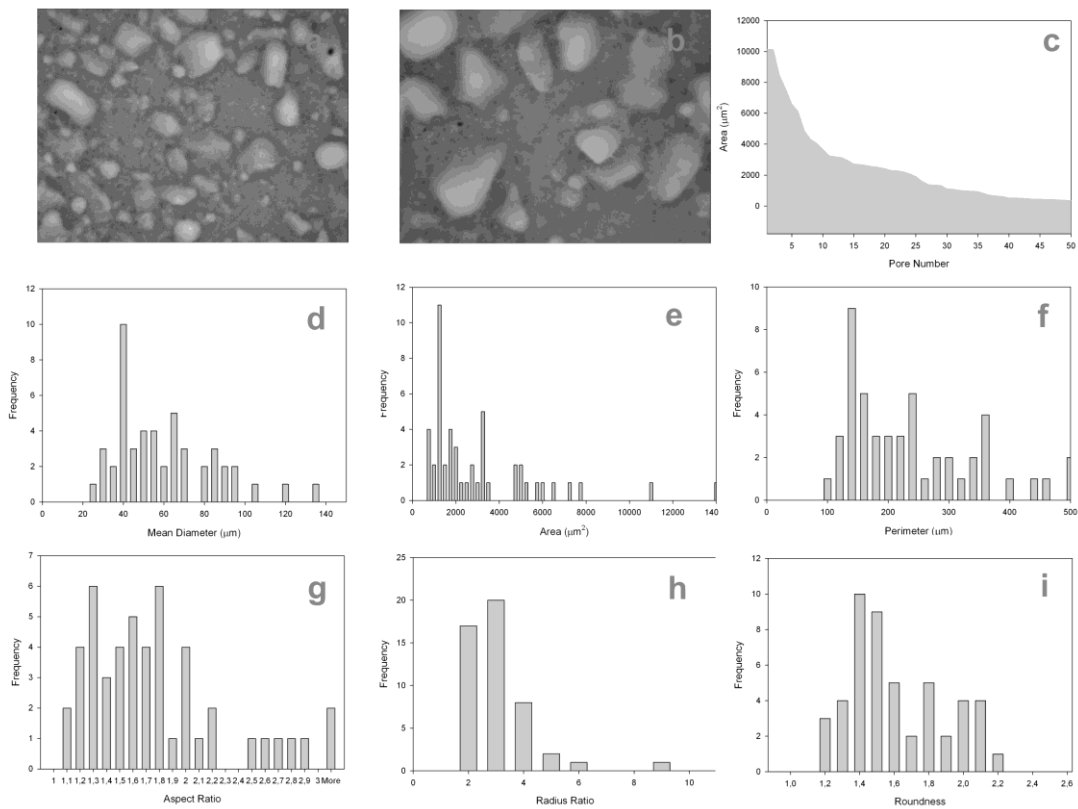


Figure A.13. Representative micrograph taken at 50x magnification (a), random micrograph taken at 100x magnification showing the interaction of pores in detail (b), area distribution (c), size distribution (d), area histogram (e), perimeter distribution (f), aspect ratio distribution (g), roundness distribution (h), radius ratio distribution (i) of pores of the representative sample.

Table A.28. Overall morphological properties of the sample

Total Area ( $\mu\text{m}^2$ )	Total Perimeter ( $\mu\text{m}$ )	3 Highest Areas ( $\mu\text{m}^2$ )	%	3 Highest Perimeters ( $\mu\text{m}$ )	%	Pore Count	Macro-porosity %	Expected Macroporosity %	Effectiveness Factor
149435	11488	29683	24	1127	12	50	24.08	36.58	4.57

## A.14. Morphological Analysis of Sample Set 14

Increase in number of fine porogens was not effective in void filling as rare interconnections were only observed between coarse adjacent particles as seen in Fig.A.14(b). The size distribution seen in Fig.A.14(d) is not proportional to the added amount given in Table A.29 due to low contrast of the micrograph. Fig.A.14(g-i) show presence of irregular shaped coarse pores.

Table A.29. Size distributions of NaCl porogens added into the sample

	-38 $\mu\text{m}$ size group	-53 $\mu\text{m}$ size group	-75 $\mu\text{m}$ size group	-106 $\mu\text{m}$ size group	-150 $\mu\text{m}$ size group	-212 $\mu\text{m}$ size group	Total
By mass (gr)	0.000	0.600	0.315	0.317	0.309	0.320	1.862
By number	0	1862739	345108	122941	42317	15513	2388618

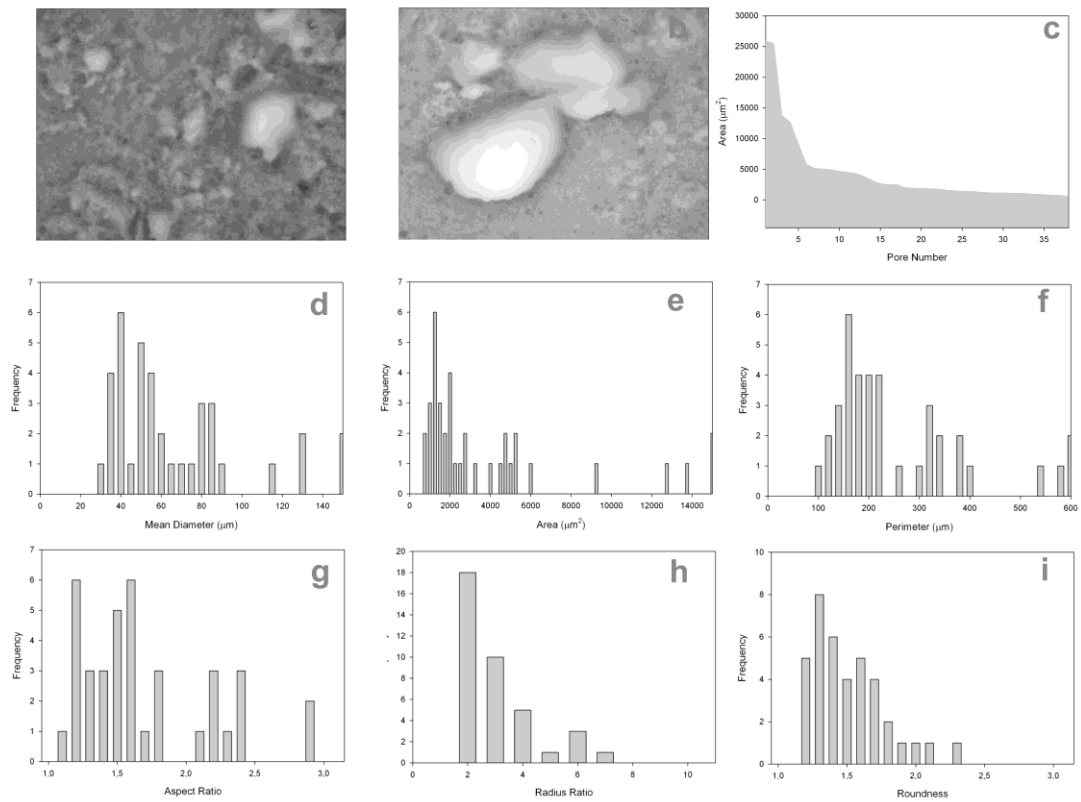


Figure A.14. Representative micrograph taken at 50x magnification (a), random micrograph taken at 100x magnification showing the interaction of pores in detail (b), area distribution (c), size distribution (d), area histogram (e), perimeter distribution (f), aspect ratio distribution (g), roundness distribution (h), radius ratio distribution (i) of pores of the representative sample.

Table A.30. Overall morphological properties of the sample

Total Area ( $\mu\text{m}^2$ )	Total Perimeter ( $\mu\text{m}$ )	3 Highest Areas ( $\mu\text{m}^2$ )	46 %	3 Highest Perimeters ( $\mu\text{m}$ )	25 %	Pore Count	Macro- porosity %	Expected Macroporosity %	Effectiveness Factor
159992	9644	62778	46	1908	25	38	25.78	36.36	26.06

## A.15. Morphological Analysis of Sample Set 15

High number of fine porogens were not observed in micrographs seen in Fig.A.15(a,b) due to the low contrast of the micrographs, resulting in the low macroporosity and effectiveness factor given in Table A.32. Interactions between porogens are limited with low amount of intermediates

Table A.31. Size distributions of NaCl porogens added into the sample

	-38 $\mu\text{m}$ size group	-53 $\mu\text{m}$ size group	-75 $\mu\text{m}$ size group	-106 $\mu\text{m}$ size group	-150 $\mu\text{m}$ size group	-212 $\mu\text{m}$ size group	Total
By mass (gr)	0.407	0.741	0.000	0.378	0.441	0.000	1.966
By number	3428911	2297824	0	146486	60310	0	5933532

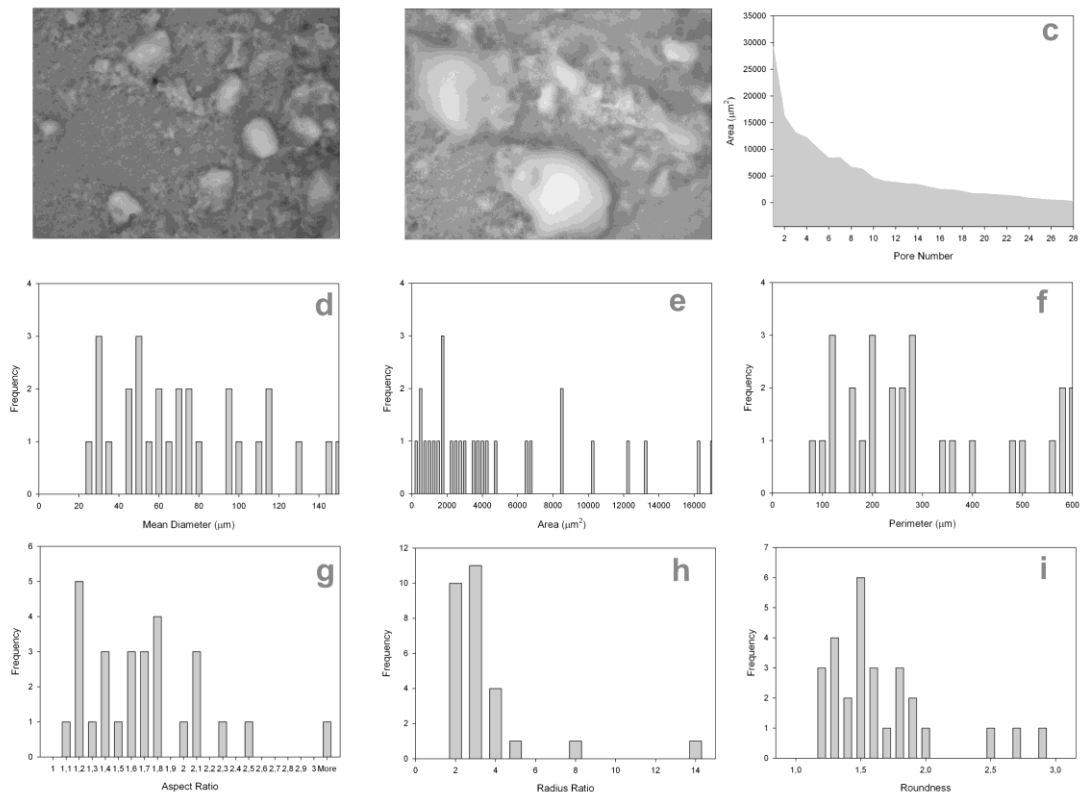


Figure A.15. Representative micrograph taken at 50x magnification (a), random micrograph taken at 100x magnification showing the interaction of pores in detail (b), area distribution (c), size distribution (d), area histogram (e), perimeter distribution (f), aspect ratio distribution (g), roundness distribution (h), radius ratio distribution (i) of pores of the representative sample.

Table A.32. Overall morphological properties of the sample

Total Area ( $\mu\text{m}^2$ )	Total Perimeter ( $\mu\text{m}$ )	3 Highest Areas ( $\mu\text{m}^2$ )	3 Highest Perimeters (%)	3 Highest Perimeters ( $\mu\text{m}$ )	Pore Count	Macro-porosity (%)	Expected Macroporosity (%)	Effectiveness Factor	
132361	7727	49525	44	1836	29	28	21.33	35.96	11.79

## A.16. Morphological Analysis of Sample Set 16

Sample 16 is an extreme case with no size distribution. All porogens are in the -212  $\mu\text{m}$  size group as seen in Table A.33. The lowest interconnectivity and effectiveness factor are obtained as seen in Table A.34. Notice the concave down shape of Fig.A.16 (c) that is opposite to the “c” shaped concave up curve observed in well interconnected samples.

Table A.33. Size distributions of NaCl porogens added into the sample

	-38 $\mu\text{m}$ size group	-53 $\mu\text{m}$ size group	-75 $\mu\text{m}$ size group	-106 $\mu\text{m}$ size group	-150 $\mu\text{m}$ size group	-212 $\mu\text{m}$ size group	Total
By mass (gr)	0.000	0.000	0.000	0.000	0.000	1.690	1.690
By number	0	0	0	0	0	81913	81913

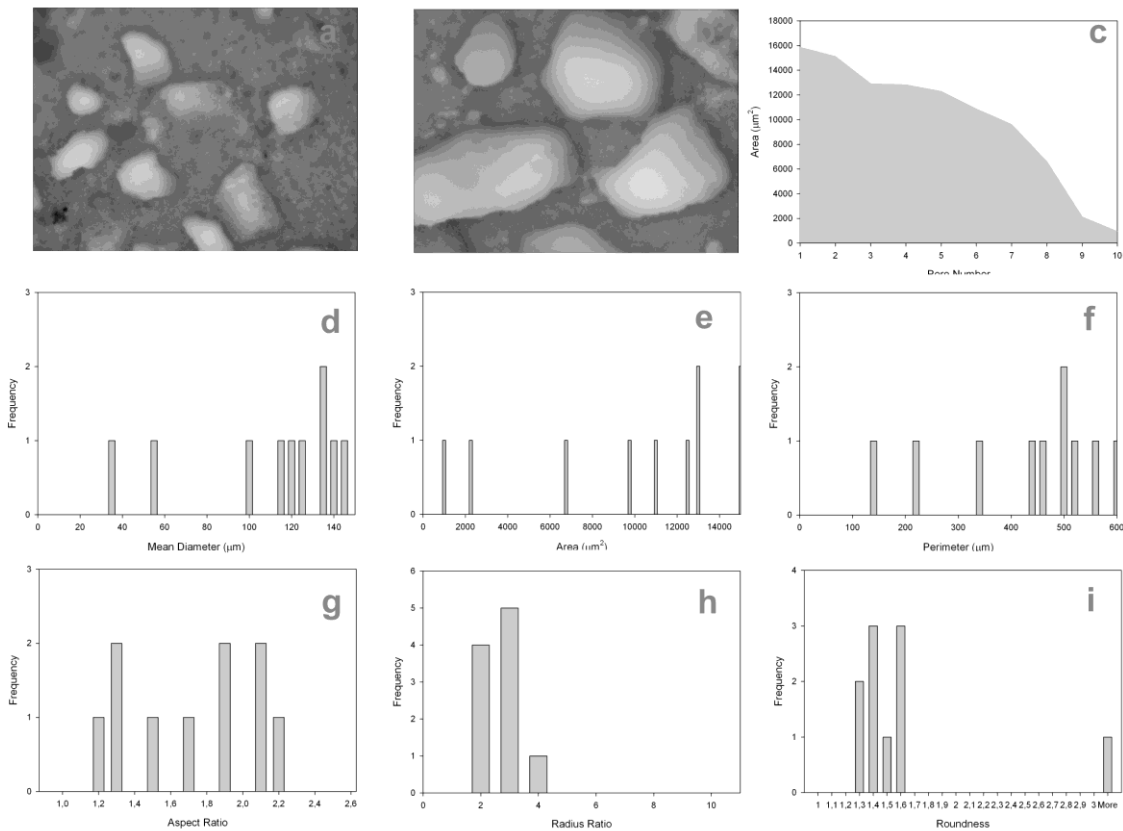


Figure A.16. Representative micrograph taken at 50x magnification (a), random micrograph taken at 100x magnification showing the interaction of pores in detail (b), area distribution (c), size distribution (d), area histogram (e), perimeter distribution (f), aspect ratio distribution (g), roundness distribution (h), radius ratio distribution (i) of pores of the representative sample.

Table A.34. Overall morphological properties of the sample

Total Area ( $\mu\text{m}^2$ )	Total Perimeter ( $\mu\text{m}$ )	3 Highest Areas ( $\mu\text{m}^2$ )	%	3 Highest Perimeters ( $\mu\text{m}$ )	%	Pore Count	Macro-porosity %	Expected Macroporosity %	Effectiveness Factor
103961	4814	42934	46	1596	37	11	16.75	35.19	0.52

## A.17. Morphological Analysis of Sample Set 17

Unique size distribution of intermediate porogens as seen in Table A.35 makes it possible to observe the interactions of intermediate porogens closer in Fig.A.17(a,b). Some interconnections are present at adjacent pores but even the high number of -75  $\mu\text{m}$  size group porogens is not enough to induce interconnection in the absence of coarse center porogens.

Table A.35. Size distributions of NaCl porogens added into the sample

	-38 $\mu\text{m}$ size group	-53 $\mu\text{m}$ size group	-75 $\mu\text{m}$ size group	-106 $\mu\text{m}$ size group	-150 $\mu\text{m}$ size group	-212 $\mu\text{m}$ size group	Total
By mass (gr)	0.000	0.000	1.012	0.784	0.000	0.000	1.797
By number	0	0	1108202	304219	0	0	1412421

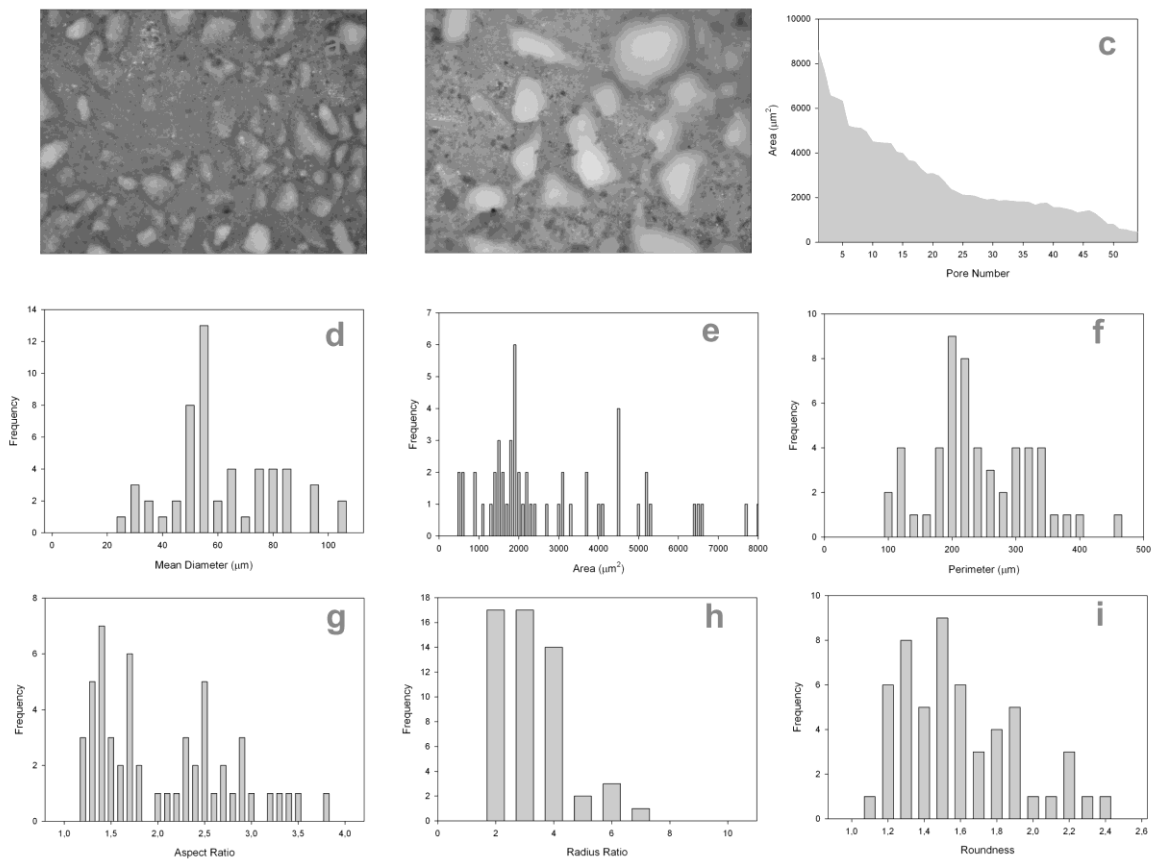


Figure A.17. Representative micrograph taken at 50x magnification (a), random micrograph taken at 100x magnification showing the interaction of pores in detail (b), area distribution (c), size distribution (d), area histogram (e), perimeter distribution (f), aspect ratio distribution (g), roundness distribution (h), radius ratio distribution (i) of pores of the representative sample.

Table A.36. Overall morphological properties of the sample

Total Area ( $\mu\text{m}^2$ )	Total Perimeter ( $\mu\text{m}$ )	3 Highest Areas ( $\mu\text{m}^2$ )	%	3 Highest Perimeters ( $\mu\text{m}$ )	%	Pore Count	Macro-porosity %	Expected Macroporosity %	Effectiveness Factor
159361	12924	20359	16	1054	10	57	25.68	34.31	2.46

## A.18. Morphological Analysis of Sample Set 18

Presence of fine porogens among abundant intermediate and coarse porogens produced some interconnectivity by bridging between the larger porogens as seen in Fig.A.18(b). Size distribution shown in Fig.A.18(d) is not proportional to the distribution given in Table A.37 due to poor detection of the fine pores in micrographs.

Table A.37. Size distributions of NaCl porogens added into the sample

	-38 $\mu\text{m}$ size group	-53 $\mu\text{m}$ size group	-75 $\mu\text{m}$ size group	-106 $\mu\text{m}$ size group	-150 $\mu\text{m}$ size group	-212 $\mu\text{m}$ size group	Total
By mass (gr)	0.470	0.000	0.397	0.448	0.540	0.224	2.079
By number	3954903	0	434582	173831	73908	10864	4648089

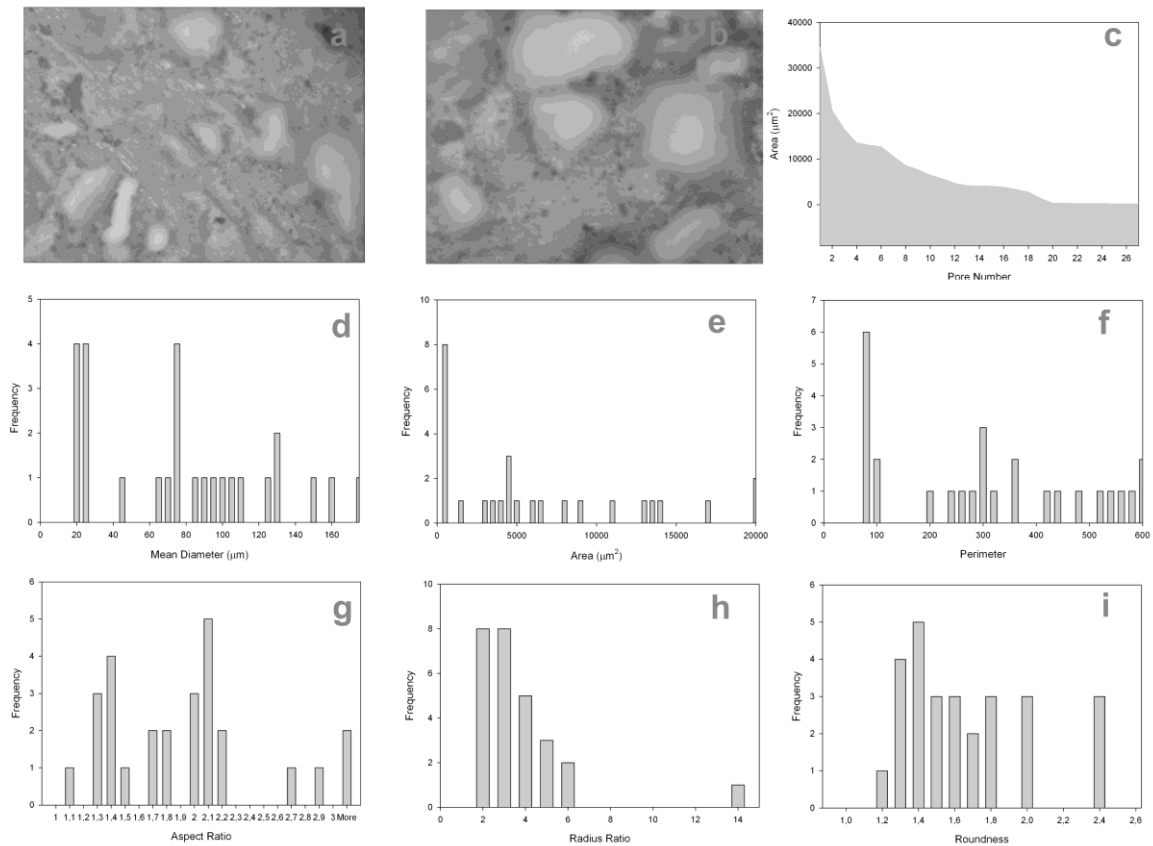


Figure A.18. Representative micrograph taken at 50x magnification (a), random micrograph taken at 100x magnification showing the interaction of pores in detail (b), area distribution (c), size distribution (d), area histogram (e), perimeter distribution (f), aspect ratio distribution (g), roundness distribution (h), radius ratio distribution (i) of pores of the representative sample.

Table A.38. Overall morphological properties of the sample

Total Area ( $\mu\text{m}^2$ )	Total Perimeter ( $\mu\text{m}$ )	3 Highest Areas ( $\mu\text{m}^2$ )	3 Highest Perimeters ( $\mu\text{m}$ )	Pore Count	Macro-porosity (%)	Expected Macroporosity (%)	Effectiveness Factor
201058	9871	67998	2106	28	32.40	36.54	104.04



## A.19. Morphological Analysis of Sample Set 19

A large fraction of the finest porogens added in sample 19 were not detected as seen in Fig.A.19(d). Presence and interaction of intermediates with coarse porogens produced some grouping as observed in Fig.A.19(a,b) with missing fine size group. Not many interconnected pores formed although the packing was well.

Table A.39. Size distributions of NaCl porogens added into the sample

	-38 $\mu\text{m}$ size group	-53 $\mu\text{m}$ size group	-75 $\mu\text{m}$ size group	-106 $\mu\text{m}$ size group	-150 $\mu\text{m}$ size group	-212 $\mu\text{m}$ size group	Total
By mass (gr)	0.417	0.083	0.432	0.000	0.596	0.596	2.125
By number	3512220	258902	473140	0	81576	28895	4354732

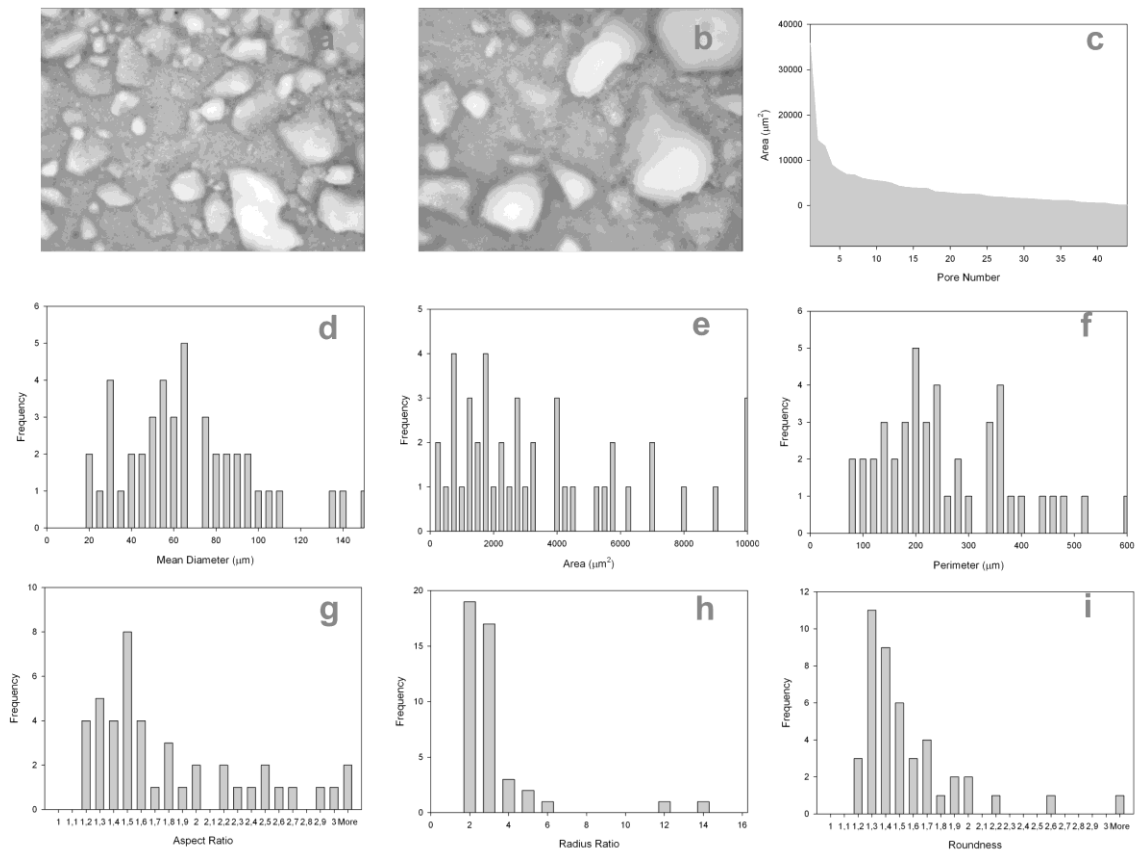


Figure A.19. Representative micrograph taken at 50x magnification (a), random micrograph taken at 100x magnification showing the interaction of pores in detail (b), area distribution (c), size distribution (d), area histogram (e), perimeter distribution (f), aspect ratio distribution (g), roundness distribution (h), radius ratio distribution (i) of pores of the representative sample.

Table A.40. Overall morphological properties of the sample

Total Area ( $\mu\text{m}^2$ )	Total Perimeter ( $\mu\text{m}$ )	3 Highest Areas ( $\mu\text{m}^2$ )	3 Highest Perimeters (%)	3 Highest Perimeters ( $\mu\text{m}$ )	Pore Count	Macro-porosity (%)	Expected Macroporosity (%)	Effectiveness Factor	
180407	11199	47818	31	1585	17	45	29.07	39.00	16.78

## A.20. Morphological Analysis of Sample Set 20

A sequence of fine, intermediate, coarse porogen size groups was not well analyzed due to the misdetection of fine porogens. Rare occurrences of grouping of intermediate porogens were observed as seen in Fig.A.20(b) but the low number of coarse porogens seen in Table A.41 prevented its extent.

Table A.41. Size distributions of NaCl porogens added into the sample

	-38 $\mu\text{m}$ size group	-53 $\mu\text{m}$ size group	-75 $\mu\text{m}$ size group	-106 $\mu\text{m}$ size group	-150 $\mu\text{m}$ size group	-212 $\mu\text{m}$ size group	Total
By mass (gr)	0.000	0.740	0.000	0.740	0.000	0.392	1.872
By number	0	2295388	0	286924	0	19009	2601320

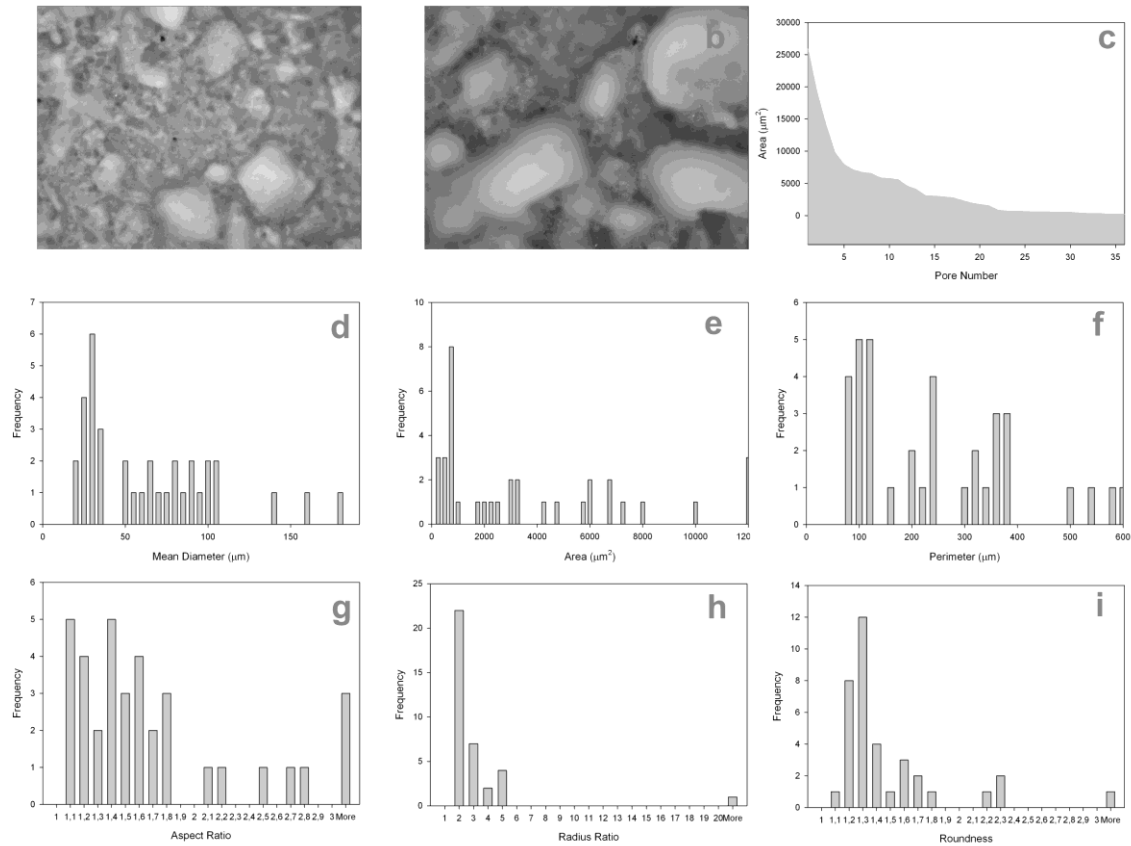


Figure A.20. Representative micrograph taken at 50x magnification (a), random micrograph taken at 100x magnification showing the interaction of pores in detail (b), area distribution (c), size distribution (d), area histogram (e), perimeter distribution (f), aspect ratio distribution (g), roundness distribution (h), radius ratio distribution (i) of pores of the representative sample.

Table A.42. Overall morphological properties of the sample

Total Area ( $\mu\text{m}^2$ )	Total Perimeter ( $\mu\text{m}$ )	3 Highest Areas ( $\mu\text{m}^2$ )	3 Highest Perimeters (%)	3 Highest Perimeters ( $\mu\text{m}$ )	Pore Count	Macro-porosity (%)	Expected Macroporosity (%)	Effectiveness Factor	
153904	9654	36130	26	1370	17	39	24.80	35.46	6.35

## A.21. Morphological Analysis of Sample Set 21

Sequential void filling produced a well packed progen structure in sample 21 similar to sample 6. Interaction of intermediates combined with void filling of fine porogens resulted in improved interconnectivity. The increase in total mass and number of porogens was also effective. Extraordinarily sharp curve in Fig.A.21(c) indicates the presence of mostly connected pores.

Table A.43. Size distributions of NaCl porogens added into the sample

	-38 $\mu\text{m}$ size group	-53 $\mu\text{m}$ size group	-75 $\mu\text{m}$ size group	-106 $\mu\text{m}$ size group	-150 $\mu\text{m}$ size group	-212 $\mu\text{m}$ size group	Total
By mass (gr)	0.762	0.159	0.004	0.347	0.297	0.594	2.163
By number	6411998	493927	4170	134412	40657	28803	7113967

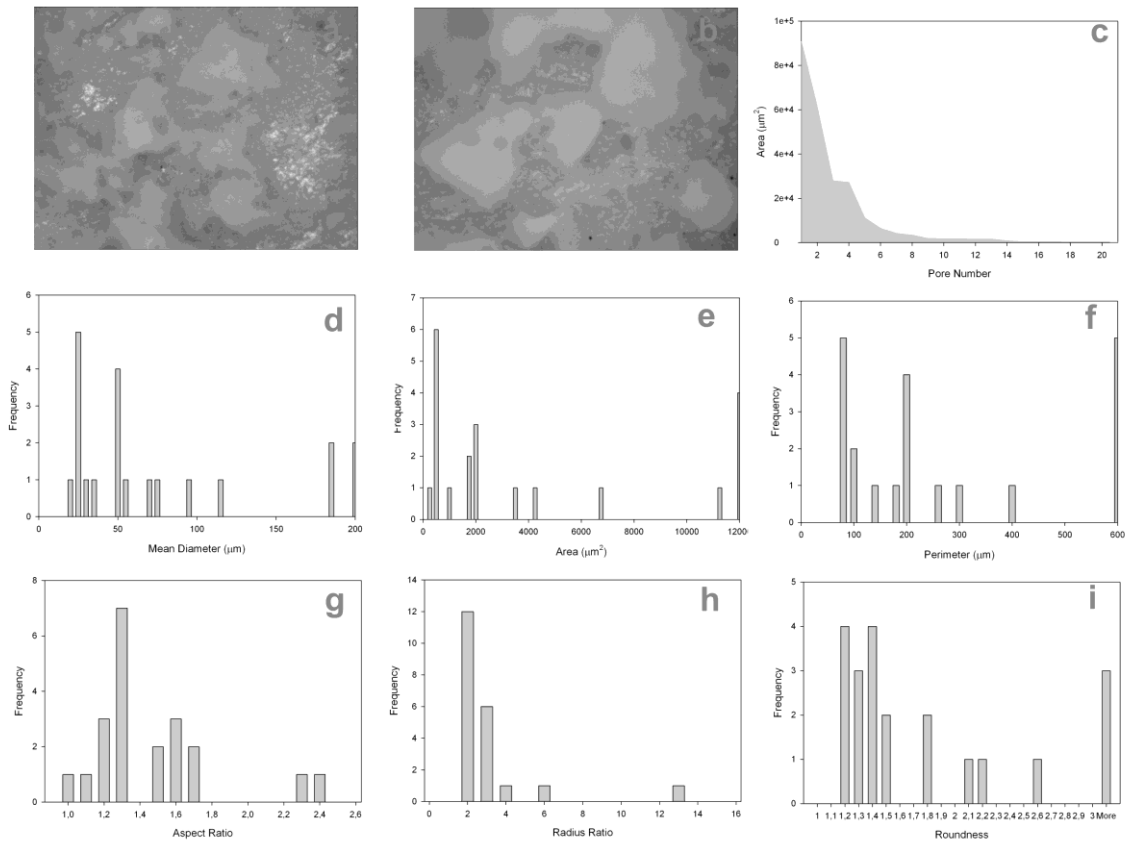


Figure A.21. Representative micrograph taken at 50x magnification (a), random micrograph taken at 100x magnification showing the interaction of pores in detail (b), area distribution (c), size distribution (d), area histogram (e), perimeter distribution (f), aspect ratio distribution (g), roundness distribution (h), radius ratio distribution (i) of pores of the representative sample.

Table A.44. Overall morphological properties of the sample

Total Area ( $\mu\text{m}^2$ )	Total Perimeter ( $\mu\text{m}$ )	3 Highest Areas ( $\mu\text{m}^2$ )	3 Highest Perimeters (%)	3 Highest Perimeters ( $\mu\text{m}$ )	Pore Count	Macro-porosity (%)	Expected Macroporosity (%)	Effectiveness Factor	
246998	9440	133839	59	3792	44	20	39.80	38.43	187.91

## A.22. Morphological Analysis of Sample Set 22

Size distribution of sample 22 is a combination of fine and coarse porogens that are close to the intermediate range. This produced pores of high variety as seen in Fig.A.22(d-i). Attachment of fine porogens on coarse ones were limited in the absence of intermediate porogens as seen in Fig.A.22 (a,b).

Table A.45. Size distributions of NaCl porogens added into the sample

	-38 $\mu\text{m}$ size group	-53 $\mu\text{m}$ size group	-75 $\mu\text{m}$ size group	-106 $\mu\text{m}$ size group	-150 $\mu\text{m}$ size group	-212 $\mu\text{m}$ size group	Total
By mass (gr)	0.077	0.774	0.050	0.000	0.484	0.774	2.160
By number	651575	2401528	55087	0	66210	37524	3211923

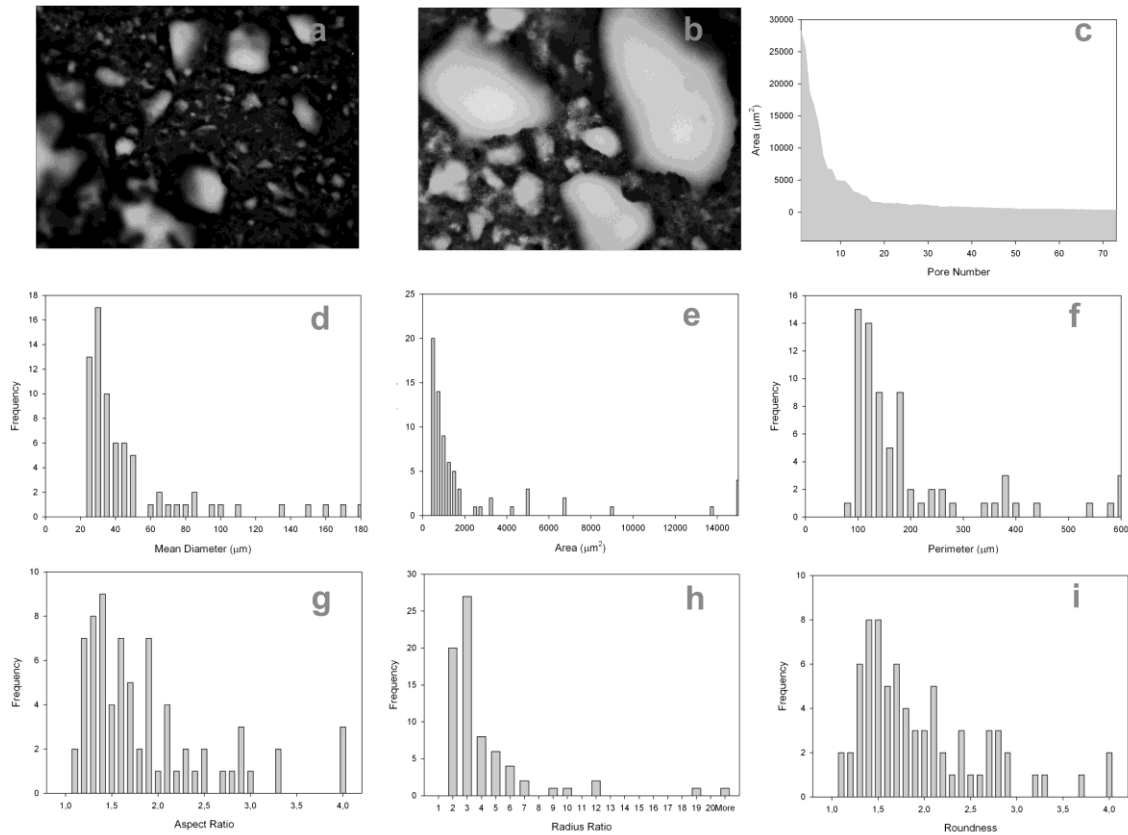


Figure A.22. Representative micrograph taken at 50x magnification (a), random micrograph taken at 100x magnification showing the interaction of pores in detail (b), area distribution (c), size distribution (d), area histogram (e), perimeter distribution (f), aspect ratio distribution (g), roundness distribution (h), radius ratio distribution (i) of pores of the representative sample.

Table A.46. Overall morphological properties of the sample

Total Area ( $\mu\text{m}^2$ )	Total Perimeter ( $\mu\text{m}$ )	3 Highest Areas ( $\mu\text{m}^2$ )	3 Highest Perimeters ( $\mu\text{m}$ )	Pore Count	Macro- porosity %	Expected Macroporosity %	Effectiveness Factor
198985	14077	63258	2346	68	32.06	38.31	68.78

## A.23. Morphological Analysis of Sample Set 23

Size distribution of sample 23 was concentrated at the fine side, producing a sequential void filling mechanism. Total perimeter was high as given in Table A.48 due to the high surface area of fine porogens. Well packed close pores were interconnected by fine necks as seen in Fig.A.23 (a,b).

Table A.47 Size distributions of NaCl porogens added into the sample

	-38 $\mu\text{m}$ size group	-53 $\mu\text{m}$ size group	-75 $\mu\text{m}$ size group	-106 $\mu\text{m}$ size group	-150 $\mu\text{m}$ size group	-212 $\mu\text{m}$ size group	Total
By mass (gr)	0.199	0.722	0.722	0.000	0.000	0.000	1.643
By number	1672117	2241079	790863	0	0	0	4704059

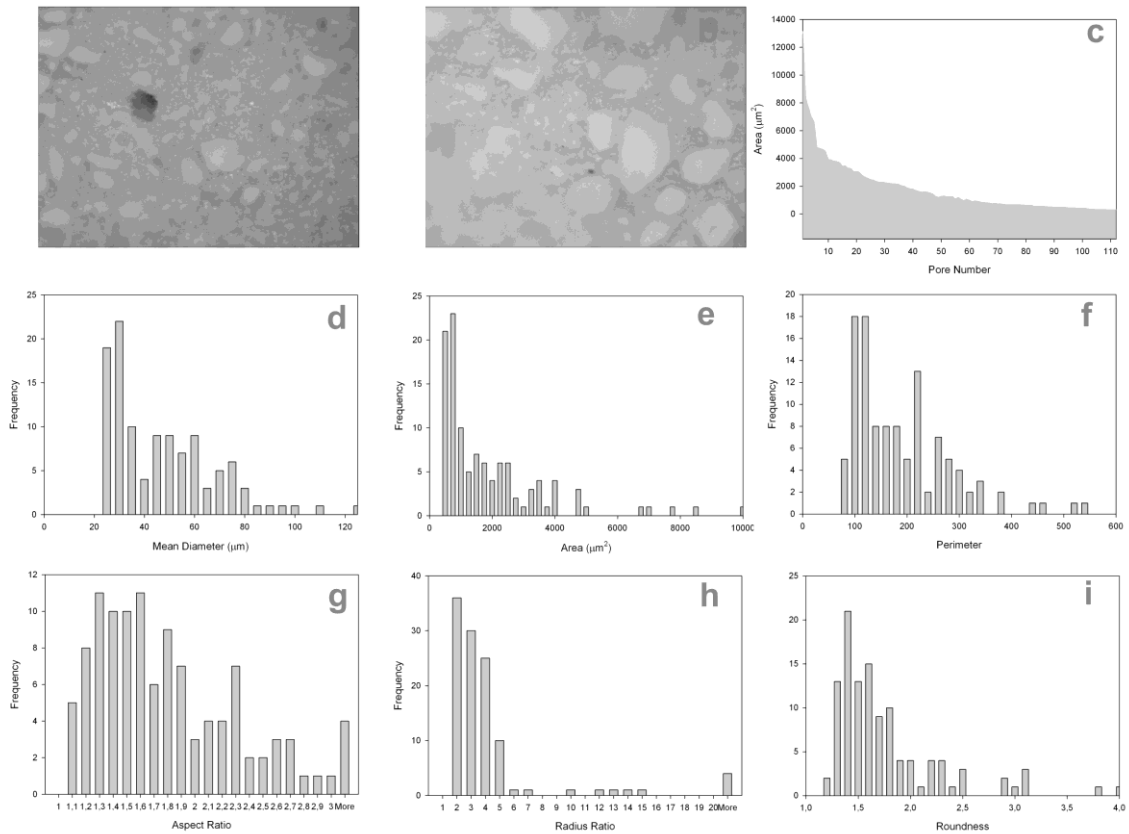


Figure A.23. Representative micrograph taken at 50x magnification (a), random micrograph taken at 100x magnification showing the interaction of pores in detail (b), area distribution (c), size distribution (d), area histogram (e), perimeter distribution (f), aspect ratio distribution (g), roundness distribution (h), radius ratio distribution (i) of pores of the representative sample.

Table A.48. Overall morphological properties of the sample

Total Area ( $\mu\text{m}^2$ )	Total Perimeter ( $\mu\text{m}$ )	3 Highest Areas ( $\mu\text{m}^2$ )	%	3 Highest Perimeters ( $\mu\text{m}$ )	%	Pore Count	Macro- porosity %	Expected Macroporosity %	Effectiveness Factor
227354	20630	34933	20	1708	11	95	36.63	31.16	103.85

## A.24. Morphological Analysis of Sample Set 24

A high mass and number of porogens were added to sample 24 as seen in Table A.49. However the size distributions in Fig.A.24(d-f) and total area given in Table A.50 do not reflect the porogen input as a result of poor detection of the fine pores in the low contrast micrographs.

Table A.49. Size distributions of NaCl porogens added into the sample

	-38 $\mu\text{m}$ size group	-53 $\mu\text{m}$ size group	-75 $\mu\text{m}$ size group	-106 $\mu\text{m}$ size group	-150 $\mu\text{m}$ size group	-212 $\mu\text{m}$ size group	Total
By mass (gr)	0.522	0.522	0.300	0.467	0.063	0.144	2.018
By number	4396321	1620364	328795	181076	8577	6963	6542095

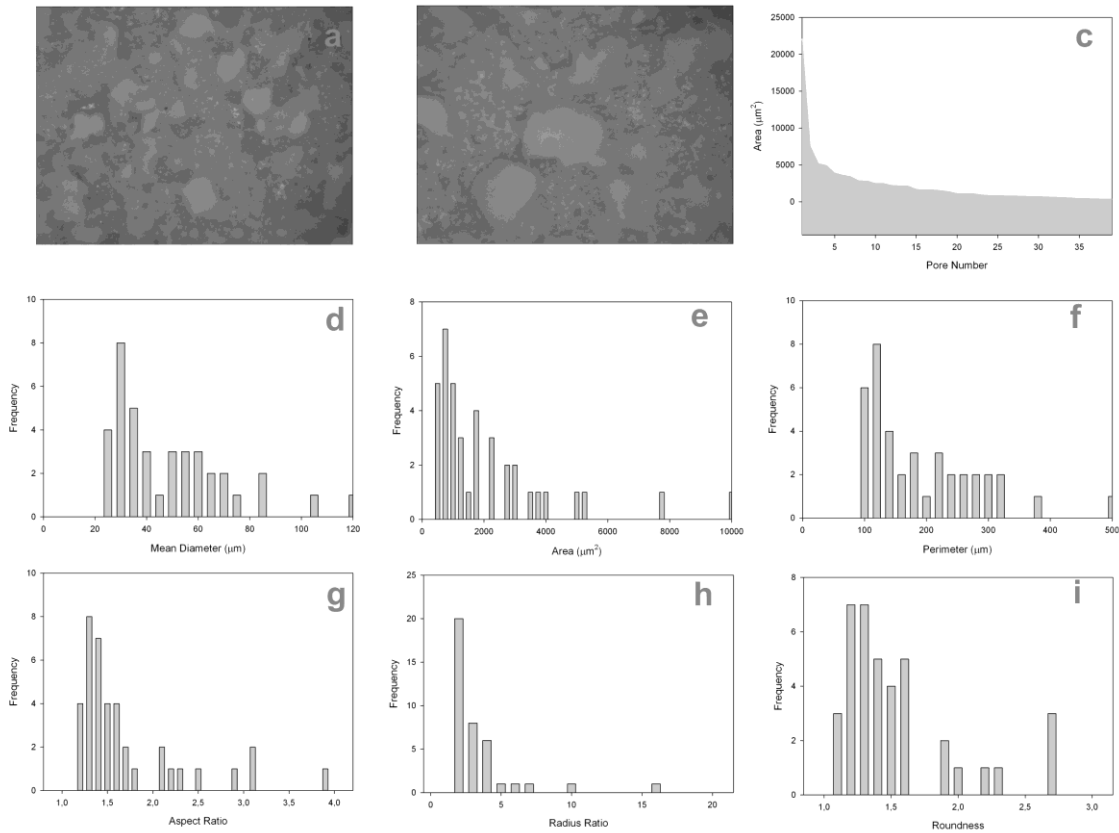


Figure A.24. Representative micrograph taken at 50x magnification (a), random micrograph taken at 100x magnification showing the interaction of pores in detail (b), area distribution (c), size distribution (d), area histogram (e), perimeter distribution (f), aspect ratio distribution (g), roundness distribution (h), radius ratio distribution (i) of pores of the representative sample.

Table A.50. Overall morphological properties of the sample

Total Area ( $\mu\text{m}^2$ )	Total Perimeter ( $\mu\text{m}$ )	3 Highest Areas ( $\mu\text{m}^2$ )	%	3 Highest Perimeters ( $\mu\text{m}$ )	%	Pore Count	Macro- porosity %	Expected Macroporosity %	Effectiveness Factor
107541	8427	25682	31	1115	17	45	17.33	35.91	2.23

## A.25. Morphological Analysis of Sample Set 25

A balanced porogen size distribution that is concentrated at the intermediate size groups as reflected in Fig.A.25(d-f) resulted in an effective pore structure consisting of necks around both coarse and intermediate pores as seen in Fig.A.25 (a,b). Sequential void filling of finer porogens and interaction of intermediate size groups were both effective in improving the interconnectivity.

Table A.51. Size distributions of NaCl porogens added into the sample

	-38 $\mu\text{m}$ size group	-53 $\mu\text{m}$ size group	-75 $\mu\text{m}$ size group	-106 $\mu\text{m}$ size group	-150 $\mu\text{m}$ size group	-212 $\mu\text{m}$ size group	Total
By mass (gr)	0.224	0.306	0.471	0.471	0.252	0.287	2.010
By number	1882547	949487	515490	182594	34473	13923	3578513

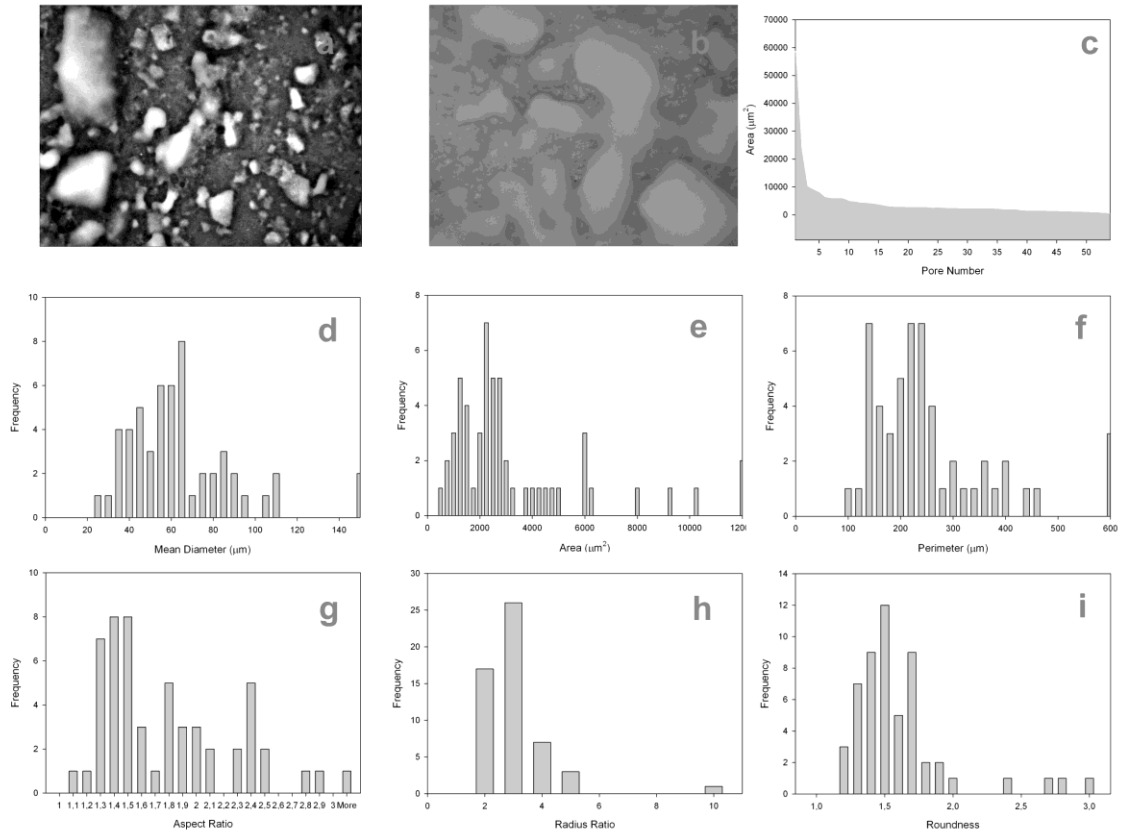


Figure A.25. Representative micrograph taken at 50x magnification (a), random micrograph taken at 100x magnification showing the interaction of pores in detail (b), area distribution (c), size distribution (d), area histogram (e), perimeter distribution (f), aspect ratio distribution (g), roundness distribution (h), radius ratio distribution (i) of pores of the representative sample.

Table A.52. Overall morphological properties of the sample

Total Area ( $\mu\text{m}^2$ )	Total Perimeter ( $\mu\text{m}$ )	3 Highest Areas ( $\mu\text{m}^2$ )	%	3 Highest Perimeters ( $\mu\text{m}$ )	%	Pore Count	Macro-porosity %	Expected Macroporosity %	Effectiveness Factor
233504	14290	88179	43	2669	23	54	37.62	35.73	288.76

## A.26. Morphological Analysis of Sample Set 26

Size distribution of porogens into one fine and one coarse group produced low interconnectivity due to the absence of intermediate size groups. High number of finest porogen group was not reflected in Fig.A.26(d) partly because of coagulation of pores and partly due to the low contrast of the micrograph. This is seen from low total perimeter given in Table A.54 while area was high.

Table A.53. Size distributions of NaCl porogens added into the sample

	-38 $\mu\text{m}$ size group	-53 $\mu\text{m}$ size group	-75 $\mu\text{m}$ size group	-106 $\mu\text{m}$ size group	-150 $\mu\text{m}$ size group	-212 $\mu\text{m}$ size group	Total
By mass (gr)	1.050	0.000	0.000	0.000	1.050	0.000	2.099
By number	8834843	0	0	0	143640	0	8978483

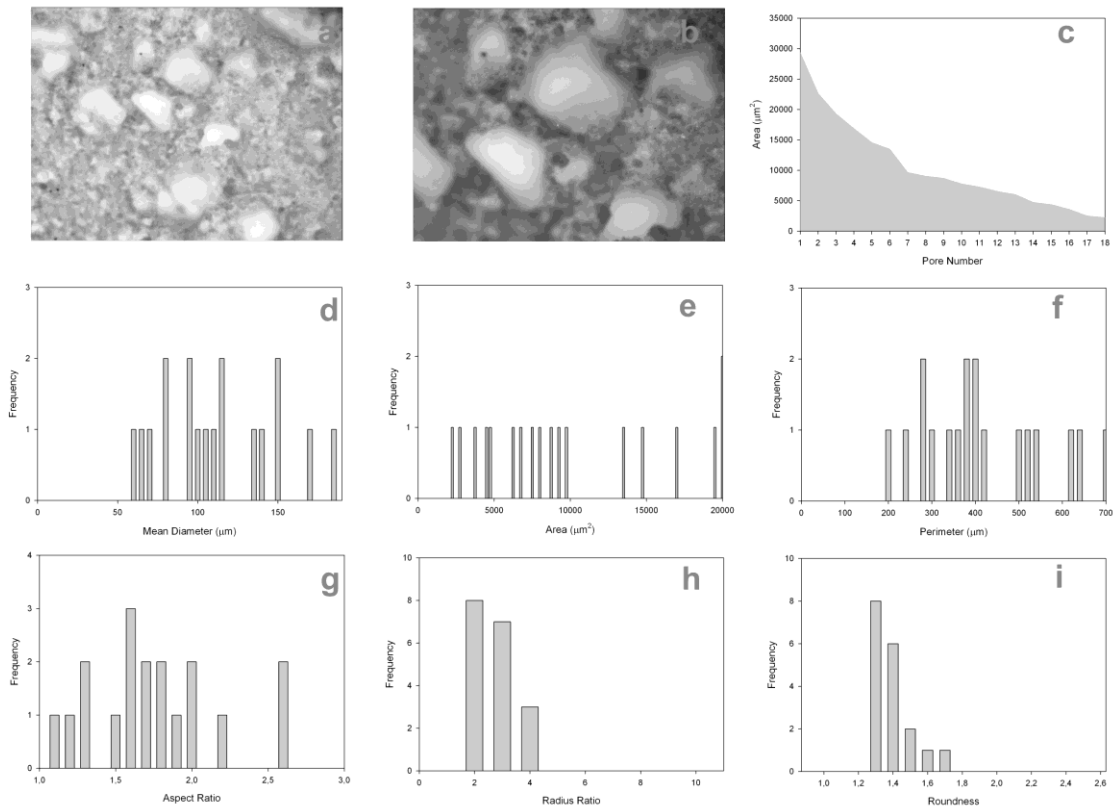


Figure A.26. Representative micrograph taken at 50x magnification (a), random micrograph taken at 100x magnification showing the interaction of pores in detail (b), area distribution (c), size distribution (d), area histogram (e), perimeter distribution (f), aspect ratio distribution (g), roundness distribution (h), radius ratio distribution (i) of pores of the representative sample.

Table A.54. Overall morphological properties of the sample

Total Area ( $\mu\text{m}^2$ )	Total Perimeter ( $\mu\text{m}$ )	3 Highest Areas ( $\mu\text{m}^2$ )	%	3 Highest Perimeters ( $\mu\text{m}$ )	%	Pore Count	Macro-porosity %	Expected Macroporosity %	Effectiveness Factor
209739	7898	83383	43	2052	29	20	33.80	37.73	15.14



## A.27. Morphological Analysis of Sample Set 27

The highest porogen mass added among all samples resulted in the highest effectiveness factor and one of the highest total perimeters in sample 27 as seen in Table A.56. The balanced size distribution similar to samples 21 and 25 and the resulting well packed, well grouped structure was also significant in achieving a high concentration of necks among both intermediate and coarse pores as seen in Fig.A.27(a,b).

Table A.55. Size distributions of NaCl porogens added into the sample

	-38 $\mu\text{m}$ size group	-53 $\mu\text{m}$ size group	-75 $\mu\text{m}$ size group	-106 $\mu\text{m}$ size group	-150 $\mu\text{m}$ size group	-212 $\mu\text{m}$ size group	Total
By mass (gr)	0.344	0.458	0.310	0.399	0.000	0.688	2.200
By number	2897519	1420369	339185	154852	0	33373	4845299

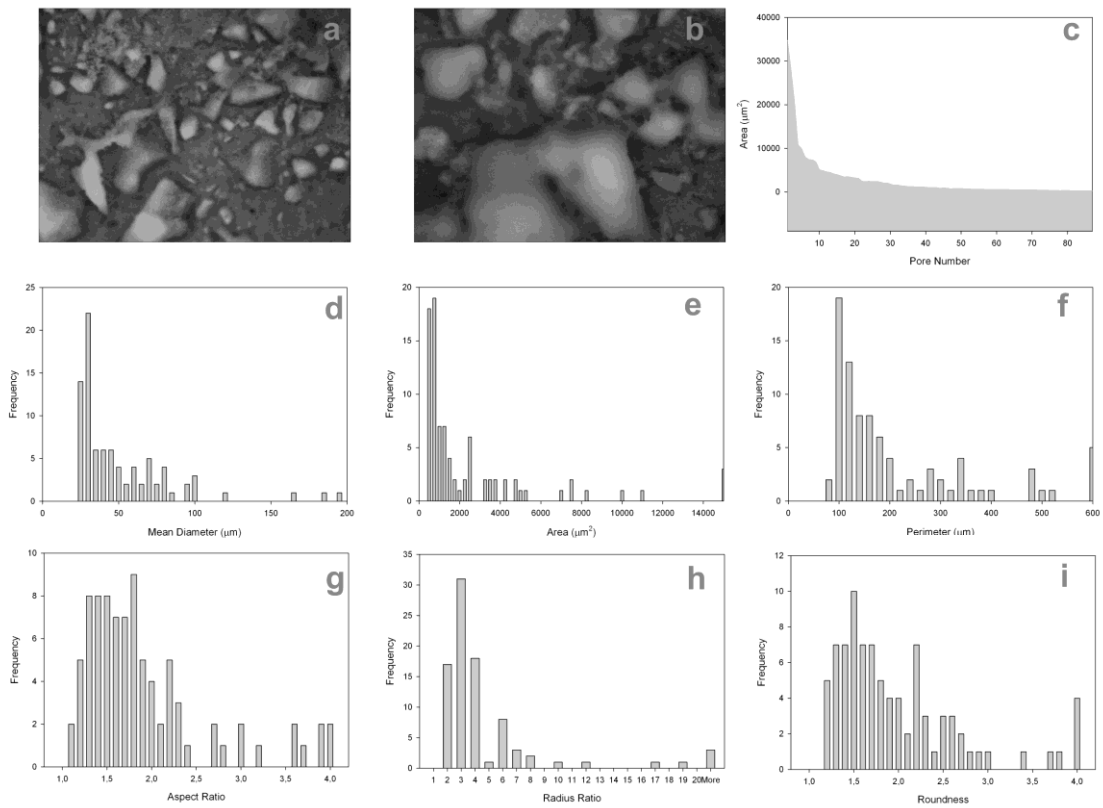


Figure A.27. Representative micrograph taken at 50x magnification (a), random micrograph taken at 100x magnification showing the interaction of pores in detail (b), area distribution (c), size distribution (d), area histogram (e), perimeter distribution (f), aspect ratio distribution (g), roundness distribution (h), radius ratio distribution (i) of pores of the representative sample..

Table A.56. Overall morphological properties of the sample

Total Area ( $\mu\text{m}^2$ )	Total Perimeter ( $\mu\text{m}$ )	3 Highest Areas ( $\mu\text{m}^2$ )	%	3 Highest Perimeters ( $\mu\text{m}$ )	%	Pore Count	Macro-porosity %	Expected Macroporosity %	Effectiveness Factor
259944	20752	79734	37	3036	18	90	41.88	38.27	757.13

## A.28. Morphological Analysis of Sample Set 28

Again a balanced size distribution producing well interconnected pore structure is seen in Fig.A.28(a). Well detection of abundant fine pores gave sample 28 the highest total perimeter among all samples. The high extent of interconnectivity is indicated in Fig.A.28(f) as pores of all surface areas in a wide range exist.

Table A.57. Size distributions of NaCl porogens added into the sample

	-38 $\mu\text{m}$ size group	-53 $\mu\text{m}$ size group	-75 $\mu\text{m}$ size group	-106 $\mu\text{m}$ size group	-150 $\mu\text{m}$ size group	-212 $\mu\text{m}$ size group	Total
By mass (gr)	0.479	0.479	0.479	0.000	0.105	0.479	2.020
By number	4028961	1484965	524035	0	14411	23203	6075575

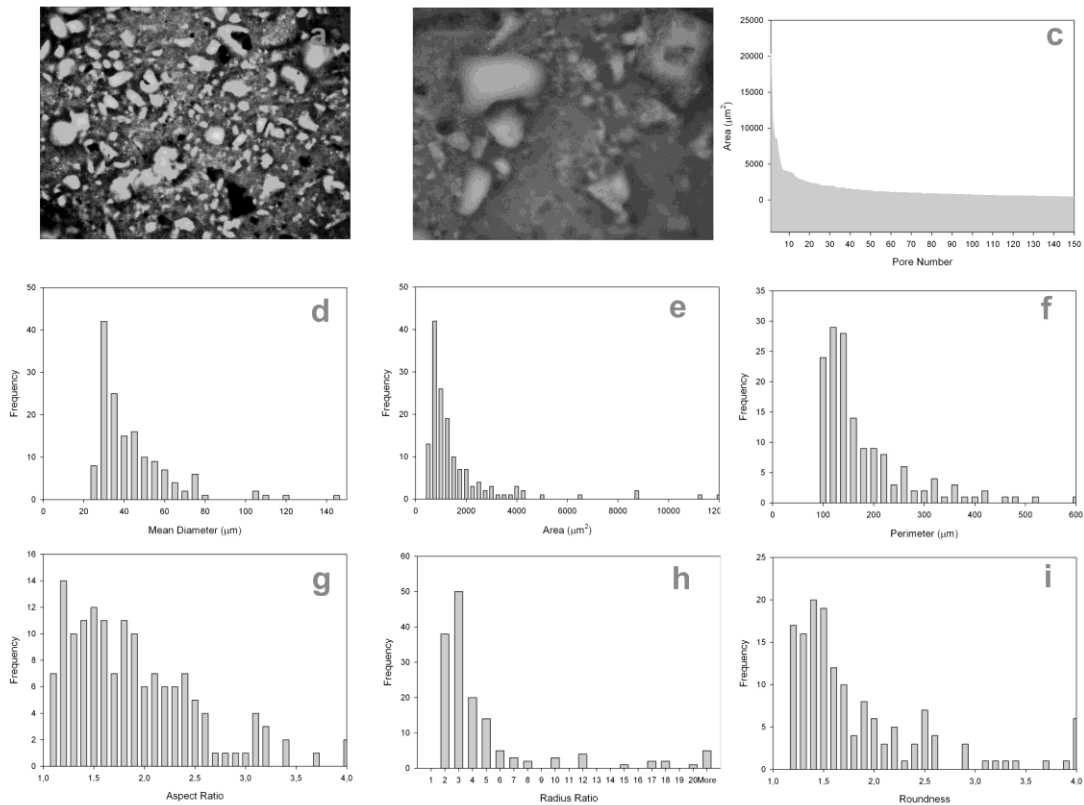


Figure A.28. Representative micrograph taken at 50x magnification (a), random micrograph taken at 100x magnification showing the interaction of pores in detail (b), area distribution (c), size distribution (d), area histogram (e), perimeter distribution (f), aspect ratio distribution (g), roundness distribution (h), radius ratio distribution (i) of pores of the representative sample.

Table A.58. Overall morphological properties of the sample

Total Area ( $\mu\text{m}^2$ )	Total Perimeter ( $\mu\text{m}$ )	3 Highest Areas ( $\mu\text{m}^2$ )	%	3 Highest Perimeters ( $\mu\text{m}$ )	%	Pore Count	Macro- porosity %	Expected Macroporosity %	Effectiveness Factor
251573	25616	43472	25	1748	9	146	40.54	36.43	202.71

## A.29. Morphological Analysis of Sample Set 29

Size distribution of sample 29 was concentrated at the coarser side as seen in Table A.59. Although a large fraction of porogen mass was in coarse size group, they were scarcely present in the micrographs due to low number as seen in Fig.A.29(a,b). Intermediate porogens were present in great number but their interacting groups were not present which resulted only in an ineffective void filling mechanism.

Table A.59. Size distributions of NaCl porogens added into the sample

	-38 $\mu\text{m}$ size group	-53 $\mu\text{m}$ size group	-75 $\mu\text{m}$ size group	-106 $\mu\text{m}$ size group	-150 $\mu\text{m}$ size group	-212 $\mu\text{m}$ size group	Total
By mass (gr)	0.000	0.385	0.827	0.004	0.143	0.658	2.017
By number	0	1195091	905084	1678	19547	31891	2153291

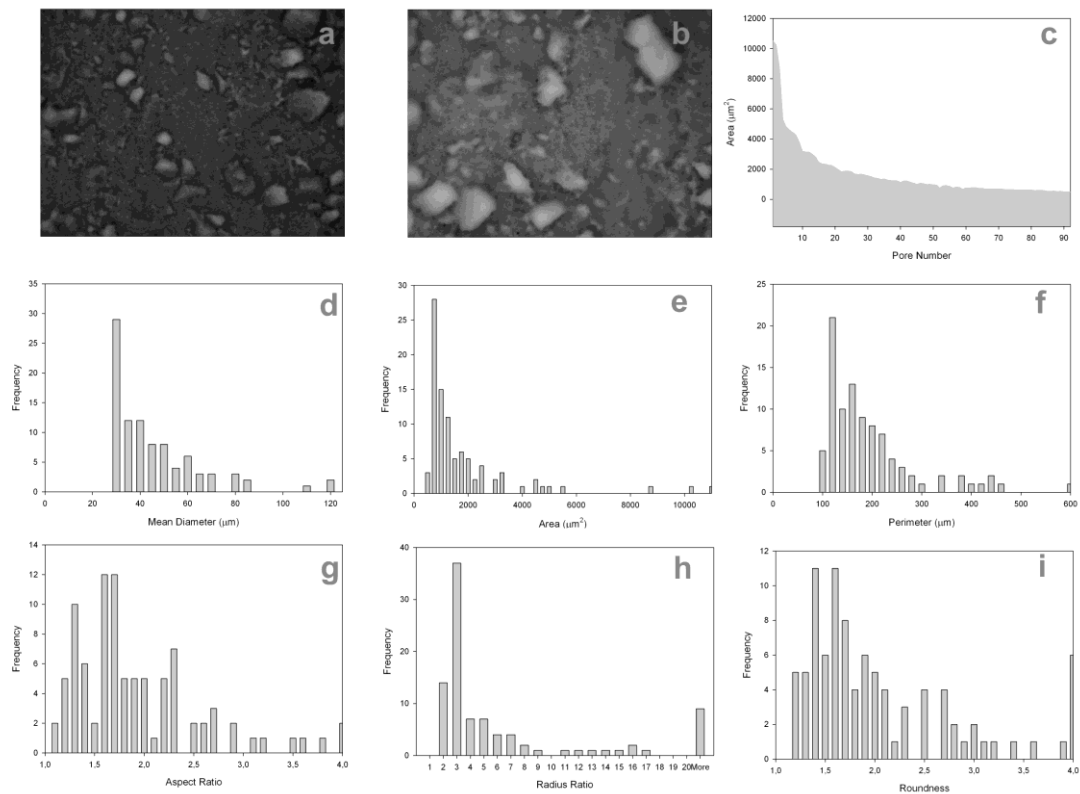


Figure A.29. Representative micrograph taken at 50x magnification (a), random micrograph taken at 100x magnification showing the interaction of pores in detail (b), area distribution (c), size distribution (d), area histogram (e), perimeter distribution (f), aspect ratio distribution (g), roundness distribution (h), radius ratio distribution (i) of pores of the representative sample.

Table A.60. Overall morphological properties of the sample

Total Area ( $\mu\text{m}^2$ )	Total Perimeter ( $\mu\text{m}$ )	3 Highest Areas ( $\mu\text{m}^2$ )	%	3 Highest Perimeters ( $\mu\text{m}$ )	%	Pore Count	Macro-porosity %	Expected Macro-porosity %	Effectiveness Factor
157403	17229	29601	26	1401	11	87	25.36	36.91	28.73

### A.30. Morphological Analysis of Sample Set 30

Sample 30 is an example of formation of interconnected pores without fine porogens. The sole interconnection mechanism is the interaction of adjacent intermediate size groups with no void filling effect as seen in Fig.A.30(a,b). Abundance of intermediate size groups is critical in achieving interconnection without fine porogens as indicated by the high total perimeter given in Table A.62.

Table A.61. Size distributions of NaCl porogens added into the sample

	-38 $\mu\text{m}$ size group	-53 $\mu\text{m}$ size group	-75 $\mu\text{m}$ size group	-106 $\mu\text{m}$ size group	-150 $\mu\text{m}$ size group	-212 $\mu\text{m}$ size group	Total
By mass (gr)	0.004	0.000	0.523	0.817	0.470	0.212	2.027
By number	34398	0	572683	316957	64315	10301	998654

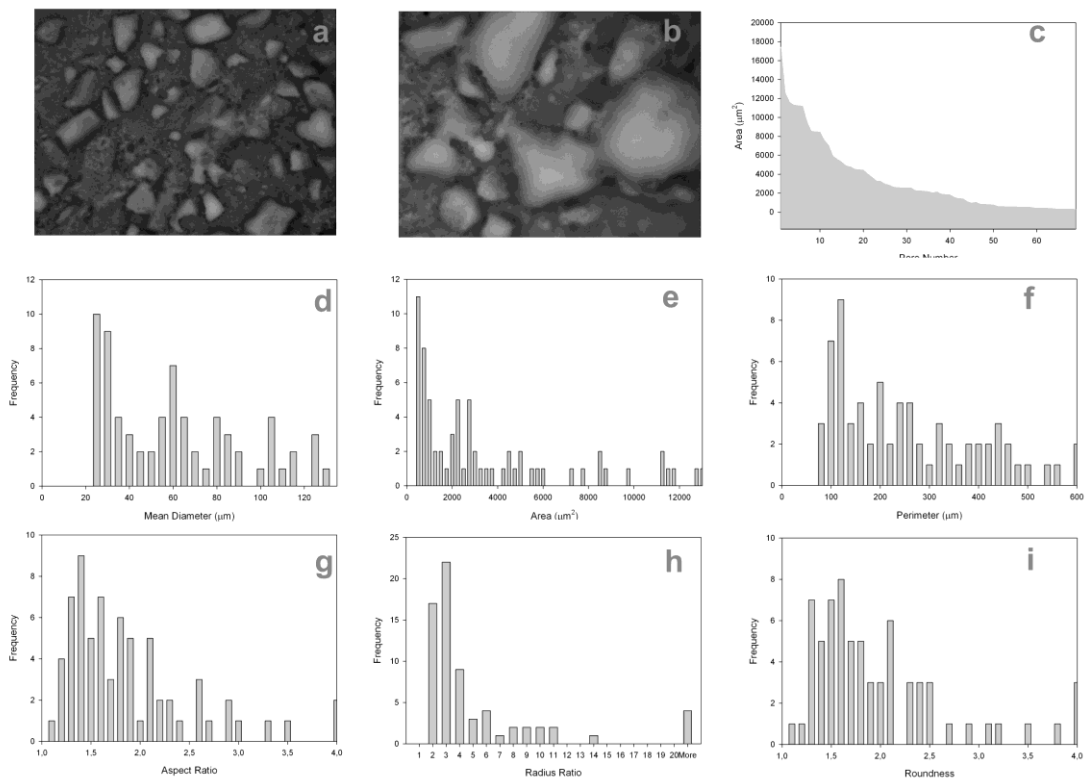


Figure A.30. Representative micrograph taken at 50x magnification (a), random micrograph taken at 100x magnification showing the interaction of pores in detail (b), area distribution (c), size distribution (d), area histogram (e), perimeter distribution (f), aspect ratio distribution (g), roundness distribution (h), radius ratio distribution (i) of pores of the representative sample.

Table A.62. Overall morphological properties of the sample

Total Area ( $\mu\text{m}^2$ )	Total Perimeter ( $\mu\text{m}$ )	3 Highest Areas ( $\mu\text{m}^2$ )	3 Highest Perimeters (%)	3 Highest Perimeters ( $\mu\text{m}$ )	Pore Count	Macro-porosity (%)	Expected Macroporosity (%)	Effectiveness Factor	
211884	17128	41756	24	1790	13	71	34.14	36.92	63.68

### A.31. Morphological Analysis of Sample Set 31

Narrow size distribution of porogens demonstrates beneficial interaction of adjacent size groups on total area and perimeter. Interconnectivity is limited due to the low total number of porogens but rare occurrences of necks are present as seen in Fig.A.31(b). A packing mechanism induced by extra void filling fine porogens would enhance the contact points greatly. High aspect ratio and low roundness seen in Fig.4A.31(g-i) are a consequence of shape irregularity of porogens under study.

Table A.63. Size distributions of NaCl porogens added into the sample

	-38 $\mu\text{m}$ size group	-53 $\mu\text{m}$ size group	-75 $\mu\text{m}$ size group	-106 $\mu\text{m}$ size group	-150 $\mu\text{m}$ size group	-212 $\mu\text{m}$ size group	Total
By mass (gr)	0.000	0.000	0.900	0.000	0.900	0.000	1.800
By number	0	0	985459	0	123182	0	1108641

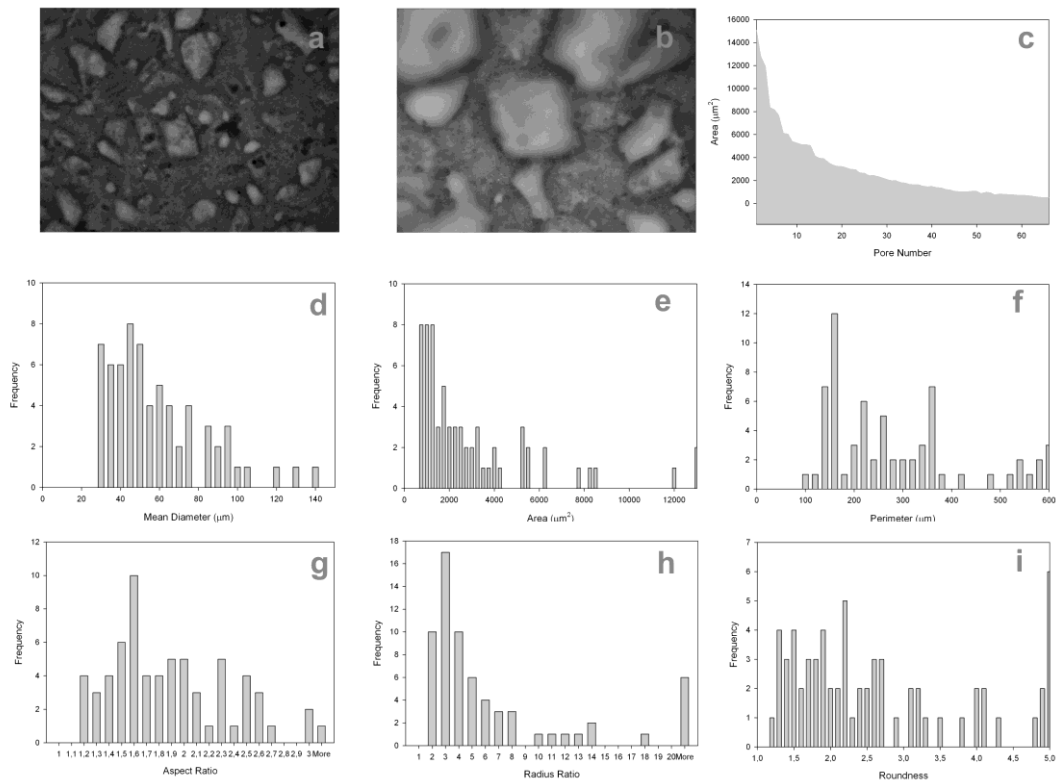


Figure A.31. Representative micrograph taken at 50x magnification (a), random micrograph taken at 100x magnification showing the interaction of pores in detail (b), area distribution (c), size distribution (d), area histogram (e), perimeter distribution (f), aspect ratio distribution (g), roundness distribution (h), radius ratio distribution (i) of pores of the representative sample.

Table A.64. Overall morphological properties of the sample

Total Area ( $\mu\text{m}^2$ )	Total Perimeter ( $\mu\text{m}$ )	3 Highest Areas ( $\mu\text{m}^2$ )	3 Highest Perimeters ( $\mu\text{m}$ )	Pore Count	Macro-porosity %	Expected Macroporosity %	Effectiveness Factor
201618	17764	40151	1736	68	32.49	34.99	64.26

### A.32. Morphological Analysis of Sample Set 32

Size distribution concentrated at the coarser side with some intermediate porogen inclusion produced limited interconnectivity despite high mass of added porogen as seen in Table A.65. High total area and medium perimeter given in Table A.66 is characteristic of coarse porogens. Pore grouping by coagulation effect is the only effective mechanism due to the low number of void filling fine porogens as seen in Fig.A.32(a,b)

Table A.65. Size distributions of NaCl porogens added into the sample

	-38 $\mu\text{m}$ size group	-53 $\mu\text{m}$ size group	-75 $\mu\text{m}$ size group	-106 $\mu\text{m}$ size group	-150 $\mu\text{m}$ size group	-212 $\mu\text{m}$ size group	Total
By mass (gr)	0.000	0.090	0.420	0.000	0.748	0.849	2.107
By number	0	279087	459611	0	102428	41165	882291

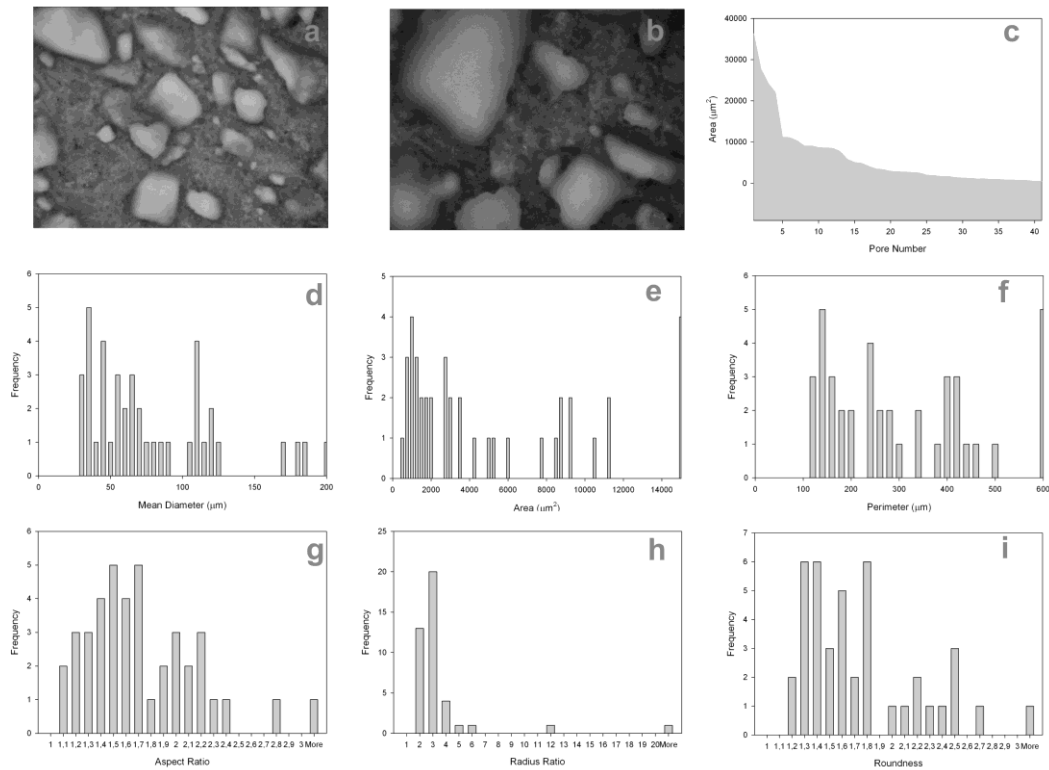


Figure A.32. Representative micrograph taken at 50x magnification (a), random micrograph taken at 100x magnification showing the interaction of pores in detail (b), area distribution (c), size distribution (d), area histogram (e), perimeter distribution (f), aspect ratio distribution (g), roundness distribution (h), radius ratio distribution (i) of pores of the representative sample.

Table A.66. Overall morphological properties of the sample

Total Area ( $\mu\text{m}^2$ )	Total Perimeter ( $\mu\text{m}$ )	3 Highest Areas ( $\mu\text{m}^2$ )	%	3 Highest Perimeters ( $\mu\text{m}$ )	%	Pore Count	Macro- porosity %	Expected Macroporosity %	Effectiveness Factor
250649	13297	74973	34	2199	19	44	40.39	39.01	65.63

### A.33. Morphological Analysis of Sample Set 33

Balanced size distribution concentrated at the finer side produced a hierarchy of adjacent pores that form necks due to abundance of fine porogens as seen in Table A.68. Part of the -38  $\mu\text{m}$  size group was not detected as indicated by the relatively low amount seen in Fig.A.33(d). Both a combination of void forming coarse and void filling fine porogens and interacting intermediate porogens favor high interconnectivity.

Table A.67. Size distributions of NaCl porogens added into the sample

	-38 $\mu\text{m}$ size group	-53 $\mu\text{m}$ size group	-75 $\mu\text{m}$ size group	-106 $\mu\text{m}$ size group	-150 $\mu\text{m}$ size group	-212 $\mu\text{m}$ size group	Total
By mass (gr)	0.403	0.515	0.306	0.000	0.537	0.220	1.981
By number	3389410	1599032	335047	0	73475	10671	5407635

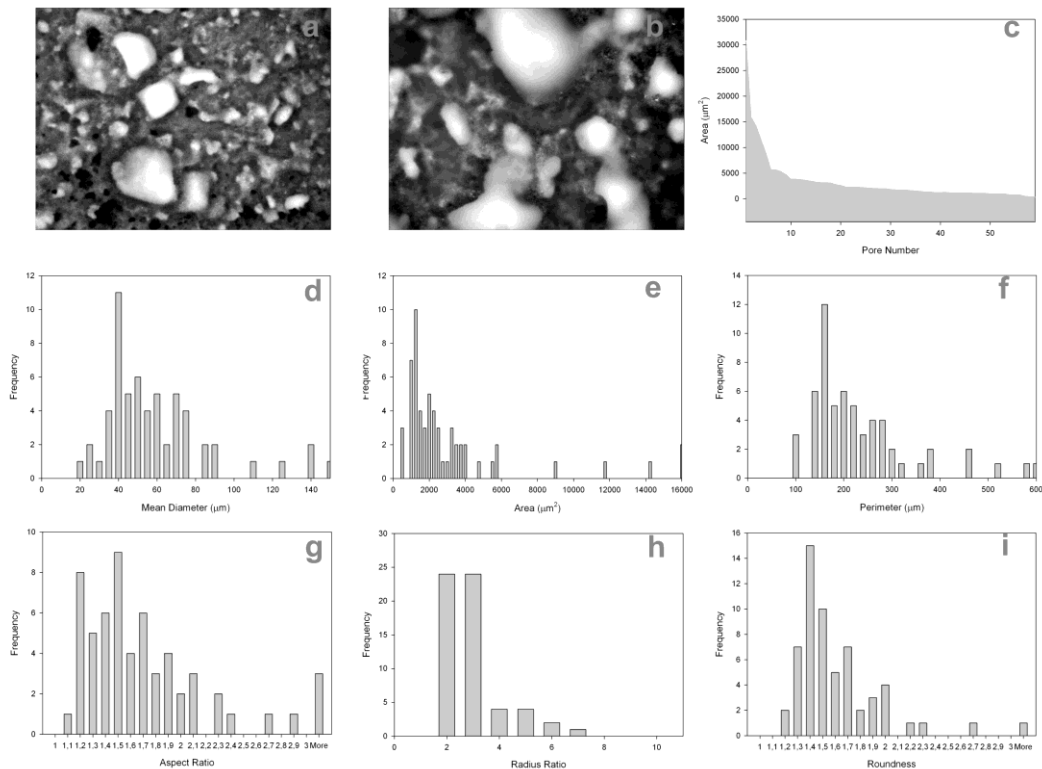


Figure A.33. Representative micrograph taken at 50x magnification (a), random micrograph taken at 100x magnification showing the interaction of pores in detail (b), area distribution (c), size distribution (d), area histogram (e), perimeter distribution (f), aspect ratio distribution (g), roundness distribution (h), radius ratio distribution (i) of pores of the representative sample.

Table A.68. Overall morphological properties of the sample

Total Area ( $\mu\text{m}^2$ )	Total Perimeter ( $\mu\text{m}$ )	3 Highest Areas ( $\mu\text{m}^2$ )	3 Highest Perimeters (%)	3 Highest Perimeters ( $\mu\text{m}$ )	Pore Count	Macro- porosity %	Expected Macroporosity %	Effectiveness Factor	
186959	13314	58341	37	1881	18	62	30.12	35.88	51.41

### A.34. Morphological Analysis of Sample Set 34

High number of fine porogens were not detected as seen in Fig.A.34(d) which accounts for the relatively low total area and effectiveness factor given in Table A.70. The hierarchy of pores as fine-intermediate-coarse exists which should provide both well packing and well grouping of porogens around coarse ones.

Table A.69. Size distributions of NaCl porogens added into the sample

	-38 $\mu\text{m}$ size group	-53 $\mu\text{m}$ size group	-75 $\mu\text{m}$ size group	-106 $\mu\text{m}$ size group	-150 $\mu\text{m}$ size group	-212 $\mu\text{m}$ size group	Total
By mass (gr)	0.730	0.000	0.679	0.097	0.205	0.399	2.110
By number	6143544	0	742888	37592	28092	19349	6971465

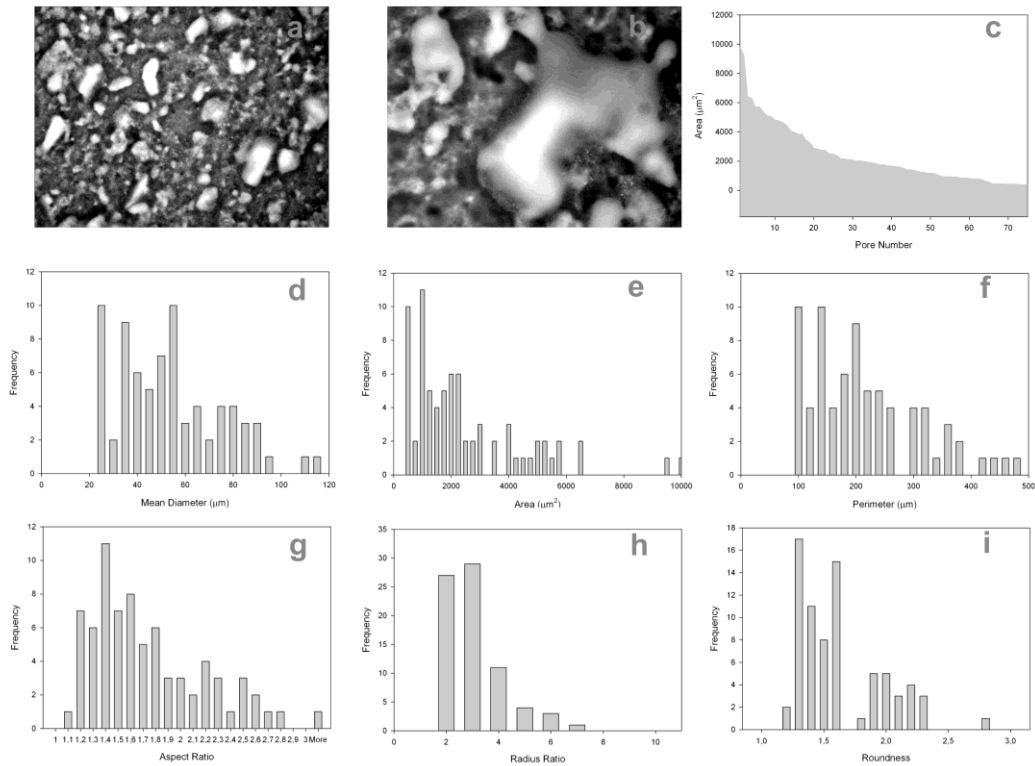


Figure A.34. Representative micrograph taken at 50x magnification (a), random micrograph taken at 100x magnification showing the interaction of pores in detail (b), area distribution (c), size distribution (d), area histogram (e), perimeter distribution (f), aspect ratio distribution (g), roundness distribution (h), radius ratio distribution (i) of pores of the representative sample.

Table A.70. Overall morphological properties of the sample

Total Area ( $\mu\text{m}^2$ )	Total Perimeter ( $\mu\text{m}$ )	3 Highest Areas ( $\mu\text{m}^2$ )	3 Highest Perimeters ( $\mu\text{m}$ )	Pore Count	Macro-porosity %	Expected Macroporosity %	Effectiveness Factor
180253	15635	29062	1269	73	29.04	37.80	12.49



### A.35. Morphological Analysis of Sample Set 35

Sample 35 had the highest total area but relatively low total perimeter due to the abundance of coarse porogens. Interconnectivity was limited to the interaction between adjacent size groups as seen in Fig.A.72(b). Rare occurrence of necks was due to absence of void filling mechanism similar to samples 29-32

Table A.71. Size distributions of NaCl porogens added into the sample

	-38 $\mu\text{m}$ size group	-53 $\mu\text{m}$ size group	-75 $\mu\text{m}$ size group	-106 $\mu\text{m}$ size group	-150 $\mu\text{m}$ size group	-212 $\mu\text{m}$ size group	Total
By mass (gr)	0.027	0.000	0.257	0.598	0.338	0.598	1.818
By number	226574	0	281601	231970	46251	28996	815392

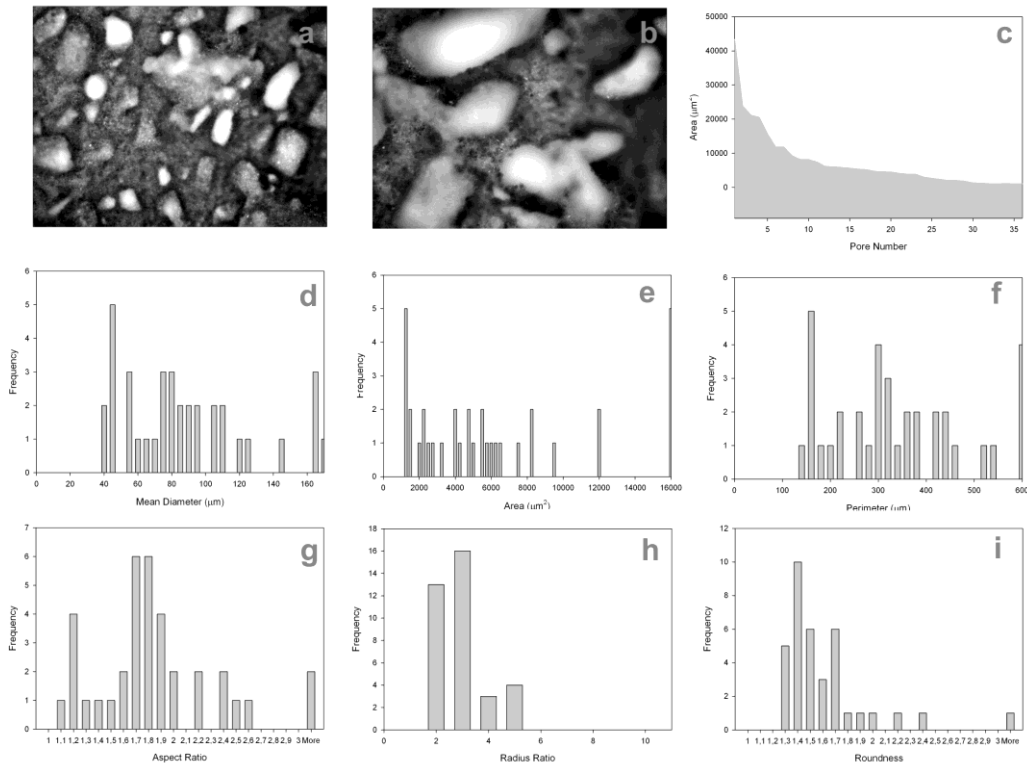


Figure A.35. Representative micrograph taken at 50x magnification (a), random micrograph taken at 100x magnification showing the interaction of pores in detail (b), area distribution (c), size distribution (d), area histogram (e), perimeter distribution (f), aspect ratio distribution (g), roundness distribution (h), radius ratio distribution (i) of pores of the representative sample.

Table A.72. Overall morphological properties of the sample

Total Area ( $\mu\text{m}^2$ )	Total Perimeter ( $\mu\text{m}$ )	Highest Areas ( $\mu\text{m}^2$ )	3 Highest Areas (%)	3 Highest Perimeters ( $\mu\text{m}$ )	3 Highest Perimeters (%)	Pore Count	Macro-porosity (%)	Expected Macroporosity (%)	Effectiveness Factor
270572	12918	72464	28	2173	20	37	43.60	N/A	53.07

### A.36. Morphological Analysis of Sample Set 36

Balanced porogen size distribution concentrated at the intermediate size groups had some degree of interconnectivity. Some necks are seen in Fig.A.36(a,b) with the interaction of adjacent size groups. A fraction of fine porogens were not detected as seen in Fig.A.36(d) which is the reason of low total perimeter given in Table A.74.

Table A.73. Size distributions of NaCl porogens added into the sample

	-38 $\mu\text{m}$ size group	-53 $\mu\text{m}$ size group	-75 $\mu\text{m}$ size group	-106 $\mu\text{m}$ size group	-150 $\mu\text{m}$ size group	-212 $\mu\text{m}$ size group	Total
By mass (gr)	0.225	0.308	0.474	0.474	0.253	0.289	2.023
By number	1894097	955312	518652	183714	34685	14008	3600468

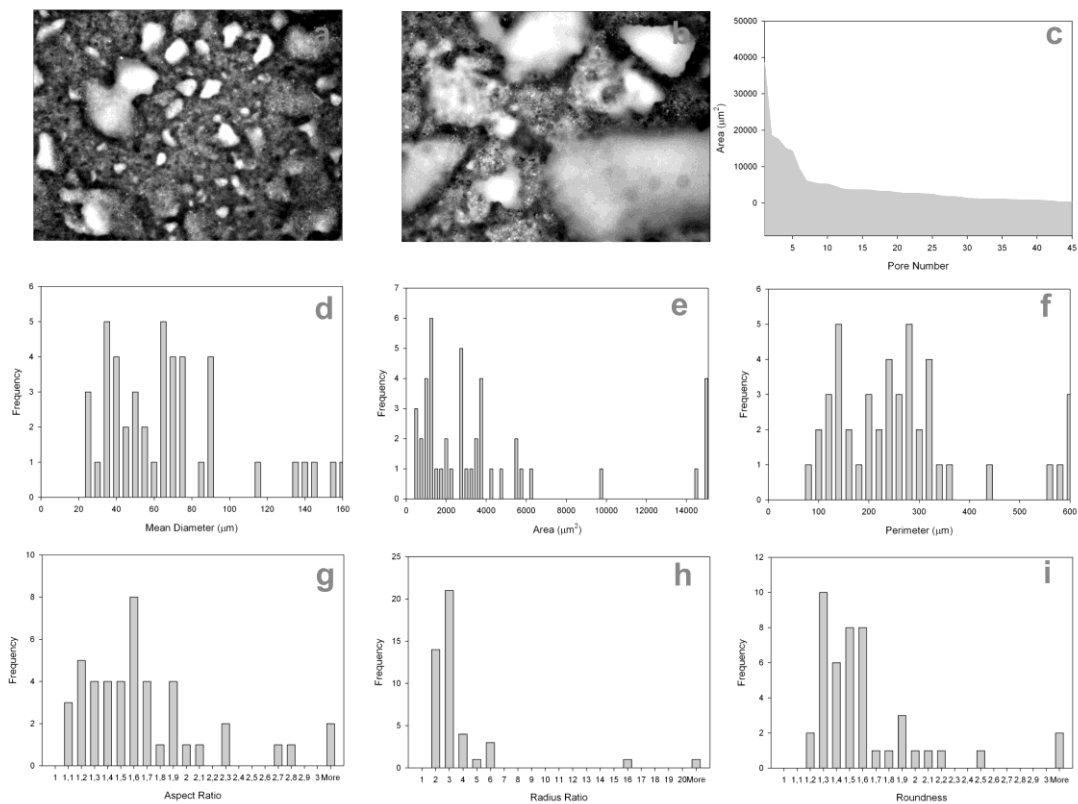


Figure A.36. Representative micrograph taken at 50x magnification (a), random micrograph taken at 100x magnification showing the interaction of pores in detail (b), area distribution (c), size distribution (d), area histogram (e), perimeter distribution (f), aspect ratio distribution (g), roundness distribution (h), radius ratio distribution (i) of pores of the representative sample.

Table A.74. Overall morphological properties of the sample

Total Area ( $\mu\text{m}^2$ )	Total Perimeter ( $\mu\text{m}$ )	3 Highest Areas ( $\mu\text{m}^2$ )	3 Highest Perimeters (%)	Pore Count	Macro-porosity (%)	Expected Macroporosity (%)	Effectiveness Factor		
209265	13138	53308	30	1848	16	51	33.72	36.34	40.05

### A.37. Morphological Analysis of Sample Set 37

Size distribution between fine and coarse porogens with small intermediate amount is expected to produce limited interconnectivity similar to sample 26. The limitation of the microscope to capture representative micrographs with high contrast prevents a sound analysis of sample 37 as almost all -38  $\mu\text{m}$  size group pores were omitted, resulting in low total area, perimeter and macroporosity values given in Table A.76.

Table A.75. Size distributions of NaCl porogens added into the sample

	-38 $\mu\text{m}$ size group	-53 $\mu\text{m}$ size group	-75 $\mu\text{m}$ size group	-106 $\mu\text{m}$ size group	-150 $\mu\text{m}$ size group	-212 $\mu\text{m}$ size group	Total
By mass (gr)	0.833	0.174	0.004	0.379	0.325	0.650	2.365
By number	7011088	540076	4560	146971	44456	31494	7778643

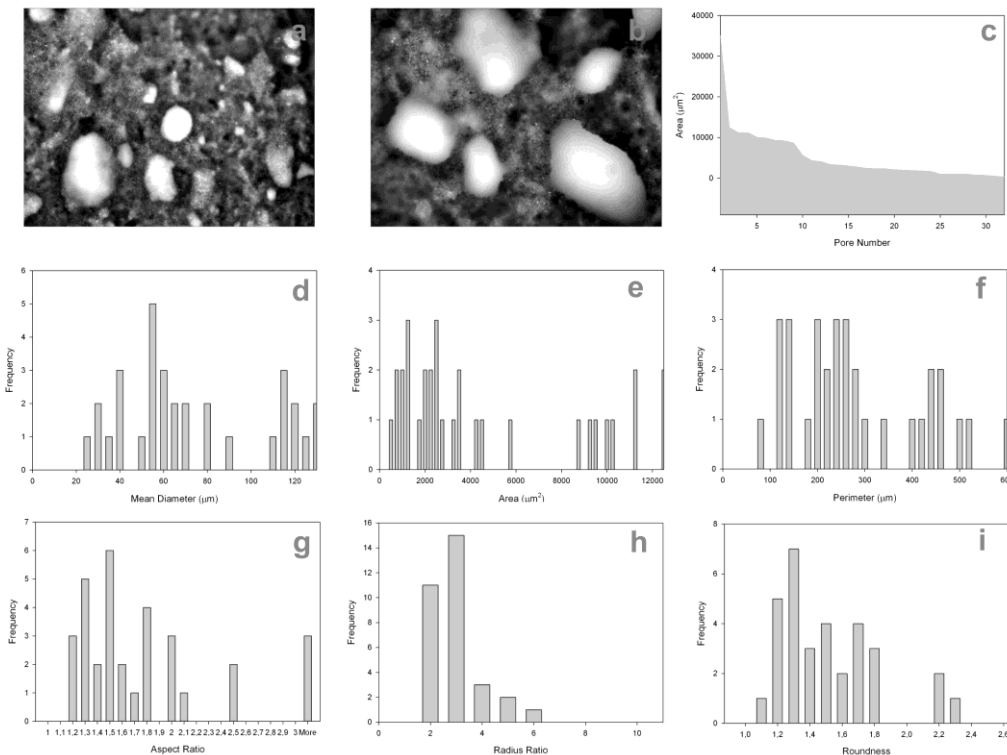


Figure A.37. Representative micrograph taken at 50x magnification (a), random micrograph taken at 100x magnification showing the interaction of pores in detail (b), area distribution (c), size distribution (d), area histogram (e), perimeter distribution (f), aspect ratio distribution (g), roundness distribution (h), radius ratio distribution (i) of pores of the representative sample.

Table A.76. Overall morphological properties of the sample

Total Area ( $\mu\text{m}^2$ )	Total Perimeter ( $\mu\text{m}$ )	3 Highest Areas ( $\mu\text{m}^2$ )	3 Highest Perimeters (%)	3 Highest Perimeters ( $\mu\text{m}$ )	Pore Count	Macro-porosity (%)	Expected Macroporosity (%)	Effectiveness Factor	
154628	8472	59469	44	1796	26	36	24.92	39.95	15.13

### A.38. Morphological Analysis of Sample Set 38

Sequential void filling of the fine, among intermediate and coarse porogens give sample 38 some degree of interconnectivity although most fine pores were again not detected as seen in Fig.A.38(d). Both total area, total perimeter and macroporosity are expected to increase to a level of well connected pore structure if instrument related error is removed.

Table A.77. Size distributions of NaCl porogens added into the sample

	-38 $\mu\text{m}$ size group	-53 $\mu\text{m}$ size group	-75 $\mu\text{m}$ size group	-106 $\mu\text{m}$ size group	-150 $\mu\text{m}$ size group	-212 $\mu\text{m}$ size group	Total
By mass (gr)	0.755	0.000	0.702	0.100	0.212	0.413	2.182
By number	6353928	0	768328	38879	29054	20011	7210201

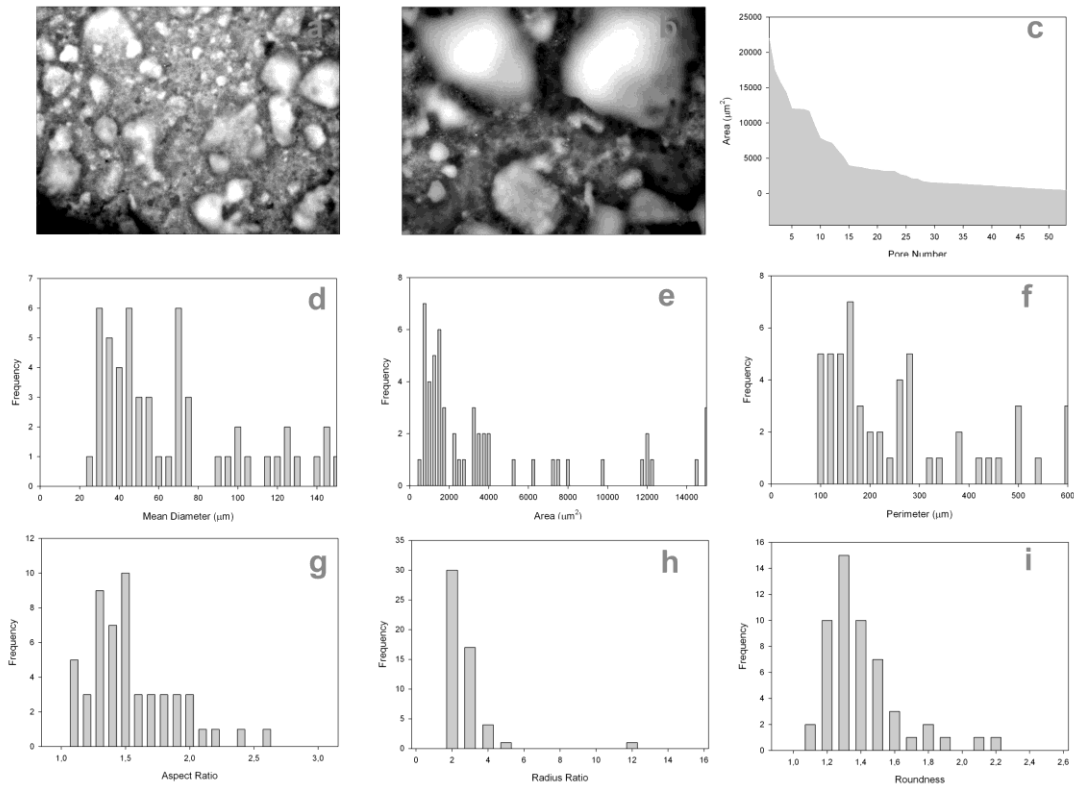


Figure A.38. Representative micrograph taken at 50x magnification (a), random micrograph taken at 100x magnification showing the interaction of pores in detail (b), area distribution (c), size distribution (d), area histogram (e), perimeter distribution (f), aspect ratio distribution (g), roundness distribution (h), radius ratio distribution (i) of pores of the representative sample.

Table A.78. Overall morphological properties of the sample

Total Area ( $\mu\text{m}^2$ )	Total Perimeter ( $\mu\text{m}$ )	3 Highest Areas ( $\mu\text{m}^2$ )	3 Highest Perimeters (%)	Pore Count	Macro-porosity (%)	Expected Macroporosity (%)	Effectiveness Factor		
217629	13013	66541	36	1993	19	51	35.07	38.35	59.47

Simply put, its mass, density, and architecture can change in accordance with prevailing, local mechanical conditions. The skeleton can add or remove bone tissue where appropriate to alter its functional architecture, typically to reduce stress or resulting strain.



Figure 2.1. Cross section of a human femur.  
(Source: Buckwalter, 1995)

The stiffness of cortical and trabecular bone are approximately 17 GPa and 100–200 MPa, respectively (Turner et al. 1999), (Brown et al. 2002). The compressive strength of trabecular bone is reported as 2.5 MPa (Brown et al. 2002). The tensile strength of cortical bone is estimated to be close to 130 MPa (Cullinane 2005). Bone, unlike a uniform material like steel, is extremely anisotropic and thus its material properties vary widely with the direction and orientation of loading. This anisotropy in cortical bone has been linked to its constituent layers or lamellae, where each layer has been shown to demonstrate its own unique elastic properties via changes in preferred collagen fibril orientation. It is these multiple layers, piled upon one another, that serve to give cortical bone its generalized material properties (Bensamoun et al. 2004).

absence of relevant and necessary information from bone biologists, Hench assumed that the role of the cement line was replaced by that of the calcium phosphate-rich surface reaction layer on bioactive glass used in his pioneering work. However Davies presents histological evidence of bone cement layer as seen in Figure 3.1 and argues that both biology and material surface play a part in the ultimate bonding phenomenon (Brown et al. 2002).

The formation of bone requires not only the recruitment and migration of a potentially osteogenic cell population but also the differentiation of this population into mature secretory cells. The potentially osteogenic population will migrate through the resolving blood clot and will reach the surface of bone fragments, or the implant, within the wound site. According to Davies' another study on the mechanism of peri-implant healing, this stage termed osteoconduction is the most important aspect of peri-implant healing. The implant surface design can have a profound influence on osteoconduction not only by modulating the levels of platelet activation, but also by maintaining the anchorage of the temporary scaffold of fibrin and proteins through which these cells reach the implant surface. Cells that reach the solid surface will initiate matrix synthesis by secreting the first proteinaceous matrix of the cement line directly on the implant surface. This stage, the de novo formation of bone can therefore be considered as a separate and distinct phenomenon which, in time, will be followed by the remodeling of the peri-implant bone (Davies 2003).

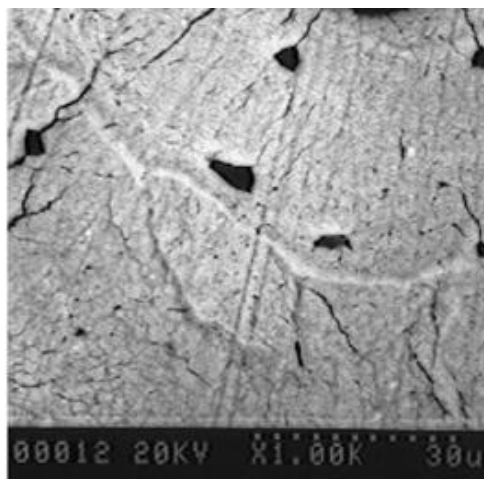


Figure 3.1. Backscattered electron image of a secondary osteon in rat femur clearly showing the relatively hypermineralized cement line forming the interface between the new bone (top) and the old bone (bottom) (Source: Davies and Baldan, 1997)

However, there is always a trade-off in ceramics between the porosity needed for bone ingrowth and the mechanical properties of the scaffold. Therefore, a particular effort should be given to balance the porosity of a scaffold with the need for mechanical properties when implanted in the specific site. Macropore induction by porogens is a solid approach to increase the effective porosity and minimize the useless micropores in scaffolds. Among the diverse techniques used to build macroporous ceramic scaffolds are polymer sponge replica template (Miao et al. 2004; Descamps et al. 2008), pore forming emulsifier (Bohner 2001; Bohner 2005), freeze casting (Qi et al. 2009), combustible porogen (Bouler et al. 1996; del Real et al. 2002), leachable porogen (Takagi et al. 2001; Tadic 2004) and three dimensional printing (Taboas et al. 2003; Gbureck et al. 2007) techniques. Morphology of scaffolds prepared with the respective techniques are seen in the SEM images in Figure 3.2.

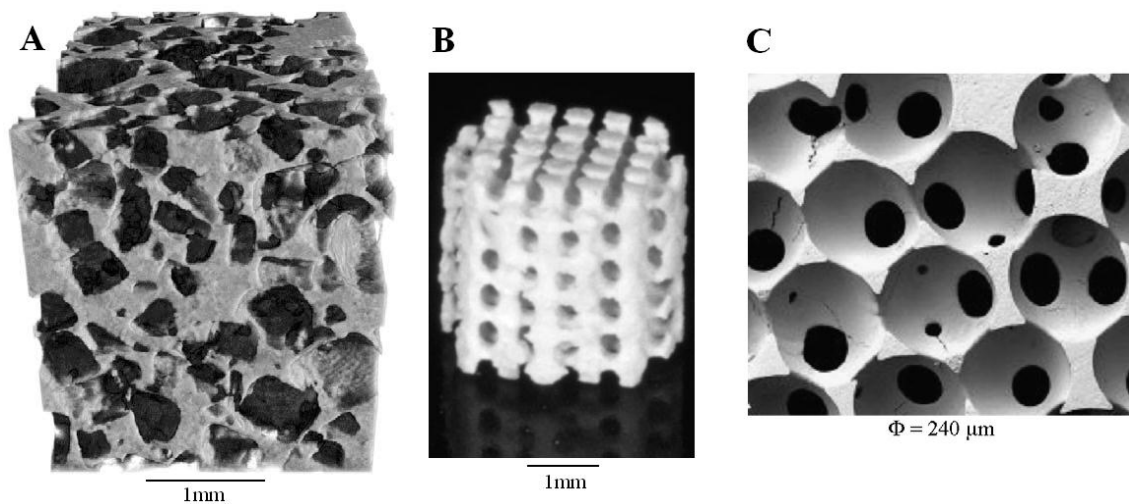


Figure 3.2. Macroporous scaffolds prepared by (a) NaCl/PVA fiber leaching (Source: Tadic et al., 2004) (b) solid free form fabrication (Source: Taboas and Maddox 2003), (c) polymer reverse replica (Source: Descamps and Duhoo 2008) techniques.

In the study by Ginebra et al. where the hardening of  $\alpha$ -TCP to calcium deficient hydroxyapatite is investigated, four stages can be distinguished in the evolution of the microstructure as seen in Figure 4.2. In the first stage, which runs up to 30 minutes, the initial powder exhibits a detached and granular morphology. In the second stage, from 30 minutes to 8 hours, the smaller  $\alpha$ -TCP particles have dissolved completely, whereas the bigger ones become surrounded by a layer of small CDHA crystals, which can be expected to retard the reaction. In the third stage, which runs from 8 to 64 hours, the remaining  $\alpha$ -TCP particles keep dissolving but at a lower rate. Some platelike crystals of CDHA can be seen within the interstices, which are much bigger than the first CDHA crystals precipitated. At the end of this stage, particles of  $\alpha$ -TCP are hardly detected, but one can still see where they have been. The rims of small crystals formed in the first stages can still be distinguished, but the space previously occupied by the  $\alpha$ -TCP particles is now occupied by the big platelike crystals. In the last stage, for  $t > 64$  hours, radial or parallel orientations of the crystals occur with a more compact form, probably due to crystal growth (Ginebra et al. 1997).



Figure 4.2. SEM pictures of cement at various periods of reaction: (a) after 15 min; (b) after 1 hr; (c) after 64 hrs; (d) after 360 hrs. (Source: Ginebra et al. 1997)



chains of Ca-PO<sub>4</sub> arranged parallel to each other (Wang et al. 2008). Lattice water molecules are interlayered between the calcium phosphate chains. The crystal structure seen in Figure 4.6 is basically a layer structure bound together by hydrogen bonding. Zig-zag chains of CaO<sub>8</sub> polyhedra running parallel to the a axis are bound together by similar zig-zag chains of PO<sub>4</sub><sup>3-</sup> tetrahedra, resulting in corrugated sheets normal to the b axis. These sheets are weakly bound together through hydrogen bonding associated with a layer of H<sub>2</sub>O molecules. The phosphate tetrahedra is asymmetric, containing four non-equivalent P–O bond lengths; the longest of these P–O bonds involves hydroxyl oxygen where the acidic proton resides. This acidic proton forms a short hydrogen bond of 1.69 Å to O in which the O–H–O angle is 167.9° (Schofield et al. 2004). Two of the oxygen atoms bonded to the Ca<sup>2+</sup> cations belong to H<sub>2</sub>O molecules and the remaining six oxygen atoms are bonded to the phosphate groups. The H<sub>2</sub>O molecules form a layer which binds together the polyhedral layers via the O–H hydrogen bonds, which act almost entirely along the b axis.

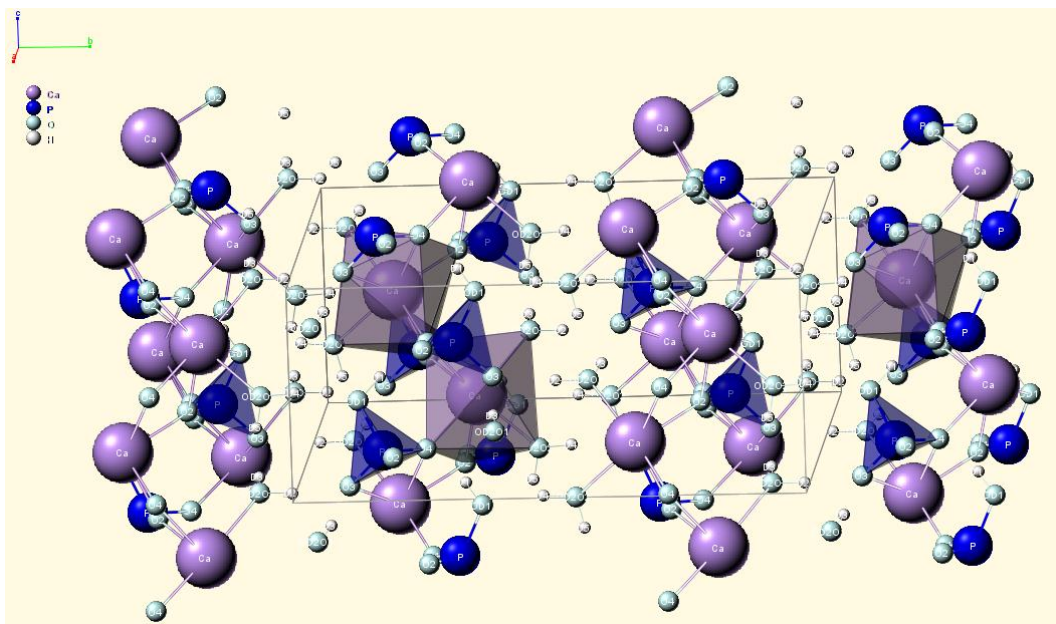


Figure 4.6. Representation of the crystal structure of brushite viewed along the a axis with the b axis horizontal and the c axis vertical. (Source: Webmineral.com)

Anhydrous calcium hydrogen phosphate or monetite is less soluble than DCPD due to the absence of water inclusions. The morphology of DCPD is shown in Figure 4.7. DCPD crystals are characteristically smooth plates. DCPD powders can easily be

precursors. At pH 6.7, OCP was observed to form at intermediate supersaturation, and DCPD was observed at lower pH values. The kinetics of formation of OCP was described by a flashlike nucleation step in combination with surface nucleation and growth based on a mononuclear growth model. Certain calcium positions in DCPD and HA are closely aligned, enabling epitaxial intergrowth and transformation of DCPD to HA. In situ AFM studies showed that the precipitation of HA occurred after the dissolution of DCPD, and no evidence of direct structural transformation from DCPD to HA was observed (Wang et al. 2008). This indicates that DCPD acts as a heterogeneous growth center for HA without requiring any structural modification. Various authors have demonstrated transformation of both DCPD and DCPA to HA upon soaking the samples in aqueous solutions, Hank's salt solution and simulated body fluid (Kumar 2000; Tas et al. 2004; Jalota et al. 2008). Crystal morphology of DCP particles is shown in Figure 4.9.

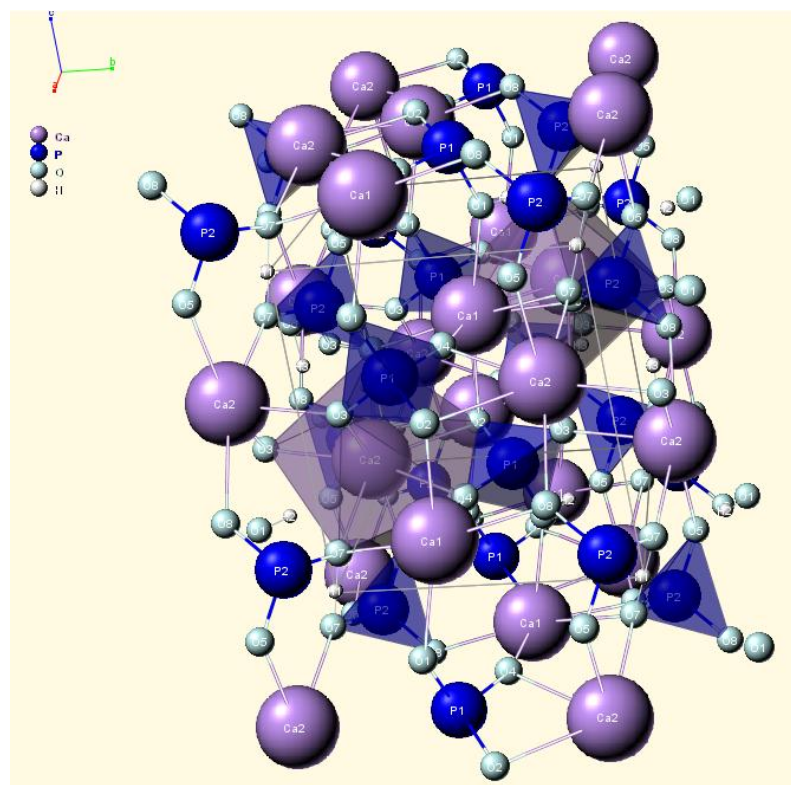


Figure 4.8. Representation of the crystal structure of monetite viewed along the a axis with the b axis horizontal and the c axis vertical. (Source: Webmineral.com)

- The growth rate of systems with a low solubility  $< 10^{-7}$  is diffusion controlled for  $S > 10$
- This is also true for systems with solubility  $< 10^{-4}$  for the relative supersaturation  $S > 1$ .
- In general, both mechanisms, volume diffusion and integration, contribute to growth when  $0.1 < \text{solubility} < 10^{-4}$  and  $10^{-3} < S < 0.1$ .
- The integration of units is the decisive step for crystal growth when solubility  $< 10^{-4}$  and  $S < 0.1$

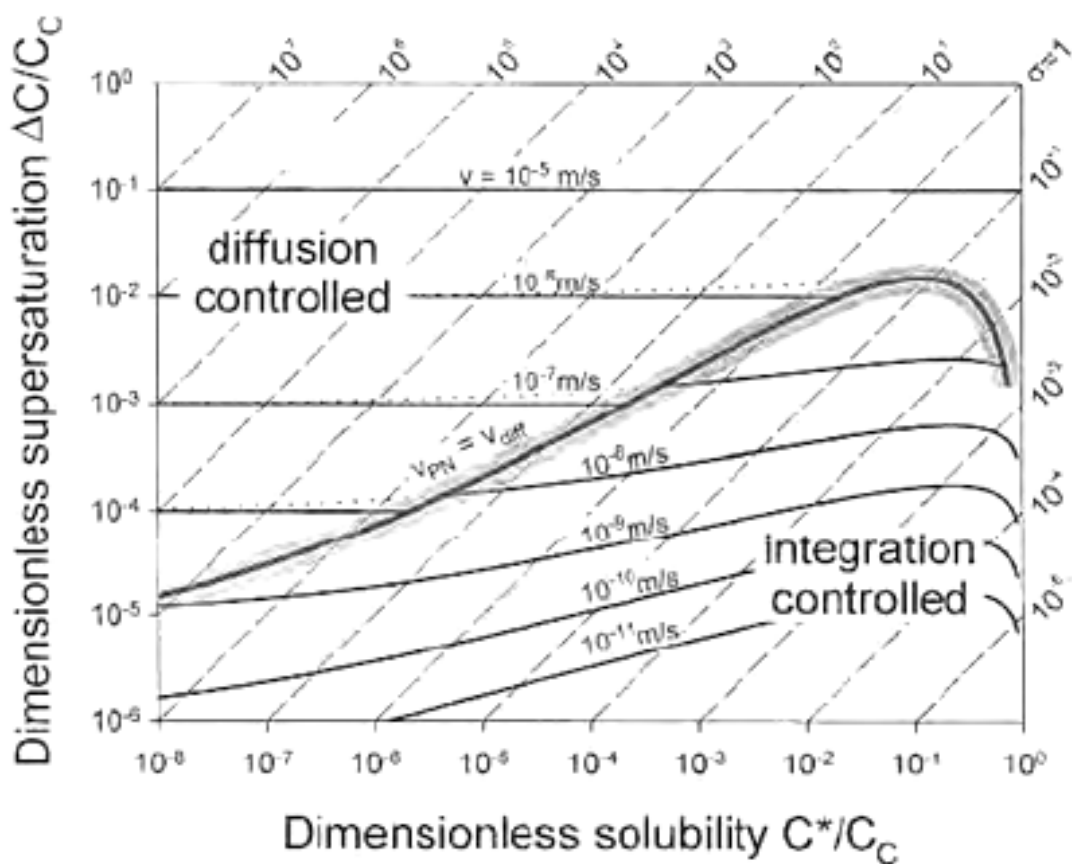


Figure 4.21. Generally applicable prediction of growth rates as a function of supersaturation and solubility. (Source: Mersmann, 2001)

Therefore the governing equilibrium growth mechanism for brushite cement in pure water at acidic pH is integration controlled growth since the precursors are highly soluble reaching solubilities around  $10^{-1}$ . Surface integration is slower than diffusion even for relatively high supersaturations as seen in Figure 4.21. The supersaturation of

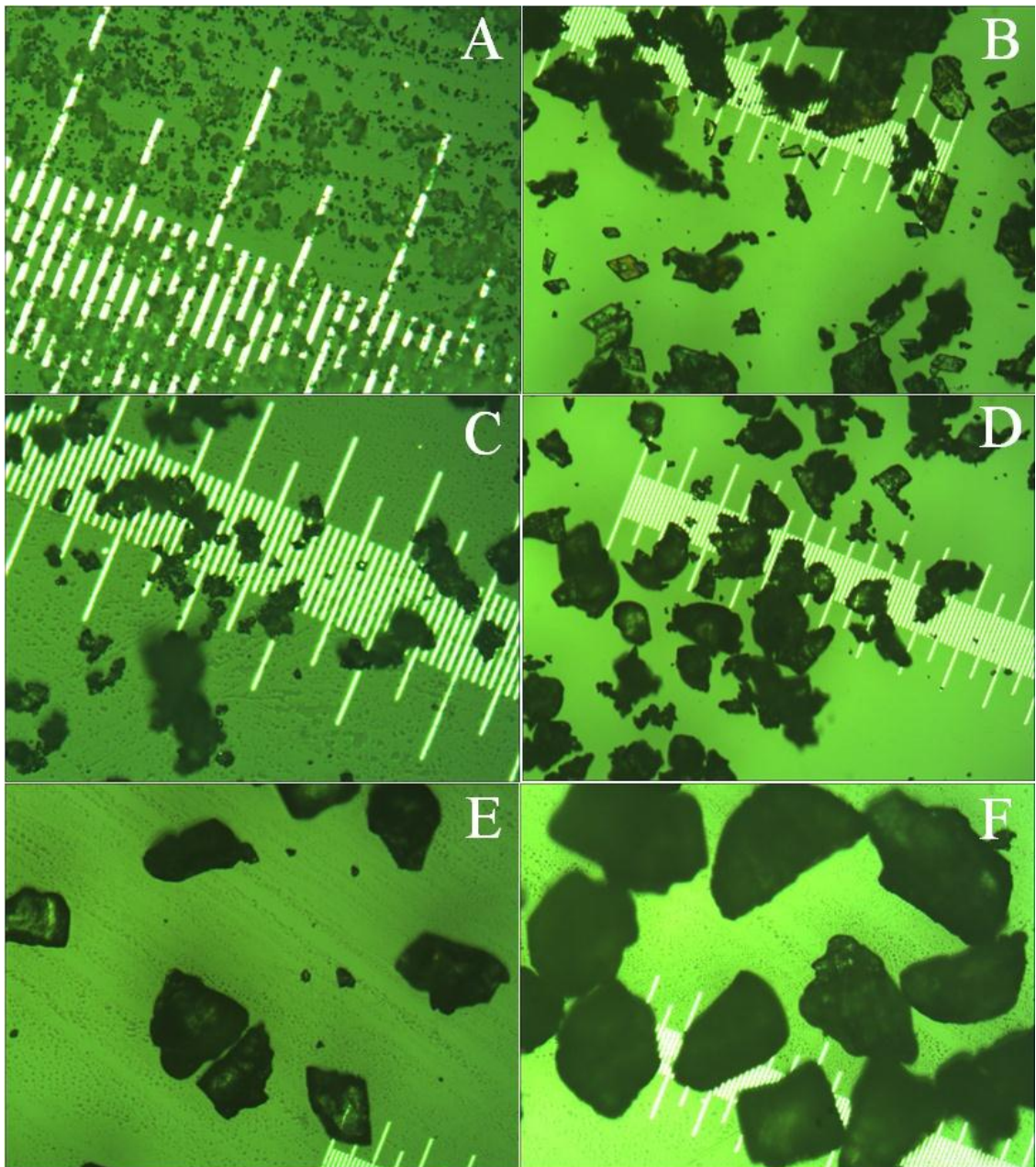


Figure 5.1. Optical microscope images of cement precursor (A)  $\beta$ -TCP, (B) MCPM, NaCl less than (C) 38  $\mu\text{m}$ , (D) 75  $\mu\text{m}$ , (E) 150  $\mu\text{m}$ , and (F) 212  $\mu\text{m}$ . The scale is 1 mm, smallest ticks corresponding to 10  $\mu\text{m}$ .

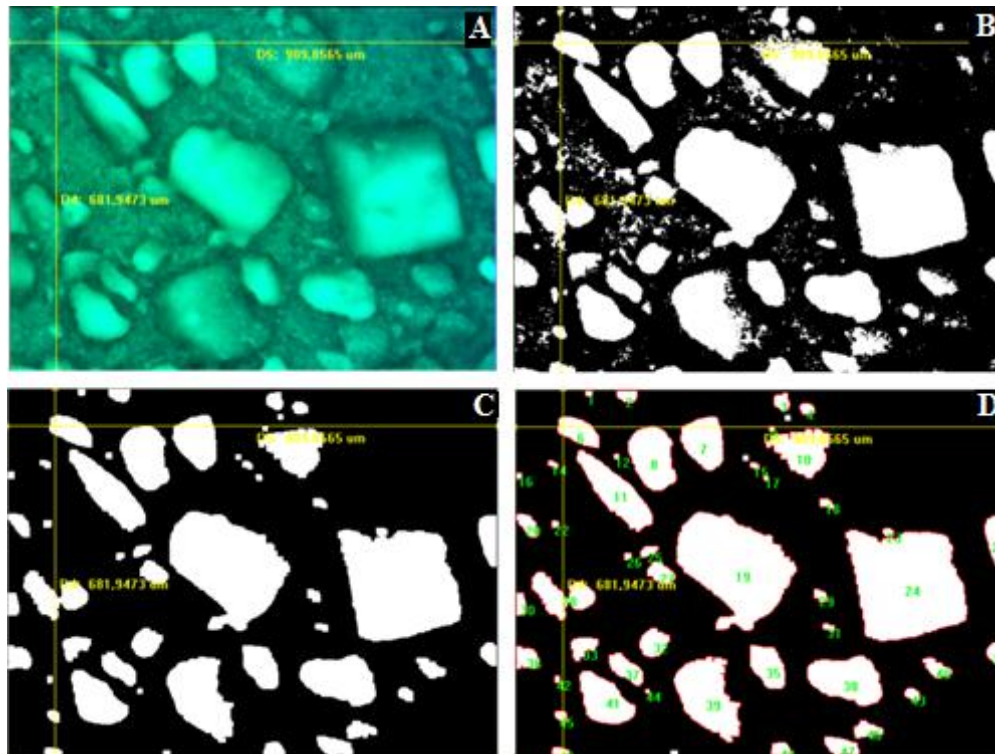


Figure 5.3. Image processing sequence for sample 32.

<p>Diameter (max)</p> <p>Length of longest line joining two points of object's outline and passing through the centroid.</p>	<p>Diameter (min)</p> <p>Length of shortest line joining two points of object's outline and passing through the centroid.</p>	<p>Diameter (mean)</p> <p>Average length of diameters measured at 2 degree intervals and passing through object's centroid.</p>	<p>Perimeter</p> <p>Length of the object's outline.</p>	<p>Area</p> <p>Area included in the polygon defining the object's outline.</p>
<p>Size (length)</p> <p>Feret diameter (i.e. caliper length) along major axis of object.</p>	<p>Size (width)</p> <p>Feret diameter (i.e. caliper length) along minor axis of object.</p>	<p>Radius Ratio</p> <p>Ratio between Max. Radius and Min. Radius.</p>	<p>Aspect Ratio</p> <p>Ratio between major axis and minor axis of ellipse equivalent to object.</p>	<p>Roundness</p> <p><math>(\text{perimeter}^2) / (4 * \pi * \text{area})</math></p>

Figure 5.4. Morphological parameters measured in the image analysis.

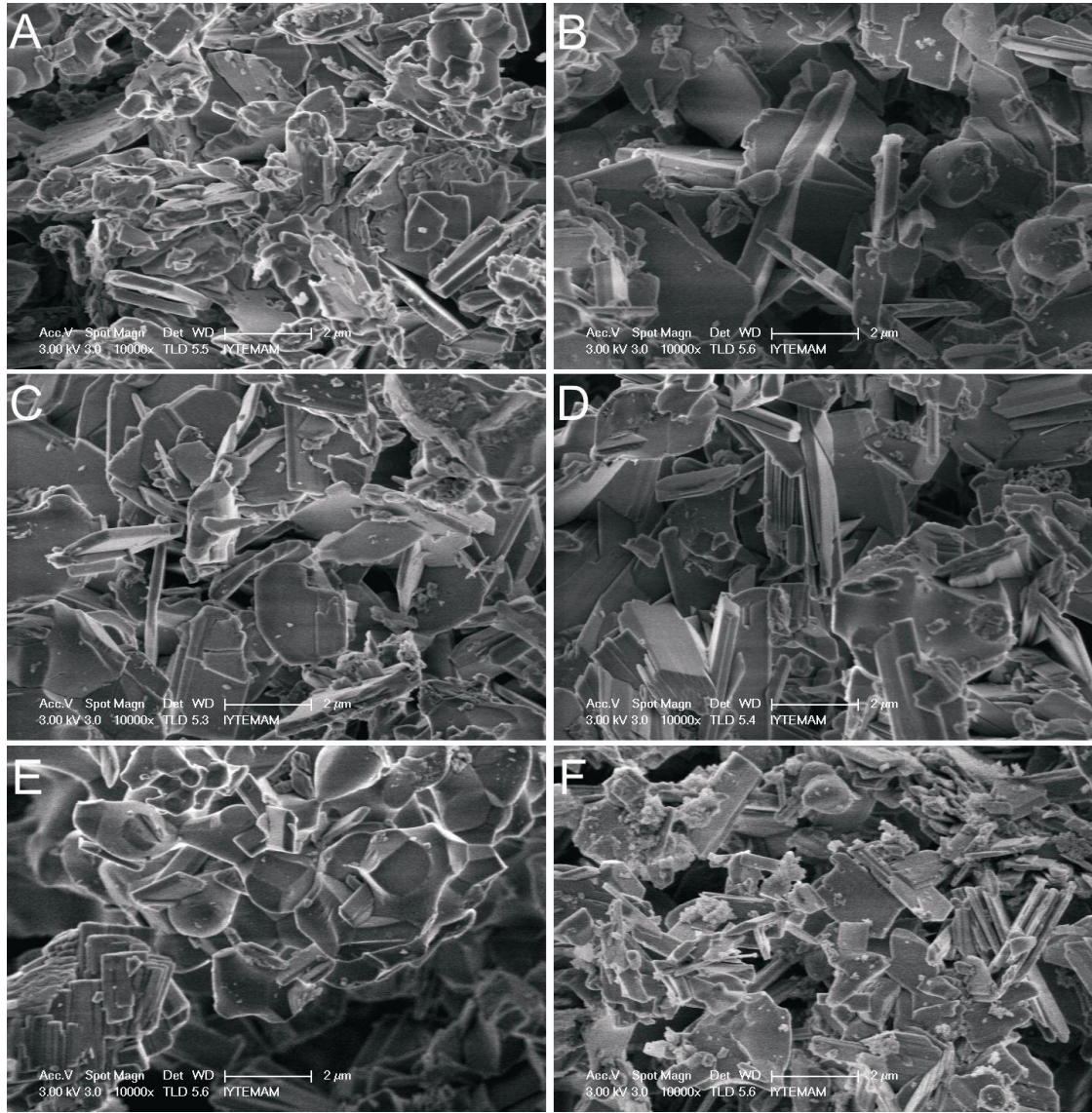


Figure 6.24. Crystal morphology of samples set in 1-6 M NaCl aqueous solution (A-F).

Table 6.4. Elemental analysis of samples set in 1-6 M NaCl aqueous solution

NaCl M	EDX				XRD			
	O%	P%	Ca%	Ca/P	O%	P%	Ca%	Ca/P
1	67.25	15.81	16.95	1.07	68.26	14.16	17.59	1.24
2	66.75	15.41	17.84	1.16	68.44	14.09	17.47	1.24
3	65.92	15.23	18.85	1.24	68.46	14.11	17.43	1.24
4	66.72	15.59	17.69	1.13	68.3	14.15	17.55	1.24
5	67.29	15.56	17.15	1.10	68.19	14.25	17.56	1.23
6	68	15.15	16.85	1.11	68.08	14.35	17.57	1.22

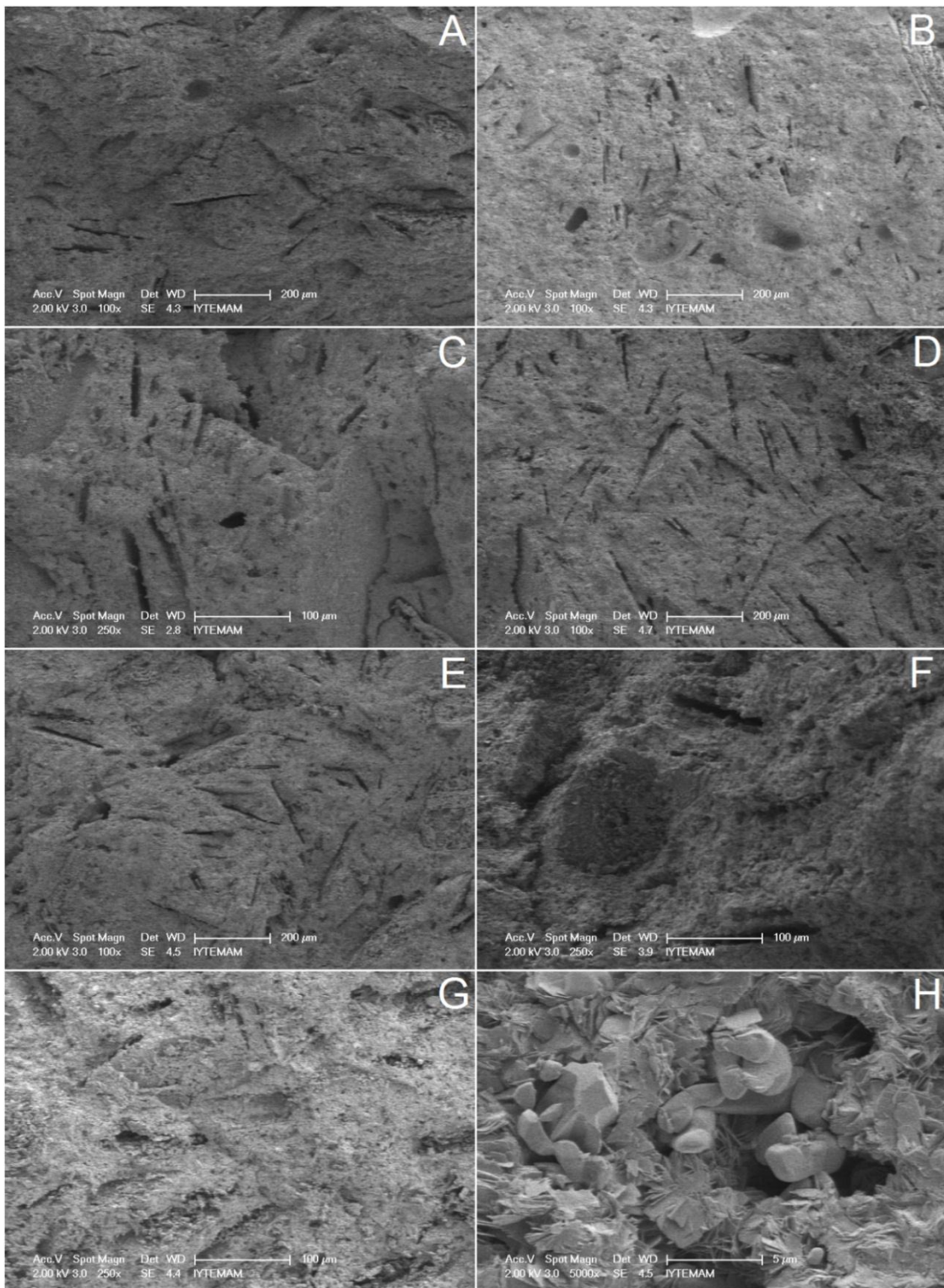


Figure 6.44. (a-g) SEM images of samples prepared with NaCl concentration varying from 0 to 6 M respectively. (h) Morphology of monetite and brushite crystals from sample prepared with 6 M NaCl.

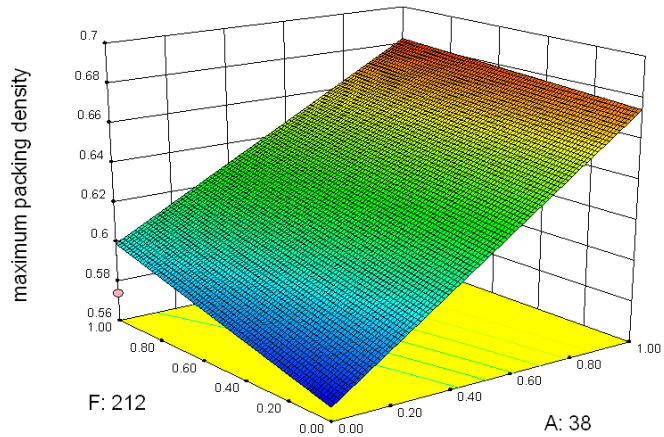


Figure 7.6. Variation of maximum packing density in the binary system.

As seen in the design cube given above, the synergistic effect of three size groups, -38, -53, and -212 further enhances the packing density. This is seen more clearly on the response surface graphs given in Figure 7.7. The left graph shows the synergistic effect of -38 and -212 size groups alone. The second and third show their synergistic effects in the presence of 0.5 and 1.0 parts of -53 micrometer size group. While the maximum packing density in the presence of high -38 and -212 size groups increase with addition of -53 size group, it decrease when the large particle size group amount is low. In other words -53 size group is only effective in increasing the packing density when it is utilized as a filler, not the larger particle.

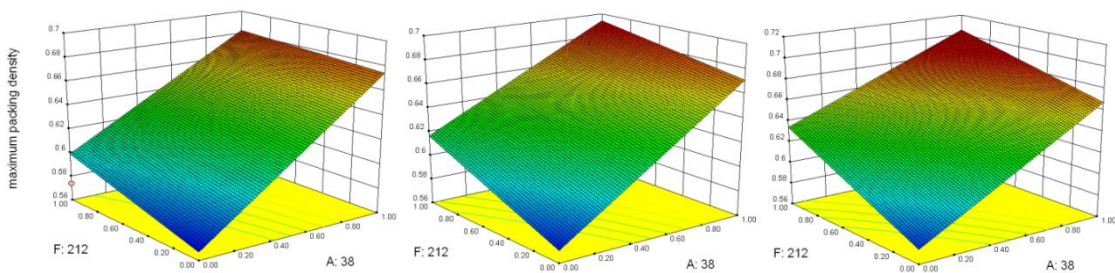


Figure 7.7. Synergistic effect of -53, -38, -212 size groups on the packing density.

A similar relationship is present in the distribution of three size groups, -38, -75 and -212. As seen in Figure 7.8, -75 micrometers group is also more effective as a filler between larger -212 micrometers group and is a better substitute for -38 micrometers group. Such a relationship is not valid for the other two particle size groups -106



and -150 micrometers probably because they are too large to fill the gaps between the largest particles. They are not as effective large particles as the -212 micrometers group and enable only moderate packing even in the presence of maximum particles -38 micrometers.

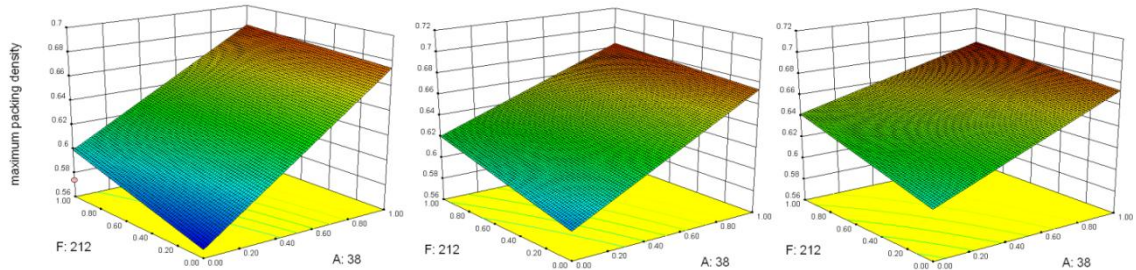


Figure 7.8. Synergistic effect of -75, -38, -212 size groups on the packing density.

Although the two small particle size groups -53 and -75 reinforce the synergistic effect of the large and small particle groups, their combined use alters the packing densities adversely. As seen in Figure 7.9, equal half part additions of both size groups lowers the packing density compared to both the synergistic effect of -38 and -212, and the three component synergistic effects of the individual small size groups given above. This is clearly seen when the middle graph in in Figure 7.9 is compared to the third graphs of Figures 7.7 and 7.8. What's more, packing densities deteriorate considerably when all four particle size groups are added in equal maximum amounts. That means the two small particle size groups, -53 and -75 micrometers should be used only as substitutes, not simultaneously. The synergistic adverse effect of the two small size groups was also revealed by the analysis of variance.

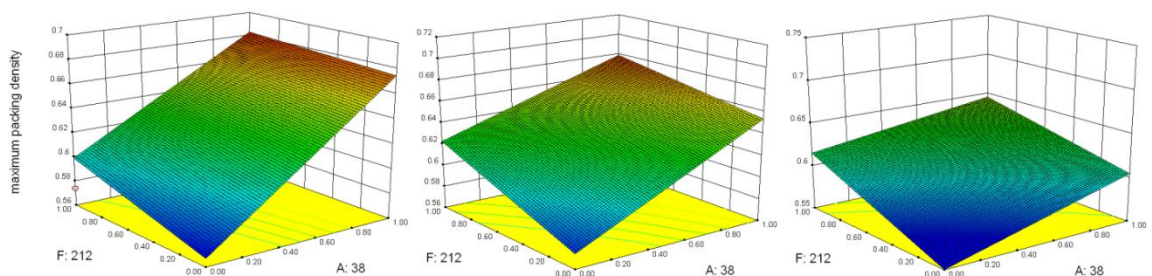


Figure 7.9. Adverse effect of combination of -53 and -75 size groups on packing density.

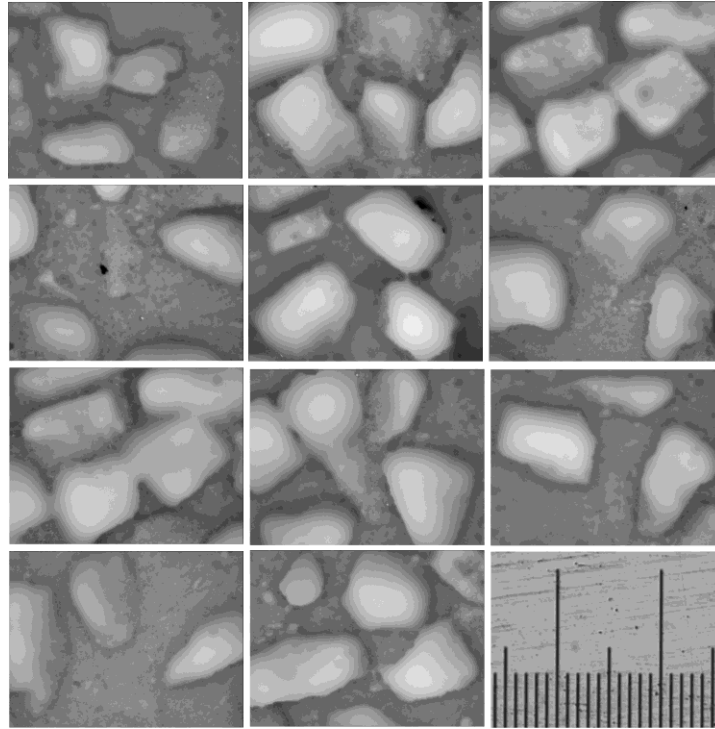


Figure 7.59. Mosaic display of micrographs for sample 16 taken at 100x magnification (scale: 100  $\mu\text{m}$  between two long lines).

Porogens in the size range of 30-150  $\mu\text{m}$  exist in the micrographs given in Fig.7.60. Interconnections mostly occur around the coarser porogens by contacting intermediate porogens. The abundance of coarser porogens indicate wall effect for the fine cement precursor. Fineness of the precursor limited the size of the gaps originating from the wall effect, thereby conserving well packing. Loosening effect between fine, intermediate porogens and finer cement is thought to be responsible for loose packing that result in separation of fine and intermediate porogens. It is seen that porogens in the same size group are closer due to small interaction. Loosening effect is more effective between lower intermediate porogens and the fine cement precursors as loose packing separates the finer porogens more than the coarse porogens. The unstable arrangement of intermediate and fine porogens directs them away toward coarse porogens with low particle interaction in the presence of the hydrodynamic shear stress. In other words porogens group up around the coarser porogens and interconnection is formed easily. These groups or coagulates provide local interconnections as the average coagulate size does not exceed a few hundred microns. Spicer et al. similarly reported a universal flocculation size of around 10 diameters of unisized polymer spheres coagulated in an agitated vessel, regardless of the shear rate (Spicer et al. 1996). Relative numbers of

different size groups are important in the synergistic combination of loosening, wall and coagulation effects. Not an optimum combination but many high interconnectivities should exist in the porogen-cement system with so many size variations in addition to the ultimate variable, the porogen amount. It is certain that a porogen configuration that is well interconnected at low porogen amount, such as sample 7, will have enhanced interconnectivity with increasing porogen amount.

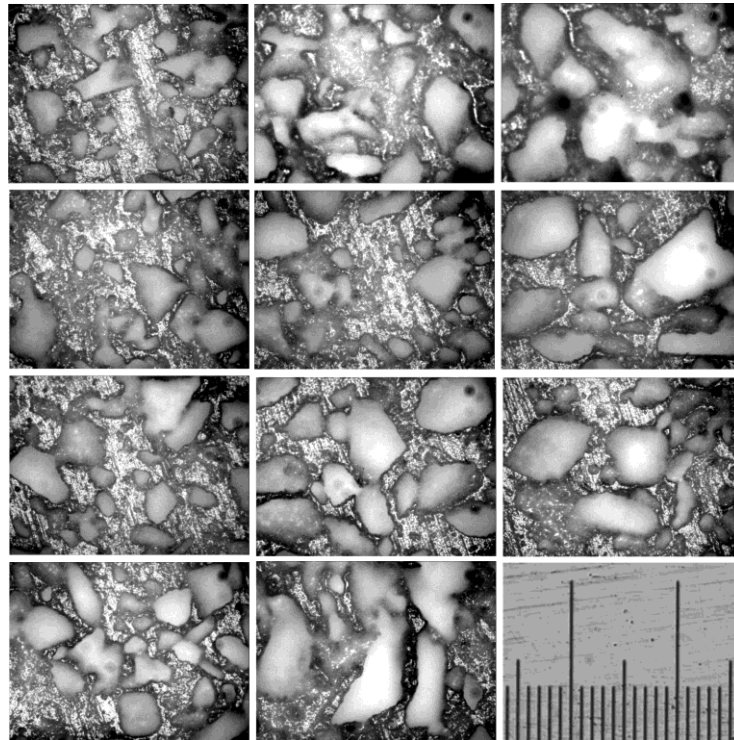


Figure 7.60. Mosaic display of micrographs for sample 7 taken at 100x magnification (scale: 100  $\mu\text{m}$  between two long lines).

One representative micrograph sample that has pore dimensions closest to the mean pore morphological features given in Table A.2, is chosen for the detailed morphological analysis of each sample set. Distributions of size and various other morphological parameters for all pores in the representative micrograph sample are given as well as the micrograph itself and a random higher magnification micrograph showing the details of pore interconnection. A correlation between pore interconnectivity and porogen size distribution is sought based on the data given. A balanced porogen size distribution may not give the highest interconnectivity as equal masses of size groups do not produce comparable number of individual pores. Sequential void filling mechanism between the adjacent size groups or void filling

between non-interacting porogen size groups may be effective as discussed in the detailed morphological analysis results given in the appendix.

Macroporous cement blocks were analyzed by both optical and scanning electron microscopes. SEM images provide information on the crystal structure of the constituent phases while optical micrographs give idea about the porogen configuration and the interconnectivity. High magnification SEM image of sample 2 shows the fine stacked monetite crystals as seen in Figure 7.61. Sample 2 contains 71% monetite, 20% brushite and 9%  $\beta$ -TCP in average. Stacked monetite sheets are seen to deposit over the thicker brushite plates in Figure 7.61. Brushite crystal morphology is seen in a brushite rich region of sample 2 in Figure 7.62. Notice that fine monetite sheets are deposited on the pore walls adjacent to the NaCl crystals before their dissolution.

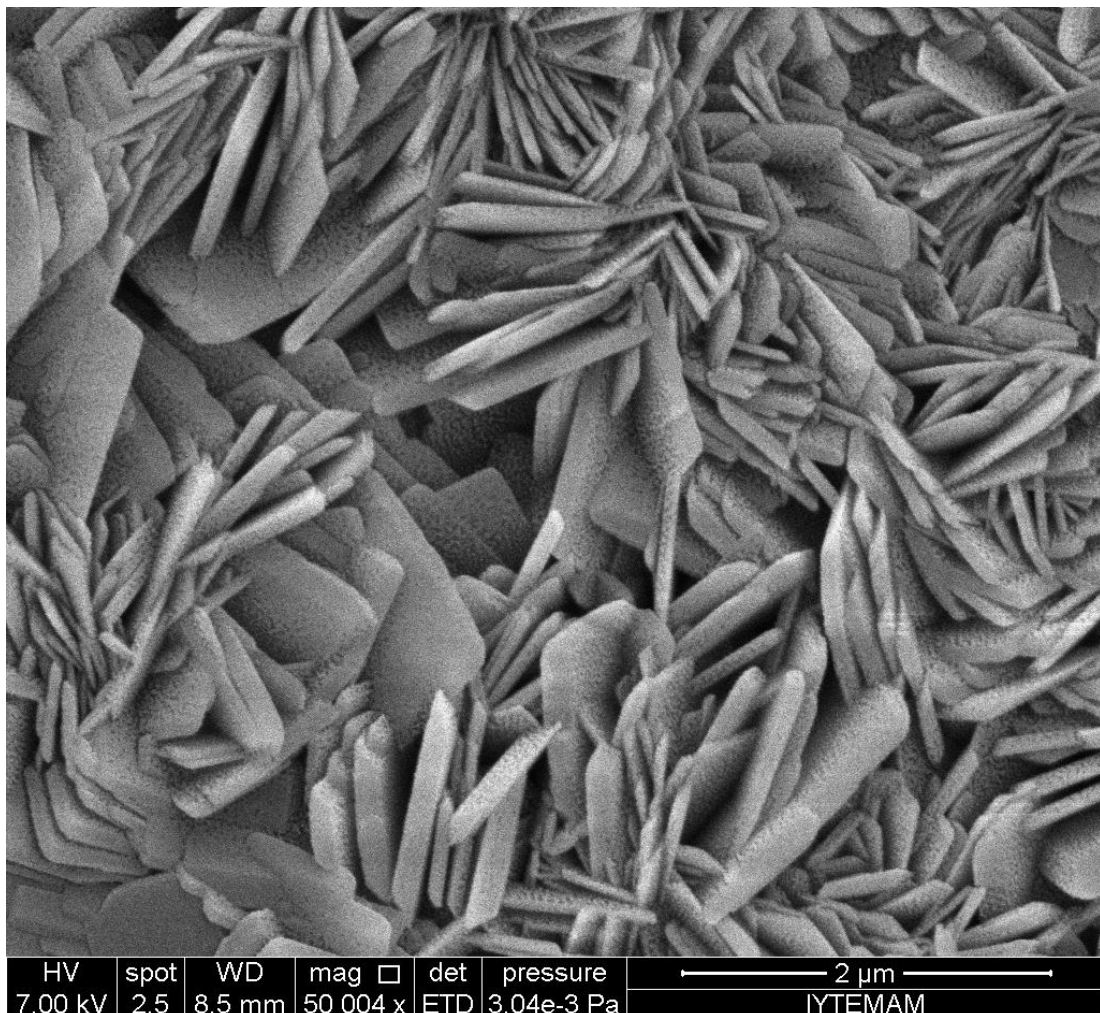


Figure 7.61. Monetite crystals of sample 2 in focus.

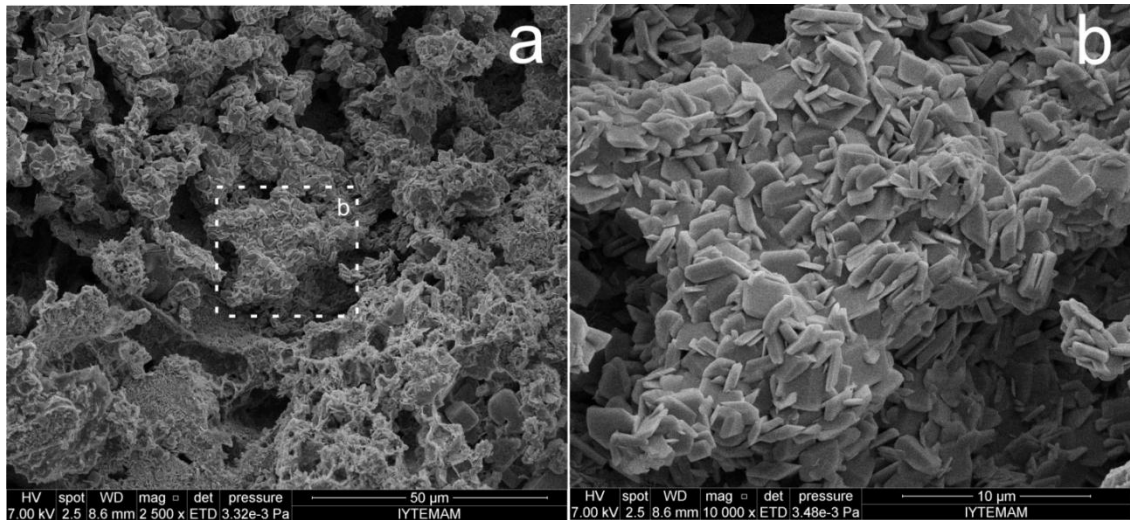


Figure 7.62. Brushite rich region of sample 2

The finer crystal structure of monetite observed in Figure 7.61 in contrast to the more bulky brushite crystal structure seen in Figure 7.62, may result in higher surface area in monetite rich cements. The surface topography of macroporous scaffolds based on monetite rich cement may therefore be more favorable for cellular response and attachment. On the contrary, specific surface area measurements conducted by BET analysis show that increase in brushite content is accompanied generally by an increase in surface area as seen in Figure 7.63. Low variation in the results despite the large number of analyzed samples is assuring that brushite cement has higher surface area than monetite cement. The only objection to the general applicability of this finding is the misleading assumption derived from comparing Figures 7.61 and 7.62 that monetite cement has a finer stacked-sheet structure than brushite. Close examination of samples containing above 80% monetite reveals a different monetite crystal structure especially next to pores created by NaCl crystals. The cellular wall structure is characteristic of monetite rich cements studied that has monetite content higher than 80%. The cellular wall structure may be responsible for the lower surface area of higher monetite containing cements as half of the samples characterized by BET high monetite content.

Sample 1 which on the average has 10% more monetite content than sample 2 exhibits the interesting cellular structure around pore walls as seen in Figure 7.64. Vertical monetite sheets that connect to form polygon cells may have nucleated adjacent to the NaCl crystals before leaching. These cellular regions seem to be entirely consisted of monetite crystals with no brushite and  $\beta$ -TCP in the vicinity. Another sample with the cellular monetite structure around NaCl is sample 11 which has almost

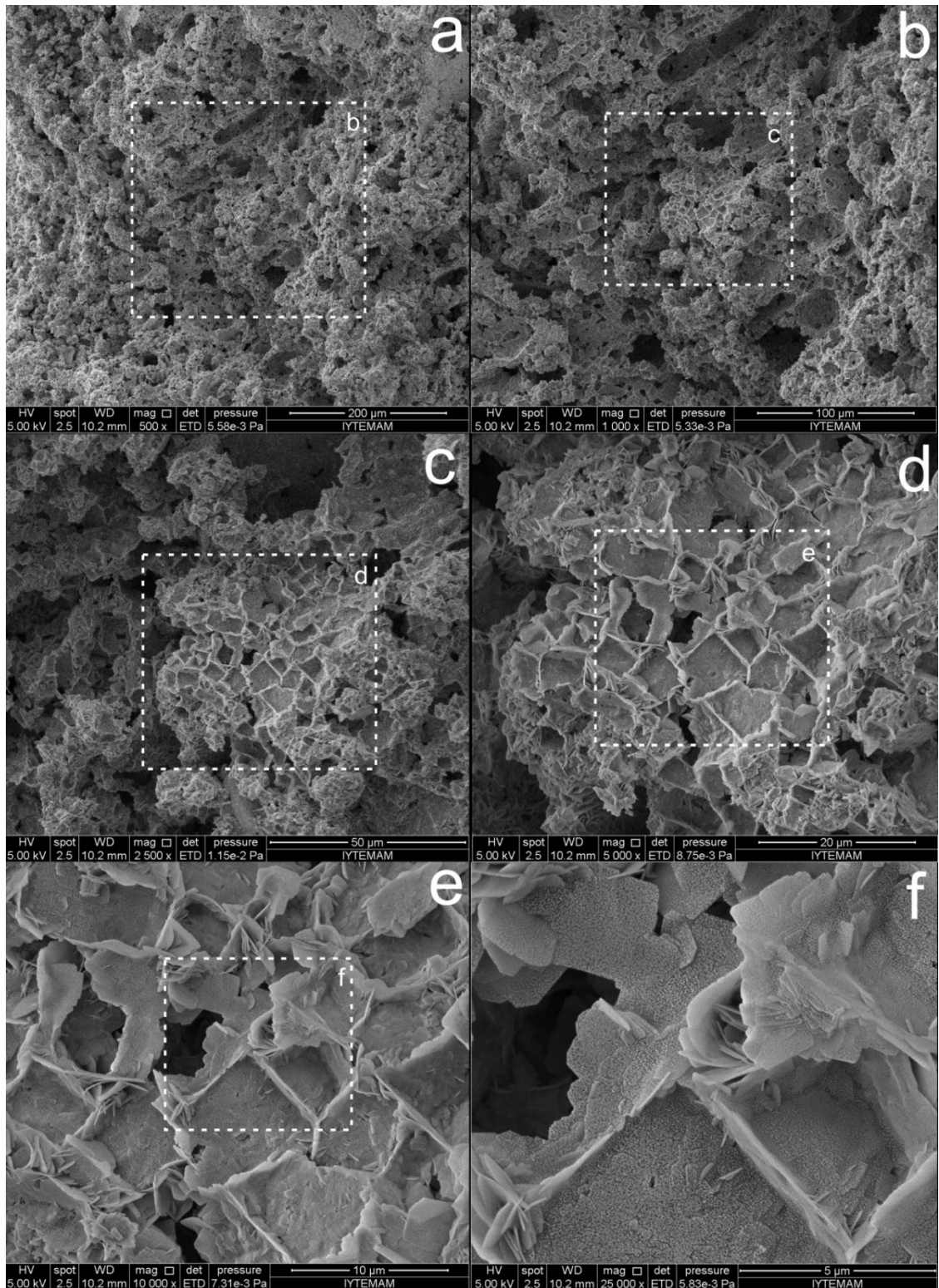


Figure 7.64. Monetite rich region of sample 1 in focus.

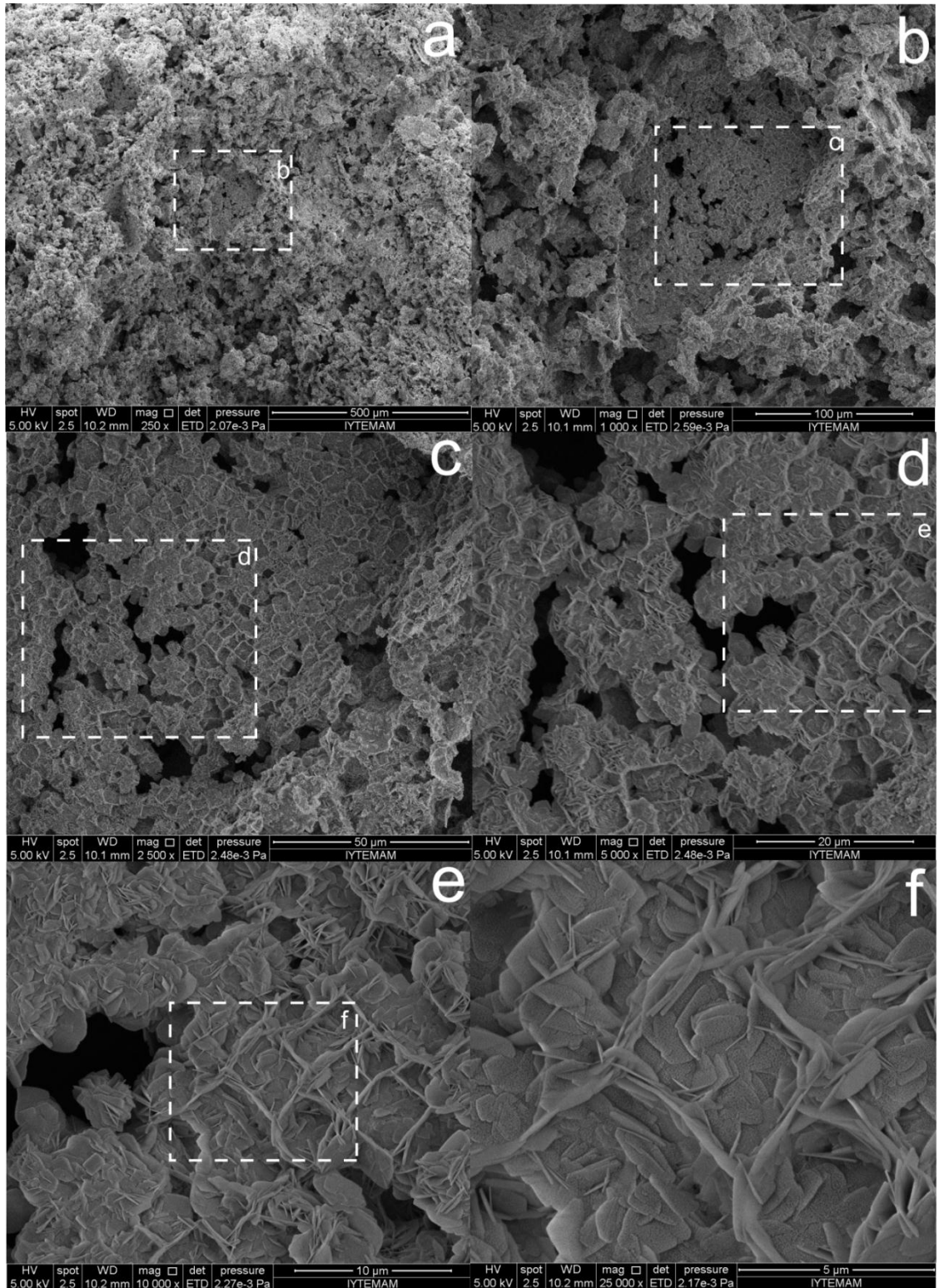


Figure 7.65. Cellular monetite crystals of sample 1 on a pore wall.

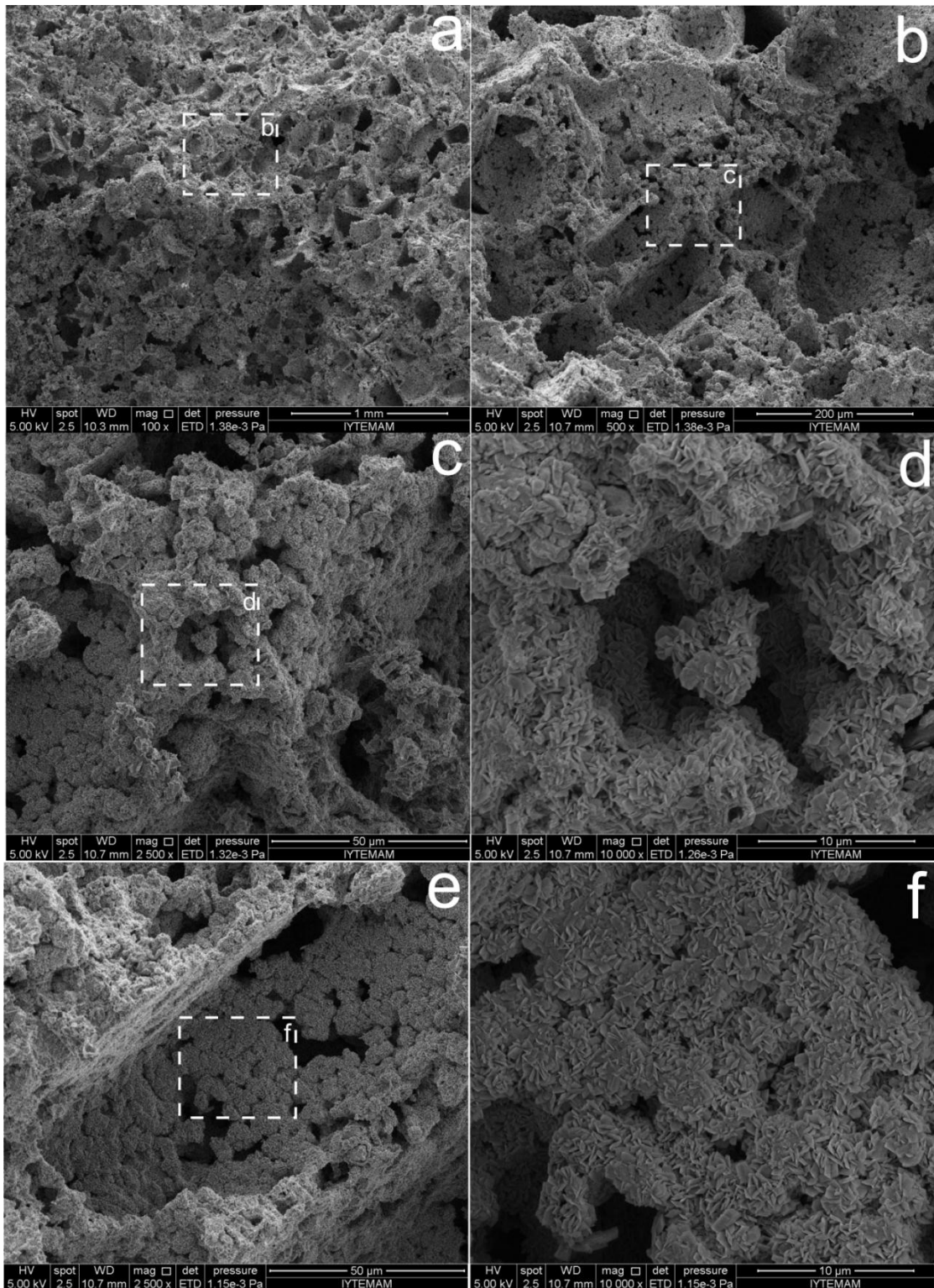


Figure 7.66. Microstructure of sample 37 around macropore walls.



walls seen in Figure 7.71 reveals the characteristic monetite morphology and a few rounded crystals that resemble sintered  $\beta$ -TCP residue.

Table 7.11. Optimum size distribution deduced from the morphological analysis

	-38 $\mu\text{m}$ size group	-53 $\mu\text{m}$ size group	-75 $\mu\text{m}$ size group	-106 $\mu\text{m}$ size group	-150 $\mu\text{m}$ size group	-212 $\mu\text{m}$ size group	Total
Distribution for shortrange interconnection		0.2-0.25g #776398 - 621118	0.6-0.75g #821468 - 657174	0.6-0.75g #290698 - 232558	0.2-0.25g #34200 - 27260		1.6-2g #1538110 - 1922764
Distribution for well packing	0.125- 0.325g #1050420 - 2731092					0.125- 0.325g #6068- 15777	0.25- 0.65g #1056488 - 2746869
Overall Distribution	0.125- 0.325g #1050420 - 2731092	0.2-0.25g #776398 - 621118	0.6-0.75g #821468 - 657174	0.6-0.75g #290698 - 232558	0.2-0.25g #34200 - 27260	0.125- 0.325g 6068 - 15777	2.25g #2979252 - 4284979

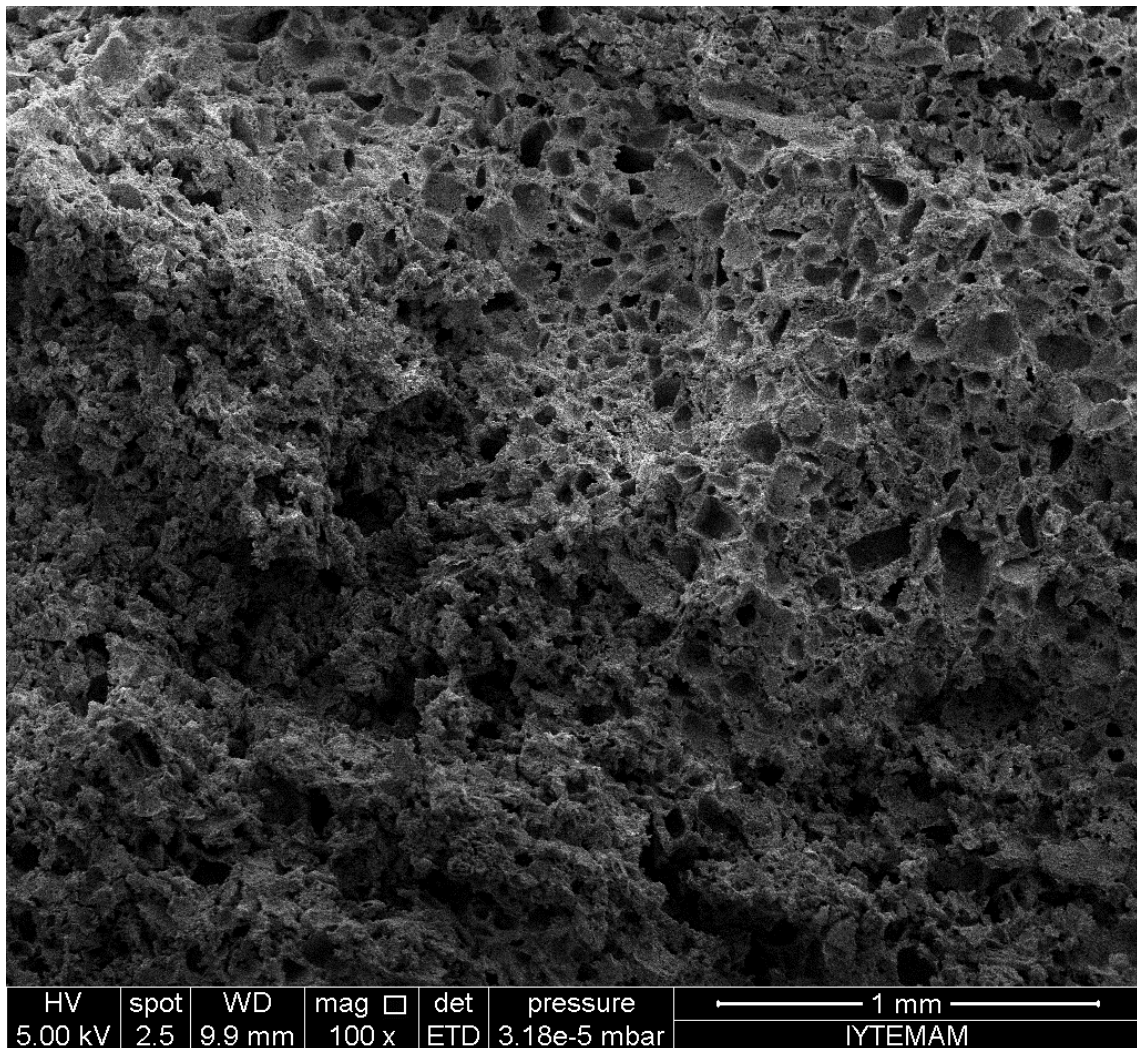


Figure 7.67. SEM image of the microstructure of sample containing 80% porosity at 100 times magnification.

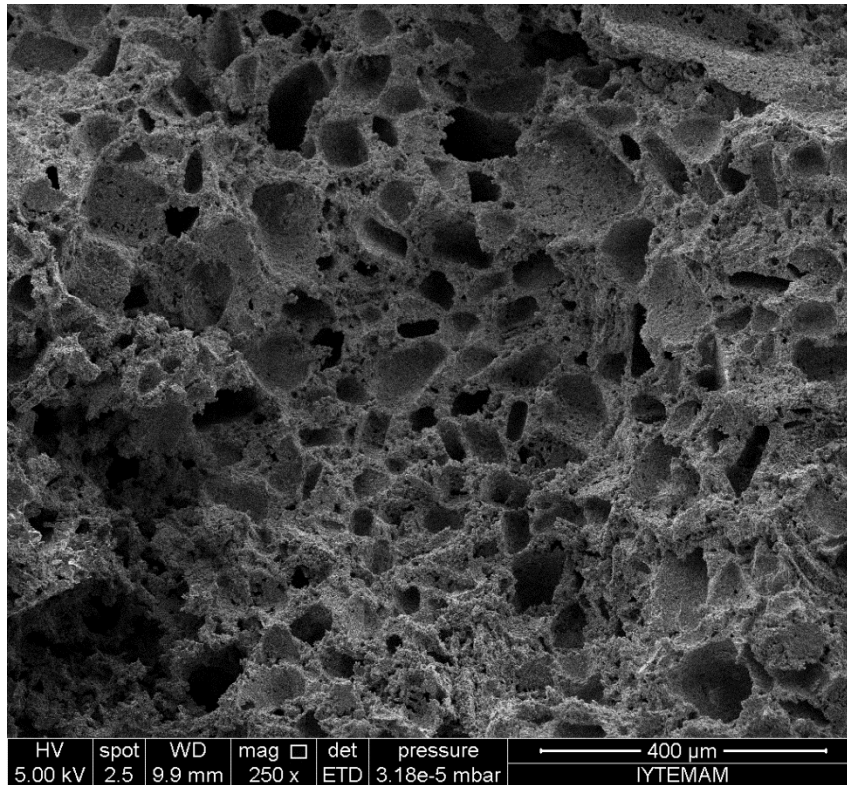


Figure 7.68. SEM image of the microstructure of sample containing 80% porosity at 250 times magnification.

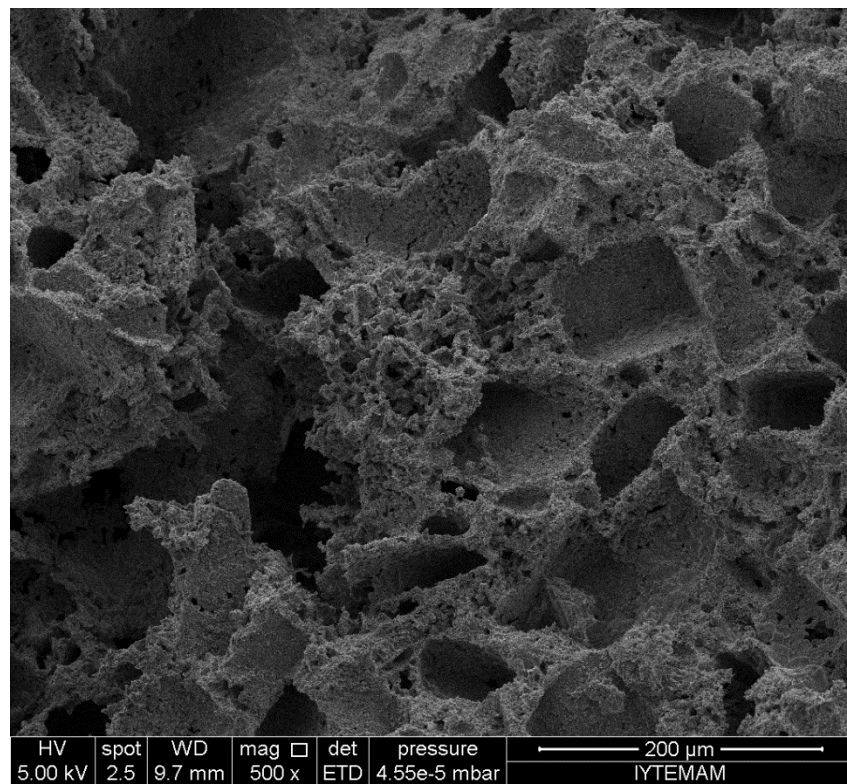


Figure 7.69. SEM image of the microstructure of sample containing 80% porosity at 500 times magnification.

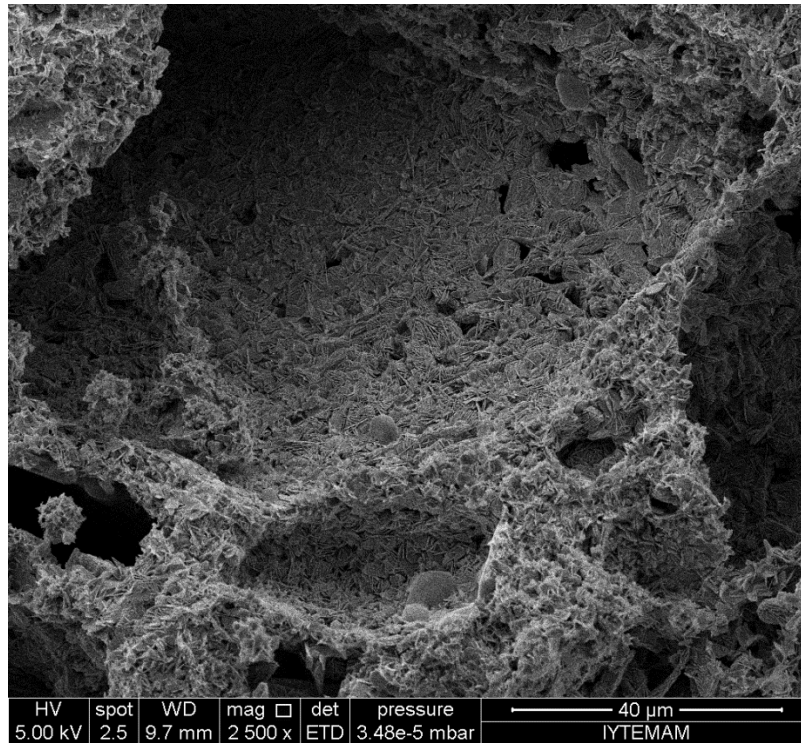


Figure 7.70. SEM image of the microstructure of sample containing 80% porosity at 2500 times magnification.

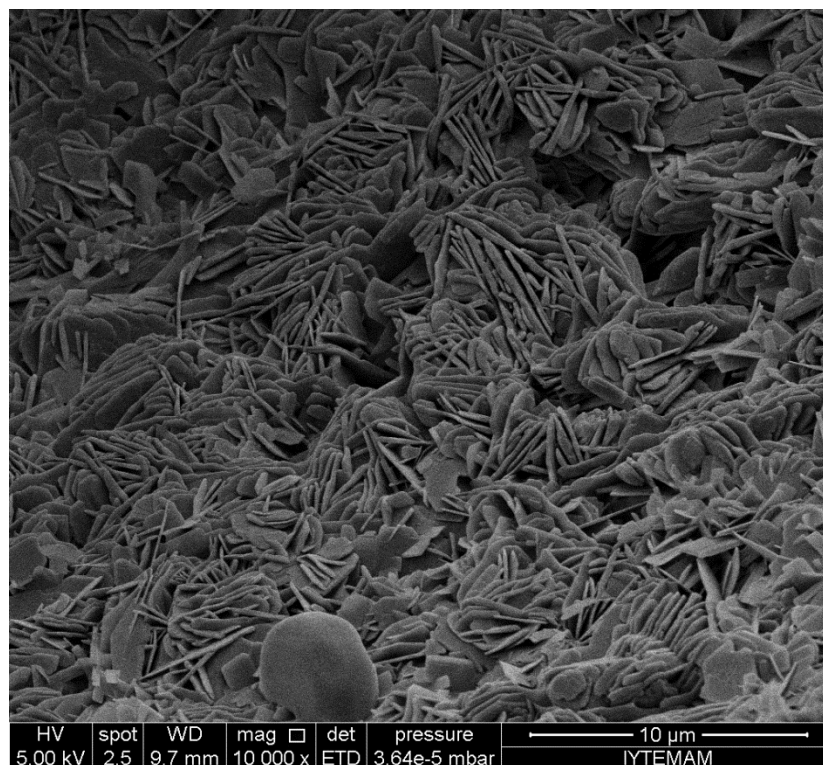


Figure 7.71. SEM image of the microstructure of sample containing 80% porosity at 10000 times magnification.

## VITA

**Name, Surname:** Erdem Şahin

**Date and Place of Birth:** 19.05.1980, Isparta

**Contact:** erdemsahin@yahoo.com, +90542 2612246



### Education:

Degree	Area	Institute	Year
High School	Science	İzmir American Collegiate Institute	1998
BSc Major	Metallurgical & Materials Engineering	Middle East Technical University	2003
MSc	Materials Science & Engineering	İzmir Institute of Technology	2006
PhD	Chemical Engineering	İzmir Institute of Technology	2012

### Academic Work Experience:

Research Assistant, İzmir Institute of Technology, Chemical Engineering 2004-2012

### Scientific Articles Published in International Journals:

1. E. Şahin, F. Y. Mahlicli, S. Yetgin, D. Balköse, "Preparation and characterization of flexible poly(vinyl chloride) foam films", Journal of Applied Polymer Science, Volume 125, Issue 2, 1448-1455, 2012

### Studies Presented at International Conferences and Published in the Proceedings:

1. E. Şahin, M. Çiftçioğlu, "Controlling the phase composition and porosity of brushite cements by ionic modifiers", Proceedings of the 12th International congress of European Ceramic Society, June 19-22, 2011, Stockholm

2. E. Şahin, M. Çiftçioğlu, "Synergistic effect of NaCl and citric acid on brushite cement setting kinetics", Proceedings of the 23rd Symposium and annual meeting of international society for ceramics in medicine, November 6-9, 2011, İstanbul